David Zhou
Elias Greenbaum
Editors

BIOLOGICAL AND MEDICAL PHYSICS, BIOMEDICAL ENGINEERING

Implantable Neural Prostheses 1

Devices and Applications

Springer

BIOLOGICAL AND MEDICAL PHYSICS, BIOMEDICAL ENGINEERING

BIOLOGICAL AND MEDICAL PHYSICS, BIOMEDICAL ENGINEERING

The fields of biological and medical physics and biomedical engineering are broad, multidisciplinary and dynamic. They lie at the crossroads of forntier research in physics, biology, chemistry, and medicine. The Biological & Medical Physics/Biomedical Engineering Series is intended to be comprehensive, covering a broad range of topics important to the study of the physical, chemical and biological sciences. Its goal is to provide scientists and engineers with textbooks, monographs, and reference works to address the growing need for information.

For other volumes in this series, go to:
www.springer.com/series/3740

David D. Zhou
Elias Greenbaum
Editors

Implantable Neural Prostheses 1

Devices and Applications

Springer

Editors
David D. Zhou
Second Sight Medical Products Inc.
12744 San Fernando Road
Sylmar CA 91342
USA
dzhou@2-sight.com

Elias Greenbaum
Oak Ridge National Laboratory
P.O.Box 2008
Oak Ridge TN 37831-6194
USA
greenbaum@ornl.gov

ISBN 978-0-387-77260-8 e-ISBN 978-0-387-77261-5
DOI 10.1007/978-0-387-77261-5
Springer Dordrecht Heidelberg London New York

Library of Congress Control Number: 2009921898

Preface

Significant progress has been made in the development of neural prostheses to restore human functions and improve the quality of human life. Biomedical engineers and neuroscientists around the world are working to improve design and performance of existing devices and to develop novel devices for artificial vision, artificial limbs, and brain–machine interfaces.

This book, *Implantable Neural Prostheses 1: Devices and Applications*, is part one of a two-book series and describes state-of-the-art advances in techniques associated with implantable neural prosthetic devices and their applications. Devices covered include sensory prosthetic devices, such as visual implants, cochlear implants, auditory midbrain implants, and spinal cord stimulators. Motor prosthetic devices, such as deep brain stimulators, Bion microstimulators, the brain control and sensing interface, and cardiac electro-stimulation devices are also included. Progress in magnetic stimulation that may offer a non-invasive approach to prosthetic devices is introduced. Regulatory approval of implantable medical devices in the United States and Europe is also discussed.

Advances in biomedical engineering, micro-fabrication technology, and neuroscience have led to many improved medical device designs and novel functions. However, many challenges remain. This book focuses on the device designs and technical challenges of medical implants from an engineering perspective. We are grateful to leading researchers from academic institutes as well as design engineers and professionals from the medical device industry who have contributed to the book. Part two of this series will cover techniques, engineering approaches, and R&D advances in developing implantable neural prosthetic devices. We hope a better understanding of design issues and challenges may encourage innovation and interdisciplinary efforts to push forward the frontiers of R&D of implantable neural prostheses.

Los Angeles, California — David D. Zhou
Oak Ridge, Tennessee — Elias Greenbaum

Contents

Contributors

Eric Basham Department of Electrical Engineering, University of California, Santa Cruz, CA 95064, USA, basham.eric@gmail.com

Kerry Bradley Boston Scientific Neuromodulation Corporation, 25155 Rye Canyon Loop, Valencia, CA 91355, USA, kerry.bradley@bsci.com

Rafael Carbunaru Boston Scientific Neuromodulation Corporation, 25155 Rye Canyon Loop, Valencia, CA 91355, USA, rafael.carbunaru@bsci.com

Xinyu Chai Institute for Laser Medicine and Biophotonics, Department of Biomedical Engineering, Shanghai Jiao Tong University, Shanghai 200240, China, xychai@sjtu.edu.cn

Mike Colvin Boston Scientific Neuromodulation Corporation, 25155 Rye Canyon Loop, Valencia, CA 91355, USA, michael.colvin@bsci.com

Haihong Feng The Institute of Acoustics, Academia Sinica, Beijing 100190, China, fenghaihong@263.net

Robert J. Greenberg Second Sight Medical Products, Inc., Sylmar Biomedical Park, 12744 San Fernando Road, Sylmar, CA 91342, USA, robert.greenberg@2-sight.com

Martin Han Neural Engineering Program, Huntington Medical Research Institutes, 734 Fairmount Ave. Pasadena, CA 91105, USA, martinhan@hmri.org

William V. Harrison Silere Medical Technology, Inc., Kirkland, WA 98034, USA, vanbrooks@gmail.com

Kristen N. Jaax Boston Scientific Neuromodulation Corporation, 25155 Rye Canyon Loop, Valencia, CA 91355, USA, kristen.jaax@bsci.com

Dongchul C. Lee Boston Scientific Neuromodulation Corporation, 25155 Rye Canyon Loop, Valencia, CA 91355, USA, dongchul.lee@bsci.com

Minoo Lenarz Otorhinolaryngology Department, Hannover Medical University, Hannover 30625, Germany, lenarz.minoo@mh-hannover.de

Thomas Lenarz Otorhinolaryngology Department, Hannover Medical University, Hannover 30625, Germany, lenarz.thomas@mh-hannover.de

Liming Li Institute for Laser Medicine and Biophotonics, Department of Biomedical Engineering, Shanghai Jiao Tong University, Shanghai 200240, China, lilm@sjtu.edu.cn

Xiaoxin Li Eye Center, Peking University People's Hospital, Beijing 100044, China, drlixiaoxin@vip.sina.com

Hubert H. Lim Department of Biomedical Engineering, University of Minnesota, 7-105 Hasselmo Hall, 312 Church St SE, Minneapolis, MN 55455, USA; Otorhinolaryngology Department, Hannover Medical University, Hannover, Germany, hlim@umn.edu

Wentai Liu Department of Electrical Engineering, University of California, Santa Cruz, CA 95064 USA; Nat'l Chiao Tung University, Taiwan, wentai@soe.ucsc.edu

Douglas B. McCreery Neural Engineering Program, Huntington Medical Research Institutes, 734 Fairmount Ave, Pasadena, CA 91105, USA, dougmc@hmri.org

Rick McVenes Leads Research, Cardiac Rhythm Disease Management Division, Medtronic, Inc., MVC 52, 8200 Coral Sea St. NE, Mounds View, MN 55112, USA, rick.mcvenes@medtronic.com

Michael A. Moffitt Boston Scientific Neuromodulation Corporation, 25155 Rye Canyon Loop, Valencia, CA 91355, USA, michael.moffitt@bsci.com

Stephen Rebscher Department of Otolaryngology-Head and Neck Surgery, University of California, San Francisco, San Francisco, CA 94143, USA, srebscher@ohns.ucsf.edu

Qiushi Ren Institute for Laser Medicine and Biophotonics, Department of Biomedical Engineering, Shanghai Jiao Tong University, Shanghai 200240, China, renqsh@sjtu.edu.cn

Joseph H. Schulman Mann Medical Research Organization, 25155 Rye Canyon Loop Valencia, CA, USA, joes@mannfbe.org

Ken Stokes Brady Leads Research, Cardiac Rhythm Disease Management Division, Medtronic, Inc., 11052 Robinwood Lane, Brainerd, MN 56401, USA, kbstokes@mlecwb.net

Natalia Tchemodanov Department of Electrical Engineering, University of California, Santa Cruz, CA 95064, USA, ntchemod@gmail.com

Xiaohong Sui, Institute for Laser Medicine and Biophotonics, Department of Biomedical Engineering, Shanghai Jiao Tong University, Shanghai 200240, China, suixhong@sjtu.edu.cn

Xiaoan Sun Nurotron Biotechnology Inc., Irvine, CA 92618, USA, xsun@nurotron.com

Xiaodong Sun Department of Ophthalmology, Shanghai First People's Hospital, Shanghai 200080, China, sun_xiaodong@hotmail.com

Zhi Yang, Department of Electrical Engineering, University of California, Santa Cruz, CA 95064 USA, yangzhi@soe.ucsc.edu

Todd K. Whitehurst Boston Scientific Neuromodulation Corporation, 25155 Rye Canyon Loop, Valencia, CA 91355, USA, todd.whitehurst@bsci.com

Kaijie Wu Institute for Laser Medicine and Biophotonics, Department of Biomedical Engineering, Shanghai Jiao Tong University, Shanghai 200240, China, kaijiewu@sjtu.edu.cn

Xun Xu Department of Ophthalmology, Shanghai First People's Hospital, Shanghai 200080, China, drxuxun@sjtu.edu.cn

Fan-Gang Zeng Departments of Anatomy and Neurobiology, Biomedical Engineering, Cognitive Sciences and Otolaryngology – Head and Neck Surgery, University of California, Irvine, 364 Med Surg II, Irvine, CA 92697, USA, fzeng@uci.edu

Chuanqing Zhou Institute for Laser Medicine and Biophotonics, Department of Biomedical Engineering, Shanghai Jiao Tong University, Shanghai 200240, China, zhoucq@sjtu.edu.cn

David D. Zhou Second Sight Medical Products, Inc., Sylmar Biomedical Park, 12744 San Fernando Road, Sylmar, CA 91342, USA, dzhou@2-sight.com

List of Acronyms

A1	Primary auditory cortex
ABI	Auditory brainstem implant
ACI	Auditory cortex implant
AF	Activating function
AF	Atrial fibrillation
AIROF	Activated iridium oxide film
AMD	Age-related macular degeneration
AMI	Auditory midbrain implant
ANI	Auditory nerve implant
ASIC	Application specific integrated circuit
AV	Atrioventricular
BBS	Bicarbonate buffered saline
BCI	Brain–machine interface
BJT	Bipolar junction transistor
BON	Bed of nails
CCD	Charge coupled device
CFR	Code of federal regulations
CHF	Congestive heart failure
CI	Cochlear implant
CIS	Continuous-interleaved-sampling
CL	Current level
CMOS	Complementary metal-oxide semiconductor
CRT	Cardiac resynchronization therapy
CS	Coronary sinus
CSF	Cerebrospinal fluid
CSP	Chip-size packages
cTMS	Controllable pulse-width TMS
CV	Cyclic voltammetry
DAC	Digital analog converter
DBS	Deep brain stimulation
DRIE	Deep reactive ion etching
DRth	Excitable dorsal root
DSP	Digital signal processor

EEP	Electrically evoked potential
EIROF	Electroplated iridium oxide film
EIS	Electrochemical impedance spectroscopy
EMI	Electromagnetic interference
ERG	Electroretinograms
ESC	Environmental stress cracking
EtO	Ethylene oxide
FBC	Field balancing and cycling
FDA	Food and Drug Administration
FEM	Finite element method
FES	Functional electrical stimulation
FMEA	Failure modes & effects analysis
FMS	Functional magnetic stimulation
FOA	Focus of attention
FRCB	Frequency-related conduction block
FS	Field steering
GABA	Gamma-aminobutyric acid
GCL	Ganglion cell layer
GERD	Gastroesophageal reflux disease
GPi	Globus pallidus internus
HDE	Humanitarian device exemption
HMD	Head-mounted display
HUD	Humanitarian use device
IC	Inferior colliculus
ICC	Its central nucleus
ICD	Implantable cardioverter defibrillators
ICP	Inductively-coupled plasma
IDE	Investigational device exemption
IGBT	Insulated gate bipolar transistor
ILM	Internal limiting membrane
INL	Inner nuclear layer
IPG	Implantable pulse generator
IPL	Inner plexiform layer
IR	Infrared
IRB	Institutional review board
IR drop	Voltage drop across a resistance - current (I) x resistance (R)
IrOx	Iridium oxide
LCR	Inductance capacitance resistance
LES	Lower esophageal sphincter
LGN	Lateral geniculate nucleus
LiI	Lithium iodide
LPCVD	Low-pressure chemical vapor deposition
MEA	Microelectrode arrays
MEMS	Micro-electro-mechanical system

MIDAS	Migraine disability assessment
MIO	Metal ion oxidation
MPTP	1-methyl-4-phenyl-1, 2, 3, 6-tetrahydropyridine
NF2	Neurofibromatosis type 2
NFL	Nerve fiber layer
NRT	Neural response telemetry
OCT	Optical coherence tomography
OLM	Outer limiting membrane
ONL	Outer nuclear layer
OPL	Outer plexiform layer
PCU	Prosthetic control unit
PBS	Phosphate-buffered saline
PD	Parkinson's disease
PDCA	Plan-do-check-act
PDMS	Polydimethylsiloxane
PECVD	Plasma-enhanced chemical vapor deposition
PGC	Programmable gain control
PMA	Premarket approval
PSA	Pacing system analyzer
PSD	Power spectral density
PU	Pressure ulcer
PW	Pulse width
RF	Radio frequency
RMS	Root mean square
RP	Retinitis pigmentosa
RPE	Retinal pigment epithelium
rTMS	Repetitive TMS
SBON	Slanted bed of nails electrode
SC	Superior colliculus
SCR	Silicon controller rectifier
SCS	Spinal cord stimulation
SD	Standard deviation
SDRAM	Synchronous dynamic random access memory
Si_3N_4	Silicon nitride
SiC	Silicon carbide
SiO_2	Silicon dioxide
SNR	Signal-to-noise ratio
SIROF	Sputtered iridium oxide film
SOI	Silicon-on-insulator
STN	Subthalamic nucleus
SVO	Silver vanadium oxide
Ta_2O_5	Tantalum pentoxide
T cell	Transmission cell
TDMA	Time domain multiplexed access

TiN	Titanium nitride
TMS	Transcranial magnetic stimulation
TTS	Transverse tripolar system
V1	Visual cortex
VEP	Visual evoked potentials
UF	Urgency frequency syndrome
UNCD	Ultrananocrystalline diamond
UUI	Urinary urge incontinence
VF	Ventricular fibrillation
VLSI	Very large-scale integrated circuit

Microelectronic Visual Prostheses

David D. Zhou and Robert J. Greenberg

Abstract Research efforts worldwide are developing microelectronic visual prostheses aimed at restoring vision for the blind. Various visual prostheses using neural stimulation techniques targeting different locations along the visual pathway are being pursued. Retinal prostheses have proved to be capable of offering blind subjects in advanced stages of outer retinal diseases the opportunity to regain some visual function. With relatively low-density retinal implants, simple visual tasks that are impossible with the blind subject's natural light perception vision can be accomplished. Blind subjects can spatially resolve individual electrodes within the array of the implanted retinal prosthesis and can use the system to discriminate and identify oriented patterns. This chapter reviews progress in the development of visual prostheses including visual cortex and optic nerve stimulation devices and retina stimulation devices such as epiretinal, subretinal, and extraocular implants. Second Sight Argus 16 and Argus II 60-electrode Retinal Implants are described. Some engineering challenges for the development of visual prostheses, especially retinal prostheses, are discussed.

1 Introduction

Blindness has a devastating impact on people's quality of life and economy. In 1997 the US Census Bureau reported that about 8 million individuals over the age of 15 had difficulty seeing and of those, 1.8 million were unable to read [1]. Hereditary retinal degenerative diseases, such as retinitis pigmentosa (RP) and age-related macular degeneration (AMD), are among the more frequent causes of blindness through photoreceptor loss. In the United States, retinal blindness alone costs $4 billion annually in lost benefits and taxable income to the government. RP has an incidence rate of approximately 1 in 4000 births, and

D.D. Zhou (✉)
Second Sight Medical Products, Inc., Sylmar Biomedical Park, Sylmar, CA 91342, USA
e-mail: dzhou@2-sight.com

D.D. Zhou, E. Greenbaum (eds.), *Implantable Neural Prostheses 1*,
Biological and Medical Physics, Biomedical Engineering,
DOI 10.1007/978-0-387-77261-5_1,

therefore affects more than 100,000 people in the United States [2]. It is projected that the incidence for AMD among people aged over 65 may be as high as 5.5% in 10 years [3, 4].

Inspired by the success of cochlear implants, which restore hearing for the deaf, research efforts worldwide are developing microelectronic visual prostheses (visual implants) aimed at restoring vision for the blind [5–10]. Many recent developments from research teams to industrial groups working on visual prostheses have raised hopes for the possibility of creating retinal implants and other strategies for restoring vision in blind subjects. In particular, a retinal prosthesis has the potential to provide increased vision to some subjects who are blind from degeneration of the outer retina. In fact, there is theoretical and some experimental clinical evidence that suggests that direct electrical stimulation of the retina might be able to provide some vision to subjects who have lost the photoreceptive elements of their retinas.

This chapter will review the progress of the development of visual prostheses, especially in retinal implants. Some technical challenges will be discussed.

2 Biomedical Engineering Approaches for Restoring Vision to the Blind

2.1 Visual Pathway

The visual pathway consists mainly of the eye, optic nerve, lateral geniculate nucleus (LGN), and visual cortex (also known as striate cortex or V1) (Fig. 1). When the light reaches the retina through the cornea and the pupil, photoreceptors on the outer boundary layer of the retina membrane convert photons into electrical neural signals. These signals are processed by cells in the retina structure and are sent to the brain along the optic nerves. Optic nerves send

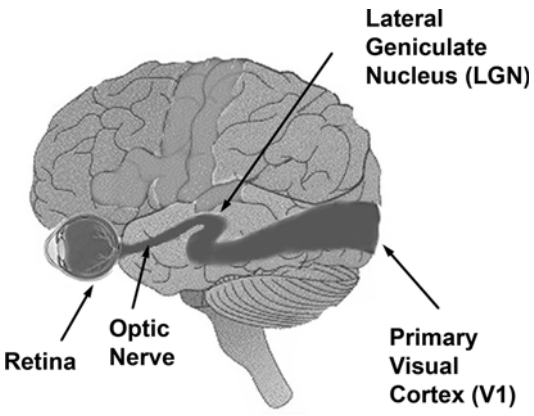

Fig. 1 Visual pathway

neural signals to the visual cortex of the brain via the LGN, a relay station deep in the brain hemisphere. Blindness can result from diseases or injuries to any part of this visual pathway. For example, glaucoma may cause damage to the optic nerve due to excessively high intraocular pressure, while stroke, brain tumor, and head trauma may cause damage to the visual cortex.

2.2 Eye and the Retina

The eyeball is slightly ellipsoidal and has a volume of about 10 cm^3 in an adult 18–30 years of age [11]. The axial length is approximately 24 mm from the cornea to the retina. The space inside the eye has a volume of about 4–6.5 ml and is filled with clear vitreous humor. The vitreous is a gel that consists of collagen fibers that are separated and stabilized by hyaluronic acid [12]. Approximately 98% of this gel is water; diffusion of low molecular-weight solutes such as inorganic ions, glucose, and amino acids is unimpeded through the vitreous.

Table 1 lists the concentrations of some chemicals in the vitreous humor [13]. Oxygen is largely supplied by the atmosphere. The major substrate for respiration in the retina is glucose. Most of the glucose (~70%) utilized by the retina is converted to lactate. Glutamate, one of many neuro-active amino acids, has been found in higher concentration within the retina. The glutamate is actively metabolized by normal retina tissue. Vitrectomy and subsequent vitreous fluid exchange alter chemical and physical properties of the vitreous. A study by Manzanas et al. [14] indicated that changes in proteins, lactic acids, and ascorbic acids return to normal after 7 days.

Table 1 The concentrations of some chemicals in the vitreous humor [13] in comparison to those in plasma

Chemicals	In plasma	In vitreous
Na^+	146 μM	144 μM
Cl^-	109 μM	114 μM
K^+	–	7.7 μM
HCO_3^-	28 μM	20–30 μM
Ascorbate	0.04 mM	2.21 mM
Lactate	10.3 mM	7.78 mM
Glucose	6 mM	3.44 mM
Hyaluronate	–	32–240 μg/ml
Collagen	–	286 μg/ml
L-Glutamate	–	~0.1–10 μM

The human retina that lines the back of the eye is approximately 250 μm thick and resembles a thin single ply wet tissue paper in strength. The thinnest part of the retina, about 150 μm, is at the center of the fovea, while the thickest part of the retina at the fovea rim is about 400 μm. The human retina is a delicate multilayered organization of neurons, cells, and nourishing blood vessels (Fig. 3) [15]. The retina is organized both vertically and horizontally.

Fig. 2 The human eye

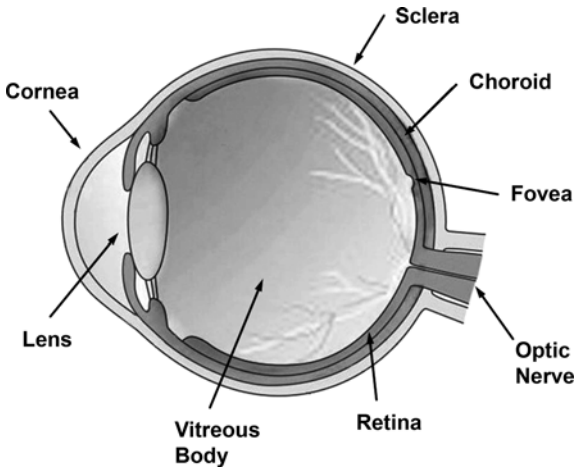

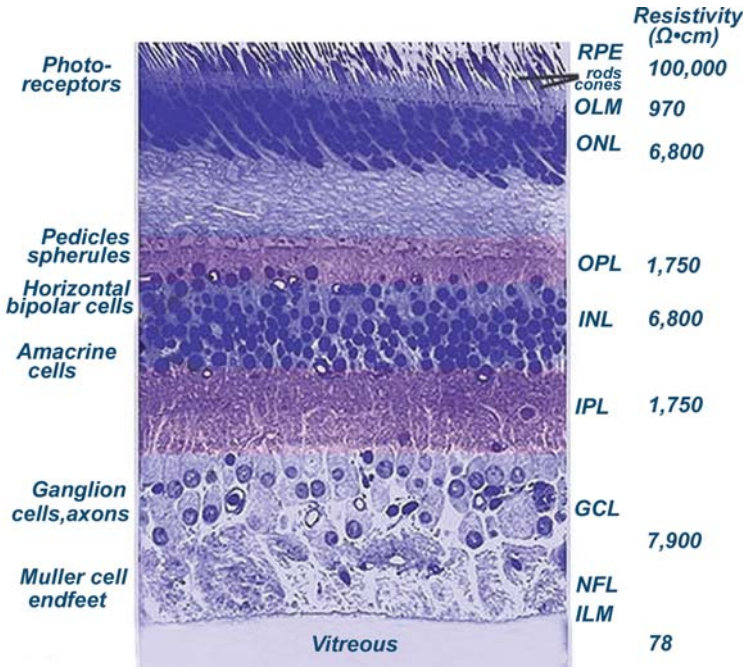

Fig. 3 The human retina layered structure and retinal neural cells. From *top* to *bottom*, the retina layers are: RPE, the retinal pigment epithelium, rod and cone layer; OLM, outer limiting membrane; ONL, outer nuclear layer; OPL, outer plexiform layer; INL, inner nuclear layer; IPL, inner plexiform layer; GCL, ganglion cell layer; NFL, nerve fiber layer; and ILM, internal limiting membrane (image adapted from Ref. [15] with permission). Listed on the right side are the resistivities of different retinal layers [17]

The vertically oriented cells are photoreceptors of rods and cones, the bipolar cells and the ganglion cells. The horizontally oriented cells are the horizontal cells and the amacrine cells.

A circular field of approximately 5–6 mm around the fovea is considered the central retina, and it is thicker than the peripheral retina due to increased packing density of photoreceptors. This central retina area is a preferred site for a retinal implant.

Vitreous has resistivity similar to saline (60–80 $\Omega \cdot$cm). However, the layered retina has much higher impedance than vitreous [16]. Estimated conductivity data from multiple sources and unpublished data are listed in Fig. 3 [16, 17]. Each layer in the retina has different resistivity. In particular, the retina pigment epithelium, the nuclear layers and the ganglion cell layer have been found to have higher resistivity than other parts of the retina.

2.3 Candidate Retina Diseases for the Retinal Implants

Retinitis pigmentosa (RP) and age-related macular degeneration (AMD) are two likely candidate diseases from retinal blindness that a retinal implant may help. For RP, the progression of the disease is generally slow, but the eventual impact on vision and quality of life is often devastating. For example, patients afflicted with RP for 25 years are usually left with a visual field of 10° or less (i.e., legally blind). As the disease progresses and further photoreceptor loss occurs, even this constricted field may be lost. Unfortunately, many of the people who have RP tragically lose their vision before the age of 40. Figure 4 shows a fundus photo of human retina with retinitis pigmentosa. The gradual onset and the relatively late age at which most RP and AMD patients become legally blind adds to personal and familial difficulties in adjusting to being blind [18, 19]. As lifespan increases within the United States and other counties, these degenerative diseases will affect a growing number of patients.

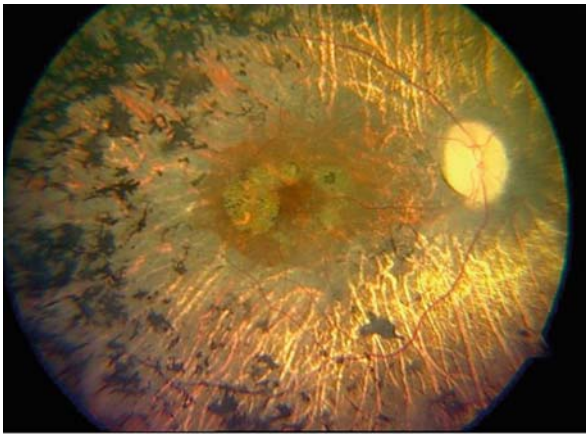

Fig. 4 Fundus photo of a human retina with retinitis pigmentosa

Macular degeneration results in legal blindness. In practical terms, this means vision of less than 20/200 or visual loss which results in the inability to watch TV, recognize faces, drive, or read. AMD is expected to become the single leading cause of legal blindness. Although some treatments to slow the progression of AMD are available, no treatment exists that can replace the function of lost photoreceptors [20].

2.4 Biomedical Engineering Approaches for Visual Implants

The possibility to restore vision in blind subjects using electricity began with the discovery that an electric charge delivered to a blind eye produces a sensation of light. This discovery was made by LeRoy in 1755 [21]. LeRoy passed the discharge of a Leyden jar through the orbit of a man who was blind from cataract and the subject saw "flames passing rapidly downwards". However, it was not until 1966 that the first human experiments in this field began with Brindley and Lewin's experiments on electrical stimulation of visual cortex [22]. While cortical stimulation approaches have made progress, it has been hampered by the complexity of the physiology [5]. The processing that has occurred by the time the neural signals have reached the cortex is greater than the more distal sites such as the retina. This results in more complex phosphenes being perceived by the blind subjects. Cortical prostheses provide additional risks such as intracranial hemorrhage and infection to a blind subject who has an otherwise normal brain. These factors and the lack of availability of implantable electronics have limited the clinical application of these devices.

The limitations of the cortical approach encouraged several groups worldwide over the past 20 years to explore the possibility of producing vision in patients with an intact optic nerve and damaged photoreceptors by stimulating the retina, the optic nerve, and recently the LGN [23–25]. Worldwide efforts to develop various microelectronic visual implants and to investigate various aspects of visual stimulations are increasing in recent years. Figure 5 shows some research teams and industrial groups in the United States, Europe, Asia, and Australia pursuing different approaches to restore vision in the blind.

3 Microelectronic Visual Implant Technologies

Depending on the location of stimulating electrodes, visual prostheses can be divided into three groups: retinal, optic nerve, and visual cortex (V1) including LGN devices. In retinal devices, three approaches are pursued and there are intraocular devices for epiretinal and subretinal stimulations and extraocular devices for transretinal stimulation. Retina stimulation differs from optic nerve

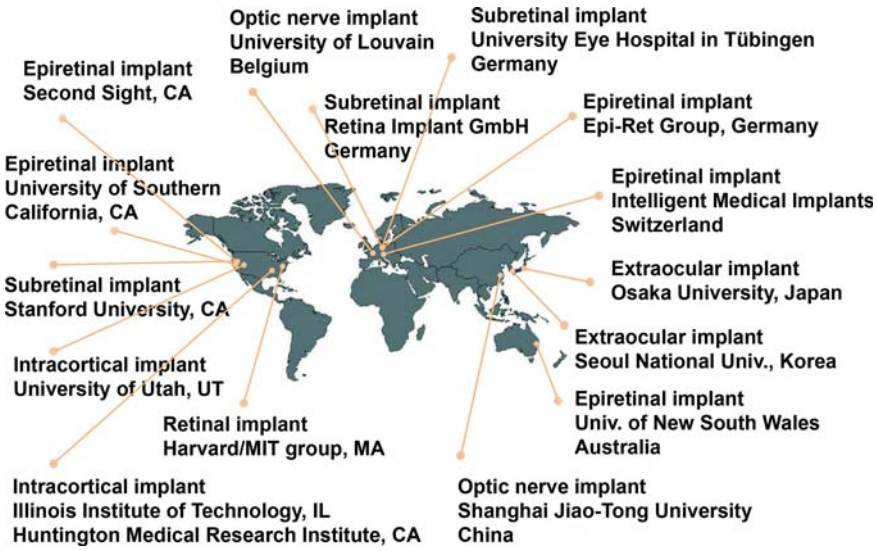

Fig. 5 Some research teams and industrial groups worldwide that are developing implantable visual prostheses

or cortex stimulation. Retinal implants stimulate remaining retinal neural cells to bypass lost photoreceptors and allow the visual signal to reach the brain via the normal visual pathway.

3.1 Retinal Stimulation and Retinal Implants

In retinal diseases like retinitis pigmentosa, blindness is caused by a loss of photoreceptors. Inspite of nearly complete degeneration of the retinal architecture, there is relative preservation of the inner retinal neurons [26, 27]. The approach of retinal stimulation by a retinal prosthesis positioned intraocular or extraocular is to electrically stimulate the remaining retinal cells. Three major approaches to retinal stimulation have emerged: epiretinal, subretinal, and extraocular (Fig. 6). Epiretinal approaches involve placing electrodes on the top side of the retina near ganglion cells [26, 28, 29], whereas subretinal approaches involve placing electrodes and most of the electronics under the retina in the location of the degenerated photoreceptors between the retina and the retinal pigment epithelium [30, 31]. In the extraocular approach electrodes are placed on the posterior scleral surface of the eye. Both epiretinal and subretinal implants have been tested chronically in humans while the extraocular devices have been limited to animal models and acute studies.

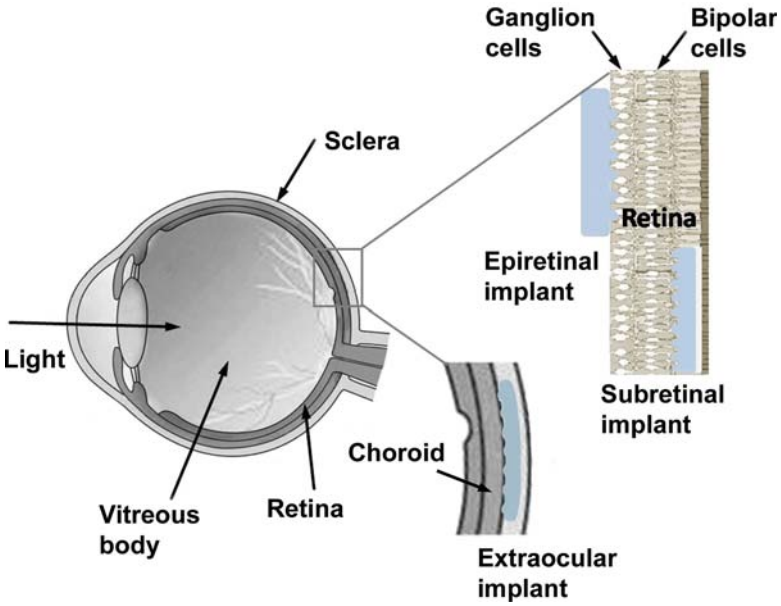

Fig. 6 Schematic of three approaches for an implantable retina implant: an epiretinal implant is placed on the ganglion cell side of the retina. A subretinal implant is positioned between the retina and the retinal pigment epithelium. An extraocular implant is placed on the scleral surface of the eye

3.2 Epiretinal Implant

The epiretinal approach has been pursued by several research teams [23, 28, 29, 32] and industrial groups [5, 35, 37]. Early acute experiments demonstrated that electrical stimulation could restore visual perception of dots and possibly more complex shapes. In one acute human trial by Humayun and co-workers [26], a single electrode array was placed onto the retina surface, no devices were implanted (Fig. 7). Prior to the introduction of the array, a majority of the vitreous gel was removed. A stimulus was transmitted to the retina through the electrode and a perception of a bright spot was formed in the patient's eye. Rizzo and Wyatt's group [33] have performed acute tests in six human subjects (5 RP patients and 1 normal vision subject as a control). Thin-film microelectrode arrays with a thickness of 10 μm and different diameters (50, 100, and 400 μm) were placed on the retina of subjects who were awake. Stimulation charges were delivered to the electrodes from an extraocular current source. This type of acute testing led to the design of the chronic retinal implants.

Second Sight and the Humayun group at USC have been continuously developing the intraocular retinal prosthesis since 1999. A large portion of this research and development for the first generation long-term retinal implant

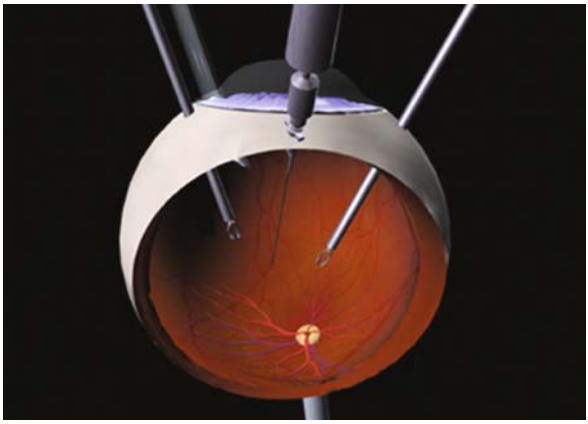

Fig. 7 The configuration of one of the very first patient tests conducted 12 years ago at Johns Hopkins [26]

was done in collaboration with several universities funded by National Eye Institute (NEI). Between 2002 and 2004, the Humayun group has chronically implanted the Second Sight retinal prostheses in six blind subjects with retinitis pigmentosa [6].

The intraocular retinal prostheses implanted were the Argus™ 16 Retinal Implants – the devices developed based on existing cochlear implant technology of Advanced Bionics (Valencia, CA) with modified electronics, novel retinal electrode arrays, and novel video processing technologies. The Argus™ 16 device consists of a wearable external device and an implantable stimulator (Fig. 8).

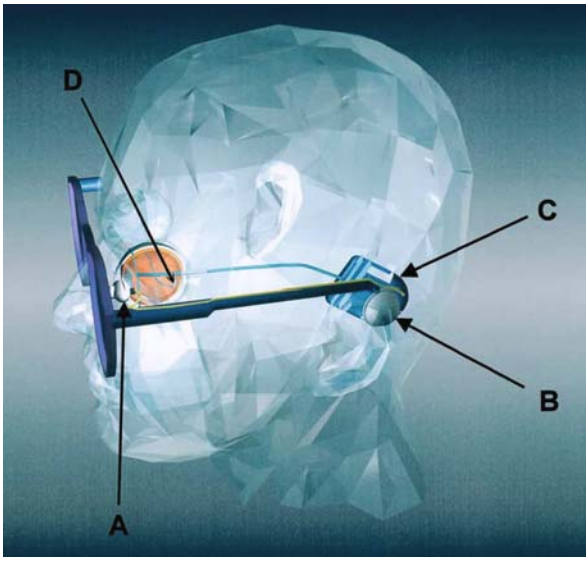

Fig. 8 A schematic design of a retinal prosthesis with (A) camera in the glass frame; (B) wireless transmitter; (C) extraocular stimulator; and (D) intraocular electrode array (reproduced from Ref. [20] with permission from Elsevier)

In this design, a small camera is housed in the glasses that connects to a belt-worn visual processing unit (VPU)^{TM} (Fig. 9a). The VPU encodes visual information acquired from the camera and transmits electrical stimulation signals to the implanted unit. The data transfer is accomplished via a wireless inductive link using an external coil that is magnetically stabilized over the electronic implant. Personal computer-based custom software was also used to actively control the electrical stimulation command through the VPU.

Fig. 9 The Second Sight Argus 16 electrode retinal stimulator implant. (**a**). The Argus 16 external system consisting of a pair of glasses housing a camera, a hip worn visual processing unit (VPU), and a primary coil that is magnetically attached to the scalp just behind the ear (where a secondary coil in a stimulator is implanted). (**b**) The electronic stimulator is implanted in the bone behind the ear. The cable connecting the electronics package to the array is tunneled up into the orbit where it encircles the eye and enters through a pars planar incision. The array is fixed on the epiretinal surface with a metal tack

The Argus^{TM} 16 implanted unit consists of an extraocular stimulator and an intraocular electrode array (Fig. 9b). The extraocular stimulator is surgically attached to the temporal area of the skull. A subcutaneous cable connected to the stimulator is used to deliver a charge across the eye wall to an intraocular electrode array placed on the retinal surface. The electrode array consists of 16 disc-shaped platinum electrodes in a square 4×4 layout embedded in silicone. Each electrode is approximately 500 μm in diameter. In some subjects, 250 μm electrodes or a combination of 250 μm and 500 μm electrodes were used. Edge-to-edge separation between two adjacent electrodes is approximately 200 μm [20].

Prior to introduction of the implant, the majority of the vitreous gel is removed. The electrode array is then positioned just temporal to the fovea on the top side of the retina near ganglion cells and a metal retinal tack was inserted through the electrode array and into the sclera. The threshold level of electrical stimulus charge remains below 0.35 mC/cm^2, which is an established long-term safety limit for platinum [34]. The timing of the pulse is typically a biphasic, cathodic first current pulse, 1 ms/phase with a 1 ms interphase delay [20]. The threshold currents to elicit the responses are considerably lower than previously reported acute tests [26]. Electrical stimulation produces phosphenes in the

human subjects. In general, the size and brightness of the phosphenes increase with higher stimulation current. The results are both reliable and reproducible with respect to the spatial location of the stimulating electrodes on the retina and the stimulating electrical current [6, 20]. In addition, the implanted devices with only 16 electrodes have enabled blind subjects to detect when lights are on or off, describe an object's motion, count distinct items, as well as locate and differentiate basic objects in an environment.

In early 2007, Second Sight received the FDA approval to conduct a clinical study of the Argus^{TM} II Retinal Prosthesis System. This smaller and higher resolution implant is the second generation of an electronic retinal implant. The Argus^{TM} II device has a thin-film array of 60 platinum electrodes that are attached to the epiretinal surface (Fig. 10). This phase I of a 3-year investigational device exemption (IDE) trial on blind RP subjects with four US centers, several European sites, and Mexico is underway. At the time of this writing, 18 subjects have been implanted. The development of retinal implant technology is supported by the National Eye Institute (NEI) of the National Institutes of Health (NIH), the Department of Energy's Office of Science (DOE) Artificial Retina Project, and National Science Foundation (NSF).

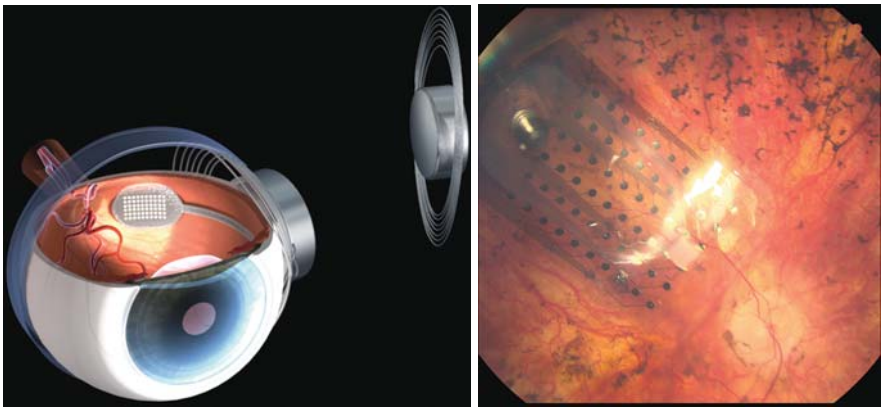

Fig. 10 *Left*: The second sight Argus II 60 electrode retinal stimulator implant. *Right*: A second sight thin-film 60 electrode array in the eye of a RP subject

Another industrial effort to develop epiretinal implants is Intelligent Medical Implants (IMI) AG (Zurich, Switzerland, and IIP Technologies AG – a subdivision in Bonn, Germany). The company's retinal implant has been implanted chronically in four blind RP subjects [35]. An epiretinal stimulator developed by IMI is shown in Fig. 11a [36]. An intraocular part of the implant is a thin-film polyimide array of 49 platinum electrodes (Fig. 11b). The array is placed in the macular area and fixed by a retinal tack with a silicone retainer ring. An extraocular part of the retinal stimulator is fixed onto the sclera.

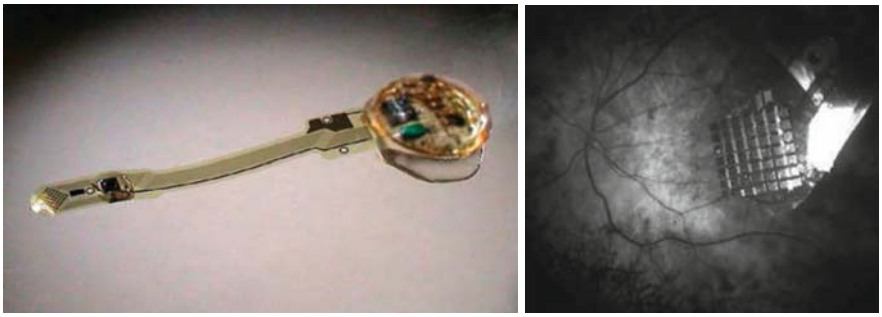

Fig. 11 *Left*: An epiretinal stimulator developed by Intelligent Medical Implants (IMI) AG with a thin-film polyimide cable of gold traces. Reproduced from [36] with permission from Springer. *Right*: The electrode array has 49 platinum electrodes (reproduced from Ref. [37] with permission from Dr. G. Richard, University Eye Clinical Center, Hamburg, Germany)

Unlike the Second Sight implants in which both power and data are transferred through RF links, the power for the IMI retinal stimulator is provided through a RF link, while the stimulation data is transmitted via an optical link. The transmitters for both power and data are housed in a handheld unit. Based on the 9-month follow-up results, the implant is well tolerated in the eye. The subjects were able to distinguish between different points and recognize simple patterns such as horizontal bars [35].

3.3 Subretinal Implant

In the subretinal approach, photodiodes are implanted underneath the retina and used to generate currents that stimulate the retina. In Germany, a consortium led by Eberhart Zrenner [31] is being sponsored by the German government to develop subretinal implants. In the United States, Optobionics (Naperville, Illinois) is a private company founded in 2000 by the Chow brothers Alan and Vincent Chow, an ophthalmologist and an engineer, respectively, that had pursued the subretinal approach [8, 30] before filing for bankruptcy in 2007. The artificial silicon retina (ASR) microchip they developed is a 2-mm diameter silicon-based device that contains approximately 5000 microelectrode tipped microphotodiodes and is powered by incident light. Each pixel is 20×20 μm square and is fabricated with a 9×9 μm iridium oxide (IrOx) electrode electrochemically deposited to each pixel. Pixel current is 8–12 nA with approximately 800 foot-candles of illumination. In the pilot clinical trial for safety and efficacy studies reported in 2004, the ASR was implanted in six RP subjects from three centers.

The ASR microchip was placed within a fabricated Teflon sleeve and secured intraoperatively to a saline-filled syringe injector; it was then deposited within the subretinal space by fluid flow. From follow-up results ranging from 6 to 18

months, all ASRs functioned electrically with no implant rejection or retinal detachment. They reported that visual function improvements occurred in all subjects and included unexpected improvements in retinal areas distant from the implant. They claimed that the presence of the implanted ASR (either alone or coupled with low-level electrical stimulation) induced a "neurotrophic effect" or improved the visual function of the retina.

Optoelectronic subretinal implants rely on transformation of incident light to electrical signal via photodiodes. It is doubtful that current photodiodes are efficient enough to generate charges required to stimulate retinal cells. In fact, in vivo and in vitro studies indicated that a pure photovoltaic current was not sufficient to provide charge capacities for stimulating the bipolar cells [7, 38]. Additional energy inputs such as near-infrared radiation or RF power transmission are required [38, 39]. Powered subretinal implants using microelectrode arrays instead of microphotodiodes have been proposed by Zrenner [40] and the Harvard/MIT group [41].

A hybrid subretinal device with both microphotodiodes and microelectrodes has been developed by Retina Implant AG (Reutlingen, Germany) and Zrenner's team [40]. The device consists of an active chip ($3\times3\times0.1$ mm) with 1540 microphotodiodes and an additional 16 titanium nitride electrode (diameter 50 μm) array of 4×4 layout with a 280 μm intra-electrode space for direct stimulation powered externally (Fig. 12). Each microphotodiode cell has an area of 72×72 μm. When powered by a pulsed power supply at about 20 Hz with an active time per period about 500 μs, the cell delivers charge between 0.5 and 10 nC [42]. The maximum amplitude of the output pulses is set to 2 V to avoid exceeding the water window (see discussion in Section 4.4).

A polyimide carrier foil with 22 gold traces connects intraocular electrodes and photodiode chip to an extraocular connector which connects to a silicone cable (diameter 3 mm) with 22 coiled gold wires. This long cable of ~15 cm leads to an external plug behind a patient's ear for an external stimulator which

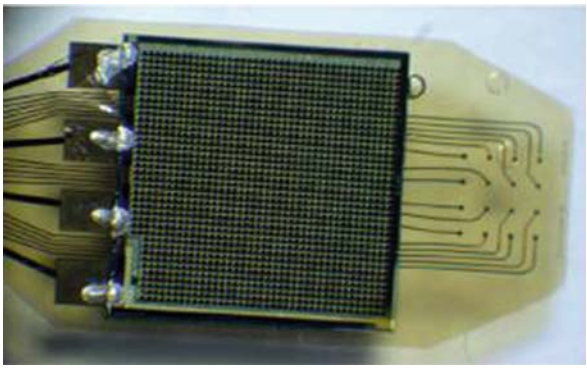

Fig. 12 A hybrid subretinal device with both microphotodiodes and microelectrodes developed by Retina Implant AG, Reutlingen, Germany (Couresy of Dr. Walter-Gerhard Wrobel, Retina Implant AG)

provides control signals, power, and stimuli. The devices have been successfully used in a 4-week clinical trial in seven blind RP subjects [43, 44]. Direct stimulation using electrodes approximately 1° apart produced phosphenes and subjects could recognize different spatial patterns, such as dots, lines, angles, or a square [40, 44].

It is critically important that visual stimulation electrodes are placed close to the target neuron cells to achieve low threshold charge and high resolution. Commonly this is achieved by using protruding or penetrating electrodes. Alternatively, neuron cells could be attracted to the electrodes. Daniel Palanker and co-workers [45, 46] at Stanford University, CA have designed a photodiode-based subretinal implant with micro-channels that prompts migration of retinal cells into the proximity of stimulating electrodes. In vitro and in vivo experiments confirmed that the cells preserved axonal connections to the rest of the retina during migration and thus maintained the signal transduction path, but an integrated device has not yet been built. In a recent animal study by the same group [47], they compared three configurations (flat, pillars, and chambers) of passive subretinal arrays and found that three-dimensional pillars had minimal alteration of the inner retinal architecture (Fig. 13). In the microchamber design, encapsulation of cell bodies inside the chambers causes cell isolation and limits their access to diffusing metabolites, which may affect cells' long-term viability.

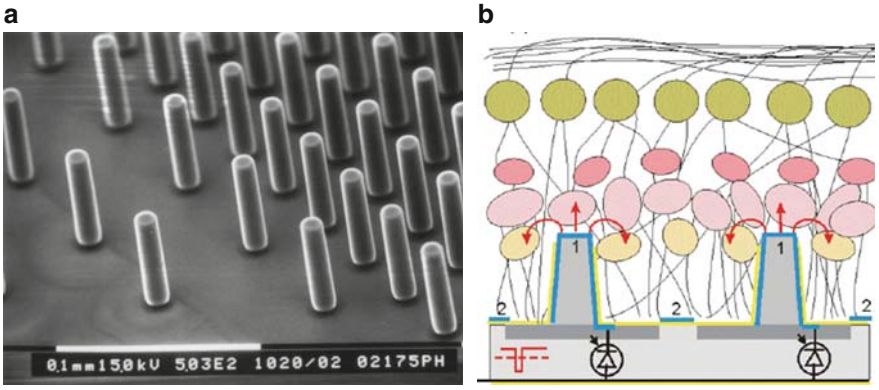

Fig. 13 (**a**) An SEM micrograph of the microfabricated SU-8 (an epoxy-based photosensitive polymer) pillar arrays. Each pillar is about 10 μm in diameter and 40–70 μm in height. (**b**) A pillar array may attract retinal cells to migrate into three-dimensional pillars in a subretinal implant for achieving intimate electrode-cell proximity (reproduced from Ref. [47] with permission from IOP Publishing Ltd)

Both epiretinal and subretinal approaches have advantages and disadvantages [7]. The epiretinal implants do not rely on the signal processing capability of the retina when stimulating the ganglion cells on the top of the retina [38].

Epiretinal implants are also significantly easier to safely surgically install when compared to subretinal implants. One theoretical advantage of the subretinal approach is that it may be able to take advantage of the complex processing circuitry of the retina by replacing the input signals from the photoreceptors with direct electrical input. However, recent data show that degeneration of the photoreceptors causes severe disorganization of the retinal circuitry [48], so stimulating with subretinal electrodes may result in a scrambling of the signal as it passes through the disordered circuitry.

3.4 Extraocular Implant

Chowdhury [49] studied the feasibility of using a retinal prosthesis for extraocular stimulation in anaesthetized adult cats. They found that electrodes placed on the exterior of the eye could reliably evoke visual cortex responses for a variety of configurations. Electrodes of Pt disks and Ag balls placed on the posterior scleral surface of the eye after a craniotomy and lateral orbital dissection. Cortical potentials evoked by electrical stimulation lower than 100 μA with single pulses were recorded at the primary visual cortex. These findings suggested that it is possible to electrically stimulate the retina with electrodes placed in an extraocular location, but thresholds are likely higher than for intraocular stimulation.

There is also a group from the Department of Ophthalmology at Osaka University in Japan that focuses on transretinal electrical stimulation [50]. They conducted acute electrophysiological experiments in rats. For electrical stimulation, a 0.2–0.3 mm in diameter silver-ball electrode was used as a stimulation electrode and an epoxy-coated stainless steel wire 0.2 mm in diameter was used as a return or reference electrode. The Ag-ball electrode was inserted into a small lamellar scleral resection made at a short distance from the optic nerve in the upper temporal part of the sclera. The stainless steel return electrode with about 2 mm of the tip exposed was inserted approximately 4 mm into the vitreous. In most stimulation experiments, the return electrode in the vitreous was used as the cathode. A single monophasic pulse of electrical current ranging from 5 to 300 μA was applied between these two electrodes for various pulse widths of 0.05, 0.2, or 0.5 ms.

The electrically evoked potentials (EEPs) from transretinal stimulation were recorded from the superior colliculus (SC) in rats. A silver-ball recording electrode (Ag/AgCl, 0.2–0.3 mm in diameter) was positioned on the exposed SC surface by a three-dimensional micromanipulator. A stainless steel screw was implanted into the occipital bone approximately 1 mm behind the lambda and used as a reference electrode for recording. EEP recordings confirmed that transretinal electrical stimulation did generate focal excitation in retinal ganglion cells in normal animals and in those with degenerated photoreceptors. Since the study was acute, long-term effects of retina or choroid damages could not be accessed.

A similar approach was used by Sung June Kim's group at Seoul National University, Korea for suprachoroidal stimulation [51, 52]. The prototype implant, which was built based on a cochlear implant, has two unique features (Fig. 14). Rather than inserting a reference electrode into the vitreous as in Tano's approach [50], they placed the reference electrode on the outer scleral surface without penetrating the vitreous cavity. This design will simplify surgical procedures and reduce possible ocular damage from penetrating the vitreous cavity.

Fig. 14 A suprachoroidal (extraocular) implant for transretinal stimulation. The device consists of a receiver coil, hermetically sealed titanium package, and polyimide-based gold stimulation and reference electrodes (reproduced from Ref. [52])

The second feature was that the implant was powered by a small rechargeable battery so that the external components, such as power supply and data control parts, could be removed during a chronic stimulation experiment. Transfer of data and charging the batteries were accomplished through inductive links. The power consumption determined on a dummy resistor of 1.3 kΩ was around 2 mW at 520 μA, 1 ms, and 4 Hz biphasic current. Under these conditions, the battery could supply the power to the stimulator for over 30 h. The rechargeable battery with a capacity of 75 mAh (4.2 V) in the implant could be fully recharged within 3 h with 25 mA charging current through a RF inductive link.

The 7 channel stimulator developed by Kim's group was hermetically packed in a titanium case. The feedthroughs connected the electrode array and receiver coil to the retinal stimulator. A ceramic sintering process was used to fix the feedthroughs in the ceramic plate that provided electrical isolation. Brazing and laser welding techniques were employed to achieve hermetic sealing of the titanium housing [52, 53]. The electrode array has an integrated stimulation electrode array and a large reference electrode. The seven stimulation electrodes have an exposed strip-shaped area of 750×300 μm that is arranged in a 4 mm × 4 mm area. The reference electrode, also made of polyimide insulated thin-film gold, has a diameter of 1.5 mm. The electrodes have typical impedances of 1.3 kΩ and 300 Ω in PBS at 1 kHz for the stimulation and reference electrode, respectively.

Surgical implantation into rabbits was performed to verify the functionality and safety of this newly designed system. A polyimide-based gold electrode array was implanted in the suprachoroidal space. EEPs were recorded via stainless steel needle electrodes from the cortex during electrical stimulation of the retina. They found that the placement of the reference electrode in the

extraocular space resulted in effective stimulation of the retina. Long-term follow-up using optical coherence tomography (OCT) showed no chorioretinal abnormality due to implantation of the electrodes.

One advantage of extraocular implants is that they are surgically less invasive. However, transretinal stimulation may require considerably higher charges and may have lower resolution due to the distance between stimulating electrodes and the retina in comparison to epiretinal or subretinal stimulations. Yamauchi et al. [54] directly compared the threshold electrical charge density of the retina in rabbits for the generation of EEPs using microelectrode arrays implanted into either the subretinal or the suprachoroidal space. They found that the retinal threshold charges to elicit an EEP are significantly lower with subretinal stimulation ($9 + /–7$ nC or $23 + /–16$ μC/cm^2) compared to transretinal (extraocular) stimulation ($150 + /–122$ nC or $375 + /–306$ μC/cm^2). An approach to use a penetrating electrode array placed in the suprachoroidal space has been explored to reduce the electrode–retina distance for transretinal stimulation, but controlling the depth of penetration has been difficult [55].

3.5 Visual Stimulation in the Brain

3.5.1 Cortical Stimulation

Early experiments performed by Brindley, Dobelle and others [22, 56–59] demonstrated that visual cortical stimulation could elicit predictable phosphenes. Brindley and Lewin used 80 cortical surface electrodes in a subject who was able to perceive phosphenes. Approximately 32 independent visual percepts were obtained. Another subject received a second 80 channel implant in 1972 [56, 60]. Of the 80 implanted electrodes and stimulators, 79 of them produced visual percepts of varied size and shape. However, because relatively large surface electrodes were used for cortical stimulation, the threshold current to produce phosphenes was very high and the resolution of produced phosphenes was low.

Since these early experiments, efforts have been underway to produce penetrating arrays of electrodes that offer the possibility of more closely spaced electrodes and therefore higher resolution cortical devices [10, 61–63]. Schmidt et al. [64] studied the feasibility of a visual prosthesis using intracortical microstimulation of the visual cortex in a totally blind subject due to glaucoma. They used IrOx penetrating microelectrodes and the electrodes were implanted in the right visual cortex, near the occipital pole, for a period of 4 months. A total of 34 out of the 38 implanted penetrating microelectrodes produced percepts with low threshold currents typically less than 25 μA with cathodic first pulse trains of 3 s duration, 200 μs pulse width at 100 Hz. The subject reported phosphenes ranging from a pinpoint to a disk shape. Phosphene recognition was improved after replacing a long pulse train (3000 ms) with 10 short ones (200 ms) at 1 s

intervals. They found that resolution was improved by using intracortical microelectrodes instead of the surface electrodes used in early cortical stimulation. Penetrating electrodes spaced 500 μm apart generated separate phosphenes, but microelectrodes spaced 250 μm typically did not. The current threshold for phosphene generation with intracortical microelectrodes is dramatically reduced by two orders of magnitude compared to that of surface stimulation. Two challenges, however, with intracortical stimulation is depth control of the electrodes and damage to brain tissue.

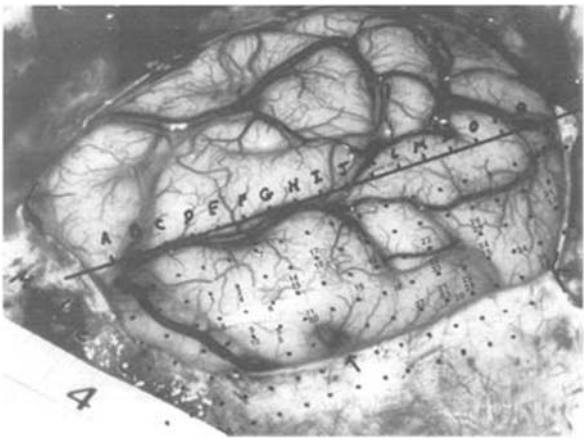

Fig. 15 Photograph of exposed surface of the right visual cortex of the blind subject. The overlaid dots, at ~2.4 mm spacing, were reference points for surface stimulation. The numbers in the figure have been placed on the approximate positions of the intracortical microelectrodes. The terminal portion of the calcarine fissure is marked by an arrow and superior is to the left of the arrow. A centimeter scale is shown at the lower left (reproduced from Ref. [64] with permission from Oxford University Press)

Philip Troyk et al. [65] reported the use of an animal model for intracortical visual prosthesis research. They have made extensive use of trained monkeys to investigate stimulation strategies in developing a multichannel sensory cortical interface.

As shown in Fig. 16, the envisioned intracortical visual stimulation system in the study consists of external components such as camera, video process module and coil, implantable stimulation modules, and implantable electrode arrays. The image captured by a camera is converted by a video processing module and the stimulation signals and power required are transmitted through a transcutaneous inductive link to fully implanted stimulation modules. The penetrating microelectrode arrays are implanted on the surface of the cortex. The electrodes are connected to fully implanted electronic stimulation modules through lead

Fig. 16 A conceptual design of an intracortical visual prosthesis. The image captured by a camera is converted by a video process module and the stimulation signals are transmitted through a transcutaneous inductive link to implanted stimulation modules. Stimulation of microelectrodes implanted in the visual cortex results in a perception of the image (reproduced from Ref. [65] with permission from Wiley-Blackwell)

wire cables. Stimulation of microelectrodes implanted in the visual cortex would result in a perception of the image. The camera would be integrated into eyeglass frames and tied to eye movements. There were a total of 192 electrodes from 24 arrays (each with 8 electrodes) implanted in area V1 of a male macaque. The electrodes were made from parylene (poly-dichloroparaxylylene) coated fine iridium wires 30 μm in diameter. The exposed electrode tips with two different areas of 500 μm^2 and 200 μm^2 were activated to form iridium oxide to increase charge storage capacity. Their findings suggested that using an animal model for visual prosthesis research to compensate for the absence of a language report is feasible. However, these studies are very challenging.

3.5.2 Visual Stimulation in LGN of the Thalamus

In the past, the development of visual prostheses has focused on three out of four main locations of the visual pathway, i.e., the retina, optic nerve, and visual cortex. The lateral geniculate nucleus of the thalamus (LGN), which is located in the midbrain to relay signals from the retina to the visual cortex, has limited access due to surgical difficulty. The recent success of deep brain stimulation techniques targeting the midbrain has encouraged research to pursue the approach of LGN stimulation for a visual prosthesis. Pezaris and Reid [25] examined the concept in animal models for a visual prosthesis based on thalamic stimulation. They inserted polyimide coated tungsten wire bundle electrodes through the surgical cranial opening and into the brain by using a 32 ga

tapered transdural guide tube. The saccading reaction of alert monkeys from electrical stimulation applied to the LGN was used to assess the effects of stimulation. They concluded that electrical microstimulation in the LGN creates visual normal percepts or phosphenes. Surgical and implant challenges, however, remain for an LGN device with more than a few electrodes.

3.6 Optic Nerve Stimulation

A group led by Claude Veraart [66] at the Neural Rehabilitation Engineering Laboratory in Brussels, Belgium has implanted a nerve cuff with four electrodes around the optic nerve of an RP subject. That subject is able to reliably identify the quadrant in which she sees a phosphene and may be able to differentiate other phosphenes as well [66–68]. To make the optic nerve visual prosthesis more acceptable, implantation techniques safer and less invasive than those previously used have been developed [69]. Unlike prostheses previously implanted in the intracranial part of the optic nerve, which required more invasive surgery, a transconjunctival approach is now used to implant a stimulating electrode around the intraorbital section of the optic nerve. This technique allows sufficient exposure of the nerve after detaching only one rectus muscle and performing a lateral canthotomy. A 68-year-old RP subject underwent long-term implantation using such an implantation technique.

Fang and co-workers [70] from Tano's group investigated a transvitreal approach to stimulate the optic nerve. They inserted epoxy-coated platinum wire electrodes (50 μm in diameter) through the vitreous and fixed the electrodes in the optic disc of rabbit eyes. EEPs from the bipolar optic nerve stimulation were made through cortical recording. The threshold charges to elicit EEPs in the visual cortex were low and comparable to retinal stimulation. However, some optic nerve damage around the electrode track was observed after the electrodes were implanted in the optic disc for less than 1 h.

A team led by Ren Qiushi at Shanghai JiaoTong University, China has joined the race to develop visual prostheses using optic nerve stimulation. The multi-disciplinary team named C-Sight (Chinese Project for Sight), which is sponsored by the National Basic Research Program of China, was founded in 2004 [24]. They are exploring both surface and penetrating electrode arrays using animal models to target the axons of the optic nerve.

4 Engineering Challenges in the Development of Visual Prostheses

Building a high density, high resolution, and long-term visual prosthesis involves engineering challenges not yet solved by other neural stimulator researches. The highest resolution cochlear implants in the market today (nearly 30 years after the first human implant) have a package and interconnect

that support only 24 electrodes and are much larger than any device that could fit in the eye socket. The challenges for visual prostheses include developing a biocompatible hermetic electronics packaging with high-density electrical connection feedthroughs from inside the package to outside, low power consumption, a high-density stimulator capable of driving a large number of electrodes simultaneously, a system for efficient power and data transmission and robust high-density electrode arrays for safe chronic stimulation. All of this must fit within the confined space of the eye socket or cortical spaces while withstanding the corrosive environment of the body for many years. Some challenges that exist in the development of visual implants, especially for retinal implants, will now be discussed.

4.1 Implant Packaging and Biocompatibility of Materials

Encapsulation of implanted medical devices is one of the greatest challenges in the biomedical industry [71]. One such factor that makes it so challenging is the corrosive environment, such as biological fluid containing salts and proteins among other cellular structures, in which the medical device has to survive [72]. Another factor is the biocompatibility and blood compatibility of the encapsulant material [73]. It is crucial for the life of a device and the protection of the body to use a material that would satisfy both needs.

Biomaterials are used in contact with living tissue, resulting in an interface between living and nonliving substances [74]. All medical implants are coated or packaged by biomaterials that are inert substances designed for implantation or incorporation with the human body. However, not all the materials used inside the medical implants are biocompatible. The materials used to make the medical implants such as electronic components, active metals, or alloys are not biocompatible. For a reliable medical implant, especially an active device such as a retinal implant, the package or coating should have a lifetime of 10 years or longer. Should this coating or package fail during the implantation, toxic materials may leach out and cause possible tissue or neural damages. The leakage may also cause the failure of electronic devices inside the implants.

Three approaches have been pursued in the active implant packages: hard cases including metal, ceramic, or glass cases; soft cases including various polymer encapsulations and thin-film chip-size packages (CSP). The hard-case approach has been used exclusively by various implantable device manufacturers for CI, DBS, SCS, and pacemakers and by many research groups for prototype visual devices. Titanium appears to be the material of choice for the hard-case packages [52, 75]. A hard case is bulky and it is difficult to make very small devices. However, it provides the most reliable hermetic packages with years of device lifetime and is the only technology used in commercial implants.

Soft-case materials include silicone (polydimethylsiloxane, PDMS), epoxies, and various polymers such as parylene, polyurethane, and polyimide [76].

A typical example of a soft-case retinal implant was developed by Stieglitz's group [77]. The device has been completely coated with parylene C then encapsulated in silicone (Fig. 17). The device has survived 14 months of implantation in animals. The implantation was passive as the device was only periodically powered to check for functionality. Continuously powered stimulation in saline (active device) is a much tougher test to pass.

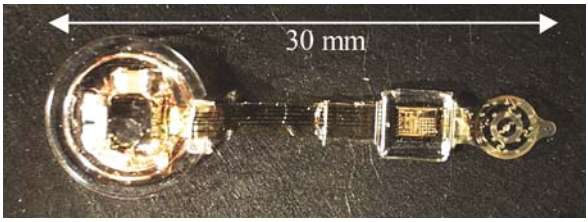

Fig. 17 An epiretinal vision prosthesis with assembled electronic components after coating with parylene C and silicone encapsulation (reproduced from Ref. [77] with permission from IEEE)

A combination of polymers has been used to protect a 100 electrode array on a multiplexer chip for an extraocular implant [75]. The device was coated by two layers of parylene, first 1 μm parylene N for excellent dielectric strength, then 5 μm parylene C for its low permeability to moisture. Finally, the device was molded with silicone. The devices were tested in saline at room temperature for 3 days and passively implanted in rabbits for 10 days without failure.

Parylene is a conformal protective polymer coating material used in coatings for many medical devices. One attractive feature of parylene coating is that it conforms to virtually any shape, even on sharp edges or crevices. The parylene is applied at the molecular level at room temperature by a chemical vapor deposition process [78]. In the deposition process, the polymer dimers are converted under vacuum and heat to dimeric gas, pyrolized to cleave the dimer, and finally deposited as a clear polymer film. No catalysts or solvents are required and no foreign substances are introduced that could degrade the coated surface. Thick coatings can be easily applied in a single operation. Parylene C (poly-dichloropara-xylylene) is the most widely used dimer to have a very low permeability to moisture, chemicals, and other corrosive gases while parylene N (poly-para-xylene) provides high dielectric strength and a dielectric constant.

Thin-film chip-size package or chip-scale package (CSP) technology has been adopted for medical implant protection. The technology developed for semiconductor industries will potentially result in a slim hermetic package that is virtually the same size as the bare stimulator chip. The thin-film coating approach has been actively pursued by a group at Argonne National Labs led by Orlando Auciello [50, 79, 80]. Thin-film CSP coating materials include silicon oxide, silicon nitride, silicon carbide, alumina, diamond-like-carbon, and polycrystalline diamond. Some of those passivation layers are commonly used as moisture and mobile ion barriers to protect the silicon-based electronic components.

In vitro accelerated corrosion tests were carried out on Si chip samples coated with silicon oxide and silicon nitride at different temperatures in bicarbonate buffered saline (BBS) for 2 to 3 months [81]. Severe pitting corrosion has been detected on unprotected silicon samples after soaked in saline for only 4–5 weeks. After 25 days in BBS, the Si samples at 77°C showed obvious corrosion while the samples at 57°C had partially corroded. Corrosion of the sample at 37°C can only be detected by chemical analysis of soaking solutions. Pitting corrosion of these Si samples, characterized by the loss of Si cubic crystals under the attack of saline, was observed. The localized pitting corrosion on the Si surface developed with soaking time and the corrosion area increased after 2 months of immersion for the samples soaked at 57°C and 77°C. The original shiny Si surface became dull and rough. The samples immersed at 37°C or lower showed no visible signs of corrosion (under microscopic examination) after soaking in BBS for 2 months. The corrosion rate at room temperature was very low and no significant corrosion was noticed even for a longer term immersion test (3 months). It was clear that the Si corrosion had been accelerated by elevated temperatures. The corrosion rates calculated based on the chemical analysis were 0.0049, 0.077, 0.44, and 0.69 MPY (Mils per year) for samples soaked at 23, 37, 57, and 77°C, respectively.

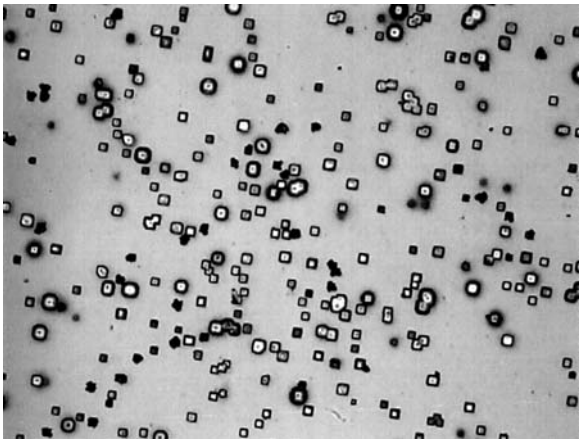

Fig. 18 Pitting corrosion on Si wafer after soaking in BBS for 2 months at 57°C (magnification ×500)

In vivo experiments revealed a decay of the passivation layer of the Si chip-based device when implanted for less than a year [82]. Microphotodiode arrays with a silicon oxide passivation layer have been examined for surface changes before and after 10 months of implantation in the rabbit eye. Microscopic damage of the silicon oxide passivation layer and pitting corrosion of the underlying silicon were clearly visible. These microphotodiode arrays are manufactured on a silicon wafer using CMOS process technology similar to those made by Optobionics [8].

Various thin-film coating materials for subretinal implants have been assessed for biocompatibility [83–85]. The materials implanted in the subretinal spaces of Yucatan pigs for 3 months included amorphous aluminum oxide, polyimide, amorphous carbon, parylene, poly(vinylpyrrolidone), and poly(ethylene glycol). Acute retinal damage with severe disorganization of the retina was observed in pigs implanted with amorphous aluminum oxide [83].

Cogan and co-workers [86] evaluated the stability of amorphous silicon carbide (SiC) films as a coating material. The SiC was deposited by plasma-enhanced chemical vapor deposition (PECVD) and it was compared for dissolution rate and biocompatibility with silicon nitride (Si_3N_4) formed by low-pressure chemical vapor deposition (LPCVD). Their results indicated that the coating dissolution rate was considerably accelerated by soaking temperatures. Dissolution rates of Si_3N_4 rose from 0.4 nm/day at 37°C to 24 nm/day at 90°C, a 120-fold increase. Under the same conditions, SiC had a low dissolution rate of 2.4 nm/day at 90°C and no measurable dissolution at 37°C. They found that SiC was more stable in physiological saline than Si_3N_4 and well tolerated in the cortex.

The ultrananocrystalline diamond (UNCD) coatings have been evaluated for protecting retinal stimulator chips [80, 87]. The in vitro and in vivo results have shown evidence of stability and biocompatibility.

Despite some progresses made in the development of thin-film packaging, none of the thin-film coatings available to date have been shown to have sufficient lifetimes to protect implants for long-term applications. Hermetic packaging using hard cases consumes the most space in biomedical implants. Thin-film coating technology increases the possibility of developing chip-sized implants that are less invasive and further research is warranted.

4.2 Thermal Effects of Stimulator on Tissues and Heat Damage

Most neural stimulators use a current stimulation mode. For an implantable neural stimulator, the current output is limited by the device's compliance voltage and the load impedance of electrode and tissue [88]. For a given compliance voltage, the higher the load impedance, the lower the current output of a stimulator. It was noted that the electrode and tissue interface impedance was greater than the electrode impedance in saline [89]. To improve the efficiency of neural stimulation, bringing stimulating electrodes closer to the target cells is critical. However, electrodes closer to the tissue will increase the load impedance. Figure 19 shows the increase in impedance when a retinal electrode is placed on the epiretinal surface in the vitreous in a canine. The voltage excursion that was an indication of electrode impedance under the same stimulation current was much higher for the electrode on the retinal surface than that in the vitreous. The impedance of the electrode and tissue interface largely defines the output load for the stimulator circuit, and thus the power consumption of the implanted system.

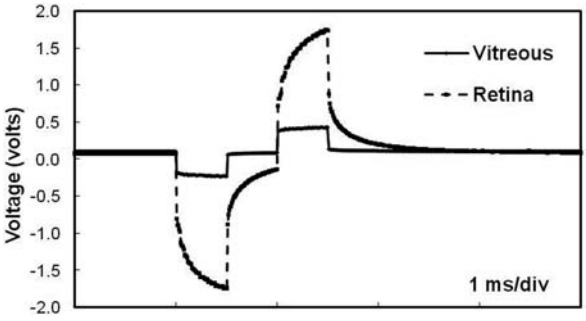

Fig. 19 Electrode impedance measured in an acute stimulation experiment in a canine. The electrode impedance indicated by the voltage excursion was increased significantly by moving the electrode closer to the retina. Unpublished data

One strategy to ensure sufficient current output is to design an integrated circuit with a higher compliance voltage. However, the cost of that approach is higher power consumption, a larger integrated circuit, and increased device temperature [89]. For retinal implants, the implanted electronics are located in or near the eye. The power must be dissipated in the surrounding tissue, which will result in a local temperature rise. Thermal effects of the implant on tissue are one of the primary safety concerns related to visual prostheses. The technical challenge is quite substantial in regard to heat dissipation of electronic components [38].

Studies of thermal effects of the implants on tissue have been carried out for retinal and subretinal prostheses [39, 90]. Piyathaisere et al. [90] studied the heat and power dissipation effect of an intraocular electronic heater on the retina. They used a resistive load heat probe briefly placed on the retina surface or held in the vitreous cavity for 2 h. They observed acute retina damage at 50 mW or higher and permanent retina damage from power consumption over 100 mW or higher when the heater touched the retina. When the heater was held in the vitreous cavity, much more heat could be tolerated. With a power consumption of 500 mW for 2 h, temperature increases of 5°C in the vitreous and 2°C near the retina were measured. Those results indicated that a significant amount of power can be dissipated by the fluid in the eye. To place the retinal implant on the retinal surface, the majority of vitreous gel will be removed and the vitreous cavity will be filled with liquid. The liquid in the eye acts as a heat sink in helping thermal dissipation of implanted microstimulators. To reduce possible thermal damages, the electronic stimulator package should be positioned away from the tissue surface of stimulation sites.

Recently, Sailer et al. [38] studied the thermal effects of infrared (IR) irradiation onto the retina. IR irradiation has been considered as an option to supply additional energy for microphotodiode-based subretinal implants. They implanted thin-film polyimide strips that carried a temperature probe and an optical sensor into the subretinal space of the eyes in rabbits. The maximum temperature rise with 40 mW was found to be about 4.5°C. Under this condition, no acute damage was noted by histological examination. However, the thermal effects of longer term irradiation were not assessed in the study.

They suggested that choroidal blood flow contributed to the heat dissipation and stabilized the temperature increase for the subretinal devices.

Gosalia et al. [91] have modeled integrated circuits operating in the eye using a three-dimensional head model and a finite-difference-based numerical method. The temperature increase in the eye and surrounding head tissues due to the operation of the implanted stimulator IC chip of a retinal prosthesis was evaluated. Induced temperature increase in the eye and surrounding tissues was estimated for several different operational conditions of the implanted chip. In the vitreous cavity, temperature elevation of 0.26°C was observed after 26 min for a chip dissipating 12.4 mW when positioned in the mid-vitreous cavity while 0.16°C was observed when the chip was positioned in the anterior portion between the eye's ciliary muscles. Corresponding temperature rises observed on the chip were 0.82°C for both positions of the chip. Simulation results show that temperature increases induced from a 60 electrode retinal prosthesis chip in the mid-vitreous of the human eye are approximately 0.6 and 0.4°C in the absence and presence of choroidal blood flow, respectively. Correspondent temperature rises of approximately 0.19 and 0.004°C on the retina are obtained for these cases. The thermal model and method used were validated by comparison with in vivo measurements of intraocular heating performed in the eyes of canines.

4.3 Stimulation Microelectrode Arrays

One of the key components of visual implants is the stimulating electrode array. The electrode array, when in contact with living tissue, forms an interface between the electronic device and the biological tissues [34]. There are mainly two types of electrode arrays used in visual implants; planar type or three-dimensional needle or pillar type.

For the cortical and optic nerve stimulations, needle-type electrode arrays are mostly being used today, although Dobelle [57, 92] implanted surface arrays in subjects in Portugal. A typical example for this type of electrode is the Utah array [10]. The Utah array is a 4.2 mm square grid with 100 silicon microelectrodes, 1.0 mm long, and a spacing of 0.4 mm [61].

The needle-type electrode array developed by McCreery's group at Huntington Medical Research Institute, Pasadena, CA (HMRI) has been successfully used for implantation in cortical and other stimulation studies [65, 93]. The HMRI array has the long stabilizer pins to help maintain the position of the array in the cortex. The microelectrode tip of the HMRI array is coated by parylene insulation and the exposed electrode tip is iridium.

A pillar-shaped gold electrode array on thin-film polyimide has been tested as an extraocular implant in rabbits for 4 weeks. The protruding electrodes in suprachoroidal space were observed to cause some retinal layer detachment during retinal surgery [94].

Needle-type electrode arrays, especially the high-density arrays, have been rarely used in the retinal implants due to the possible damage of retina by the electrode insertion. In vitro and in vivo tests conducted by Gerding et al. [55, 95] revealed that forced penetration of electrodes during surgery (immediate penetration) led to retinal damage at the site of penetration. However, slow penetration proved to be less traumatic and worked well. Slow electrode penetration was achieved by suturing electrode arrays on the scleral surface with mild tension of the sutures without forcing the penetration of electrodes during surgery. Slow insertion occurred postoperatively days or even weeks until the electrode carrier reached the outer sclera surface. Figure 20 shows a fundus photo of a ten-electrode array in a monkey eye 2 months post implantation. Preliminary pathohistological results exhibit a well-preserved retinal structure around the electrode tips. However, control of penetration depth remained a problem.

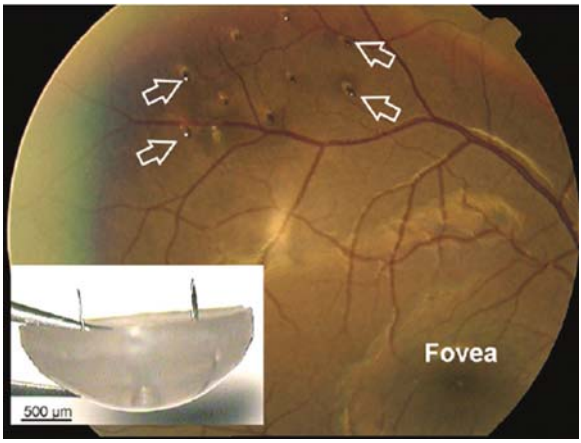

Fig. 20 Fundus photo of a monkey eye 2 months after implantation of ten passive penetrating electrodes. Four of the ten penetrating electrodes are indicated by arrows. The inset shows a two-electrode array with diameters 90–120 µm (reproduced from Ref. [55] with permission from IOP Publishing Ltd)

4.3.1 Planar Electrodes

Planar electrode arrays are usually made from flexible polymers, such as silicone, polyimide, and parylene. The electrode arrays used in the early clinical studies by Humayun's group are mainly silicone-based flexible arrays [20, 96]. Figure 21 shows a fundus photograph of an implanted silicone electrode array developed by Second Sight. The electrode array was composed of 16 platinum disks arranged in a 4×4 square array. A single 25 µm diameter platinum wire was attached to each disk. The disks and wire were encapsulated in medical grade silicone, except for the surface of the platinum disks juxtaposed against the retina, which was not enclosed by the silicone.

The exposed surface of the platinum disks formed an array of planar, stimulating electrodes in a silicone matrix [97]. The disks were approximately 500 µm in diameter and mounted on 600 µm centers. The side of the implant

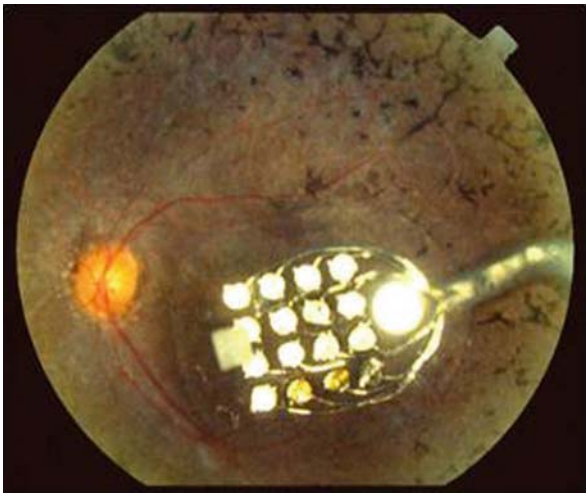

Fig. 21 A fundus photograph of an implanted silicone electrode array as a part of the Argus™ 16 retinal implant developed by Second Sight. The electrode array was composed of 16 platinum disks arranged in a 4×4 square array. The white silicone tube to the left of the electrodes is a handle that allows the surgeon to hold and manipulate the electrode array. The array is approximately 6 mm long and 5.5 mm wide. The electrode size is approximately 500 μm or 250 μm

that was placed next to the retina measured 5.5×6 mm and was curved to match the retina. The implant was less than 1 mm thick. The 16 wires from the disks formed a cable, extending from the electrode array. Each wire was individually insulated. The cable was about 10 cm long, a sufficient length to allow the cable to exit the eye through the sclerotomy wound, and is sutured to the sclera in the superotemporal quadrant under the conjunctiva.

4.3.2 Flexible Thin-Film Electrode Arrays

Polyimide has been widely used in the construction of flexible electrode arrays for visual implants [51, 75, 98–100]. An example of a flexible polyimide electrode array is shown in Fig. 22. This type of array was used in acute stimulation tests in canines.

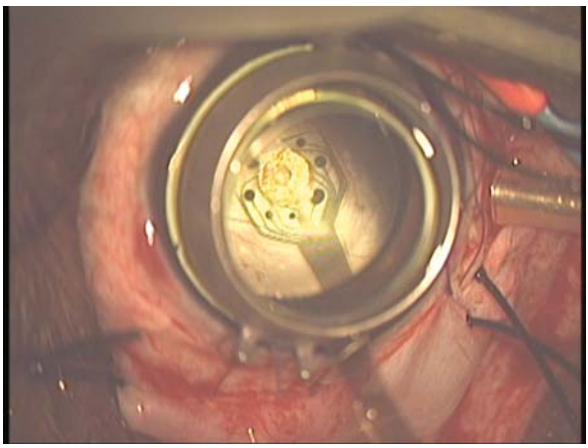

Fig. 22 A thin-film polyimide array used in an acute test in a canine's eye. The array has 16 platinum disks from 50 to 400 μm in diameter arranged in two circles of eight electrodes

The microelectrode array was composed of 16 platinum disks with different surface areas, arranged in two circles of eight electrodes embedded in polyimide. The sizes of electrodes were from 50 to 400 μm in diameter. A flat cable with thin-film Pt traces connected the electrodes and the extraocular micro-connector.

Parylene-based electrode arrays have also been developed for retinal stimulation. Single- and dual-metal-layer fabrication processes were used to produce Pt and Ir electrode arrays and showed biostability in canine eyes for 6 months [78, 101, 102]. One such retinal electrode array shown in Fig. 23 had 1024 electrode contacts, each electrode 75 μm in diameter. However, only 60 of those electrodes were connected for measurements, with each connected electrode having a looped trace (two 8-μm-wide traces of 20 mm length). The electrode impedance for the 75 μm evaporated Pt electrode was about 5 kΩ. The via step junctions were used to connect underlying traces to the overlying electrode in the dual-metal-layer design. Each via of 6 μm × 6 μm introduced a low resistance of 12.5 Ω. The top and bottom parylene C layers were 7 and 8 μm thick, respectively. A very thin insulation layer (∼1 μm) between two metal layers was capable of minimizing capacitive crosstalk between overlapping and adjacent metal lines due to the low dielectric constant of parylene. These arrays were heat molded so that the retained spherical curvature would match the curvature of the canine retina. A similar array of iridium was built using parylene HT, a high temperature, stable and biocompatible fluorinated variant of parylene.

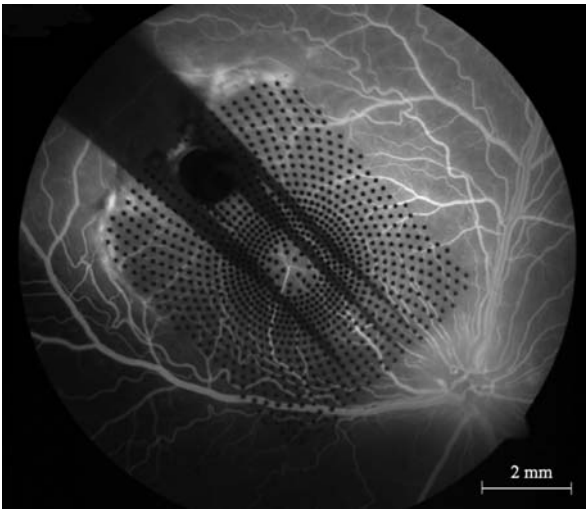

Fig. 23 Fundus photographs showing a parylene microelectrode array tacked to the retina of a canine. The array has 1024 electrodes and 60 of them were wired out through thin-film traces (reproduced from Ref. [78] with permission from Elsevier)

An electrode array design that utilizes both polyimide and parylene has been reported by Terasawa et al. [103]. The platinum bump electrode arrays were fabricated using a polyimide base layer sandwiched between 5 μm parylene layers. They used a layer of 8 μm polyimide as the base for sputtered Ti/Au seed layers. The 10 × 10 electrodes, each with a diameter of ∼220 μm, were built up by 25-μm-thick plated Au and 1-μm plated Pt. The array cable width was 4.2 μm

with line/space of 9 μm/10 μm for Ti/Au traces. After electroplating and removal of photoresist, a layer of 5 μm thick parylene C was coated on the top surface to take advantage of its conformal coating feature and good insulation property. This parylene coating process was repeated on the polyimide surface on the backside of the array after removal of a stainless steel sacrificial layer. Finally, each electrode array was singulated and each platinum electrode tip of 200 μm in diameter was exposed by laser ablation. The authors observed some cracks on the electrode surfaces due to the high energy of the laser pulse (<1 mJ/pulse), and black scorch marks left on the surface of electrodes after laser ablation. Removal of such marks by Ar plasma treatment sometimes damaged the polyimide-parylene adhesion and caused parylene delamination. This array design has been incorporated in an extraocular implant and was tested acutely in vitro and in rabbits without failure [75].

4.4 Electrode Materials

Various electrode materials have been explored for visual stimulation electrodes. Some examples of electrode materials are platinum, iridium, iridium oxide, titanium nitride (TiN), tantalum pentoxide, and conducting polymers [104, 105]. An electrode must be able to deliver a higher charge density without generating irreversible electrochemical reactions such as metal corrosion or dissolution, gas evolution, or introduction of toxic chemical reaction products. Electrical Stimulation of biological tissue with metal electrodes requires the flow of ionic charge in the biological tissue. This flow of charge can be induced by two mechanisms: capacitive and Faradaic. The Faradaic mechanism of charge injection involves electron transfer across the electrode–tissue interface. This may induce harmful electrochemical reactions and cause tissue or nerve damage. The capacitive mechanism involves charging or discharging of the electrode double layer. Ions in the tissue are attracted or repelled by the charge on the electrode to produce pulses of ionic current. There is no charge transfer across the electrode–tissue interface. Charging or discharging the double layer capacitance is an ideal mechanism of charge injection because no electrochemical reactions can occur in the electrode/tissue interface. Water hydrolysis is the most common electrochemical reaction during pulse stimulation, which limits the charge-injection capacity of an electrode. The potential range defined by hydrogen evolution at cathode and oxygen evolution at anode is called the water window.

4.4.1 Capacitive Electrodes

Electrodes that have a dielectric film such as TiO_2, Ta_2O_5, and $BaTiO_3$ are extensively studied materials for capacitive stimulation electrodes. Among them, anodically formed Ta_2O_5 appears to be the best dielectric material to use for stimulation in biological media [34, 106, 107]. Ta_2O_5 surface (Fig. 24),

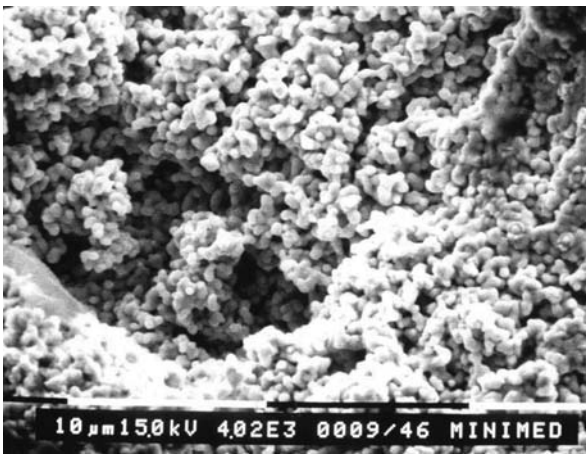

Fig. 24 Tantalum capacitive microelectrode surface made of sintered higher density powders produced by Second Sight

made of sintered higher density powders and anodized at different forming voltages, was found very stable during prolonged pulse stimulation at levels which exceed the water window potentials [108]. However, the charge-injection limit for Ta_2O_5 was generally lower than that of the metal or metal oxide electrodes, especially for electrodes anodized at higher forming voltage. Electrochemical studies indicated that anodizing Ta to Ta_2O_5 did extend the anodic water window, but had no significant effects on the cathodic potential window. This means that the pulse stimulation using a Ta electrode will be limited by the cathodic potential excursion.

4.4.2 Titanium Nitride

Titanium nitride (TiN) coating has been widely used as a biomaterial for orthopedic prostheses, cardiac valves and as electrode materials for sensing and charge-injecting electrodes [109, 110]. Titanium is sputtered at high pressure in a nitrogen atmosphere to obtain nanoporous TiN stimulation electrodes on the implant. The TiN deposition enhances electrode surface area by a factor of up to 100, which is a critical prerequisite for efficient charge transfer from the chip to the retinal tissue. Titanium nitride electrodes proved to be biostable over an implantation period exceeding 18 months [111]. TiN electrode arrays have been used in a 4 week clinical trial in seven RP patients by Retinal Implant AG and Zrenner Group [43]. However, cell culture results in an animal study did show that exposure of TiN to retinal cell culture increased cell death, especially for culturing periods longer than 2 weeks [112].

TiN thin-film microelectrodes (Fig. 25) for charge-injection applications have been studied by various electrochemical techniques [113]. Within water window potentials, TiN electrodes have a very stable surface and the charge transfer through the electrode/electrolyte interface is mainly through a

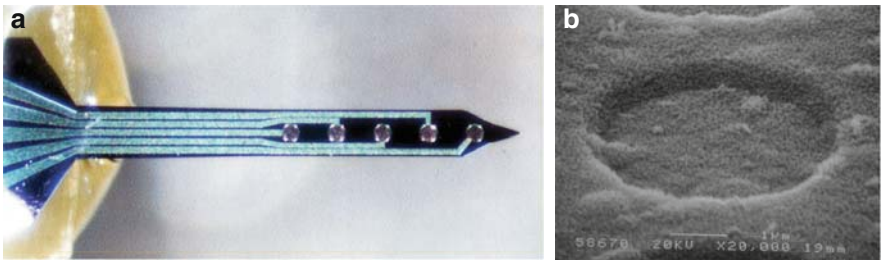

Fig. 25 (**a**) A five electrode microarray coated with thin-film TiN from University of Michigan. The diameter of the electrode surface is 71.8 μm and it has an area of 4.05×10^{-5} cm^2. The electrode has multi-layers of thin-film coatings including ~1 μm TiN as the top layer of electrode material. (**b**) SEM micrograph of TiN electrode surface. At 20,000 times magnification, the micro-roughness of TiN is revealed (reproduced from Ref. [113] with permission from IEEE)

capacitive mechanism. Gentle gassing of the TiN electrode surface generated by cathodic voltage bias did not damage the electrode in terms of charge delivery capacity and adhesion. However, when the surface was subjected to a wider voltage bias and more vigorous gassing, there was damage to the TiN coating. In some cases, a total loss of charge-injection capacity was observed.

4.4.3 Iridium Oxide

Iridium oxide (IrOx) has been reported to hold higher safe stimulation limits of 1–4 mC/cm^2 [105, 114]. IrOx has been shown to be biocompatible in several studies on cortical implants [64, 93]. However, chronic aggressive stimulation resulted in degradation of IrOx and adverse tissue response [115]. In order to utilize its high charge capacity, IrOx electrodes need to be biased anodically [116].

Electrochemically activated IrOx has been used as the electrode material on the "hat-pin" microelectrodes for intracortical stimulation of the visual cortex [64], on the needle electrode made by McCreery's group [93], and on the microphotodiode chips made by Optobionics [47]. Electroplated then activated IrOx has been used in the acute animal studies and acute clinical trials conducted by IMI [36]. Implants coated with parylene and IrOx evaluated 6 weeks after implantation in rats were generally well tolerated in the subretinal space, inducing only a mild gliotic response [46].

4.4.4 Platinum Gray

Solid platinum (Pt) electrodes were reported to handle the charge injection up to 0.35 mC/cm^2 [34]. A new electrode material named "Platinum Gray" developed by Second Sight performs better than smooth solid Pt material. Platinum gray is similar to the more familiar platinum black except that it is prepared in a way to make it significantly more mechanically stable [117].

An SEM picture of platinum gray is shown in Fig. 26 along with pictures of smooth platinum and very soft platinum black. For a given electrode material, the ability of an electrode to transfer charge during neural stimulation is proportional to the electrochemical surface area of the electrode instead of its geometric surface area. Electrode capacitance determined by electrochemical impedance spectroscopy (EIS) is a measurement of a combination of the electrodes' geometric and electrochemical surface areas. These measurements show that the platinum gray coating increases electrode capacitance 50–100 times more than smooth platinum and lowers effective current density of the electrodes significantly, therefore increasing the electrode's charge delivery capacity.

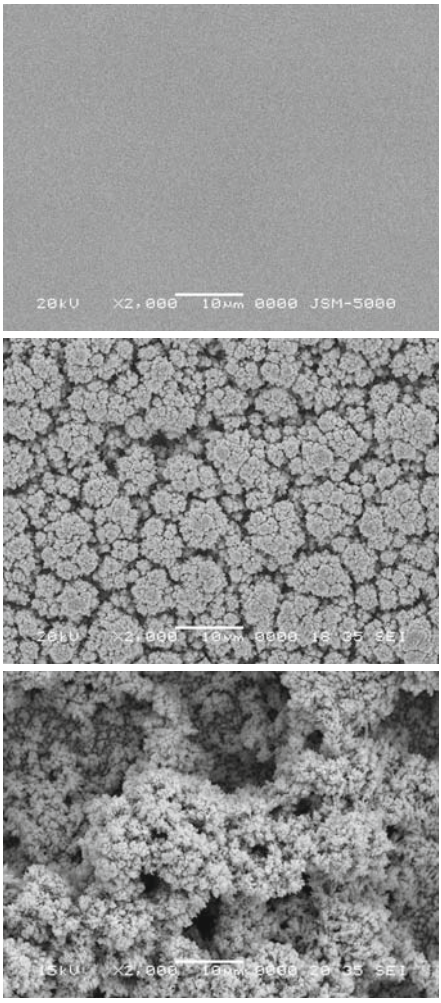

Fig. 26 SEM micrographs of Second Sight Platinum *Gray* (*middle*) electrode material showing the fractal nature and high surface area compared to that of smooth platinum (*top*) and soft platinum *black* (*bottom*)

The area estimated by integrating the cyclic voltammogram within the water window indicates the charge delivery capacity of an electrode. Figure 27a shows a comparison of cyclic voltammograms of sputtered thin-film Pt and Pt gray-coated electrodes. The increased cyclic voltammograms for Pt gray electrodes over the sputtered thin-film Pt (Fig. 27b) allows increased charge delivery capacities for neural stimulation. Platinum gray has been fully verified with soak tests for over 10 years and has more than sufficient chronic charge density capacity – up to 1.0 mC/cm^2 for retinal stimulation.

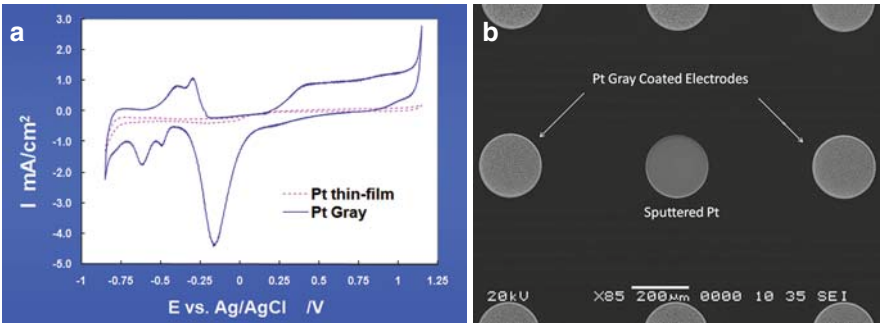

Fig. 27 (**a**) Cyclic voltammograms taken on sputtered thin-film Pt and Pt *gray*-coated electrodes. The CV measurements were carried out in a Phosphate-Buffered Saline (PBS) solution with a potential scan rate of 50 mV/s. (**b**) SEM micrograph of a thin-film array with a sputtered Pt and Pt *gray*-coated electrodes. Unpublished data

Smaller and thinner electrode arrays with flexible polymer substrates to follow the curvature of the retina are the main trends in the development of micro-stimulating electrodes for retinal implants. Planar array configurations with a three-dimensional microelectrode structure to increase charge-injection capability is one proposed idea by Second Sight's team [118]. Using novel nanotechnology combined with well-established MEMS methods will produce batch-fabricated, low-cost electrodes for neural stimulation, recording, and chemical and biochemical sensing inside the eye [119].

4.5 Surgical Attachment of Stimulation Microelectrode Arrays

Surgical attachment that results in a stable implant without creating force that can harm the neural interface such as the retina is another challenge. For cortical and optic nerve stimulations, long needle-type electrodes were used to stabilize electrode arrays. For retinal implants, various methods for chronically affixing the array to the retina have been explored, including biocompatible adhesives or glues, magnetic attachment, MEMS-based silicon tacks, and machined metal retinal tacks. Micromachined silicon tacks

were easy to make by using MEMs technology [51]. However, silicon is brittle and suffers from pitting corrosion in the body. Mechanical strength and long-term biocompatibility are two remaining challenges for the silicon tacks. The most promising of these methods is the metal retinal tacks resulting in firm attachment [120, 121]. In vivo studies conducted by Gerding and co-workers [55, 122] in rabbits demonstrated that tack insertion through the retina, choroid, and sclera did not cause choroidal hemorrhage, major secondary proliferations, or other adverse effects. They reported that reduction of tack diameter reduced the induced secondary tissue reactions and retinal layer disorganization.

The intraocular fixation of the electrode array using tacks has also been proven to be surgically feasible in clinical trials [20, 35]. The follow-up period of more than 9 months clearly shows that the implants are very well tolerated in the subject's eyes. No incidence of cell growth has been observed, and no irritation has occurred as evidenced by fluorescein angiograms and optical coherence tomography. The close proximity between the electrode array and the retina enables the fixation with one retina tack [35]. Berk and co-workers studied retina tack effects in rabbits and they found that the retinal visual function and the retinal architecture underneath the implant were unaffected by the fixation of the implant using a tack [123].

In six human subjects with Second Sight Argus 16 implants, retinal tacks proved to be effective in the array fixation (Fig. 28) [6, 20]. There are over 5 years of implant experience with the Second Sight Argus 16 implants. The array movements were accessed by serial photographs obtained of the implant both preoperatively and on scheduled post-operative dates. The photographs reveal minimal, if any, movement of the device. A comparison of pre-operative and post-operative fluorescein angiograms showed no changes in the vasculature of the retina and choroid.

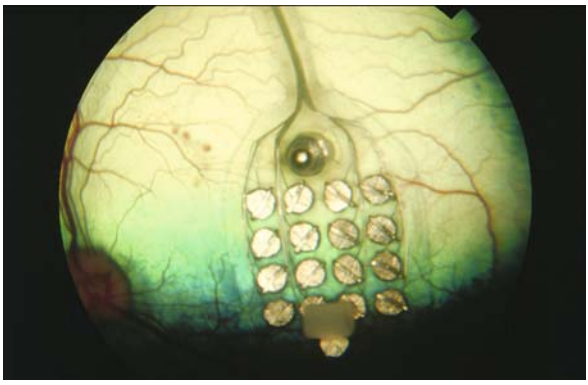

Fig. 28 A fundus photo shows an Argus 16 electrode silicone array being fixed by a tack on the epiretinal surface in a canine

Unlike epiretinal devices, the implant attachment for microphotodiode and thin-film array-based subretinal devices did not require a tack. The microphotodiode devices and thin-film electrode arrays implanted in animals and human subjects remained stable under the subretinal space without tacks [8, 43, 124]. However, subretinal implants are prone to retinal detachments.

5 Conclusion

Visual prostheses have proved to be capable of offering blind subjects in advanced stages of outer retinal diseases the opportunity to regain some visual function. With relatively low-density retinal implants produced so far by Second Sight, simple visual tasks that are impossible with the blind subject's natural light perception vision can be accomplished. Blind subjects can spatially resolve individual electrodes within the array of the implanted retinal prosthesis and can use the system to discriminate and identify oriented patterns. Visual prosthesis research suggests that higher density devices will provide higher spatial resolution vision and enable precision activities for blind subjects [125]. To accomplish this, advances in various engineering aspects, such as low power consumption and an implantable microelectronic stimulator, slim hermetical packaging with long-term biocompatibility, and high-density electrode arrays capable of delivering high charges with a geometrical dimension of micrometers or even nanometers, are needed. Newer models of visual implants will have higher resolution and someday may allow blind subjects to recognize faces, read, and even watch television.

Acknowledgments This work was supported by the National Institute of Health – National Eye Institute (NEI), under NIH Grant EY012893 and by the Artificial Retina Project of Department of Energy (DOE Lab 01-14 Project). Authors are grateful to Chase Byers for his help in preparing the manuscript.

References

1. Census (1997) Americans with Disabilities: US Census Bureau
2. Heckenlively JR, Boughman J, Friedman L (1988) Diagnosis and classification of retinitis pigmentosa. In: Heckenlively JR (Ed) Retinitis pigmentosa, JB Lippincott Philadelphia, Philadelphia
3. Klein R, Klein BE, Jensen SC, et al. (1997) The five-year incidence and progression of age-related maculopathy: the beaver dam eye study. Ophthalmology 104:7–21
4. Klein R, Klein BE, Tomany SC, et al. (2002) Ten-year incidence and progression of age-related maculopathy: The Beaver Dam eye study. Ophthalmology 109:1767–1779
5. Greenberg R (2000) Visual prostheses: A review. Neuromodulation 3:161–165
6. Humayun MS, Freda R, Fine I, et al. (2005) Implanted intraocular retinal prosthesis in six blind subjects. IOVS 46:1144
7. Zrenner Z (2002) Will retinal implants restore vision? Science 295:1022–1025

8. Chow A, Chow V, Packo K, et al. (2004) The artificial silicon retina microchip for the treatment of vision loss from retinitis pigmentosa. Arch Ophthalmol 122:460–469
9. Rizzo J, Wyatt J, Humayun M, et al. (2001) Retinal prosthesis: an encouraging first decade with major challenges ahead. Ophthalmology 108:13–14
10. Normann RA, Maynard EM, Rousche PJ, et al. (1999) A neural interface for a cortical vision prosthesis. Vision Res 39:2577–2587
11. Hahn FJ, Chu WK (1984) Ocular volume measured by CT scans. Neuroradiology 26:419–420
12. Foulds WS (1976) Clinical significance of trans-scleral fluid transfer. Trans Ophthalmol Soc UK 96:290–308
13. Berman E (1991) Retina. In: Berman ER (ed) Biochemistry of the eye. Plenum Press, NY, pp 309–315
14. Manzanas LL, Pastor JC, Munoz R, et al. (1992) Intraocular irrigating solutions and vitrectomy-related changes (in protein, lactic and ascorbic acid) in rabbit vitreous. Ophthalmic Res 24:61–67
15. Kolb H, Fernandez E, Nelson R (2008) Webvision, the Organization of the Retina and Visual system, http://webvision.med.utah.edu, Accessed 10 December, 2008
16. Geddes LA, Baker LE (1967) The specific resistance of biological material-A compendium of data for the biomedical engineer and physiologist. Med Biol Eng 5:271–291
17. Greenberg R (1998) Analysis of electrical stimulation of the vertebrate retina: Work towards a retinal prosthesis. Johns Hopkins University, Baltimore, MD
18. Allen M (1990) Adjusting to visual impairment. J Ophthalmic Nurs Technol 9:47–51
19. Leinhaas MA, Hedstrom NJ (1994). Low vision: how to assess and treat its emotional impact. Geriatrics 49:53–56
20. Humayun MS, Weiland JD, Fujii GY, et al. (2003) Visual perception in a blind subject with a chronic microelectronic retinal prosthesis. Vision Res 43:2573–2581
21. Clausen J (1955) Visual sensations (Phosphenes) produced by AC sine wave stimulation. Acta Physiol Neurol Scand Supp 94:1–101
22. Brindley G, Lewin W (1968) The sensations produced by electrical stimulation of the visual cortex. J Physiol (London) 196:479–493
23. Weiland JD, Humayun MS (2008) Visual prosthesis. Proc IEEE 96:1076–1084
24. Niu J, Liu Y, Ren Q, et al. (2008) Vision implants: An electrical device will bring light to the blind. Sci China Ser F-Inf Sci 51:101–110
25. Pezaris JS, Reid RC (2007) Demonstration of artificial visual percepts generated through thalamic microstimulation. PNAS 104:7670–7675
26. Humayun M, de Juan E, Dagnelie G, et al. (1996) Visual perception elicited by electrical stimulation of the retina in blind humans. Arch Ophthalmol 114:40–46
27. Humayun M, de Juan E, Weiland J, et al. (1999) Pattern electrical stimulation of the human retina. Vision Res 39:2569–2576
28. Eckmiller R (1997) Learning retina implants with epiretinal contacts. Ophthalmic Res 29:281–289
29. Rizzo J, Wyatt J (1997) Prospects for a visual prosthesis. Neuroscientist 3:251–262.
30. Chow AY, Chow VY (1997) Subretinal electrical stimulation of the rabbit retina. Neurosci Lett 225:13–16
31. Zrenner, E, Miliczek KD, Gabel VP, et al. (1997) The development of subretinal microphotodiodes for replacement of degenerated photoreceptors. Ophthalmic Res 29:269–280
32. Wyatt J, Rizzo J (1996) Ocular implants for the blind. IEEE Spectrum 33:47–53
33. Rizzo JF, John Wyatt J, Loewenstein J, et al. (2003) Perceptual efficacy of electrical stimulation of human retina with a microelectrode array during short-term surgical trials. IOVS 44:5362–5369
34. Robblee LS, Rose TL (1990) Electrochemical guidelines for selection of protocols and electrode materials for neural stimulation, In: Agnew WF, McCreery DB (eds) Neural Prostheses fundamental studies, Prentice Hall, Englewood Cliffs, NJ, pp 26–66

35. Richard G, Hornig R, Keseru M, et al. (2007) Chronic epiretinal chip implant in blind patients with retinitis pigmentosa: Long-term clinical results. Presented at the ARVO Annu. Meeting, Ft. Lauderdale, FL
36. Hornig R, Zehnder T, Velokay-Parel M, et al. (2007) The IMI Retinal Implant System. In: Humayun MS, et al. (eds) Artificial Sight, Basic Research, Biomedical Engineering, and Clinical Advances, Chapter 6, Springer, New York, pp 111–128
37. Wickelgren I (2006) A Vision for the blind. Science 312:1124–1126
38. Meyer JW (2001) Retina Implant – A BioMEMS Challenge. The 11th International Conference on Solid-State Sensors and Actuators, June 10–14, 2001, Munich, Germany
39. Sailer H, Shinoda K, Blatsios G, et al. (2007) Investigation of thermal effects of infrared lasers on the rabbit retina: a study in the course of development of an active subretinal prosthesis. Graefe's Arch Clin Exp Ophthalmol 245:1169–1178
40. Zrenner E, Besch D, Bartz-Schmidt KU, et al. (2006) Subretinal chronic multi-electrode arrays in blind patients: Function testing and pattern recognition. Proceeding of 5th International meeting on substrate-integrated micro electrode arrays, July 4–7, 2006, Germany, p 90
41. Winter JO, Cogan SF, Rizzo JF (2007) Retinal prostheses: current challenges and future outlook. J Biomater Sci Polymer Ed 18:1031–1055
42. Graf H, Dollberg A, Spuntrup JS (2007) HDR Sub-retinal Implant for the Vision Impaired. In: High-Dynamic-Range (HDR) Vision. Springer Berlin Heidelberg, pp 141–146
43. Besch D, Sachs H, Szurman P, et al. (2008) Extraocular surgery for implantation of an active subretinal visual prosthesis with external connections: feasibility and outcome in seven patients. Br J Ophthalmol 92:1361–1368
44. Zrenner E (2007) Restoring neuroretinal function: New potentials. Doc Ophthalmol 115:56–59
45. Palanker D, Vankov A, Huie P, et al. (2005) Design of a high-resolution optoelectronic retinal prosthesis. J Neural Eng 2:105–120
46. Butterwick A, Huie P, Jones BW, et al. (2008) Effect of shape and coating of a subretinal prosthesis on its integration with the retina. Experimental Eye Research, doi:10.1016/j.exer.2008.09.018. Available online 10 October 2008
47. Loudin JD, Simanovskii DM, Vijayraghavan K (2007) Optoelectronic retinal prosthesis: System design and performance. J Neural Eng 4:S72–S84
48. Marc RE, Jones BW, Watt CB, et al. (2003) Neural remodeling in retinal degeneration. Prog Retin Eye Res 22:607–655
49. Chowdhury V, Morley JW, Coroneo MT (2005) Feasibility of extraocular stimulation for a retinal prosthesis. Can J Ophthalmol 40:563–572
50. Sakaguchi H, Fujikado T, Fang X, et al. (2004) Transretinal electrical stimulation with a suprachoroidal multichannel electrode in rabbit eyes. Jpn J Ophthalmol 48:256–261
51. Seo J, Zhou J, Kim E, et al. (2007) A Retinal Implant System Based on Flexible Polymer Microelectrode Array for Electrical Stimulation. In: Tombran-Tink J, Barnstable CJ and Rizzo JF (eds) Visual prosthesis and ophthalmic devices new hope in sight. Humana Press, New Jersey
52. Zhou JA, Woo SJ, Park SI, et al. (2008) A Suprachoroidal Electrical Retinal Stimulator Design for Long-Term Animal Experiments and In Vivo Assessment of Its Feasibility and Biocompatibility in Rabbits. J Biomedicine and Biotech doi:10.1155/2008/547428,10 pages.
53. An SK, Park SI, Jun SB, et al. (2007) Design for a simplified cochlear implant system. IEEE Trans Biomed Eng 54:973–982
54. Yamauchi Y, Franco LM, Jackson DJ, et al. (2005) Comparison of electrically evoked cortical potential thresholds generated with subretinal or suprachoroidal placement of a microelectrode array in the rabbit. J Neural Eng 2:S48–S56
55. Gerding H (2007) A new approach towards a minimal invasive retina implant. J Neural Eng 4:S30–S37

56. Brindley G, Donaldson P, Falconer M, et al. (1972) The extent of the region of occipital cortex that when stimulated gives phosphenes fixed in the visual field. J Physiol (London) 225:57–58
57. Dobelle WH, Mladejovsky MG, Girvin JP (1974). Artificial vision for the blind: electrical stimulation of visual cortex offers hope for a functional prosthesis. Science 183:440–444
58. Dobelle WH, Mladejovsky MG, Evans JR, et al. (1976) Braille' reading by a blind volunteer by visual cortex stimulation. Nature 259:111–112
59. Pollen DA (1975) Some perceptual effects of electrical stimulation of the visual cortex in man. In: Tower DB (ed) The nervous system, Vol 2: the clinical neurosciences. Raven Press, New York
60. Brindley G (1972) The variability of the human striate cortex. J Physiol (London) 225:1–3
61. Rousche P, Normann R (1998) Chronic recording capability of the Utah Intracortical Electrode array in cat sensory cortex. J Neurosci Methods 82:1–15
62. Hoverer A, Wise K (1994) A three-dimensional micro-electrode array for chronic neural recording. IEEE Trans Biomed Eng 41:1136–1146
63. Bak M, Girvin J, Hambrecht F, et al. (1990) Visual sensations produced by intracortical microstimulation of human occipital cortex. Med Biol Eng Comp 28:257–259
64. Schmidt EM, Bak MJ, Hambrecht FT, et al. (1996) Feasibility of a visual prosthesis for the blind based on intracortical micro stimulation of the visual cortex. Brain 119:507–522
65. Troyk P, Bak M, Berg J, et al. (2003) A model for intracortical visual prosthesis research. Artif Organs 27:1005–1015
66. Veraart C, Raftopoulos C, Mortimer J (1998) Visual sensations produced by optic nerve stimulation using an implanted self-sizing spiral cuff electrode. Brain Res 813:181–186
67. Veraart C, Delbeke J, Wanet-Defalque MC, et al. (1999) Chronic electrical stimulation of the optic nerve in a retinitis pigmentosa blind volunteer. Invest Ophthalmol Vis Sci 40:S783
68. Veraart C, Wanet-Defalque MC, Gerard B, et al. (2003) Pattern recognition with the optic nerve visual prosthesis. Artif Organs11:996–1004
69. Brelen ME, De Potter P, Gersdorff M, et al. (2006) Intraorbital implantation of a stimulating electrode for an optic nerve visual prosthesis, case report. J Neurosurg 104:593–597
70. Fang X, Sakaguchi H, Fujikado T (2005) Direct stimulation of optic nerve by electrodes implanted in optic disc of rabbit eyes. Graefe's Arch Clin Exp Ophthalmol 243:49–56
71. Nichols MF (1994) The challenges for hermetic encapsulation of implanted devices – A review. Biomed Eng 22:39–67
72. Babak Z, Von Arx JA, Dokmeci MR, et al. (1996) A hermetic glass-silicon micropackage with high- density on-chip feedthroughs for sensors and actuators. J Microelectromech Syst 5:166–177
73. Kanda Y, Aoshinma R, Takada A (1981) Blood compatibility of components and materials in silicon integrated circuits. Electron Lett 17:558–559
74. Yuen T, Agnew W, Bullara L, et al. (1990) Biocompatibility of electrodes and materials in the central nervous system. In: Agnew W, McCreery D (eds) Neural prostheses: Fundamental studies. Prentice Hall, Englewood Cliffs, NJ, pp 171–321
75. Terasawa Y, Uehara A, Yonezawa E, et al. (2008) A visual prosthesis with 100 electrodes featuring wireless signals and wireless power transmission. IEICE Electron Express 5:574–580
76. Wong CP (1995) Recent advances in hermetic equivalent flip-chip hybrid IC packaging of Microelectronics. Mater Chem Phys 42:25–30
77. Stieglitz T, Haberer W, Lau C, et al. (2004) Development of an inductively coupled epiretinal visual prosthesis. Proceedings of the 26th Annul International Conference of the IEEE EMBS, San Francisco, pp 4178–4181
78. Rodger DC, Fong AJ, Li W, et al. (2008) Flexible parylene-based multielectrode array technology for high-density neural stimulation and recording. Sens Actuators B 132: 449–460

79. Auciello O (2005) Science and Technology of Ultrananocrystalline Diamond Films as Hermetic Bioinert Coatings for Artificial Retina Microchip Encapsulation. Proceedings of the Second DOE International Symposium on Artificial Sight, April 29, 2005, Ft. Lauderdale, Florida
80. Xiao X, Wang J, Liu C, et al. (2006) In vitro and in vivo evaluation of ultrananocrystalline diamond for coating of implantable retinal microchips. J Biomed Mater Res B: Appl Biomater 77:273–281
81. Zhou D, Mech B, Greenberg R (2000) Accelerated corrosion tests on Silicon wafers for implantable medical devices. Proceedings of the 198th Electrochemical Society Meeting, October, 2000, p 363
82. Meyer JU (2002) Retina implant – A bioMEMS challenge. Sens Actualors A-Phys 97–98:1–9
83. Montezuma S, Loewenstein J, Scholz C, et al. (2006) Biocompatibility of materials implanted into the subretinal space of Yucatan pigs. Invest Ophthal Vis Sci 47:3514–3522
84. Scholz C (2007) Perspectives on: Materials Aspects for Retinal Prostheses. J Bioact Compat Polym 22:539–568
85. Sweitzer R, Montezuma S, Rizzo J, et al. (2006) Evaluation of subretinal implants coated with amorphous aluminum oxide and diamond-like carbon. J Biodegradable Compat Polym 21:5–22
86. Cogan SF, Edell D, Guzelian A, et al. (2003) Plasma-enhanced chemical vapor deposited silicon carbide as an implantable dielectric coating. J Biomedical Mater Res A67: 856–867
87. Xiao X, Wang J, Carlisle JA, et al. (2005) Ultrananocrystalline diamond as a hermetic, bio-inert coating for implantable medical devices. Proceeding of Materials Research Society Meeting, March 28–April 1, 2005, San Francisco
88. Liu W, Sivaprakasam M, Wang G, et al. (2007) Challenges in realizing a chronic high-resolution retinal prosthesis. In: Humayun MS, et al. (Eds.) Artificial Sight, Basic Research, Biomedical Engineering, and Clinical Advances, Chapter 7, Springer, New York, pp 129–150
89. Shah S, Hines A, Zhou D, et al. (2007) Electrical properties of retinal-electrode interface. J Neural Eng 4:S24–S29
90. Piyathaisere DV, Eyal M, Chen S, et al. (2003) Heat effects on the retina. Ophthalmic Surg Lasers Imaging 34:114–120
91. Gosalia K, Weiland J, Humayun M, et al. (2004) Thermal elevation in the human eye and head due to the operation of a retinal prosthesis. IEEE Trans Biomed Eng 51:1469–1477
92. Klomp GF, Womack MV, Dobelle WH (1977) Fabrication of large arrays of cortical electrodes for use in man. J Biomed Mater Res 11:347–364
93. McCreery D, Lossinsky A, Pikov V, et al. (2006) Microelectrode array for chronic deep-brain microstimulation and recording. IEEE Trans Biomed Eng 53(4):726–737
94. Kim ET, Seo JM, Se Woo SJ, et al. (2008) Fabrication of pillar shaped electrode arrays for artificial retinal implants. Sensors 8:5845–5856
95. Gerding H, Ezelius H, Niggemann B (2006) The minimal invasive Retinal Implant (miRI) project: a novel approach towards the restoration of vision in patients with degenerative retinal diseases (ARVO abstract 3214)
96. Majji A, Humayun M, Weiland J, et al. (1999) Long-term histological and electrophysiological results of an inactive epiretinal electrode array implantation in dogs. Invest Ophthalmol Vis Sci 40:2073–2081
97. Yanai D, Weiland JD, Mahadevappa M, et al. (2007) Visual performance using a retinal prosthesis in three subjects with retinitis pigmentosa. Amer J Ophthalmol 143:820–827
98. Hesse L, Schanze T, Wilms M, et al. (2000) Implantation of retina stimulation electrodes and recording of electrical stimulation responses in the visual cortex of the cat. Graefe's Arch Clin Exp Ophthalmol 238:840–845
99. Stieglitz T, Beutel H, Schuettler M, et al. (2000) Micromachined, polyimide-based devices for flexible neural interfaces. Biomed Microdevices 2:283–294

100. Sachs HG, Gabel V (2004) Retinal replacement-the development of microelectronic retinal prostheses experience with subretinal implants and new aspects. Graefe's Arch Clin Exp Ophthalmol 242:717–723
101. Rodger DC, Weiland JD, Humayun MS, et al. (2006) Scalable high lead-count parylene package for retinal prostheses. Sens actuators B Chem 117:107–114
102. Rodger DC, Li W, Ameri H (2007) Dual-metal-layer parylene-based flexible electrode arrays for intraocular retinal prostheses. Invest Ophthalmol Vis Sci 48:E-Abstract 657
103. Terasawa Y, Tashiro H, Uehara A (2006) The development of a multichannel electrode array for retinal prostheses. J Artif Organs 9:263–266
104. Cui X, Zhou D (2007) Poly(3,4-ethylenedioxythiophene) for chronic neural stimulation. IEEE Trans Neural Syst Rehabil Eng 15:502–508
105. Weiland JD, Liu WT, Humayan MS (2005) Retinal Prosthesis. Annu Rev Biomed Eng 7:361–401
106. Rose TL, Kelliher EM, Robblee LS (1985) Assessment of capacitor electrodes for intracortical neural stimulation. J Neurosci Methods 12:181–193
107. Guyton DL, Hambrecht FT (1974) Theory and design of capacitor electrodes for chronic stimulation. Med Biol Eng 9:613–620
108. Zhou D, Greenberg, R (2001) Tantalum capacitive microelectrode array for neural prosthesis. In: Butler M, Vanysek P, Yamazoe N (eds) Chemical and biological sensors and analytical methods II. Electrochemical Society, Pennington, New Jersey, pp 622–629
109. Janders M, Egert U, Stelzle M, et al. (1996) Novel thin film titanium nitride microelectrodes with excellent charge transfer capability for cell stimulation and sensing applications. 18th Annual international Conference of the IEEE Engineering in medicine and biology society, Amsterdam, pp 245–247
110. Schaldach M, Hubmann M, Weikl A, et al. (1990) Sputter-deposited TiN electrode coatings for superior sensing and pacing performance. Pace 3:1891–1895
111. Meyer JU, Stieglitz T, Scholz O, et al. (2001) High density interconnects and flexible hybrid assemblies for active biomedical implants. IEEE Trans Adv Packging 24:366–374
112. Guenther E, Troger B, Schlosshauer B, et el. (1999) Long-term survival of retinal cell cultures on retinal implant materials. Vision Res 39:3988–3994
113. Zhou D, Greenberg R (2003) Electrochemical Characterization of Titanium Nitride Microelectrode Arrays for Charge-Injection Applications. Proceedings of 25th Annual International Conference of the IEEE Engineering in Medicine and Biology Society, Cancun, paper1.2.4-1 (CD ROM)
114. Cogan SF (2008) Neural Stimulation and Recording Electrodes. Annu Rev Biomed Eng 10:14.1–14.35
115. Cogan SF, Guzelian AA, Agnew WF, et al. (2004) Over-pulsing degrades activated iridium oxide films used for intracortical neural stimulation. J Neurosci Methods 137:141–150
116. Cogan SF, Troyk RP, Ehrlich J, et al. (2005) In vitro comparison of the charge-injection limits of activated iridium Oxide (AIROF) and Platinum-Iridium Microelectrodes. IEEE Trans Biomed Eng 52:1612–1614
117. Zhou D (2005) Platinum electrode and method for manufacturing the same. US Patent 6,974,533
118. Hung A, Zhou D, Greenberg R, et al. (2002) Micromachined Electrodes for High Density Neural Stimulation Systems, 2nd Annual International, IEEE-EMBS Special Topic Conference on Microtechnologies in Medicine & Biology, Madison, Wisconsin, pp 76–79
119. Zhou D, Greenberg R (2005) Microsensors and microbiosensors for retinal implants. Front Biosci 10:166–179
120. Walter P, Szurman P, Vobig M, et al. (1999) Successful long-term implantation of electrically inactive epiretinal microelectrode arrays in rabbits. Retina 19:546–552
121. Margalit E, Fujii GY, Lai JC, et al. (2000) Bioadhesives for intraocular use. Retina 20:469–477

122. Taneri S, Bollmann FP, Uhlig C, et al. (1999) The retina implant—project: in vitro and in vivo testing of different tack types for intraocular fixation of retina implants Invest. Ophthalmol Vis Sci 40:733
123. Berk H, Vobig M, Walter P, et al. (1999) Long-term visual function after tach fixation of epiretinal stimulators in rabbits. IOVS 40:S732
124. Sachs HG, Schanze T, Wilms M, et al. (2004) Subretinal implantation and testing of polyimide film electrodes in cats. Graefe's Arch Clin Exp Ophthalmol 243:464–468
125. McMahon MJ, Caspi A, Dorn JD, et al. (2007) Spatial vision in blind subjects implanted with the Second Sight retinal prosthesis. Invest Ophthalmol Vis Sci 48: E-Abstract 4443.

Visual Prosthesis for Optic Nerve Stimulation

Xiaohong Sui, Liming Li, Xinyu Chai, Kaijie Wu, Chuanqing Zhou, Xiaodong Sun, Xun Xu, Xiaoxin Li, and Qiushi Ren

Abstract The C-Sight visual prosthesis is based on optical nerve stimulation with a penetrating electrode array. A silicon-based microprobe by MEMS process techniques and Pt–Ir microwire arrays by electrochemical etching were fabricated in our project. Noise and impedance analyses were applied to optimize the electrode configuration. A multichannel microcurrent neural electrical stimulator and an implantable CMOS-based micro-camera were developed for neural stimulation and image acquisition, respectively, with a DSP-based system processing the captured image. Electrical evoked potentials (EEPs) from rabbit models were recorded using multichannel stainless-steel screws mounted on the primary visual cortex. The mean charge threshold density was $20.99 \pm 5.52\ \mu C/cm^2$ considering the exposed surface of the stimulating electrode. Current threshold decreased as the pulse duration of the stimulus increased while the corresponding charge threshold increased. The amplitude of P1 increased when the pulse duration increased from 0.4 to 1.0 ms while the latency of P1 changed little. Experiments also showed that different distribution maps of EEPs were elicited by different pairs of stimulating electrodes. The stimulating electrode pair along the axis of the optic nerve elicited cortical responses with much lower thresholds than that perpendicular to the axis of the optic nerve. The visual prosthesis with stimulating electrodes penetrating into the optic nerve has been validated in animal experiments.

1 Introduction

In the past several years, many approaches have been pursued to provide neural electrical simulation at various positions along the visual pathway, such as the retina [1–4], suprachoroid [5], visual cortex [6, 7], or optic nerve

Q. Ren (✉)
Institute for Laser Medicine and Biophotonics, Department of Biomedical Engineering, Shanghai Jiao Tong University, Shanghai 200240, China
e-mail: renqsh@sjtu.edu.cn

D.D. Zhou, E. Greenbaum (eds.), *Implantable Neural Prostheses 1*,
Biological and Medical Physics, Biomedical Engineering,
DOI 10.1007/978-0-387-77261-5_2,

[8, 9] to restore the vision of blind patients. One issue [10] with electrically stimulating the visual cortex or retina is that the visual field is represented over a relatively large area, making coverage of the entire visual field nearly impossible with current electrode array technologies. In the visual pathway, the optic nerve is one place where the entire visual field is represented in a relatively small area.

The ultimate goal of artificial vision systems, also known as vision prostheses [10], is to artificially produce visual perception in individuals with profound loss of vision due to disease or injury, that can be used to perform activities for which current assistive technologies have severe limitations. Such activities include reading text, recognizing faces, negotiating unfamiliar spaces, etc. Although the most significant difference between these approaches is the interface to the nervous system, all of them share a common set of components, such as a micro-camera, a visual information extraction and processing system, a power and information transmission system, a neural electrical simulator and electrode arrays [11].

The C-Sight (Chinese Project for Sight) is the first multidisciplinary research project on visual prosthesis in China funded by the Chinese Ministry of Science and Technology under the National Key Basic Research Program (973 Program, 2005CB724300) and by the Science and Technology Commission of Shanghai Municipality(STCSM). The C-Sight project aims at developing an implantable visual prosthesis for optic nerve stimulation by penetrating microelectrode arrays (MEAs) to restore helpful vision for RP (retinitis pigmentosa) and AMD (age-related macular degeneration) patients.

Visual information is transmitted via the optic nerve composed of millions of axons of ganglion cells. Visual phosphenes are created during optic nerve stimulation by cuff or penetrating microelectrode arrays. In 1998, Veraart et al. proved that electrical stimulation of the optic nerve in a 59-year-old volunteer with retinitis pigmentosa could elicit phosphenes. The contact spiral cuff electrode was used in their experiment. However, the spatial resolution of recovered vision was limited because surface stimulating electrodes were used. To improve spatial resolution, penetrating microelectrode arrays are invasively inserted into the optic nerve with endurable tissue trauma. Optic nerve visual restoration by penetrating microelectrode arrays has been verified in our animal experiments. With processing techniques advancing, the size of the microelectrode arrays can be minimized greatly, resulting in reduced optic nerve damage and high spatial resolution.

In the C-Sight project, we proposed specific penetrating microelectrode arrays as the neural interface to transmit the outside encoded electrical stimuli into the optic nerve bundles for visual recovery. Figure 1 shows the schematic diagram of the C-Sight approach and the details are presented in Fig. 2.

The total visual prosthesis was composed of two parts: outside the body and inside the body. In view of Fig. 2, the outer part included image capturing, processing, and transmitting. The surrounding images are captured by a

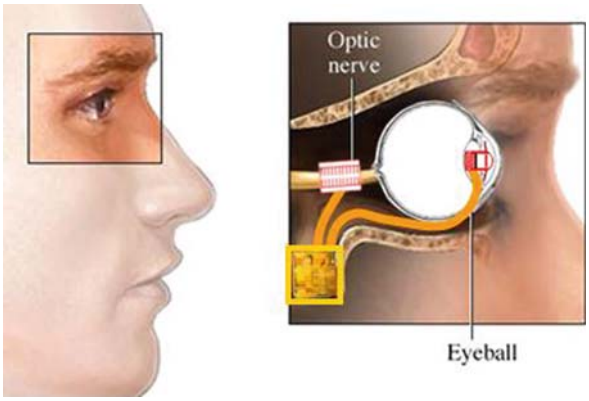

Fig. 1 Optic nerve visual prosthesis using penetrating microelectrode arrays

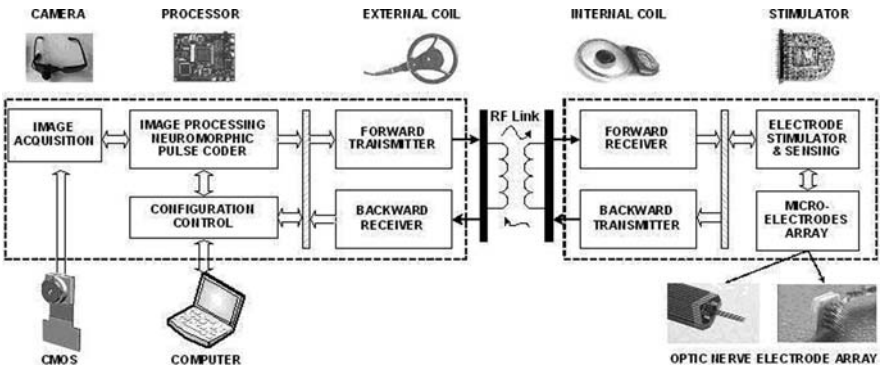

Fig. 2 Block diagram of optic nerve stimulation using penetrating microelectrode arrays

CMOS micro-camera implanted into the lens of the RP or AMD patients. This method will enhance the synchronization between outside images and visual phosphenes compared with the glasses-based image shot. Then, the key features of images are extracted from the original scenes by advanced image processing algorithms and encoded into trains of digital signals with a specific spatiotemporal stimulation pattern. These electrical pulses are forwarded by radio transmission. In the inner part, the internal coil transfers the received radio power and data to the implanted microcurrent stimulator which is electrically connected to the implanted microelectrode arrays. Considering these two parts, the outside images can be transformed into multichannel microcurrent pulses to stimulate the optic nerve where action potentials are generated and conveyed to the visual cortex.

2 Penetrating Microelectrode Arrays

The implantable microelectrodes are considered in different ways such as biocompatibility, tissue trauma, uniformity, low cost, and so on. Metal microwires and silicon microelectrode arrays are usually selected as the neural interface for neural recording and stimulation. Metal microwires made of stainless steel, tungsten, and platinum/iridium (Pt/Ir) alloy were prevalent in the early stage of neural prosthesis applications. With the development of MEMS (micro-electro-mechanical system) micromachining technique, silicon-based microelectrodes can be fabricated in batches and have satisfactory uniformity, high yield, and low cost. Several different types of MEAs were fabricated in our group.

2.1 Noise and Impedance Analyses

The in vivo neural recording or stimulating setup is unavoidably affected by main-frequency disturbance, background noise, and thermal (Johnson) noise of the microelectrode. Disturbance from the main frequency can be eliminated by a shielded cover, and the background noise results from respiration and excitation of thousands of neurons far from the exposed microelectrode sites and closely relates to the animal conditions, and so the thermal noise analysis is detailed here. After the microelectrode was implanted in vivo, the exposed metal sites were electrically related with the physiological saline solution. The equivalent circuit of metal–electrolyte interface [12] was illustrated in Fig. 3. Rmet denotes the interconnecting metal wire resistance on the order of tens of ohms, and Ce and Re denote the double-layer capacitance and resistance, respectively. E is the half-cell voltage at the metal–electrolyte interface.

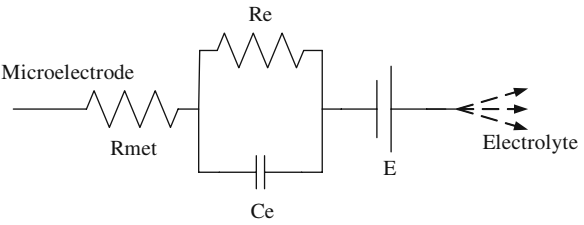

Fig. 3 Equivalent circuit of microelectrode–electrolyte interface

According to Fig. 3, thermal noise was dominated by Rmet, Re–Ce network. Rmet and the resulted PSD (power spectral density) of thermal noise were shown in equations (1) and (2), respectively.

$$Rmet = \rho \times \frac{L}{S} \tag{1}$$

$$S(f) = 4kTRmet \tag{2}$$

where $k(= 1.38\times10–23$ J/K) is the Boltzmann's constant, T is the absolute temperature with the unit of Kelvin, ρ is the metal resistivity, L is the connecting wire length of several millimeters, and S denotes the cross-section area. The thermal noise from the small-value metal resistance Rmet is neglected. Therefore, the noise is mainly produced from Re–Ce network shown in Fig. 4.

Figure 4(a) shows the practical parallel network of resistor and capacitor,

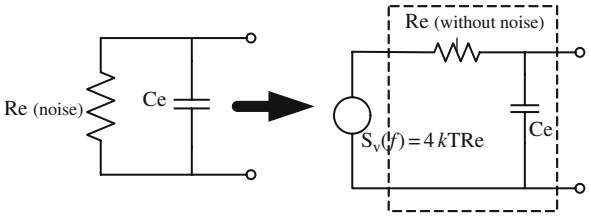

Fig. 4 Noise-analysis model of Re–Ce network

and Fig. 4(b) is the equivalent noise model of this network considering thermal noise from Re. The dashed-line block denotes the ideal network. PSD of Re and the transfer function $h(f)$ are, respectively, expressed in equations (3) and (4), PSD of the output terminals $S_{\text{out}}(f) = S_{\text{v}}(f)|h(f)|^2$ is shown in equation (5), and the total noise $P_{\text{n,out}}$ within the total frequency range is shown in equation (6)

$$S_v(f) = 4kT\,\text{Re} \tag{3}$$

$$h(f) = \frac{1}{1 + j2\pi f\,\text{Re}Ce} \tag{4}$$

$$S_{out}(f) = \frac{4kT\,\text{Re}}{1 + 4\pi^2\text{Re}^2Ce^2f^2} \tag{5}$$

$$P_{n,out} = \int_0^\infty S_{out}(f)df = \frac{kT}{Ce} \tag{6}$$

The unit of kT/Ce is V^2. $(kT/\text{Ce})^{1/2}$ is the equivalent noise voltage with units of Vrms. It was clear that the equivalent noise voltage of the Re–Ce network within the total frequency range was in inverse proportion to Ce. With settled temperature, increasing Ce can reduce thermal noise voltage, which means increasing the site area of the multichannel microelectrode with planar metal sites exposed. At body temperature of 310 K, the equivalent thermal noise voltage at the total frequency range was 65.4 μVrms with Ce of 1 pF.

Thermal noise analyses resulted in the size selection of the exposed planar site, and the impedance Z was mainly determined from Re and Ce in equation (7).

$$Z = \frac{\mathrm{Re}}{1 + j2\pi f \mathrm{Re}Ce} \tag{7}$$

In view of equations (6) and (7), low thermal noise means large signal-to-noise ratio (SNR), large site size, low impedance, and low spatial resolution.

Microelectrodes for neural stimulation possessed satisfactory charge transmission ability and large double-layer capacitance resulting in low impedance of several to tens of kΩ. Meanwhile the selectivity was affected, so the exposed site area must be compromised to satisfy the requirements of low thermal noise or high-sensitivity and high-spatial resolution or high selectivity.

2.2 The Tungsten Shafts

Tips of the implanted tungsten microwires were electrochemically etched with a tungsten probe as the working electrode (anode) and a carbon rod as the counter electrode (cathode). A 1 mol/l NaOH solution was used as the electrolyte. The experiment setup included a voltage power source, a switch, an ammeter, and an electrochemical cell with a pair of electrodes as shown in Fig. 5. The applied AC voltage was 50 Hz of frequency and 6 V of amplitude. After shaping a certain taper, the probe was insulated by Teflon and a 200 μm-long tip was exposed. The impedance characteristics were measured by the Precision LRC Meter Agilent

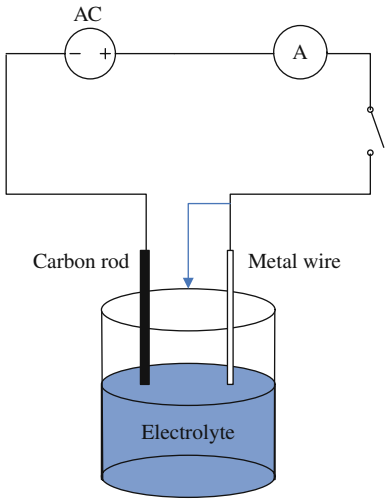

Fig. 5 Electrochemical etching setup

E4980A with a three-electrode method at room temperature. The typical impedance at 1 kHz was 10 kΩ.

Five microelectrodes were mounted on a 0.4-mm-thick plastic pedestal. The size of the pedestal was 2.5 mm long and 1.5 mm wide with the electrodes spaced 275 μm apart from the center. The shaft of the electrodes was 100 μm in diameter with one end etched electrolytically to a penetrating cone-shaped tip with an included angle of 15° and the radius of curvature of 0.5–0.7 μm. This microelectrode array had a height of 0.5 μm. The electrode was insulated with Teflon with the tip exposed to yield a surface area of $3155 \pm 100\ \mu m^2$. The lead cables were enameled wires and were connected to a 6-pin connecter. The electrode array was encapsulated with medical grade silicon gel in an innovative designed mold, which was hemispheroidal with a 3-mm-wide and 2-mm-deep notch across the axis on the surface of the mold. The radius of the hemispheroid was 12 mm in accordance with the size of the human eye ball (Fig. 6). Due to the non-stable physical and chemical characteristics of tungsten material, the microelectrode array based on tungsten microwires was only for acute experiment purposes.

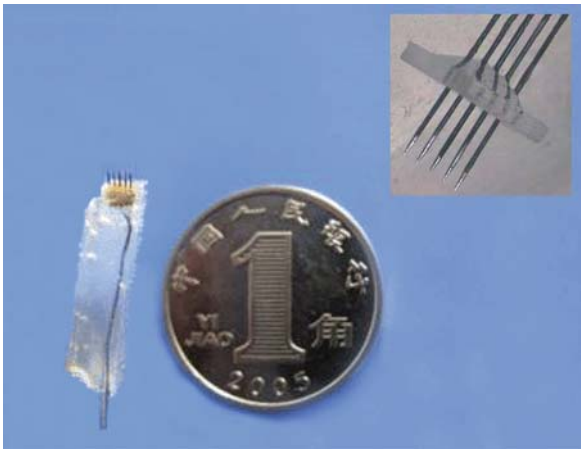

Fig. 6 Five probes were mounted on the substrate with the enameled wire connected individually: the zoom-in penetrating microprobes were shown in the *upper right corner*

2.3 The Pt/Ir Alloy Shafts

In order to improve the biocompatibility and biostability of the implanted microelectrode array, noble metals platinum, and iridium were considered as the stimulating metal material. With the addition of iridium, hardness can be enhanced for optic nerve penetration. The Pt/Ir microelectrode arrays were also selected in our lab.

Different kinds of FMAs (floating multielectrode arrays) were customized by Micro-Probe Incorporated in the United States in the optic nerve stimulation

experiment. The lengths of microprobes ranged from 0.80 mm to 1.50 mm, and the impedance was 10 kΩ at 1 kHz shown in Fig. 7(a). Figure 7(b) shows the 1×5 electrode array (100% Ir) with the probe lengths steeply increasing from 0.90 mm to 1.50 mm, and the exposed tip length of 100 μm. Each shaft had an impedance of 10 kΩ. Figure 7(c) shows the 16-shaft FMA (70%Pt-30%Ir) with the shaft length of 0.2 mm and per-shaft impedance of 20 kΩ.

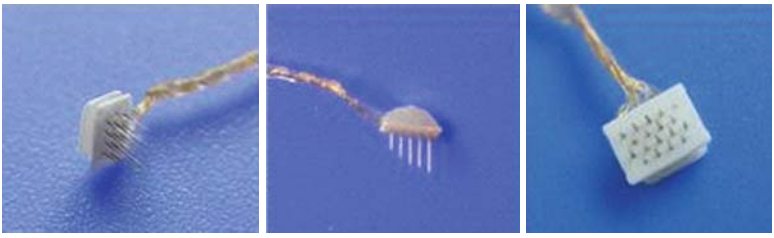

(a) (b) (c)

Fig. 7 (**a**) Thirteen probes with length from 0.80 mm to 1.50 mm; (**b**) five probes with length from 0.90 mm to 0.50 mm; (**c**) sixteen probes with the same length of 0.2 mm

2.4 Silicon-Based Microelectrode Arrays

With the development of the MEMS (micro-electro-mechanical system) micromachining technique, silicon-based microelectrodes can be fabricated in batches and have satisfactory uniformity, high yield, and low cost. The silicon microelectrodes bear relatively good flexibility and mechanical strength compared with silicon/silicon dioxide ones [13, 14]. Si (silicon), SiO_2 (silicon dioxide), and Si_3N_4 (silicon nitride) are biocompatible with biological tissue and suitable for in vivo application [15]. As a result, silicon-based microelectrodes have attracted much interest in recent years. Two- or three-dimensional silicon microelectrodes have been fabricated [13–16] in Michigan and Utah. The silicon microelectrodes or microprobes can be fabricated based on a single-crystal silicon or SOI (silicon-on-insulator) wafer. Based on the single-crystal silicon substrate, a deep p^{++} boron diffusion process is usually included to determine the outline of the silicon microelectrodes with higher concentration grades between the p^{++} layer and the silicon substrate. This presents rigid requirements for the diffusion process. In contrast, based on the SOI wafer, the top silicon or silicon device layer determines the thickness of the silicon microelectrode with precisely controlled uniformity. Besides, the buried SiO_2 layer is an etch stop while releasing the microelectrode.

The original SOI wafer was manufactured by bonding a top silicon layer of 15 μm, a buried silicon dioxide layer of 1 μm, and a bottom silicon layer of 500 μm. The fabrication process is detailed as follows: (a) Lower 3000 Å silicon nitride was deposited on the SOI wafer by plasma-enhanced chemical vapor deposition (PECVD) to electrically separate the top silicon from the SOI wafer and metal connecting wires; (b) Lower titanium/gold (Ti/Au) of 1000 Å/3000 Å

was sputtered on the lower silicon dioxide and patterned as conductor traces by diluted buffered oxide etching (BOE) and gold corrosive, respectively. Then the probe was annealed at 380°C for 40 min; (c) Upper 3000Å SiO_2 was deposited by plasma-enhanced chemical vapor deposition to insulate the metal layer from the tissue solution. (d) The upper SiO_2 layer was etched by BOE to open Φ-6 μm contact holes near the tip and bond pads at the rear. (e) According to step (b), seven Φ-10-μm circular recording sites were formed with the central space of 120 μm. (f) Thick photoresist was used as the mask layer, and the horizontal architecture of the microelectrode was determined by an ICP (inductively coupled plasma) dry etching process technique. (g) The wafer was thinned to 200 μm by physical ablation of the bottom silicon and adhered to a glass plate by black wax. Then the wafer could be further thinned to 50 μm by BOE solution. (h) The wax was removed and the top side of wafer was protected and adhered to another silicon wafer by photoresist. The bottom silicon layer of the wafer was plasma dry etched using gas SF6. Because of the low selectivity ratio between silicon and silicon dioxide, the buried silicon dioxide layer was removed at the same time. Consequently, the individual silicon microelectrodes were completed after performing photoresist-removing techniques using acetone.

Figure 8 shows the silicon microelectrode. The released microelectrode is shown in Fig. 9.

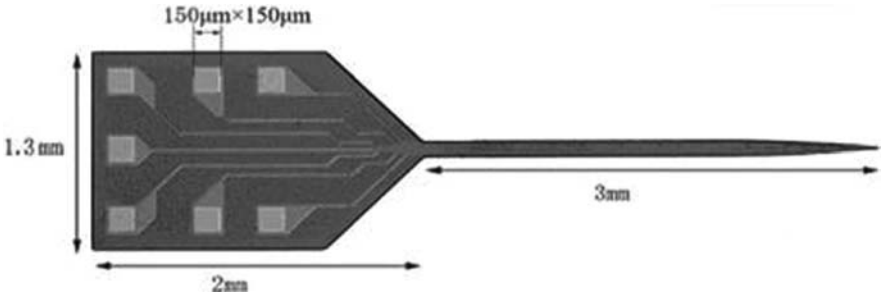

Fig. 8 The top view of silicon-based MEAs after ICP etching: single probe with seven sites

Fig. 9 The released SOI-based silicon microelectrodes

According to Figs. 8 and 9, seven bond pads corresponding to seven different recording sites are clearly shown with the lateral dimensions marked. The probe shank is 3 mm long and 100 μm wide, and the seven recording sites are located in the center of the shank within the range of 1 mm from the tip. Since the shank is narrowed down like a sharp-edged sword near the tip, it is able to penetrate into the optic nerve with the tip angle of 6°.

3 Neural Electrical Stimulator

Some electrical stimulators for chronic pain treatment use battery power and rely on repeated surgery to replace the battery. Alternatively, it is possible to power implants without a physical connection by using an inductive link, in which current through a primary coil driven by a signal and energy source induces current in a secondary coil [16]. In this design, the external and internal parts exchange information by radio frequency (RF) telemetry.

The neural stimulator consists of three main parts: the communication unit, the processing and control unit, and the electrode driver unit. Figure 10 is the schematic architecture of the micro-stimulator.

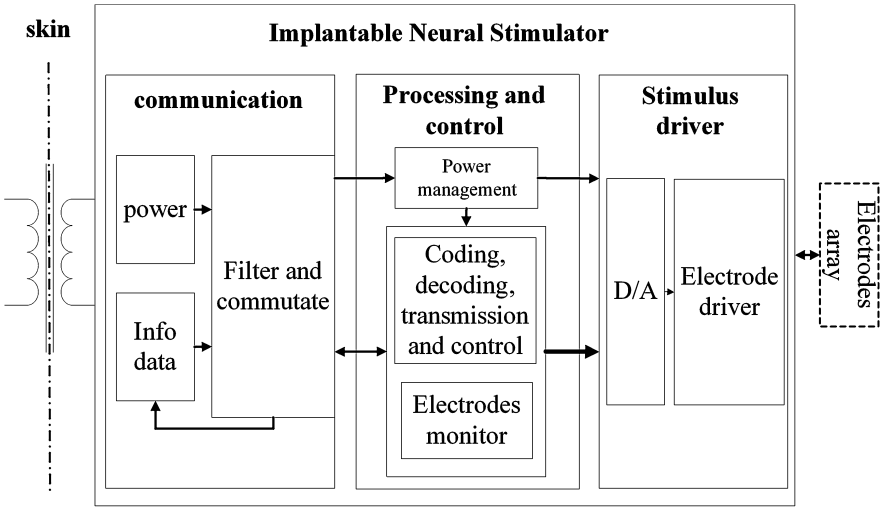

Fig. 10 Schematic architecture of the neural electrical stimulator

3.1 Communication Unit

The communication unit receives power and data signal packets. Similarly, when the state information of electrode arrays is needed, the state packets are sent out by this unit too.

A high-efficiency Class-E amplifier is used to transmit power to the internal unit. The power is generated by the induced RF signal. The voltage swing of the

induced signal is as high as the need of the stimulator. Therefore, the signal must be rectified and regulated before it is delivered to the other parts of the stimulator.

The control data and stimulus information are provided by the external part. The valid packets in the system protocol include synchronization, start, data, and end packets. The basic format of each packet is: the start bit (1bit, 0), the information bits (8bits, include control and data information), the end bit (1bit, 1). The data packet format follows the format shown in Fig. 11.

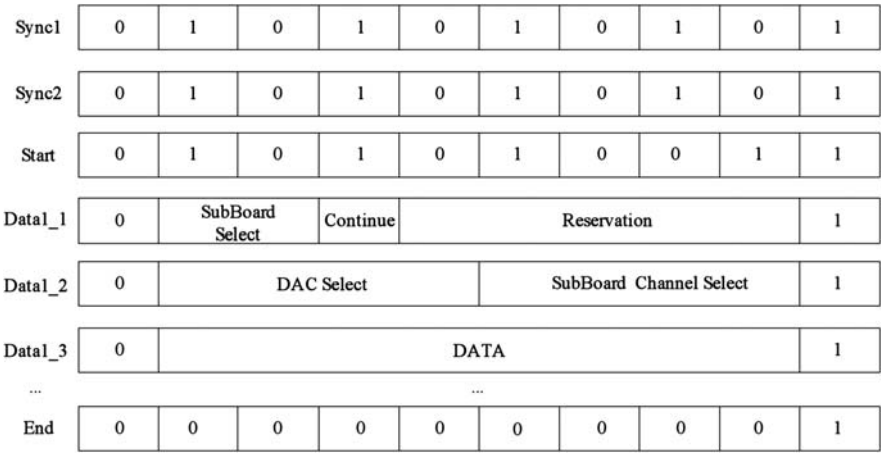

Fig. 11 Data packet format for the stimulator

As we all know, the information after image acquisition and processing is transferred from the external part to the internal stimulator according to the format of the frame. Each frame will consist of many data packets. If the continue bit is set to 1, it means the process of transmission needs transfer control and data information continuously. After finishing the transmission of information of one frame, the end packet will be added in the transmitting sequence. It shows the system has finished the transmission of one frame image. If we want to transfer the next frame, the synchronization packets should be sent over again.

3.2 Processing and Control Unit

The processing and control unit shown in Fig. 12 is responsible for managing power, coding, decoding data information, and monitoring the state of electrode array. Considering the feasibility of integration, the main function of the processing and control unit is implemented based on FPGA.

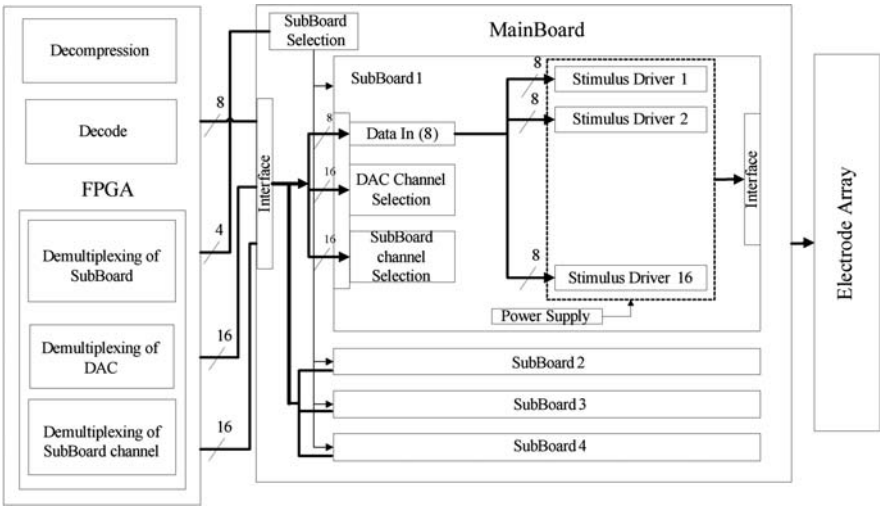

Fig. 12 Schematic of the main control circuit

The parameter collector also measures power supply voltage, electrode resistance, interference between electrodes, and other important internal parameters. These messages can be transmitted back to the outer controller by the reverse data transmission module. This part of the function is under research and development.

3.3 Electrode Driver Unit

The electrode driver unit converts digital signals into analog signals by a digital analog converter (DAC) and supplies biphasic current pulses of variable amplitudes and durations to the electrode array with penetrating electrodes.

Because the design style of the subboard and mainboard is used in the electrode driver unit, four subboards are plugged into four slots on the mainboard vertically. On each subboard, there is one DAC which has a 16-channel output and two octal SPST switches which are used to control which electrode is selected. Therefore, we need to design the circuit to control 64 electrodes aggregately. The schematic of the electrode driver unit is shown in Fig. 13.

To avoid stimulation current flowing to other electrodes freely, it is necessary that only two electrodes generate stimulation current every time. Besides, the accumulation of charge would induce a permanent injury in human tissues. According to the experiment results of Claude Veraart et al. [17, 18], stimulation based on the optic nerve needs biphasic current pulses. Therefore, two-phase pulse stimulation is adopted to balance the total charge. Fig. 14 shows the current stimulation pulses.

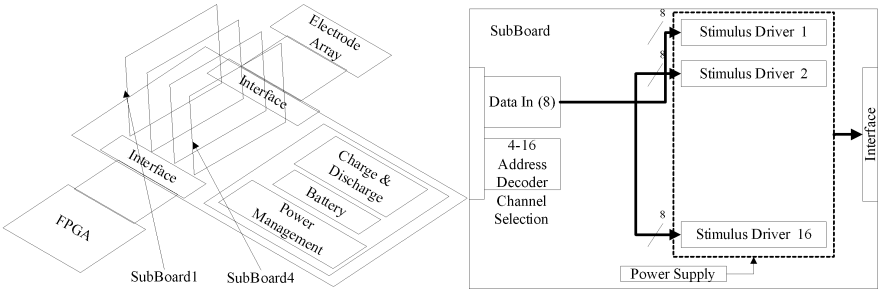

Fig. 13 Schematic of electrode driver unit

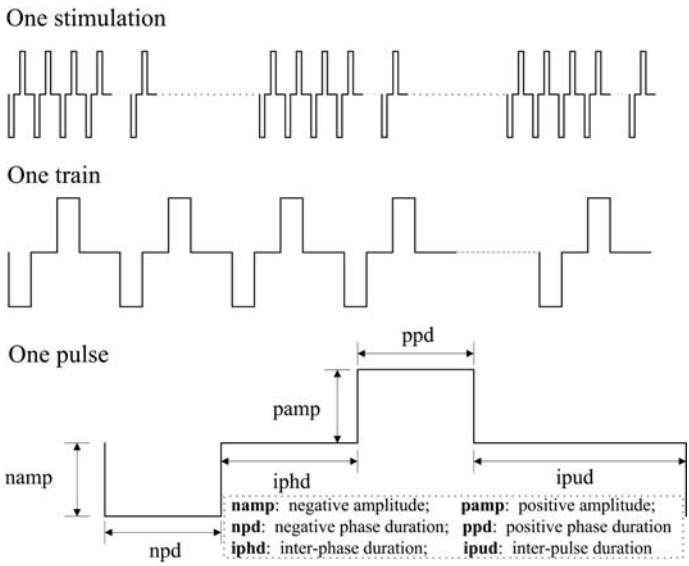

Fig. 14 Current stimulation pulses

The design is capable of controlling the electrode driver with the style of subboard and mainboard to generate biphasic current, from several μA up to several mA variable amplitudes, from tens of microseconds (μs) up to hundreds of microseconds (μs) in pulse duration and single or multiple pulses train. In the project, the main control unit uses FPGA to realize the decompression, coding, decoding, and demultiplexing control. In our design, it can offer single pulse or multiple pulse sequences which vary in range from 10 μA to 4 mA current amplitudes, from 25 to 400 μs duration, from 40 to 350 Hz frequency, etc. Due to the use of demultiplexing, we cannot give the 64 electrodes stimulus signal simultaneously. As in many imaging systems, for perceiving a continuous image, the retinal stimulation needs to be above a specific rate in order to

achieve flicker-free vision. The threshold stimulation rate above which the image appears continuous is between 40 and 50 Hz [19]. This parameter provides the opportunity to demultiplex one output from DAC to drive multiple stimulus drivers.

4 Image Acquisition and Processing

The visual information processing system is a very important portion of the application of the visual prosthesis. It is necessary to research and develop the hardware of the image processing system dedicated to visual prostheses as well as the image processing strategies applying to visual prostheses.

From Figs. 2 and 15, it is clear that the micro-camera and image processor are absolutely essential parts of visual prosthesis in our project.

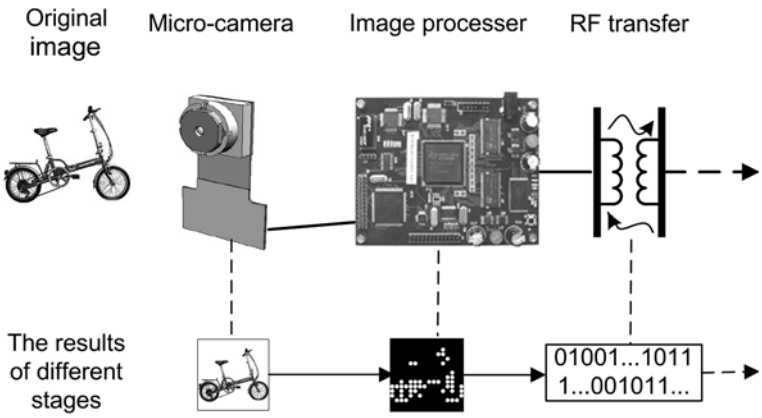

Fig. 15 Schematic of image acquisition and processing system

4.1 Image Acquisition

As the prosthesis will be implanted into the human eye, all the components should be small in size with low weight and low power dissipation. A number of image acquisition devices or mini-cameras are available and suitable for this application, such as charge-coupled device (CCD) or complementary metal-oxide semiconductor (CMOS) cameras. Although a CMOS camera is more susceptible to noise and has lower light sensitivity than CCD, it is more suitable for implantable visual prosthesis applications with some crucial features, such as lower power dissipation, small size, and camera-on-a-chip integration. Based on such reasons, the OV6650FS (Omnivision Co.) was chosen as the photo-

sensor in our image acquisition system, for it is the smallest CMOS camera on the market and has relatively low power dissipation. As the former research mentioned, Stiles et al. have found that only 625 pixels are enough for object recognition by blind people [20]. Therefore, the resolution of CIF (352 × 288) of OV6650FS is enough for a visual prosthesis prototype.

4.2 DSP-Based Image Processing System

4.2.1 Hardware of Image Processing System

Image real-time processing is necessary in visual prostheses. The digital signal processor, due to strong operation capability and its special soft and hard structure, has been widely used in image processing. The computational complexity for the algorithms which can be applied to visual prostheses is very high, so our image processing system is based on TMS320DM642. It has a VLIW architecture which is a highly parallel architecture in which multiple instructions are executed per cycle, making it an excellent choice for visual image processing application.

Figure 16 shows our image processing system designed for visual prostheses, which consists of a digital signal processor (DSP), a synchronous dynamic random access memory (SDRAM), a FLASH, an advanced RISC machine (ARM), a special memory, an adjusting circuit, a data transmit interface, a data receive interface, and a power management.

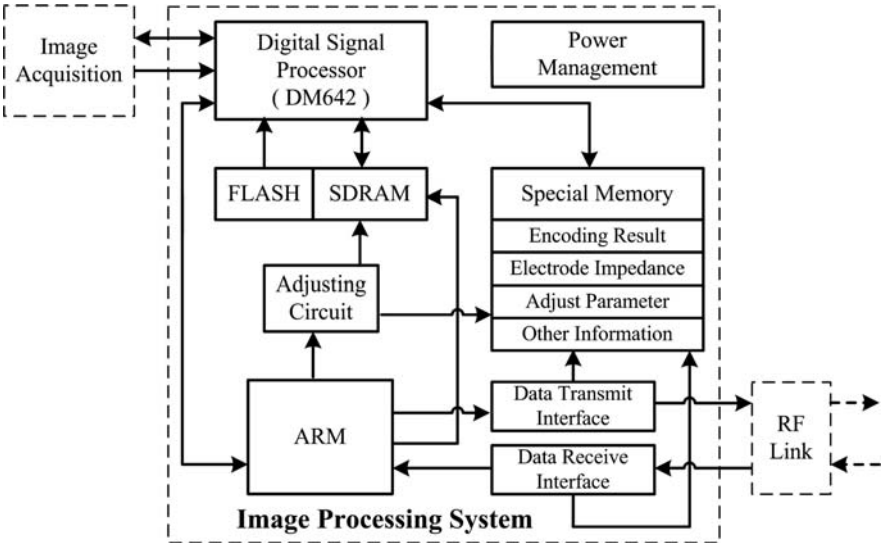

Fig. 16 Image processing system designed for visual prostheses

The DSP connects with the image acquisition system. It receives the image information from the image acquisition system and takes charge of the main functions of image processing, such as information reduction, extracting, encoding, and so on. The ARM connects with the DSP. It has a high ability of controlling the transmission of the information in the image processing system. SDRAM stores the image information with the specific format which was received from the image acquisition system. The special memory deposits the encoding results, electrode information, adjust information, as well as other information at the different addresses. The FLASH connects with the DSP. The program of the image processing strategies for the visual prostheses is stored in the FLASH. The adjusting circuit is used to emendate the image information deposited in the SDRAM and improve the image quality. The power management is in charge of offering the power supply to the whole image processing system.

4.2.2 Image Processing Strategies

The image processing strategies are the most important part of the software design in our system. These strategies are used in the flow of whole image processing. As Fig. 17 shows, the original images are acquired by the camera and sent to the DSP (digital signal processor) for the pre-processing. After that,

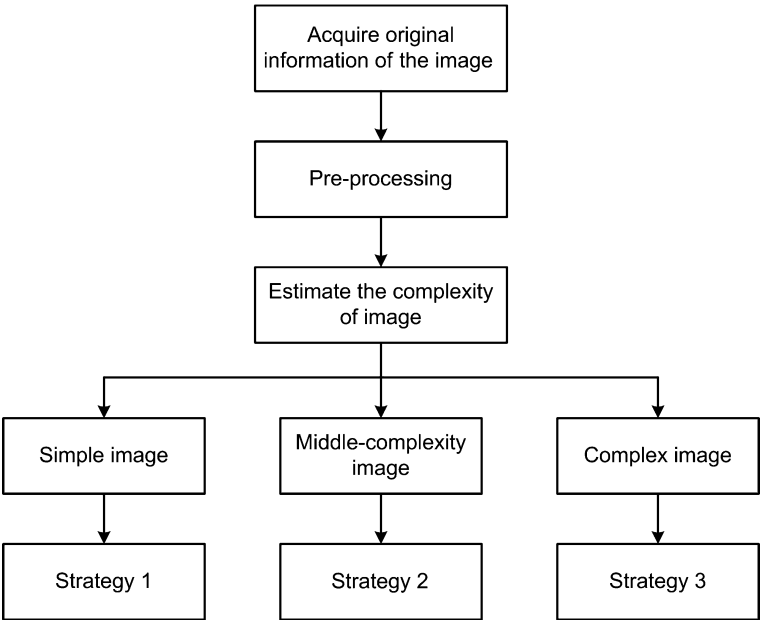

Fig. 17 Schematic of image processing strategies

the images will be classified according to complexity: simple images, middle-complexity images, and complex images.

Image Classification

The first key issue of image processing strategies is image classification. The approach is to use simple and effective mathematic methods to calculate and get an eigenvalue of image, then classify the different images according to this value. Based on former research, there are several methods to estimate the complexity of an image, such as local gray complexity [21], template [22], and two-dimensional C0 complexity [23], etc. Different measures can be adapted to process surrounding images in the daily life of blind patients. According to the analysis of comparative results, the method of two-dimensional C0 complexity gave the better distinction. Figure 18 shows the complexity of different object and scene images using the two-dimensional C0 complexity method.

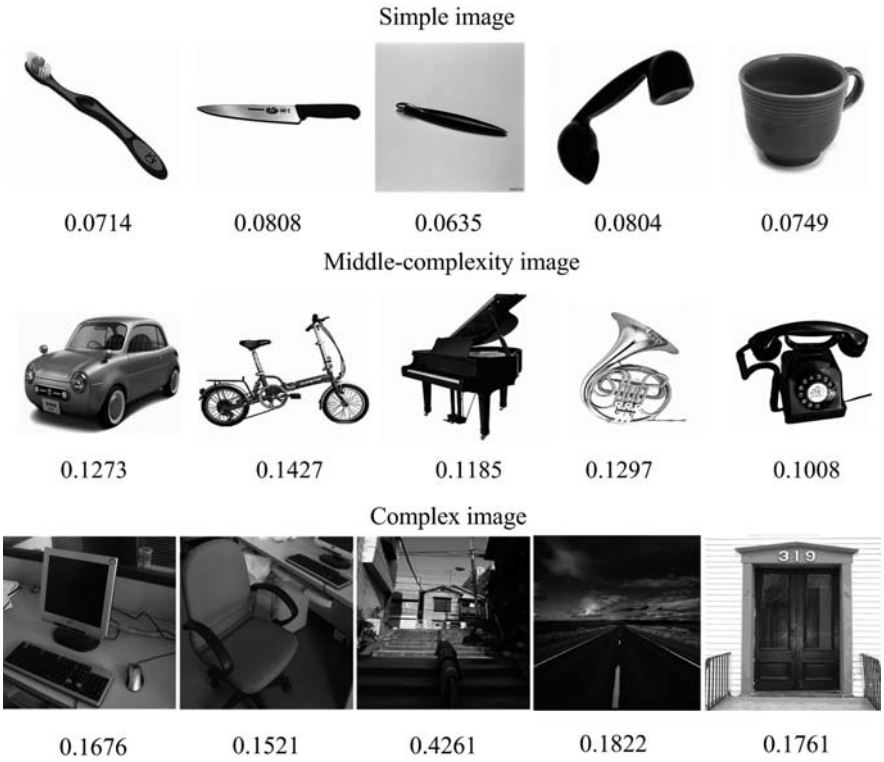

Fig. 18 The complexity of different object and scene images using two-dimensional C0 complexity method

Different Image Processing Strategies According to Various Complexities

For different images, various image processing strategies are used to reduce the computation. If the simple strategy cannot get a better result, the image processing system will use a more complex processing strategy automatically.

(A) Strategy 1: Simple Image

Simple images include simple objects, characters, or words. As we can see in the Fig. 19, using the image reduction arithmetic reduced the original 288×288 image to 32×32 directly. The adaptive threshold binary method was applied to the simplified image. Then, four orientation kernels were used to extract the useful information. Finally the result (32×32 binary images) can be gotten after then edge detection process of the binary image.

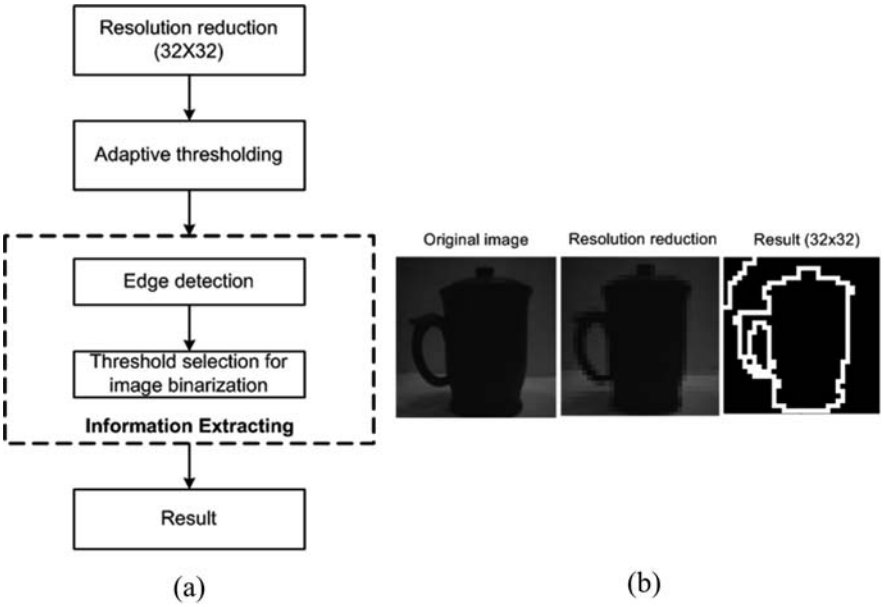

Fig. 19 Strategy 1: (**a**) schematic of simple image processing strategy and (**b**) a series of results for different processing steps

(B) Strategy 2: Middle-Complexity Image

The middle-complexity images include more complex objects and simple scenes. Figure 20 shows the Strategy 2 for a middle-complexity image. After the estimation of complexity, the images (288×288) were reduced to 96×96. Then, the useful information was extracted from the pixelized image (using the method which was mentioned in Strategy 1). Some morphological operations like

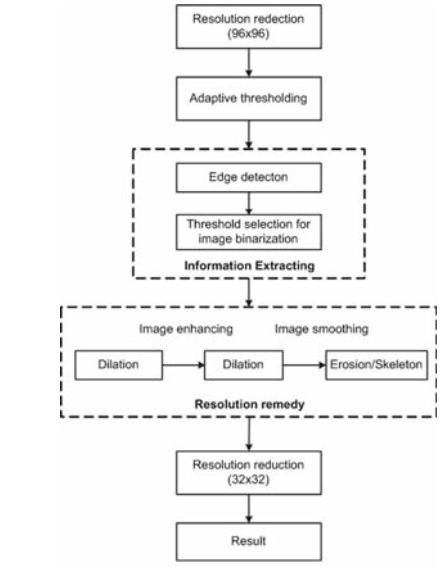

Fig. 20 Strategy 2: (**a**) schematic of middle-complexity image processing strategy and (**b**) a series of results of different processing steps

dilation, erosion, as well as a skeleton were used to enhance and mend the images. A process of erosion was executed which focuses on depressing the affection of noise and false contour. A skeleton was very useful in processing images of words. In the end, the results were regulated or reduced to 32×32.

(C) Strategy 3: Complex Image

Complex images will be the real objects and scenes we meet in daily life. It is hard to get satisfactory results when we use simple processing methods such as Strategy 1 and 2. Therefore, it is necessary to select the most important or interesting region (called focus of attention – FOA) as the focus. Then, Strategy 2 is used to process this region (focus image) to get satisfactory result. Figure 21 shows the schematic of Strategy 3.

To sum up, due to the limited electrode numbers and existing techniques, it will be difficult to increase the pixel number for the actual visual prosthesis, and only low-resolution image information can be transmitted to the brain. Therefore, currently the goal of visual prostheses is not to regenerate detailed vision, but to provide visual perception that is useful for blind individuals to perform common daily tasks such as text reading, facial recognition, and unfamiliar

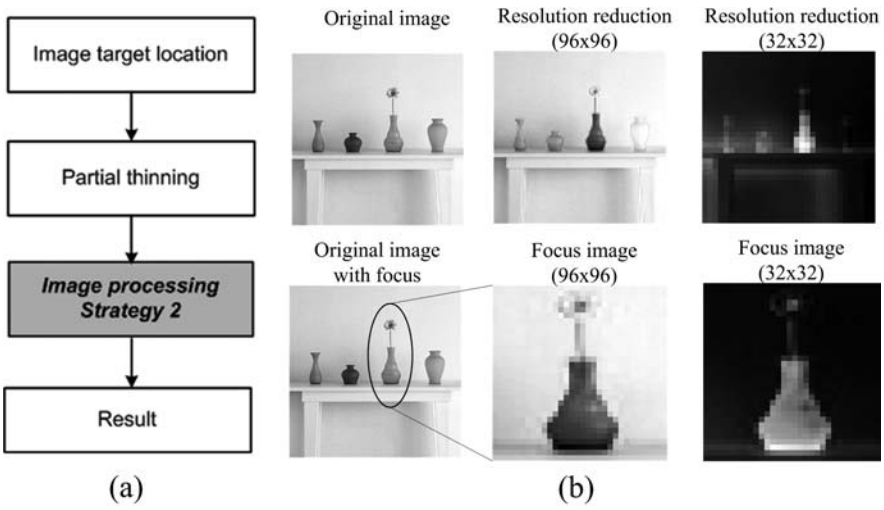

Fig. 21 Strategy 3: (**a**) schematic of complex image processing strategy and (**b**) a series of results for different processing steps and focus image

environment navigation. In the near future, with the development of technology and improvement of relative theories, the function of visual prostheses will be perfected to satisfy more requirements of blind people in their normal lives.

5 Psychophysical Study for Visual Prosthesis

The brain is able to function only if it is provided with sufficient information. Using visual prostheses, what the patients will see are pixelized images. Due to limited numbers of microelectrodes, the images are of low resolution which largely impairs the development of visual prostheses. To restore functional vision, we must know the minimum requirements that the brain needs.

Psychophysical experiments using simulated prosthetic vision can provide the minimum requirements of visual prostheses to realize certain tasks. These experiments simulate scenes of daily life in normal sighted people. Simulated experiments can control individual variables and experiments can be repeated on specific subjects. Many parameters could be adjusted in a large range. The psychophysical experiment on simulated prosthesis vision is an important way to study the minimum information requirement. The importance of simulated experiments has been proved by the success of multichannel cochlear implants.

Several groups all over the world have carried out such simulated experiments on different aspects as pixelized reading [24–26], human face recognition [27, 28], eye–hand coordination [27, 29], and movement [30].

Our team conducted some simulated experiments on normal sighted people to study the recognition of pixelized Chinese characters [31] and pixelized images in daily life. We also studied the positioning of simulated phosphenes based on psychophysical experiments [32].

5.1 Recognition of Chinese Characters with a Limited Number of Pixels

Visual prosthesis is based on point-to-point interconnection between stimulating microelectrode contacts and neural elements. The image captured by the camera is translated into electrical signals and then delivered by bypassing regions of the malfunctioned visual pathways. What the subjects "see" is a pixelized image, and a limited number of microelectrodes result in low resolution.

Most previous studies of pixelized reading focused on reading speed with Latin words as the experimental objects, while little attention has been paid to the reading and recognition of Chinese characters.

In order to acquire systematical knowledge about the optimal and economical recognition of pixelized Chinese characters with limited numbers of pixels, we conducted two phases of experiments.

5.1.1 Recognition Accuracy of Pixelized Chinese Characters Using Simulated Prosthetic Vision

We used the first set of GB 2312-80 International Standard Code promulgated by the Standardization Administration of China as our experimental character set. A self-developed platform, HanziConvertor with digital image processing capacities was developed to convert original Chinese characters into pixelized optical stimulus.

Three experiments were carried out to study the discernible differences among the classes of pixel numbers, the character typefaces and stroke numbers in recognition of Chinese characters, respectively.

The subjects were asked to identify the pixelized images and wrote down the recognizable characters as quickly as they could. If the characters could not be identified, the subjects should write down "X". The results were recorded and compared with the original characters saved in advance.

It was found that the pixel number is the crucial factor that determines the accuracy of recognition. The accuracy rises constantly with the array size. The accuracy of the pixel array size 6×6 is nearly zero. Nearly all the characters sampled in size of 6×6 were indecipherable except for several characters with very few strokes. In size of 8×8 or 10×10, the recognition accuracy increases rapidly, and reached nearly 50%. When pixel number was 12×12, all the subjects could identify every character without error.

The four tested fonts were set as Fangsong Ti, Hei Ti, Kai Ti, and Song Ti, respectively. When Song Ti and Hei Ti were applied, the recognition accuracy was higher compared to the other two fonts, Kai Ti and Fangsong Ti. Especially in the pixel array size of 10×10, the disparity was obvious. It was mainly because Song Ti and Hei Ti occupy much more space than the other two fonts with the same pixel sizes.

We also found that the complexity of each character, measured by the number of strokes it contains, affected the recognition accuracy. Characters

with 1–4 strokes were identified correctly in all kinds of pixel array sizes, while satisfactory recognition accuracy of characters with 5–8 strokes could be achieved when pixel size was larger than 8×8. As for characters with more than nine strokes, only 12×12 arrays were able to provide enough information for the subjects. When pixel size was lower than 12×12, the recognition accuracy decreased as the number of strokes increased.

5.1.2 Recognition of Chinese Characters with a Limited Number of Pixels Based on Complexity Analysis

All the information that the visual prosthesis translates and processes is based on the image captured by the camera. The stroke number of Chinese characters is not a clear conception for vision prosthesis. In view of the calculation speed and the applicability, the black pixel statistic algorithm was chosen in the study.

The 631 most commonly used Chinese characters were classified into six groups based on black pixel statistic algorithm complexity (0–0.16, 0.16–0.20, 0.20–0.24, 0.24–0.28, 0.28–0.32, and 0.32–0.36) as experimental characters set. Hei font was chosen in our experiment to minimize any unexpected confounding effects.

The experiment was performed in a quiet and dark room to shield from ambient light. The setup included a DSP-based embedded system, a head-mounted display (HMD) with an experimental software package developed by our team written in the C++ language. The pixelized images of Chinese characters with different resolutions (6×6, 8×8, 10×10, and 12×12) were rendered on a head-mounted display screen (Fig. 22).

Fig. 22 The experimental scene of recognition of Chinese characters with a limited number of pixels: it was performed in a quiet and dark room to shield from ambient light. The pixelized images of Chinese characters with different resolutions (6×6, 8×8, 10×10, and 12×12) were rendered on head-mounted display screen

The complexity of the 631 most commonly used Chinese characters was evaluated by the black pixel statistic algorithm. The mean complexity and the number of Chinese characters with stroke numbers from 1 to 16 can be found in (Table 1). In general, Chinese characters with a high number of strokes will be more complicated than those with fewer strokes. Mean complexity increases gradually with the increase of the stroke number. The complexity rises rapidly when the stroke number is less than 4. From 4 to 16 strokes, the rate of rise slows down.

The mean recognition accuracy of Chinese characters is $98.29 \pm 2.04\%$, $91.98 \pm 7.56\%$, $69.75 \pm 24.80\%$, and $28.40 \pm 27.97\%$ for 12×12, 10×10, 8×8, and 6×6 pixels arrays, respectively, regardless the complexity of the characters.

The results indicate that the mean recognition accuracy increases with the increase of the pixel array number. The binary pixel arrays 10×10 and 12×12 are sufficient for recognition of Chinese characters, so that more than 90% of experimental samples can be identified correctly. A result of less than 30% of experimental samples identified correctly for 6×6 pixel arrays indicates that 6×6 pixel arrays are not suitable for recognition of Chinese characters. The pixel arrays 8×8 are the threshold, with about 70% of characters identified correctly. As to our expectation, the mean recognition accuracy decreased with the increase of complexity for a given pixel array number. The more complicated a character is, the more difficult it is for a subject to identify.

5.2 Image Processing Based Recognition of Images with a Limited Number of Pixels

The purpose of this study was to investigate the primary factors in recognition of images of common objects and scenes and optimize the recognition rate on low resolution using image processing technologies. Two image processing methods ("threshold-binarization" images and "edge" images) and two kinds of pixel arrays (square pixel array and circular pixel array) were adopted in different image arrays, respectively (8×8, 16×16, 24×24, 32×32, 48×48, and 64×64).

Twenty objects and five scene images were chosen from the databases which were familiar to almost everyone. The original images were captured using the mini CMOS image sensor which was a part of an embedded system based on DSP developed by ourselves.

The experiment was performed in a quiet and dark room to shield from ambient light. Setup was the same as mentioned above. The images were captured and processed by the embedded system, and then the results were transmitted to the computer through the USB device. The HMD was controlled by the computer (Fig. 23).

Table 1 Mean complexity and number of Chinese characters with stroke number from 1 to 16

Number of strokes	1	2	3	4	5	6	7	8	9	10	11	12	13	14	15	16
Mean complexity	0.05	0.14	0.16	0.20	0.22	0.24	0.25	0.27	0.28	0.29	0.30	0.30	0.31	0.31	0.32	0.32
Number of characters	1	9	32	53	71	89	78	81	73	52	36	26	14	9	4	3

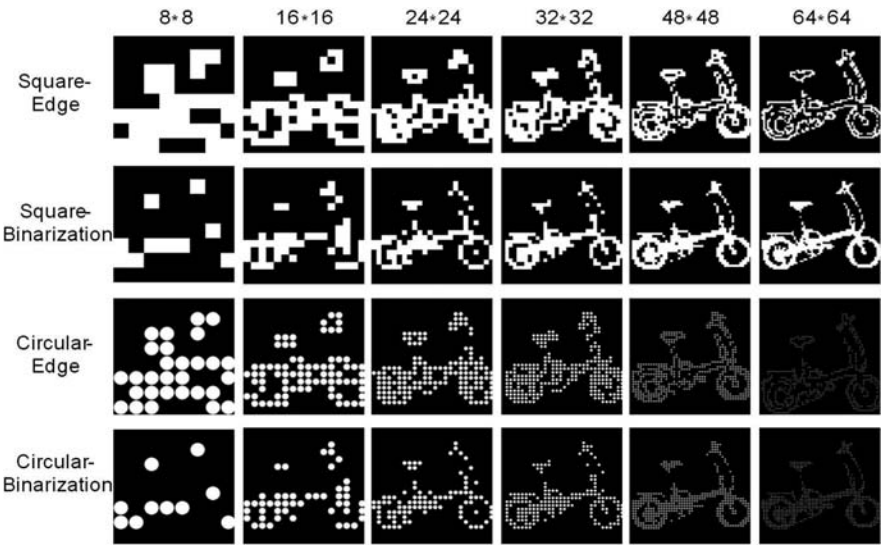

Fig. 23 Sample images used in the experiment. Each column corresponds to a given number of pixels (6×6, 8×8, 10×10, and 12×12) and each row corresponds to a given processing method and shape of pixel. The image pixelized by white binary matrix pixels. Visual angle of each image was set in 5°

The object recognition was close to zero in 8×8 pixel arrays. When the pixel number increased to 16×16 pixels, the recognition showed noticeable differences with two image processing strategies. Binarization showed better results than Edge strategy, the impact produced by the shape of pixels was relatively small. However, different pixel shapes with the same processing method produced no significant differences in image recognition. Furthermore, with the pixel number increased to 24×24, there was a great increase in recognition accuracy. The Circular-Binarization (69.57 ± 9.42) image was still the most easily identifiable, but the distinction was comparatively small. The fluctuant trend of recognition with higher pixel numbers demonstrated a relatively slow growth from the 32×32 resolutions to 64×64. At the same time, the accuracy increased from 80% to nearly 100% (Fig. 24).

Scene images were very hard to identify without sufficient prior information when the resolution was lower than 32×32. With 32×32 pixel arrays, there was a great diversity of recognition accuracy for two strategies and two pixel shapes from Square-Binarization (30.44 ± 7.32) to Square-Edge (9.57 ± 8.60). The diversity of recognition accuracy of different image modes became negligible at the resolution of 48×48 pixels. Meanwhile, the mean recognition accuracy of different strategies and pixel shapes had an obvious growth (near 60%). For 64×64 pixels, the mean recognition accuracy had reached near 80%. Binarization showed better results than Edge strategy in 32×32 pixel arrays. However,

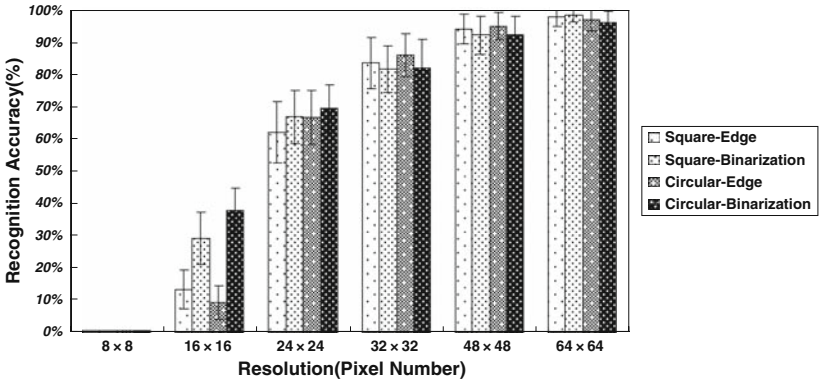

Fig. 24 Experiment results: the recognition accuracy of objects

with the number increasing to 48×48, the Edge got better results than the Binarization method. Different pixel shapes with the Edge method did not show distinct differences, while with the Binarization method, square pixels got better results than circular pixels when the pixel number increased to 32×32. "Circular-Edge" images were easier to recognize (Fig. 25).

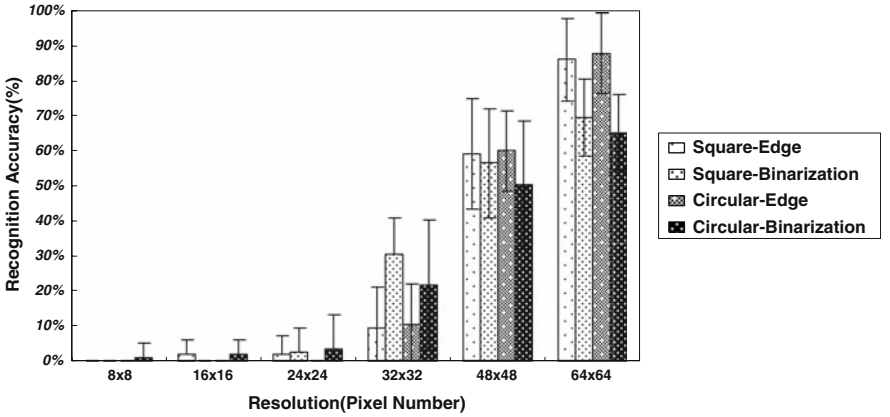

Fig. 25 Experiment results: the recognition accuracy of simple scenes

5.3 Dispersion and Accuracy of Simulated Phosphene Positioning

With the rapid development of prosthetic vision evaluating the characteristics of phosphenes after implantation of electrode arrays will become increasingly important in future research. Mapping phosphenes was of great importance after electrode array implantation of visual prostheses. Several methods have

been developed by our team to map phosphenes and evaluate their characteristics. Two phases of experiments were carried out in this regard.

5.3.1 Tactile Perception Based on Phosphene Positioning Using Simulated Prosthetic Vision

The setup included a head-mounted display, which was connected to the computer in order to generate simulated phosphenes, a 19-inch touch screen to record the subject's tactile position, a simple tactile guide that directs the subject to recognize the origin of the system, and an inverted "L" shaped short horizontal stick pointed toward the center of the touch screen. During the experiment, the subject's hands were placed at the tip of the short horizontal stick in order to help him/her realize where the center of the touch screen was. Moreover, the setup also included a chin rest placed 30 cm in front of the touch screen in order to hold the subject's head stable, and a Dell computer with a C++ experimental program to create the circular phosphene. The phosphene's size was 16×16 mm (Fig. 26).

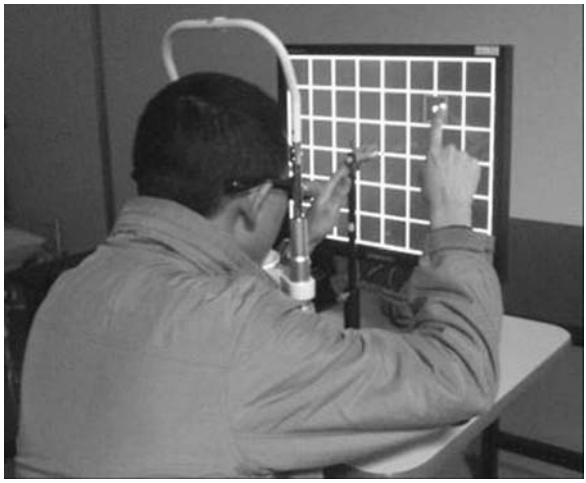

Fig. 26 The setup of the simulated phosphene positioning system. It is totally dark in the HMD before the program is running. The image in the HMD is the same as that on the touch screen except for the resolution. The image also displays on the touch screen to help the experimenter track the experimental procedure. (From Chai et al., 2007b)

The experiment included two modes: without and with a visual guide. The visual guide was used to reduce the visual perception error. The equidistant horizontal and vertical lines divide the touch screen and the screen in the HMD into 8×6 grids. In this situation, the visual perception error is reduced as the locations of simulated phosphenes are observed with more accuracy. Each mode included training and formal parts.

The visual guide increased the accuracy of tactile perception as the distribution was larger when the error was under 20 mm and became inverse as the error went above 20 mm.

Dispersion and response time have a significant relation to the distance to the origin. There are two main aspects that affect accuracy: the error of judgment and individual differences. The error of judgment can be explained using the visual guide, which obviously increases the accuracy as well as the other two parameters. The individual differences could be solved by systematic training (Figs. 27 and 28).

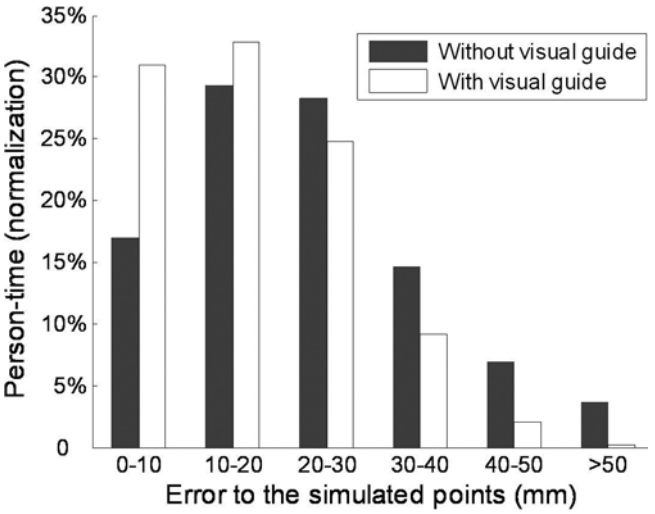

Fig. 27 Contrast of tactile accuracy distribution in two modes (without and with visual guide). The statistics are based on three simulated points (the distance to the center of the touch screen is 16, 60, and 80 mm each) in 20 subjects. Each point is repeated 10 times. (From Chai et al., 2007b)

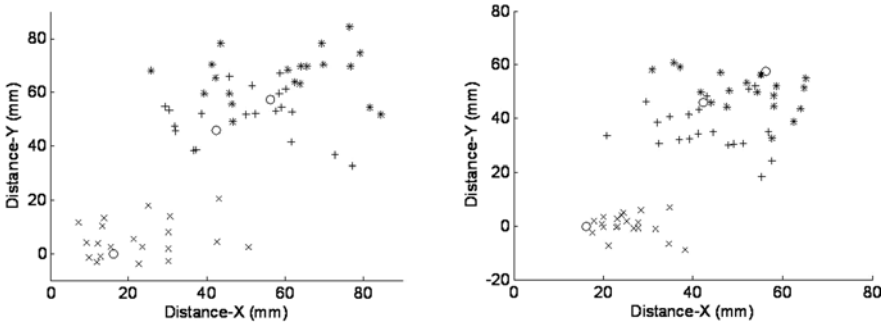

Fig. 28 The scatter of simulated phosphenes and the mean values of the subject's judged points in the mode without the visual guide (*left*). The scatter of simulated phosphenes and the mean values of the subject's judged points in the mode with the visual guide (*right*). The *open circle* represents the three simulated phosphenes whose distances to the origin were 16, 60, and 80 mm, respectively. The *product sign*, *plus sign*, and *asterisk sign* represent the mean value of the subject's judged points toward the 16, 60, and 80 mm simulated phosphenes, respectively. The 20 determinative signs toward each simulated phosphene represent the 20 subjects in the experiment. (From Chai et al., 2007b)

5.3.2 Dispersion and Accuracy of Simulated Phosphene Positioning Using Tactile Board

Three experiments were designed to evaluate the performance of phosphene positioning based on a tactile board using simulated prosthetic vision. They measured the effect of distance, the effect of quadrant, and the long-term effect.

The tactile board was a self-developed apparatus designed on Cartesian coordinates in order to reduce the tactile perception error. It consisted of a basic board, a pushbutton array, and adjustable retainers (Fig. 29).

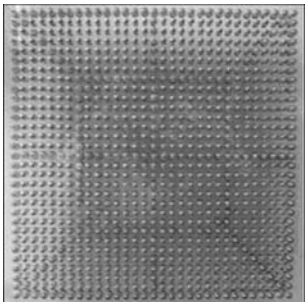

Fig. 29 The tactile board

The setup of the phosphene positioning system included a self-developed tactile board, a head-mounted display, a 19-inch touch screen, a personal computer with a self-developed experimental software system written in the C++ language (Fig. 30).

Fig. 30 The setup of simulated phosphene positioning system

Each experiment included two processes: the training and the formal experiment. The procedures of the training part and the formal experiment were completed in a dark, quiet room so that the subjects could concentrate on the experiments.

The values of standard deviation (SD) were less than 6 mm. All of the values were in the range of 4–6 mm. The range of mean error was 4–9 mm. The response time for the distances of 56 mm, 79 mm, 113 mm, and 136 mm was from 24.5 to 28.3 seconds, while the response time for 11 mm distance was 17.7 seconds.

The dispersion based on the tactile board was significantly improved in evaluating simulated phosphenes in two aspects. One was that the dispersion of all judged points decreased in using the tactile board, while the other was that the differences of dispersion were small enough to be ignored as the distance to the origin increased.

The conclusion was that the tactile board increased accuracy. Using the tactile board not only decreased the mean error, but also reduced the accuracy's fluctuation as the distance to the origin changed.

Long-term experiments improved both dispersion and accuracy, and both SD and mean error were decreased in the long-term experiments, especially in the first two experiments.

6 Surgical Approach to Expose the Optic Nerve

Anatomically, the retrobulbar segment of the optic nerve is located in the closed orbit. There is no way to access it except surgery. Therefore, a surgical approach should be selected and its efficiency and safety should be evaluated.

6.1 Surgical Technique

Anesthesia and sedation were introduced by intramuscular injections of ketamine hydrochloride and xylazine hydrochloride. Body temperature was maintained at a level of 39°C during the experiment and electrocardiogram was supervised so that the anesthesia could also be monitored. Atropine eye solution was administered into the conjunctival sac of the surgical eye to lessen the edema of the conjunctiva and the third eyelid.

Surgery was performed on right eyes only. After shaving the surgical area, povidone-iodine was used for disinfection and the surgical eye was routinely draped. A lateral canthotomy was performed and the conjunctiva was incised at the superior fornix. The superior rectus muscle was dissected with a thermal cauter; in order to avoid unnecessary bleeding, the vortex vein along the rectus muscle needed to be ligated. Then, the eye was rotated inferonasally. Care needed to be taken to avoid tearing or breaking the intraorbital venous sinuses. The soft tissue surrounding the posterior aspect of the globe was dissected superotemporally with care along the ciliary blood vessels on the sclera, until the optic nerve became visible. The outlet of the optic nerve was gently freed from the surrounding soft tissue and made ready for implanting the stimulation microelectrodes or electrode array.

6.2 *Efficiency and Safety*

Electrically evoked cortical responses generated by implanting the microelectrodes or electrode array into the retrobulbar segment of the optic nerve are shown in Fig. 31. In our investigation, the visual conduction function in terms of implicit time and amplitude in visually evoked potential recordings would be influenced transiently. However, these transient changes could be recovered naturally without any intervention about 1 month after surgery (Fig. 32). Moreover, the histological examination also provided no abnormal structural alterations at a level of light microscopy.

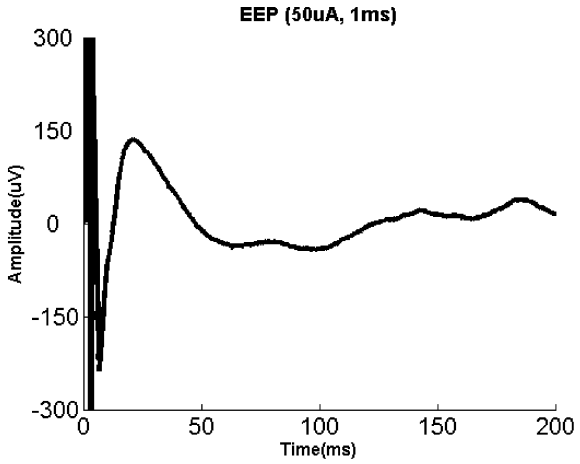

Fig. 31 EEP generated by current of 50 μA with duration of 1 ms

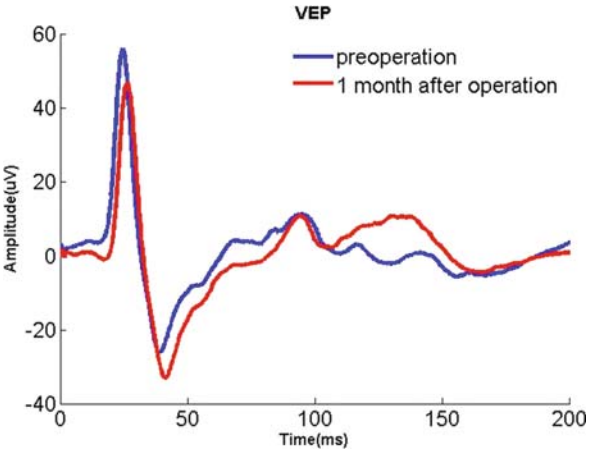

Fig. 32 A complete recovery of VEP in one month after surgery

As a whole, lateral canthotomy was a relatively safe and efficient surgical approach which served in the implementation of the visual prosthesis investigation.

7 In Vivo Electrophysiological Study

By applying a penetrating electrode array in the optic nerve, the axons of the ganglion cells local to each electrode could be stimulated. This approach may potentially increase the spatial resolution of the visual prosthesis while lowering the thresholds of the stimulating current when compared with the surface cuff electrodes. To obtain the appropriate stimulating parameters and pattern, we investigated the feasibility and basic spatiotemporal properties of cortical responses evoked by optic nerve stimulation with penetrating electrodes in this study, using multichannel recording electrode arrays positioned at the visual cortex area in rabbits.

7.1 Subjects

Thirty-six healthy adult Chinese albino rabbits, weighing about 2.0–3.0 kg, were used in this study. After intravenous anesthetization with 5% pentobarbital sodium, orbital surgery was performed to expose the intraorbital optic nerve of the rabbits. The temporal and spatial properties of electrically evoked potentials (EEP) evoked by optic nerve stimulation with penetrating electrodes were investigated, respectively.

7.2 Temporal Properties

7.2.1 Stimulations

To investigate the temporal properties of EEP evoked by optic nerve stimulation with penetrating electrodes, two microelectrodes (each with 100 μm diameter and 300 μm tip exposure) were used to stimulate the optic nerve of rabbits. Each electrode was made of Teflon-insulated tungsten wire and the impedance of the electrode ranged from 2.5 to 3.5 kΩ at 1 kHz, 50 mV sinusoidal wave. The insertion site of the stimulating and return electrodes was about 1 mm and 2 mm, respectively, posterior to the eyeball (Fig. 1).

A single charge-balanced symmetrical cathode-first biphasic current pulse, generated by an isolated stimulator (MS16, Tucker-Davis Technologies, Alachua, FL, USA), was applied between the stimulating and return electrodes. When determining the charge threshold, a duration fixed current was used. The lowest current for eliciting reproducible EEP was found. Then the corresponding charge was calculated by multiplying current by duration.

Pulse amplitude and duration of the stimuli were varied to study their effects on EEP. The effects of stimulus pulse amplitude on EEP were investigated by using current intensity ranging from 40 to 120 μA with fixed pulse duration of 0.5 ms. The effects of stimulus pulse duration on EEP were studied over a range of 0.4–1.2 ms with fixed pulse amplitude of 100 μA. By fixing the charge as a constant value, the effects of varying pulse duration and pulse amplitude on EEP were examined. For the above experiments, the frequency of the pulses was 1 Hz. The influence of stimuli frequency on EEP was studied as well. The stimuli frequency was varied from 1 Hz to 10 Hz.

7.2.2 Recordings

In order to detect the maximal response of EEP, a nine-recording-electrode array was positioned over the contra-lateral visual cortex area of the stimulated eye. The skull was exposed through a skin incision at the top of the head along the midline, and nine stainless crew-type electrodes were drilled into the skull over the visual cortex (Fig. 33). The nine electrodes formed a 3×3 array with 2 mm spacing. EEP from the visual cortex contra-lateral to the stimulated eye were recorded by a multichannel neurophysiology workstation (System 3, Tucker-Davis Technologies, Alachua, FL, USA). Signals from the nine recording electrodes were amplified and filtered with a band-pass of 3–2000 Hz. Fifty evoked responses were averaged.

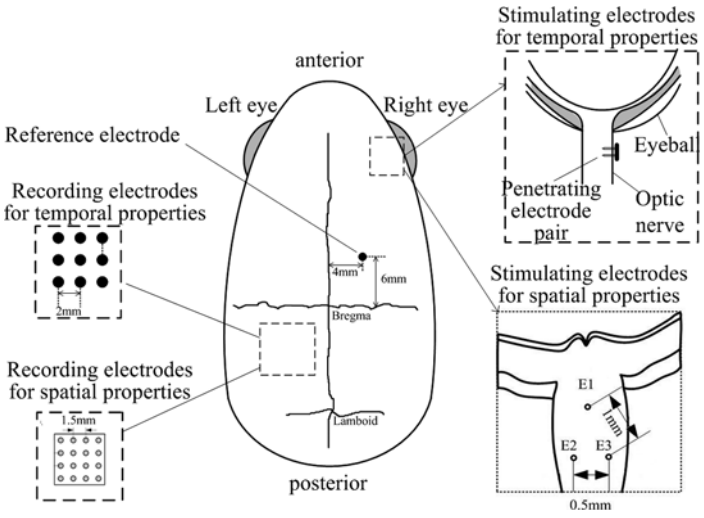

Fig. 33 The strategy for electrical stimulation and cortical recording in rabbits

7.2.3 Temporal Properties of EEP

Electrical stimulation of the optic nerve evoked EEP in the visual cortex of all the rabbits. The waveform of the induced EEP was similar to that of VEP, while the latency of P1 of EEP was shorter compared with that of VEP.

The mean charge threshold for eliciting EEPs in the visual cortex was 16.04 ± 4.22 nC (Mean $\pm$ SD). Considering that the exposed surface of the stimulating electrode was about 7.64×10^{-4} cm^2, the mean charge threshold density was 20.99 ± 5.52 μC/cm^2.

The strength–duration curve was also investigated as displayed in Fig. 34. Current threshold decreased as the pulse duration of the stimulus increased (solid), while the corresponding charge threshold increased when increasing the pulse duration.

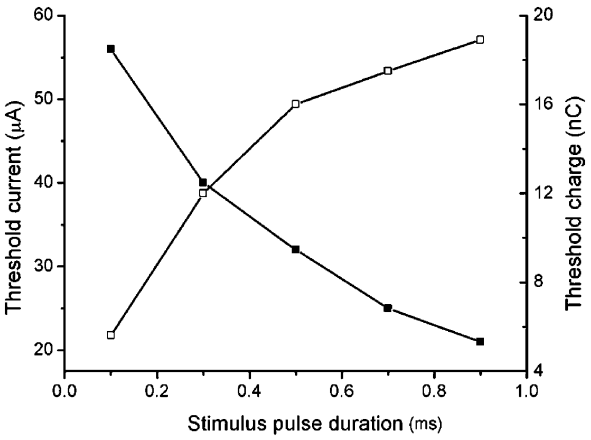

Fig. 34 Current threshold and corresponding charge threshold as functions of stimulus pulse duration in one rabbit. *Solid*: current threshold and *hollow*: charge threshold. Unpublished data

Figure 35 depicts the EEP waveforms to stimuli with varying pulse amplitude. The amplitude of P1 increased when increasing the stimulus pulse amplitude while the latency of P1 decreased.

The EEP waveforms to stimuli with the varying pulse duration are shown in Fig. 36. As can be seen, the amplitude of P1 increased when the pulse duration increased from 0.4 to 1.0 ms. But the latency of P1 changed little with increasing stimulus pulse duration.

Figure 37 displays the typical EEP waveforms elicited by stimuli with a fixed pulse, but different pulse amplitude and pulse duration. The amplitude of P1 decreased and the latency increased when the pulse duration increased from 0.2 ms to 1.0 ms and the pulse amplitude decreased from 250 μA to 50 μA accordingly.

The influence of stimulation frequency on EEP was studied. For comparison, the influence of stimulation frequency on VEP was studied as well. Figure 38 shows the typical VEP and EEP responses as the stimulation

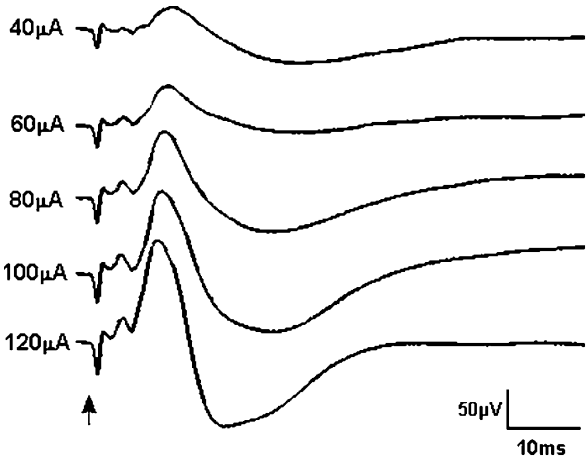

Fig. 35 EEP waveforms to stimuli with varying pulse amplitude in one rabbit (pulse duration = 0.5 ms). *Arrow*: onset of the stimuli. Unpublished data

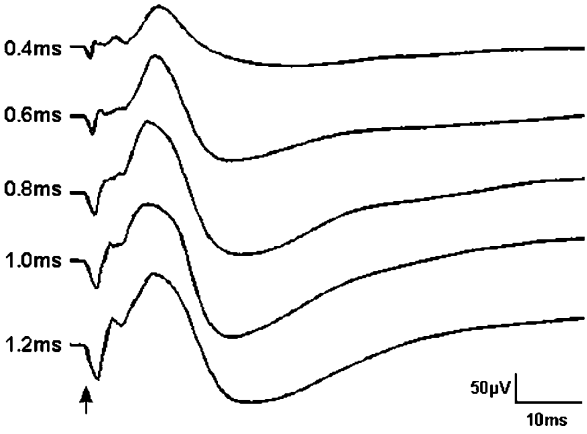

Fig. 36 EEP waveforms to stimuli with varying pulse duration in one rabbit (pulse amplitude = 100 μA). *Arrow*: onset of the stimuli. Unpublished data

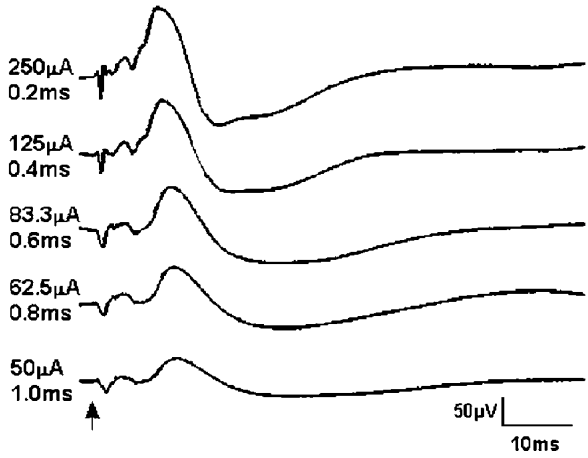

Fig. 37 EEP waveforms to stimuli with fixed charge (50 nC) but different pulse amplitude and pulse duration in one rabbit. *Arrow*: onset of the stimuli. Unpublished data

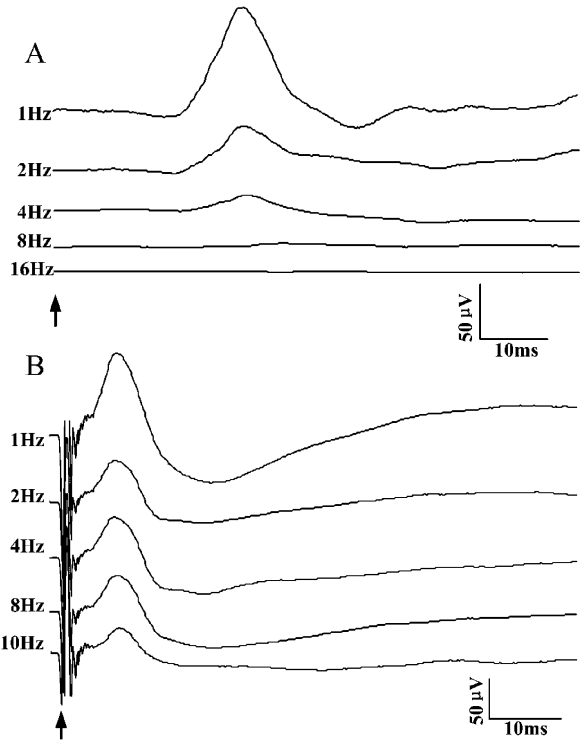

Fig. 38 (**A**) VEP waveforms to optic stimuli with different frequency; (**B**) EEP waveforms elicited by electrical stimuli with different frequency but fixed pulse amplitude and duration (100 μA, 0.5 ms). Unpublished data

frequency was varied. As depicted in the figure, the amplitudes of both VEP and EEP decreased with the increase of stimulation frequency. But the VEP was depressed with lower stimulation frequency compared with EEP. This may be due to the direct electrical stimulation to the optic nerve, bypassing the retinal synaptic transmission, and therefore, the EEP could be elicited with a wider frequency range than VEP did.

7.3 Spatial Properties

7.3.1 Stimulations

To investigate the spatial properties of cortical responses elicited by optic nerve stimulation, three triangularly or linearly configured microelectrodes were inserted into the optic nerves of the rabbits (Fig. 33). The home-made needle-type electrodes were fabricated by micro-electric wires made of Platinum–Iridium alloy insulated by Teflon (80 μm diameter, 100 μm tip exposure). The uncoated area was about 2.7×10^{-4} cm^2 and the impedance was 5∼12 kΩ at 1 kHz, 50 mV sinusoidal wave.

Electrical stimulation was applied to the different pairs of three stimulating electrodes. Biphasic charge-balanced rectangular stimuli with the cathode-first pulse were used. The pulse duration was fixed at 0.5 ms, while the pulse amplitude varied from 10 μA to 100 μA, with the frequency of 1 Hz.

7.3.2 Recordings

The recording electrode array was made up of 4×4 silver-ball electrodes with 0.3–0.4 mm in diameter. The silver wire (diameter = 0.2 mm) behind the silver ball was insulated by a glass tube. The 16 electrodes were fixed on a base plate in a matrix format, with the central distance of 1.5 mm between the two adjacent electrodes. One solid shaft was extended from the plate in order to be fixed onto a three-dimensional micromanipulator. The impedance of the silver-ball electrodes ranged from 500 to 800 Ω measured under 100 μA, 1 kHz, AC stimulation.

The EEP responses of 16 channels at the contra-lateral visual cortex to the stimulated eye were recorded subdurally to investigate the spatial properties of EEPs (Fig. 33). The recording electrode array was moved within the cortex in order to cover the whole area of the visual cortex.

7.3.3 The Spatial Responses to the Optic Nerve Stimulation

Our experimental results showed that the extent of EEP increased as the stimulating intensity increased. Figure 39 illustrates normalized P1 amplitude of EEP as a function of recording distance from the response center (the maximal channel). The relation of normalized EEP amplitudes and recording distances was fitted by Gaussian function. As seen from the figure, the amplitude of P1 decreased when the recording distance from the response center increased, and the stimuli with larger amplitude evoked a larger response area in the visual cortex.

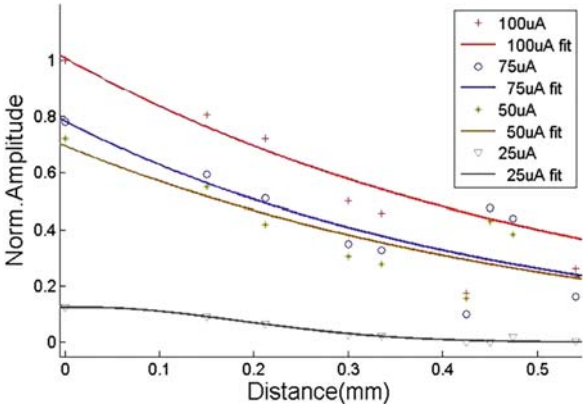

Fig. 39 The normalized P1 amplitude of EEP as a function of recording distance from the channel with maximal response. The data was fitted by Gaussian function. The stimulus pulse duration was 0.5 ms. Unpublished data

We also investigated the spatial properties of EEP as the optic nerve was stimulated by different stimulating electrode pairs. Our experimental results showed that different distribution maps of EEP were elicited by different pairs of stimulating electrodes. The stimulating electrode pairs along the axis of the optic nerve elicited cortical responses with much lower thresholds than that perpendicular to the axis of the optic nerve. Figure 40 illustrates the spatial extension of EEP under the same stimulating parameters as the optic nerve was stimulated by different pairs of the stimulating electrodes in one rabbit. The horizontal axis represents the recording distance from the channel with the maximal response. The vertical axis represents the normalized P1 amplitude of EEP recorded by one channel. The relation of normalized amplitudes and distances was fitted by Gaussian function. As shown in Fig. 40, the spatial area of EEP elicited by the electrode pairs approximately parallel with the axis of the optic nerve (Pair-1 and Pair-2) were much larger than that elicited by the electrode pair perpendicular to the axis of the optic nerve (Pair-3). The attenuating speed under the same stimulating intensity by the electrode pairs approximately parallel with axis of the optic nerve was faster than that perpendicular to the axis of the optic nerve. When the optic nerve was stimulated by linearly arranged electrodes, larger EEPs were elicited by the electrode pair with a larger distance than the one with a smaller distance.

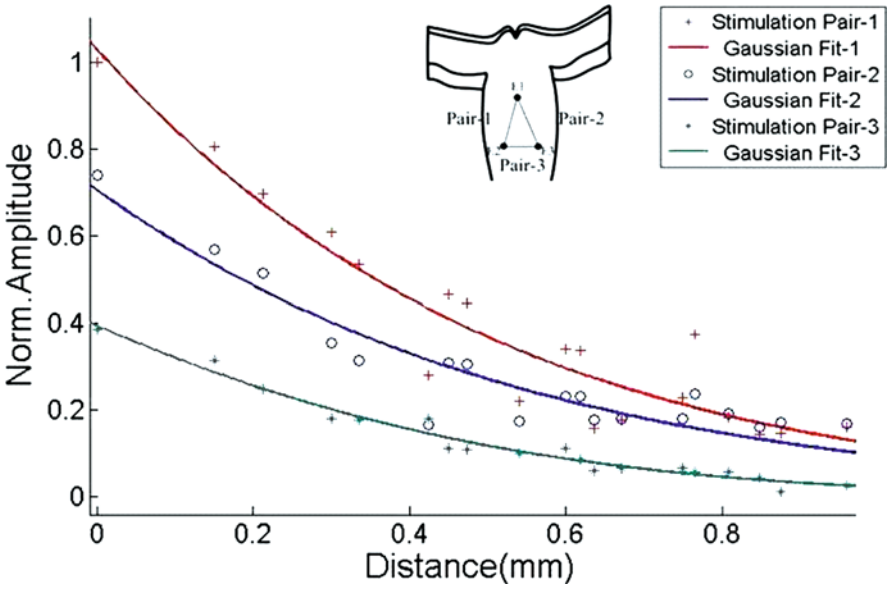

Fig. 40 The spatial extension of EEP as the optic nerve was stimulated by different pairs of stimulating electrodes in one rabbit. Stimulating electrode pairs along the axis of the optic nerve elicited larger cortical responses than those perpendicular to the axis of the optic nerve. The stimulus pulse amplitude and pulse duration were 100 μA and 0.5 ms, respectively. Unpublished data

7.4 Assessment of the Damage to the Optic Nerve

Electroretinograms (ERG) and visual evoked potentials (VEP) were monitored as a control at the different stages of all the experiments. Histological analysis of the optic nerve was performed after the experiments.

The experimental results showed that ERG did not vary significantly, but the P1 amplitude of VEP declined after the orbital surgery to expose the optic nerve. Histological analysis showed mild damage to the optic nerve tissue induced by electrical stimulation in acute experiments.

8 Conclusion

In the foregoing chapter, we have described an implantable visual prosthesis with a stimulating microelectrode array penetrating into the optic nerve, and animal experiments have validated the feasibility of this kind of visual restoration. The design of the microelectrode can be optimized from noise analyses. Two different types of penetrating electrode arrays were presented including a silicon-based microprobe produced by MEMS process techniques and *Pt-Ir* microwire arrays produced by electrochemical etching. Both of them are ideal candidates for optic nerve stimulation with the key difficulty in chronically in vivo fixing. As compared with cuff electrode arrays, penetrating ones can improve spatial resolution. In addition, our group accomplished a great achievement with the multichannel microcurrent stimulator. A commercial low-resolution CMOS micro-camera was adopted for image capturing, and a DSP processed these images in real time. Now our optic nerve visual prosthesis has been validated by animal experiments, and more such experiments will be conducted to optimize the penetrating microelectrode arrays.

Acknowledgments This research is supported by the National Basic Research Program of China (973 Program, 2005CB724302), National Science Fund for Distinguished Young Scholars from The National Natural Science Foundation of China (60588101), the National Natural Science Foundation of China (60871091), National Natural Science Foundation of China for the Youth (30700217), Shanghai Pujiang Program (07PJ14050), the 111 Project from the Ministry of Education of China (B08020).

References

1. Koury CB (2006) Epiretinal prosthesis shows promise for blind patients. Retina Today 12
2. Humayun MS, Weiland JD, Fujii GY, et al. (2003) Visual perception in a blind subject with a chronic microelectronic retinal prosthesis. Vision Res 43:2573–2581
3. Chow AY, Chow VY, Packo KH, et al. (2004) The artificial silicon retina microchip for the treatment of vision loss from retinitis pigmentosa. Arch Ophthalmol 122:460–469
4. Chow AY, Pardue M, Chow VY, et al. (2001) Implantation of silicon chip microphotodiode arrays into the cat subretinal space. IEEE Trans Neural Syst Rehabil Eng 9:86–95

5. Kanda H, Morimoto T, Fujikado T, et al. (2004) Electrophysiological studies of the feasibility of suprachoroidal-transretinal stimulation for artificial vision in normal and RCS rats. Invest Ophthalmol Vis Sci 45:560–566
6. Troyk P, Bak M, Berg J, et al. (2003) A model for intracortical visual prosthesis research. Artif Organs 27:1005–1015
7. Brindley GS, Lewin WS (1968) The sensations produced by electrical stimulation of the visual cortex. J Physiol 196:479–493
8. Delbeke J Oozeer M, Claude V (2003) Position, size and luminosity of phosphenes generated by direct optic nerve stimulation. Vision Res 43:1091–1102
9. Veraart C, Raftopoulos C, Mortimer JT, et al. (1998) Visual sensations produced by optic nerve stimulation using an implanted self-sizing spiral cuff electrode. Brain Res 813:181–186
10. Maynard EM (2001) Visual prostheses. Annu Rev Biomed Eng 3:145–168
11. Yu W, Tian Y, Chai X, et al. (2006) Image processing strategies dedicated to the optic nerve stimulation. 2006 International Symposium on Biophotonics Nanophotonics and Metamaterials 147–150
12. Merrill DR, Bikson M, Jefferys JGR (2004) Electrical stimulation of excitable tissue: design of efficacious and safe protocols. J Neurosci Methods 141:171–198
13. Sui X, Pei W, Zhang R, et al. (2006) A micromachined SiO_2/Silicon probe for neural signal recordings. Chinese Phys Lett 23:1932–1934
14. Sui X, Zhang R, Pei W, et al. (2007) A novel implantable multichannel silicon-based microelectrode. Chinese Phys 16:2116–2119
15. Normann RA, Maynard EM, Rousche PJ, et al. (1999) A neural interface for a cortical vision prosthesis. Vision Res 39:2577–2587
16. Margalit E, Maia M, Weiland JD, et al. (2002) Retinal prosthesis for the blind. Surv Ophthalmol 47:335–356
17. Veraart C, et al. (1998) Visual sensations produced by optic nerve stimulation using an implanted self-sizing spiral cuff electrode. Brain Res 813:181–186
18. Brelén ME, Duret F, Gérard B, et al. (2005) Creating a meaningful visual perception in blind volunteers by optic nerve stimulation. J Neural Eng 2:22–28
19. Sivaprakasam M, Liu W, Humayun MS, et al. (2005) A Variable Range Bi-Phasic Current Stimulus Driver Circuitry for an Implantable Retinal Prosthetic Device. IEEE J Solid-State Circuits 40:763–771
20. Stiles NR (2004) Intraocular camera for retinal prostheses: Restoring vision to the blind California State Science Fair, S0322.
21. Yang X, Zhou C (2000) Analysis of the complexity of remote sensing image and its role on image classification. IEEE Int Geosci Remote Sens Symp 5:2179–2181
22. Zheng G, Cai Z (2005) Two Dimensional Pattern Complexity. J Fudan Univ 44:332–337
23. Gonzalez RC, Woods RE (1992) Digital Image Processing. Addison-Wesley Publishing Company, New Jersey
24. Cha K, Horch KW, Normann RA, et al. (1992) Reading speed with a pixelized vision system. J Opt Soc Am A 9:673–677
25. Dagnelie G, Thompson RW, Barnett GD, et al. (2000) Visual perception and performance under conditions simulating prosthetic vision. Perception. 29 (suppl.). 84(abstract)
26. Thompson RW, Barnett GD, Humayun MS, et al. (2000) Reading speed and facial recognition using simulated prosthetic Pixelized vision. Invest Ophthalmol Vis Sci 44:5035–5042
27. Humayun MS (2001) Intraocular retinal prosthesis. Trans Am Ophthalmol Soc 99:271–300
28. Thompson RW, Barnett GD, Humayun MS, et al. (2003) Facial recognition using simulated prosthetic pixelized vision. Invest Ophthalmol Vis Sci 44:5035–5042
29. Hayes JS, Yin VT, Piyathaisere D, et al. (2003) Visually guided performance of simple tasks using simulated prosthetic vision. Artif Organs 27:1016–1028

30. Dagnelie G, Keane P, Narla V, et al. (2007) Real and virtual mobility performance in simulated prosthetic vision. J Neural Eng 4:92–101
31. Chai X, Yu W, Wang J, et al. (2007a) Recognition of pixelized chinese characters using simulated prosthetic vision. Artif Organs 31:175–182
32. Chai X, Zhang L, et al. (2007b) Study of tactile perception based on phosphene positioning using simulated prosthetic vision. Artif Organs 32:110–115

Cochlear Implants

Fan-Gang Zeng, Stephen Rebscher, William V. Harrison, Xiaoan Sun, and Haihong Feng

Abstract The cochlear implant has not only provided partial hearing to more than 120,000 persons worldwide but also served as a model for successful academic and industrial collaboration. The present chapter reviews the development of modern cochlear implants and the dynamic interactions between academia and industry. The chapter takes a system approach to the cochlear implant system design and specifications. The design goals, principles, and methods of the subsystem components are identified from the external speech processor and radio frequency transmission link to the internal receiver, stimulator, and electrode arrays. Safety and reliability issues are considered in the context of the system design and the regulatory requirements. Future directions are discussed with regard to the expanded role of the cochlear implant in treatment of hearing impairment and in development of other neural prostheses.

1 Introduction

The research and development of the cochlear implant has served as a model of dynamic and fruitful collaboration between academia and industry. Figure 1 shows how the cochlear implant was started in academia, transferred to industry, and successfully commercialized to have restored or provided partial hearing to more than 120,000 adults and children worldwide as of 2008.

Modern cochlear implant research started in California, USA, in the 1960s and 1970s. In 1961, William House in Los Angeles implanted a crude single electrode device in two deaf patients. House's initial device only lasted 2 weeks before they were rejected but both patients reported useful hearing with electric stimulation. House and his engineer collaborator, Jack Urban, later developed

F.-G. Zeng (✉)
Departments of Anatomy and Neurobiology, Biomedical Engineering, Cognitive Sciences and Otolaryngology – Head and Neck Surgery, University of California, 364 Med Surg II, Irvine, CA 92697, USA
e-mail: fzeng@uci.edu

D.D. Zhou, E. Greenbaum (eds.), *Implantable Neural Prostheses 1*, Biological and Medical Physics, Biomedical Engineering,
DOI 10.1007/978-0-387-77261-5_3,

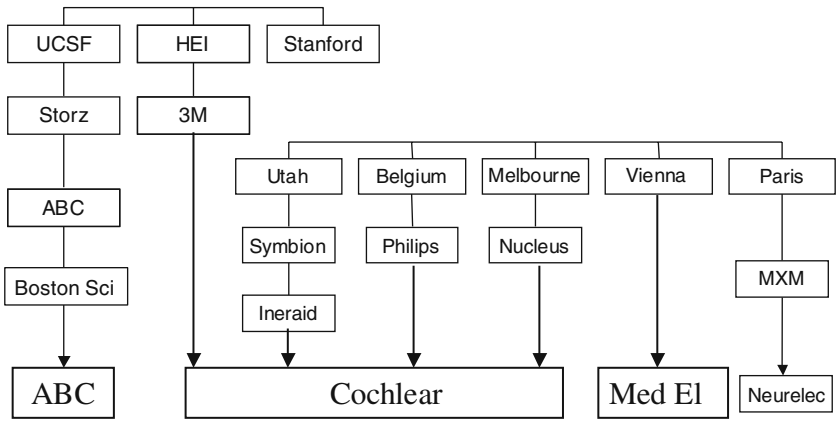

Fig. 1 An organizational chart depicting the development of the cochlear implant from academic research to industrial commercialization. UCSF stands for University of California, San Francisco, HEI for House Ear Institute, and ABC for Advanced Bionics Corporation

a complete single-channel cochlear implant system that was commercialized by 3 M and became the first device to obtain the US FDA approval in 1984 [1]. The 3 M/House device was a market leader with a few hundred annual sales in the middle 1980s. Due to its inferior performance, the 3 M/House single-channel system was phased out of the market and was eventually taken over by the Cochlear Corporation.

In 1964, Blair Simmons at Stanford University implanted a cluster of six stainless-steel electrodes into the auditory nerve through the modiolus in a 60-year-old deaf person [2]. Robert White, also at Stanford, supervised several outstanding Ph.D. dissertations and developed a VLSI-based multi-channel cochlear implant system [3]. Stanford entered an agreement with Biostem in 1983 but their joint effort did not produce any commercial devices.

In 1971, Robin Michelson in University of California, San Francisco (UCSF) implanted a form-fitting single-channel electrode pair in four deaf patients [4]. The UCSF team then developed an analog, four-channel device, which was transferred to Storz but its commercialization was not successful. Advanced Bionics Corporation obtained the UCSF electrode design in 1993 and has since produced the Clarion series devices. Advanced Bionics was acquired by Boston Scientific in 2004 for $742 million but had been bought back by its principals as a private company in 2007 (www.advancedbionics.com).

In 1978, Graeme Clark in Australia developed a 22-electrode cochlear implant system and implanted two deaf patients. Supported by a grant from the Australian Department of Productivity, the University of Melbourne and Nucleus Limited entered a public and private cooperative agreement in 1979 to manufacture and market the 22-electrode cochlear implant. In mid 1980s, NIH also helped speed up the acceptance of multi-electrode cochlear implants by

directly funding the University of Melbourne device development (1RO1-NS21027) and hosting the first consensus conference concluding that "multi-channel implants may have some superior features in adults when compared with the single-channel type." As a spin-off of Nucleus, Cochlear went public in 1995 and has been a dominating player controlling 70–80% of the cochlear implant market worldwide (www.cochlear.com).

Donald Eddington at the University of Utah developed an analog, six-electrode implant with a percutaneous plug interface [5, 6]. Its commercial version was first called the Symbion device and was later called the Ineraid device. Because of the direct access to the intracochlear electrodes, the Ineraid device was uniquely suited for research purposes [7–10]. The University of Antwerp in Belgium developed the Laura device that could deliver either 8-channel bipolar or 15-channel monopolar stimulation. The Laura device was marketed by Philips Hearing Instruments for a short period of time. Both Ineraid and Laura devices were bought out by Cochlear and are no longer available commercially.

Ingeborg Horchmair-Desoyer and Erwin Hachmair at the Technical University of Vienna, Austria, designed several multi-electrode cochlear implant devices and, working with their otologic surgeons, implanted five patients in the 1970s [11].They later switched to a simpler single-channel device and entered an agreement with 3 M to market the device. Because the single-channel device failed commercially, the Austrian group founded Mel-El in 1989 and has produced three generations of multi-electrode cochlear implants (www.medel.com).

Chouard in France implanted 21 patients with a multi-electrode (5–7 monopolar) and percutaneous device in the 1970s [12]. This early effort led to the development of a 15-channel monopolar device called Digisonic and was marketed by the MXM laboratories in 1986. The Digisonic MX20 device is currently marketed by Neurelec, a company founded in 2006 (www.neurelec.com).

Based on research at universities, several startup companies are also developing advanced and low-cost multi-electrode cochlear implants, including Advanced Cochlear Systems (www.advcoch.com) in Seattle, Washington, Nurobiosys Corporation in Seoul, Korea [13], and Nurotron Biotechnology Inc. based in both Irvine, CA and Hangzhou, China (www.nurotron.com). It remains to be seen whether these startup companies will become successful and impact the worldwide cochlear implant market.

This chapter will first provide a system review on modern cochlear implant systems, then detailed analysis on critical components of the cochlear implant, and finally system evaluation and validation.

2 System Review

The original goal of a cochlear implant is to safely use electric stimulation to provide or restore functional hearing in totally deafened persons. The utility of the cochlear implant has been expanded to enhance residual hearing in persons with severe hearing impairment. Recently, the design principle of the cochlear

implant has been adopted for development of similar hearing implants such as the auditory brainstem implant as well as other neural prostheses such as vestibular and retinal implants. Figure 2 shows schematically a typical modern cochlear implant system. A microphone (1) picks up the sound and transmits it via a wire (2) to the behind-the-ear external processor with ear hook and a battery case (3). The external processor converts the sound into a digital signal, processes and encodes the digital signal into a radio frequency (RF) signal, and sends it to the antenna inside a headpiece (4). The headpiece is held in place by a magnet attracted to an internal unit (5) placed under the skin behind the ear. The hermetically sealed internal unit contains active electronic circuits that derive power from the RF signal, decode the signal, convert it into electric currents, and send them along wires (6) threaded into the cochlea. The intracochlear electrodes (7) at the end of the wire stimulate the auditory nerve (8) connected to the central nervous system, where the electrical impulses are interpreted as sound.

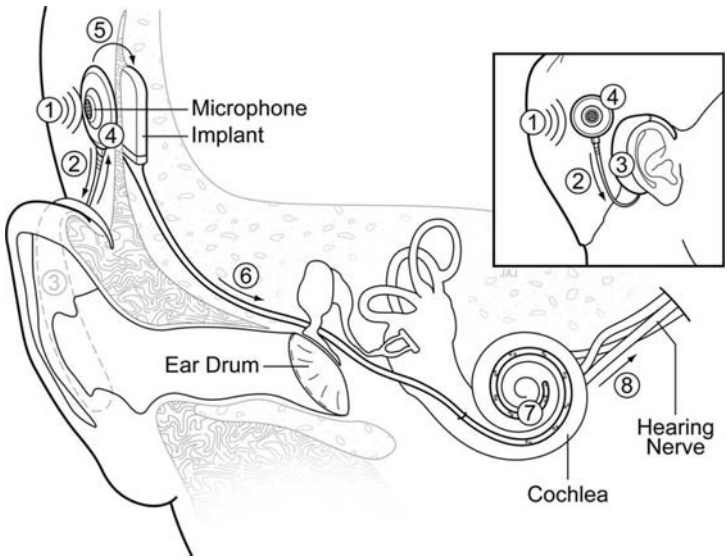

Fig. 2 A typical modern cochlear implant system that converts sound to electric impulses delivered to the auditory nerve

Figure 3 shows the cochlear implant system's architecture and functional blocks. An external unit, also known as the speech processor, consists of a digital signal processing (DSP) unit, a power amplifier, and an RF transmitter. The DSP extracts features from the sound and converts the features into a stream of bits that can be transmitted by the RF link. The DSP also contains memory units or "maps" that store patient-specific information. Depending on

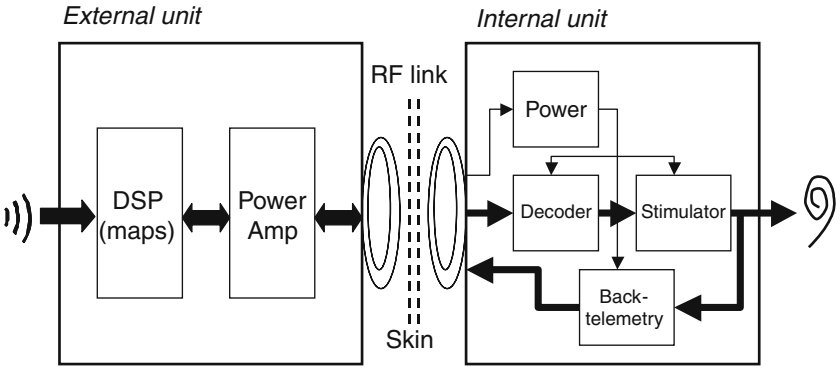

Fig. 3 Architecture and functional block diagram of a modern cochlear implant

the design and the specific implementation, the DSP may also process back telemetry information from the internal unit.

An internal unit consists of the RF receiver and a hermetically sealed stimulator. Because the internal unit has no battery, the stimulator must first derive power from the RF signal. The charged up stimulator will then decode the RF bit stream and convert it into electric currents to be delivered to appropriate electrodes. All modern systems also contain a feedback loop that can monitor critical electric and neural activities in the implants and transmit these activities back to the external unit.

There has been a convergence in technology from the viewpoint of system specifications in the last two decades. For example, the input dynamic range (IDR) was set at 30 dB in the early Nucleus 22 device, but has now increased to be 75–80 dB with a default value of 45–60 dB in the latest devices to match the range of amplitude variations of natural speech and environmental sounds [14–16]. Similarly, the frequency range has broadened to include components lower than 300 Hz to take advantage of the temporal pitch code in attempt to improve pitch and tonal language perception [17–19]. The latest devices all contain the standard CIS plus other proprietary multiple speech-processing strategies.

The Nucleus device is slightly ahead of other devices in the field in adopting sound field processing, a directional microphone, and other cosmetic (e.g., water resistant) technologies. The Nucleus device also has the longest history and the best reliability record, but it appears to lag behind in the internal unit design and technology. The latest system, the Nucleus Freedom, is still the slowest in terms of RF transmission frequency and data rate and hence the lowest in overall stimulation rate. Nucleus has kept to its original design from the 1980s with only one current source, unable to provide simultaneous stimulation and electrical field imaging. Detailed presentation and analysis of these subsystem components, functions, and specifications will be provided in the following section.

3 External Unit

Figure 4 shows a functional block diagram of the continuous interleaved sampling (CIS) strategy, which has been implemented by all major manufacturers and is still available in their latest devices (see Table 1). The sound is first subject to a number of band-pass filters with the number ranging from as few as 5 in the original CIS implementation [20] to as many as 20 in the Nucleus Freedom device [21]. The temporal envelope from each band is extracted by rectification followed by a low-pass filter. The cutoff frequency of the low-pass envelope filter is typically set at 400 Hz or slightly lower, requiring at least 800 Hz carrier for faithful representation of these envelopes [20]. The envelope is then logarithmically compressed to match the widely varying acoustic amplitudes to the narrow electric dynamic range [16, 22]. The compressed envelope amplitude modulates a fixed-rate biphasic carrier, whose rate can vary from several hundred to several thousand hertz per second. To avoid simultaneous electrical field interference, the biphasic carriers are time interleaved between the bands so that no simultaneous stimulation occurs between the bands at any time. Because of this non-simultaneous stimulation, only one current source with a multiplexer, as opposed to the parallel current sources in Fig. 4, is needed to achieve the CIS strategy.

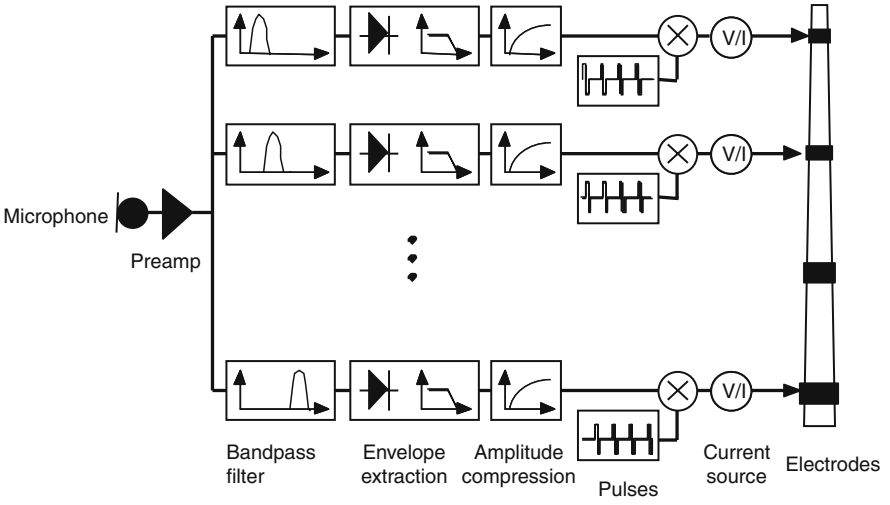

Fig. 4 Block diagram of the continuous interleaved –sampling (CIS) strategy

Figure 5 shows a functional block diagram of the "n-of-m" strategy, which was first described by Wilson and colleagues [23] and had been refined in subsequential development as the SPEAK and ACE strategies in the Nucleus devices [21, 24]. The pre-processing in the n-of-m strategy is similar to the CIS strategy, including the band-pass filters and the envelope extraction blocks. However, there are several major differences between the two strategies. One

Table 1 Properties of cochlear implant electrode arrays

	Advanced bionics 1j	Advanced bionics helix	Cochlear contour advance	Med-El combi 40 +
Length (mm)	20	20	25	31.5
Diameter (mm)	0.8–0.4	1.2–0.7	0.8–0.5	0.8–0.6
Number of contacts	16	16	22	12
Contact spacing (mm)	1.1	0.85	0.75	2.4
Shape	Pre-curved	Spiral	Spiral	Straight
Stylet	No	Yes	Yes	No

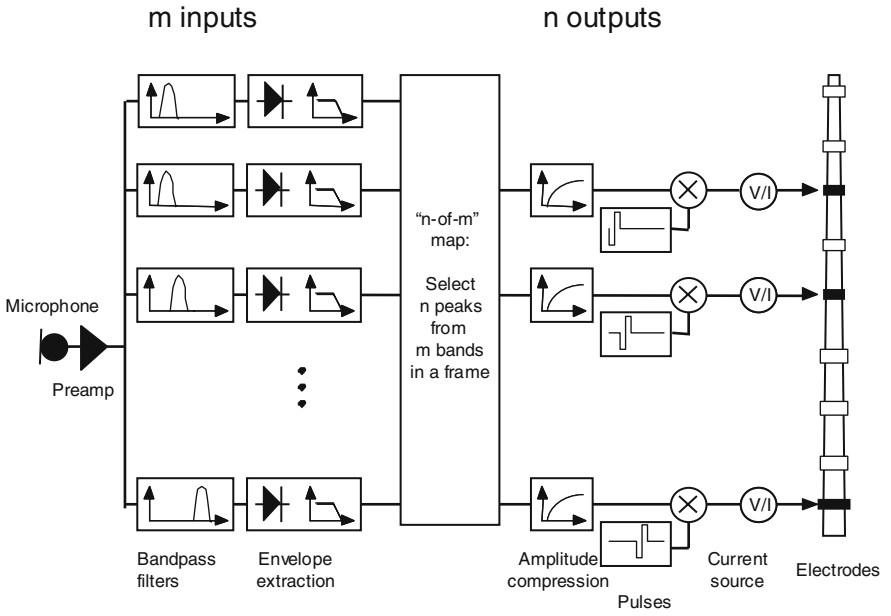

Fig. 5 Block diagram of the "n-of-m" strategy

difference is that the n-of-m strategy has a greater number of band-pass filters, e.g., m = 22 in the Nucleus implementation, than the CIS strategy. The number of band-pass filters is typically set to equal the number of intracochlear electrodes. The second difference is that the n-of-m strategy is based on temporal frames, typically lasting 2.5–4 msec, whereas the CIS strategy does not have any explicit processing frames. In each frame of the n-of-m strategy, an "n" number of bands with the largest envelope amplitude are selected (by definition, n•m). Recent studies have shown that selection of the largest peaks based on psychophysical-masking properties can improve performance [25]. Envelopes from the selected bands are subject to the same amplitude compression and used to determine the current level of the biphasic pulse. The biphasic pulses are interleaved between the output channels, with the per channel stimulation

rate being determined by the frame rate. Finally, only the corresponding "n" electrodes (dark bands in the figure) out of the "m" electrodes are stimulated in a particular frame. The SPEAK strategy selects 6–8 largest peaks and has a fixed 250 Hz per channel rate. The ACE strategy has a larger range of peak selection and higher rate than the SPEAK strategy. If n = m, then the SPEAK and ACE strategies are essentially same as the CIS strategy.

4 Radio Frequency Transmission Link

The RF link uses a pair of inductively coupled coils to transmit both power and data. The RF transmission has to address a host of challenging technical issues [26–28]. The external unit needs to provide not only reliable communication protocols including a signal modulation method, bit coding, frame coding, synchronization, and back telemetry detection but also high-efficiency RF power amplifier and immunity to electromagnetic interference (EMI). The internal unit, on the other hand, needs to harvest power with high efficiency and retrieve data with high accuracy. In addition, the size of the transmitting and receiving coils needs to be minimized and cosmetically appealing.

The RF link uses a frame or packet coding scheme to transmit specific stimulus parameters to the internal stimulator. In the Nucleus system, the parameters include pulse amplitude, pulse duration, pulse gap, active electrode, and return electrode that are used to define a biphasic pulse and the stimulation mode. Depending on the timing relationship between a frame and the pulses it generates, frame coding schemes can be classified by either the expanded mode or the embedded mode.

The expanded mode was first used by Cochlear in the Nucleus 22 device with a carrier frequency of 2.5 MHz and later in the Nucleus 24 device with a carrier frequency of 5 MHz [26, 29]. Figure 6 shows the expanded frame coding used in

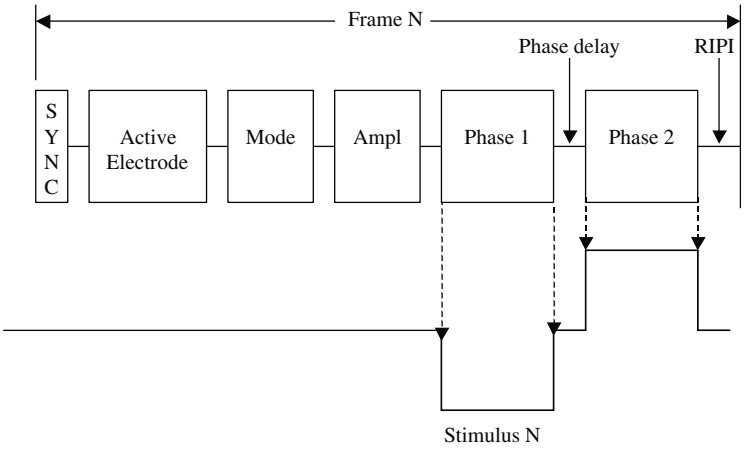

Fig. 6 The expanded mode of frame coding in the Nucleus system

the Nucleus device, in which a frame consists of a SYNC burst and an additional five bursts that specify a legal biphasic pulse [30]. The SYNC burst is short, containing no more than 7 RF clock cycles.

The number of RF cycles (n) within each burst is a multiple of eight cycles and conveys the information needed to specify the electric biphasic pulse:

- The active electrode number is determined by (n-4)/8, where $12 \leq n \leq 180$, and ranges between 1 and 22.
- The stimulation mode is determined by (n-4)/8, where $12 \leq n \leq 244$, and ranges between 1 and 30. When the stimulation mode returns a number between 1 and 22, it specifies the bipolar (BP) configuration with the return electrode being in the cochlea (however, the active and return electrodes cannot be the same). On the other hand, monopolar stimulation is specified by a stimulation mode number of 24 with the reference electrode being a ball electrode placed under the temporalis muscle (MP1), 25 being a plate electrode on the package (MP2), and 30 being both the plate and the ball electrodes (MP1 + 2).
- The pulse amplitude is coded by 271-n, where$16 \leq n \leq 271$, resulting in 256 discrete clinical units from 255 to 0.
- The pulse duration of phase 1 is determined by the duration of phase 1 burst, with the number of RF cycles from 18 to 300 or 3.6 to 600 μS.
- The phase delay determines the interval between the negative-going phase and the positive-going phase and can range from 6 to 50,000 RF cycles, or 1.2 to 10,000 μS. The polarity of phase 2 is opposite to that of phase 1, but their durations have to match for balanced charge.
- The residual inter-pulse-interval (RIPI) or inter-frame gap is inserted to produce the designed stimulation rate. The number of the RF cycles for the RIPI can range from 6 to 1,250,000, equivalent to 1.2 μS to 250 mS. This 250 mS upper limit is determined by the requirement of at least 4 Hz pulse rate to keep the internal circuit powered up.

The expanded mode requires a relatively simply decoder on the receiver side, however, it has several limitations. First, the maximal total stimulation rate is low because no stimulation is generated when parameters such as Sync, electrode, mode, amplitude, and RIPI bursts are being transmitted. Furthermore, the RIPI is not a constant between frames even at a constant stimulation rate, because it is affected by other stimulation parameters such as electrode, mode, and amplitude. Finally, the amplitude and pulse duration parameters are prone to RF cycle detection errors, which may lead to unbalanced charge.

To overcome the limitations of the expanded mode, the embedded mode frame coding scheme was developed and has become the de facto standard for current cochlear implants [31]. The basic idea is to transmit the information regarding electrode, mode, and amplitude (E, M, & A) for the next biphasic stimulus, while the present stimulus is still being delivered. Another advantage of the embedded mode is that there is a period of time between the end of the present stimulus and the start of the next stimulus for the internal circuitry to

check the validity of the stimulation parameters. In the case of errors, the stimulus can be stopped before it is actually delivered.

The maximum total stimulation rate depends upon the bit rate and the frame rate in the RF transmission link. The Nucleus 22 uses only the expanded mode to encode frames and has a theoretically maximal total stimulation rate of 5,900 Hz. In practice, this theoretical rate is not attainable with the maximum rate being just above 3,000 Hz [29]. The Nucleus 24 system supports both the expanded mode and the embedded mode, with a maximum pulse rate of 8,500 and 14,400 Hz, respectively. To further increase the maximum total stimulation rate, the electrode mode and pulse duration information can be set initially with only the electrode number and amplitude information being transmitted on a pulse by pulse basis. The Nucleus Freedom system (CI24R and CI24RE) adopts this high-rate mode and can attain a maximum total rate of 32,000 Hz [21].

Both the Advanced Bionics and Med El systems have used high RF and multiple current sources to achieve the high total stimulation rate. Compared with the 5 MHz RF in the Nucleus 24 device, the Clarion HiRes 90 K (Advanced Bionics) uses 49 MHz and the Sonata device (Med El) uses 12 MHz RF. The higher RF leads to higher bit rate in the RF transmission. The multiple current sources allow one-to-one mapping between the current source and the electrode, eliminating the need to transmit the electrode information. The HiRes 90 K device has 16 current sources corresponding to 16 electrodes and is capable of producing a maximum total stimulation of 83,000 Hz. Sonata has 12 current sources corresponding to 12 electrodes and is capable of producing a maximum total stimulation rate of 50,700 Hz pulses. Although there has been a trend for all manufacturers to push for higher stimulation rates, there is little or no scientific evidence suggesting that a higher rate produces better performance [32–34].

5 Internal Unit

5.1 Receiver and Decoder

Figure 7 shows the block diagram of a typical implanted receiver and stimulator [26, 35–37]. The centerpiece is an ASIC (application-specific integrated circuit) chip shown as a dotted box that performs critical function to ensure safe and reliable electric stimulation. Inside the ASIC chip, there is a forward pathway, a backward pathway, and control units. The forward pathway usually includes a data decoder that recovers digital information from the RF signal, error, and safety check that ensures proper decoding, and a data distributor that sends the decoded electric stimulation parameters to the right place (i.e., the programmable current source) at the right time (i.e., by switching on and off multiplexers). The backward pathway usually includes a back telemetry voltage sampler that reads the voltage over a period of time on the recording electrode.

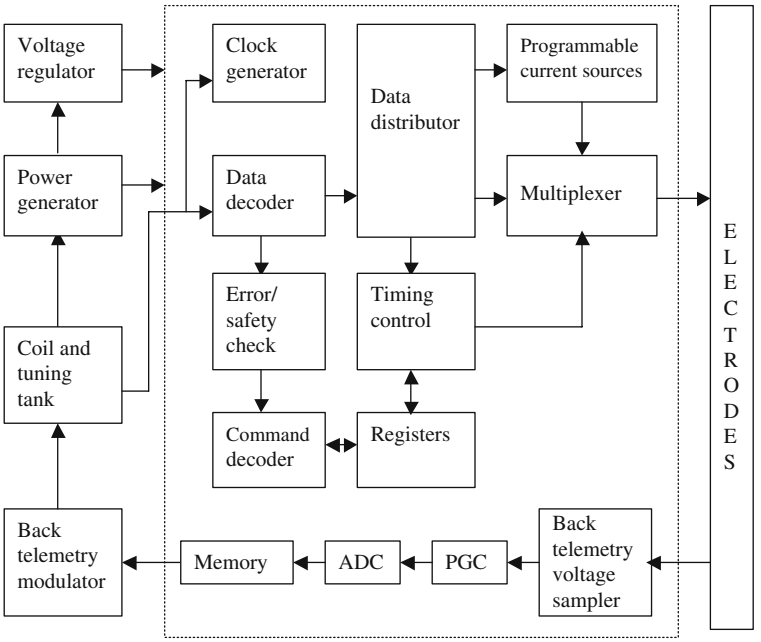

Fig. 7 Block diagram of the cochlear implant internal unit

The voltage is then amplified by the programmable gain control (PGC), converted into digital form by an analog to digital converter (ADC), and stored in memory to be sent out to the external unit via back telemetry. The ASIC chip also includes many control units from the clock generated from the RF signal to command decoder and registers. There are several circuits and devices that cannot be easily integrated into the ASIC chip, including the voltage regulator, the power generator, the coil and RF tuning tank, and the back telemetry data modulator.

Stimulation safety is a top priority in the receiver and stimulator design. Under no circumstance should harmful electrical stimulation such as over stimulation or unbalanced stimulation be delivered to the cochlea. Additional considerations are needed to prevent erratic functions of the receiver stimulator in cases of unpredictable events, such as a drop of the headpiece, strong electromagnetic interference, or malfunction of the external DSP unit. Several levels of safety checks are commonly implemented in current cochlear implants, including

- A parity check to detect bit error from either RF transmission or data decoding.
- A stimulation parameter check to ensure the validity of electrode number, mode, amplitude, pulse duration, and inter-pulse gap.

- A maximum charge check to prevent over stimulation, with the charge density being typically less than 15–65 $\mu C/cm^2$/phase dependent on the electrode material, size, and shape [38, 39].
- A charge balance check to prevent unbalanced stimulation and DC stimulation because they generate gases, toxic oxychlorides, corrosion products, and associated pH changes that can cause tissue damage [40].
- To prevent DC stimulation, capacitors are serially connected to the electrodes to block any unbalanced charge being delivered to electrodes. The Clarion and Med El devices have used this method.
- To prevent accumulated unbalanced charges, especially with high-rate stimulation, Nucleus cochlear implants short all stimulating electrodes between pulses [41].

5.2 Stimulator

The current source generates a stimulating current according to the amplitude information from the data decoder. The complete system usually consists of a digital to analog converter (DAC) and current mirrors. The design of an accurate current source is demanding. In the Nucleus 22 device, a trimmer network was needed to fine tune the reference current to deal with the process variation of integrated circuit fabrication. Recent devices no longer use this trimmer network method, but instead combine multiple DACs to obtain the desired amount of current.

In addition to accuracy, an ideal current source should have infinite impedance. In practice, the impedance of a current source should be high relative to the impedance of the load. Several techniques have been developed to design a high-impedance current source. For example, Cascode current mirrors are commonly used to increase the current source output impedance, but the increased impedance usually comes at the expense of reduced voltage compliance and power dissipation [42].

For cochlear implants with multiple current sources, e.g., the Advanced Bionics HiRes 90 k and the Med El Sonata devices, a switching network is no longer needed to connect one current source to multiple electrodes. Instead, multiple current sources are used sequentially or simultaneously, in which both the N-channel and the P-channel current sources are used to generate positive and negative phases of stimulation [43]. Matching the N-channel current source and the P-channel current source is needed to ensure that the positive and negative charges be balanced.

To handle a wide range of electrode impedance, the current source in a cochlear implant typically requires high-compliance voltage, thus leading to high-power consumption. Minimizing voltage drop in the devices is one way to achieve low power consumption. Using adaptive compliance voltages is another way to balance the need between the low power consumption and the wide impedance range [44, 45].

5.3 Electrodes

After external signal processing and transmission to an implanted receiver/stimulator, the electrical output of a cochlear implant is delivered to the cochlea via a sequential array of stimulating contacts. These stimulus pulses depolarize auditory neurons in the spiral ganglion or peripheral dendrites in the osseous spiral lamina. Over the past three decades, the design of these electrodes has evolved from simple single-channel devices to multiple site arrays consisting of 12–22 stimulating contacts. In all currently manufactured devices, these stimulating contacts are formed from platinum–iridium alloy, usually Pt:Ir 90:10, and are molded into a carrier of silicone elastomer. This carrier holds the contacts in their intended orientation within the scala tympani, facilitates handling of the electrode array during insertion, and acts as an insulator to reduce the spread of stimulus current within the volume of the scala tympani. Table 1 lists the basic parameters of the most frequently used cochlear implants from the three major manufacturers.

The first generation of multichannel cochlear implant electrodes consisted of both straight (Nucleus 22 banded and Med-El) and spiral-shaped (Advanced Bionics Clarion^{TM}) models. Temporal bone insertion studies revealed that, in general, after insertion straight arrays were located along the lateral margin of the scala tympani and the spiral Clarion^{TM} array was located near the center of the scala tympani. These studies also revealed that at least some of these arrays often deviated from their intended location in the scala tympani into the scala media or scala vestibuli [46–69]. It was hypothesized that these traumatic insertions might lead to greater loss of spiral ganglion neurons in the vicinity of the lesion [55, 70, 71] and additional loss of performance due to unpredictable current flows within the three compartments of the cochlea. Also, computer models [72–77] and animal physiological experiments [78–83] have demonstrated that the location of an intracochlear array and the configuration of the stimulating sites were important factors in determining the amount of current that was required to illicit a perceptual response, i.e., the efficiency of stimulation, and the selectivity of the response to each channel of stimulation. In response to this growing body of research, which included clinical studies, temporal bone trials, computer modeling, and animal studies, a second generation of intracochlear electrodes was developed beginning in the late 1990s and continuing to the present. Primary design goals for the development of these new electrodes include deeper insertion to better match the tonotopic place of stimulation to the frequency band assigned to each electrode channel, improving efficiency of stimulation, and reducing insertion related trauma.

5.3.1 Current Electrodes, Efficiency, and Intracochlear Trauma

Figure 8 illustrates three current intracochlear electrode arrays. Although similar in many respects each have features that attempt to achieve the goals

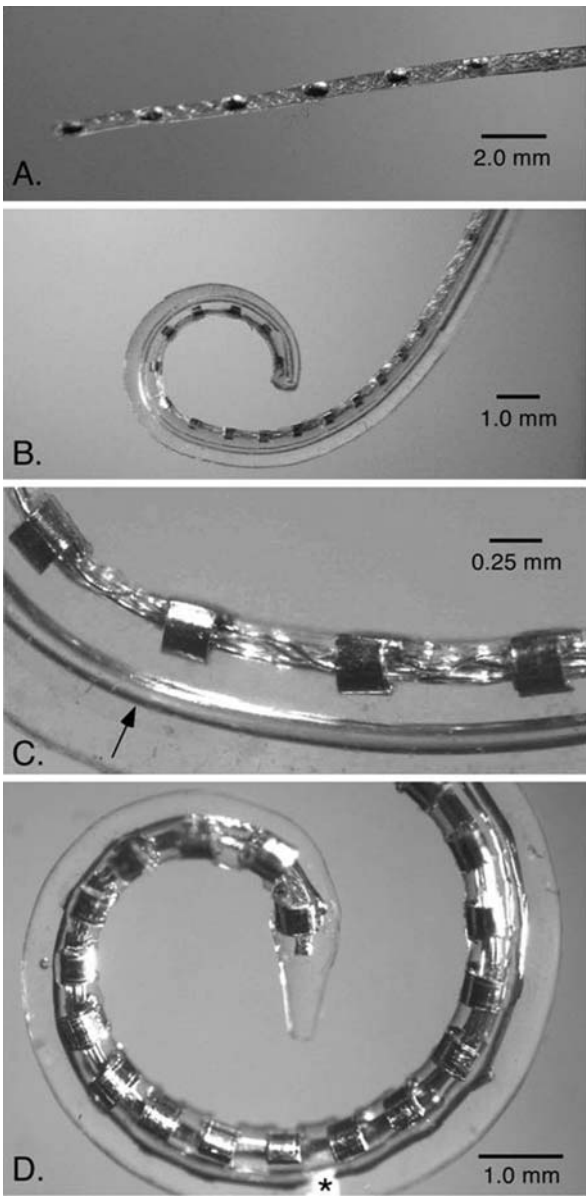

Fig. 8 Cochlear implant electrodes manufactured by Med-El, Cochlear Corporation and Advanced Bionics, Inc. are shown above. The Med-El Combi 40 + ™ electrode (**A**) is a straight electrode with 12 paired contacts. The second contact site of each pair is not visible in this image. The Combi 40 + ™ and the Advanced Bionics Helix™ (shown in **B** and **C**) both use crinkled lead wires to increase flexibility and reliability. The Helix™ and Contour Advance™ electrodes (shown in **B–D**) are pre-molded spirals designed to be located near the modiolus after insertion. To facilitate surgical insertion both are held on a straight wire stylet which is held in a molded channel within the array as shown in **C**. The Helix™ insertion system holds the stylet in place after it is inserted approximately 6 mm into the cochlea. At this point, the electrode is advanced off of the stylet to its full insertion depth. With the Contour™ electrode, the array and stylet are positioned approximately 9 mm within the cochlea (see the *white marker, asterisk* in **D**) and the electrode is advanced off of the stylet

presented above in different ways. The current Med El Combi 40 + ™ intracochlear array (Fig. 8A) is a straight electrode and is the longest of the electrodes shown (31.5 mm in length). Because a straight cylindrical electrode can be inserted into the scala tympani in any orientation this electrode has a pair of foil-stimulating contacts at each stimulus site to ensure that no single site faces directly away from the target neurons within the modiolus. To increase

flexibility and reliability, the lead wires within the silicone carrier are crinkled as they are in the Helix™ and Med El electrode as well. Although the Combi 40+™ electrode has been inserted to a depth of greater than two turns, in temporal bone studies insertion depths of one full cochlear turn or greater resulted in increased trauma in 50% or more of the trial insertions [59].

The Advanced Bionics Helix™ (Fig. 8B,C) and Cochlear Contour™ electrodes (Fig. 8D) are spiral shaped. They are designed to be positioned near the modiolus and are thus often referred to as perimodiolar electrodes. Both of these devices have flattened foil contacts oriented to face the modiolus when the electrodes are fully inserted. Temporal bone studies and clinical threshold data confirm that perimodiolar electrodes are located nearer their intended sites of stimulation in the spiral ganglion and that this position results in more efficient activation of these neurons [84–88].

Insertion of a tightly coiled electrode array within the anatomical restrictions of the surgical field without straightening the array would be difficult or impossible in most subjects. Thus, a fine channel is molded into each spiral array (see Fig. 8C, arrow) to allow the use of a fine straight wire stylet. This stylet holds the electrode straight during the initial phase of insertion. After the tip of the electrode has been inserted to a point just beyond the beginning of the first cochlear turn the stylet is held in place and the electrode is advanced off of the stylet to its full insertion depth. Thus, this technique is often referred to as the advance off stylet or AOS technique. Although the AOS technique should, in theory, result in little if any contact with the lateral wall of the scala tympani, shown to be critical in the initiation of trauma [64], recent temporal bone studies with the Contour™ electrode indicate that damage may result with this electrode. We have hypothesized that this damage may occur if the straightened Contour™ electrode with the stylet in place is inserted too deeply into the scala tympani. The white marker on each Contour™ array (shown with an asterisk in Fig. 8D) is located approximately 9 mm from the tip of the electrode. However, we recently reported that the distance from the anterior edge of the round window to the beginning of the first cochlear turn varies from 4.6 to 8.2 mm (mean = 6.7 mm, n = 62) [89]. Most electrodes are inserted through a cochleostomy placed anterior to the round window which further reduces this critical distance. Thus, in at least some cases, it appears that inserting the Contour™ electrode to this marker while still fully loaded on the stylet might lead to trauma as the straight stiffened electrode contacts the outer wall of the first cochlear turn. Unfortunately, there is currently no routine method to determine the size of the individual cochlea during, or prior to, surgery to better allow the surgeon to anticipate the ideal insertion depth prior to advancing the array in each patient. It appears that the Advanced Bionics Helix™ electrode will be less prone to this mechanism of trauma as the insertion system for the Helix™ is designed to insert the electrode only 6 mm into the scala tympani before advancing the array off of the stylet.

Both the Contour™ and the Helix™ electrodes also include mechanical features intended to minimize the occurrence of trauma. The latest version of

the Contour™ electrode, the Contour Advance or Softip™, has an elongated tip molded with soft silicone elastomer. In a temporal bone comparison study with the standard Contour™ array this modified tip design appeared to reduce the incidence of trauma [85]. The Helix™ electrode and Advanced Bionics 1 J electrode (a slightly pre-curved array very similar to the Helix™ in all other aspects) increased mechanical stiffness in the vertical plane of the array to minimize the probability that the electrode will deviate upwardly through the basilar partition into the scala vestibuli. This strategy has been effective in reducing intracochlear trauma in several electrode designs manufactured by Advanced Bionics [49, 86, 89, 90].

5.3.2 Insertion Depth

Clinical studies using both modified acoustic speech in hearing subjects and altered stimulus locations in cochlear implant subjects have shown that a correct match between the frequency band of the signal delivered to the cochlea and the tonotopic location of that electrical stimulus may be a critical factor in cochlear implant performance [91–96]. Until recently it was difficult to estimate the location of electrode sites in each subject or to estimate the frequency map in a given patient because of insufficient resolution in medical imaging systems, the problem of strong imaging distortion created by the metal contacts in the cochlear implant electrode, and the lack of an accurate frequency map for the spiral ganglion which is the most probable site of activation for most cochlear implant subjects. Recent improvements in imaging methods [97–99] and an accurate map of the human spiral ganglion based on cochlear size [100] now make it possible to design an electrode array to better match the tonotopic frequency distribution of the average human subject and to better customize the frequency-to-place mapping parameters for each patient following surgery.

From an electrode design standpoint, an insertion depth of approximately 540°, or 1.5 cochlear turns, as measured from the round window will permit stimulation of the full range of speech formant frequencies. Because the path of neurons in the spiral ganglion becomes highly compressed at more apical locations in the cochlea it may not be effective to stimulate significantly lower frequency locations and preliminary human studies confirm that stimulation of these more apical locations may not produce significant increases in performance [46, 47]. Temporal bone insertion data for the current clinical cochlear implant electrodes indicate that none of these electrode arrays can be consistently inserted to this target depth (540° from the round window) without severe trauma. In these studies, the Contour™ electrode was inserted to average depths of 340° [85] to 405° [89], the Helix™ was inserted to an average depth of 435° [86] and the Med El Combi 40+ electrode was inserted to an average depth of 277° with minimal trauma [59]. Clearly, we can infer from this data that the stimulating channel locations for most current cochlear implant subjects do not match the acoustic frequency bands which are being delivered to those

locations and it is probable that speech perception in the majority of subjects suffers due to this mismatch.

5.3.3 Future Cochlear Implant Electrode Design

It is clear that the development of cochlear implant electrode arrays will continue to play an important role in improved subject performance. No single electrode manufactured today meets all of the criteria for an optimum device; insertion depth to match the primary speech frequency spectrum increased coupling efficiency and minimal insertion damage. What other areas of development might also impact the performance and satisfaction of cochlear implant users or increase the number of hearing impaired subjects that would benefit from this technology?

One way to increase the spectral resolution of a cochlear implant system is to increase the number of perceptually distinct channels. Computer modeling and animal research indicate that to have greater functional channel density will require optimized electrode location very near to the spiral ganglion or peripheral dendrites. With the perimodiolar Helix^{TM} array and HiRes 120 software Advanced Bionics uses "current steering" to create several perceptual frequencies or "virtual channels" between pairs of electrode contacts by varying the proportion of current sent to each contact site. In this way a large number of channels can be created using a relatively small number of electrode sites [101,102]. An alternate location for highly selective auditory stimulation is the body of auditory nerve fibers within the modiolus. Preliminary results with an intramodiolar or intraneural stimulating array indicate that activation of these fibers may produce very efficient and very selective activation of the auditory nerve [103, 104]. More accurate representation of the spectral content of acoustic energy may not only increase the speech performance of cochlear implant users but also allow greater appreciation of music and other environmental sounds which have been difficult for implant users to recognize or appreciate with current systems.

As cochlear implant subject performance steadily increases, the number of hearing impaired subjects which might clearly benefit from this technology is increasing rapidly. Patients that receive marginal benefit from conventional hearing aids have shown significantly better performance with a cochlear implant [105]. Subjects with significant levels of hearing at low frequencies, i.e., in the apical region of the cochlea, appear to benefit from simultaneous use of electrical stimulation in the base of the cochlea and amplified acoustic stimulation in the apical cochlea. To decrease the probability that insertion of the electrode will result in damage to the cochlea and a reduction in a subject's remaining acoustic performance, several shortened intracochlear electrodes have been designed and the efficacy of these electrodes has been compared to that of standard cochlear implant electrodes in similar patients [106–111]. Table 2 lists the specifications of several electrodes designed for use in these hybrid electric/acoustic or EAS implant systems.

Table 2 Properties of the EAS electrode arrays

	Cochlear Hybrid	Cochlear Hybrid – L	Med-El Flex EAS
Length (mm)	6	15	20.9
Diameter (mm)		0.35 (tip)	0.8–0.6
Number of contacts	6	22	12
Contact spacing (mm)	0.75	0.75	1.9
Shape	Straight	Straight	Straight
Stylet	No	No	No

To achieve deeper insertion with minimal associated damage may require significant innovation. The capability to mechanically steer an electrode as it passes along the length of the scala tympani may be one method used to meet this challenge. One design concept developed to "steer" the tip of an electrode functions by forming fine fluid channels beneath the surface of the array [112]. Controlling the pressure in these channels bends the array in the desired direction. Other strategies use fine filaments or temperature sensitive shape memory metal elements within the array to control electrode shape. Additionally, the most effective use of mechanical steering during insertion will probably require some form of feedback to accurately direct the electrode and avoid trauma.

5.3.4 Summary

In the past decade improvement in the design of intracochlear electrodes has led to the production of devices with greater efficiency and reduced intracochlear damage. Still, current electrodes do not allow routine insertion to the cochlear depth that is required to locate stimulating contacts adjacent to tonotopically appropriate sectors of essential speech frequency components. In addition, temporal bone studies demonstrate that at least some insertions with each type of electrode currently in use result in damage to the cochlea. This damage may result in accelerated degeneration of the spiral ganglion neurons upon which the cochlear implant depends for activation. Damage also results in idiosyncratic location of the electrode array within the scala tympani as location of the array is restricted at the point of damage from following its usual course. These variations in distance from the electrode to each neural activation site affect the efficiency and spread of excitation for each channel in unique ways making it difficult to optimally fit patients with severe intracochlear damage [113,114].

Finally, the role of the surgeon must be carefully addressed as cochlear implants move from application in relatively small populations of deaf individuals to larger populations of subjects with greater residual hearing. It is important to note that the studies which demonstrate reductions in the occurrence of damage with the latest electrode designs are, for the most

part, conducted by experienced surgeons that have completed many temporal bone studies of these devices. For this reason, it is very difficult to separate the effects of their increasing expertise from the effects of iterative changes in electrode design. Improvements in electrode design must be effective across the broad spectrum of surgical experience and training if these modifications are going to result in increased performance for all subjects.

5.4 Back Telemetry

Back telemetry allows the external unit to check the status of the internal unit, such as regulated voltage, compliance voltage, register values, and hand shaking status. The function of back telemetry is critical to ensure that the internal circuit works in the proper state to correctly execute commands sent from the external unit. The other function of back telemetry is to measure and monitor critical information regarding the electrode–tissue interface, including electrode impedance, electrode field potential, and neural responses [115].

Electrode impedance is derived by measuring the voltage drop across an electrode for a given current. The current is delivered below the audible threshold, with a value in tens of μA or even lower. Extremely low electrode impedance suggests shortage, while extremely high electrode impedance suggests open circuitry. Electrodes with both extreme values are typically eliminated in the fitting process. Electrode field potential can be obtained by stimulating one electrode, while recording the potential in other non-stimulating electrodes. Electrical field imaging plots the potential distribution as a function of electrode position and can be a useful clinical tool to probe the interference and interaction between electrodes [116].

Neural response telemetry (NRT) measures the auditory neural response to electric stimulation. Because the neural response is minuscule, usually buried in the artifact of electric stimulation, special techniques are required to remove the artifact. Figure 9 shows three methods used to remove the electric artifacts [117]. First, an alternating phase assumes that the neural responses are the same to anodic and cathodic-leading stimuli so that simple averaging the two responses would cancel the artifacts while preserving the neural response. However, this assumption is not true and additionally the nerve may respond to the second phase, limiting the alternating phase utility [118]. Second, template subtraction uses either a subthreshold template or statistical properties of electric artifact to remove the artifact and recover the neural response [119, 120]. Third, forward masking takes advantage of neural refractoriness in that a probe following a masker will produce artifact but no neural response [117]. At present, forward masking is the most widely used technique.

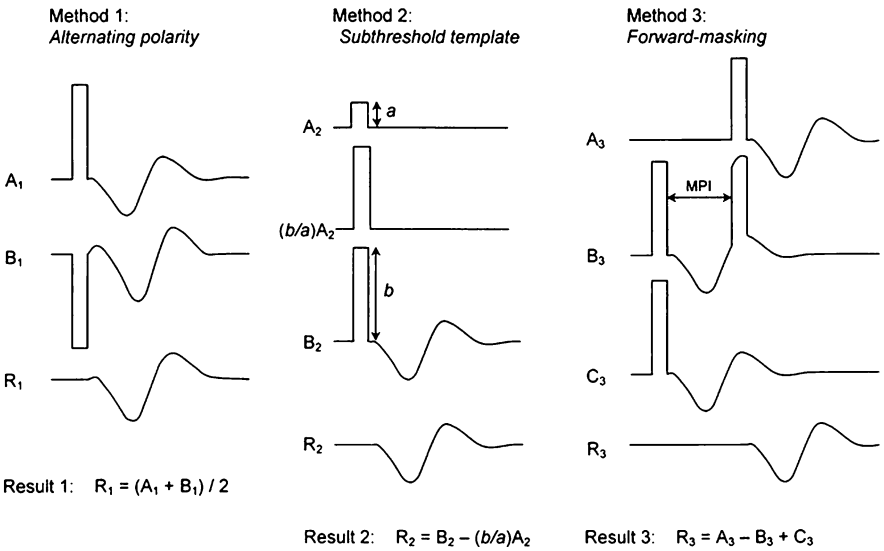

Fig. 9 Comparison of three methods to reduce electrical stimulus artifact [with permission of 117]. In method 1, stimulus polarity is sequentially alternated (traces A_1 and B_1); in the average (R_1), the stimulus artifacts cancel out. In method 2, a subthreshold stimulus (A_2) is used to obtain a template of the stimulus artifact without a neural response. The template is scaled upward (waveform $(b/a)A_2$) to match the amplitude of a suprathreshold stimulus artifact of B_2 and subtracted from that waveform to eliminate the stimulus artifact (R_2). In the third method, a high-level masker puts the nerve in a refractory state, so that a subsequent probe fails to elicit a response (B_3). This waveform is subtracted from the response to the probe alone (A_3) to eliminate the probe artifact. This subtraction, however, introduces an inverted masker and masker response (i.e., in B_3) where the probe artifact occurs in the midst of the EAP to the masker. To remove this artifact, the response to the masker alone (C_3) is added, producing the desired EAP response to the probe (R_3)

6 Safety Considerations

Safety is an important consideration in the design of any neural prosthetic device. The safety of an implantable neural prosthetic device can be segmented into four categories: (1) materials and their biocompatibility and toxicity, (2) sterilization to eliminate infection, (3) mechanical design with its potential to cause structural tissue damage, and (4) energy exposure limits and the resulting tissue and neural damage. Safety problems related to each of these categories can have both short- and long-term consequences.

6.1 Biocompatibility

All implantable materials should be biologically compatible in terms of not producing a toxic, injurious, or immunological response within the living tissue.

The materials used to fabricate implantable system components need to be compatible with the tissue and structures in the vicinity of the device and need to be appropriately selected for their specific use. There is a significant history of implantable materials demonstrating the successful biocompatibility in implantable applications. By selecting materials that already meet an FDA recognized biocompatibility standard it is possible to avoid the need for animal testing and possibly submit a declaration of conformity in place of performance data [121]. In addition to saving time and expense, declaration of conformity allows design energy and focus to be placed elsewhere. Selection of materials would then be based on factors related to their mechanical properties, electrical properties, and abilities to achieve hermetic isolation. Table 3 presents a partial list of frequently used biocompatible materials in cochlear implants.

Table 3 List of biocompatible materials and their applications

Materials		Applications
Metal	Titanium	Case; encapsulation
	Platinum	Electrode
	Iridium	Electrode
	Zirconium	Case
	Gold	Coil; encapsulation
Non metal	Ceramic	Case; feedthroughs
	Glass	Feedthroughs
	Silicone rubber	Carrier; encapsulation
	Parylene	Insulation coating
	Teflon	Insulation coating

Biocompatibility is not the only factor in selecting proper materials in cochlear implants. For example, when selecting materials for the design of electrodes used to deliver electrical stimulation, it has been found that platinum–iridium electrodes are safer and less damaging to neural tissue than titanium electrodes used at the same stimulation exposure levels [122]. Therefore, even though titanium is biocompatible, its use should be limited to specific applications that do not include delivering electrical stimulation to neural tissue. The materials most commonly used for this application in cochlear implants are 90% platinum–10% iridium alloys.

6.2 Sterilization

Even though a material used for a specific design may be biocompatible, the material must also be designed and manufactured to tolerate the process that will be used to achieve sterilization. Sterilization processes often expose materials to high temperatures and harsh chemicals. Ethylene oxide (EtO) is frequently used to sterilize cochlear implants. Other acceptable sterilization

methods are available for cochlear implants. These are covered by multiple standards and documents available from the FDA and other sources [123].

The EtO sterilization process applies both high temperatures and a chemical gas to the components to achieve sterilization. Materials exposed to the EtO process must be able to withstand exposure to both of these conditions. Additionally, the structure of implanted components and housing must be designed to avoid pockets, crevices, or other small spaces in the external surfaces where bacteria can collect, making it more difficult if not impossible for the sterilization processes to be effective.

6.3 Mechanical Safety

Tissue trauma is frequently the result of mechanical stress or chronic force applied to tissue by the implantable package and electrode. Tissue trauma can also be induced by surgeries that result from an implant designed in a way that is difficult to put in place and stabilize. Relative to the package, smaller is generally better, but this is not the only consideration. The cochlear implant package is normally placed behind the pinna of the ear embedded in bonny tissue around and adjacent to the mastoid cavity. A very small package that cannot be stabilized will probably cause more tissue damage than a well-designed package that can be stabilized in an effective bone bed. A new device implanted in a healthy subject will probably be encapsulated in tissue that will stabilize the device after several weeks, the design goal is to provide stabilization until this encapsulation occurs. The top surface of the package needs to be shaped to reduce internal tissue trauma that could result in long-term problems. Softly rounded corners and soft silicone rubber encapsulation helps prevent these problems. There have been cases of severe tissue necrosis reported with some implants and this usually results in an explant and a subsequent reimplant with a different device or a different placement method. Designers need to work carefully with skilled surgeons to ensure the final design meets the surgical needs and minimizes the potential for chronic tissue trauma.

6.4 Energy Exposure

Electricity, heat, light, and sound are several types of energy encountered by cochlear implants. The bio-effects of light and sound energy sources, particularly the interaction between tissue and laser or ultrasonic sound, are well documented. Stimulation of the cochlea requires exposure to adequate amounts of electrical energy to achieve sufficient neural recruitment to achieve loudness. Increasing requirements to improve tonotopic selectivity is forcing a reduction in contact surface area along with a higher density electrode pitch. The trends are placing an additional burden of keeping electrical energy at safe exposure levels. The standard parameter used to quantify energy delivery for neural

activation is charge density. The maximum total charge, charge density, and its delivery must be specified for safe operation of the stimulator. Most modern cochlear implants use current source stimulation drivers. The charge is the product of current and time of the signal applied to the contact. Driver currents in cochlear implants range from a few micro-amps to as high as two milliamps. Electrical contacts vary in range from 0.12 mm^2 up to over 1.5 mm^2. Typically, the charge density is less than 15–65 $\mu C/cm^2$/phase although higher values have been considered safe in electric stimulation of the nerve tissue [38, 39].

External devices that maintain surface contact with the skin must not have chronic temperatures that exceed 41°C. This criterion allows considerable rise if the environmental temperature is low but may be difficult to achieve in very hot climates. The temperature rise of implanted electronics must be minimized to safe levels. Implanted devices must not have surface temperatures that exceed 39° C under any condition in vivo. The implant environment must be considered during design and testing to ensure the final device meets requirements [124]. In addition, the temperature may rise as a result of exposure to outside energy sources such as MRI. Analytical treatment of this topic is difficult and early in vivo modeling and testing is suggested.

7 Evaluation

Over the last three decades, the cochlear implant has evolved from a single-channel device that merely provided help in lip reading and identification of environmental sounds to modern multi-channel devices that allow average users to understand 70–80% of open-set speech in quiet. This level of understanding is sufficient to carry a conversation in person or even over the telephone. Figure 10 shows sentence recognition in quiet by the latest cochlear implant users from three major manufacturers. There is no statistically significant difference between the three devices.

With improved performance, the audiological criteria for cochlear implantation have been accordingly relaxed. In the early days, cochlear implant performance was judged in comparison to vibrotactile aid performance [128], then the hearing aid performance [129], and now normal auditory performance [130]. The present audiological criteria are not based on pure tone audiograms, but rather on speech performance in the best-aided condition. If the best-aided sentence intelligibility is less than 50%, the subject can now be a candidate for cochlear implantation regardless of his or her pure tone thresholds.

8 Future Direction

Despite impressive performance by modern cochlear implant users, they face tremendous challenges in pitch-related tasks and in realistic listening situations. Intensive research has been initiated to address these challenges and beyond:

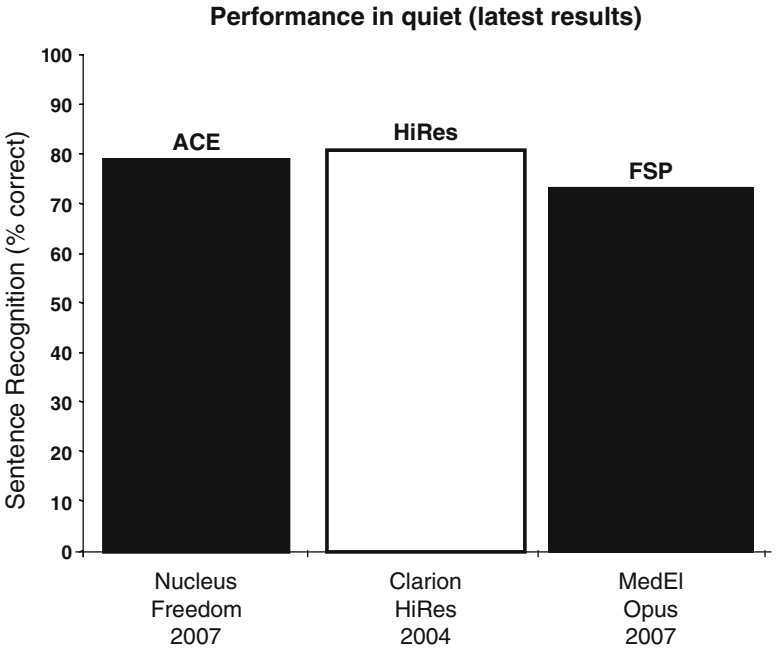

Fig. 10 Sentence recognition scores in a quiet background using the Nucleus Freedom system [125], the Clarion HiRes 90 k system [126], and the Med-El Opus system [127]

- Front-end processing in hearing aid technology such as directional microphone, noise reduction, and sound field or scene analysis is being incorporated into cochlear implants for improved speech recognition in noise [131, 132].
- Bilateral cochlear implants guarantee the implantation of the best ear and offer improved localization and speech recognition in noise [133]. However, for bilateral implants to behave like binaural implants, significant design of the present implants is required, including coordinated and novel stimulation patterns between the two implants [e.g., 134, 135].
- Combined acoustic and electric hearing [136, 137] extends the utility of the cochlear implant to those with little or significant residual acoustic hearing. In many cases, the residual hearing occurs only at low frequencies below 300 Hz, which are not transmitted by the telephone because they provide little or no speech intelligibility [138]. Surprisingly, these low-frequency acoustic sounds, when combined with a cochlear implant, can improve the implant performance in noise and in music perception [139–141].
- The auditory nerve implant (ANI), which was first attempted by Simmons at Stanford, is also revived with improved signal-processing and electrode technology [142, 143]. Compared with the cochlear implant, the ANI can improve spatial selectivity and lower power consumption.

- The auditory brainstem implant (ABI) that stimulates the surface of the cochlear nuclei has been introduced for more than 20 years with several hundred patients, but the clinical results are mixed and generally poor [144]. Recent development of penetrating ABI should improve tonotopic access in theory but the clinical outcome is less than desirable [145]. The reason for the generally poor performance with ABI may be the presence of acoustic tumors because there are successful ABI users who typically do not have acoustic tumors [146].
- The auditory middlebrain implant (AMI) offers an alternative, and potentially effective stimulation site because the inferior colliculus (IC) has relatively convenient surgical access and clearly defined anatomical structure, [147]. Several patients have received AMI recently, producing useful hearing [148].
- Feasibility of an auditory cortex implant (ACI) has also been studied and may someday provide useful functional hearing in special patient populations [149].
- Finally, cochlear implant design can be adapted to develop other neural prostheses such as the retinal implant to help restore vision [150] and balance [151, 152].

Acknowledgments Part of the materials presented here are from a comprehensive review paper by the same authors (IEEE Review on Biomedical Engineering, 2008). The authors thank Abby Copeland for proofreading the manuscript. The preparation of this manuscript was supported in part by the National Institutes of Health, US Department of Health & Human Services (RO1-DC002267, RO1-DC008858, P30-DC008369, and HHS-N-263-2007-00054-C), The Chinese Academy of Sciences Pilot Project of the Knowledge Innovation Program (KGCX2-YX-607), and The Key Technologies R&D Program of Ministry of Science and Technology of the People's Republic of China (No.2008BAI50B08).

References

1. House WF, Urban J (1973) Long term results of electrode implantation and electronic stimulation of the cochlea in man. Ann Otol Rhinol Laryngol 82:504–517.
2. Simmons FB, Epley JM, Lummis RC, et al. (1965) Auditory nerve: Electrical stimulation in man. Science 148:104–106.
3. White RL (1982) Review of Current Status of Cochlear Prostheses. IEEE Trans Biomed Eng BME 29:233–238.
4. Michelson RP (1971) Electrical stimulation of the human cochlea. Arch Otolaryngol 93:317–323.
5. Eddington DK, Dobelle WH, Brackmann DE, et al. (1978) Auditory prosthesis research with multiple channel intracochlear stimulation in man. Ann Otol Rhinol Laryngol 87:1–39.
6. Eddington DK (1980) Speech discrimination in deaf subjects with cochlear implants. J Acoust Soc Am 68:885–891.
7. Wilson BS, Lawson DT, Finley CC, et al. (1991) Coding strategies for multichannel cochlear prostheses. Am J Otol 12 Suppl:56–61.

8. Zeng FG, Shannon RV (1994) Loudness-coding mechanisms inferred from electric stimulation of the human auditory system. Science 264:564–566.
9. Dorman MF, Soli S, Dankowski K, et al. (1990) Acoustic cues for consonant identification by patients who use the Ineraid cochlear implant. J Acoust Soc Am 88:2074–2079.
10. Shannon RV (1992) Temporal modulation transfer functions in patients with cochlear implants. J Acoust Soc Am 91:2156–2164.
11. Hochmair-Desoyer IJ, Hochmair ES, Burian K, et al. (1981) Four years of experience with cochlear prostheses. Med Prog Technol 8:107–119.
12. Chouard CH (1980) The surgical rehabilitation of total deafness with the multichannel cochlear implant. Indications and results. Audiology 19:137–145.
13. An SK, Park SI, Jun SB, et al. (2007) Design for a simplified cochlear implant system. IEEE Trans Biomed Eng 54:973–982.
14. James CJ, Skinner MW, Martin LF, et al. (2003) An investigation of input level range for the nucleus 24 cochlear implant system: Speech perception performance, program preference, and loudness comfort ratings. Ear Hear 24:157–174.
15. Spahr AJ, Dorman MF, Loiselle LH (2007) Performance of patients using different cochlear implant systems: Effects of input dynamic range. Ear Hear 28:260–275.
16. Zeng FG, Grant G, Niparko J, et al. (2002) Speech dynamic range and its effect on cochlear implant performance. J Acoust Soc Am 111:377–386.
17. Zeng FG (2002) Temporal pitch in electric hearing. Hear Res 174:101–106.
18. Green T, Faulkner A, Rosen S (2004) Enhancing temporal cues to voice pitch in continuous interleaved sampling cochlear implants. J Acoust Soc Am 116:2298–2310.
19. Laneau J, Wouters J, Moonen M (2004) Relative contributions of temporal and place pitch cues to fundamental frequency discrimination in cochlear implantees. J Acoust Soc Am 116:3606–3619.
20. Wilson BS, Finley CC, Lawson DT, et al. (1991) Better speech recognition with cochlear implants. Nature 352:236–238.
21. Patrick JF, Busby PA, Gibson PJ (2006) The development of the Nucleus Freedom Cochlear implant system. Trends Amplif 10:175–200.
22. Zeng FG, Shannon RV (1992) Loudness balance between electric and acoustic stimulation. Hear Res 60:231–235.
23. Wilson BS, Finley CC, Farmer JC, Jr. et al. (1988) Comparative studies of speech processing strategies for cochlear implants. Laryngoscope 98:1069–1077.
24. McDermott HJ, McKay CM, Vandali AE (1992) A new portable sound processor for the University of Melbourne/Nucleus Limited multielectrode cochlear implant. J Acoust Soc Am 91:3367–3371.
25. Nogueira W, Buchner A, Lenarz T, et al. (2005) A psychoacoustic "NofM"-Type speech coding strategy for cochlear implants. EURASIP J Appl Signal Processing 2005:3044–3059.
26. Crosby PA, Daly CN, Money DK, et al. (1985) Cochlear implant system for an auditory prosthesis. United States Patent 4532930: Commonwealth of Australia Dept. of Science & Technology (Belconnan AU).
27. Hochmair IJ, Hochmair ES (1991) Transcutaneous power and signal transmission system and methods for increased signal transmission efficiency. United States Patent 5070535.
28. Zierhofer CM, Hochmair ES (1996) Geometric approach for coupling enhancement of magnetically coupled coils. Biomed Eng, IEEE Trans 43:708–714.
29. Shannon RV, Adams DD, Ferrel RL, et al. (1990) A computer interface for psychophysical and speech research with the Nucleus cochlear implant. J Acoust Soc Am 87: 905–907.
30. Robert ME, Wygonski J (2002) House Ear Institute Nucleus Research Interface (HEINRI) Users Guide. Los Angeles, CA: House Ear Institute.
31. Daly CN, McDermott H (1998) Embedded data link and protocol. United States Patent 5741314.

32. Vandali AE, Whitford LA, Plant KL, et al. (2000) Speech perception as a function of electrical stimulation rate: Using the Nucleus 24 cochlear implant system. Ear Hear 21:608–624.
33. Friesen LM, Shannon RV, Cruz RJ (2005) Effects of stimulation rate on speech recognition with cochlear implants. Audiol Neurootol 10:169–184.
34. Plant K, Holden L, Skinner M, et al. (2007) Clinical evaluation of higher stimulation rates in the nucleus research platform 8 system. Ear Hear 28:381–393.
35. Zierhofer CM (2003) Multichannel cochlear implant with neural response telemetry. United States Patent 6600955: Med-El Elektromedizinishe Geraete GmbH (Innsbruck AT).
36. Schulman JH, Whitmoyer DI, Gord JC, et al. (1997) Multichannel cochlear implant system including wearable speech processor. United States Patent 5603726: Alfred E. Mann Foundation For Scientific Research (Sylmar CA).
37. McDermott H (1989) An advanced multiple channel cochlear implant. IEEE Trans Biomed Eng 36:789–797.
38. Shannon RV (1992) A model of safe levels for electrical stimulation. IEEE Trans Biomed Eng 39:424–426.
39. McCreery DB, Agnew WF, Yuen TG, et al. (1990) Charge density and charge per phase as cofactors in neural injury induced by electrical stimulation. IEEE Trans Biomed Eng 37:996–1001.
40. Huang CQ, Shepherd RK, Carter PM, et al. (1999) Electrical stimulation of the auditory nerve: Direct current measurement in vivo. IEEE Trans Biomed Eng 46:461–470.
41. Huang CQ, Shepherd RK, Seligman PM, et al. (1998) Reduction in excitability of the auditory nerve following acute electrical stimulation at high stimulus rates: III. Capacitive versus non-capacitive coupling of the stimulating electrodes. Hear Res 116:55–64.
42. Ghovanloo M, Najafi K (2005) A compact large voltage-compliance high output-impedance programmable current source for implantable microstimulators. IEEE Trans Biomed Eng 52:97–105.
43. Gord JC (2001) Programmable current output stimulus stage for implantable device. United States Patent 6181969: Advanced Bionics Corporation (Sylmar CA).
44. Money D (2001) High compliance output stage for a tissue stimulator. United States Patent 6289246: Cochlear Pty. Ltd. (Lane Cove AU).
45. Karunasiri RT (2006) Digitally controlled RF amplifier with wide dynamic range output. United States Patent 7016738: Advanced Bionics Corporation (Valencia CA US).
46. Baumann U, Nobbe A (2006) The cochlear implant electrode-pitch function. Hear Res 213:34–42.
47. Gani M, Valentini G, Sigrist A, et al. (2007) Implications of deep electrode insertion on cochlear implant fitting. JARO 8:69–83.
48. Wardrop P, Whinney D, Rebscher SJ, et al. (2005) A temporal bone study of insertion trauma and intracochlear position of cochlear implant electrodes. I: Comparison of Nucleus banded and Nucleus Contour electrodes. Hear Res 203:54–67.
49. Wardrop P, Whinney D, Rebscher SJ, et al. (2005) A temporal bone study of insertion trauma and intracochlear position of cochlear implant electrodes. II: Comparison of Spiral Clarion and HiFocus II electrodes. Hear Res 203:68–79.
50. Welling DB, Hinojosa R, Gantz B, et al. (1993) Insertional trauma of multichannel cochlear implants. Laryngoscope 103:995–1001.
51. Tykocinski M, Saunders E, Cohen LT, et al. (2001) The contour electrode array: Safety study and initial patient trials of a new perimodiolar design. Otol Neurotol 22:33–41.
52. Shepherd RK, Clark GM, Pyman BC, et al. (1985) Banded intracochlear electrode array: Evaluation of insertion trauma in human temporal bones. Ann Otol Rhinol Laryngol 94:55–59.
53. Richter B, Aschendorff A, Lohnstein P, et al. (2001) The nucleus contour electrode array: A radiological and histological study. Laryngoscope 111:508–513.

54. Richter B, Aschendorff A, Lohnstein P, et al. (2002) Clarion 1.2 standard electrode array with partial space-filling positioner: Radiological and histological evaluation in human temporal bones. J Laryngol Otol 116:507–513.
55. Nadol JB, Shiao JY, Burgess BJ, et al. (2001) Histopathology of cochlear implants in humans. Ann Otol Rhinol Laryngol 110:883–891.
56. Eshraghi AA, Yang NW, Balkany TJ (2003) Comparative study of cochlear damage with three perimodiolar electrode designs. Laryngoscope 113:415–419.
57. Eshraghi AA (2006) Prevention of cochlear implant electrode damage. Curr Opin Otolaryngol Head Neck Surg 14:323–328.
58. Aschendorff A, Klenzner T, Richter B, et al. (2003) Evaluation of the HiFocus™ electrode array with positioner in human temporal bones. J Laryngol Otol 117:527–531.
59. Adunka O, Kiefer J (2006) Impact of electrode insertion depth on intracochlear trauma. Otolaryngol Head Neck Surg 135:374–382.
60. Adunka O, Unkelbach M, Mack M, et al. (2004) Cochlear implantation via the round window minimizes trauma to cochlear structures: A histologically controlled study. Acta Otolaryngol 124:807–812.
61. Marsh MA, Coker NJ, Jenkins HA (1992) Temporal bone histopathology of a patient with a nucleus 22-Channel cochlear implant. Am J Otol 13:241–248.
62. Fayad J, Linthicum FH, Otto SR, et al. (1991) Cochlear implants: Histopathologic findings related to performance in 16 human temporal bones. Ann Otol Rhinol Laryngol 100:807–811.
63. Fayad JN, Luxford W, Linthicum FH (2000) The clarion electrode positioner: Temporal bone studies. Am J Otol 21:226–229.
64. Roland JT (2005) A model for cochlear implant electrode insertion and force evaluation: Results with a new electrode design and insertion technique. Laryngoscope 115: 1325–1339.
65. Roland JT, Fishman AJ, Alexiades G, et al. (2000) Electrode to Modiolus proximity: A flouroscopic and histologic analysis. Am J Otol 21:218–225.
66. Gstoettner W, Plenk H, Franz P, et al. (1997) Cochlear implant deep electrode insertion: Extent of insertional truama. Acta Otolaryngol 117:274–277.
67. Ketten DR, Skinner MW, Wang G, et al. (1998) In vivo meaures of cochlear length and insertion depth of nucleus cochlear implant electrode arrays. Ann Otol Rhinol 107:1–16.
68. Skinner M, Ketten D, Holden L, et al. (2002) CT-derived estimation of cochlear morphology and electrode array position in relation to word recognition in Nucleus-22 recipients. J Assoc Res Otolaryngol 3:332–350.
69. Skinner MW, Ketten DR, Vannier MW, et al. (1994) Determination of the position of nucleus cochlear implant electrodes in the inner ear. Am J Otol 15:644–651.
70. Nadol JB (1990) Degeneration of cochlear neurons as seen in the spiral ganglion of man. Hear Res 49:141–154.
71. Nadol JB (1984) Histological considerations in implant patients. Arch Otolaryngol 110:160–163.
72. Finley CC, Wilson BS, White MW (1987) A finite-element model of bipolar field patterns in the electrically stimulated cochlea – A two dimensional approximation. IEEE – Ninth Ann Conf Eng Med Biol Soc 1901–1903.
73. Finley CC (1989) A finite-element model of radial bipolar field patterns in the electrically stimulated cochlea – Two and three dimensional approximations and tissue sensitivities. IEEE – 11th Ann Int Conf Eng Med Biol Soc 1059–1060.
74. Finley CC, Wilson BS, White MW (1989) Models of Neural Responsiveness to Electrical Stimulation. In: Spellman FA, (Ed.), Cochlear Implants: Models of the Electrically Stimulated Ear. New York: Springer-Verlag.
75. Finley CC, Wilson BS, White MW (1990) Models of neural responsiveness to electrical stimulation. In: J.M. Miller and F.A. Spelman (Eds.), Cochlear Implants: Models of the Electrically Stimulated Ear. New York: Springer-Verlag, pp. 55–96.

76. Frijns JHM, Snoo SLd, Schoonhoven R (1995) Potential distributions and neural excitation patterns in a rotationally symmetric model of the electrically stimulated cochlea. Hear Res 87:170–186.
77. Frijns JHM, Snoo SLd, Kate JHt (1996) Spatial selectivity in a rotationally symmetric model of the electrically stimulated cochlea. Hear Res 95:33–48.
78. Snyder RL, Bierer JA, Middlebrooks JC (2004) Topographic spread of inferior colliculus activation in response to acoustic and intracochlear electric stimulation. J Assoc Res Otolaryngol 5:305–322.
79. Snyder RL, Rebscher SJ, Cao K, et al. (1990) Chronic intracochlear electrical stimulation in the neonatally deafened cat. I. expansion of central representation. Hear Res 50:7–33.
80. Shepherd RK, Hatsushika S, Clark GM (1993) Electrical stimulation of the audtitory nerve: The effect of electrode position on neural excitation. Hear Res 66:108–120.
81. Rebscher SJ, Snyder RL, Leake PA (2001) The effect of electrode configuration and duration of deafness on threshold and selectivity of responses to intracochlear electrical stimulation. J Acoust Soc Am 109:2035–2048.
82. Pfingst BE, Morris DJ, Miller AL (1995) Effects of electrode configuration on threshold functions for electrical stimulation of the cochlea. Hear Res 85:76–84.
83. Snyder R, Middlebrooks J, Bonham B (2008) Cochlear implant electrode configuration effects on activation threshold and tonotopic selectivity. Hear Res 235:23–38.
84. Cords SM, Reuter G, Issing PR, et al. (2000) A silastic positioner for a modiolus-hugging position of intracochlear electrodes: Electrophysiologic effects. Am J Otol 21:212–217.
85. Stover T, Issing P, Graurock G, et al. (2005) Evaluation of the advance off-stylet insertion technique and the cochlear insertion tool in temporal bones. Otol Neurotol 26:1161–1170.
86. Wright CG, Roland PS, Kuzma J (2005) Advanced bionics thin lateral and helix II electrodes: A temporal bone study. Laryngoscope 115:2041–2045.
87. Gstoettner W, Franz P, Hamzavi J, et al. (1999) Intracochlear Position of Cochlear Implant Electrodes. Acta Otolaryngol 119(2):229–233.
88. Tykocinski M, Cohen LT, Pyman BC, et al. (2000) Comparison of electrode position in the human cohclea using various perimodiolar electrode arrays. Am J Otol 21:205–211.
89. Rebscher S, Hetherington A, Bonham B, et al. (2008) Considerations for design of future cochlear implant electrode arrays: Electrode array stiffness, size and depth of insertion. J Rehab Res Dev 45:731–747.
90. Rebscher SJ, Heilmann M, Bruszewski W, et al. (1999) Strategies to improve electrode positioning and safety in cochlear implants. IEEE Trans Biomed Eng 46:340–352.
91. Fu QJ, Shannon RV (1999) Effects of electrode configuration and frequency allocation on vowel recognition with the Nucleus-22 cochlear implant. Ear Hear 20:332–344.
92. Fu QJ, Shannon RV, Galvin J (2002) Perceptual learning following changes in the frequency-to-electrode assignment with the Nucleus-22 cochlear implants. J Acoust Soc Am 112:1664–1674.
93. Oxenham AJ, Bernstein JGW, Penagos H (2004) Correct tonotopic representation is necessary for complex pitch perception. Proc Nat Acad Sci 101(5):1421–1425.
94. Baskent D, Shannon R (2003) Speech recognition under conditions of frequency-place compression and expansion. J Acoust Soc Am 113(4):2064–2076.
95. Baskent D, Shannon R (2004) Frequency-place compression and expansion in cochlear implant listeners. J Acoust Soc Am 116:3130–3140.
96. Baskent D, Shannon R (2005) Interactions between cochlear implant electrode insertion depth and frequency-place mapping. J Acoust Soc Am 117:1405–1416.
97. Escude B, James C, Deguine O, et al. (2006) The size of the cochlea and predictions of insertion depth angles for cochlear implant electrodes. Aud Neurotol 11(suppl 1):27–33.
98. Aschendorff A, Kubalek R, Turowsi B (2005) Quality control after cochlear implant surgery by means of rotational tomography. Otol Neurotol 26:34–37.
99. Aschendorff A, Kromeier J, Klenzner T (2007) Quality control after insertion of the nucleus contour and contour advance electrode in adults. Ear Hear 28:75S–79S.

100. Stakhovskaya O, Sridhar D, Bonham B, et al. (2007) Frequency Map for the Human Cochlear Spiral Ganglion: Implications for Cochlear Implants. JARO 8:220–233.
101. Buechner A, Brendel M, Krueger B, et al. (2008) Current steering and results from novel speech coding strategies. Otol Neurotol 29:203–207.
102. Bonham BH, Litvak LM (2008) Current focusing and steering: Modeling, physiology, and psychophysics. Hear Res 242:141–153.
103. Middlebrooks J, Snyder R (2007) Auditory prosthesis with a penetrating nerve array. J Assoc Res Otolaryngol 8:258–279.
104. Middlebrooks J, Snyder R (2008) Intraneural stimulation for auditory prosthesis: Modiolar trunk and intracranial stimulation sites. Hear Res 242:52–63.
105. Fraysse B, Dillier N, Klenzner T, et al. (1998) Cochlear implants for adults obtaining marginal benefit from acoustic amplification. Am J Otol 19:591–597.
106. Adunka O, Kiefer J, Unkelbach M, et al. (2004) Development and evaluation of an improved electrode design for electric acoustic stimulation. Laryngoscope 114: 1237–1241.
107. Roland JT, Zeitler D, Jethanamest D, et al. (2008) Evaluation of the short hybrid electrode in human temporal bones. Otol Neurotol 29:482–488.
108. Fraysse B, Macias AR, Sterkers O, et al. (2006) Residual hearing conservation and electroacoustic stimulation with the nucleus 24 contour advance cochlear implant. Otol Neurotol 27:624–633.
109. Lenarz T, Stover T, Buechner A, et al. (2006) Temporal bone results and hearing preservation with a new straight electrode. Aud Neurotol 11(suppl 1):34–41.
110. James C, Albegger K, Battmer R, Burdo S, Deggouj N, Deguine O, Dillier N, Gersdorff M, Laszig R, Lenarz T, Rodriguez MM, Mondain M, Offeciers E, Macías AR, Ramsden R, Sterkers O, Von Wallenberg E, Weber B, Fraysse B (2005) Preservation of residual hearing with cochlear implantation: How and why. Acta Otolaryngol 125(5):481–491.
111. Briggs RJS, Tykocinski M, Xu J, et al. (2006) Comparison of round window and cochleostomy approaches with a prototype hearing preservation electrode. Aud Neurotol 11(suppl 1):42–48.
112. Arcand B, Bhatti P, Butala N, et al. (2004) Active positioning device for a perimodiolar cochlear electrode array. Microsyst Technol 10:478–483.
113. Skinner MW, Holden TA, Whiting BR, et al. (2007) In vivo estimates of the position of advanced bionics electrode arrays in the human cochlea. Ann Otol Rhinol Laryngol Suppl 197:2–24.
114. Finley CC, Holden TA, Holden LK, et al. (2008) Role of electrode placement as a contributor to variability in cochlear implant outcomes. Otol Neurotol 29:920–928.
115. Abbas PJ, Brown CJ, Shallop JK, et al. (1999) Summary of results using the nucleus CI24M implant to record the electrically evoked compound action potential. Ear Hear 20:45–59.
116. van der Beek FB, Boermans PP, Verbist BM, et al. (2005) Clinical evaluation of the Clarion CII HiFocus 1 with and without positioner. Ear Hear 26:577–592.
117. Miller CA, Abbas PJ, Brown CJ (2000) An improved method of reducing stimulus artifact in the electrically evoked whole-nerve potential. Ear Hear 21:280–290.
118. Miller CA, Abbas PJ, Rubinstein JT (1999) An empirically based model of the electrically evoked compound action potential. Hear Res 135:1–18.
119. Hashimoto T, Elder CM, Vitek JL (2002) A template subtraction method for stimulus artifact removal in high-frequency deep brain stimulation. J Neurosci Methods 113:181–186.
120. Heffer LF, Fallon JB (2008) A novel stimulus artifact removal technique for high-rate electrical stimulation. J Neurosci Methods 170:277–284.
121. September 17 (2007) Guidance for Industry and FDA Staff - Recognition and Use of Consensus Standards: U.S. Food and Drug Administration.

122. Harnack D, Winter C, Meissner W, et al. (2004) The effects of electrode material, charge density and stimulation duration on the safety of high-frequency stimulation of the subthalamic nucleus in rats. J Neurosci Methods 138:207–216.
123. Mendes GC, Brandao TR, Silva CL (2007) Ethylene oxide sterilization of medical devices: A review. Am J Infect Control 35:574–581.
124. Lazzi G (2005) Thermal effects of bioimplants. IEEE Eng Med Biol Mag 24:75–81.
125. Balkany T, Hodges A, Menapace C, et al. (2007) Nucleus Freedom North American clinical trial. Otolaryngol Head Neck Surg 136:757–762.
126. Koch DB, Osberger MJ, Segel P, et al. (2004) HiResolution and conventional sound processing in the HiResolution bionic ear: Using appropriate outcome measures to assess speech recognition ability. Audiol Neurootol 9:214–223.
127. Arnoldner C, Riss D, Brunner M, et al. (2007) Speech and music perception with the new fine structure speech coding strategy: Preliminary results. Acta Otolaryngol 127: 1298–1303.
128. Skinner MW, Binzer SM, Fredrickson JM, et al. (1988) Comparison of benefit from vibrotactile aid and cochlear implant for postlinguistically deaf adults. Laryngoscope 98:1092–1099.
129. Miyamoto RT, Osberger MJ, Robbins AM, et al. (1991) Comparison of speech perception abilities in deaf children with hearing aids or cochlear implants. Otolaryngol Head Neck Surg 104:42–46.
130. Wilson BS, Dorman MF (2007) The surprising performance of present-day cochlear implants. IEEE Trans Biomed Eng 54:969–972.
131. Chung K, Zeng FG, Acker KN (2006) Effects of directional microphone and adaptive multichannel noise reduction algorithm on cochlear implant performance. J Acoust Soc Am 120:2216–2227.
132. Chung K, Waltzman S, Zeng FG (2004) Using hearing aid directional microphones and noise reduction algorithms to enhance cochlear implant performance. Acoust Res Lett Online 5:56–61.
133. Schleich P, Nopp P, D'Haese P (2004) Head shadow, squelch, and summation effects in bilateral users of the MED-EL COMBI 40/40 + cochlear implant. Ear Hear 25:197–204.
134. Laback B, Majdak P (2008) Binaural jitter improves interaural time-difference sensitivity of cochlear implantees at high pulse rates. Proc Natl Acad Sci USA 105:814–817.
135. Long CJ, Carlyon RP, Litovsky RY, et al. (2006) Binaural unmasking with bilateral cochlear implants. J Assoc Res Otolaryngol 7:352–360.
136. von Ilberg C, Kiefer J, Tillein J, et al. (1999) Electric-acoustic stimulation of the auditory system. New technology for severe hearing loss. ORL J Otorhinolaryngol Relat Spec 61:334–340.
137. Gantz BJ, Turner C (2004) Combining acoustic and electrical speech processing: Iowa/Nucleus hybrid implant. Acta Otolaryngol 124:344–347.
138. Chang JE, Bai JY, Zeng FG (2006) Unintelligible low-frequency sound enhances simulated cochlear-implant speech recognition in noise. IEEE Trans Biomed Eng 53: 2598–2601.
139. Kong YY, Stickney GS, Zeng FG (2005) Speech and melody recognition in binaurally combined acoustic and electric hearing. J Acoust Soc Am 117:1351–1361.
140. Dorman MF, Gifford RH, Spahr AJ, et al. (2008) The benefits of combining acoustic and electric stimulation for the recognition of speech, voice and melodies. Audiol Neurootol 13:105–112.
141. Turner C, Gantz B, Vidal C, et al. (2004) Speech recognition in noise for cochlear implant listeners: Benefits of residual acoustic hearing. J Acoust Soc Am 115:1729–1735.
142. Badi AN, Kertesz TR, Gurgel RK, et al. (2003) Development of a novel eighth-nerve intraneural auditory neuroprosthesis. Laryngoscope 113:833–842.
143. Middlebrooks JC, Snyder RL (2007) Auditory prosthesis with a penetrating nerve array. J Assoc Res Otolaryngol 8:258–279.

144. Schwartz MS, Otto SR, Shannon RV, et al. (2008) Auditory brainstem implants. Neurotherapeutics 5:128–136.
145. McCreery DB (2008) Cochlear nucleus auditory prostheses. Hear Res 242:64–73.
146. Colletti V (2006) Auditory outcomes in tumor vs. nontumor patients fitted with auditory brainstem implants. Adv Otorhinolaryngol 64:167–185.
147. Lenarz T, Lim HH, Reuter G, et al. (2006) The auditory midbrain implant: A new auditory prosthesis for neural deafness-concept and device description. Otol Neurotol 27:838–843.
148. Lim HH, Lenarz T, Joseph G, et al. (2007) Electrical stimulation of the midbrain for hearing restoration: Insight into the functional organization of the human central auditory system. J Neurosci 27:13541–13551.
149. Rousche PJ, Normann RA (1999) Chronic intracortical microstimulation (ICMS) of cat sensory cortex using the Utah Intracortical Electrode Array. IEEE Trans Rehabil Eng 7:56–68.
150. de Balthasar C, Patel S, Roy A, et al. (2008) Factors affecting perceptual thresholds in epiretinal prostheses. Invest Ophthalmol Vis Sci 49:2303–2314.
151. Della Santina CC, Migliaccio AA, Patel AH (2007) A multichannel semicircular canal neural prosthesis using electrical stimulation to restore 3-d vestibular sensation. IEEE Trans Biomed Eng 54:1016–1030.
152. Merfeld DM, Haburcakova C, Gong W, et al. (2007) Chronic vestibulo-ocular reflexes evoked by a vestibular prosthesis. IEEE Trans Biomed Eng 54:1005–1015.

A New Auditory Prosthesis Using Deep Brain Stimulation: Development and Implementation

Hubert H. Lim, Minoo Lenarz, and Thomas Lenarz

Abstract The auditory midbrain implant (AMI) is a new auditory prosthesis designed for stimulation of the inferior colliculus, particularly its central nucleus (ICC), in deaf patients who cannot sufficiently benefit from current auditory implants (i.e., cochlear and brainstem implants). We have begun clinical trials in which three patients have been successfully implanted with the AMI. Although the intended target was the ICC, the AMI array was implanted into different regions across patients due to our learning experience with the surgical approach. The first patient was implanted into the dorsal cortex of the inferior colliculus, the second patient into the lateral lemniscus, and the third patient into the ICC. Nevertheless, all patients receive hearing benefits on a daily basis with their device, which has been encouraging for the potential of the AMI as a hearing alternative for deaf patients. The greatest improvements have been observed in the patient implanted into the target region of the ICC, indicating the importance of proper placement of the array into the midbrain. Furthermore, we have observed large differences in perceptual effects depending on location of stimulation. This chapter will provide an overview of the different steps that were taken to ensure safe and reliable translation and implementation of a new implant concept to clinical application. The first section of the chapter provides the rationale and issues that needed to be considered in the design of the AMI system. Section 2 covers the safety and feasibility studies performed in vitro and in animals to ensure the device would be safe and functional in humans. Section 3 describes our experience in determining how to implant and implement a new device into patients as well as the overall hearing performance achieved with the device. Finally, the last section provides some future directions for how to improve the AMI based on what we have learned from the human and animal findings. The underlying

H.H. Lim (✉)
Department of Biomedical Engineering, University of Minnesota, Minnesota, MN, USA; Otorhinolaryngology Department, Hannover Medical University, Hannover, Germany
e-mail: hlim@umn.edu

D.D. Zhou, E. Greenbaum (eds.), *Implantable Neural Prostheses 1*, Biological and Medical Physics, Biomedical Engineering,
DOI 10.1007/978-0-387-77261-5_4,

theme of this chapter is to provide the reader with a complete and realistic overview of the thought process, steps, and obstacles that were involved in translating an idealistic concept to a practical clinical device.

1 Introduction

1.1 Rationale

The thought of implanting a computer chip into the brain to enhance or restore some sensory or motor function seems at first fanciful as if from a science fiction movie. However, over the past decade, brain–machine interfaces have become more than just a reality, but a daily necessity for a large patient population. One such device, which has become the success story of the neural prosthesis field, is the cochlear implant (CI). Over 100,000 patients worldwide have been implanted with a CI, which consists of an electrode array that is inserted into the cochlea and designed to electrically stimulate the remaining nerve fibers (Fig. 1). Sound is recorded on an external microphone and processed into a pulse sequence that is transmitted through a telemetry interface across the skin

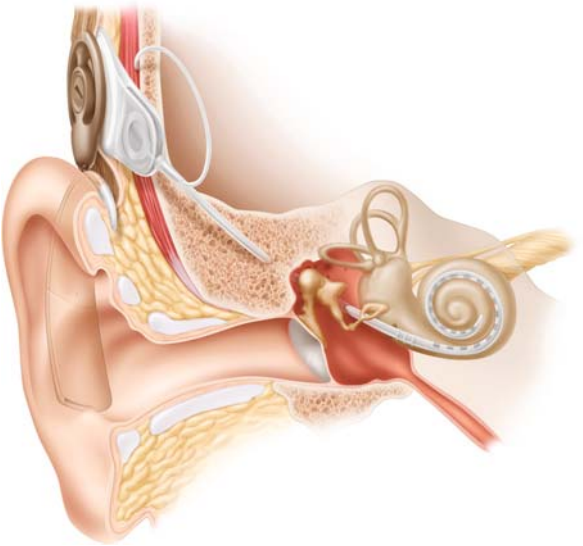

Fig. 1 Cochlear implant (CI) system. There are many types of CI systems with different processor designs and electrode arrays. This image presents a behind-the-ear CI system developed by Cochlear Ltd. It consists of a small processor that fits behind the ear with a microphone located near the *white tip* (not shown). The processor is connected to the receiver–stimulator implanted in a bony bed in the skull beneath the skin surface through a telemetry interface (*brown coil*). The ground ball electrode connected to the receiver–stimulator is placed within the temporalis muscle, while the electrode array is positioned within the cochlea with the 22 electrodes aligned along its tonotopic gradient. The electrodes are designed to stimulate the remaining nerve fibers that exit to the *right* of the image

(receiver is implanted in a bony bed in the skull behind the ear within the temporoparietal area) to different electrodes aligned along the tonotopic gradient of the cochlea. There are several types of CI devices and stimulation strategies developed by different companies. For a review, see ref. [1]. However, most modern implants use a general stimulation paradigm. The sound signal is bandpass filtered into N signals corresponding to different frequency bands within the human hearing range. The envelopes of these signals are then used to amplitude modulate a pulse train (usually a set pulse rate) that is delivered to M ($N > M$) sites corresponding to the largest energy components. Remarkably, patients can extract sufficient information from these stimulation sequences to understand speech with many even being able to converse over the telephone [2].

Unfortunately, there are many patients who cannot benefit from a CI because they do not have a viable auditory nerve to stimulate (e.g., due to nerve avulsion or aplasia) or an implantable cochlea (e.g., due to ossification). For these patients, the auditory brainstem implant (ABI) can be used to restore some auditory function. For a review, see Ref. [3]. The ABI consists of a planar electrode array that is implanted onto the surface of the cochlear nucleus (Fig. 2). The initial motivation for the ABI was to restore hearing in neurofibromatosis type 2 (NF2) patients. NF2 is associated with bilateral acoustic neuromas in which removal of these tumors usually leads to complete deafness. Since the brainstem is approached during tumor removal surgery, the patient can be implanted with an ABI with minimal added risk. The ABI has provided enhancements in lip-reading capabilities and environmental awareness. However, only a few of over 500 patients have achieved some open set speech perception without lip reading. More recently, nontumor deaf patients have been implanted with the ABI. Although the same technology and stimuli are used for both the nontumor and the NF2 ABI patients, many of the nontumor patients have obtained high levels of speech perception similar to what is

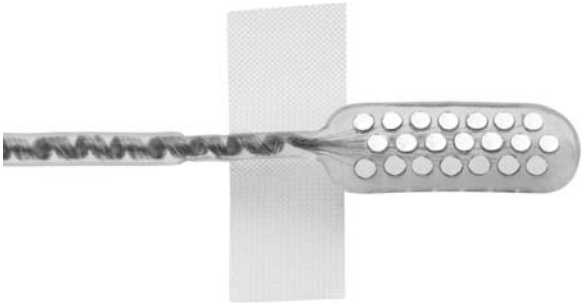

Fig. 2 ABI array. An example of an electrode array, developed by Cochlear Ltd., designed for surface stimulation of the cochlear nucleus for hearing restoration. This array consists of 21 active platinum disk electrodes mounted on a 3 × 8.5 mm silicone carrier backed with PET mesh (additional flaps to fix array to tissue surface). Each of the electrodes has a diameter of about 0.7 mm

observed for top CI patients [4]. This is interesting in that it suggests that the limited performance observed in NF2 ABI patients may be associated with tumor-related damage at the level of the cochlear nucleus where the tumors are located. The fact that many NF2 patients can still understand speech up until tumor removal suggests that auditory nuclei beyond the cochlear nucleus are still functional and the limited performance with ABI stimulation is more associated with activation issues with the cochlear nucleus. Therefore, a new auditory prosthesis that bypasses this damaged region is needed for deaf NF2 patients. The NF2 disease occurs in about 1 in 40,000 births [5], thus there are an ample number of patients who would benefit from such a device. Furthermore, such a device could serve as an alternative for nontumor patients who do not sufficiently benefit from the CI or ABI.

The question arises as to which auditory structure would serve as an alternative location for a new auditory prosthesis. The region must be surgically accessible in humans, provide a well-defined neuronal organization that would enable systematic spatial stimulation of different functional regions, and is not located too far along the auditory pathway associated with more complex coding properties. An appropriate balance among these criteria resulted in our selection of the inferior colliculus (IC), particularly its central nucleus (ICC). The location of the IC along the auditory pathway and relative to the other auditory structures is shown in the simplified schematic in Fig. 3 (taken from Ref. [6]). The ICC is a converging center for almost all ascending auditory brainstem projections [7], which should provide access to pathways necessary for sound perception. It also consists of a well-defined laminated organization (Fig. 4). Based on anatomical similarities across mammalian species and the fact that these laminae have shown to correspond to different frequency layers in animals [8, 9], it is inferred that the human ICC also consists of well-defined tonotopic layers. This is important for an auditory prosthesis considering that the ability to transmit specific frequency information has shown to be important for achieving high levels of speech perception in normal hearing and CI subjects [10, 11]. Furthermore, the IC is surgically accessible in humans, especially as part of the NF2 tumor removal approach (see Section 3.1), and it is possible to modify commonly used DBS stereotactic approaches to the midbrain for safe implantation of an electrode array into the IC [12, 13].

Although the auditory cortex is more superficially located (Fig. 3) and surgically accessible than the IC, it consists of a less defined functional organization (e.g., the tonotopic map is less consistent across animal subjects), in part due to its more plastic nature [14, 15], and exhibits more complex coding of perceptual sound features. Lower auditory nuclei, such as the superior olivary nuclei and the lateral lemnisci, may exhibit less complex processing compared to the IC since they are lower along the auditory pathway. However, these nuclei code sound in a more diffuse manner (i.e., no one nucleus serves as a converging center of information) and with a less defined and/or skewed tonotopic organization compared to the ICC [16]. Although the medial geniculate body can be approached using stereotactic methods [13, 17] and provides access to most auditory projections ascending from lower centers to the auditory cortex, it will

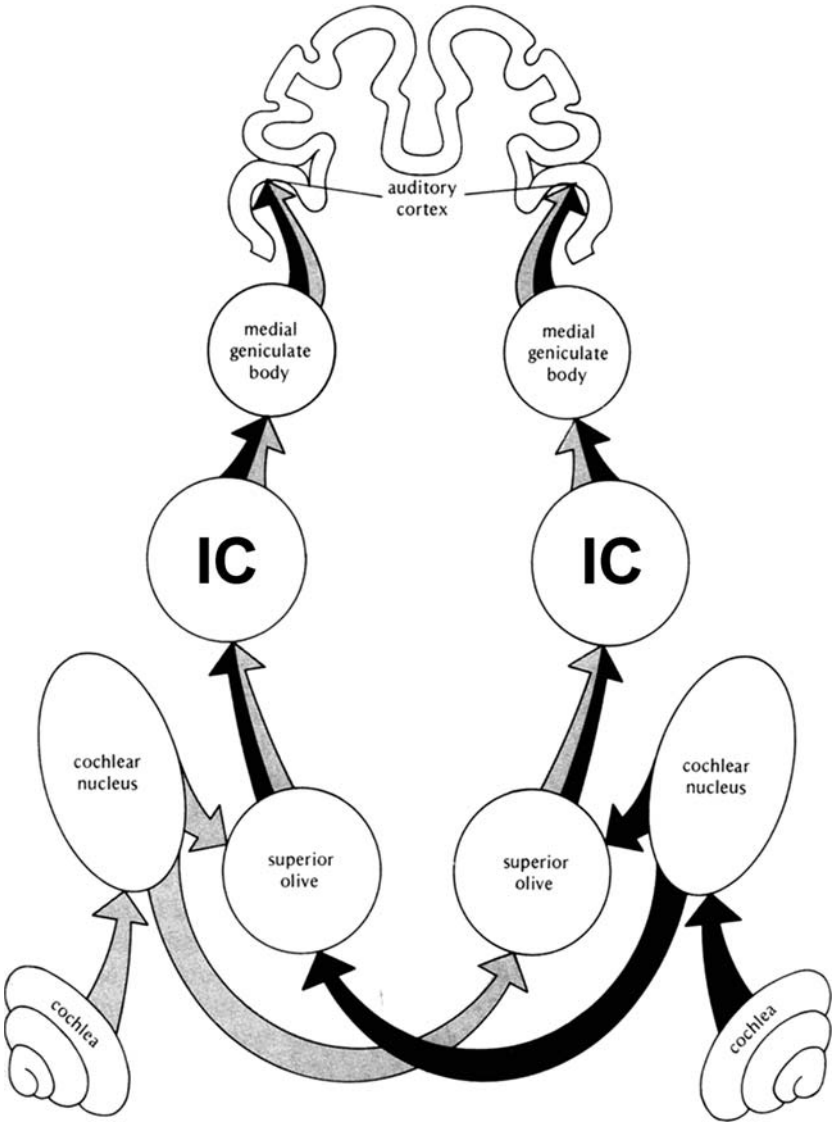

Fig. 3 Auditory pathway. Simplified schematic showing most of the major nuclei along the auditory pathway from the cochlea up through the inferior colliculus (IC) to the auditory cortex. There are extensive projections across the different nuclei as well as descending pathways that are not shown. Taken from Ref. [6] and reprinted with permission from Elsevier

likely exhibit more complex processing compared to the IC since it is higher along the auditory pathway [16].

Therefore, we selected the IC as our target structure for a new auditory prosthesis, the auditory midbrain implant (AMI).

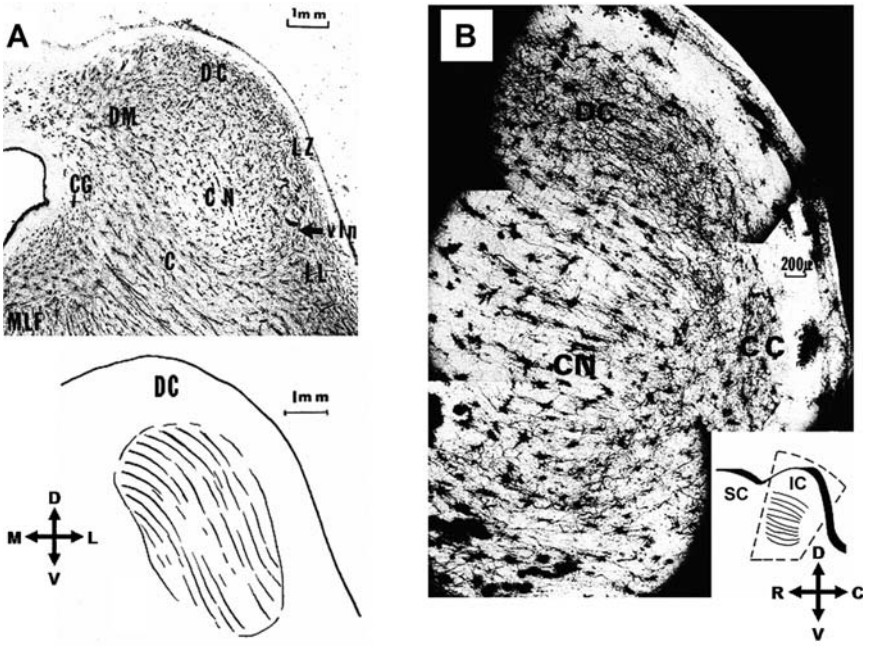

Fig. 4 Anatomy of inferior colliculus. Histological sections of the human inferior colliculus (IC) depicting its different subdivisions and layered structure using the Golgi–Cox method. (**A**) Axial section (*top*) at the junction of the caudal and middle thirds of the IC of a 55-year-old man and its simplified schematic (*bottom*) showing the orientation of the dendritic laminae within the central nucleus. (**B**) Parasagittal section at the junction of the medial and middle thirds of the IC of a 53-year-old man; inset provides orientation of the dendritic laminae within the central nucleus and indicates the location of the section (*dashed lines*). C, cuneiform area; CC, caudal cortex; CG, central gray; CN, central nucleus; DC, dorsal cortex; DM, dorsomedial nucleus; LL, lateral nucleus and dorsal nucleus of lateral lemniscus; LZ, lateral zone; MLF, medial longitudinal fasciculus; SC, superior colliculus; vln, ventrolateral nucleus. Anatomical directions: C, caudal; D, dorsal; L, lateral; M, medial; R, rostral; V, ventral. Images taken from Ref. [8] and reprinted with permission from Taylor and Francis Group

1.2 Design Considerations

The IC is a three-dimensional structure that is somewhat spherical (Fig. 4). It consists of different regions associated with different coding features [9, 18, 19]. The ICC is the main ascending auditory region of the midbrain whereas the dorsal cortex receives substantial descending projections from higher auditory and nonauditory centers and is designed for modulating information transmitted along the ascending pathway. The lateral nucleus has been associated with multimodal information processing as well as modulation of ascending and descending projections to and from lower auditory centers. There are other regions within the IC along with differences in regions across species that have been identified. Although it is important to understand the coding features

within the different regions of the IC across species and especially within humans for developing stimulation strategies for the AMI, our initial focus is in the coding features of the ICC since it is our implant target for the first patients. Implanting arrays into other IC regions in addition to the ICC may be required to achieve perception of complex sound stimuli. However, to simplify the design and implementation of the AMI in the first patients, we focused on the ICC because it receives almost all ascending pathways from the brainstem en route to higher perceptual centers [7]. Thus, we should have access to most ascending information required for speech perception.

One of the advantages of stimulating the ICC is that it has a well-defined tonotopic organization in which its three-dimensional structure is made up of two-dimensional isofrequency layers that are aligned roughly 45° from the parasagittal plane (Fig. 4). As mentioned earlier, the ability to systematically activate different frequency regions, thus elicit distinct spectral percepts, has shown to be important for speech perception in CI as well as normal hearing subjects [10, 11]. Thus, the systematic tonotopic organization of the ICC makes it a promising location for an auditory prosthesis. However, if frequency is coded along one dimension of the three-dimensional structure, then what is coded along the other dimensions? It is not yet clear how sound is coded along the isofrequency layers. Some studies have shown that different features of sound are systematically coded along these ICC laminae. For example, in mice it has been shown that ICC neurons with lower pure tone thresholds, sharper frequency tuning, and greater sensitivity to slower frequency sweep speeds are located more centrally within a lamina and these properties systematically change in more concentrically outward regions [20, 21]. In cats, it has been shown that a periodotopic (best modulation frequency) map exists along the dorsomedial-to-ventrolateral dimension of the ICC laminae [22] and shorter pure tone latencies are represented in more ventrolateral regions [23]. These findings suggest that frequency may be coded in one dimension while temporal, level, and even frequency interactions are coded along the other dimensions. From an engineering point of view, such an organization would be advantageous for a three-dimensional array in which appropriate spatial stimulation of the ICC could elicit different spectral, temporal, and level percepts, all features that make up the structure of a sound signal. However, there is some controversy over whether such spatial maps exist across different sound levels [24, 25] and it is still unknown how these maps vary across species, especially in humans. Furthermore, the question remains how we could electrically stimulate different sites, which results in synchronized activation of clusters of neurons rather than discrete activation of individual neurons, throughout the ICC to elicit the appropriate temporal and spatial neural interactions that can be decoded by higher order neurons as meaningful auditory percepts.

Attempting to understand the intricate coding circuitry of the ICC and then being able to interpret the findings to appropriately stimulate this circuitry to restore speech perception may prove to be an ambitious feat. It may be more practical to simply implant a large number of sites throughout the ICC. In this

way, a broad range of varying stimuli across the nuclei could be investigated until effective stimulation patterns are identified using more of a heuristic approach. However, this approach has its own limitations. In designing a new auditory prosthesis, especially one that will be implanted within the center of the brain, it is crucial to take every precaution to ensure that the array can be safely and chronically implanted into the brain. Demonstrating the safety of a new electrode array takes carefully planned, long-term animal studies and requires extensive steps for human approval through the appropriate governmental and clinical agencies. For an array with a greater number of sites and larger dimensions, more neural tissue will need to be displaced during implantation and stronger forces will be required to push the array into the tissue, which can result in greater brain damage. Thus obtaining approval for such a device may be more difficult. From an engineering perspective, designing an array with a greater number of sites becomes more technologically challenging. For example, the current DBS array has four large sites each connected to the processor via wire leads (Fig. 5A). It is not possible to use the same technology to develop a three-dimensional array with a high density of small sites (e.g., 100 closely spaced 2000 μm^2 sites with a site-to-site distance of 100 μm) due to the large volume of space required for the wire leads and the inability to accurately space the sites with such small dimensions. New fabrication technologies used to develop silicon or polyimide electrode arrays can achieve such specifications (Fig. 6) [26]. However, these types of electrode technologies are not yet approved for chronic human use since it is not clear how safe and functional they are over long periods of time within the brain, though some initial studies have provided encouraging results [3, 27]. Extensive safety studies still need to be performed to translate this technology into a neural prosthesis for humans. Even if the number of sites can be dramatically increased, there are other limitations, such as a limited bandwidth for transferring data from the processor to the implanted stimulator (i.e., the stimulation sequences are transmitted across a wireless interface) and a limited amount of power than can drive the stimulator especially if current steering techniques with multi-site stimulation algorithms are used. Implants with large number of sites may require appropriate switching electronics to stimulate a subset of the total number of sites at any given time. Furthermore, the complexity of the algorithm will increase with site number in a combinatorial sense. Considering that patients would rather wear a small behind-the-ear processor (as shown in Fig. 1) than a large body-worn device at the cost of less processing power, it becomes crucial to simplify the algorithms to run on smaller processors with less energy requirements.

Based on these different design considerations and issues, a balance must be reached between complexity and feasibility. On one end, we would like a three-dimensional array that can sufficiently stimulate across the entire IC. On the other end, we would like an array that is safe for human use and will not take extensive animal and in vitro studies to develop and obtain approval for clinical trials. Our research and clinical team decided to use an electrode array technology already approved for human use. The human prototype AMI array was

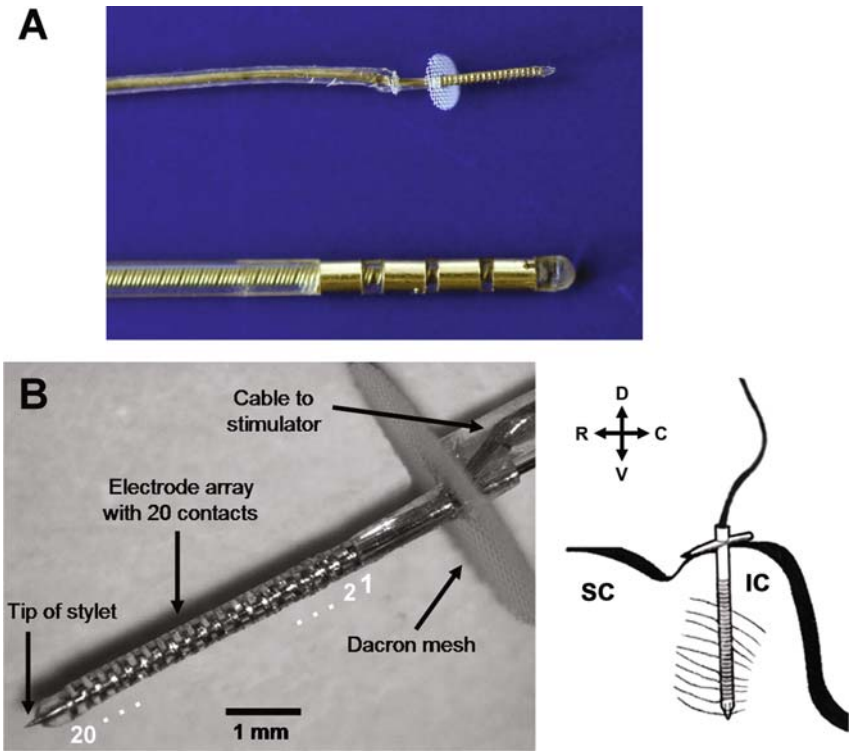

Fig. 5 AMI array. (**A**) Image of the AMI array next to a standard DBS array (Medtronic Inc., Minneapolis, MN, USA). The DBS array consists of four platinum–iridium contacts (2 mm center-to-center separation) each with a ring diameter of 1.27 mm, width of 1.5 mm, and surface area of ~6 mm^2. (**B**) Magnified image of the AMI array, which is 6.2 mm long (from Dacron mesh to tip of silicone carrier without stylet). Each of the 20 platinum ring electrodes (0.2 mm center-to-center separation) has a diameter of 0.4 mm, width of 0.1 mm, and surface area of ~0.00126 mm^2. The AMI array is designed to be positioned along the tonotopic gradient of the central nucleus of the inferior colliculus (IC). The array was developed by Cochlear Ltd. SC, superior colliculus. Anatomical directions: C, caudal; D, dorsal; R, rostral; V, ventral

derived from a clinically approved CI array developed by Cochlear Ltd (Lane Cove, Australia) (Fig. 5). This meant that the AMI would consist of only a single-shank array similar to that of the CI. Although it was not possible to technologically develop an array with much more than 20 sites and significantly reduce the array dimensions due to the wire leads, the overall size of the array is still dramatically smaller than the current DBS array (Fig. 5A). Through sufficient in vitro tests and animal studies (see Section 2), the safety, mechanical robustness, and functionality of the AMI array were demonstrated and approval for human use was obtained in a short period of time (within 3 years). The disadvantage of the array was that we only had one shank to implant into a three-dimensional structure. Thus, we were left with the critical

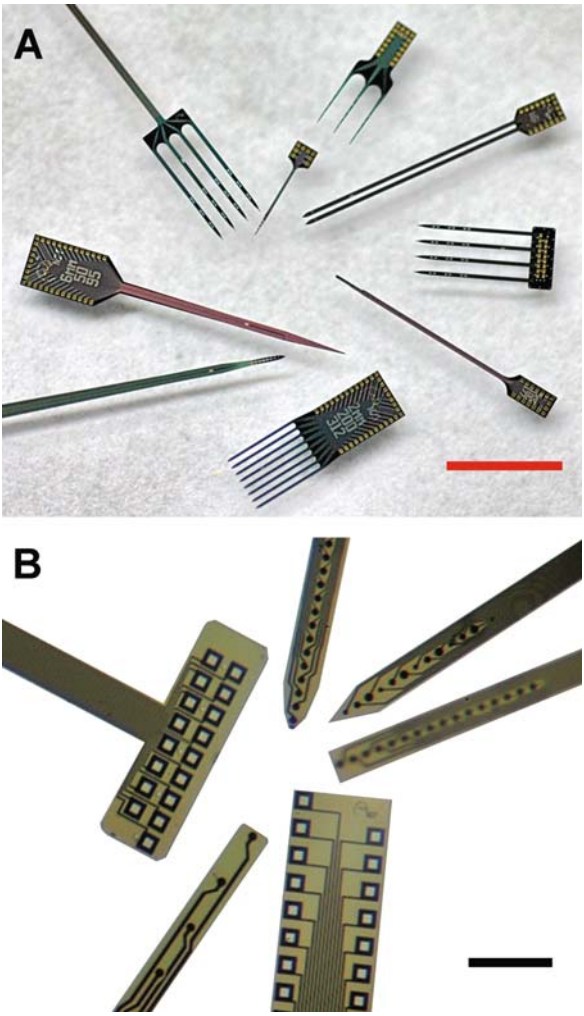

Fig. 6 New planar electrode technologies. (**A**) Silicon substrate multisite probes of different two-dimensional configurations. Each probe has multiple sites linearly organized along a given shank with micron level precision. Bond pads (*gold squares*) providing connection to each site are visible on the probes. Red scale bar is 4 mm. **(B)** Polyimide multisite probes. Both sites (*black dots*) and bond pads (*silver squares*) are shown. Polyimide probes are more flexible and resistant to breakage than the silicon probes, thus may be more appropriate for long-term use in humans. Black scale bar is 0.5 mm. Three-dimensional probes can also be developed by bonding several two-dimensional probes inserted into a three-dimensional construct. These probes and new electrode technologies are developed by NeuroNexus Technologies (Ann Arbor, Michigan, USA)

decision of where to implant this array within the ICC, a question we are still investigating. After obtaining approval for clinical trials, we implanted three patients. Section 3 provides an overview of our human findings and the

systematic steps involved in appropriately fitting each patient with the AMI. The chapter ends (Section 4) with an overview of what design features need to be implemented in the next generation of the AMI system in order to improve overall hearing performance based on both our animal and human findings.

2 Device Development and Testing

2.1 Human Prototype Array

The AMI consists of a single-shank multi-site array designed according to the dimensions of the human IC with the goal of stimulating the different layers of the ICC (Fig. 5). The AMI electrode array is 6.4 mm long (from Dacron mesh to tip of stylet) with a diameter of 0.4 mm. It consists of 20 platinum ring electrodes linearly spaced at an interval of 200 μm. Each site has a width of 100 μm (surface area of 126,000 μm^2) and is connected to a parylene-coated 25-μm-thick wire (90% platinum/10% iridium). The body (carrier) of the electrode array is made from silicone rubber (30 durometer hardness) and is concentrically hollow. A stiffening element (stylet) made of stainless steel is positioned through the axial center of this silicone carrier to enable insertion of the electrode array into the IC. After the electrode array is in its final position in the midbrain, the stylet is removed and the softer silicone carrier remains in the tissue. The Dacron mesh anchors the electrode array onto the surface of the neural tissue to minimize movement after implantation. This Dacron mesh also prevents overinsertion of the electrode array into the IC during implantation.

The other components of the AMI system are similar to the latest nucleus CI system (Fig. 1) consisting of a behind-the-ear microphone and processor that transmits the electromagnetic signals to the receiver–stimulator implanted under the skin. This receiver–stimulator is implanted in a bony bed on the skull near the craniotomy and is connected with a cable to the electrode array.

The successful design and development of the AMI array was a result of applying the Plan–Do–Check–Act (PDCA) principle (Fig. 7). This is a recursive process in which each phase of the cycle applies the PDCA principle creating a fractal process encompassing aspects of the design and development cycle. The scientists and engineers at Cochlear Ltd., particularly James F. Patrick, Frank Risi, Godofredo (JR) Timbol, and Peter Gibson, ensured successful execution of the PDCA principle on the development of the AMI.

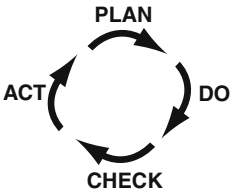

Fig. 7 Schematic of PDCA (Plan–Do–Check–Act) process used for AMI development

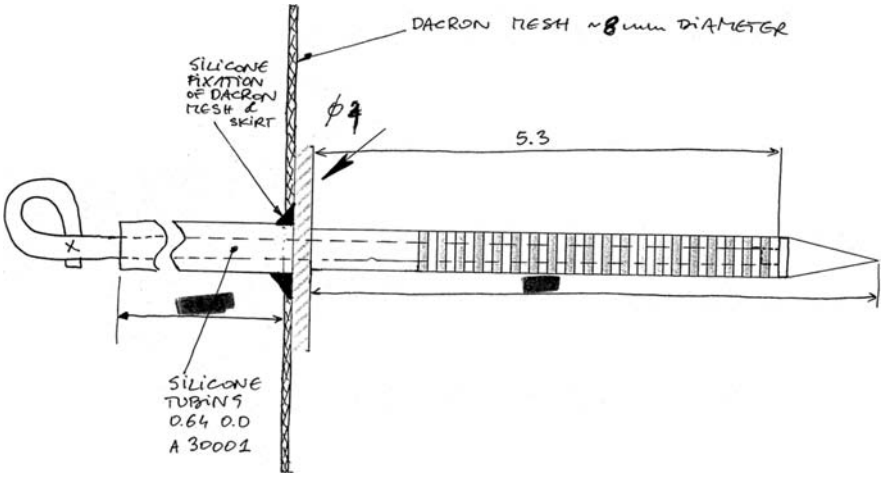

Fig. 8 Original AMI schematic

Plan: A number of meetings were held between researchers, otolaryngologists, and neurosurgeons at Hanover Medical University and engineers and scientists from Cochlear Ltd. During these meetings a number of creative and innovative draft concepts for an AMI array were created (Fig. 8). In addition, dimensional, functional, reliability, and surgical requirements were highlighted.

Do: Engineers at Cochlear Ltd. used the original concepts and ideas to generate detailed designs using advanced CAD modeling and prototypes (Fig. 9). As part of the "Do" process, they used FMEA (failure modes and effects analysis) to identify and estimate potential risks or hazards associated with each design. FMEA is a step-by-step approach for identifying all possible failures in a design, a manufacturing or assembly process, or a product or service and prioritizing them based on their seriousness, frequency of occurrence, and detectability. It relies on bringing together people with in-depth

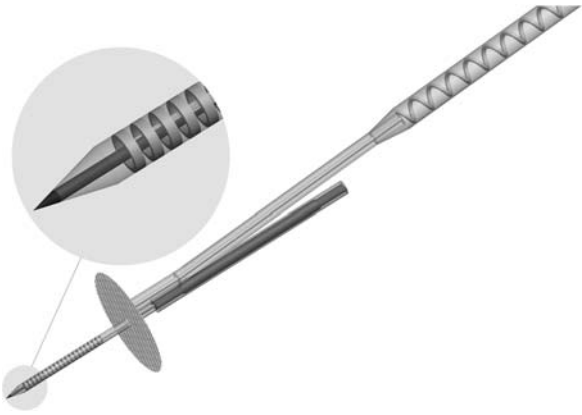

Fig. 9 An example CAD drawing of the AMI array

knowledge spanning all aspects (e.g., design, manufacturing, testing, marketing, sales) of the specific process, product, or service in order to efficiently and effectively address the potential failures of the system. For example, the penetrating tip in the original concept (Fig. 8) consisted of a separate titanium conical tip that remained implanted after removal of the stylet. However, the FMEA identified a number of risks with this concept, especially the potential for neural damage due to the hard tip remaining implanted in the soft tissue. This resulted in a modified design in which the tip, which is now part of the stylet, would be removed after the electrode array is positioned into the neural tissue (Figs. 5B and 9). Furthermore, materials and manufacturing processes were based as much as possible on existing commercial CI electrode technologies to reduce both potential risks and development time. However, due to specific design requirements for the AMI, such as the dimensional constraints, the stylet required for surgical insertion of the array into the brain with minimal insertion trauma, and electrode reliability concerns for the reduced dimensions, this phase required the development of some manufacturing processes, tools, equipment, and assessment protocols.

Check: After a theoretical engineering design review, the AMI array was subjected to a series of tests to verify safety and reliability of the design and also to validate clinical safety and performance. The "Check" phase of the PDCA cycle is generally the longest, requiring the controlled manufacture of a large number of sample devices for testing. Prior to testing, the design was evaluated analytically using FEA (finite element analysis) methods to quickly identify risk areas or areas of weakness, specifically focusing on wire bond strength and potential high-stress areas resulting from long-term use (Fig. 10).

In vitro life testing of the AMI array, including severe stress and fatigue testing, was performed based on protocols developed to mimic conditions expected in vivo and typical use cases. One example was flexing the electrode array around a known bend radius multiple times to failure similar to the type of testing performed on CI arrays (Fig. 11). This test was designed to assess the resistance of the AMI arrays to excessive handling and deflection during and after implantation. The AMI electrodes were monitored during testing by

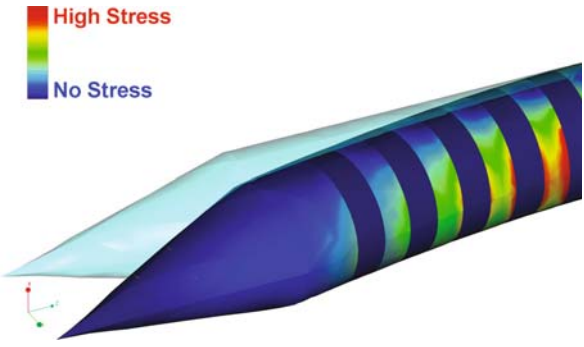

Fig. 10 Finite element analysis to simulate and assess bending stresses in the array

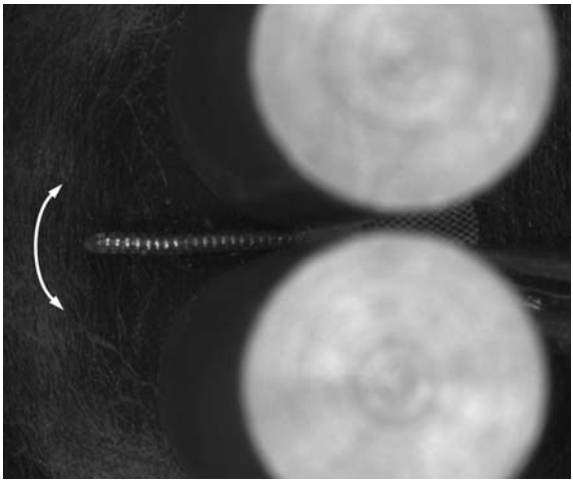

Fig. 11 In vitro bending test. The AMI array was positioned between two rollers and continuously bent and stressed to assess failures and material defects associated with excessive handling of the array that could occur during and after implantation

measuring continuity and impedances within a conductive medium. Failures only occurred well beyond the acceptance criteria developed for accelerated life testing, while visual inspection of the arrays under high magnification confirmed that the failure mechanisms were as expected and not a result of material defects.

The design verification process ensured that the AMI implant was reliable and suitable for clinical use and identified potential areas of weakness that needed to be addressed prior to human implantation. In parallel, we performed acute and chronic animal studies as well as fresh cadaver preparations to provide additional data relating to insertion trauma, electrode stability, surgical usability, and long-term functional reliability (see Sections 2.2 and 3.1).

Act: The results of the verification and validation tests were reviewed against the stringent company requirements with any identified issues being addressed through the iterative application of the PDCA process, generating appropriate design or manufacturing changes. For example, during the animal studies we realized that the original long stainless steel stylet handle was difficult to grip with surgical tools and safely insert the array into the brain tissue. The design was modified, resulting in a much shorter handle with a silicone coating that provided greater stability during insertion.

Overall, the application of the PDCA principal, innovative design practices, advanced design tools, and thorough analyses resulted in the original AMI electrode array concept becoming a clinical reality.

2.2 Feasibility and Safety Studies

In addition to extensive in vitro tests performed by the engineers at Cochlear Ltd., we performed electrophysiology and histological studies in animals to assess the functionality, reliability, and safety of the AMI array in living tissue. These experiments were also part of the PDCA process described in the

previous section. The animal studies consisted of acute electrophysiology experiments in guinea pigs to determine the effects of electrical stimulation of the ICC on activation of higher auditory regions and chronic experiments in cats to evaluate the effects of long-term implantation and stimulation on tissue damage. This section provides a brief overview of these results with further details presented in previously published work [28–30].

One major rationale for selecting the ICC as the target site for an auditory prosthesis is its well-defined tonotopic organization. We designed our AMI array based on this organization and the dimensions of the human IC and hypothesized that AMI stimulation of the ICC would achieve frequency-specific activation. Furthermore, we expected lower thresholds than CI stimulation because of the ability to directly stimulate ICC neurons compared to the distant nature of neural activation (across the bony modiolar wall) for cochlear stimulation. The AMI sites are large due to limitations in electrode technology. Yet this should also result in lower charge densities for ICC activation, thus providing a safer range of current levels for central nervous system stimulation. To test our hypotheses, we performed experiments in a ketamine-anesthetized guinea pig model in which we electrically stimulated different regions along the tonotopic axis of the ICC and recorded the corresponding neural activity across the tonotopic gradient of the primary auditory cortex (A1) (Fig. 12). We used

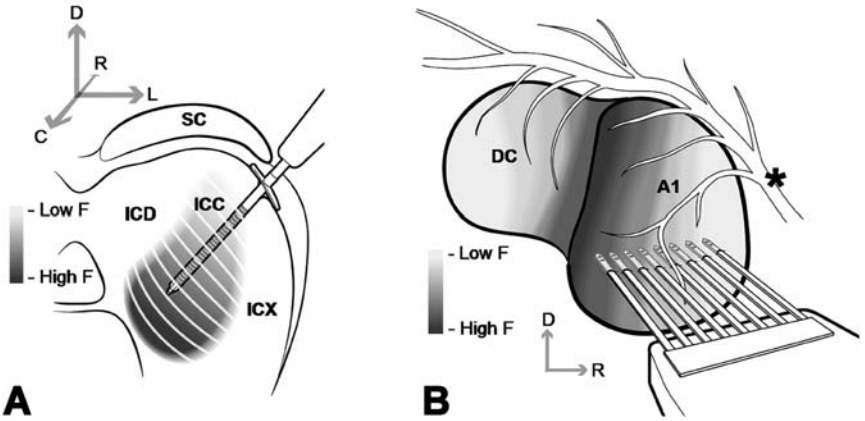

Fig. 12 Electrophysiology setup. Drawings of the AMI array and an 8-shank silicon-substrate Michigan probe (Center for Neural Communication Technology, University of Michigan, Ann Arbor, MI) positioned along the tonotopic gradient of the central nucleus of the inferior colliculus (ICC) (**A**) and primary auditory cortex (A1) (**B**), respectively. Anatomy in (**A**) and (**B**) was derived from images presented in Ref. [31, 32], respectively (not drawn to scale). Electrode sites (~400 μm^2) are represented by *black dots* along each A1 probe shank (sites separated by 50 μm, shanks separated by 200 μm). The asterisk corresponds to blood vessels. DC, dorsocaudal cortex; F, frequency; ICD, inferior colliculus dorsal cortex; ICX, inferior colliculus external cortex; SC, superior colliculus. Anatomical directions: C, caudal; D, dorsal; L, lateral; R, rostral. Taken from Ref. [29] and reprinted with permission from the Association for Research in Otolaryngology

single biphasic monopolar pulses (200 μs/phase, cathodic leading) within the ICC where the return was through a wire positioned in a neck muscle. Each ICC site was stimulated with levels between 1 and 100 μA in logarithmic (dB) steps. The A1 neural activity (evoked potentials and spikes) was filtered and processed for analysis.

In summary, the mean threshold for A1 spike activity to ICC stimulation was 27.4 μA (SD: 12.3 μA; n = 75). This value corresponds to the thresholds of A1 neurons with a similar best frequency (i.e., most sensitive to a specific pure tone stimulus) to that of the stimulated ICC neurons. Although in most cases stimulation of a specific frequency region within the ICC elicited the lowest spike thresholds in a similar frequency region in A1 (67%, n = 75), thus achieving frequency-specific activation, there were cases in which the lowest threshold was elicited by A1 neurons with different best frequencies. The mean value when taking the lowest A1 threshold for a stimulated ICC site regardless of best frequency was 20.7 μA (SD: 9.6 μA; n = 75). For cochlear stimulation, A1 thresholds of about 67.2 μA (median value) have been reported [33], which is 10 dB higher than our median value of 20 μA. Even accounting for differences in the threshold method used, these results suggested that the AMI could provide lower thresholds than CIs, which would potentially reduce overall energy consumption during daily use. Furthermore, current levels for AMI activation appeared to be safe for central nervous system stimulation. Our thresholds ranged from about 6 to 60 μA, which for a 200 μs/phase pulse results in a total charge per phase of 1.2–12 nC. For 126,000 μm^2 sites, this results in a charge density per phase ranging between about 1 and 10 $\mu C/cm^2$. Using a charge density per phase of about 10 $\mu C/cm^2$ (7 h of continuous stimulation at 50 Hz, anodic-leading biphasic pulses, 400 μs/phase, 0.5 cm^2 surface electrodes) in cat parietal cortex, McCreery et al. [34] demonstrated that safe neural stimulation up to 5000 nC/phase was possible (neural damage appears to be related to both charge density and total charge). Using much smaller sites (6,500 μm^2) than our AMI sites and a higher charge density of 1600 $\mu C/cm^2$, they still could safely stimulate up to 100 nC/phase. Both cases result in much higher charge and charge density values than our stimulation values. Even considering the differences in pulse duration (200 versus 400 μs/phase) and brain region (guinea pig midbrain versus cat cortical tissue), especially since we stimulated with much fewer pulses (less than 7 h at 2 Hz), it was expected that our stimulation levels would not cause noticeable tissue damage. We could not determine the maximum current level needed for AMI stimulation with our experimental setup due to the limit of the stimulator. However, even if levels reach up to 500 μA, the total charge per phase and charge density per phase will still only be about 100 nC and 80 $\mu C/cm^2$, respectively, which are still well within the safe limits described above and presented in [34–36]. At higher levels, frequency-specific activation was also still possible. For example, when stimulating at 5 dB above threshold, 77% (n = 69) of the stimulated ICC sites elicited the largest evoked potential within an A1 region of similar best frequency.

The acute guinea pig experiments provided the initial evidence demonstrating that stimulation of the ICC with our AMI array could achieve low threshold, frequency-specific, and potentially safe activation of the central auditory system. The latter was inferred from empirical safety data collected from stimulation of the cat cortex using slightly different parameters than in our study. Furthermore, stimuli were only presented for a few hours whereas future AMI patients would be stimulated on a daily basis with much faster rates. To obtain a more realistic sense of the safety of the array to both chronic implantation and stimulation for longer periods, we performed a histomorphological study in cats [28]. The cat was selected as the animal model because its IC is similar in cytoarchitecture and size to the human IC. Eight cats were chronically implanted for 3 months, in which four of them were additionally stimulated for 60 days (4 h/day) starting 4 weeks after implantation to assess if clinically relevant stimuli further affected the tissue response. The stimuli consisted of cathodic-leading, charge-balanced pulses in common ground mode (100 μs/phase, 250 pps, 45 μs phase gap) using the SPEAK strategy (Cochlear Ltd.) and driven by continuous sound from a radio. Across animals and throughout the 3-month implant period, the threshold (T) and comfortable (C) levels used to program the processor ranged from 84 to 209 μA and 93 to 256 μA, respectively. An important component of this study was that we used a similar surgical approach to expose the IC surface and implant the AMI array as would be used in the human patients.

In our experiments, we analyzed the histomorphological effects 3 months after initial array implantation, which generally corresponds to the long-term sustained tissue response. In Giemsa-stained sections, the electrode tracks in both nonstimulated and stimulated cats were surrounded by a thin fibrillary sheath (Figs. 13A and 14A). There was no significant difference in the thickness of the reactive fibrillary sheath between the nonstimulated and the stimulated cats suggesting that the encapsulation process is more affected by the

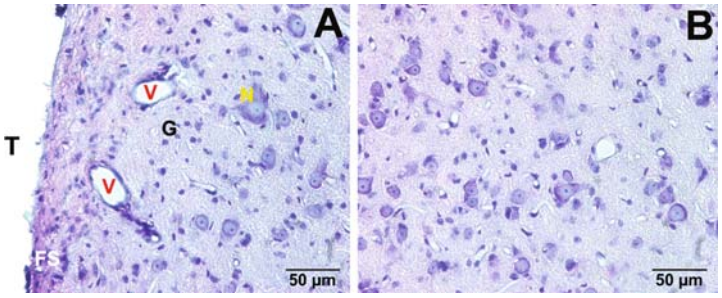

Fig. 13 Tissue reaction to nonstimulated AMI array. Giemsa-stained histological sections showing the distribution of neurons and glial cells adjacent to the track of a chronically implanted nonstimulated electrode array (**A**) in comparison to those in a similar location in the contralateral (control) inferior colliculus of the same cat (**B**). The fibrillary sheath around the track can also be seen. FS, fibrillary sheath; G, glial cell; N, neuron; T, track; V, vessel. Taken from Ref. [28] and reprinted with permission from Lippincott Williams and Wilkins

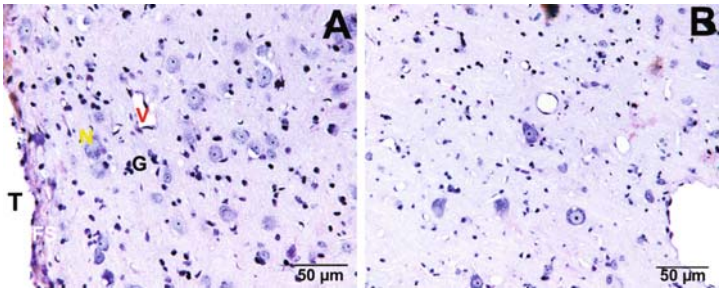

Fig. 14 Tissue reaction to stimulated AMI array. Giemsa-stained histological sections showing the distribution of neurons and glial cells adjacent to the track of a chronically stimulated electrode array (**A**) in comparison to those in a similar location in the contralateral (control) IC of the same cat (**B**). The fibrillary sheath around the track can also be seen. FS, fibrillary sheath; G, glial cell; N, neuron; T, track; V, vessel. Taken from Ref. [28] and reprinted with permission from Lippincott Williams and Wilkins

implantation of a foreign object rather than chronic stimulation. The average thickness of the fibrillary sheath across all nonstimulated and stimulated data was 58.1 μm (SD: 62.7). Around the fibrillary sheath, reactive gliosis was detected in both nonstimulated and stimulated cats (Figs. 13 and 14). The stimulated cats exhibited significant elevation of glial cells out to about 250 μm from the electrode track, while the nonstimulated cats had elevated glial cells out to about 350 μm (Fig. 15C,D). Intact and healthy neurons could be observed around the electrode track in both stimulated and nonstimulated ICs (Figs. 13 and 14). However, there were fewer neurons in the immediate vicinity of the electrode tracks in both animal groups. The neuron density increased to normal at about 50 μm from the track in the stimulated cats and at about 100 μm from the track in nonstimulated cats (Fig. 15A,B). In comparing the plots in Fig. 15, it is apparent that the extent of neuronal survival is inversely related to the level of glial reaction such that a greater number of glial cells corresponds to a fewer number of neurons at each distance from the electrode track. Furthermore, it appears that chronic stimulation improved the tissue reaction (i.e., less glial cells relative to control) and led to better survival of the neurons around the electrode array. Further studies need to be performed to confirm this finding since it is based on only a few animals.

Overall, these histomorphological findings demonstrated that minimal neuronal damage occurs around the electrode array due to chronic implantation and stimulation of our AMI array. These results are similar to what has been observed with other deep brain neural implants currently used in human patients [37, 38] and were encouraging as to the potential safety of our array for clinical use. Furthermore, all eight animals were healthy throughout the 3-month implant period and we did not observe any complications associated with the surgical approach. In electrically stimulating the IC in cats, as well as in humans, it is possible to stimulate neighboring structures that may elicit nonauditory and even adverse effects [8, 39–41]. Activation of the spinothalamic tract (caudal and

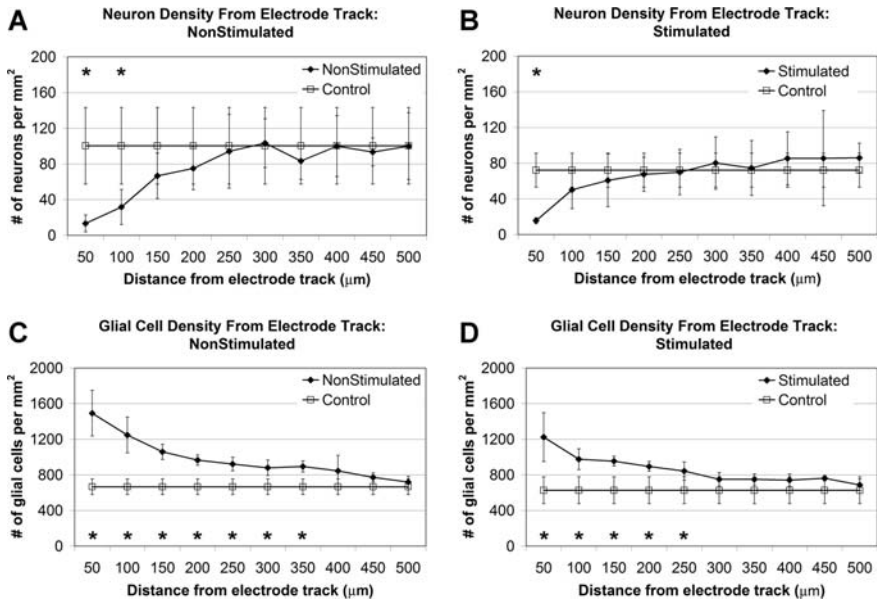

Fig. 15 AMI histological summary. (**A, B**) Neuron density versus distance from electrode track for the nonstimulated and stimulated cats. (**C, D**) Glial cell density versus distance from electrode track for the nonstimulated and stimulated cats. Includes mean across all animals (four nonstimulated and four stimulated), standard deviation bars, and asterisks above the implanted/stimulated mean values that were significantly different from the control values. For further details on the analysis methods, see Ref. [28]. Taken from Ref. [28] and reprinted with permission from Lippincott Williams and Wilkins

ventral to the IC) and the trigeminal tract (medial and ventral) can elicit pain, temperature, and pressure sensations in the body and face, respectively. The trochlear nerve (caudal) and the superior colliculus (rostral) are associated with ocular movements. Stimulation of regions more medial and ventral to the IC, such as the periaqueductal gray and cuneiform area, can elicit pain sensations and changes in arterial blood pressure and heart rate. In all four of our stimulated animals, we did not observe any abnormal eye movements, irregular heart rates, or behavioral responses indicative of painful sensations. It is possible that the animals may have experienced some of the minor sensory effects described above, which we were unable to measure. However, if they did occur, the level of discomfort experienced by the animals was not visually noticeable.

3 Implementation in Humans

3.1 Surgical Approach

Considering that NF2 patients are the largest initial group of candidates for an AMI, we needed to develop a combined surgical approach that enables removal

of acoustic neuromas and AMI implantation at the same surgical setting. The typical midline and paramedian supracerebellar-infratentorial approaches both provide good exposure of the IC but do not provide an appropriate lateral exposure to the cerebellopontine angle and internal auditory canal, which is necessary for tumor removal. However, a lateral suboccipital craniotomy provides access to the internal auditory canal and cerebellopontine angle as well as the IC via a lateral supracerebellar-infratentorial approach. Figure 16A shows the location of the skin incision and craniotomy required for this approach. Once the neurosurgeon cuts through the dura and folds it over the edges to expose the brain (to later allow the dura to be closed via sutures), the cerebellum and tentorium become visible (Fig. 16B). The cerebellum must be retracted medially (to the right) to expose the auditory nerve behind the cerebellum. This is where the acoustic neuroma is located. Once the neurosurgeon removes the tumor, the cerebellum can be retracted downward to expose the surface of the IC. Due to the semi-sitting position and gravity, the cerebellum actually drops downward without any forced retraction as shown in Fig. 16C. Figure 16C,D shows the surface of the IC after the neurosurgeon has carefully cut through the surrounding arachnoid and pushed aside several blood vessels covering the midbrain surface. Once the surface of the IC is exposed, the AMI can be inserted into the IC (Fig. 16D). There are several advantages to this approach. First of all, the insertion pathway shown in Fig. 16D actually enables the placement of the array along the tonotopic gradient of the ICC. Second, minimal manipulation of the cerebellum and surrounding midbrain regions is required to expose the IC surface and implant the array. Furthermore, with regard to vestibular schwannoma surgery, this approach enables removal of even large tumors with the possibility of hearing preservation in patients who undergo surgery in the last hearing ear. In these cases, the function of the auditory nerve must be monitored during and after tumor removal, in which implantation would only be performed in the case of complete hearing loss.

We tested the surgical approach described above in several fresh human cadavers in a semi-sitting position. Details of these experiments are presented in [42]. Briefly, we observed that approaching the tentorial hiatus and dorsolateral aspect of the mesencephalon through the lateral supracerebellar-infratentorial route does not endanger the major midline venous structures in the quadrigeminal cistern. It also provides direct access to the IC with an appropriate angle for AMI insertion along the hypothesized tonotopic gradient of the ICC. Potential risks of this combined approach are partly related to tumor removal through the typical lateral suboccipital approach in the semi-sitting position and partly due to the supracerebellar-infratentorial approach to the IC [43–46]. In experienced hands, tumor removal through this approach is associated with no mortality and a low rate of minor complications [47]. Intraoperative Doppler sonography allows early detection and thereby exclusion of additional morbidity due to air embolism. Risks regarding exposure of the IC and AMI implantation include cerebellar bleeding or infarction, which may result from either extensive retraction of the cerebellum or interruption or coagulation of the cerebellar bridging veins. In performing the operation in the semi-sitting

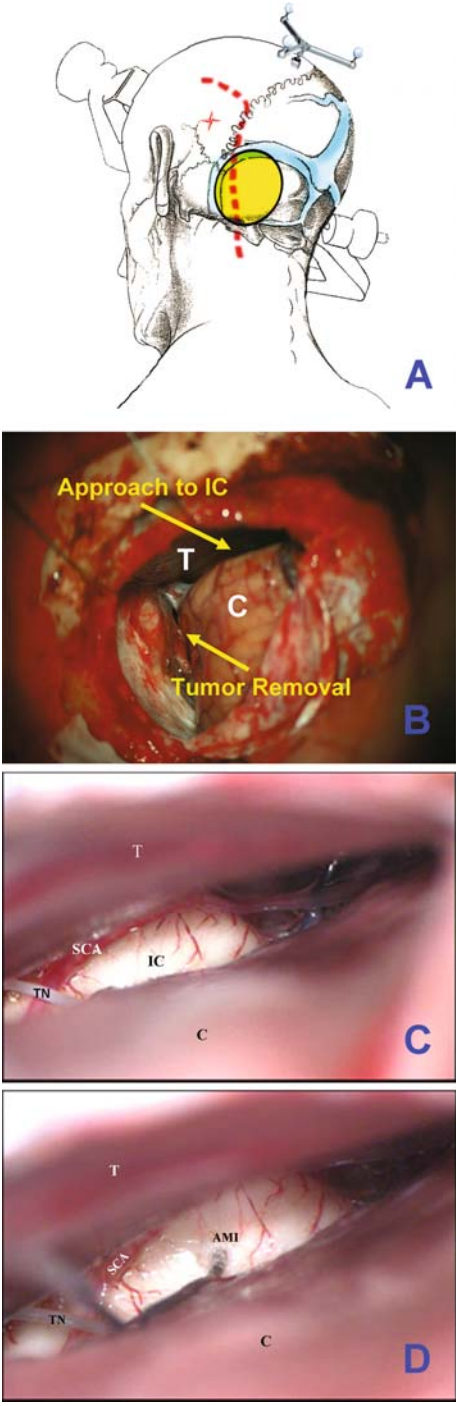

Fig. 16 Surgical approach to the inferior colliculus. (**A**) Schematic drawing of the fixed head in a semi-sitting position and showing the skin incision (*red dotted line*), appropriate location

position, there is no need for cerebellar retraction, and approaching the tentorial notch laterally helps in preserving the cerebellar bridging veins, which are mostly located medial to the trajectory of our approach. The major midline venous structures are not exposed and are therefore not in danger. The only cranial nerve surrounding the IC is the trochlear nerve, which emerges at the side of the frenulum veli below the IC and encircles the cerebral peduncle. Exposing this nerve immediately after opening the arachnoid adhesions reduces the risk for accidental damage to the nerve (Fig. 11C,D). Also, swelling of the superior colliculus because of either manipulation in the quadrigeminal cistern or inevitable coagulation of the quadrigeminal veins may lead to a transient Parinaud syndrome consisting of a combination of impaired extraocular movements (impaired up-gaze or convergence), nystagmus, and impaired papillary reactions. These deficits are almost always transient and rarely cause permanent neurological sequelae [48].

The human and animal findings provided the necessary evidence to obtain approval for and pursue clinical trials. Three patients have been implanted with the AMI thus far. Consistent with our cadaver and chronic cat studies, none of the patients developed any complications due to either tumor removal or AMI implantation. There were no transient or permanent sensory or motor deficits due to implantation trauma in the midbrain. Also none of the patients experienced transient or permanent pain sensations postoperatively due to potential lesions in the midbrain. The only complication associated with the surgery was in identifying the appropriate location to insert the AMI array on the IC surface. The goal is to implant the array along the tonotopic gradient of the ICC. To aid in placement, we used three-dimensional intraoperative navigation (Vector Vision Navigation System; Brainlab, Heimstetten, Germany) with CT and MRI images based on the bone-anchored registration method, which proved to be quite effective in identifying the IC borders during our cadaver studies. However, during live surgery, we noticed that brain shifts as much as several millimeters could occur once the dura was opened, which was minimal in the cadaver preparations. Since the ICC is not a surface structure, it was

Fig. 16 (continued) for the receiver–stimulator of the AMI in the temporoparietal area (*red star*), and the location of the modified lateral suboccipital craniotomy (*yellow circle*) exposing the inferior margin of the transverse sinus and the medial margin of the sigmoid sinus (*blue shaded regions*). The antenna placed at the top of the head is for the three-dimensional intraoperative navigation system. (**B**) After the skull is removed and the dura flaps pulled to the side, the tentorium (T) and cerebellum (C) are visible. The cerebellum is retracted medially (*right*) to expose the auditory nerve and tumor. Due to gravity, the cerebellum drops downward to expose the inferior colliculus (IC). (**C**) View of the left IC, trochlear nerve (TN), and the caudal branch of the superior cerebellar artery (SCA) through the lateral supracerebellar infratentorial approach and after the neurosurgeon has removed the overlying arachnoid and pushed aside several blood vessels. No retraction was used to push the cerebellum downward to view the IC. (**D**) The cable extends from the AMI array that has been implanted into the IC

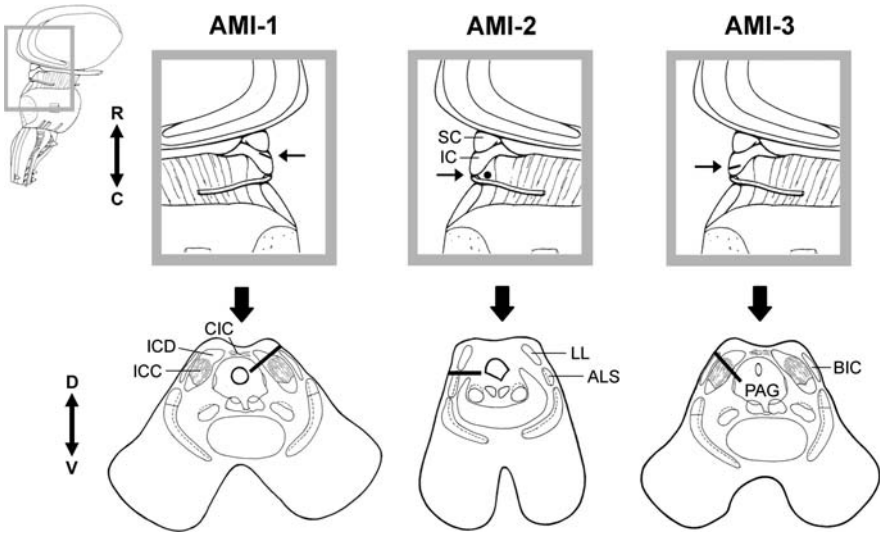

Fig. 17 Array placement across patients. Parasagittal (*top*) and axial (*bottom*) sections showing the location and orientation of the array within the midbrain of each patient. *Arrow* in parasagittal section points to the caudorostral location of the array and the corresponding axial section below. The *black line* (or dot for AMI-2) representing the array in each section corresponds to the trajectory of the array across several superimposed CT-MRI slices. ALS, anterolateral system; BIC, brachium of IC; CIC, commissure of IC; IC, inferior colliculus; ICC, inferior colliculus central nucleus; ICD, inferior colliculus dorsal nucleus; LL, lateral lemniscus; PAG, periaqueductal gray; SC, superior colliculus. Taken from Ref. [49] and reprinted with permission from the Society for Neuroscience

difficult to accurately insert the array into the ICC without any reliable three-dimensional mapping of the IC borders.

Figure 17 provides a summary of the different locations of the array across the three patients. In the first patient (AMI-1), we implanted the array too rostral and medial resulting in its placement into the dorsal cortex of the IC. In response to the first placement, in the second patient (AMI-2) we attempted to insert the array more caudally and laterally resulting in its placement along the surface of the lateral lemniscus. From our learning experiences with the first two patients, we became more familiar with the IC surface landmarks (i.e., IC–SC border, midline, exit point of the trochlear nerve) and the extent of brain shift during surgery. Thus in AMI-3, we were able to improve our surgical techniques and position the array into the ICC.

The next step is to determine where to implant the AMI array within the ICC in future patients. We have animal data suggesting that stimulation of the rostral and lateral regions of the ICC provides better frequency, temporal, and level coding properties as well as more excitatory and spatially synchronized activity in A1 [50, 51]. Thus implantation of the array into such a region within the human ICC may provide improvements in coding properties that have shown to be important for speech perception [10, 11, 52–55]. Since it is not clear if our animal

electrophysiological findings will translate to consistent human perceptual effects, we will need to assess psychophysical and speech performance across a larger number of AMI patients implanted into different ICC regions to answer the question of optimal implant location with the single-shank array. Although we will attempt to position the array in a more rostral and lateral location within the ICC in the next few patients, the main focus will be to simply ensure the array is implanted within the ICC using our improved surgical techniques. We are also developing surface IC stimulation techniques (i.e., stimulating with bipolar electrode spheres) in which we record the corresponding cortical evoked potentials with surface EEG arrays. The idea is to identify specific patterns of evoked potentials associated with different locations along the IC surface that correlate with where to insert the AMI array to penetrate the ICC.

3.2 Patient Fitting

A summary of the demographic and implant-related information for each patient is presented in Table 1. All three patients were diagnosed with the NF2 disease and required acoustic neuroma removal on one side where they were already deaf. AMI-1 had residual tonal hearing in the right ear (30–50 dB

Table 1 Patient summary

Name	AMI-1	AMI-2	AMI-3
Gender	F	M	F
Age	71	28	42
Hearing status[1]	Residual right ear	Hearing aid left ear	None
Tinnitus	Sometimes	Always	Always
Implant side	Left	Right	Right
Implant date	07/04/06	08/08/06	10/25/06
Turn on date	08/07/06	09/11/06	12/13/06
Side effect sites	12–20	1–9, 20	12–20
Side effects	Dizziness, contra facial twitch, head/chest sensations & warmness	Paresthesia in contra upper body and face, coldness in contra face	Paresthesia in contra thigh, leg, and foot
Active sites[2]	1, 2, 4–9	10, 11, 13–19	1–9
Processor strategy[1]	ACE, 6-8 maxima	SPEAK, 8 maxima	SPEAK, 6 maxima

[1]Further details provided in Section 3.2.
[2]Other sites not listed either caused unpleasant sounds (i.e., a low-pitch screechy sound or sensation that was uncomfortable but difficult to describe) or were shorted to other sites and thus were not used for daily stimulation.
Taken from Ref. [49] and reprinted with permission from the Society for Neuroscience.

HL for 0.125–1 kHz; >70 dB HL for >1 kHz). However, she scored poorly on our standard speech test used to assess implant eligibility (<10% at 110 dB HL for Freiburger monosyllable word test; CI criteria: <30% at 65 dB HL) indicating her inability to benefit from hearing aids. AMI-2 had residual tonal hearing in the left ear (>90 dB HL) and could obtain some improvements in lip-reading capabilities using a hearing aid. However, he was experiencing rapid deterioration in his hearing, which justified AMI implantation. AMI-3 was completely deaf for 6 years and had previously been implanted two times with the ABI on the left side. In both cases, the ABI became postoperatively displaced into the fourth ventricle due to the enlarged facial recess created by the large tumor that was removed. AMI-3 was then implanted with the AMI during removal of a residual acoustic neuroma on the right side. All three patients had varying degrees of tinnitus that were affected by midbrain stimulation but not in any obvious manner.

The patients returned 5–7 weeks after AMI implantation for their first fitting session. Since our AMI patients are the first cases of stimulation within the midbrain for hearing restoration, we were faced with the difficult task of figuring out how best to stimulate these patients to restore useful hearing. For the first few testing sessions, it was crucial to have a physician present in case of any adverse reactions to electrical stimulation since it was not yet known how stimulation within the midbrain would induce different sensory and motor effects. More importantly, we had to be cautious of pain sensations, heart rate changes, and blood pressure effects associated with various midbrain regions. Fortunately, we did not observe any adverse or painful side effects to electrical stimulation. Nonauditory sensations consisted of paresthesia, mild temperature changes in different parts of the face and body, some dizziness, and mild facial twitches (see Table 1). However, all these side effects were avoided by turning off the corresponding sites for daily stimulation. As for auditory sensations, the patients described the percepts as tonal in nature but that some sites elicited a broad spectral percept with multiple pitches. The patients also described the sounds as having an electronic quality mixed in with the tonal percept. Furthermore, pitch and temporal percepts could be altered by changing the stimulation pulse rate and pattern as well as location of activation. These qualitative results were encouraging for AMI implementation since they suggest that at the level of the midbrain sound still appears to be somewhat coded into elementary perceptual features of sound (i.e., tonal sounds that can be systematically elicited with varying temporal percepts). This is in contrast to stimulation of the auditory cortex in which more complex sound sensations (e.g., “swooshing of jumping rope”, “whining”, “jet engine”, “crickets”) and even a lack of perceptual changes to varying stimulus parameters (e.g., different pulse rates) have been reported [56–58].

In addition to assessing the functional effects of midbrain stimulation, we also frequently measured the impedances of the sites to assess the functionality of the implanted array over time. Cochlear Ltd. has developed a testing and fitting software, Custom Sound, that enables impedance measurements and

implementation of different stimulation strategies. The level unit used in this software is known as Current Level (CL), which for the AMI system (i.e., all their Nucleus Freedom systems) corresponds to $CL = 127.5 \times \log (L/17.5)$ where L is level in μA. For measuring impedances, monopolar or common ground configurations can be used with the latter allowing identification of shorts (i.e., impedance equal to zero). Impedances are calculated by presenting a single biphasic pulse (80 CL, 25 μs/phase, 7 μs inter-phase gap) and dividing the measured voltage by the pulse current level. The calculation is based on the average of eight pulses presented at 5000 pps. Generally, the site impedances range from 3 to 20 kΩ across our patients. For most sites, the impedances remained relatively stable over time. However, we did observe some electrode shorts that appeared over time. AMI-1 had several shorts, AMI-2 had no shorts, and AMI-3 had one short. It is still not clear as to what may be causing these shorts. As described earlier, we performed extensive in vitro tests to ensure that excessive manipulation and bending of the array did not induce any shorts. We also chronically implanted the array into cats for 3 months and did not observe any obvious issues with shorts. We are currently investigating this issue to improve the design of the array through the PDCA process. This is just an example of how extensive in vitro and animal testing may not predict all issues that can arise during human use of the implant. Thus careful and thorough monitoring of the functionality and safety of the implant is essential throughout the entire clinical trial. For our purposes, we simply turned off all but one of the sites of the shorted set to prevent current from flowing through more than one location during daily stimulation.

The main challenge we initially faced in fitting the patients was in reducing the enormous parameter space for stimulation to just the essential elements required for speech perception. For the same reasons we developed an AMI array based on previously approved CI technology (i.e., concerning safety and practicality), we eventually decided to implement the first AMI patients with a CI stimulation strategy. This is not to claim that auditory coding is the same at the level of the midbrain as in the cochlea. However, there is evidence from animal studies suggesting that some general coding features of complex sound (e.g., to varying pitch or animal vocalizations) are maintained from the cochlea up to the auditory cortex [59–62]. In particular, many neurons still respond in synchrony to the envelope of the sound signal and with a spatial representation for frequency information at the level of the midbrain as occuring within the cochlea [24, 63]. Although many neurons located higher along the auditory pathway also tend to exhibit more complex and variable response patterns, we do not yet have any clear indications as to how to more optimally stimulate the midbrain, particularly the ICC. Furthermore, since some ABI patients (particularly those without tumors) can converse over the telephone with CI strategies at the level of the brainstem [4], it is not too implausible to assume that CI-derived strategies may work, to some degree, at the level of the midbrain.

We could have taken the more conservative approach in that before implanting any patient, we performed excessive electrophysiology and behavioral

animal studies to understand the intricate coding circuitry of the IC and how electrical stimulation of its different regions affects higher auditory processing. However, behavioral studies are quite time consuming and, in the end, can only provide a limited, experimentally constrained view of how the auditory system will process sound in a natural environment, especially in relation to processing in humans. At some point, the decision to implant patients with the available knowledge must be made since it is not possible to know ahead of time which strategies will be most effective in restoring hearing in humans until it is actually performed, especially since artificial neural activation is induced with electrical stimulation. Based on the available data from animal and human studies on auditory processing and our series of safety and AMI stimulation studies [28–30, 42, 50, 51, 64, 65], we made the decision to implant patients with the AMI and to implement CI-based strategies, which we did not believe to be optimal for the IC but would provide some basic features of sound that the patients could use to dramatically improve their daily hearing condition. Then we would optimize the strategy based on their psychophysical and hearing performance.

There are various types of stimulation strategies used in CI patients and developed by the different implant companies. However, the general architecture is similar across strategies as described in the Introduction. The two types of strategies arbitrarily employed in our AMI patients are the SPEAK and ACE strategies. Except for minor differences, such as a different inter-phase gap and pulse rate limit, these strategies are quite similar. For further details, see Ref. [66]. The main point is that in order to implement these strategies, the threshold and comfortable levels must be set for each site, the sites must be ordered to correspond to different frequency ranges of sound information (i.e., pitch ordering), a pulse rate and pulse width of stimulation needs to be selected, and various minor parameters need to be adjusted. Thus, our goal of the first testing sessions was to determine these different parameters. Based on various psychophysical tests presented in detail in [67], we selected a pulse rate of 250 pps, pulse width of 100 μs/phase, and monopolar configuration (bipolar and common ground are also possible). Briefly, 250 pps was high enough to avoid noticeable rate pitch effects (i.e., lower rates elicit confounding low-pitch percepts) and the lowest rate available for daily stimulation to minimize adaptive effects (i.e., high-rate stimulation can cause the loudness to decrease over time). These parameters also achieved the largest drop in thresholds in which using longer pulse widths and higher pulse rates (thus greater total charge) did not decrease the thresholds by much more, whereas using shorter pulse widths and slower pulse rates substantially increased threshold levels. This was important for identifying stimuli that requires less total charge (thus more energy efficient activation) yet was still reasonably within the compliance voltage limits of the stimulator and the safety limit for brain stimulation. The threshold and comfortable levels as well as the site (i.e., pitch) order were adjusted as needed during each testing session based on standard fitting methods used for CI patients.

For the most part, fitting the AMI patients with the CI strategies was straightforward, similar to the fitting of CI patients. However, we did encounter

a particularly interesting situation in one of the patients. With daily stimulation, threshold levels began to rise in AMI-1 over time such that after 125 days, we had to turn off the implant because the levels required to elicit auditory sensations exceeded the limit of the stimulator. After 48 days of recovery, the levels decreased but not to the original levels observed during the first testing session. Furthermore, the patient expressed that the loudness of the incoming sound faded away after tens of seconds of continuous sound input. It appears that stimulation of the dorsal cortex of the IC, the region where AMI-1 is implanted, is not designed to sustain a constant loudness with continuous stimulation. This is not surprising considering that the dorsal cortex of the IC has shown in animal studies to receive a large number of descending and modulating projections from auditory and nonauditory centers [19] and to adapt to constant stimuli [68]. Currently, we are developing a new stimulation strategy for this patient that attempts to stimulate in a more distributed pattern across sites to prevent any one site from being excessively and continuously stimulated. However, in future patients, we will avoid the dorsal cortex until effective stimuli for this region are identified.

3.3 Hearing Performance

Even with the use of a single-shank array in a three-dimensional auditory structure and stimulation strategies originally designed for the cochlea, all three patients have obtained hearing benefits from the AMI on a daily basis. In particular, they all obtain improvements in lip-reading capabilities and environmental awareness. Details of the hearing results, including the effects of midbrain stimulation on temporal, pitch, level, and location percepts, are presented in Ref. [49]. Briefly, AMI-1 obtained auditory sensations that all appeared to originate simultaneously from both ears, AMI-2 perceived all sounds from the ipsilateral side, and AMI-3 perceived all sounds from the contralateral side. This finding is interesting in that it suggests that neurons coding for different location percepts are organized in a somewhat segregated manner considering that the active sites in each patient spanned almost 2 mm throughout the midbrain. All three patients obtained monotonic loudness growth functions in which higher current levels produced louder auditory sensations. This is particularly important for implementing the CI strategy since it requires that loudness is coded by current level in which pulse trains presented on a given site are amplitude modulated by the envelope of the filtered sound signal. All three patients can also detect temporal changes in the stimulus, such as gaps in pulse trains as short as 10 ms. Although each patient can detect differences in pitch percepts depending on the stimulated site, we only observed a systematic pitch organization in AMI-3. This is consistent with findings from animal studies in that the array in AMI-1 and AMI-2 is not aligned along any known tonotopic organization whereas the array in AMI-3 is

aligned along the tonotopic gradient of the ICC (i.e., lower pitch percepts more superficially and higher pitch percepts in deeper regions). It must be emphasized that we did not observe this systematic pitch organization for the first 6 months of stimulation. In fact, stimulation of all sites elicited predominantly low-pitch sounds. These results are presented in Ref. [49]. However, during the 6-month follow-up session, AMI-3 expressed that annoyingly high-pitch percepts could be perceived during daily stimulation. After performing extensive pitch tests, we identified a systematic pitch organization consistent with animal findings [51]. It appears that dramatic plastic effects to midbrain stimulation is possible and may be reversing deficits induced by long periods of deafness (AMI-3 was deaf for 6 years and had only low frequency residual hearing prior to complete deafness). Consistent with this idea, we also observed dramatic improvements in temporal resolution, such as gap detection (100 ms down to 10 ms), in AMI-3 over time with daily stimulation that cannot be solely explained by learning improvements on the tasks. This has important implications for speech-coding strategies that will be discussed in the next section.

Overall, it is apparent that location of stimulation can affect different perceptual features as well as hearing performance. AMI-1, who is implanted in the dorsal cortex of the IC, obtains the least benefit from the AMI. This is mainly due to the adaptive effects experienced during daily stimulation in which the loudness decreases and thresholds increase over time. During the speech tests, in which silent (recovery) periods are followed by speech presentation as well as during daily situations when intermittent sound is presented and perceived at a loud enough level, the patient is able to extract some temporal and pitch information from the sound signal. Generally, improvements in hearing have been limited to lip-reading enhancement and environmental awareness. On the other hand, AMI-2, who is implanted on the surface of the lateral lemniscus, obtains additional improvements in vowel, number, and consonant recognition with the AMI alone. The greatest improvements have been observed in AMI-3, who was implanted in the intended target of the ICC. As shown in Fig. 18, AMI-3 obtained about 50% correct for vowels, 20% for consonants, and 40% for numbers with AMI alone indicating that she obtains a significant amount of sound information with her implant alone after 1 year of daily stimulation. The most encouraging result was her speech-tracking scores. Generally, ABI NF2 patients in our clinic ($n = 27$) do not obtain any speech tracking with the implant alone. The average lip-reading enhancement (difference between lip reading plus ABI and lip reading alone) for the ABI is about 14 words per minute (H. H. Lim, Unpublished observations). AMI-3 achieved a lip-reading enhancement of 26 words per minute (tested by the same speech therapist using the same protocol), which suggests that if the AMI can be implanted into the correct target of the ICC, then it has potential to provide improvements in hearing performance over the average ABI patient. This is encouraging for the AMI since its goal is to provide a hearing alternative to the ABI in NF2 patients. However, we still need to provide further improvements in overall hearing. Normal hearing subjects obtain a speech-tracking score of about 85–100 words

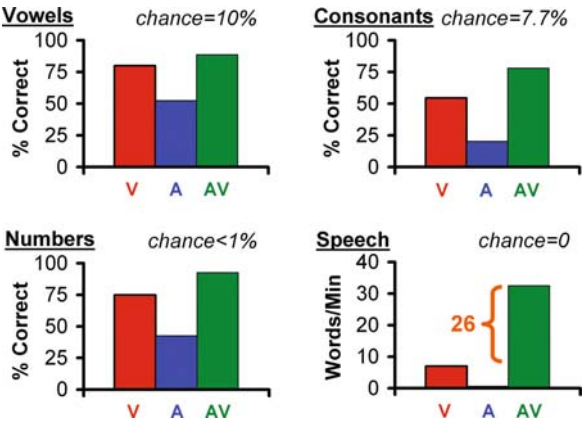

Fig. 18 Speech scores for AMI-3 at 1 year. Vowel test (chance level of 10%) consisted of five long (e.g., BAAT, GAAT) and five short (e.g., BAT, GAT) words randomly read to the patient (four times) and the patient had to repeat the word. Consonant test (chance level of 7.7%) consisted of 13 meaningless consonant words (e.g., ABA, AGA) repeated four times. Freiburger number test (open set, chance level < 1%) consisted of 20 German numbers between 13 and 99 (2–5 syllables). Speech tracking (modified open set, chance level of 0%) involved reading a story to the patient who was asked to repeat the words of the cited sentences. The number of correct words in 5 min was obtained and divided by five to obtain the correct number of words per minute. V, lip reading (visual) alone; A, AMI (audio) alone; AV, lip reading and AMI (audiovisual). Lip-reading enhancement is the difference between AV and V. All scores are the average across three testing sessions. Further details on the methods are presented in Ref. [68]

per minute [69], which is much greater than the 30 words per minute obtained by AMI-3. Furthermore, many CI patients can converse over the telephone, thus obtain speech perception without lip reading (i.e., with the implant alone).

4 Future Directions

Generally, the performance of the AMI across our three patients has been encouraging as to its potential as an alternative hearing solution for patients who cannot sufficiently benefit from the CI or ABI. The AMI has also shown to be safe for human use. However, hearing performance is still much lower than what is typically achieved by the top CI patients and normal hearing subjects. This is likely due to suboptimal activation throughout the IC. Currently we are stimulating along a single trajectory within a three-dimensional structure with stimuli originally designed for the cochlea. The fact that we observed dramatic adaptive effects when stimulating certain IC regions (in AMI-1), while no or minimal adaptation when stimulating in other regions, confirms that different IC neurons code sound information in different ways as has been shown in animal studies (for a detailed coverage of the IC, see Ref. [70]). This is in contrast to cochlear neurons that generally exhibit quite similar coding

properties and are effectively activated through CI stimulation strategies. Therefore, in order to improve overall hearing performance, new electrode technologies and stimulation strategies designed for more naturalistic activation across the IC needs to be investigated. Both aspects are discussed below.

4.1 Electrode Technologies

With the current single-shank array, we have approval to implant a total of five patients. Through our surgical experience in the last three patients, we have improved our methods for implanting the array into the ICC. However, since the ICC is not a surface structure that can be visually localized, we will likely have difficulties in ensuring placement of the array into specific regions within the ICC in our next two patients. As discussed in Section 1.2, ideally we would like to develop a three-dimensional array with a large number of closely spaced sites, which would increase the probability of placing sites within the appropriate regions of the IC. Furthermore, based on our human psychophysical results, stimulation location within the IC affects different perceptual features. Thus, implanting an array with a greater number of sites will ensure that we have sufficient access to the different coding mechanisms within the IC. Unfortunately, such technology is still not approved for human use.

As a compromise, we have developed a new double-shank array (Fig. 19) that consists of two shorter single-shank arrays connected through separate cables (i.e., the two cables merge together into one cable before connecting to the receiver–stimulator). Since we are limited to a total of 22 sites by the

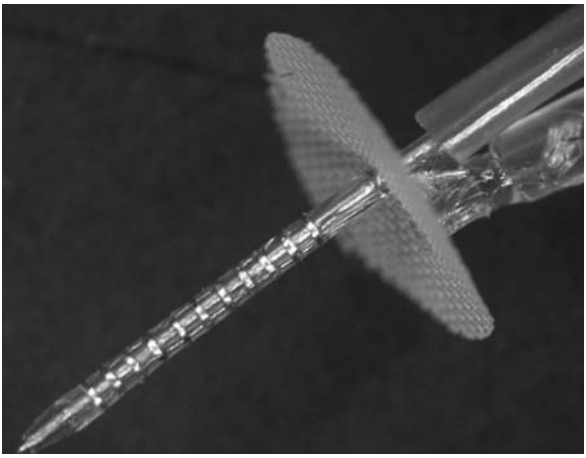

Fig. 19 Double-shank array. Image of one of the two shanks of the new AMI array. Materials and development of this array are similar to the single-shank array in Fig. 5, except the shank is 5 mm long, sites span a distance of 3.1 mm (edge-to-edge), and the site spacing is 0.3 mm (center-to-center). The sites are still 0.1 mm wide with a diameter of 0.4 mm and surface area of $\sim$0.00126 mm^2. The array was developed by Cochlear Ltd

processor interface, we developed two shanks each with 11 sites. These shanks are similar in design to the single-shank array, except with fewer sites that are more widely spaced apart (300 μm center-to-center). The original single-shank array had 20 sites spaced at 200 μm intervals, thus spanned 3.8 mm (3.9 mm from the site edges). Based on the number of active sites we obtained in AMI-3 (that still spanned a wide range of pitches) and the anatomical dimensions of the human ICC [8], reducing the total span of the sites to 3.0 mm (3.1 mm from the site edges) should still provide sufficient coverage across the different frequency regions of the ICC. To achieve this, however, we had to increase the site spacing by 50%. The plan is to implant both shanks along the tonotopic gradient of the ICC but in different isofrequency locations. In particular, we hope to place one shank in a more rostral–lateral location while the other shank in a more caudal–medial location. This is based on animal findings in which the ICC appears to be divided into these two smaller subregions with different coding properties [50, 71]. The benefit of the double-shank array is that we can stimulate each shank independently of each other and/or in synchrony by aligning sites within the same isofrequency layer. We can also steer current across different combinations of sites throughout the ICC. Although stimulation of other IC regions, such as the dorsal cortex or external nucleus, in combination with the ICC may provide greater improvements in hearing performance, we will first focus on stimulating across multiple regions throughout the ICC to reduce the complexity of the investigation.

One advantage of the design of the new double-shank array is that we do not need to repeat animal safety studies since it simply consists of two single-shank arrays that have already been approved for human use. We do, however, need to test the array in fresh cadaver preparations to determine the best approach for implanting both shanks into the IC. With the single-shank array, the neurosurgeon manually inserts the array into the neural tissue and then removes the stylet. For the double-shank array, there is the added risk of manually implanting two shanks separately. The surgical opening to the IC surface is quite small and it is possible that the neurosurgeon may displace or collide with the first implanted array during implantation of the second array. For this reason, we are currently developing a surgical positioner that will enable the neurosurgeon to easily insert the double-shank array into the tissue, either one at a time or simultaneously, without having to reach into the small cavity surrounding the IC surface.

Although we have not yet attempted to implant a three-dimensional array based on silicon and polyimide technologies into our patients mainly due to the additional obstacles in obtaining approval for clinical trials, we will begin to investigate those technologies in animal models. Eventually, brain–machine interfaces will rely on such technologies to provide greater improvements in performance and flexibility in terms of implementation. In addition, we will also investigate stereotactic approaches to the midbrain. Considering the success and safety of DBS for a multitude of neurological applications, especially those associated with midbrain regions [12, 13], it is to our advantage to

translate many of the surgical techniques and technologies already developed and approved for DBS surgery to AMI implantation. This includes the use of penetrating microarrays for mapping the borders of the IC for array implantation. Although the patients will not have functional hearing to drive neural activity in the IC for recording purposes, it will be possible to electrically stimulate different regions and characterize the site locations based on the perceptual responses elicited in the awake patient during stereotactic surgery.

4.2 Stimulation Strategies

Several key findings have surfaced from our animal and human experiments that provide some guidance toward how we could better stimulate the IC to restore useful hearing. The major finding is that location of stimulation affects auditory percepts. Some IC regions are designed to robustly transmit continuous and repetitive sound stimuli, whereas other regions respond only to transient inputs. Different regions appear to code for different sound location percepts. Certain regions also appear to better code for temporal, level, and spectral features of sound information. Together, these findings suggest that an appropriate stimulation strategy may actually require different stimulation sequences for different regions. For example, a patient may be implanted with a double-shank array or even a three-dimensional array. Fitting of the processor would require stimulation of each site followed by classification of that site based on its perceptual effects. Once the different sites are classified into different groups, the appropriate stimuli would be presented to those sites. Some sites may receive stimuli corresponding to only the transient components of the signal (e.g., just the onset or offset of a sound segment), which could alleviate some of the strong loudness adaptation effects we observed for continuous stimulation of certain IC regions, whereas other sites may receive the stationary components (e.g., stimulated for the entire stimulus duration). Certain sites could be presented with fine changes in sound features, whereas other sites would code for more coarse components of the sound. The range of coding properties across IC regions as well as identification and classification of the features that are most critical for speech perception need to be more thoroughly investigated and ultimately implemented into the stimulation strategy.

The fact that we also observed dramatic plastic effects in AMI-3 over time with daily stimulation further suggests that stimulation strategies will require some adaptive features that can accommodate these changes as well as optimize them to enable greater improvements in hearing performance. In the same way electrical stimulation of the IC may improve coding properties toward normal conditions in a deafened system, it is also possible that suboptimal stimuli may degrade coding mechanisms or at least introduce confounding effects that may prevent further improvements in hearing with the AMI over time. Thus, the appropriate type of stimuli, not only to elicit useful hearing but also to induce

positive plastic changes within the IC, needs to be determined. Future AMI goals will be directed toward developing stimulation strategies that activate the IC in a more naturalistic pattern in combination with improvements in electrode technologies.

Acknowledgments We would like to thank Gert Joseph, Urte Rost, Joerg Pesch, and Rolf-Dieter Battmer for involvement with AMI patient testing and fitting; Madjid Samii, Amir Samii, and the International Neuroscience Institute (Hanover, Germany) for successful AMI surgery; and the engineers and scientists at Cochlear Ltd. (Lane Cove, Australia) for AMI development and technical assistance. We would also like to thank David J. Anderson for providing the scientific pathway for performing the initial AMI feasibility experiments at the University of Michigan; and Günter Reuter, Uta Reich, Gerrit Paasche, and Alexandru C. Stan for involvement with the animal safety studies at Hanover Medical University. We appreciate the contributions by Frank Risi and James F. Patrick from Cochlear Ltd. in the writing of Section 2.1. Funding was mostly provided by Cochlear Ltd. with contributions from the German Research Foundation (SFB 599) and NIH through P41 EB2030, P30 DC05188, T32 DC00011, and F31 DC007009.

References

1. Zeng FG. Trends in cochlear implants. *Trends Amplif* 8: 1–34, 2004.
2. Adams JS, Hasenstab MS, Pippin GW, and Sismanis A. Telephone use and understanding in patients with cochlear implants. *Ear Nose Throat J* 83: 96, 99–100, 102–103, 2004.
3. McCreery DB. Cochlear nucleus auditory prostheses. *Hear Res* 242: 64–73, 2008.
4. Colletti V, and Shannon RV. Open set speech perception with auditory brainstem implant? *Laryngoscope* 115: 1974–1978, 2005.
5. Evans DG, Huson SM, Donnai D, Neary W, Blair V, Teare D, Newton V, Strachan T, Ramsden R, and Harris R. A genetic study of type 2 neurofibromatosis in the United Kingdom. I. Prevalence, mutation rate, fitness, and confirmation of maternal transmission effect on severity. *J Med Genet* 29: 841–846, 1992.
6. Yost WA. *Fundamentals of Hearing: An Introduction*. New York: Academic Press, 2000.
7. Casseday JH, Fremouw T, and Covey E. The inferior colliculus: A hub for the central auditory system. In: *Springer Handbook of Auditory Research: Integrative Functions in the Mammalian Auditory Pathway (Vol 15)*, edited by Oertel D, Fay RR, and Popper AN. New York: Springer-Verlag, pp. 238–318, 2002.
8. Geniec P, and Morest DK. The neuronal architecture of the human posterior colliculus. A study with the Golgi method. *Acta Otolaryngol Suppl* 295: 1–33, 1971.
9. Oliver DL. Neuronal organization in the inferior colliculus. In: *The Inferior Colliculus*, edited by Winer JA, and Schreiner CE. New York: Springer Science + Business Media, Inc., pp. 69–114, 2005.
10. Friesen LM, Shannon RV, Baskent D, and Wang X. Speech recognition in noise as a function of the number of spectral channels: comparison of acoustic hearing and cochlear implants. *J Acoust Soc Am* 110: 1150–1163, 2001.
11. Shannon RV, Fu QJ, and Galvin J, 3rd. The number of spectral channels required for speech recognition depends on the difficulty of the listening situation. *Acta Otolaryngol Suppl* 50–54, 2004.
12. Green AL, Wang S, Owen SL, Xie K, Bittar RG, Stein JF, Paterson DJ, and Aziz TZ. Stimulating the human midbrain to reveal the link between pain and blood pressure. *Pain* 124: 349–359, 2006.

13. Wichmann T, and Delong MR. Deep brain stimulation for neurologic and neuropsychiatric disorders. *Neuron* 52: 197–204, 2006.
14. Dahmen JC, and King AJ. Learning to hear: plasticity of auditory cortical processing. *Curr Opin Neurobiol* 2007.
15. Keuroghlian AS, and Knudsen EI. Adaptive auditory plasticity in developing and adult animals. *Prog Neurobiol* 82: 109–121, 2007.
16. Ehret G, and Romand R. *The Central Auditory System*. New York: Oxford University Press, Inc., 1997.
17. Owen SL, Green AL, Nandi DD, Bittar RG, Wang S, and Aziz TZ. Deep brain stimulation for neuropathic pain. *Acta Neurochir Suppl* 97: 111–116, 2007.
18. Ehret G. The auditory midbrain, a "shunting yard" of acoustical information processing. In: *The Central Auditory System*, edited by Ehret G, and Romand R. New York: Oxford University Press, Inc., pp. 259–316, 1997.
19. Winer JA. Three systems of descending projections to the inferior colliculus. In: *The Inferior Colliculus*, edited by Winer JA, and Schreiner CE. New York: Springer Science + Business Media, Inc., pp. 231–247, 2005.
20. Hage SR, and Ehret G. Mapping responses to frequency sweeps and tones in the inferior colliculus of house mice. *Eur J Neurosci* 18: 2301–2312, 2003.
21. Stiebler I. Tone-threshold mapping in the inferior colliculus of the house mouse. *Neurosci Lett* 65: 336–340, 1986.
22. Schreiner CE, and Langner G. Periodicity coding in the inferior colliculus of the cat. II. Topographical organization. *J Neurophysiol* 60: 1823–1840, 1988.
23. Langner G, Schreiner C, and Merzenich MM. Covariation of latency and temporal resolution in the inferior colliculus of the cat. *Hear Res* 31: 197–201, 1987.
24. Krishna BS, and Semple MN. Auditory temporal processing: responses to sinusoidally amplitude-modulated tones in the inferior colliculus. *J Neurophysiol* 84: 255–273, 2000.
25. Seshagiri CV, and Delgutte B. Response properties of neighboring neurons in the auditory midbrain for pure-tone stimulation: a tetrode study. *J Neurophysiol* 98: 2058–2073, 2007.
26. Anderson DJ. Penetrating multichannel stimulation and recording electrodes in auditory prosthesis research. *Hear Res* 242: 31–41, 2008.
27. McCreery D, Lossinsky A, and Pikov V. Performance of multisite silicon microprobes implanted chronically in the ventral cochlear nucleus of the cat. *IEEE Trans Biomed Eng* 54: 1042–1052, 2007.
28. Lenarz M, Lim HH, Lenarz T, Reich U, Marquardt N, Klingberg M, Paasche G, Reuter G, and Stan A. Auditory Midbrain Implant: Histomorphological effects of long-term implantation and electrical stimulation of a new DBS array. *Otol Neurotol* 28: 1045–1052, 2007.
29. Lenarz M, Lim HH, Patrick JF, Anderson DJ, and Lenarz T. *Electrophysiological validation of a human prototype auditory midbrain implant in a guinea pig model. JARO* 7: 383–398, 2006a.
30. Lim HH, and Anderson DJ. Auditory cortical responses to electrical stimulation of the inferior colliculus: Implications for an auditory midbrain implant. *J Neurophysiol* 96: 975–988, 2006.
31. Malmierca MS, Rees A, Le Beau FE, and Bjaalie JG. Laminar organization of frequency-defined local axons within and between the inferior colliculi of the guinea pig. *J Comp Neurol* 357: 124–144, 1995.
32. Wallace MN, Rutkowski RG, and Palmer AR. Identification and localisation of auditory areas in guinea pig cortex. *Exp Brain Res* 132: 445–456, 2000.
33. Bierer JA, and Middlebrooks JC. Auditory cortical images of cochlear-implant stimuli: dependence on electrode configuration. *J Neurophysiol* 87: 478–492, 2002.
34. McCreery DB, Agnew WF, Yuen TG, and Bullara L. Charge density and charge per phase as cofactors in neural injury induced by electrical stimulation. *IEEE Trans Biomed Eng* 37: 996–1001, 1990.

35. Merrill DR, Bikson M, and Jefferys JG. Electrical stimulation of excitable tissue: design of efficacious and safe protocols. *J Neurosci Methods* 141: 171–198, 2005.
36. Shannon RV. A model of safe levels for electrical stimulation. *IEEE Trans Biomed Eng* 39: 424–426, 1992.
37. Haberler C, Alesch F, Mazal PR, Pilz P, Jellinger K, Pinter MM, Hainfellner JA, and Budka H. No tissue damage by chronic deep brain stimulation in Parkinson's disease. *Ann Neurol* 48: 372–376, 2000.
38. McCreery DB, Shannon RV, Otto S, and Waring MD. A cochlear nucleus auditory prosthesis based on microstimulation, Quarterly Report #3, Contract NO1-DC-4-0005, National Institute on Deafness and Other Communication Disorders: Neural Prosthesis Development Program. 2005.
39. Kretschmann HJ, and Weinrich W. *Cranial Neuroimaging and Clinical Neuroanatomy: Magnetic Resonance Imaging and Computed Tomography*. New York: Thieme Medical Publishers, Inc., p. 375, 1992.
40. Moore JK. The human auditory brain stem: a comparative view. *Hear Res* 29: 1–32, 1987.
41. Trepel M. *Neuroanatomie. Struktur und Funktion*. Muenchen: Elsevier GmbH, p. 396, 2004.
42. Samii A, Lenarz M, Majdani O, Lim HH, Samii M, and Lenarz T. Auditory midbrain implant: a combined approach for vestibular schwannoma surgery and device implantation. *Otol Neurotol* 28: 31–38, 2007.
43. Ammirati M, Bernardo A, Musumeci A, and Bricolo A. Comparison of different infratentorial-supracerebellar approaches to the posterior and middle incisural space: a cadaveric study. *J Neurosurg* 97: 922–928, 2002.
44. Hitotsumatsu T, Matsushima T, and Inoue T. Microvascular decompression for treatment of trigeminal neuralgia, hemifacial spasm, and glossopharyngeal neuralgia: three surgical approach variations: technical note. *Neurosurgery* 53: 1436–1441; discussion 1442-1433, 2003.
45. Ulm AJ, Tanriover N, Kawashima M, Campero A, Bova FJ, and Rhoton A, Jr. Microsurgical approaches to the perimesencephalic cisterns and related segments of the posterior cerebral artery: comparison using a novel application of image guidance. *Neurosurgery* 54: 1313–1327; discussion 1327-1318, 2004.
46. Vougioukas VI, Omran H, Glasker S, and Van Velthoven V. Far lateral supracerebellar infratentorial approach for the treatment of upper brainstem gliomas: clinical experience with pediatric patients. *Childs Nerv Syst* 21: 1037–1041, 2005.
47. Samii M, Gerganov V, and Samii A. Improved preservation of hearing and facial nerve function in vestibular schwannoma surgery via the retrosigmoid approach in a series of 200 patients. *J Neurosurg* 105: 527–535, 2006.
48. Stein BM. Supracerebellar-infratentorial approach to pineal tumors. *Surg Neurol* 11: 331–337, 1979.
49. Lim HH, Lenarz T, Joseph G, Battmer RD, Samii A, Samii M, Patrick JF, and Lenarz M. Electrical stimulation of the midbrain for hearing restoration: Insight into the functional organization of the human central auditory system. *J Neurosci* 27: 13541–13551, 2007.
50. Lim HH, and Anderson DJ. Spatially distinct functional output regions within the central nucleus of the inferior colliculus: Implications for an auditory midbrain implant. *J Neurosci* 27: 8733–8743, 2007.
51. Lim HH, Lenarz M, Joseph G, Battmer RD, Samii A, and Lenarz T. Hearing performance in the first auditory midbrain implant patients. *Internat Conf Cochlear Implants and Other Implantable Auditory Technologies* 10: 76, 2008a.
52. Loizou PC, Dorman M, and Fitzke J. The effect of reduced dynamic range on speech understanding: implications for patients with cochlear implants. *Ear Hear* 21: 25–31, 2000.
53. Rance G, Cone-Wesson B, Wunderlich J, and Dowell R. Speech perception and cortical event related potentials in children with auditory neuropathy. *Ear Hear* 23: 239–253, 2002.

54. Shannon RV, Zeng FG, Kamath V, Wygonski J, and Ekelid M. Speech recognition with primarily temporal cues. *Science* 270: 303–304, 1995.
55. Zeng FG, and Galvin JJ, 3rd. Amplitude mapping and phoneme recognition in cochlear implant listeners. *Ear Hear* 20: 60–74, 1999.
56. Dobelle WH, Stensaas SS, Mladejovsky MG, and Smith JB. A prosthesis for the deaf based on cortical stimulation. *Ann Otol Rhinol Laryngol* 82: 445–463, 1973.
57. Howard MA, Volkov IO, Mirsky R, Garell PC, Noh MD, Granner M, Damasio H, Steinschneider M, Reale RA, Hind JE, and Brugge JF. Auditory cortex on the human posterior superior temporal gyrus. *J Comp Neurol* 416: 79–92, 2000.
58. Penfield W, and Perot P. The brain's record of auditory and visual experience. A final summary and discussion. *Brain* 86: 595–696, 1963.
59. Cariani PA, and Delgutte B. Neural correlates of the pitch of complex tones. I. Pitch and pitch salience. *J Neurophysiol* 76: 1698–1716, 1996.
60. Suta D, Kvasnak E, Popelar J, and Syka J. Representation of species-specific vocalizations in the inferior colliculus of the guinea pig. *J Neurophysiol* 90: 3794–3808, 2003.
61. Syka J, Suta D, and Popelar J. Responses to species-specific vocalizations in the auditory cortex of awake and anesthetized guinea pigs. *Hear Res* 206: 177–184, 2005.
62. Wang X, Merzenich MM, Beitel R, and Schreiner CE. Representation of a species-specific vocalization in the primary auditory cortex of the common marmoset: temporal and spectral characteristics. *J Neurophysiol* 74: 2685–2706, 1995.
63. Joris PX, Schreiner CE, and Rees A. Neural processing of amplitude-modulated sounds. *Physiol Rev* 84: 541–577, 2004.
64. Lenarz T, Lim HH, Reuter G, Patrick JF, and Lenarz M. *The auditory midbrain implant: a new auditory prosthesis for neural deafness-concept and device description*. *Otol Neurotol* 27: 838–843, 2006b.
65. Lim HH, and Anderson DJ. Feasibility experiments for the development of a midbrain auditory prosthesis. In: *Proc 1st Internat IEEE EMBS Conf Neural Eng*. Capri Island, Italy, pp. 193–196, 2003.
66. Patrick JF, Busby PA, and Gibson PJ. The development of the Nucleus Freedom Cochlear implant system. *Trends in amplification* 10: 175–200, 2006.
67. Lim HH, Lenarz T, Joseph G, Battmer RD, Patrick JF, and Lenarz M. Effects of phase duration and pulse rate on loudness and pitch percepts in the first auditory midbrain implant patients: Comparison to cochlear implant and auditory brainstem implant results. *Neuroscience* 154: 370–380, 2008c.
68. Perez-Gonzalez D, Malmierca MS, and Covey E. Novelty detector neurons in the mammalian auditory midbrain. *Eur J Neurosci* 22: 2879–2885, 2005.
69. Strauss-Schier A, Battmer RD, Rost U, Allum-Mecklenburg DJ, and Lenarz T. Speech-tracking results for adults. *Ann Otol Rhinol Laryngol Suppl* 166: 88–91, 1995.
70. Winer JA, and Schreiner CE editors. *The Inferior Colliculus*. New York: Springer Science + Business Media, Inc., p. 736, 2005.
71. Lim HH, Lenarz T, Anderson DJ, and Lenarz M. The auditory midbrain implant: Effects of electrode location. *Hear Res* 242: 74–85, 2008b.

Spinal Cord Stimulation: Engineering Approaches to Clinical and Physiological Challenges

Michael A. Moffitt, Dongchul C. Lee, and Kerry Bradley

Abstract Spinal cord stimulation is an effective therapy for the management of chronic pain with historical origins dating back to the 1960s. The therapy consists of electrical stimulation of the spinal cord to 'mask' pain. One effect of stimulation is generation of tingling paresthesia in the patient, and overlap of the paresthesia with the pain is important to successful therapy. Clinical and anatomical challenges to successful and durable concordant paresthesia include: contact impedance changes, lead migration, clinical programming time requirements, unknown anatomic variables, and optimal lead design. In this chapter we review these challenges, the principles guiding engineering solutions and tradeoffs, and the use of computational tools to guide design of system components. Topics include a historical overview, stimulation waveform and clinical effects of waveform parameters such as pulse width, voltage vs. current control, multiple-source systems, real-time programming methods, contact size and spacing, use of field potentials for electrical imaging, modeling methods, and others.

1 Introduction to Spinal Cord Stimulation Therapy

1.1 Brief History of Spinal Cord Stimulation

In 1965, Melzack and Wall proposed the Gate Control Theory of pain [1]. The theory was an integration of previous observations on the nature of pain transmission and modulation in humans and animals. A brief summary of the theory is as follows. In a particular region of the body (e.g., a hand, arm, or leg), innocuous pressure and touch sensations, transduced by specific receptors in the skin, are carried by relatively large afferent fibers (Aβ, Aγ) in the peripheral nervous system. From the same body part, painful sensations are usually

M.A. Moffitt (✉)
Boston Scientific Neuromodulation Corporation, 25155 Rye Canyon Loop,
Valencia, CA 91355, USA
e-mail: Michael.Moffitt@bsci.com

D.D. Zhou, E. Greenbaum (eds.), *Implantable Neural Prostheses 1*,
Biological and Medical Physics, Biomedical Engineering,
DOI 10.1007/978-0-387-77261-5_5,

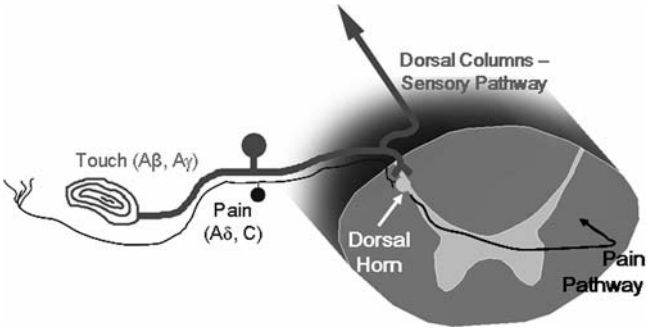

Fig. 1 Relevant sensory anatomy in the spinal cord

transmitted by smaller afferent fibers (Aδ, C). As shown in Fig. 1, both types of fibers enter the spinal cord through the dorsal roots. The small pain fibers enter the dorsal horn and after processing in the dorsal horn the pain information travels up the opposite side of the spinal cord. The large cutaneous fibers also enter the spinal cord and contribute to the processing in the dorsal horn, but additionally send branches up the dorsal columns of the spinal cord. It is in the dorsal horn where the 'gating' is believed to take place.

The Gate Theory purports that there is a central transmission cell which communicates pain to higher centers. Input to this transmission cell (T cell) comes from three basic sources: large pressure/touch fibers, small pain fibers, and a special type of interneuron.

As shown in Fig. 2, this interneuron has an inhibitory effect on both the large and the small fiber inputs to the transmission cell (effectively 'gating' their input to the T cell). However, the large and small fibers also influence the interneuron, having opposing effects. Greater activity in small fibers inhibits the interneuron (thereby opening the 'gate') which allows more small fiber and large fiber input to the T cell, and thus more pain signaling to the brain. However, if there is greater activity in large fibers, the interneuron's inhibitory

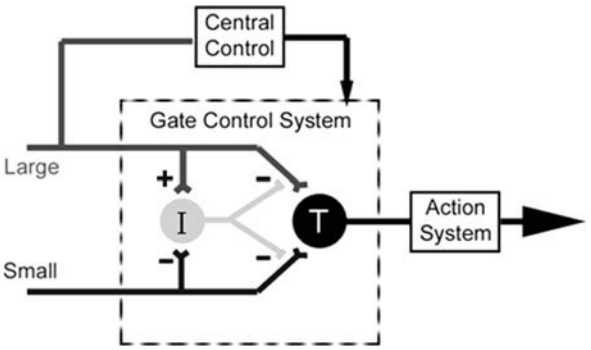

Fig. 2 Schematic of gate control system in modulation of pain transmission (adapted from Melzack and Wall, 1965)

output is increased (closing the 'gate') and now large and small fiber activity will less influence the T cell and the transmission of peripheral pain sensations will be reduced.

The Gate Theory, while now considered somewhat simplistic and incomplete,[1] provided a theoretical construct for Shealy et al. [6] to attempt spinal cord stimulation (SCS) as a clinical treatment for chronic pain in 1967. The Shealy group hypothesized that a viable and efficient target for large fiber, innocuous stimulation would be the dorsal columns of the spinal cord. The dorsal columns are predominantly made up of projection collaterals of the large pressure and touch fibers that enter the spinal cord. The 'efficiency' of dorsal column stimulation lies in the fact that, at any vertebral level, the dorsal columns carry information from nearly all body regions caudal to that level. Activation of the dorsal columns will send action potentials both toward the brain (orthodromic direction; see also *Paresthesia: A serendipitous 'side effect'*) and away from the brain (antidromic direction) down the spinal column to where the fibers initially entered via the dorsal roots. Focusing for now on the antidromic effects, action potentials propagate down the spinal cord and enter the gray matter (i.e., approach the 'gating interneuron'), mimicking action potentials coming from the periphery. Thus, activation of large fibers in the dorsal columns at a given vertebral level (e.g., T9) can theoretically 'close the gate' for all regions below that vertebral level (e.g., stimulating at T9 may relieve pain throughout the legs and low back).

At the time of Shealy's work, chronically implantable electrical stimulation had recently become feasible. In particular, neurostimulators (e.g., carotid sinus nerve stimulators or 'baropacers') consisted of implantable electrode systems driven by external RF stimulator systems [7]. The external stimulator consisted of a battery-driven pulse generator coupled to a transmitter and antenna, and the implantable electrode system consisted of a fully implanted receiver coupled to pulse generation circuitry and stimulating leads. The external programmable system generated the pulse trains, which then modulated a carrier. This

[1] The failure of the Gate Theory to adequately explain the incomplete response of chronic pain patients to SCS led investigators to explore other aspects of the chronic pain condition [2, 3]. Most animal and clinical studies of neuropathic pain have focused on the individual 'signatures' of the disease: changing homeostasis (local blood flow, neurotransmitter release, and regulation) [2], perceptual sensation (pain quality, paresthesia), and behavior (disturbed sleep, depression) [4]. In 2005, Ronald Melzack revisited the 'gate theory' [5] and replaced the 'gate' with a more system-oriented concept, which he termed the 'neuromatrix.' He defined the neuromatrix as 'an array of neural circuit elements (genetically programmed) to perform a specific function as interconnected and to produce awareness and action.' He proposed that pain is 'a multidimensional experience produced by characteristic "neurosignature" patterns of nerve impulses generated by a widely distributed neural network – the "body-self neuromatrix" – in the brain.' Therefore, chronic pain is likely produced by a combination of neural activities – perceptual, homeostatic, and behavioral programs – and activated by the 'body-self neuromatrix.' In future assessments, SCS might be better understood as a therapy that modulates the output patterns of this neuromatrix by electrically activating a few key components of the matrix (e.g., the dorsal columns, the dorsal roots, etc.).

combined signal was transcutaneously delivered to the implant via inductive coupling to a coil and demodulated to reproduce the pulse train, which was then delivered to the implanted contacts. With such capability, Shealy et al. conceived of an implantable, portable system that could be used to treat chronic intractable pain. The primary innovation of the Shealy group was to locate the electrodes in the spinal column, initially placed subdurally, directly atop the dorsal columns. Early patients reported reasonable degrees of pain relief, though complications were highly prevalent, both clinical (cerebrospinal fluid (CSF) leakage, acute neurologic deficit, etc.) and technical (broken electrode connectors, failed stimulator electronics, etc.) [8].

Over the course of the next three and a half decades, SCS became an established modality for the treatment of a broad and diverse range of pain disorders, including reflex sympathetic dystrophy, peripheral neuropathy, phantom limb pain, and failed spinal surgery [9-12]. The most successful results have been in the treatment of neuropathic pain, often with a vascular component [13]. Improvements have been made in both the clinical and technical aspects of SCS, including psychological patient screening and consistent follow-ups, and equipment design and functionality [14]. In general, technology improved to address several clinical problems:

- percutaneous leads (similar to transvenous pacemaker leads) developed as a response to the high morbidity and relative irreversibility of the flat, 'paddle' electrodes (i.e., laminectomy or surgical electrodes) that were first employed for SCS [15];
- leads were designed with greater numbers of contacts to compensate for post-operative migration and for shaping stimulation fields [16];
- stimulators became fully implantable, initially powered by primary cell batteries, and more recently by rechargeable Li-ion sources [17];
- stimulators also gained multiple channels, to allow for more independent control of therapy delivered to multiple body parts [18].

Interestingly, one clinical advance has led to greater technical challenges. The transition from subdural placement of contacts to epidural placement greatly reduced the risk and morbidity of SCS implantation, and opened the therapy to anesthesiologists who could introduce leads through percutaneous needles [15]. However, placement in the dorsal epidural space meant that the contacts are now separated from the neural target by a layer of cerebrospinal fluid, typically a few mm thick [19]. This dorsal CSF layer thickness (dCSF) makes selectively targeting the dorsal column fibers difficult, for several reasons that will be discussed in this chapter. In fact, many of the technological improvements to contact spacing, size, orientation, and number have been made to deal with the variable dCSF in the spinal column.

Modern SCS equipment commonly includes an implantable pulse generator (IPG), connected to one or more leads with at least two stimulating contacts (see Fig. 3).

Fig. 3 Rechargeable fully implantable spinal cord stimulator that supports one (as shown) or two percutaneous eight-contact leads

The IPG can have single or multiple stimulation sources, and these sources can deliver controlled-voltage or controlled-current pulses (see *Electrical sources for stimulation*). All IPG's commercially available today have multiple stimulation channels, where each channel delivers a programmable pulse train. The patient can control the IPG via telemetry with a handheld remote control device. Rechargeable devices come with an external charger, which is used periodically (e.g., once a week) to recharge the implant [17]. All SCS systems now employ sophisticated external programmers that allow a vast range of stimulation parameters to be adjusted to 'fit' the SCS stimulation to each individual patient's needs.

This chapter will review the clinical requirements and constraints when designing an SCS device, focusing on the engineering aspects of stimulation programming, generation of electrical fields, and how these relate to a successful and durable clinical outcome. Most of the design concepts behind SCS device development seek to provide adequate *neural selectivity*; that is, stimulation of the targeted fibers while avoiding stimulation of undesired fibers, thus maximizing therapeutic outcome.

1.2 Paresthesia: A Serendipitous 'Side Effect'

In the preceding section we described that electrical stimulation of dorsal column fibers will generate action potentials that propagate in three directions: (1) into the spinal cord gray matter (evoking the theoretical 'gate' effect), (2) out into the periphery, and (3) up toward the brain. The volleys of action potentials that go to the brain are thought to be primarily responsible for generating an effect called paresthesia. Paresthesia is reported to be a 'tingling' or 'buzzing' sensation with highly variable secondary sensations, such as 'pulsing,'

'thumping,' 'throbbing,' 'sharp,' 'cool.' [18] The closest analogous sensation that has been reported by patients is that 'it feels like when your (limb) falls asleep.'

Paresthesia sensations are used in SCS for mapping stimulation to the appropriate neurons. It is believed that, if a paresthesia is perceived by a patient in a specific body region, then the sensory fibers that innervate that region have been activated. Per the tenets of the Gate Theory, activation of innocuous sensory fibers for a specific body region should result in reduced transmission of pain signals to the brain from that body region. Paresthesia has the valuable characteristic that its response to changes in the stimulation field is relatively rapid (on the order of a second), compared to assessments of pain relief from stimulation, which may take from seconds to several hours [15]. Since paresthesia is due to fibers which mediate mechanoreceptive input, these fibers respond rapidly and tonically to external inputs [20]. This short latency response has enabled programming systems which make small, comfortable changes in the location of the electric field which the patient can then assess and determine paresthesia overlap with the painful body area. One commercially available programming system even allows the patient to adjust the stimulation field location using a joystick, with which he/she can 'steer' the paresthesia to different parts of his/her body [21] (see *Real-time programming strategies*). Overlap of paresthesia with pain (concordance) has been shown to be a necessary, though not sufficient, component to pain relief. Concordant paresthesia is one of the few statistically significant predictors of successful SCS; it is a crucial technical result that is correlated to a successful clinical outcome [15]. Given that paresthesia can be used for therapeutic targeting, it is thus a serendipitous 'side effect.'

Still, the presence of paresthesia introduces clinical challenges. Some patients who trial SCS may report pain relief, yet do not opt for permanent implant because they did not like the sensation of paresthesia [22]. Other patients may have perfect concordance of paresthesia with their pain, yet receive little or no pain relief in those body regions [8]. And most patients who use SCS report the need to adjust the stimulation amplitude during posture changes to maintain the intensity of the paresthesia at a comfortable level (such intensity changes may be a result of the changing dCSF: as the patient moves from an upright position to a supine position, the spinal cord moves dorsally toward the contacts, which results in an increased electric field intensity in the dorsal columns and thus more fibers excited and more intense paresthesia) [23]. An ideal SCS system might behave in a closed-loop manner, employing a sensor to estimate the dCSF and adjust the pulse amplitude to maintain comfortable paresthesia intensity. One method, using ultrasonic distance estimation, has been designed and investigated in vitro [24]. The other significant engineering challenge involving the maintenance of comfortable paresthesia arises during stimulation programming, as will be discussed below.

1.3 Introduction to Clinical and Physiological Challenges

SCS is an extensively technical therapy. At implant, the physician focuses on accurate and stable placement of the contacts over the spinal segment which enables concordant paresthesia, which provides the critical foundation for SCS success. Even still, once the lead has been positioned well and securely sutured in place, the post-operative technical factors involved in maintaining a successful outcome are manifold.

The first of these is the required 'fine-tuning' of the stimulation program after permanent implant. It is common for patients to return to the physician's office for optimization of their stimulation programs several times post-implant [25]. These programming sessions may be even more extensive and demanding than those during the trial, since the patient is not only more experienced with paresthesia, but may desire more precise targeting of their painful area and/or coverage of areas that were not achieved during trial stimulation. In the follow-up clinical phase, it has been shown that exhaustive programming of a single quadripolar lead (i.e., assessing all possible contact combinations) yields a statistically significant improvement in concordance of paresthesia [26]. The clinical cost, however, is extended programming time because traditional methods of contact combination programming are inefficient. In response, newer technologies have been introduced that allow more efficient programming, where paresthesia sensations are maintained while the contact combination is adjusted (see *Device programming in the operating room and post-implant*).

Another physiologic challenge to maintaining successful paresthesia concordance may be the development of fibrosis along the contact array. It is well established that the foreign object response of the body results in the development of a fibrotic scar to immobilize the implanted lead to prevent further mechanical trauma. The challenge to the stimulator system is that the developing scar tissue results in a higher contact resistance [27]. In controlled-voltage stimulator systems, the pulses delivered to the contacts have fixed voltages. By Ohm's law, a fixed voltage which sees an increased resistance will yield a reduced current. SCS stimulates tissue 'at a distance,' i.e., it is the current that flows remotely from the contacts in the dorsal columns which activates the neurons. Thus, the scar tissue that develops at the contacts may reduce the current flowing to the nervous tissue.

Even stimulator systems that use controlled-current pulses (where the voltage at the contact(s) is automatically adjusted to guarantee the programmed current) can be challenged by the development of fibrosis along the contact array. If a stimulator system uses a single current or voltage source and the patient requires a contact combination more complex than a mono- or bipole to achieve concordant paresthesia, the fibrosis that develops along the array can compromise the stimulation field (see *Single- and multiple-source systems*).

In SCS, the monopolar impedance along the implanted contacts has been shown to vary from contact to contact, both at implant and over time [28] (see Fig. 4).

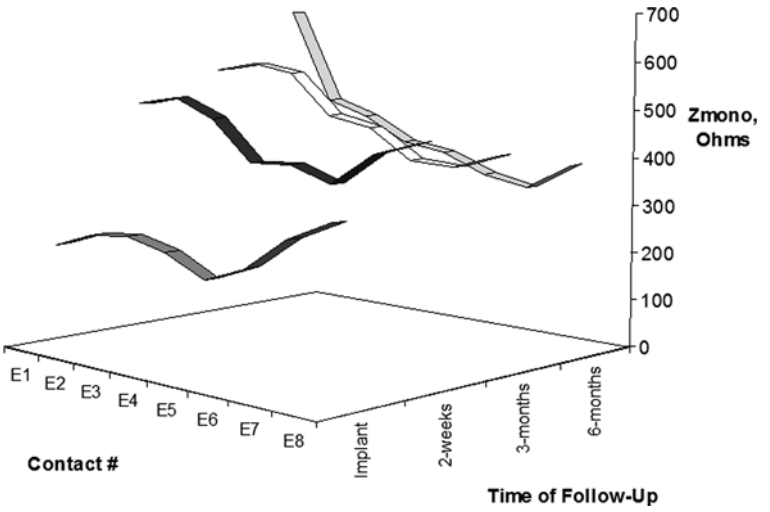

Fig. 4 Variability of monopolar impedance along multicontact percutaneous SCS lead at implant, 2 weeks, 3 months, and 6 months post-implant

This variability has been attributed to the inhomogeneity of the tissues in the epidural space adjacent to the contacts. At implant, the contacts may be adjacent to epidural fat, connective tissue, blood vessels, ligament, etc. [29]. As time passes, the wound healing process progresses for approximately 6–12 weeks post-implant and culminates in the final phase of scar formation [30]. The measured impedance variability from contact to contact along the leads suggests that the fibrotic capsule surrounding the lead may have variable thickness. Whatever the source, the changing, variable profile of impedance along the lead means that the current flow pattern achieved acutely post-implant, perhaps yielding excellent concordant paresthesia, may change over time when a single-source system is used with a complex contact combination [31]. Only systems in which the current at every contact is independently controlled may mitigate this time- and spatially variable impedance problem.

2 Optimization of the Electric Field

2.1 Number of Implanted Contacts

Most modern SCS leads employ multiple contacts distributed in single or multiple columns and rows along the lead for at least two reasons: (1) percutaneous leads with at least four contacts require less revision surgery to maintain concordant paresthesia, because they can be reprogrammed non-invasively [15]; (2) having multiple contacts allows one to shape the stimulation field to optimize the neural selectivity (and thereby the paresthesia-pain overlap) by strategic deployment of anodes and cathodes [15, 32, 33].

2.2 Contact Size and Spacing

As the number of contacts supported by percutaneous leads has increased, an appropriate question has arisen: 'How should the contacts be physically arranged on the lead to optimize the likelihood of clinical success for an SCS patient?' One might begin by asking: 'What are the spatial characteristics of the SCS target?' The characteristics of the SCS target, often termed the 'sweet spot' [18], have not been rigorously studied, but would be expected to be sensitive to a number of parameters including an individual's anatomy, lead placement, the pathology, and other considerations. This clinical and anatomical variability, and other engineering considerations and trade-offs must be evaluated to arrive at a design. Here we review some of the guiding design considerations for an SCS lead.

The contact length will affect the contact impedance and may affect the threshold of stimulation (dependent on the distance between the contact and the target neural tissue) [34, 35]. In particular, a small contact length will result in reduced surface area for charge transfer, and therefore, higher contact impedances. Model-based results[2] shown in Fig. 5A illustrate the effect of contact

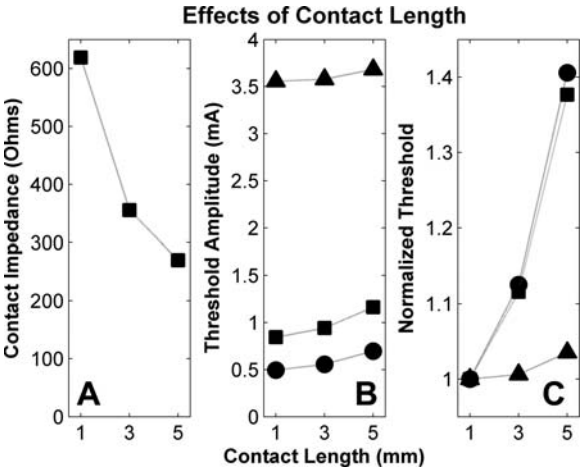

Fig. 5 Effect of contact length on contact impedance (**A**) and stimulation thresholds (**B, C**). Symbols indicate the dCSF as 1 (*circle*), 3 (*square*), or 6 (*triangle*) mm. In (**A**), monopolar contact impedances decreased as contact length increased. Note that the term impedance is commonly used, but clinical measurements are made with a short pulse (~20 μs), and the result is effectively the contact resistance. Stimulation thresholds increased with contact length at all dCSF values (**B**), but the percent change was greatest at lower dCSF values and was less than 5% at dCSF = 6 mm (**C**)

[2] The results illustrated in Figures 5, 6, 7, 9, 18, 19, 20, 21 and 22 were generated with the model by Lee et al. [93]. Voltage and activating function waveforms were low pass filtered (1 mm running average) for smoothness.

length on contact impedance. A typical contact length for percutaneous leads is 3 mm, and resulting clinically evaluated impedances are approximately 350 ohms [28]. Longer contact lengths, such as 6 mm, exist on commercially available leads and may have lower contact impedances. Overall contact impedance is an important consideration with clinical impact, because impedance will affect expected battery life (primary cell) or battery recharge intervals (rechargeable cell).

Stimulation thresholds can also be affected by contact length, and this effect is dependent on the distance of the lead from the target neural tissue. Figure 5B illustrates that larger contact lengths can lead to higher stimulation thresholds, particularly when the contact is close to the spinal cord (Figure 5C).

A discussion on how contact size affects stimulation threshold merits a brief review of the *activating function* concept. Ranck qualitatively discussed how changes in the extracellular voltage in the vicinity of an axon cause some regions of the axon membrane to depolarize (i.e., move toward action potential initiation), and others to hyperpolarize (i.e., move away from action potential initiation) [36], and this is illustrated in Fig. 6. Using an electrical cable model

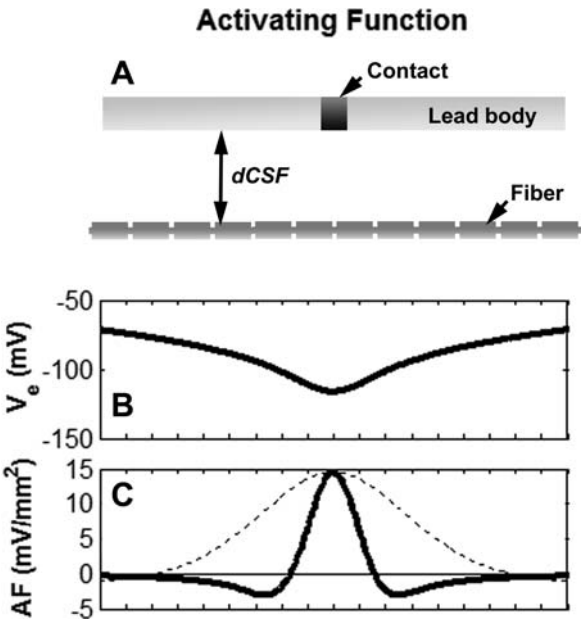

Fig. 6 Illustration of the activating function concept. Panel (**A**) shows a diagram of a lead with a contact (length = 1 mm) a distance of 3 mm from a nearby dorsal column fiber (axon). When the contact is used as a monopolar cathode (distant anode), then the extracellular voltage (V_e) observed at the fiber is shown in panel (**B**). Panel (**C**) shows the activating function, which is the second difference of V_e (*solid line*) (where $\Delta x = 1.25$ mm). Where the AF is positive, depolarization (change toward excitation) of the axon is predicted to occur, and where the AF is negative, hyperpolarization is expected to occur. As dCSF increased to 6 mm, the AF was broader and had a lower peak amplitude (~20 times smaller). (The dashed line of panel (C) shows AF when dCSF = 6 mm, with the amplitude normalized to highlight the change in AF shape.)

of the axon, McNeal and Rattay formalized mathematically [37, 38] the activating function (AF) as:

$$AF = V_{e,i-1} - 2^{*}V_{e,i} + V_{e,i+1} \quad (1)$$

where $V_{e,i}$ is the extracellular potential at the i^{th} node of Ranvier. Positive values of the AF correspond to depolarization, and negative values correspond to hyperpolarization of the axon membrane. The AF can be thought of as a predictor of the relative response of the axon transmembrane potential at $t = 0^{+}$. Figure 6 illustrates that for an axon with a straight trajectory, a nearby cathode causes a strong depolarization of the axon near the cathode, flanked by weaker hyperpolarization. Note that the shapes of the AF change as a function of distance from the target axon (Fig. 6C).

Because the AF is linear, using it as a predictor of stimulation is limited because it does not capture the non-linear behaviors of the axon [39, 40], but nevertheless remains conceptually useful for understanding first-order effects. Also note that Eq. (1) is the second difference of the extracellular voltage and applies to myelinated axons. The AF for unmyelinated axons is the second derivative of the extracellular voltage along the trajectory of the axon.

Returning to contact length and applying the AF concept, we recognized that change in the extracellular voltage gradient is required to promote stimulation. When close to the target fiber, small contacts have larger activating function peaks, as shown in Fig. 7. By increasing the contact length, a nearby axon (with trajectory parallel to the contact) will observe strongest changes of the extracellular voltage near the edges of the contact. This can cause the AF to be largest beneath the edges of the contact, as shown in Fig. 7. At larger

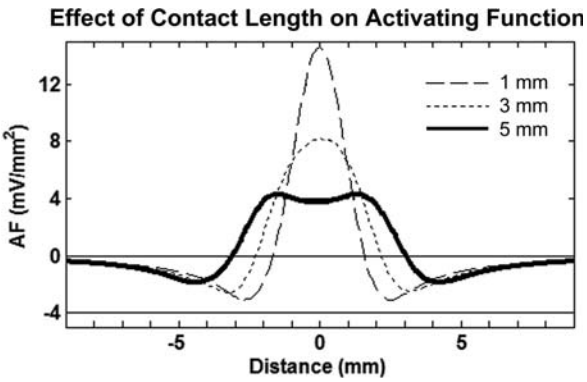

Fig. 7 Effect of contact length on the activating function (AF) at a dorsal column fiber when dCSF = 3 mm. As contact length increased, the peak AF amplitude decreased. Note that when the contact length was 5 mm, local maxima were observed near the edges of the contact. This shape is consistent with the expectation that the AF will be highest where change in the voltage gradient is observed

distances from the target axon(s), increased contact lengths may be acceptable and may be chosen because of their lower impedance properties. In SCS, this distance is approximately the thickness of the cerebrospinal fluid, which varies as a function of the vertebral level at which the lead is placed, and is variable from patient to patient [41, 42]. Typical values range from 1.5 to 8.5 mm at mid-to-low thoracic vertebral levels, a common SCS target [42].

Available center-to-center contact spacings vary widely, and include common values of 4, 4.5, 7, and 9 mm (see Fig. 8). Principles guiding the choice of contact spacing include (1) increasing the span of the contact array on the lead (using a wide spacing); (2) improving the resolution of the excitable region (using a tight spacing); and (3) promoting dorsal column axon stimulation relative to dorsal root axon stimulation [43, 44]. For a given number of contacts, there is a trade-off between principle 1, and principles 2, and 3. A wide center-to-center spacing ($\geq$ 7 mm) has the advantage of distributing target locations along a greater vertebral span. However, it should be noted that depending on the dCSF there may be gaps within that span, i.e., locations along the dorsal columns and within the span of the contact array at which stimulation cannot be initiated (inferred by AF analysis, see Fig. 9). Employing the AF concept, we expect that tight center-to-center spacing (e.g., 4 mm) may be used to improve the resolution of stimulation loci within the span of the contact array and to reduce the likelihood of gaps between adjacent cathodes (see Fig. 9) (although the possibility always exists if the lead is close enough to the spinal cord). Note also that when multiple electrical sources are available (see '*Electrical sources for stimulation*' below), the interaction of contacts spaced close enough together may be desirable to enable fine-tuning of stimulation in a region of interest.

Certain variables that are not determined a priori complicate the trade-off between span and resolution (e.g., the dCSF for a given patient is unknown and is expected to change with posture [23, 45]). First, the AF dependence on dCSF means that optimal contact spacing is also expected to be dCSF dependent. For a particularly large dCSF, a lead with widely spaced contacts will have diminished or an absence of gaps and the advantages of span persist, while the lead with tightly spaced contacts gains imperceptible resolution at the cost of span. In contrast, for a small dCSF, a lead with widely spaced contacts will have wider gaps (conceivably missing the 'sweet spot' within the span of the lead contacts) at the cost of greater span, while the lead with tightly spaced contacts has a useful targeting resolution within its smaller span. Second, a characterization of

Fig. 8 Illustration of common contact spacings and spans observed in commercial products. As a dimensional reference, all contacts are 3 mm in length, and lead diameters are approximately 1.3 mm. Panels A, B, and C show 8-contact leads with center-to-center contact spacings of 4, 7, and 9 mm, respectively

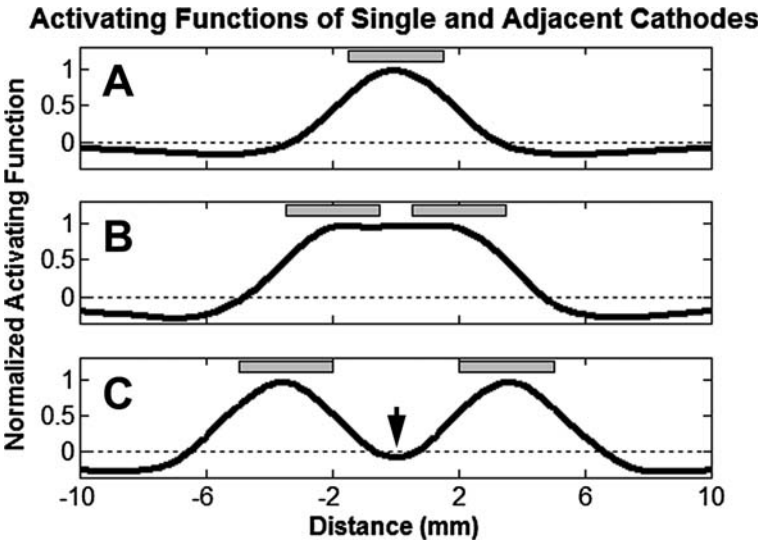

Fig. 9 Normalized activating functions (AF) of single and adjacent cathodes. The AF for a single monopolar cathode (**A**) and for two adjacent cathodes (**B, C**) are shown for dCSF = 3 mm. Panels (**B**) and (**C**) illustrate the effect of contact spacing when adjacent contacts are assigned as cathodes. In (**B**), the tight contact spacing (4 mm) yields an AF that is broad compared to the AF of a single contact (**A**), and with a strong AF in between the two contacts. In (**C**), the wide contact spacing (7 mm) yielded an AF with two local maxima and a gap in between the contacts. Of note, between the two widely spaced contacts, a region of hyperpolarization (negative AF) was observed (*arrow* in panel (**C**))

the size, and in particular the rostral-caudal length, of the 'sweet spot' has not been determined through clinical study and is expected to vary from patient to patient. A more thorough understanding in this regard would also contribute to lead spacing decisions.

Finally, work with a computational model of SCS (including a non-linear axon model) has indicated that tightly spaced bipoles and tripoles promote dorsal column activation over dorsal root (often considered a source of undesirable side effects) activation [43, 44] at the cost of higher amplitudes. While this concept has not yet been validated through clinical study, it is noteworthy that leads with tightly spaced contacts make available to the clinician these theoretically optimal combinations, where leads with widely spaced contacts do not.

2.3 Electrical Sources for Stimulation

In SCS, and other indications, patient's benefit from thorough, and often time-consuming, device programming [26, 46], so system architectures amenable to expanded and faster tunability are desirable (see also *Real-time programming*

strategies). In this section, we discuss electrical sources of stimulation and their applicability to this problem. We also discuss theoretical effects of the architecture of the electrical sources on maintenance of the programmed field over time, with inferences of therapeutic stability.

Electrical stimulation of neural tissue is typically done with periodic pulse-based waveforms consisting of three phases per period: the stimulation phase, the interphase, and the charge recovery phase. These three phases are illustrated in Fig. 10A. The stimulation phase is an active phase responsible for exciting the target neural elements and typical durations consist of tens to several hundreds of μs. Some neural elements will be approaching excitation at the end of the stimulation phase, and will reach it shortly after (within ~100 μs) if not interrupted. The interphase is a short (tens to a few hundreds of μs) rest (open-circuit) phase between the stimulation and charge recovery phases that allows

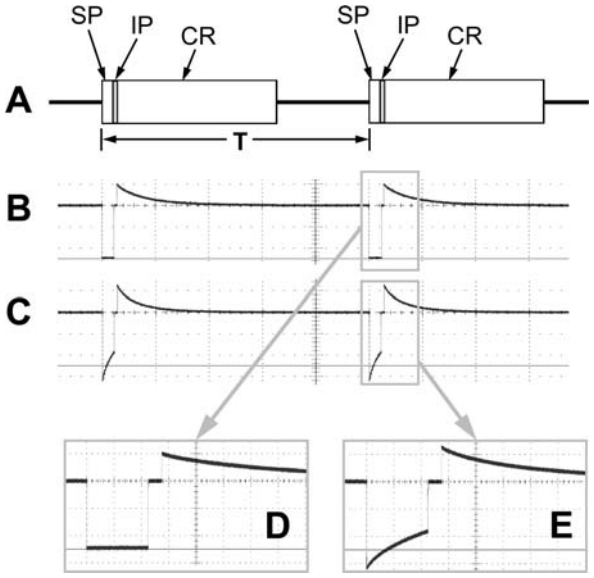

Fig. 10 Phases of a typical stimulation waveform (**A**), and illustrations with current-controlled (**B**, **D**) and voltage-controlled (**C**, **E**) devices. The stimulation waveform consists of a stimulation phase (SP; typically current or voltage regulated) and a charge recovery phase (CR; may be active or passive), separated by an interphase (IP; rest phase). These three phases are repeated with period (T). Most devices have output capacitors on each contact, and charge is recovered passively during the CR phase by connecting the capacitors. Panels (**B**–**E**) show the current as a function of time during the waveform, when in a bench test a lead was placed in saline with a series sampling resistor (100 Ohm), and connected to either a current-regulated device (Boston Scientific Precision^{TM}) (**B**, **D**) or a voltage-regulated device (Medtronic Restore^{TM}) (**C**, **E**). Note that with a current-regulated device, the current is constant during the stimulation phase (**B**, **D**). With a voltage-regulated device, the current decays during the stimulation pulse (**C**, **E**). In all bench tests shown, the SP and IP phases were 450 μs and 100 μs in duration, respectively

action potential generation in these neural elements, and can be used to promote efficiency [47, 48]. The charge recovery phase is used to recover the injected charge such that the steady-state waveform is charge balanced, and this is important to minimize corrosion and tissue damage as discussed in other chapters of this book (Chapters 1 and 6). To ensure charge balance, contemporary systems typically include output capacitors on each contact, and charge recovery is achieved passively by shorting the output capacitors during the charge recovery phase. The duration of this phase is typically on the order of thousands of μs, and much longer than the stimulation phase to reduce the peak amplitude and minimize the likelihood of stimulating from this phase. Some current-regulated systems also use active charge-recovery mechanisms to better control the amplitude of current during this phase.

Other waveform paradigms exist that exploit the non-linear properties of neurons to achieve specific stimulation objectives (e.g., excite cells or axons preferentially [49, 50], excite small axons preferentially to large axons [51, 52]). These advanced waveforms have yet to be implemented in clinical systems but may be part of future systems.

2.3.1 Voltage and Current Regulation

The stimulation phase can consist of a regulated voltage pulse or a regulated current pulse. In both cases, current is injected and the amplitude of the accompanying activating function observed in the target tissue is directly proportional to the amplitude of the current being injected. With respect to stimulation, there are two primary differences between current- and voltage-regulated pulses.

First, consider a single active monopolar electrode (with a return electrode far enough away to make it inconsequential). In the case of a current-regulated pulse, the amplitude of the current injected is the programmed value, independent of the contact impedance. In the case of a voltage-regulated pulse, the amplitude of the current injected is dependent on the contact impedance and is given by Ohm's law as $I = V/R$. So, *in the case of the voltage-regulated pulses, the intensity of stimulation is subject to the contact impedance*. The contact impedances on SCS leads change over time, as illustrated in Fig. 4, and so the stimulation intensity at a given voltage level may change over time. In SCS therapy, patients are very aware of the stimulation intensity (manifest as paresthesia) and are able to compensate for these intensity changes with a patient controller. This difference may become more apparent in other indications (e.g., deep brain stimulation for tremor control), where the patient is not so directly aware of the stimulation intensity.

Second, because of capacitive and other effects at the electrode interface [53], the current delivered by a voltage-regulated source is initially V/R, but diminishes during the stimulation phase, as illustrated in Fig. 10C, E. Note also that the rate of decay is dependent on the contact impedance. In contrast, a current-regulated source requires the voltage on the electrode to change during the stimulation phase to maintain constant current delivery, and the strength of the field is constant during the pulse. So, a primary difference is that the current

waveforms generated by the two sources are different (see Fig. 10). In SCS, it is not yet clear if one waveform is preferred over the other, although clinical differences have been reported anecdotally [54, 55].

An additional difference is that the current waveform generated by a voltage-regulated source is subject to impedance and electrode surface changes and is considered less repeatable [56], and this has been a concern in the academic setting [57]. Another difference is that the amount of charge injected may be controlled with a current-regulated source (a current regulator for each contact is particularly desirable), and this capability facilitates existing and future strategies for abiding charge injection limits [53, 56, 58].

2.3.2 Single- and Multiple-Source Systems

In SCS, devices are often programmed with multiple contacts of the same polarity (e.g., a tripole combination has two anodes). In these cases, single-source systems may control the net current (i.e., if it is a current source), but are not able to control the currents through the like-polarity contacts that are ganged to the lone source, as illustrated in Fig. 11. There are two consequences of not controlling the currents that may have clinical impact.

First, the electric field, and therefore the stimulation response, may change over time. This is hypothesized to occur because the amplitudes of the currents delivered through the ganged contacts will depend on the contact impedances and field effects (the effects of other active contacts). While the mechanisms and clinical impact are not well defined, the contact impedances in SCS are known to change over time [28, 59, 60] (see also Fig. 4), implicating impedance changes as one possible contributor (of many candidates) to some observations of therapeutic instability over time [61].

A multiple current-source system that avoids ganging contacts will maintain the currents in the face of changing impedances. Changes in the electrical properties of the volume conductor (e.g., the presence of encapsulation tissue that did not exist at implant) may still impact the electric field, but maintaining the currents passed through each electrode presently represents the best opportunity to maintain the electric field at the target.

Second, multiple-source systems are able to generate many electric fields that a single-source system cannot, illustrated in Fig. 11. Therefore, for a given lead, a multiple-source system is expected to have greater ability to fine-tune or improve the resolution of the electric field near a region of interest. With the large numbers of contacts often used in SCS, the number of permutations of contact combination is large even with single-source systems (e.g., assuming 16 contacts, a single-source system has $\sim 4.3 \times 10^7$ permutations, and a multiple currents source system has $\sim 2 \times 10^{16}$ permutations (assuming 2.5% resolution)). Despite this large number of options on a single-source system, the ability to make incremental modifications in the field is not as straightforward as with a multiple-source system. Consider a thought experiment involving two electrodes that may be assigned as a cathodes, and they are first connected to a single-source system (Fig. 11A). Only three assignments exist for contact 1/contact 2: cathode/off, off/cathode, and

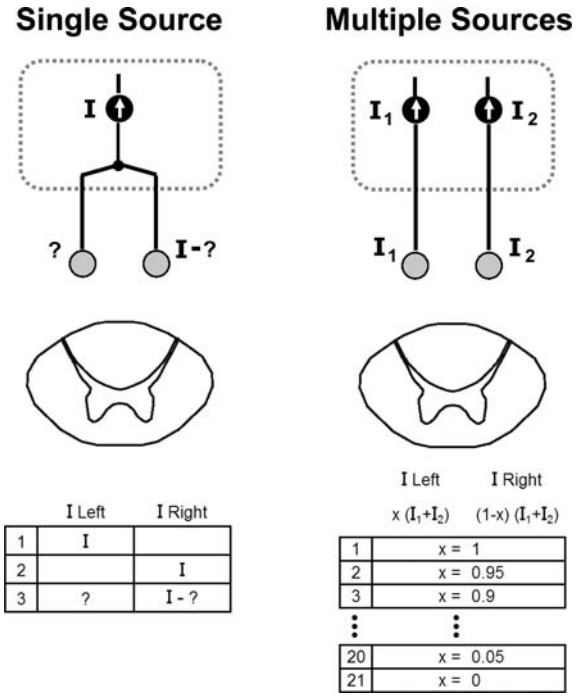

Fig. 11 Illustration of single and multiple current-source architectures in a two-contact thought experiment. Consider two contacts that may be assigned as cathodes or as 'off.' With a single-source system (*Left*), the contacts can be assigned as cathodes independently, or simultaneously. When both contacts are assigned as cathodes simultaneously, they are ganged together, and while the net current is programmable (I), the current through each contact will depend on the contact impedances. With a multiple-source system (*Right*), the two contacts may be assigned as cathodes independently or simultaneously, and in each case the current through the contacts is programmable (I_1 and I_2). Note that with multiple sources, the current through a contact is not dependent on impedance and enables generation of electric fields that cannot be explicitly programmed with a single source (compare tables of possible combinations; right-hand table generated assuming 5% resolution)

cathode/cathode. Connecting the same two contacts to a multiple-source system enables additional combinations (e.g., 21 combinations assuming current can be shifted in 5% increments) due to the ability to adjust the relative fractions of the total amplitude to the two contacts (Fig. 11B).

Both single-source and multiple-source systems have been used in clinical studies and both are presently available commercially. Clinical work with the multiple-source system has shown that balancing the relative amplitudes on multiple electrodes does result in modulation of the location and the span of the paresthesia [21, 62, 63]. While some clinical comparisons have been made [62, 64], attempts to rigorously evaluate and quantify clinical efficacy differences between single- and multiple-source systems have not yet been made.

2.3.3 Examples of Multiple-Source Systems

Until recently, commercial SCS systems have used a single source for generating the fields used for stimulation. However, multiple-source systems have been considered academically for many years in animal work [65] and in clinical study [62, 63]. Here we briefly review three multiple-source systems of note, including two SCS systems.

In 1993, Veraart et al. [65] reported on the use of multiple-current sources and a 12-contact spiral cuff electrode (illustrated in Fig. 12A) to tune

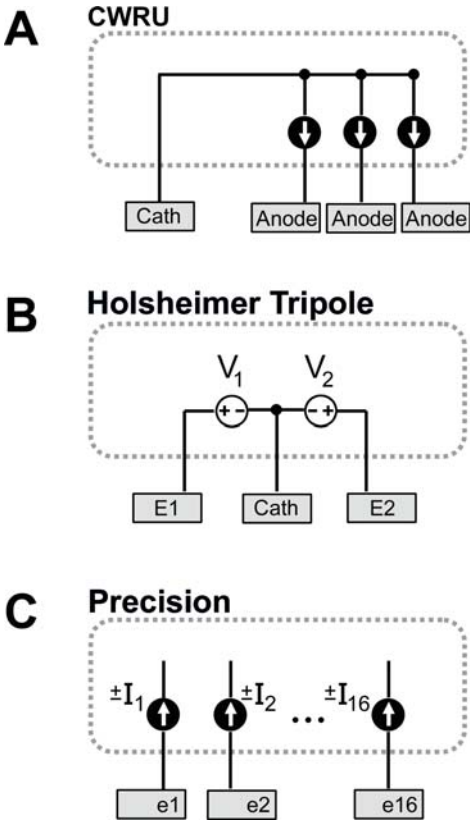

Fig. 12 Examples of multiple-source systems. Panel (**A**) shows the architecture used by Veraart et al. in an experiment at Case Western Reserve University (CWRU) to selectively stimulate fibers with a cuff electrode in cat peripheral nerve. Those experiments included up to two of the fundamental blocks shown in panel (**A**), so up to six simultaneous current sources. Panel (**B**) illustrates the original transverse tripole for SCS proposed by the Struijk and Holsheimer at the University of Twente (UT), and constructed by Medtronic for clinical studies. The original transverse tripole used two voltage sources to tune the location of paresthesia through programming. Panel (**C**) illustrates the architecture of the Boston Scientific Precision^{TM} SCS system that consists of a bidirectional current source for each of 16 contacts for wide programming flexibility

stimulation of a peripheral nerve (cat sciatic) to selectively activate each of four fascicles within the nerve. In particular, the authors showed that greater selectivity of activation was achieved using three current sources to appropriately balance currents, than could be obtained with a monopole generated with a single-current source. Further, use of six current sources was found to further improve selective activation in some cases.

In 1996, Struijk and Holsheimer proposed a two voltage source SCS system [66] that relied on a specialized paddle lead (three contacts arranged transversely), and this multiple-source system is shown in Fig. 12B. This system, commonly known as the transverse tripolar system (TTS), was fabricated by Medtronic and studied clinically at multiple centers [62, 63]. A strong conclusion of the multi-center study was that the multiple sources could be used to tune the location of the paresthesia, and the pattern of the tunability was consistent with contemporary understanding of the dorsal column anatomy. This multiple-source system has not been made commercially available.

In 2004, Advanced Bionics introduced a spinal cord stimulator that utilized 16 current sources (bidirectional), one for each contact supported (see Fig. 12C). This system enabled the user to incrementally change the electrode combination at a non-zero amplitude to achieve real-time tunability of the paresthesia (see also *Real-time programming strategies*). In this system, all 16 contacts may be active without ganging contacts together.

2.4 Electrical Management of Lead Migration

In SCS, the location of the leads within the spine is of paramount importance since it determines the possible location of the stimulation paresthesia [19, 32]. SCS outcomes are frequently compromised by lead dislocation or migration, which can lead to the loss of optimal paresthesia coverage with subsequent reduction in pain relief [67, 68]. Lead migration is considered by some to be the most common technical complication of SCS [9, 69].

Sometimes paresthesia coverage is reestablished via reprogramming, avoiding the necessity of a surgical revision [15]. However, optimal reprogramming may be difficult to achieve without confirming the new position of the leads using fluoroscopic imaging. The disadvantages of frequent fluoroscopy include patient exposure to radiation and inconsistent availability of fluoroscopic equipment in a non-surgical medical setting. Additionally, fluoroscopic imaging of leads is typically performed while the patient is supine. However, the lead position may be somewhat different when the patient is upright, i.e., the posture assumed by the patient for most of their waking hours [23]. So, even if programming is done based upon imaging, the resulting contact combination found for the supine position may be less effective when the leads move to a different orientation when the patient is upright.

A technique, similar to impedance tomography, that uses electrical measurements to estimate the relative positions of contacts in the epidural space may help deal with lead migration. Briefly, a subthreshold stimulation pulse (1 mA, 20 μs) is delivered monopolarly (i.e., the return path for current is a far-away at the IPG case) to a single contact. The spread of current in the volume conductor (i.e., body) will generate grossly spherical potential contours in the tissue surrounding the source contact (see Fig. 13) [70]. The other implanted contacts are also positioned within this potential field, and the voltage measured on each contact provides a 'sampling' of the generated potential field. Since the geometry of the leads is known a priori, the sampled potential field can be partially reconstructed from these measurements.

A useful application of this technique in SCS is to determine the relative orientation of parallel leads. For example, just after implant in a hypothetical patient, the leads may be positioned in a 'perfect parallel' arrangement, and initial programming may be done based upon knowledge of this orientation. Some time later, however, the patient may return to the clinic reporting less-than-optimal paresthesia concordance. If the field-potential measurement technique is used, a suspected relative lead migration may be confirmed without the use of fluoroscopy (see Fig. 14).

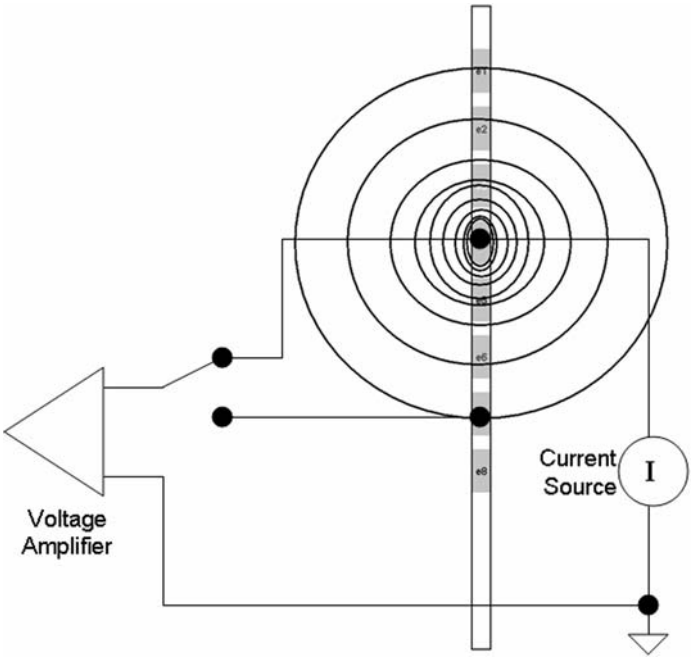

Fig. 13 Measurement of field potentials by stimulator

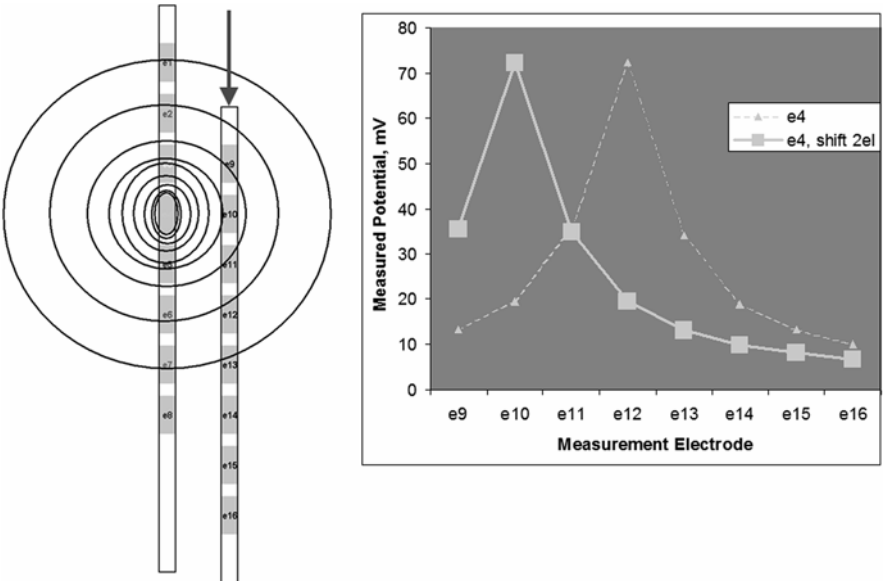

Fig. 14 Detection of two-contact relative lead migration using field-potential technique. Note that the maximum of the field-potential plot indicates which contact on the second lead is aligned with the source contact (e4) on the first lead

Knowledge of relative lead orientation for programming has been shown to be anecdotally useful. Figure 15A shows programming of dual parallel leads, such that side-by-side anode–cathode interaction is dominant. The resulting paresthesia is limited in extent, as the stimulation field consists of two laterally oriented bipoles, which appear to recruit only the lateral dorsal columns. When programming is done in the same patient with knowledge of the relative orientation of the parallel leads, cross-lead cathode–cathode interaction can be maximized and anode–cathode interaction minimized. This can result in greater midline superposition of stimulation fields, and, as shown in Fig. 15B, an increase in the paresthesia extent.

The field-potential technique has been implemented in one commercially available spinal cord stimulation system and has been shown to agree to within 2 mm of coincident fluoroscopy [71].

A further advantage of the technique is that it is purely electrical and very low power, which makes it suitable for use and management by the implanted stimulator at any time. A candidate future implementation may include automatic adjustment based on updated information on relative lead positions. For example, if a patient is away from the clinic and undergoes some temporary lead migration, the IPG, using field-potential measurements and knowledge of the patient's desired programs, might automatically adjust the stimulation program to minimize changes in the stimulation field and ideally maintain concordant paresthesia.

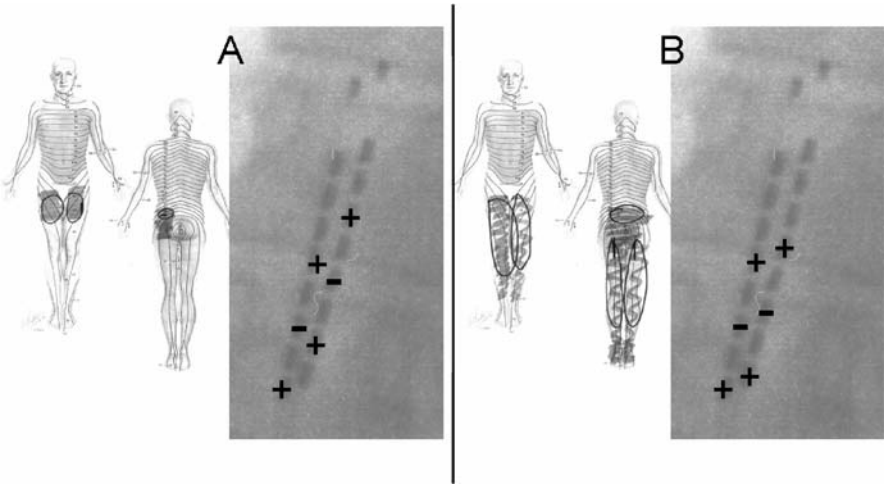

Fig. 15 Clinical importance of relative lead orientation for dual parallel lead programming in SCS. Colorings on the dermatome maps were made by a patient when stimulation was at a 'comfortable' level, using either the mis-aligned cathodes (**A**) or aligned cathodes (**B**) as a stimulation program. Note that aligned cathodes yielded substantial increase in paresthesia coverage. Knowledge of relative lead positions is important to ensure aligned cathodes and can be estimated electrically via the field-potential technique described in the text

3 Clinical Programming Time

3.1 Historical Programming Approach

Early SCS systems were typically mono- or bipolar, so concordance of paresthesia was critically dependent upon the positioning of the stimulating contacts in the spine [8, 72, 73]. Programming was rudimentary, as there were usually only two choices for contact polarity: negative (cathode) and positive (anode). Cathodes were chosen most frequently, since the site of stimulation under a cathode is near the contact (see 'Contact size and spacing'), and an active cathode has a lower threshold than an anode [72]. As SCS systems gained more contacts, the number of programmable combinations increased exponentially and there was growing awareness that the stimulation field could be optimized by judicious selection of anodes and cathodes on a per-patient basis [74-76].

Law was the first to report on the technical results of exhaustively testing contact combinations in SCS therapy for pain [33, 74, 75]. He showed that a 'narrowly spaced' (< 9 mm center to center), rostral bipole located on the physiological midline gave a statistically superior technical and clinical result. North et al. [15] and Alo et al [77, 78] have both published clinical data that is in agreement with the modeling work of Struijk et al. [29] and Holsheimer et al. [32, 35, 43, 79], which suggest that, for a lead placed on or very close to the physiological midline,

the optimal combination is a 'guarded cathode' (+ − +). The rationale is straightforward: to maximize the depth of penetration in the dorsal columns, it is important to promote the peak of the activating function beneath the cathode. This is best achieved by flanking the cathode with anodes (see '*Contact size and spacing*'), as the positive side-lobes of the anodic activating function superimpose atop the cathodic activating function, thereby increasing its relative value.

However, Holsheimer has stated that, while the guarded cathode is optimal for a population of patients, it may not be the best programmed combination for an individual patient [80]. This is primarily due to the great variability of patient anatomy, lead placement and orientation, and targeted nerve fibers (such as segmental paresthesias from dorsal root activation, which are promoted by the use of monopolar stimulation).

Barolat et al. performed extensive analyses of the technical characteristics of stimulation at different vertebral levels and medio-lateral positions of the contact array [81]. In their report, they indicated that the best paresthesia result required that (a) the leads were appropriately located and (b) that all possible contact combinations were attempted. North et al. have shown that exhaustive testing of contact combinations significantly improves both pain-paresthesia overlap as well as patient satisfaction with SCS [26].

Thus, since contact combination programming can contribute significantly to concordance of paresthesia, and modern SCS systems have multiple contacts, the challenges of optimizing the stimulation field via contact combination selection are a factor in successful use of SCS. The following sections detail the specific challenges of contact combination programming in the operating room during implant and during post-operative follow-up.

3.2 Device Programming in the Operating Room and Post-implant

When the physician implants the leads during the trial, he/she has an initial vertebral target in mind for locating the contacts, based upon the location of the patient's pain. Once the leads are positioned, the challenge in the OR is to identify if (a) concordant paresthesia can be generated with the leads in that position and (b) if the active contacts which generate that paresthesia are 'conservatively' located, i.e., toward the center of the contact array [82]. It is important to program the stimulator quickly and efficiently, since extended OR time puts the patient at greater risk for infection and is very costly [17].

Historically, during the implantation of percutaneous leads, two modes of stimulation testing have been typically performed. The first type is the discrete combination adjustment, where a specific contact combination is programmed and then the amplitude is increased until the patient feels paresthesia [83]. If the location of the paresthesia does not cover the patient's painful areas, the stimulation is first turned off before further contact combination adjustments are made. This is necessary, because SCS systems limited to discrete

combination adjustments may cause patient discomfort when switching to a new discrete combination if the stimulation amplitude is suprathreshold; the patient may experience jolting sensations from the abrupt and large shift of the electric field.

Once the stimulator is off, the combination is then changed; the amplitude is then slowly increased until paresthesia is felt. Several stimulation combinations may be tried and, if no concordant paresthesia is felt at the lead location, the lead is moved and the process is repeated. This can be a time-consuming process and implies that only a few combinations can be tried for a single lead position during implantation.

In response to this clinical inefficiency, a second method used intraoperatively is 'mechanical trolling' [83]. In this technique, the lead is initially placed at a position beyond the assumed target spinal segment. A contact combination is programmed on the lead and the amplitude is then increased until the patient feels paresthesia. The physician then gently pulls the lead from the spinal needle, thus dragging the lead along the dura and shifting the electric field along the nerves while the patient reports paresthesia location. While the physician is performing this 'mechanical trolling,' the stimulation amplitude is adjusted by the clinician controlling the stimulator to maintain a comfortable paresthesia intensity. This method can be a general improvement over discrete combination programming in terms of time efficiency, but carries the risk of significant overstimulation if the clinician control of the amplitude is not well synchronized to the actions of the physician *and* the verbal feedback of the patient. In the event of overstimulation, the patient can become refractory to paresthesia sensitivity for several minutes. This can further increase the time for implant. Recently, a user friendly electrical version of trolling was introduced. This method allows the lead to remain in place while the electric field is incrementally "trolled" using field steering (see *Real-Time Programming Strategies*).

3.3 Device Reprogramming

In contrast to intraoperative programming, during a standard follow-up visit, stimulator programming tends to be more extensive, since more time is available and the patient can provide detailed feedback on the paresthesia location. Anywhere from a few minutes to hours can be spent in the follow-up visit, depending upon the difficulty of covering a particular body region with paresthesia and the capabilities of the stimulator and programmer system [81]. Finding the contact combination that results in the best paresthesia may be a numerically overwhelming task, particularly with historic programming tools [76]. Either an exhaustive search is undertaken which may take hours or a limited (and possibly sub-optimal) subset of discrete combinations are tried within an allotted, likely brief, period of clinical time [26].

3.4 Real-Time Programming Strategies

For both programming in the operating room, and in the post-operative setting, an efficient real-time programming method is desirable. To date, two principal strategies have been used to enable real-time programming. The first is based on modulating the amplitudes of two or more component fields (we will refer to this approach as field balancing and cycling (FBC)). The second strategy is based on incremental modulation of the field at clinical amplitudes using multiple sources (we will refer to this approach as field steering (FS)).

The FBC approach requires the use of multiple timing channels. In typical stimulator architectures, a timing channel consists of a contact combination (i.e., anode/cathode assignment) and the timing parameters for generating the stimulation waveform described previously (see *Electrical sources for stimulation*), as shown in Fig. 10. Important for this discussion is the fact that a timing channel has assigned to it only one electric field (defined by the contact assignments) with a clinical stimulation response. Let us suppose that a second timing channel is defined with a different assigned electric field (see Fig. 16). By running the two timing channels simultaneously in an interleaved fashion, a stimulation effect from both fields can be generated. The FBC real-time programming approach must use two or more fields (interleaved from two or more timing channels) and allows the user to balance the amplitudes of the timing channels to modulate the stimulation effect (Fig. 16).

Note that as the amplitude of a timing channel is decreased below the stimulation threshold, a new field may be assigned to that timing channel. With an ideal user interface, the amplitude balancing and the cycling of fields is done automatically as the user adjusts simple controls (e.g., left/right buttons), and this way the patient is able to cycle through fields (more efficiently than through the historical approach) and modulate the paresthesia in real time.

The FBC approach has been used in its simplest form since 1999 (e.g., Medtronic Synergy™ with EZstim™ remote control), and improved user interfaces have continued to be produced to enhance its use[3]. The FBC strategy can be used by both single- and multiple-source systems (see *Electrical sources for stimulation*), and most contemporary SCS systems have multiple timing channels. While FBC can be implemented on single-source systems, in such cases the component fields remain constrained by the single-source architecture (e.g., they may be affected by impedance change over time, and the tunability is limited). Note that with the FBC approach the effective frequency is expected to be higher, which may increase total paresthesia coverage [84], but may also yield reduced battery life (or reduced recharge intervals).

[3] Commercial implementations of FBC include Medtronic TargetStim™, St. Jude Medical Dynamic MultiStim™, and Boston Scientific area balancing in the Precision™ system.

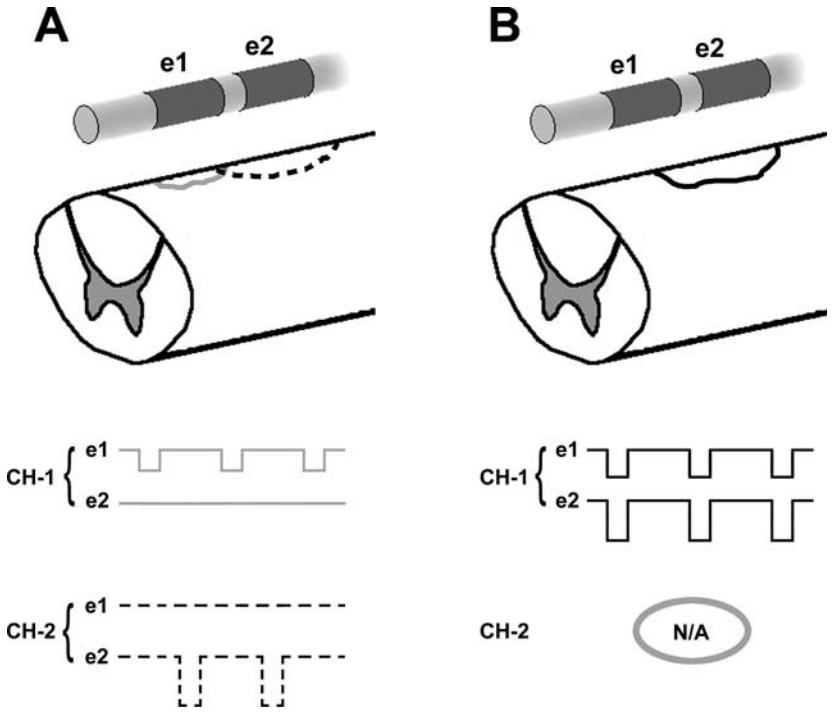

Fig. 16 Comparison of real-time programming scenarios with FBC and FS methods. With the FBC concept (**A**), multiple timing channels (CH-1 and CH-2) are used, where each may correspond to a distinct electric field (and distinct stimulated regions; *gray* and *dashed lines* on spinal cord), and stimulation pulses from each channel are interleaved (compare pulse timing of CH-1 and CH-2). During real-time programming, the amplitudes of the pulses from each channel are balanced, and when a channel's amplitude is reduced below threshold, a new field may be assigned to that channel (i.e., fields may be cycled). With the FS concept (**B**), a single-timing channel is used, and the field is incrementally changed as real-time programming steps are made resulting in incremental changes in the stimulated region (*solid line* on the spinal cord). Multiple sources are required for the FS type of real-time programming

The FS approach for real-time steering consists of using a multiple-source system, and making incremental changes to the source magnitudes at a non-zero amplitude, as illustrated in Fig. 16. The essence of the FS approach is incremental shaping of the field (i.e., the field changes with each step), with corresponding real-time shaping of the paresthesia. The FS requires a multiple-source system (with associated advantages, e.g., fine-tunability and compensation for impedance changes), and can be done with one timing channel, so may have advantages over FBC in terms of a lower effective rate and corresponding battery use. The FS[4] method is presently used in a commercially available SCS system.

[4] Commercial implementation of FS includes Boston Scientific i-Sculpt™ in the Precision™ system.

4 Stimulation Parameters

4.1 Effects of Pulse Width

Earlier reports of pulse width (PW) programming in SCS focused on energetic concerns, especially as primary cell IPG's gained acceptance. To reduce frequent surgery for replacement of IPG's with depleted batteries, SCS programming required consideration of stimulating the patient at the most energy-optimal stimulation parameters, while still providing adequate therapy [72, 85]. In electrical stimulation, the most energy-optimal PW setting is the chronaxie setting [86, 87]. In a simple stimulation model, where the electrode is modeled as a pulsed current source, and the tissue is modeled as a lumped parallel resistance and capacitance, the chronaxie is defined as the PW setting that minimizes energy delivery from the stimulator [88]. Chronaxie has been used historically in an attempt to characterize the type of tissue being stimulated. Gross differences are clearly observed (e.g., nerve vs. muscle [89]), but chronaxie seems too coarse a metric for fine divisions of nerve fiber types. Chronaxie has been shown to depend upon the distance from the electrode to the fibers [90], the distribution of the fiber diameters near the electrode [47], the size and shape of the electrode [88], and the shape of the stimulation pulse [91].

Clinically, however, the value of using chronaxie for determining therapeutic programming is questionable. A recent prospective study of PW programming in SCS found the strength-duration parameters to be grossly in keeping with most previous reports [92]. However, approximately 26% of patients, when selecting among a full range of PW settings chose values higher than chronaxie as 'favorite' settings: the median PW setting for patient 'favorite' programs was 400 μs. Additionally, the variations in paresthesia coverage and focus observed with different PW settings suggest that using only chronaxie for programming might result in sub-optimal paresthesia coverage Approximately one-third of patients showed either paresthesia coverage growth or caudal shift, sometimes both, with increasing PW (see Fig. 17).

Mathematical modeling of SCS, using a realistic distribution of fiber diameters in the dorsal columns, suggested that greater activation of smaller fibers would occur as the PW was increased [93] . Since there is a greater relative fraction of smaller fibers in the medial aspects of the dorsal columns, the modeling results predicted greater paresthesia coverage in the lumbar and sacral dermatomes with increased PW at a mid- to low-thoracic lead placement [94]. Thus, chronaxie, while academically interesting, does not seem to predict patient choice of desired programming nor provide maximal paresthesia coverage. As rechargeable neurostimulators become more prevalent, energy minimization concerns should be considered secondary to clinical effect, especially as PW is concerned.

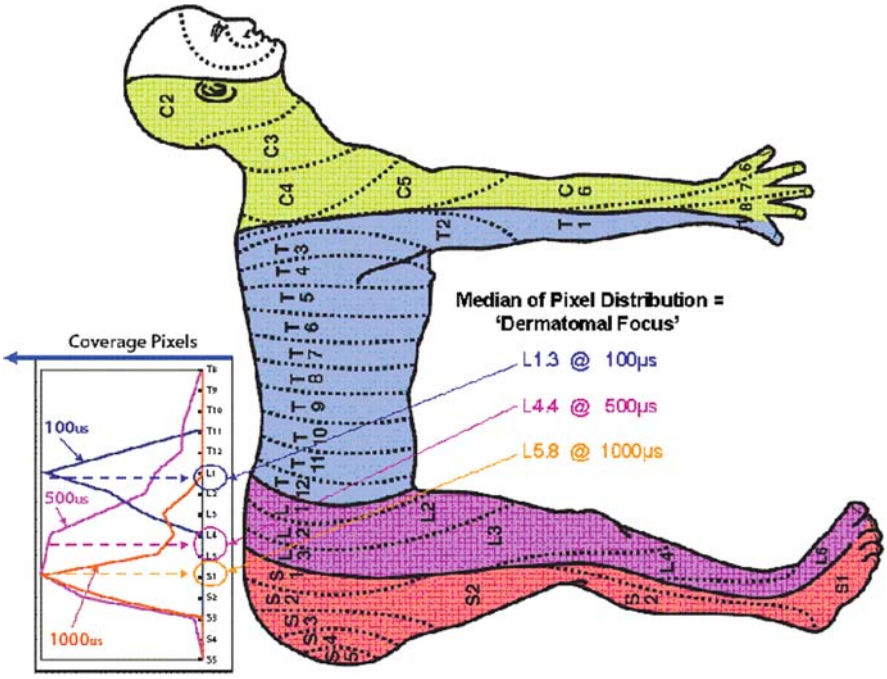

Fig. 17 Shift of 'Focus' of paresthesia distribution with pulse width [92]. At each PW setting a histogram was created of the normalized number of pixels in each dermatome; these histograms are shown in the chart at left, which is grossly aligned with the dermatomes shown on the body figure at right. The median was calculated from each histogram to characterize the 'dermatomal' focus at each PW setting. Note the caudal shift in the focus of paresthesia as the pulse width was increased

4.2 Effects of Stimulation Rate

While PW in SCS has undergone some investigation, the reported effects of stimulation rate remain primarily observational. A 20+-year retrospective review of 171 patients reported that the average stimulation rate selected by patients was 63 ± 54 Hz (range: 8–200 Hz), and suggested that this number relates to a possible mechanism of SCS called frequency-related conduction block (FRCB) [16]. In FRCB, the local ionic balance at the node of Ranvier is modified by repetitive stimulation, leading to a reduced ability for action potentials to be generated and thus reduced traffic in the axon [95]. Animal studies of peripheral nerve and dorsal column stimulation have shown that FRCB has a larger effect on smaller fibers than larger fibers [96]. Bifurcation points in the axon are especially sensitive to FRCB [97].

Another study has suggested that relatively high stimulation rates (> 250 Hz) were useful in reestablishing pain relief for some chronically implanted patients who had 'breakthrough pain' (i.e., returning pain

sensations in body areas with concordant paresthesia) [98]. In the use of SCS for spasticity, one author has suggested that rates on the order of 1500 Hz may be required for efficacy [99].

In addition to modifying axonal excitability, the synaptic connections made by these axons may also be sensitive to stimulation rate. Recent animal investigations of wide dynamic range neurons in the dorsal horn have suggested that these neurons have a characteristic post-synaptic potential profile that makes their output relatively inhibitory or excitatory depending upon the synaptic input [100]. This rate sensitivity appears also to be sensitive to the type and number of connections between interneurons in the dorsal horn. More work is necessary to characterize the technical and clinical effects of stimulation rate in SCS.

5 Computational Models as an Engineering Tool

5.1 University of Twente Computational Model: Insight and Clinical Impact

Technical advancement in computational models has provided not only theoretical tools to improve understanding of the mechanisms of electrical stimulation, but also evaluation of new stimulation technologies, such as novel electrode designs, optimal contact combinations, and stimulation pulse waveforms.

An SCS computational model was initially proposed by Coburn and Sin [101], and the bulk of the SCS modeling effort was significantly furthered by Holsheimer and colleagues, beginning with Struijk and Holsheimer's development of a three-dimensional field model of SCS [102]. When combined with a theoretical model of myelinated nerve fibers, the quality of computational models further improved the level of insight into electrical stimulation delivered in epidural space in the spinal canal [36, 37, 103]. The model provided theoretical ground for contact design and useful contact combinations [79, 104] . The computational model estimated the effect of anatomic parameters on the thresholds of dorsal column fibers [105], predicted the potential location of excitation in dorsal root fibers [29], and analyzed the effect of CSF thickness [106] with clinical validations [19, 42, 107]. The model contributed significantly to the specification of contact design parameters such as size and spacing [34, 43] to favor preferential stimulation of dorsal column fibers over root fibers [35].

In addition to the model of the electric field, the model of the myelinated sensory fiber is an important component to estimate the performance of SCS. Ion channel kinematics were derived from rabbit tibial nerve [108] and later improved to match human data [109]. Realistic parameters in the fiber model enabled estimation of fiber diameter [110] and distribution [111] in the dorsal column through comparison with clinical measurements [94].

Model-based analysis revealed that experimental measurements (e.g., chronaxie time) are device dependent and provided evidence that current-controlled

devices have better potential to estimate physiological parameters [91]. Computational models inferred that it is important to place a lead on the midline for optimal paresthesia coverage [32], and this prediction has been supported by clinical evidence [112] in SCS.

Using the computational model, Struijk and Holsheimer proposed a new stimulation paradigm for SCS, called 'Transverse Tripolar Stimulation' (TTS) [66]. The proposed TTS combination consisted of a cathode over the midline, with independently-controlled anodes lateral to the cathode, on both the left and right sides. The model was used to make two predictions: (1) the TTS could be used in SCS to preferentially stimulate dorsal column vs. root fibers which should manifest as an increase in the clinical usage range; (2) balancing of the strengths of the two anodes would result in left–right control of the paresthesia. The performance of TTS was predicted with the model [66, 113], and then evaluated clinically in single and multi-center [62-64, 114, 115] studies. The clinical trials validated the computational model by showing an increased threshold ratio (discomfort threshold over perception threshold) [114] and expanded control over the paresthesia [62]. However, commercial systems of the time used only a single source, and the full capability of the transverse tripolar contact combination could not be exploited. Full advantage of transverse tripolar stimulation relies on a multiple-source device which can optimize the electric field as predicted by the computational model [115].

In the remainder of this section, we will describe continued modeling efforts to understand: (1) sensitivities to stimulation with transverse fields, (2) current-steering with parallel percutaneous leads, (3) the effect of pulse width on fiber recruitment and the corresponding clinical effects.

5.1.1 Sensitivity Analysis of Transverse Tripolar Stimulation with Percutaneous Leads

At the advent of the transverse tripole, commercial systems used only a single source to generate the stimulation field and could not exploit the full capability of a transverse tripolar contact combination. However, three transverse contacts are sometimes used clinically to mimic the TTS, but with a single-source system.

To understand the capabilities and limitations of TTS with single- or multiple-source systems we use a computational model to evaluate the sensitivities of stimulation to variability in lead position. We focus on lead position because migration remains a significant complication in SCS [9]. Electric fields generated from TTS with possible lead migration was explored using to the computational model and the performance was compared to that of ideally placed leads (i.e., perfectly over the midline of the spinal cord). The model has three leads placed in a symmetric, parallel medio-lateral arrangement (Fig. 18A). The TTS combination was achieved by applying anodes on the two lateral contacts with a cathode on the middle lead, as shown in Fig. 18B.

To mimic lead migration (medio-lateral and dorso-ventral direction), leads were moved dorso-ventrally (Fig. 19A) or laterally (Fig. 19B). Results showed

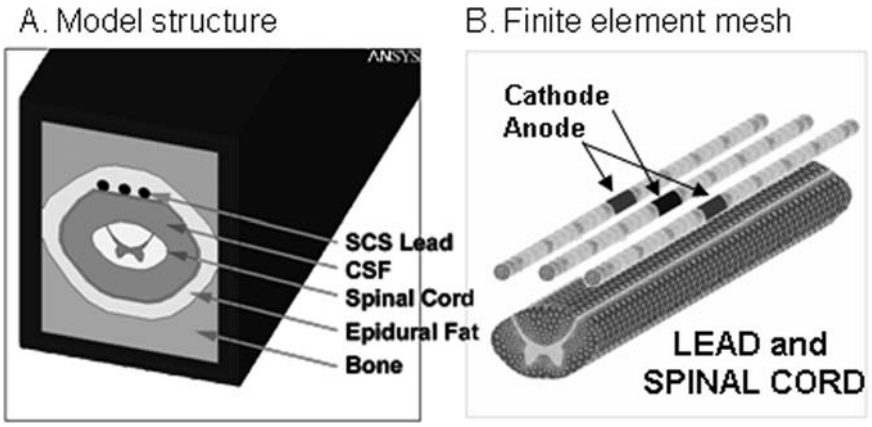

Fig. 18 (**A**) Cross-section view of the finite element model of the spinal cord. (**B**) Mesh of lead and spinal cord domains. To simulate a TTS combination, anodes were placed transverse to the cathode

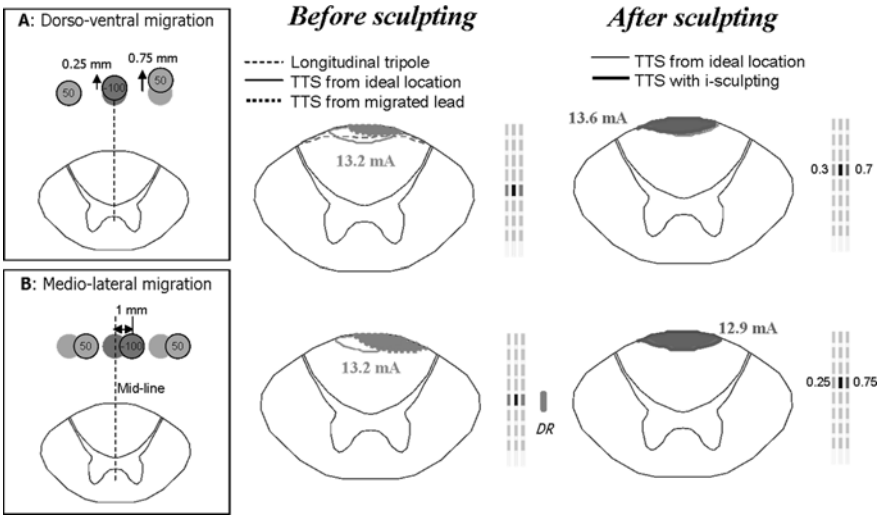

Fig. 19 Effect of lead migration during TTS. (**A**) Dorso-ventral migration shifted 'activated area' to *right* where anode got weaker by dorsal migration of the lead. Depth of penetration also changed by lead migration and was not deeper than a longitudinal tripole. However, after adjusting anode intensity with a multiple-source system (current sculpting, shown in the far *right panel*), the activated area was similar to that from ideal lead location. (**B**) Medio-lateral migration had similar effects to dorso-ventral migration. Current sculpting could realign the field to compensate for the change

that the shape and depth of the activated region of spinal cord fibers was compromised by lead offset in any direction (Fig. 19). The model predicted that the performance of TTS is highly sensitive to relative position between leads and the spinal cord. The model predicted that a multiple-source system with properly adjusted current fractionalization (Fig. 19, 'After sculpting') can reorient current

flow to mimic the ideal condition and implies the potential to restore therapeutic benefits.

The model predicted the following: (1) sensitivity of the activated region of spinal cord fibers due to small shifts (~1 mm) in lead and spinal cord positions and (2) that use of a multiple-source system, as originally proposed [66], can be used to compensate for small changes in relative lead and spinal cord positions. The asymmetries in paresthesia in these data are consistent with previous modeling results and clinical data [115].

5.1.2 Field Steering Between Contacts of Parallel Leads

Using the computer model, we studied the capability to 'sculpt' the electric field using constant current fractionalized across several contacts from two leads, as shown in Fig. 20. The model was used to quantify and visualize the volumes of activated spinal cord fibers during steering of the current from one lead to another. The model output can provide insight into the therapeutic possibilities of lead placement and programming in SCS.

Clinical evaluation of current fractionalization between two parallel leads has been initiated. Change in paresthesia was consistent with modeling results and present anatomical understanding, and paresthesia drawings made by one patient for several splits of current are shown in Fig. 20.

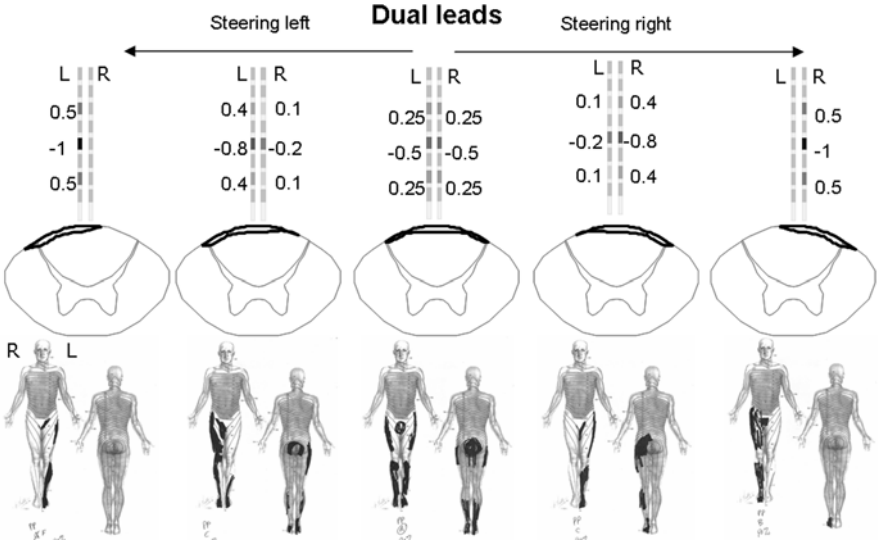

Fig. 20 Effect of current fractionalization with dual percutaneous leads. Computational model showed that current fractionalization between two leads with a multiple-source system can stimulate selectively dorsal columns. Clinical measurement of paresthesia coverage was assessed by patient drawings, and the lower panel shows drawings of paresthesia coverage from one patient at cathodic current splits of 100/0, 80/20, 50/50, 20/80, and 0/100 (from *left* to *right*; in clinical work anodes were held constant at 25% each)

5.1.3 Effect of Pulse Width

The University of Twente (UT) model has been instrumental in pioneering advances in SCS. The effects of pulse width had not been evaluated, and to investigate these effects, we generated a model of SCS (Boston Scientific model) generally based on the approach of the UT model (i.e., finite element model coupled with non-linear fiber analysis[5]), but with the addition at several myelinated fiber sizes distributed within the dorsal columns based on histological data [29, 94, 116]. The BSC model used previously developed non-linear myelinated mammalian fiber models [50]. Multiple fiber sizes were used because the effects of pulse width are known to be fiber size dependent [8]. An example of the output of the BSC model is shown in Fig. 21.

To study the effect of pulse width on dorsal column fibers of different sizes, a longitudinal guarded cathode (anode-to-cathode separations of 8 mm in center to center) combination parallel to DC fibers was applied to the model with different pulse widths (60, 210, 450, and 1000 μs) (Fig. 22). The dCSF used in this study was 3.2 mm. Two stopping criteria were used including (1) the threshold of the most excitable dorsal root (DRth) fiber (15 μm diameter) and (2) 1.4 times the threshold of the most excitable dorsal column fiber (11.5 μm diameter).

The model predicted that increasing pulse width could recruit medial fibers efficiently compared to lateral fibers, which might be related to gradually recruiting more sacral fibers located in medial portion of dorsal column (Fig. 22) with increased PW. The fiber ratio (LatF/MedF) was computed from the mathematical model (Fig. 22A), and we assumed that lateral fibers correspond to dermatomes more rostral than the medial fibers. The fiber ratio was smaller (corresponding to more caudal stimulation) for wide PW than short PW because the wide PW would recruit more medial fibers than short PW (Fig. 22B). The model also predicted that large (1000 μs) pulse widths stimulate more fibers than short (210 μs) pulse width, both in terms of activated DC 'area' (cross-sectional) and total number of fibers (3.2 times), which is expected to correspond to increased paresthesia coverage.

In summary, the computational model showed that longer PW recruited more DC fibers of any size than a short PW. Because of the abundance of small fibers located on superficial and medial dorsal columns, larger PW recruited a greater number of medial fibers relative to lateral fibers, and a greater number of total fibers. This model-based prediction is consistent with clinical data [8, 118]. Therefore, this new spinal cord model is a valuable tool for gaining theoretical insight into the stimulation parameters that may improve the efficacy of therapeutic outputs.

---

[5] In the model described by Lee et al., the spinal cord geometry (Fig. 18) was based on a histological cross section [116] and the dorsal root trajectory A1 from Struijk et al. with the dorsal root mother fiber branching into two thinner daughter fibers upon entering the spinal cord [29]. DC fibers have a straight trajectory in the rostro-caudal direction. The voltage data from the finite element model (FEM) along corresponding fibers in three-dimensional space were applied to the non-linear axon models with different fiber diameters [117].

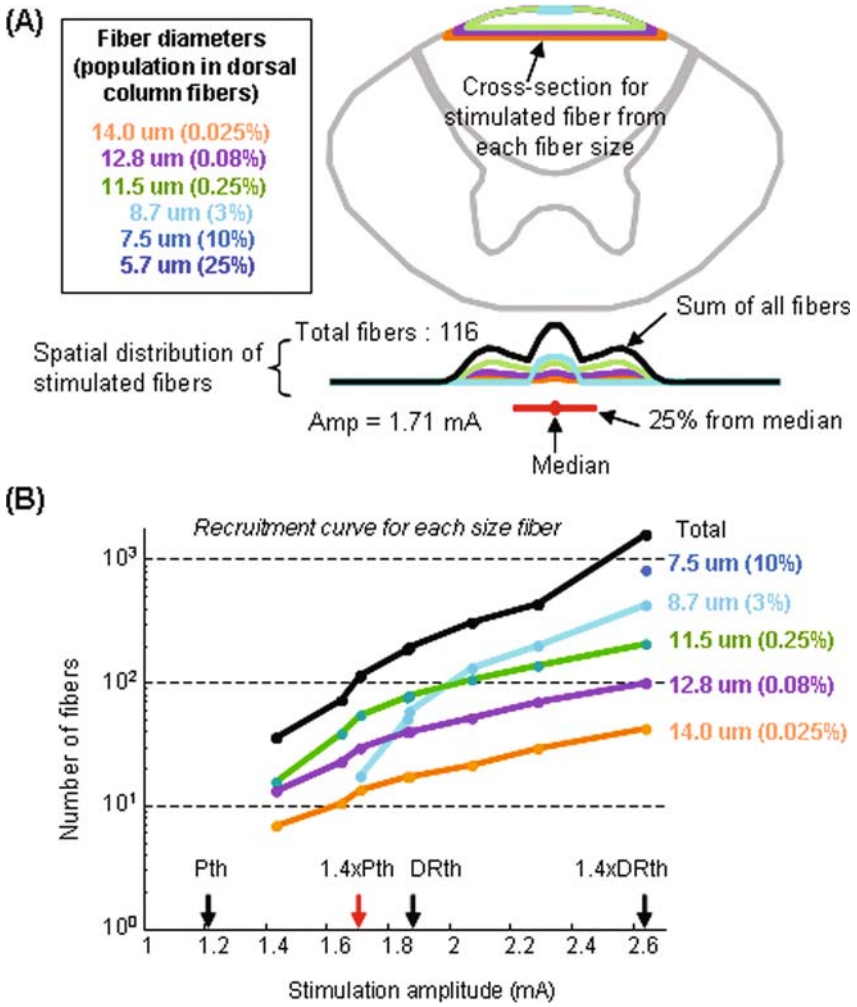

Fig. 21 (**A**) Stimulated fibers with different diameters using a longitudinal guarded cathode from a percutaneous lead (two anodes 8 mm away from the center of cathode, pulse width of 210 μs, amplitude of 1.4 times perception threshold (1.4×Pth)). The number of small fibers recruited (8.7 μm diameter) in the medial DC at 1.4×Pth, exceeded the number of recruited fibers of any other size (11.5, 12.8, and 14.0 μm diameter), even though the depth of stimulation was lower. This is possible because of the high density of small fibers. (**B**) Recruitment of fibers of each size as a function of increasing amplitude. Small fibers contribute significantly to the total number of stimulated fibers

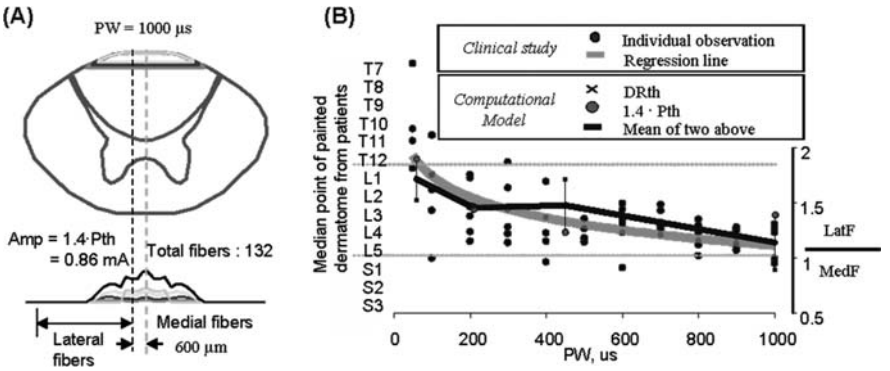

Fig. 22 (**A**) Stimulated fiber distribution by 1000 μs square pulse. Lateral and medial fibers were separated by an arbitrary line 600 μm away from midline. (**B**) Median points of paresthesia dermatome pixel drawn by six patients at maximum comfortable amplitudes and fiber ratio (LatF/MedF) from the mathematical model were plotted for different pulse width

6 Summary

In summary, spinal cord stimulation is an effective therapy for the management of some chronic pain conditions, with historical origins dating back to the 1960s. Clinically, patients feel a tingling paresthesia that when overlapped with pain will fully or partially reduce the pain, but the mechanisms are still under investigation. Technical advancements in commercially available systems are being made to overcome issues such as changes in the stimulation field with contact impedance change, lead migration, difficulty in device programming, and targeting the paresthesia to maximize concordance with pain. Computational models continue to play an important role in understanding electrical and geometrical effects of stimulation and driving design of leads and stimulation strategies.

References

1. Melzack, R. and P.D. Wall, *Pain mechanisms: a new theory*. Science, 1965, **150**(699): 971–9.
2. Linderoth, B. and R. Foreman, *Physiology of spinal cord stimulation: review and update*. Neuromodulation, 1999, **2**(3): 150–64.
3. Taub, A. and L.M. Kitahata, *Modulation of spinal-cord function by anesthesia*. Anesthesiology, 1975, **43**(4): 383–5.
4. Bennett, D. and D. Brookoff, *Complex regional pain syndromes (reflex sympathetic dystrophy and causalgia) and spinal cord stimulation*. Pain Med, 2006, **7**(S1): S64–S96.
5. Melzack, R., *Evolution of the neuromatrix theory of pain. The Prithvi Raj Lecture: presented at the third World Congress of World Institute of Pain, Barcelona 2004*. Pain Pract, 2005, **5**(2): 85–94.
6. Shealy, C.N., J.T. Mortimer, and J.B. Reswick, *Electrical inhibition of pain by stimulation of the dorsal columns: preliminary clinical report*. Anesth Analg, 1967, **46**(4): 489–91.

7. Brest, A.N., L. Wiener, and B. Bachrach, *Bilateral carotid sinus nerve stimulation in the treatment of hypertension*. Am J Cardiol, 1972, **29**(6): 821–5.
8. Burton, C., *Dorsal column stimulation: optimization of application*. Surg Neurol, 1975, **4**(1): 171–9.
9. Cameron, T., *Safety and efficacy of spinal cord stimulation for the treatment of chronic pain: a 20-year literature review*. J Neurosurg, 2004, **100**(3 Suppl Spine): 254–67.
10. Kumar, K., R. Nath, and G.M. Wyant, *Treatment of chronic pain by epidural spinal cord stimulation: a 10-year experience*. J Neurosurg, 1991, **75**(3): 402–7.
11. North, R.B., et al., *A prospective, randomized study of spinal cord stimulation versus reoperation for failed back surgery syndrome: initial results*. Stereotact Funct Neurosurg, 1994, **62**(1–4): 267–72.
12. Siegfried, J. and Y. Lazorthes, *Long-term follow-up of dorsal cord stimulation for chronic pain syndrome after multiple lumbar operations*. Appl Neurophysiol, 1982, **45**(1–2): 201–4.
13. Barolat, G., *Spinal cord stimulation for chronic pain management*. Arch Med Res, 2000, **31**(3): 258–62.
14. Barolat, G., *Current status of epidural spinal cord stimulation*. Neurosurg Q, 1995, **5**(2): 98–124.
15. North, R.B., et al., *Spinal cord stimulation for chronic, intractable pain: superiority of "multi-channel" devices*. Pain, 1991, **44**(2): 119–30.
16. North, R.B., et al., *Spinal cord stimulation for chronic, intractable pain: experience over two decades*. Neurosurgery, 1993, **32**(3): 384–94; discussion 394–5.
17. Hornberger, J., et al., *Rechargeable spinal cord stimulation versus non-rechargeable system for patients with failed back surgery syndrome: a cost-consequences analysis*. Clin J Pain, 2008, **24**(3): 244–52.
18. Oakley, J.C. and J.P. Prager, *Spinal cord stimulation: mechanisms of action*. Spine, 2002, **27**(22): 2574–83.
19. Holsheimer, J., et al., *Significance of the spinal cord position in spinal cord stimulation*. Acta Neurochir Suppl, 1995, **64**: 119–24.
20. Kandell, E., J. Schwartz, and T. Jessell, *Principles of Neural Science*. 4th ed. 2000, New York: McGraw-Hill, Health Professions Division.
21. Oakley, J.C., C. Varga, and E. Krames, Bradley K., *Real-time paresthesia steering using continuous electric field adjustment. Part I: intraoperative performance*. Neuromodulation, 2004, **7**(3): 157–67.
22. Hosobuchi, Y., J.E. Adams, and P.R. Weinstein, *Preliminary percutaneous dorsal column stimulation prior to permanent implantation. Technical note*. J Neurosurg, 1972, **37**(2): 242–5.
23. Olin, J.K., D.H. Kidd, and R.B. North,, *Postural changes in spinal cord stimulation thresholds*. Neuromodulation, 1998, **1**(4): 171–5.
24. Dijkstra, E.A., J. Holsheimer, W. Olthuis, and P. Bergveld, *Ultrasonic distance detection for a closed-loop spinal cord stimulation system*. Engineering in Medicine and Biology Society. Proceedings of the 19th Annual International Conference of the IEEE, 1997, **5**: 1954–7.
25. Barolat, G. and A.D. Sharan, *Future trends in spinal cord stimulation*. Neurol Res, 2000, **22**(3): 279–84.
26. North, R.B., et al., *Automated, patient-interactive, spinal cord stimulator adjustment: a randomized controlled trial*. Neurosurgery, 2003, **52**(3): 572–80; discussion 579–80.
27. Grill, W.M. and J.T. Mortimer, *Electrical properties of implant encapsulation tissue*. Ann Biomed Eng, 1994, **22**(1): 23–33.
28. Oakley, J.C., J. Prager, E. Krames, R. Weiner, J. Stamatos, and K. Bradley, *Variability of Contact Impedance Over Time in SCS*. in *American Society Stereotactic and Functional Neurosurgery Biennial Meeting*. 2004. Cleveland, OH: Stereotactic and Functional Neurosurgery.
29. Struijk, J.J., J. Holsheimer, and H.B. Boom, *Excitation of dorsal root fibers in spinal cord stimulation: a theoretical study*. IEEE Trans Biomed Eng, 1993, **40**(7): 632–9.

30. Vistnes, L.M., G.A. Ksander, and J. Kosek, *Study of encapsulation of silicone rubber implants in animals. A foreign-body reaction*. Plast Reconstr Surg, 1978, **62**(4): 580–8.
31. Holsheimer, J. and L. Manola, *Neuromodulation in epilepsy and chronic pain*. Neuromodulation, 2004, **9**(2): 143–53.
32. Holsheimer, J. and W.A. Wesselink, *Effect of anode-cathode configuration on paresthesia coverage in spinal cord stimulation*. Neurosurgery, 1997, **41**(3): 654–9; discussion 659–60.
33. Law, J., *Targeting a spinal stimulator to treat the 'failed back surgery syndrome'*. Appl Neurophysiol, 1987, **50**: 437–8.
34. Holsheimer, J. and J.J. Struijk, *Electrode Geometry and Preferential Stimulation of Spinal Nerve Figers Having Different Orientations: A Modeling Study*. in *14th Ann Int Conf IEEE Eng in Med & Biol Soc,* 1992, Paris, France.
35. Holsheimer, J., J.J. Struijk, and N.R. Tas, *Effects of electrode geometry and combination on nerve fibre selectivity in spinal cord stimulation*. Med Biol Eng Comput, 1995, **33**(5): 676–82.
36. Ranck, J.B., Jr., *Which elements are excited in electrical stimulation of mammalian central nervous system: a review*. Brain Res, 1975, **98**(3): 417–40.
37. McNeal, D.R., *Analysis of a model for excitation of myelinated nerve*. IEEE Trans Biomed Eng, 1976, **23**(4): 329–37.
38. Rattay, F., *Analysis of models for external stimulation of axons*. IEEE Trans Biomed Eng, 1986, **33**(10): 974–7.
39. Moffitt, M.A., C.C. McIntyre, and W.M. Grill, *Prediction of myelinated nerve fiber stimulation thresholds: limitations of linear models*. IEEE Trans Biomed Eng, 2004, **51**(2): 229–36.
40. Warman, E.N., W.M. Grill, and D. Durand, *Modeling the effects of electric fields on nerve fibers: determination of excitation thresholds*. IEEE Trans Biomed Eng, 1992, **39**(12): 1244–54.
41. Holsheimer, J. and G. Barolat, *Spinal geometry and paresthesia coverage in spinal cord stimulation*. Neuromodulation, 1998, **1**(3): 129–36.
42. Holsheimer, J., et al., *MR assessment of the normal position of the spinal cord in the spinal canal*. AJNR Am J Neuroradiol, 1994, **15**(5): 951–9.
43. Holsheimer, J. and W.A. Wesselink, *Optimum electrode geometry for spinal cord stimulation: the narrow bipole and tripole*. Med Biol Eng Comput, 1997, **35**(5): 493–7.
44. Manola, L., J. Holsheimer, and P. Veltink, *Technical performance of percutaneous leads for spinal cord stimulation: a modeling study*. Neuromodulation, 2005, **8**(2): 88–99.
45. Cameron, T. and K. Alo, *Effects of posture on stimulation parameters in spinal cord stimulation*. Neuromodulation, 1998, **1**(4): 177–83.
46. Moro, E., et al., *Subthalamic nucleus stimulation: improvements in outcome with reprogramming*. Arch Neurol, 2006, **63**(9): 1266–72.
47. Gorman, P.H. and J.T. Mortimer, *The effect of stimulus parameters on the recruitment characteristics of direct nerve stimulation*. IEEE Trans Biomed Eng, 1983, **30**(7): 407–14.
48. van den Honert, C. and J.T. Mortimer, *The response of the myelinated nerve fiber to short duration biphasic stimulating currents*. Ann Biomed Eng, 1979, **7**(2): 117–25.
49. McIntyre, C.C. and W.M. Grill, *Selective microstimulation of central nervous system neurons*. Ann Biomed Eng, 2000, **28**(3): 219–33.
50. McIntyre, C.C. and W.M. Grill, *Extracellular stimulation of central neurons: influence of stimulus waveform and frequency on neuronal output*. J Neurophysiol, 2002, **88**(4): 1592–604.
51. Grill, W.M. and J.T. Mortimer, *Stimulus waveforms for selective neural stimulation*, in *Engineering in Medicine and Biology Magazine, IEEE*, 1995, 375–85.
52. Grill, W.M. and J.T. Mortimer, *Inversion of the current-distance relationship by transient depolarization*. IEEE Trans Biomed Eng, 1997, **44**(1): 1–9.
53. Merrill, D.R., M. Bikson, and J.G. Jefferys, *Electrical stimulation of excitable tissue: design of efficacious and safe protocols*. J Neurosci Methods, 2005, **141**(2): 171–98.

54. Alo, K., *Patient-reported differences in constant current and constant voltage stimulation*, in *11th North American Neuromodulation Society*, 2007: Acapulco, Mexico.
55. Alo, K. and T. Cartwright, *Patient preferences for constant current and constant voltage stimulation*, in *11th North American Neuromodulation Society*, 2007: Acapulco, Mexico.
56. Mortimer, J.T., *Motor prostheses, Chapter 5*, in *Handbook of Physiology – The Nervous System III*, V. Brooks, Editor, 1981, American Physiological Society: Bethesda, Maryland. pp. 155–87.
57. Ranck, J.B., Jr., *Extracellular stimulation*, in *Electrical Stimulation Research Techniques: Methods in Physiological Psychology III*, Patterson, M.M. and R.P. Kesner, (ed). 1981, New York: Academic Press, pp. 1–36.
58. Scheiner, A., J.T. Mortimer, and U. Roessmann, *Imbalanced biphasic electrical stimulation: muscle tissue damage*. Ann Biomed Eng, 1990, **18**(4): 407–25.
59. Andersen, C., *Time dependent variation of stimulus requirements in spinal cord stimulation for angina pectoris*. Pacing Clin Electrophysiol, 1997, **20**(2 Pt 1): 359–63.
60. Spangenberg, P., *Time-dependent variation of stimulus requirements of single SCS (spinal cord stimulation) leads with respect to pain relief*, in *54th Annual Meeting of the German Society of Neurosurgery*. 2003: Saarbrucken, Germany, MO 18–03.
61. Kumar, K., G. Hunter, and D. Demeria, *Spinal cord stimulation in treatment of chronic benign pain: challenges in treatment planning and present status, a 22-year experience*. Neurosurgery, 2006, **58**(3): 481–96; discussion 481–96.
62. Oakley, J.C., et al., *Transverse tripolar spinal cord stimulation: results of an international multicenter study*. Neuromodulation, 2006, **9**(3):192–203.
63. Wesselink, W.A., et al., *Quantitative aspects of the clinical performance of transverse tripolar spinal cord stimulation*. Neuromodulation, 1999, **2**(1): 5–14.
64. Slavin, K.V., et al., *Efficacy of transverse tripolar stimulation for relief of chronic low back pain: results of a single center*. Stereotact Funct Neurosurg, 1999, **73**(1–4): 126–30.
65. Veraart, C., W.M. Grill, and J.T. Mortimer, *Selective control of muscle activation with a multipolar nerve cuff electrode*. IEEE Trans Biomed Eng, 1993, **40**(7): 640–53.
66. Struijk, J.J. and J. Holsheimer, *Transverse tripolar spinal cord stimulation: theoretical performance of a dual channel system*. Med Biol Eng Comput, 1996, **34**(4): 273–9.
67. Racz, G.B., R.F. McCarron, and P. Talboys, *Percutaneous dorsal column stimulator for chronic pain control*. Spine, 1989, **14**(1): 1–4.
68. Renard, V.M. and R.B. North, *Prevention of percutaneous electrode migration in spinal cord stimulation by a modification of the standard implantation technique*. J Neurosurg Spine, 2006, **4**(4): 300–3.
69. Rosenow, J.M., et al., *Failure modes of spinal cord stimulation hardware*. J Neurosurg Spine, 2006, **5**(3): 183–90.
70. Plonsey, R. and R.C. Barr, *Electric field stimulation of excitable tissue*. IEEE Trans Biomed Eng, 1995, **42**(4): 329–36.
71. Kosek, P., D. Morgan, J. Dunn, J. Oakley, R. Rosenthal, M. Moffitt, V. Grandhe, and K. Bradley, *Electronically Generated Lead (EGL) Scan: Report of First Clinical Use*, in *11th Annual North American Neuromodulation Society*, 2006, Las Vegas, NV.
72. Davis, R. and E. Gray, *Technical factors important to dorsal column stimulation*. Appl Neurophysiol, 1981, **44**(1–3): 160–70.
73. Hoppenstein, R., *Electrical stimulation of the ventral and dorsal columns of the spinal cord for relief of chronic intractable pain: preliminary report*. Surg Neurol, 1975, **4**(1): 187–94.
74. Law, J., *Spinal stimulation: statistical superiority of monophasic stimulation of narrowly separated, longitudinal bipoles having rostral cathodes*. Appl Neurophysiol, 1983, **46**: 129–37.
75. Law, J.D. and L.V. Miller, *Importance and documentation of an epidural stimulating position*. Appl Neurophysiol, 1982, **45**: 461–4.
76. North, R.B., et al., *Patient-interactive, computer-controlled neurological stimulation system: clinical efficacy in spinal cord stimulator adjustment*. J Neurosurg, 1992, **76**(6): 967–72.

77. Alo, K., V. Redko, and J. Charnov, *Four year follow-up of dual electrode spinal cord stimulation for chronic pain*. Neuromodulation, 2002, **5**(2): 79–88.
78. Alo, K., *Spinal cord stimulation for complex pain: initial experience with a dual electrode, programmable, internal pulse generator*. Pain Practice, 2003, **3**(1): 31–38.
79. Holsheimer, J., J.J. Struijk, and N.J. Rijkhoff, *Contact combinations in epidural spinal cord stimulation. A comparison by computer modeling*. Stereotact Funct Neurosurg, 1991, **56**(4): 220–33.
80. Holsheimer, J. and L. Manola, *Technical Performance of Percutaneous SCS Leads*, in *6th World Congress of the International Neuromodulation Society*, 2003, Madrid, Spain.
81. Barolat, G., S. Zeme, and B. Ketcik, *Multifactorial analysis of epidural spinal cord stimulation*. Stereotact Funct Neurosurg, 1991, **56**(2): 77–103.
82. Alo, K., M.J. Yland, D.L. Kramer, J.H. Charnov, and V. Redko, *Computer assisted and patient interactive programming of dual octrode spinal cord stimulation in the treatment of chronic pain*. Neuromodulation, 1998, **1**(1): 30–45.
83. Oakley, J.C., *Spinal cord stimulation: patient selection, technique, and outcomes*. Neurosurg Clin N Am, 2003, **14**(3): 365–80, vi.
84. North, R.B., *Spinal cord stimulation with interleaved pulses: a randomized, controlled trial*. Neuromodulation, 2007, **10**(4): 349–57.
85. Jobling, D.T., et al., *Electronic aspects of spinal-cord stimulation in multiple sclerosis*. Med Biol Eng Comput, 1980, **18**(1): 48–56.
86. Lapicque, L., *On electric stimulation of muscle through ringer's solution*. J Physiol, 1931, **73**(3): 219–46.
87. Geddes, L.A. and J.D. Bourland, *The strength-duration curve*. IEEE Trans Biomed Eng, 1985, **32**(6): 458–9.
88. Irnich, W., *The chronaxie time and its practical importance*. Pacing Clin Electrophysiol, 1980, **3**(3): 292–301.
89. Geddes, L.A., *Accuracy limitations of chronaxie values*. IEEE Trans Biomed Eng, 2004, **51**(1): 176–81.
90. Miocinovic, S. and W.M. Grill, *Sensitivity of temporal excitation properties to the neuronal element activated by extracellular stimulation*. J Neurosci Methods, 2004, **132**(1): 91–9.
91. Holsheimer, J., et al., *Chronaxie calculated from current-duration and voltage-duration data*. J Neurosci Methods, 2000, **97**(1): 45–50.
92. Yearwood, T.B. Hershey, D.C. Lee, and K. Bradley, *Pulse width Programming in Spinal Cord Stimulation: A Clinical Study Pain Medicine 2009 (In press)*.
93. Lee, D.C.B. Hershey, K. Bradley, M. Moffitt, D, Peterson, Yearwood, TL, *Dorsal Column Selectivity in Pulse Width (PW) Programming of Spinal Cord Stimulation (SCS): Computational model for the Sacral Shift*, in *11th Annual North American Neuromodulation Society Meeting*, 2007, Acapulco, Mexico.
94. Feirabend, H.K., et al., *Morphometry of human superficial dorsal and dorsolateral column fibres: significance to spinal cord stimulation*. Brain, 2002, **125**(Pt 5): 1137–49.
95. Campbell, J.N. and D.M. Long, *Peripheral nerve stimulation in the treatment of intractable pain*. J Neurosurg, 1976, **45**(6): 692–9.
96. Ignelzi, R.J., J.K. Nyquist, and W.J. Tighe, Jr., *Repetitive electrical stimulation of peripheral nerve and spinal cord activity*. Neurol Res, 1981, **3**(2): 195–209.
97. Krauthamer, V., *Modulation of conduction at points of axonal bifurcation by applied electric fields*. IEEE Trans Biomed Eng, 1990, **37**(5): 515–9.
98. Bennett, D., K.M. Aló, J, Oakley, and C. Feler,, *Spinal cord stimulation for complex regional pain syndrome i [RSD]: a retrospective multicenter experience from 1995–1998 of 101 Patients*. Neuromodulation, 1999, **2**(3): 202–10.
99. Waltz, J., *Spinal cord stimulation: a quarter century of development and investigation*. Stereotact Funct Neurosurg, 1997, **69**: 288–99.

100. Schneider, S.P., *Mechanosensory afferent input and neuronal firing properties in rodent spinal laminae III-V: re-examination of relationships with analysis of responses to static and time-varying stimuli*. Brain Res, 2005, **1034**(1–2): 71–89.
101. Coburn, B., *Electrical stimulation of the spinal cord: two-dimensional finite element analysis with particular reference to epidural electrodes*. Med Biol Eng Comput, 1980, **18**(5): 573–84.
102. Holsheimer, J. and J.J. Struijk, *Analysis of spinal cord stimulation. I. Field potentials calculated for a homogeneous medium*, in *Electrophysiological Kinesiology*, Wallinga, W., H.B. Boom, and J. de Vries, (eds.), 1988, Excerpta Medica Congress Series: Amsterdam, pp. 95–8.
103. Frankenhaeuser, B. and A.F. Huxley, *The action potential in the myelinated nerve fiber of xenopus laevis as computed on the basis of voltage clamp data*. J Physiol, 1964, **171**: 302–15.
104. Struijk, J.J., et al., *Epidural spinal cord stimulation: calculation of field potentials with special reference to dorsal column nerve fibers*. IEEE Trans Biomed Eng, 1991, **38**(1): 104–10.
105. Struijk, J.J., et al., *Recruitment of dorsal column fibers in spinal cord stimulation: influence of collateral branching*. IEEE Trans Biomed Eng, 1992, **39**(9): 903–12.
106. Struijk, J.J., et al., *Paresthesia thresholds in spinal cord stimulation: a comparison of theoretical results with clinical data*. IEEE Trans Rehab Eng, 1993, **1**(2): 101–7.
107. He, J., et al., *Perception threshold and electrode position for spinal cord stimulation*. Pain, 1994, **59**(1): 55–63.
108. Goodall, E., M. Kosternman, and J. Holsheimer, *Modeling study of activation and propagation delays during stimulation of peripheral nerve fibers with a tripolar cuff electrode*. IEEE Trans Rehabil Eng, 1995, **3**(3): 272–82.
109. Wesselink, W.A., J. Holsheimer, and H.B. Boom, *A model of the electrical behaviour of myelinated sensory nerve fibres based on human data*. Med Biol Eng Comput, 1999, **37**(2): 228–35.
110. Wesselink, W.A., et al., *Estimation of fiber diameters in the spinal dorsal columns from clinical data*. IEEE Trans Biomed Eng, 1998, **45**(11): 1355–62.
111. Holsheimer, J. and G. Barolat, *Spinal geometry and paresthesia coverage in spinal cord stimulation*. Neuromodulation, 1998, **1**(3): 129–36.
112. North, R.B., et al., *Spinal cord stimulation for axial low back pain: a prospective, controlled trial comparing dual with single percutaneous electrodes*. Spine, 2005, **30**(12): 1412–8.
113. Holsheimer, J., *Effectiveness of spinal cord stimulation in the management of chronic pain: analysis of technical drawbacks and solutions*. Neurosurgery, 1997, **40**(5): 990–6; discussions 996–9.
114. Holsheimer, J., et al., *Clinical evaluation of paresthesia steering with a new system for spinal cord stimulation*. Neurosurgery, 1998, **42**(3): 541–7; discussion 547–9.
115. Struijk, J.J., et al., *Theoretical performance and clinical evaluation of transverse tripolar spinal cord stimulation*. IEEE Trans Rehabil Eng, 1998, **6**(3): 277–85.
116. Kameyama, T., Y. Hashizume, and G. Sobue, *Morphologic features of the normal human cadaveric spinal cord*. Spine, 1996, **21**(11): 1285–90.
117. McIntyre, C.C., A.G. Richardson, and W.M. Grill, *Modeling the excitability of mammalian nerve fibers: influence of afterpotentials on the recovery cycle*. J Neurophysiol, 2002, **87**(2): 995–1006.
118. Yearwood, T., *Dorsal Column Selectivity in Pulse Width (PW) Programming of Spinal Cord Stimulation (SCS): the "Sacral Shift"*, in *11th North American Neuromodulation Society*, 2007: Acapulco, Mexico.

Microelectrode Technologies for Deep Brain Stimulation

Martin Han and Douglas B. McCreery

Abstract This chapter discusses stimulation and recording microelectrodes used in deep brain stimulation (DBS). DBS has become an established treatment for movement disorders and a promising treatment for a number of other neurological conditions. However, there is need for improved implantable devices, better tailored to specific neurological disorders and the corresponding targets in the brain. The development of miniaturized devices would permit effective treatment with minimal side effects and would facilitate research on the pathophysiology of diseases treatable by DBS. We will discuss some of the challenges in the implementation of microelectrode systems for successful clinical translation.

1 Introduction

Therapeutic electrical stimulation in deep brain structures (deep brain stimulation, DBS, see Fig. 1) has developed into an effective treatment for advanced Parkinson's disease (PD) and essential tremor (see recent reviews in [5, 17, 61, 69, 112]). DBS is also being evaluated as a treatment for other neurological conditions including intractable temporal lobe epilepsy, several types of dystonias and hyperkinetic disorders, and for intractable depression [6, 9, 59, 68, 76, 77, 95, 143]. While the range of clinical applications for DBS has expanded, its mechanism(s) of action is still not well understood [4, 89]. In addition, the present clinical devices use macroelectrodes, and the electrical stimulation tends to spread quite broadly. For instance, the human STN, a target for the relief of the motor symptoms of PD by DBS, is an ovoid with an average dimension of $3 \times 6 \times 4$ mm [10] or a volume of approximately 150–200 mm^3 [44]. The current FDA-approved clinical DBS system, manufactured by

M. Han (✉)
Neural Engineering Program, Huntington Medical Research Institutes,
Pasadena, CA 91105, USA
e-mail: martinhan@hmri.org

D.D. Zhou, E. Greenbaum (eds.), *Implantable Neural Prostheses 1*,
Biological and Medical Physics, Biomedical Engineering,
DOI 10.1007/978-0-387-77261-5_6,

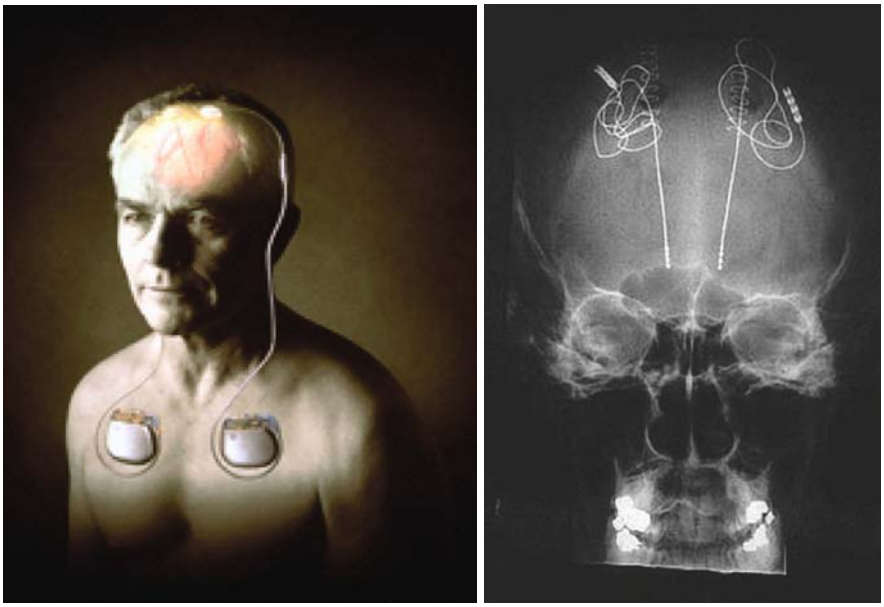

(a) (b)

Fig. 1 (**a**) Deep brain stimulation (DBS) macroelectrodes bilaterally implanted, with cables connecting to pulse generators under the skin near the collarbone (from [142]). (**b**) An X-ray image of a patient's brain showing implanted DBS macroelectrodes (from [109])

Medtronic, Inc., has a flexible "lead" 1.27 mm in diameter and 40 cm in length, with four cylindrical macroelectrodes placed along the distal 1 cm (Fig. 2(a)) [10, 35], thus spanning the linear extant of the human STN (Fig. 2(b)). The implantable stimulators (e.g., Soletra 7426) are controlled-voltage devices, and the stimulus currents can only be estimated from the resistivity of the surrounding tissue. In most patients, the stimulus voltage ranges from 1.5 to 3.5 volts [71]. When McIntyre et al. modeled the current field induced by the stimulus parameters typically used in the treatment of PD, they found that the effective stimulus may extend well beyond the boundaries of the STN [87]. This spread may account for many of the side effects that sometimes accompany DBS in the STN, including tetanic muscle contraction, speech disturbances, and ocular deviations [116].

In recent years, much has been learned about the pathophysiology of the disease states that are amenable to treatment by DBS, and there are now plausible theories concerning its mechanism of action, which in turn is helping to inform the development of the next generation of implants [86, 88]. However, a novel array for clinical DBS must retain all of the functionality of the devices now in clinical use, as well as providing new capabilities.

This chapter focuses on microelectrode technologies that are currently being used or can potentially be used in DBS. There are common issues for all implantable microelectrode systems intended for different applications, but

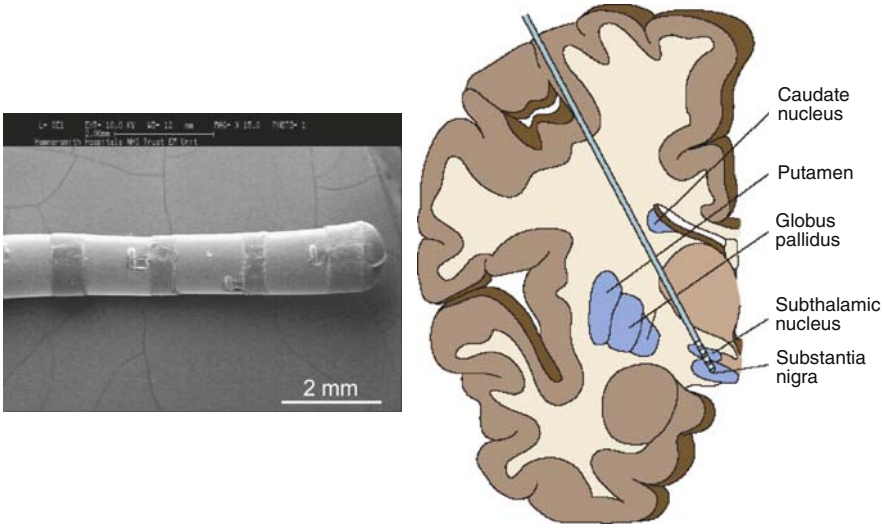

Fig. 2 (**a**) A scanning electron microscopic view of a Medtronic DBS "lead," showing four cylindrical macroelectrodes (From [96]). (**b**) A schematic of deep brain regions of the human brain, with a macroelectrode lead implanted into the subthalamic nucleus (From [37])

we will focus on those relevant to DBS. We will review and discuss several key aspects of the requirements of a device for DBS and the challenges of developing microelectrodes for these applications.

2 Implant Sites and Emerging Applications

Stimulation in the STN and in the internal segments of the globus pallidus (GPi) ameliorates many of the symptoms of PD [47]. Numerous studies have demonstrated a topographic organization of the mammalian STN [1, 3, 7, 45, 92, 94, 121, 144]. The broadest subdivision appears to be between motor, associative and limbic functions, but there is ample evidence for finer subdivisions of the topology, including a somatotopic mapping of motor functions (Fig. 3) [47]. Most of the STN neurons that are related to voluntary movement are located in the anterodorsal region of the nucleus. However, there is still some controversy as to the most efficacious site for DBS in and around the STN, and some studies have suggested that the best results are obtained by stimulating axons within the dorsolateral border of the STN and in zona inserta and/or the Fields of Forel [43, 48, 53, 114, 152, 153]. More generally, however, the STN appears to serve as a nexus that integrates the motor, cognitive, and emotional components of behavior, and might consequently be an effective target for the treatment of behavioral disorders that combine emotional, cognitive, and motor impairment [79], especially as stimulating arrays become available that can more selectively access its complex topology.

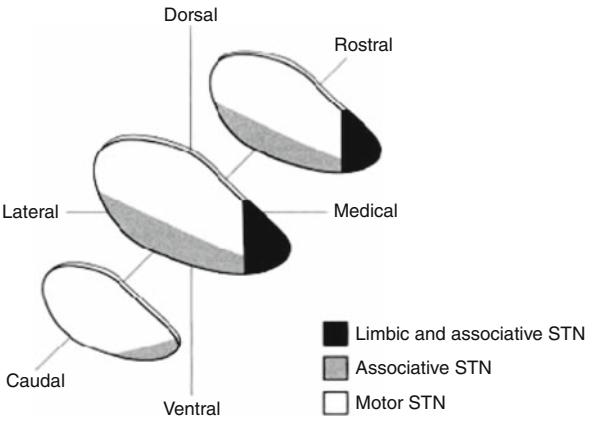

Fig. 3 A schematic of the human subthalamic nucleus (STN) illustrating the primary topographic subdivisions (from [47])

The efficacy of DBS has been established in several other types of movement disorders, and promising reports have emerged for Tourette's syndrome, obsessive-compulsive disorder, and major depression [39, 41, 52, 55, 56, 60, 72, 99, 111, 117, 134, 143]. For major depression, DBS may prove to be a reasonable option for severely ill and treatment-resistant patients who would otherwise have limited therapeutic options, and thus, a poor prognosis. The ventral intermediate nucleus of the thalamus is the most common DBS target for essential tremor, but more recent studies have demonstrated benefits in essential tremor and torticollis from DBS of the subthalamic area [24, 137], primarily the zona incerta [49, 78], while DBS in the white matter of the subgenual cingulate cortex has been shown to relieve intractable depression [59]. The pedunculopontine nucleus is another target being explored for the treatment of PD [81, 115]. The variety of implant sites employed in the clinical DBS illustrates the importance of being able to scale and otherwise customize the electrode arrays to achieve the best clinical outcomes.

3 Design Considerations and Challenges for Microelectrode Technologies in DBS

3.1 Summary of Key Requirements

Despite the success of the systems for DBS now in clinical use, it is probable that a device that can reliably and efficiently access the topographic organization of the target will provide greater flexibility, and thus, greater clinical efficacy and fewer and milder side effects than is possible with the current DBS systems. An array of independently controlled stimulating microelectrodes distributed throughout the target nucleus would permit precise control of the spatial distribution of the stimulation, and thus, allow better personalized DBS

therapy. Also, animal studies directed toward understanding the physiologic underpinnings of DBS in various brain structures and disease states would be aided greatly by a chronically implantable array that could deliver localized electrical stimulation into the target nuclei and which can also record the activity of individual neurons throughout the target.

However, there are several requirements that such a device must meet for clinical use. It must deliver the stimulation for many years, without injury to the tissue or degradation of the electrodes, and if the target is in the STN, it must deliver the stimulus at a high frequency. It is also important for the implant to be customized for different brain sites, and thus, flexibility in modifying and scaling the basic design is important. Also, the long-term biocompatibility of materials used in the implant must be established. If microelectrodes are used, they must be mechanically durable in order to reach the target without being damaged during handling by the implant surgeon or during insertion into the brain. If the device includes microelectrodes for recording neuronal activity, they must retain the ability to record the activity for many years. Uniformity of performance across the microelectrodes in a particular array and across arrays is important, and as such, measures of performance should be standardized. An additional benefit would be the inclusion of VLSI (very large scale integrated) circuit components for on-chip signal processing and channel multiplexing.

Major targets for treatment of the motor symptoms of PD are the GPi and the STN [1, 40, 47, 67, 120, 121, 133]. In the topographic organization of the mammalian STN (Fig. 3), the dorsolateral half of the STN is believed to be dedicated to motor functions [44], and presumably, it is this subdivision that the arrays should access in order to ameliorate the symptoms of movement disorders. In a clinical device, microelectrode shanks 8–10 mm in length would be sufficient to place multiple electrode sites along the dorsolateral–ventromedial span of the STN, and also, in the structures dorsolateral of the STN proper, where electrical stimulation often produces the greatest relief of the symptoms of PD. If the array is inserted into the human STN approximately along the long axis of the nucleus, via an approach lateral to the caudate nucleus and the fourth ventricle, then the array should ideally include multiple shanks encompassing a footprint 4 mm in diameter to allow for a positioning tolerance of at least 1 mm, which is consistent with the best techniques for targeting the existing clinical arrays into the human STN [121, 130]. However, the potential benefits that such a device would afford must be weighed against the risk of inducing vascular injury and interstitial hemorrhages, and thus, presenting difficult technical challenges in designing such a volume-filling array. Perhaps a prudent strategy for introducing a new technology into clinical use would be to proceed in a staged manner: (1) Begin with an array of approximately the same physical dimensions, and with all of the capabilities of the devices now in clinical use, while also introducing some capabilities for localized microstimulation and for recording of neuronal activity at multiple sites within the nucleus. (2) If these novel capabilities are shown to provide increased clinical benefit over the extant devices, then arrays of greater diameter and with additional microelectrodes

could be introduced in a staged manner, while carefully monitoring for an increase of vascular damage during implantation. This approach would also encourage the development of arrays that can deploy a large number of electrode sites from a slender "introducer" into a large volume of tissue.

An intermediary step might be a hybrid macro- and microelectrode array – basically identical to those now in clinical use (e.g., Fig. 2(a)), but with microelectrodes (for recording of neuronal activity) placed on the carrier adjacent to the existing macroelectrodes (for stimulation). This approach has an advantage of affording the stimulation functionality and programmability of the existing device, as well as adding recording capability from the microelectrodes in the same array. This design might also improve the accuracy of final placement of the macroelectrodes following the initial targeting procedure using separate microelectrodes (Section 3.6). However, it is likely that tissue damage adjacent to the single large shank would be too great for the microelectrodes to record the activity of individual or even small groups of neurons. Additionally, an initial targeting procedure with separate microelectrodes may still be necessary.

The characteristics of macroelectrodes and microelectrodes are summarized in Table 1.

Table 1 Comparison of macroelectrodes and microelectrodes for DBS applications

Issues	Macroelectrodes	Microelectrodes
Dual stimulation and recording	No	Yes
Stimulation spread	Large	Small
Stimulation spatial resolution	Low	High
Recording spatial resolution	Poor	High
Target identification by intraoperative recording	No	Yes
Closed-loop implementation	Less likely	Likely
Number of channels	Low	High
Channel number scalability	Low	High
Ease of design change	Medium	High
Long-term viability	Good	Medium
Batch processing	Low	High

3.2 Fabrication Technology and Materials

3.2.1 Substrates

There have been many efforts to develop implantable microelectrodes based on microwires and on silicon substrates. These include designs with a single stimulating (or recording) site per shank, including microwire-based microelectrodes, and those with multiple sites per shank, including most of the designs based on photolithographic technologies (see reviews in [22, 104, 127]). Typical microelectrode systems have three main components: a substrate (the "carrier"), a conductive metal layer, and insulation material. (The substrate and metal layer

would be the same in the case of microwire-based microelectrodes.) A 200-μm-diameter electrolytically sharpened tungsten microwire has been used in the hippocampus during intraoperative recordings in epileptic patients [58]. Platinum–iridium microelectrodes have been used intraoperatively in the human GPi and STN for targeting the therapeutic electrode and also for somatotopic mapping of these structures [121, 133]. Bundles of 40-μm microwires were implanted in the human hippocampus in endogenous potential recordings [46] and recording from "place cells" in the hippocampus [32]. McCreery et al. have developed an array of 75-μm-diameter iridium microwires for recording and microstimulation in the feline STN. These have been implanted for up to 415 days (Fig. 4(a)) [83]. The iridium oxide electrode site areas varied from 500 μm^2 to 2,000 μm^2 in an array of sixteen 75-μm-diameter iridium microwires. As in most microwire-based devices, there is a single electrode site at the tip of each shank, which limits the number of active electrode sites. However, Ulbert et al. have developed a "linear" array with a single shank containing a row of platinum–iridium sites, with polyimide as insulation, which has been used in human neocortex [146].

The microwire array's utility as a clinical and experimental device might be enhanced by substituting some or all of the discrete microwire-based electrodes with multisite silicon-substrate arrays. This would distribute more electrode sites along the array's long axis while also reducing the number of electrode shanks, thereby reducing the risk of tissue damage and hemorrhages. This approach could also greatly facilitate fabrication through the use of batch-processed components. There have been few animal studies utilizing silicon-based arrays for DBS. However, when considering the requirements for the next generation of DBS, microelectrodes based on semiconductor processing technology are probably the best candidates. Many laboratories are developing silicon arrays for eventual clinical application, and some potentially could be utilized for DBS with appropriate modifications, although, to date, only one device of this genre, the "Utah array," implanted into the cerebral cortex, has undergone clinical trials [145]. There are various substrates upon which batch-processed multisite microelectrodes are patterned, including silicon [16, 21, 29, 33, 36, 62, 107, 108, 124, 132, 138, 154], silicon-on-insulator [23, 34, 50, 63], polymer [2, 73, 123, 126, 135, 136], ceramic [98, 110], and metal [97]. All are fabricated using photolithography technology, and most of the microelectrode arrays have multiple microelectrode sites per shank/tines [16, 21, 23, 29, 33, 34, 62, 63, 64, 66, 73, 97, 107, 108, 132, 154]. Movable [100] and double-sided [135, 136] probes have also been reported.

Two of the best-known microelectrodes fabricated by batch processes are from the University of Michigan (conventionally described as "Michigan arrays," Fig. 4(b)) [151], and the University of Utah (the "Utah array," Fig. 4(c)) [54, 105, 106]. Both these devices utilize silicon heavily doped with boron. In the case of the "Utah arrays," this is used to achieve low resistivity for the electrodes' conductive core, while in the "Michigan array" the doping acts as an etch stop by which the probe's shape is realized. The "Michigan array" has a

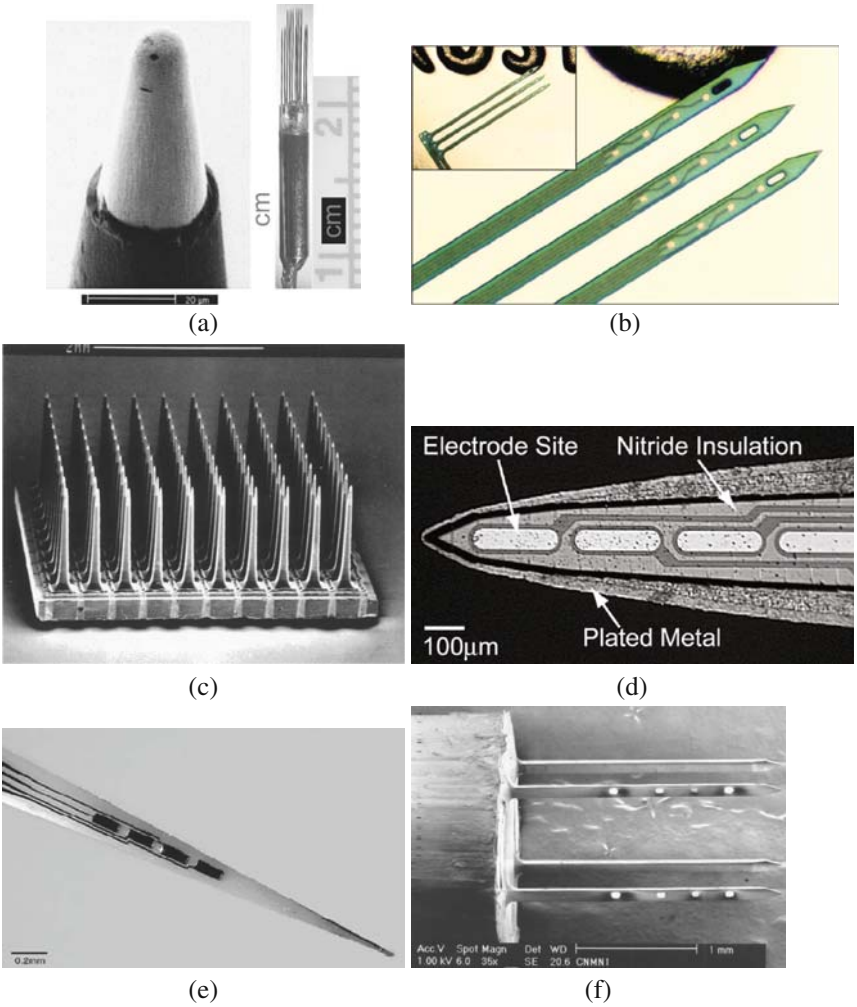

Fig. 4 Examples of microelectrode arrays based on various substrate platforms. (a) Microwire-based DBS array with 16 microelectrodes, developed at HMRI, and an enlarged view of a single-microelectrode tip [83]. (b) Silicon-based "Michigan" array with three shanks, each with four microelectrodes, placed next to a U.S. penny [150]. (c) Silicon-based "Utah" array, with an array of 10 × 10 microelectrode arrays [106]. (d) Metal-based, single-shank microelectrode array [97]. (e) Ceramic-based, single-shank microelectrodes [18]. (f) Silicon-based, four-shank, 16-channel chronic array with iridium oxide microelectrodes, fabricated from silicon-on-insulator wafers, developed at HMRI [51]

major limitation for deep brain applications, and especially for future clinical applications. The probe shape is defined by a boron-diffusion etch-stop process, which allows them to be released from the parent wafer in a wet etchant, improving the efficiency of batch processing but also effectively limiting the

probe thickness to approximately 15 μm. (The maximum diffusion depth of the boron is dependent on the probe width and operation time.) This markedly limits the mechanical strength and rigidity of the probe shanks, and probes with a high aspect ratio (length-to-width) can bend and veer off course as they are inserted into the tissue. Such probes might be implanted with the aid of special implantation techniques, including retractable introducers, but this would be difficult to adapt to an array with multiple shanks. The arrays are commercially available through NeuroNexus Technologies, Ann Arbor, MI [101]. The "Utah array," currently in pilot human trials, uses a rather unconventional method of saw-dicing in order to shape the 100 probe shanks of a 10 × 10 array. The process is followed by a combination of isotropic and anisotropic wet etching to form well-controlled electrode tip shapes. One consequence of using the saw-dicing technique is that the length of the electrode shanks is determined by the thickness of the silicon wafer, currently 1.0–1.5 mm. This is obviously too shallow to reach deep brain targets, even in small animal models. Furthermore, there is only one electrode per shank which limits flexibility in spanning a range of depths within the target. The arrays are commercially available through Cyberkinetics Neurotechnology Systems, Inc., Foxborough, MA [30].

Motta et al. have developed metal-based arrays for DBS in small animals, using a combination of photolithography and electroplating, as shown in Fig. 4(d) [97]. Their single-shank probe is 22 mm in length and tapers from 300 μm in width and 100 μm in thickness. The length of the probe shank is sufficient to reach the STN in rats. While the probe has a tapered metal tip, the electroplated metal (nickel) must be overcoated with a biocompatible material, and the physical dimension of the probe may be more difficult to control than for devices fabricated entirely by photolithography. Chen et al. developed an 11-mm-long silicon-based probe that was shaped by a YAG laser and has been implanted for mapping of evoked potentials in the rat thalamus [21]. Moxon et al. developed a ceramic (alumina)-based multisite array 7 mm in length, which is mechanically stronger than a silicon probe of similar dimensions (Fig. 4(e)) [98]. Although most of the processing is done by photolithography, each probe device is cut serially using a laser. Arrays based on silicon-on-insulator (SOI) have also been developed [65, 103], and these are based on two silicon wafers bonded with an oxide layer between them. This allows for a highly reproducible probe thickness of up to several hundred microns and does not require the use of boron-doped silicon as an etch stop as is done with the Michigan arrays. A limitation of the SOI-approach has been the lack of reliable ways to shape the probe tip after deep reactive ion etching (DRIE), which typically results in a chisel-shaped profile that is likely to inflict excessive tissue injury during insertion. Han et al. established a new reliable way of shaping the tip region following DRIE using mechanical grinding which yields tips that taper to a point with desired thicknesses (Fig. 4(f)) [50, 51].

Most silicon-based technologies will allow fabrication of probes with multiple stimulation and recording sites on each shank, whereas the microwire and Utah arrays have only one site per shank. Although it is generally believed that

the microwire-based microelectrodes perform better for long-term recording of single-unit neuronal activity, the overall performance of multisite-per-shank probes has improved [64, 147]. McCreery et al. implanted this type of stimulating electrode into the cochlear nucleus of cats for up to 314 days and reported that the thresholds of the neuronal responses evoked in the cochlear nucleus by these implants were similar to those evoked by iridium microwire electrodes implanted chronically in the same target [82]. In addition, these devices allow placement of electrode sites at different depths within the target, an important advantage in DBS applications which include recording neuronal activity.

In a device intended for clinical use, the problems that may arise from the fragility of the silicon-substrate arrays must be evaluated carefully. Young's modulus of single-crystal silicon is comparable to that of stainless steel [113]. However, when fabricated in the dimensions of typical microelectrodes, added with dopants (e.g., boron), and/or include stressed insulation layers, the microelectrode shanks can be fragile. It may be possible for the multi-shank microelectrode arrays to be guided through an introducer to the immediate vicinity of the deep brain target, with long, flexible cables leading out of the brain so that the fragile array shanks only need to penetrate through a few millimeters of brain tissue. Such a method has been successfully employed by McCreery et al. in a study of eight cats for up to 415 days in vivo [83], in which minimal inflammatory tissue responses have been observed near the microwire microelectrodes and the assembly superstructures. With this type of introducer it is likely that the greatest chance of damage to the fragile shanks would be during handling by the surgeon and support personnel (e.g., while loading the array into the introducer). This problem might be mitigated by an improved introducer in which the array is loaded into the tool while enclosed within its own protective capsule. The tips of the silicon shanks also can be modified to require less insertion force during tissue penetration, and the sharp corners of the probes, which tend to be a point of high mechanical stress and breakage, can be eliminated by proper design. If a shank of any material (e.g., silicon, ceramic or metal) should subsequently fracture while within the patient's brain, the array would sustain some loss of functionality which would be proportionately less for an array of many individual shanks. If the array had to be removed as the result of a brain abscess or a hypersensitivity response to one of the constituent materials, the fractured shank would remain in the brain, surrounded by its thin glia capsule. There is little evidence that the continued presence of such a tiny and untethered object would be deleterious (assuming of course that the patient's untoward reaction that necessitated removal of the array is not to the materials comprising the shank itself).

3.2.2 Electrode Materials

The charge capacity of commonly used platinum and platinum alloys for pulsatile stimulation ranges from about 50 $\mu C/cm^2$ to an absolute maximum of 300 $\mu C/cm^2$, for various stimulating conditions and electrodes biases [28, 122].

These charge injection limits render it unsuitable for very small stimulating electrodes, and especially microelectrodes that must operate at higher charge density. Iridium oxide (IrO_x) has been more widely accepted for microstimulation as it has an enhanced ability to inject charge by fast, reversible "faradaic" (oxidation–reduction) reactions. During pulsing, the oxide can transfer charge across the metal–tissue interface by a proton electronation reaction [8, 118]. A related feature of IrO_x is its extremely low rate of dissolution even at relatively high charge density, making it suitable for long-term stimulation at a high charge density and high pulsing rate. The impedance of IrO_x microelectrodes is also low, which is a desirable property for recording neuronal activity, since the associated thermal noise is reduced.

IrOx can be deposited by several methods: electrochemical activation of pure iridium, electroplating in a chemical bath, and reactive sputtering in vacuum deposition systems. Activated IrO_x can be formed on bulk iridium metal by potentiodynamic cycling (AIROF). McCreery et al. have used microwire-based AIROF to safely excite the neurons of the feline STN during a regimen of prolonged stimulation [83]. A stimulus of approximately 4 nC/ph (equivalent to 26.4 μA biphasic current pulses 150 μs/ph in duration) was sufficient to directly excite the neurons of the feline STN. Also, a method of electrodepositing iridium oxide (EIROF) onto gold, platinum, or platinum/iridium alloys has been demonstrated [51, 93]. Whereas both the AIROF and the EIROF employ electrolytic media as their main mechanism of formation of IrOx, the sputtered iridium oxide film (SIROF) utilizes semiconductor vacuum system-based processes, allowing for well-controlled batch deposition of films onto multiple sites, at the wafer-level as well as onto individual electrodes. Physical sputtering of metal targets by inert ionized gas (e.g., argon), coupled with reaction with reactive gases, forms SIROF, which may exhibit better stability and better charge-injection capabilities than AIROF during prolonged pulsing [27, 131]. These films strongly adhere to the metal substrate especially when the deposition of the SIROF is preceded by a pre-etch step, which can clean the substrate surface prior to deposition without breaking the vacuum. However, a post-application treatment (activation) of SIROF may be needed to maximize charge injection [149]. EIROF is attractive in certain applications because it can be electroplated onto the electrode sites, and thus, avoids the two-step process of iridium metal sputtering and electrochemical activation needed to form AIROF and SIROF.

There is still some uncertainty regarding the maximum reversible charge density that can be supported by AIROF in vivo without degradation of the oxide, and this is complicated further by the inhomogeneous charge distribution at the surface of most stimulating electrodes. At charge densities of 3,000 $\mu C/cm^2$, histology revealed iridium-containing deposits in tissue adjacent to the electrode sites, and scanning electron microscopy of explanted electrodes revealed a thickened and poorly adherent AIROF coating [26]. Microelectrodes pulsed at 2,000 $\mu C/cm^2$ or less remained intact with no histologic evidence of non-biologic deposits in the tissue, although the voltage transient was greater

than ± 1 volt, suggesting that some of the charge injection was by irreversible reactions that may have induced tissue injury. In the cat STN, tissue damage was found near the tips of AIROF electrodes which were pulsed at 4 nC/ph and at a charge density of 800 $\mu C/cm^2$ for 7 h per day for 5 days [83].

The charge-injection capacity of AIROF and EIROF can be increased by placing an anodic bias on the electrode. A particular advantage of anodic bias with iridium oxide is that by resetting the electrode potential within the interpulse period, it avoids the need for stringent charge balance in the cathodal and anodal phases of the pulse, which can be difficult to achieve even with advanced stimulators. Generally, the electrode–tissue interface impedances of stimulating microelectrodes are greater than those of macroelectrodes, and thus, for comparable charge injection, microelectrodes exhibit higher compliance/driving voltages (IR drop + polarization voltage of electrodes) and greater power consumptions. However, with the continued development of more efficient microelectrode materials with higher charge-injection capacities, such as SIROF [27], and the lower stimulus charge requirements of the more precisely targeted microstimulation, it is possible that requirements on the battery may not be much greater than in the existing DBS devices.

3.3 Stimulation Parameters and Requirements of a Clinical System

Compared to macroelectrodes, a clinical DBS system based on an array of microelectrodes could achieve more localized stimulation, with the potential for fewer side effects. However, the device must demonstrate that it can deliver the stimulation for many years. In the case of DBS in the STN, it must deliver the stimulus pulses for many hours each day, at a relatively high pulse rate (135–185 Hz). The effect of prolonged exposure to the extracellular fluid of the brain on the performance of activated iridium has not been investigated thoroughly. Thus, even the conservative charge density of 400 $\mu C/cm^2$ for iridium oxide (and the corresponding charge density values for other materials) must be validated for the demanding pulsing regimens used in DBS for PD, while the extended lifetime of a clinical device will impose additional requirements. Stimulating with a single microelectrode would yield a highly localized stimulus, and two or more microelectrodes could be pulsed simultaneously or sequentially to activate neurons within a somewhat greater, but still well-controlled volume of tissue. The ability to precisely control the spatial pattern of the electrical stimulation by superposition of the stimuli from multiple electrodes pulsed simultaneously (variously described as “current steering” or “stimulus sculpting”) certainly will be valuable in experimental studies of DBS in animal models and may emerge as an important feature of future clinical devices.

However, such functional flexibility is certain to compound the difficulty of selecting the most effective stimulation parameters, which can be a daunting

task even with the devices now in clinical use, which employ only four macroelectrodes [71]. In addition, there are issues that are unique to microelectrodes, including the fact that the charge and current densities are very high at the surface of the electrodes and in the tissue very close to the electrodes. Thus, it is especially important to carefully calibrate the stimulus parameters. A better understanding of physiological mechanisms underlying therapeutic DBS should better inform the selection of stimulus parameters.

3.4 Stimulation Safety and Tissue Response

It is well established that any material that the brain perceives as foreign triggers cascading inflammatory responses even when microelectrodes are relatively small and composed of biocompatible materials [13, 129]. In an application such as DBS, there is the additional requirement that the electrical stimulus not inflict tissue injury. It is also essential that safe stimulation limits are established not only for each microelectrode material but also for each of the various sites within the brain where microstimulation will be applied. A therapeutic window for both clinical efficacy and safety must be found within these constraints. However, the safety issues attendant to the combination of relatively high charge density and charge per phase (400 $\mu C/cm^2$ and 0.04 $\mu C/ph$), as well as the high stimulation rate (135 –185 Hz) used for therapeutic DBS in the STN, are only beginning to be investigated.

The threshold for exciting neurons in the feline STN was lower than 1 nC/ph for chronically implanted iridium microelectrodes employed by McCreery et al. [83]. The authors then determined the histologic effects of prolonged intranuclear microstimulation using suprathreshold stimulation. In each of three cats, a subset of chronically implanted microelectrodes was pulsed for 7 h per day on five successive days. Since high-frequency stimulation in the STN has been shown to most effectively ameliorate the symptoms of PD, a stimulus pulse rate of 100 Hz was used. A range of active electrode surface areas was used in these animals, and therefore, the stimulus charge per phase was invariant; however, the charge density at the surface of the electrodes differed. The authors observed dense aggregates of inflammatory cells (probably macrophages) around the tips of microelectrodes pulsed with a charge density of 800 $\mu C/cm^2$ at 4 nC/ph (Fig. 5(b)), but not at 400 $\mu C/cm^2$ and 4 nC/ph or below (Fig. 5(a)). This is similar to what was observed around pulsed microelectrodes implanted in the feline spinal cord [84] and in the cerebral cortex. The occurrence of the aggregates of inflammatory cells appears to be most closely related to the stimulus charge density. While the significance of these cellular aggregates to the viability and functionality of the neural substrate is unclear, a conservative criterion for safety of electrical stimulation is preferred, and thus, the stimulus should induce no histologically detectable changes in the tissue, and the limit for safe microstimulation in the feline STN appears to lie between

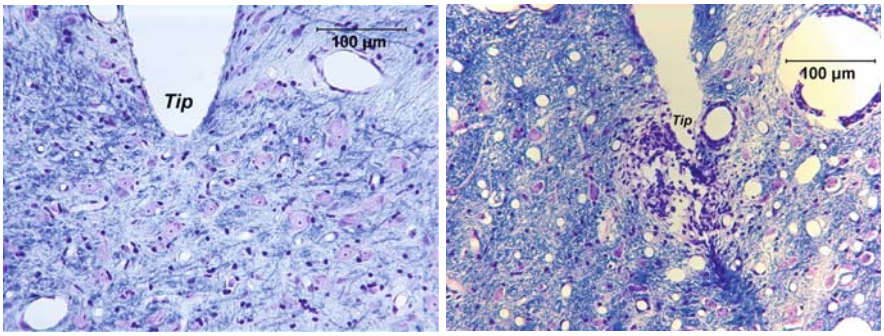

Fig. 5 Histological sections near the microelectrode tip sites following five consecutive days of stimulation for 7 h a day, with 4 nC per phase at 100 Hz at charge densities of: (**a**) 200 μC per cm^2 and (**b**) 800 μC per cm^2 [83]

400 and 800 μC/cm^2 at 4 nC/ph. (In the feline cerebral cortex, charge density and charge per phase interact synergistically to determine the threshold for tissue injury [85].) A stimulus of 4 nC/ph (26.4 μA biphasic current pulses, 150 μs/ph in duration) was sufficient to directly excite the neurons of the feline STN, and also modulated the activity of these neurons over a considerable distance within the STN, possibly by excitation of afferent axons that make synapses upon the neurons of the STN. It is yet to be determined if this somewhat widely distributed transsynaptic effect of the intra-nuclear microstimulation would be useful in the clinical treatment of movement disorders, or more generally, what might be the clinical role of highly localized microstimulation in the treatment of movement disorders. Nevertheless, the authors have demonstrated that prolonged, high-rate microstimulation can be applied in the STN without histologically detectable injury to the adjacent neurons and neuropil.

There remains the question of whether the microelectrodes would provide sufficient charge-injection capacity to produce the desired clinical effects. In a clinical device, the stimulating sites should be capable of safely injecting a charge of at least 20 nC/ph. Rodriguez et al. reported that intraoperative microstimulation in the human STN at 100 μA and with a 200 μs pulse duration (20 nC/ph) arrested tremor in a specific part of a patient's body (e.g., the foot) [119, 120]. Ideally, the relation between the spacing of the stimulating sites and their maximum safe charge per phase should be such that the clinically relevant neurons within and around the array's entire perimeter can be excited. For each of the targets of clinical DBS, it is not clear which neurons must be activated (or suppressed) to achieve the desired clinical effects, and their current–distance constants are also yet to be determined. However, if the neurons' current–distance constant is no greater than 600 μA/mm^2, a value that is typical of the larger neurons and myelinated axons of the mammalian CNS [141], then a stimulus pulse of 100 μA (20 nC/ph with a 200 μs pulse duration) would excite

neurons up to 400 μm from the electrode site. A charge of 40 nC/ph would reach even further, and would afford greater opportunities for sculpted stimulation, using the superimposed current field from a set of adjacent electrodes that are pulsed simultaneously. The optimal surface areas of the microelectrodes sites are yet to be determined, but a geometric area of 10,000 μm^2 would limit the charge density, at 40 nC/ph, to 400 $\mu C/cm^2$, which does not appear to be injurious to cat subthalamic neurons [83]. Sputtered iridium oxide film (SIROF) is reported to be capable of supporting a charge density in excess of 400 $\mu C/cm^2$ during prolonged pulsing in vitro [27]. However, in the study of McCreery et al. [83], the charge per phase used was relatively low (4 nC/ph) and the duration of the stimulation was relatively short (5 days), and additional animal studies will be required in order to verify the safety of nearly continuous, high-rate stimulation at up to 40 nC/ph.

3.5 Closed-Loop Control of DBS

The current clinical DBS systems rely on the patients' clinical response to the stimulation during surgery to confirm that the array is properly positioned, and subsequently, to adjust the stimulus parameters to achieve optimal clinical benefit. In a closed-loop control of DBS, the stimulus would be automatically adjusted to produce neuronal responses that would serve as surrogate measures of clinical efficacy. In principle, this would optimize the efficacy of the DBS while reducing reliance upon the clinical technicians, and therefore, has the potential to improve the performance and patient acceptance of DBS. It is not clear that replacing the current therapeutic array with an array of stimulating and recording microelectrodes would significantly reduce the long surgery procedures, much of which is spent while the patient is fixed to the head frame. However, the time and expense of subsequent visits to the clinics in order to adjust the stimulus parameters might be substantially reduced by a self-adjusting closed-loop system. This may be especially true for Parkinson's disease in which the type and severity of the symptoms may vary greatly during a single day and progress over a longer timescale.

The many challenges for implementing a closed-loop system include the uncertainty surrounding the mechanism of therapeutic DBS, and thus precisely what state or changes in neuronal activity the DBS should attempt to produce. Other obstacles include improving the stability and long-term viability of recording neuronal activity, and developing efficient decoding algorithms and high performance computing that must be incorporated into the implantable stimulators. However, animal studies and intraoperative results from patients undergoing implantation of deep brain electrodes do suggest some of the ways by which a closed-loop system might be implemented. Rodrigues et al. [119] recorded tremor-related activity in the STN in 12 patients with PD and found that microstimulation of the sensorimotor region of the nucleus, where these

"tremor neurons" are present, arrested the tremor with a very short latency. In monkeys which had developed parkinsonism after injection of the neurotoxin MPTP (1-methyl-4-phenyl-1, 2, 3, 6-tetrahydropyridine), Meissner et al. showed that high-rate stimulation in the STN at sites that reduced contralateral rigidity also showed a reduction in the oscillatory activity of subthalamic neurons [91].

In the treatment of Parkinson's disease, there is evidence for both inhibitory and excitatory roles of high-frequency DBS in the STN, but the efficacy of high-rate stimulation suggests the importance of suppressing or disrupting abnormal neuronal activity that is responsible for the clinical symptoms [14, 15, 70, 88, 89]. Tass et al. proposed a feedback loop using demand-controlled, coordinated pacing of neuronal subpopulation to prevent onset of symptoms [140]. Clinical trials are also underway in similar efforts to test a closed-loop system for arresting the onset of epileptic seizure using electrical stimulation in the anterior nucleus of the thalamus, based on the detection of seizure onset by monitoring the EEG [90, 102].

3.6 Recording Capability and Long-Term Stability

A microelectrode array with numerous recording sites conveys the ability to monitor the activities of numerous individual or groups of neurons. It allows for sampling of neural activity at spatial scales from single cells to neural ensembles that is not possible with larger macroelectrodes or with non-invasive methods such as magnetic resonance imaging, electroencephalograms, and magnetoencephalograms. Intraoperative recording of neuronal activity is widely used as a means of improving the accuracy of targeting during stereotactic implantation of DBS electrodes [11, 20, 38, 57, 148]. Accurate electrode placement is enabled by well-characterized neural activities in different regions of STN and GPi and in the adjacent structures [20, 44, 133], and by the responses to the stimulus by the awake patients [1, 74, 121]. For example, neuronal activity in the STN in PD includes the most commonly recorded irregular (20–30 Hz) and tonic (as high as 200 Hz) discharge patterns found in the dorsolateral region of the nucleus (related to motor functions), and rhythmical cells discharging in slow burst (about 2 Hz) frequently found in the ventral region with no sensorimotor relations [44]. On the other hand, there have also been conflicting results regarding the effectiveness of targeting with recording microelectrodes. In a study involving 20 patients implanted with the Medtronics 3389 stimulating array, Cintas et al. found no correlation between the STN target, as defined by intraoperative microelectrode recording, and the location of stimulating macroelectrodes that ultimately yielded the most effective clinical treatment over a 3- or 6-month period [25]. The authors, however, noted a potentially mild intraoperative displacement of the STN caused by the simultaneous insertions of five microelectrodes, and they also conjectured that the therapeutic electrical stimulation may have spread beyond the STN as so defined, into the Forel field or the zona incerta. Although the value of

intraoperative recording for targeting may differ for the various brain sites and disease states for which DBS is employed, this could be another application for which multisite probes may be superior to, or at least more efficient than, the single-site microelectrodes which are currently used in most of the surgeries.

The ability to chronically monitor the neuronal activity near and within the target of the DBS may prove to be especially valuable for the implementation of a closed-loop system in which an effective therapeutic stimulus protocol is determined according to its effects on the activity of the nearby neurons. The realization of this type of closed-loop system for DBS will require microelectrodes that can record neuronal activity for many years. (It is generally believed that the microwire-based microelectrodes with a single recording site at the tip perform better for long-term recording of single-unit neuronal activity than the arrays with multiple sites distributed along their length.) The potential value of single-unit recording is illustrated by the work of Meissner et al. who used four recording microelectrodes during stimulation in the STN of monkeys made parkinsonian by injection of MPTP [91]. They showed that high-rate stimulation in the STN that effectively reduced contralateral rigidity also produced a reduction of both the oscillatory activity of individual subthalamic neurons and in the correlation of the activity of pairs of these neurons. McCreery et al. were able to record the action potentials of single neurons in and around the feline STN and GPi, with and without stimulation through the adjacent microelectrodes [83]. Spontaneous neural activity with signal-to-noise ratios (SNRs) of three or greater (S/N = mean peak spike amplitude/RMS noise amplitude) was obtained in 11 cats over a period of 220–340 days after array implantation. They also showed what appeared to be inhibitory neuronal interactions in the STN. When a stimulus was applied via a microelectrode in the medial margin of the STN, a recording microelectrode of the same array in the dorsal margin of the STN showed inhibition of neuronal activity that could be mediated by the (GABA-ergic) afferents from extrinsic sources, primarily from the external segment of the globus pallidus. However, while single cell recording provides information on neural coding, topographies, and tuning of neural response, it is challenging to track the same neurons over periods of months and years [75, 125], a capability that might be of greater importance in animal studies aimed at understanding the pathophysiology of disease states treatable by DBS and the neurophysiologic mechanisms of therapeutic DBS, rather than in a closed-loop clinical device.

One of the most challenging aspects of implantable recording microelectrodes is to maintain their functionality during prolonged implantation. Many studies have examined various factors that may contribute to the progressive degradation of their ability to record neuronal activity, including inflammatory tissue reaction [12, 31, 128, 139], failure of the device itself [125], increased impedance of the surrounding tissue [19], movement of the recording sites [80], tissue micromotion [42], and silencing of nearby neurons [75]. However, the manner in which these factors interact to produce degradation of the recorded signals is not clear, and there is a mismatch between the time course of some of the proposed mechanisms of failure and the degradation of neuronal recording.

For example, the development of reactive gliosis (during the first few weeks after implantation) that is believed to contribute to the progressive deterioration of the recording quality of neuronal activity by microelectrodes does not necessarily correspond to the time at which neural recordings are typically lost (generally over a period of months after implantation).

The experiences of recent decades have affirmed the considerable challenge of designing silicon-based microelectrode systems that are capable of surviving in an in vivo environment for many years. Since the advent of silicon-based arrays a few decades ago [151], only a handful of groups have achieved successful chronic implantation of these devices for either recording or stimulation in animal subjects for 1 year or longer [64, 82], and only one device has reached clinical trials [145]. With recent advances in materials and devices development, however, it is reasonable to expect that a reliable microelectrode-based clinical DBS device can be developed in the near future.

4 Conclusions

Microelectrodes, especially multisite silicon-based devices, have the promise of being the building blocks for the next generation of devices for DBS. At the same time, there are many challenges to overcome. The complexity of optimizing the stimulus, given the enormous range of stimulus parameters, will certainly require the participation of closed-loop systems, but it is far from clear how this capability should best be implemented. The safety and efficacy of the stimulation must be evaluated in animal models from the standpoint of the potential for stimulation-induced tissue injury and the integrity of the electrodes themselves during long-term pulsing, which may be nearly continuous and at high pulse rates. Fortunately, many of these technical issues are common to other efforts to develop neural prostheses and brain–machine interfaces employing implanted microelectrodes, and synergy between these efforts is likely to benefit all of these endeavors.

Acknowledgments The authors thank the technical and animal care staffs at HMRI, and Stuart Cogan at EIC Laboratories for his help with the EIROF process. Funding for the development of the silicon microelectrode array at HMRI was provided in parts by NIH contract NO1-DC-4-0005 and grant R01NS054121.

References

1. Abosch A, Hutchison WD, Saint-Cyr JA et al. (2002) Movement-related neurons of the subthalamic nucleus in patients with Parkinson disease. J Neurosurg 97(5): 1167–72
2. Adams C, Mathieson K, Gunning D et al. (2005) Development of flexible arrays for in vivo neuronal recording and stimulation. Nucl Instrum Methods Phys Res Sect A-Accel Spectrom Dect Assoc Equip 546(1–2): 154–159

3. Afsharpour S (1985) Topographical projections of the cerebral cortex to the subthalamic nucleus. J Comp Neurol 236(1): 14–28
4. Anderson T, Hu B, Pittman Q et al. (2004) Mechanisms of deep brain stimulation: an intracellular study in rat thalamus. J Physiol 559(Pt 1): 301–13
5. Anderson WS, Lenz FA (2006) Surgery insight: deep brain stimulation for movement disorders. Nat Clin Pract Neurol 2(6): 310–320
6. Ashkan K, Wallace B, Bell BA et al. (2004) Deep brain stimulation of the subthalamic nucleus in Parkinson's disease 1993–2003: where are we 10 years on? Br J Neurosurg 18(1): 19–34
7. Beckstead RM (1983) A reciprocal axonal connection between the subthalamic nucleus and the neostriatum in the cat. Brain Res 275(1): 137–42
8. Beebe X, Rose TL (1988) Charge injection limits of activated iridium oxide electrodes with 0.2 ms pulses in bicarbonate buffered saline. IEEE Trans Biomed Eng 35(6): 494–495
9. Benabid AL (2003) Deep brain stimulation for Parkinson's disease. Curr Opin Neurobiol 13(6): 696–706
10. Benabid AL, Koudsie A, Benazzouz A et al. (2002) Imaging of subthalamic nucleus and ventralis intermedius of the thalamus. Mov Disord 17(Suppl 3): S123–9.
11. Benazzouz A, Breit S, Koudsie A et al. (2002) Intraoperative microrecordings of the subthalamic nucleus in Parkinson's disease. Mov Disord 17: S145–S149
12. Biran R, Martin DC, Tresco PA (2005) Neuronal cell loss accompanies the brain tissue response to chronically implanted silicon microelectrode arrays. Exp Neurol 195(1): 115–126
13. Biran R, Noble MD, Tresco PA (1999) Characterization of cortical astrocytes on materials of differing surface chemistry. J Biomed Mater Res 46(2): 150–9
14. Birdno MJ, Cooper SE, Rezai AR et al. (2007) Pulse-to-pulse changes in the frequency of deep brain stimulation affect tremor and modeled neuronal activity. J Neurophysiol 98(3): 1675–84
15. Birdno MJ, Grill WM (2008) Mechanisms of deep brain stimulation in movement disorders as revealed by changes in stimulus frequency. Neurotherapeutics 5(1): 14–25
16. Blanche TJ, Spacek MA, Hetke JF et al. (2005) Polytrodes: High-density silicon electrode arrays for large-scale multiunit recording. J Neurophysiol 93(5): 2987–3000
17. Breit S, Schulz JB, Benabid AL (2004) Deep brain stimulation. Cell and Tissue Res 318(1): 275–288
18. Burmeister JJ, Pomerleau F, Palmer M et al. (2002) Improved ceramic-based multisite microelectrode for rapid measurements of L-glutamate in the CNS. J Neurosci Methods 119(2): 163–171
19. Butson CR, Maks CB, McIntyre CC (2006) Sources and effects of electrode impedance during deep brain stimulation. Clin Neurophysiol 117(2): 447–454
20. Chen SY, Lee CC, Lin SH et al. (2006) Microelectrode recording can be a good adjunct in magnetic resonance image-directed subthalamic nucleus deep brain stimulation for parkinsonism. Surg Neurol 65(3): 253–261
21. Chen YY, Kuo TS, Jaw FS (2004) A laser micromachined probe for recording multiple field potentials in the thalamus. J Neurosci Methods 139(1): 99–109
22. Cheung KC (2007) Implantable microscale neural *interfaces*. Biomed. Microdevices 9(6): 923–938
23. Cheung KC, Djupsund K, Dan Y et al. (2003) Implantable Multichannel Electrode Array Based on SOI Technology. J Microelectromech Syst 12(2): 179–184
24. Chou KL, Hurtig HI, Jaggi JL et al. (2005) Bilateral subthalamic nucleus deep brain stimulation in a patient with cervical dystonia and essential tremor. Mov Disord 20(3): 377–380
25. Cintas P, Simonetta-Moreau M, Ory F et al. (2003) Deep brain stimulation for Parkinson's disease: Correlation between Intraoperative subthalamic nucleus neurophysiology and most effective contacts. Stereotact Funct Neurosurg 80(1–4): 108–113

26. Cogan SF, Guzelian AA, Agnew WF et al. (2004) Over-pulsing degrades activated iridium oxide films used for intracortical neural stimulation. J Neurosci Methods 137(2): 141–150
27. Cogan SF, Plante TD, Ehrlich J (2004) Sputtered iridium oxide films (SIROFs) for low-impedance neural stimulation and recording electrodes. Pro. 26th Ann Int Conf of the IEEE EMBS (San Francisco, CA)
28. Cogan SF, Troyk PR, Ehrlich J et al. (2005) In vitro comparison of the charge-injection limits of activated iridium oxide (AIROF) and platinum-iridium microelectrodes. IEEE Trans Biomed Eng 52(9): 1612–4.
29. Cui X, Wiler J, Dzaman M et al. (2003) In vivo studies of polypyrrole/peptide coated neural probes. Biomaterials 24: 777–787
30. Cyberkinetics Neurotechnology Systems Inc. (2008). http://www.cyberkineticsinc.com. Accessed 4 October 2008
31. Edell DJ, Toi VV, McNeil VM et al. (1992) Factors Influencing the Biocompatibility of Insertable Silicon Microshafts in Cerebral-Cortex. IEEE Trans Biomed Eng 39(6): 635–643
32. Ekstrom AD, Kahana MJ, Caplan JB et al. (2003) Cellular networks underlying human spatial navigation. Nature 425(6954): 184–187
33. Ensell G, Banks DJ, Ewins DJ et al. (1996) Silicon-Based Microelectrodes for Neurophysiology Fabrication Using a Gold Metallization/Nitride Passivation System. J Microelectromech Syst 5(2): 117–121
34. Ensell G, Banks DJ, Richards PR et al. (2000) Silicon-based microelectrodes for neurophysiology, micromachined from silicon-on-insulator wafers. Med Biol Eng Comput 38(2): 175–179
35. Finelli DA, Rezai AR, Ruggieri PM et al. (2002) MR imaging-related heating of deep brain stimulation electrodes: In vitro study. Am J Neuroradiol 23(10): 1795–1802
36. Fofonoff TA, Martel SM, Hatsopoulos NG et al. (2004) Microelectrode array fabrication by electrical discharge machining and chemical etching. IEEE Trans Biomed Eng 51(6): 890–895
37. Garcia L, D'Alessandro G, Bioulac B et al. (2005) High-frequency stimulation in Parkinson's disease: more or less? Trends Neurosci 28(4): 209–216
38. Garonzik IM, Hua SE, Ohara S et al. (2002) Intraoperative microelectrode and semimicroelectrode recording during the physiological localization of the thalamic nucleus ventral intermediate. Mov Disord 17: S135–S144
39. George MS, Nahas Z, Borckardt JJ et al. (2007) Brain stimulation for the treatment of psychiatric disorders. Curr Opin Psychiatry 20(3): 250–4
40. Ghika J, Villemure JG, Fankhauser H et al. (1998) Efficiency and safety of bilateral contemporaneous pallidal stimulation (deep brain stimulation) in levodopa-responsive patients with Parkinson's disease with severe motor fluctuations: a 2-year follow-up review. J Neurosurg 89(5): 713–718
41. Giacobbe P, Kennedy SH (2006) Deep brain stimulation for treatment-resistant depression: a psychiatric perspective. Curr Psychiatry Rep 8(6): 437–44
42. Gilletti A, Muthuswamy J (2006) Brain micromotion around implants in the rodent somatosensory cortex. J Neural Eng 3: 189–195
43. Godinho F, Thobois S, Magnin M et al. (2006) Subthalamic nucleus stimulation in Parkinson's disease : anatomical and electrophysiological localization of active contacts. J Neurol 253(10): 1347–55
44. Guridi J, Rodriguez-Oroz MC, Lozano AM et al. (2000) Targeting the basal ganglia for deep brain stimulation in Parkinson's disease. Neurology 55(12): S21–S28
45. Haber SN, Lynd-Balta E, Mitchell SJ (1993) The organization of the descending ventral pallidal projections in the monkey. J Comp Neurol 329(1): 111–28
46. Halgren E, Babb TL, Crandall PH (1978) Activity of Human Hippocampal Formation and Amygdala Neurons During Memory Testing. Electroencephalogr Clin Neurophysiol 45(5): 585–601

47. Hamani C, Saint-Cyr JA, Fraser J et al. (2004) The subthalamic nucleus in the context of movement disorders. Brain 127(Pt 1): 4–20
48. Hamel W, Fietzek U, Morsnowski A et al. (2003) Subthalamic nucleus stimulation in Parkinson's disease: correlation of active electrode contacts with intraoperative microrecordings. Stereotact Funct Neurosurg 80(1–4): 37–42.
49. Hamel W, Herzog J, Kopper F et al. (2007) Deep brain stimulation in the subthalamic area is more effective than nucleus ventralis intermedius stimulation for bilateral intention tremor. Acta Neurochirurgica 149(8): 749–758
50. Han M, Bullara LA, McCreery DB (2007) Development of a Robust Chronic Neural Probe. Proc Biomed Eng Soc Ann Fall Meeting, Los Angeles, CA. Program No. P2.146
51. Han M, McCreery DB (2008) A New Chronic Neural Probe with Electroplated Iridium Oxide Electrodes. Proc Ann Int Conf of the IEEE Eng Med Biol Soc, Vancouver, Canada. 4220–4221
52. Hardesty DE, Sackeim HA (2007) Deep brain stimulation in movement and psychiatric disorders. Biol Psychiatry 61(7): 831–5
53. Herzog J, Fietzek U, Hamel W et al. (2004) Most effective stimulation site in subthalamic deep brain stimulation for Parkinson's disease. Mov Disord 19(9): 1050–4
54. Hochberg LR, Serruya MD, Friehs GM et al. (2006) Neuronal ensemble control of prosthetic devices by a human with tetraplegia. Nature 442(7099): 164–171
55. Holtzheimer PE, 3rd, Nemeroff CB (2006) Emerging treatments for depression. Expert Opin Pharmacother 7(17): 2323–39
56. Howland RH (2008) Neurosurgical approaches to therapeutic brain stimulation for treatment-resistant depression. J Psychosoc Nurs Ment Health Serv 46(4): 15–9
57. Hutchison WD, Allan RJ, Opitz H et al. (1998) Neurophysiological identification of the subthalamic nucleus in surgery for Parkinson's disease. Annals of Neurology 44(4): 622–628
58. Ishijima B, Hori T, Yoshimasu N et al. (1975) Neuronal Activities in Human Epileptic Foci and Surrounding Areas. Electroencephalogr Clin Neurophysiol 39(6): 643–650
59. Johansen-Berg H, Gutman DA, Behrens TE et al. (2008) Anatomical connectivity of the subgenual cingulate region targeted with deep brain stimulation for treatment-resistant depression. Cereb Cortex 18(6): 1374–83
60. Kennedy SH, Giacobbe P (2007) Treatment resistant depression – advances in somatic therapies. Ann Clin Psychiatry 19(4): 279–87
61. Kern DS, Kumar R (2007) Deep brain stimulation. Neurologist 13(5): 237–252
62. Kewley DT, Hills MD, Borkholder DA et al. (1997) Plasma-etched neural probes. Sens Actuator A-Phys 58(1): 27–35
63. Kindlundh M, Norlin P, Hofmann UG (2004) A neural probe process enabling variable electrode configurations. Sens Actuator B-Chem 102(1): 51–58
64. Kipke DR, Vetter RJ, Williams JC et al. (2003) Silicon-substrate intracortical microelectrode arrays for long-term recording of neuronal spike activity in cerebral cortex. IEEE Trans Neural Syst Rehabil Eng 11(2): 151–155
65. Kisban S, Herwik S, Seidl K et al. (2007) Microprobe Array with Low Impedance Electrodes and Highly Flexible Polyimide Cables for Acute Neural Recording. 29th Ann Int Conf IEEE EMBS, Lyon, France.
66. Kovacs GT, Storment CW, Halks-Miller M et al. (1994) Silicon-substrate microelectrode arrays for parallel recording of neural activity in peripheral and cranial nerves. IEEE Trans Biomed Eng 41(6): 567–77
67. Krack P, Batir A, Van Blercom N et al. (2003) Five-year follow-up of bilateral stimulation of the subthalamic nucleus in advanced Parkinson's disease. New England Journal of Medicine 349(20): 1925–1934
68. Krauss JK, Yianni J, Loher TJ et al. (2004) Deep brain stimulation for dystonia. J Clin Neurophysiol 21(1): 18–30
69. Kringelbach ML, Jenkinson N, Owen SLF et al. (2007) Translational principles of deep brain stimulation. Nat Rev Neurosci 8(8): 623–635

70. Kuncel AM, Cooper SE, Wolgamuth BR et al. (2007) Amplitude- and frequency-dependent changes in neuronal regularity parallel changes in tremor With thalamic deep brain stimulation. IEEE Trans Neural Syst Rehabil Eng 15(2): 190–7
71. Kuncel AM, Grill WM (2004) Selection of stimulus parameters for deep brain stimulation. Clin Neurophysiol 115(11): 2431–41
72. Larson PS (2008) Deep brain stimulation for psychiatric disorders. Neurotherapeutics 5(1): 50–8
73. Lee KK, He JP, Singh A et al. (2004) Polyimide-based intracortical neural implant with improved structural stiffness. J Micromech Microeng 14(1): 32–37
74. Lenz FA, Dostrovsky JO, Tasker RR et al. (1988) Single-unit analysis of the human ventral thalamic nuclear group – somatosensory responses. J Neurophysiol 59(2): 299–316
75. Liu X, McCreery DB, Carter RR et al. (1999) Stability of the interface between neural tissue and chronically implanted intracortical microelectrodes. IEEE Trans Neural Syst Rehabil Eng 7: 315–326
76. Lyons KE, Pahwa R (2004) Deep brain stimulation and essential tremor. J Clin Neurophysiol 21(1): 2–5
77. Lyons KE, Pahwa R (2004) Deep brain stimulation in Parkinson's disease. Curr Neurol Neurosci Rep 4(4): 290–5
78. Lyons KE, Pahwa R (2008) Deep brain stimulation and tremor. Neurotherapeutics 5(2): 331–8
79. Mallet L, Schupbach M, N'Diaye K et al. (2007) Stimulation of subterritories of the subthalamic nucleus reveals its role in the integration of the emotional and motor aspects of behavior. Proc Natl Acad Sci USA 104(25): 10661–6
80. Maynard EM, Fernandez E, Normann RA (2000) A technique to prevent dural adhesions to chronically implanted microelectrode arrays. J Neurosci Methods 97(2): 93–101
81. Mazzone P, Lozano A, Stanzione P et al. (2005) Implantation of human pedunculopontine nucleus: a safe and clinically relevant target in Parkinson's disease. Neuroreport 16(17): 1877–1881
82. McCreery D, Lossinsky A, Pikov V (2007) Performance of multisite silicon microprobes implanted chronically in the ventral cochlear nucleus of the cat. IEEE Trans Biomed Eng 54(6): 1042–1052
83. McCreery D, Lossinsky A, Pikov V et al. (2006) Microelectrode array for chronic deep-brain microstimulation and recording. IEEE Trans Biomed Eng 53(4): 726–37
84. McCreery D, Pikov V, Lossinsky A et al. (2004) Arrays for chronic functional micro stimulation of the lumbosacral spinal cord. IEEE Trans Neural Syst Rehabil Eng 12(2): 195–207
85. McCreery DB, Agnew WF, Yuen TG et al. (1990) Charge density and charge per phase as cofactors in neural injury induced by electrical stimulation. IEEE Trans Biomed Eng 37(10): 996–1001
86. McIntyre CC, Grill WM, Sherman DL et al. (2004) Cellular effects of deep brain stimulation: model-based analysis of activation and inhibition. J Neurophysiol 91(4): 1457–69.Epub 2003 Dec 10.
87. McIntyre CC, Mori S, Sherman DL et al. (2004) Electric field and stimulating influence generated by deep brain stimulation of the subthalamic nucleus. Clin Neurophysiol 115(3): 589–95.
88. McIntyre CC, Savasta M, Kerkerian-Le Goff L et al. (2004) Uncovering the mechanism(s) of action of deep brain stimulation: activation, inhibition, or both. Clin Neurophysiol 115(6): 1239–1248
89. McIntyre CC, Savasta M, Walter BL et al. (2004) How does deep brain stimulation work? Present understanding and future questions. J Clin Neurophysiol 21(1): 40–50
90. Medtronic Neuromodulation (2003) Stimulation of the Anterior Nucleus of the Thalamus for Epilepsy. ClinicalTrials.gov. Identifier: NCT00101933. http://www.clinicaltrials.gov. Accessed 4 October 2008

91. Meissner W, Leblois A, Hansel D et al. (2005) Subthalamic high frequency stimulation resets subthalamic firing and reduces abnormal oscillations. Brain 128(10): 2372–82
92. Mettler FA, Stern GM (1962) Somatotopic localization in rhesus subthalamic nucleus. Arch Neurol 7: 328–9
93. Meyer RD, Cogan SF, Nguyen TH et al. (2001) Electrodeposited iridium oxide for neural stimulation and recording electrodes. IEEE Trans Neural Syst Rehabil Eng 9(1): 2–11
94. Miyata M (1986) Interconnections between the subthalamic nucleus and the cerebral cortex of the cat. Neurosci Res 4(1): 1–11.
95. Montgomery EB, Jr. (2004) Deep brain stimulation for hyperkinetic disorders. Neurosurg Focus 17(1): E1
96. Moss J, Ryder T, Aziz TZ et al. (2004) Electron microscopy of tissue adherent to explanted electrodes in dystonia and Parkinson's disease. Brain 127: 2755–2763
97. Motta PS, Judy JW (2005) Multielectrode microprobes for deep-brain stimulation fabricated with a customizable 3-D electroplating process. IEEE Trans Biomed Eng 52(5): 923–933
98. Moxon KA, Leiser SC, Gerhardt GA et al. (2004) Ceramic-based multisite electrode arrays for chronic single-neuron recording. IEEE Trans Biomed Eng 51(4): 647–656
99. Mueller J, Skogseid IM, Benecke R et al. (2008) Pallidal deep brain stimulation improves quality of life in segmental and generalized dystonia: results from a prospective, randomized sham-controlled trial. Mov Disord 23(1): 131–4
100. Muthuswamy J, Okandan M, Jackson N (2005) Single neuronal recordings using surface micromachined polysilicon microelectrodes. J Neurosci Methods 142(1): 45–54
101. NeuroNexus Technologies (2008). http://www.neuronexustech.com. Accessed 4 October 2008
102. NeuroPace (2004) Study of a Responsive Neurostimulator System to Treat Epilepsy. ClinicalTrials.gov Identifier: NCT00079781. http://www.clinicaltrials.gov. Accessed 4 October 2008
103. Norlin P, Kindlundh M, Mouroux A et al. (2002) A 32-site neural recording probe fabricated by DRIE of SOI substrates. J Micromech Microeng 12(4): 414–419
104. Normann RA (2007) Technology Insight: future neuroprosthetic therapies for disorders of the nervous system. Nat Clin Pract Neurol 3(8): 444–452
105. Normann RA, Campbell PK, Jones KE (1993) Three-dimensional electrode device. The United States of America, The University of Utah, Salt Lake City, UT, 45–81
106. Normann RA, Maynard EM, Rousche PJ et al. (1999) A neural interface for a cortical vision prosthesis. Vision Res 39(15): 2577–2587
107. Oh SJ, Song JK, Kim JW et al. (2006) A high-yield fabrication process for silicon neural probes. IEEE Trans Biomed Eng 53(2): 351–354
108. Paik SJ, Park Y, Cho DI (2003) Roughened polysilicon for low impedance microelectrodes in neural probes. J Micromech Microeng 13(3): 373–379
109. Peck ME (2007) Deep-Brain Stimulators for Parkinson's Disease Increase Impulsive Decision Making. IEEE Spectrum Online. http://www.spectrum.ieee.org/oct07/5669. Accessed 4 October 2008
110. Perale G, Giordano C, Daniele F et al. (2008) A novel process for the manufacture of ceramic microelectrodes for biomedical applications. Int J Appl Ceram Technol 5(1): 37–43
111. Pereira EA, Green AL, Nandi D et al. (2007) Deep brain stimulation: indications and evidence. Expert Rev Med Devices 4(5): 591–603
112. Perlmutter JS, Mink JW (2006) Deep brain stimulation. Annu Rev Neurosci 29: 229–257
113. Petersen KE (1982) Silicon as a Mechanical Material. Proc IEEE 70(5): 420–457
114. Plaha P, Ben-Shlomo Y, Patel NK et al. (2006) Stimulation of the caudal zona incerta is superior to stimulation of the subthalamic nucleus in improving contralateral parkinsonism. Brain 129(Pt 7): 1732–47
115. Plaha P, Gill SS (2005) Bilateral deep brain stimulation of the pedunculopontine nucleus for Parkinson's disease. Neuroreport 16(17): 1883–1887

116. Pollak P, Krack P, Fraix V et al. (2002) Intraoperative micro- and macrostimulation of the subthalamic nucleus in Parkinson's disease. Mov Disord 17(Suppl 3): S155–61.
117. Rau A, Grossheinrich N, Palm U et al. (2007) Transcranial and deep brain stimulation approaches as treatment for depression. Clin EEG Neurosci 38(2): 105–15
118. Robblee LS, Lefko JL, Brummer SB (1983) Activated Ir: An Electrode Suitable for Reversible Charge Injection in Saline Solution. J Electrochem Soc 130(3): 731–733
119. Rodriguez MC, Guridi OJ, Alvarez L et al. (1998) The subthalamic nucleus and tremor in Parkinson's disease. Mov Disord 13(Suppl 3): 111–8.
120. Rodriguez-Oroz MC, Rodriguez M, Guridi J et al. (2001) The subthalamic nucleus in Parkinson's disease: somatotopic organization and physiological characteristics. Brain 124(Pt 9): 1777–90
121. Romanelli P, Heit G, Hill BC et al. (2004) Microelectrode recording revealing a somatotopic body map in the subthalamic nucleus in humans with Parkinson disease. J Neurosurg 100(4): 611–8
122. Rose TL, Robblee LS (1990) Electrical stimulation with Pt electrodes. VIII. Electrochemically safe charge injection limits with 0.2 ms pulses. IEEE Trans Biomed Eng 37(11): 1118–20.
123. Rousche PJ, Pellinen DS, Pivin DP et al. (2001) Flexible polyimide-based intracortical electrode arrays with bioactive capability. IEEE Trans Biomed Eng 48(3): 361–371
124. Rutten WLC, Vanwier HJ, Put JHM (1991) Sensitivity and selectivity of intraneural stimulation using a silicon electrode array. IEEE Trans Biomed Eng 38(2): 192–198
125. Schmidt EM (1980) Single neuron recording from motor cortex as a possible source of signals for control of external devices. Ann Biomed Eng 8(4–6): 339–349
126. Schuettler M, Praetorius M, Kammer S et al. (2002) Recording of Auditory Evoked Potentials in Rat Using a 60 Channel Polyimide Electrode Array: Preliminary Results. Proc. 2nd Joint EMBS/BMES Conf., Houston, TX, USA.
127. Schwartz AB (2004) Cortical neural prosthetics. Annu Rev Neurosci 27: 487–507
128. Seymour JP, Kipke DR (2007) Neural probe design for reduced tissue encapsulation in CNS. Biomaterials 28(25): 3594–3607
129. Shain W, Spataro L, Dilgen J et al. (2003) Controlling cellular reactive responses around neural prosthetic devices using peripheral and local intervention strategies. IEEE Trans Neural Syst Rehabil Eng 11(2): 186–188
130. Simon SL, Douglas P, Baltuch GH et al. (2005) Error analysis of MRI and Leksell stereotactic frame target localization in deep brain stimulation surgery. Stereotact Funct Neurosurg 83(1): 1–5
131. Slavcheva E, Vitushinsky R, Mokwa W et al. (2004) Sputtered iridium oxide films as charge injection material for functional electrostimulation. J Electrochem Soc 151(7): E226–E237
132. Sreenivas G, Ang SS, Fritsch I et al. (1996) Fabrication and characterization of sputtered-carbon microelectrode arrays. Anal Chem 68(11): 1858–1864
133. Starr PA (2002) Placement of deep brain stimulators into the subthalamic nucleus or globus pallidus internus: Technical approach. Stereotact Funct Neurosurg 79(3–4): 118–145
134. Stathis P, Panourias IG, Themistocleous MS et al. (2007) Connections of the basal ganglia with the limbic system: implications for neuromodulation therapies of anxiety and affective disorders. Acta Neurochir Suppl 97(Pt 2): 575–86
135. Stieglitz T (2001) Flexible biomedical microdevices with double-sided electrode arrangements for neural applications. Sens Actuator A-Phys 90(3): 203–211
136. Stieglitz T, Gross M (2002) Flexible BIOMEMS with electrode arrangements on front and back side as key component in neural prostheses and biohybrid systems. Sens Actuator B-Chem 83(1–3): 8–14
137. Stover NP, Okun MS, Evatt ML et al. (2005) Stimulation of the subthalamic nucleus in a patient with Parkinson disease and essential tremor. Arch of Neurology 62(1): 141–143

138. Suner S, Fellows MR, Vargas-Irwin C et al. (2005) Reliability of signals from a chronically implanted, silicon-based electrode array in non-human primate primary motor cortex. IEEE Trans Neural Syst Rehabil Eng 13(4): 524–541
139. Szarowski DH, Andersen MD, Retterer S et al. (2003) Brain responses to micromachined silicon devices. Brain Res 983: 23–35
140. Tass PA (2003) A model of desynchronizing deep brain stimulation with a demand-controlled coordinated reset of neural subpopulations. Biol Cybern 89(2): 81–88
141. Tehovnik EJ (1996) Electrical stimulation of neural tissue to evoke behavioral responses. J Neurosci Methods 65(1): 1–17.
142. The Cleveland Clinic (2008) Deep Brain Stimulation. http://my.clevelandclinic.org/services/deep_brain_stimulation/ns_overview.aspx. Accessed 4 October 2008
143. Theodore WH, Fisher R (2007) Brain stimulation for epilepsy. Acta Neurochir Suppl 97(Pt 2): 261–72
144. Theodosopoulos PV, Marks WJ, Jr., Christine C et al. (2003) Locations of movement-related cells in the human subthalamic nucleus in Parkinson's disease. Mov Disord 18(7): 791–8
145. Truccolo W, Friehs GM, Donoghue JP et al. (2008) Primary motor cortex tuning to intended movement kinematics in humans with tetraplegia. J Neurosci Methods 28: 1163–1178
146. Ulbert I, Halgren E, Heit G et al. (2001) Multiple microelectrode-recording system for human intracortical applications. J Neurosci Methods 106(1): 69–79
147. Vetter RJ, Williams JC, Hetke JF et al. (2004) Chronic neural recording using silicon-substrate microelectrode arrays implanted in cerebral cortex. IEEE Trans Biomed Eng 51(6): 896–904
148. Vitek JL, Bakay RAE, Hashimoto T et al. (1998) Microelectrode-guided pallidotomy: technical approach and its application in medically intractable Parkinson's disease. J Neurosurg 88(6): 1027–1043
149. Wessling B, Mokwa W, Schnakenberg U (2006) RF-sputtering of iridium oxide to be used as stimulation material in functional medical implants. J Micromech Microeng 16(6): S142–S148
150. Wise KD, Anderson DJ, Hetke JF et al. (2004) Wireless implantable microsystems: High-density electronic interfaces to the nervous system. Proc IEEE 92(1): 76–97
151. Wise KD, Angell JB, Starr A (1970) An integrated-circuit approach to extracellular microelectrodes. IEEE Trans Biomed Eng 17(3): 238–47
152. Yokoyama T, Ando N, Sugiyama K et al. (2006) Relationship of stimulation site location within the subthalamic nucleus region to clinical effects on parkinsonian symptoms. Stereotact Funct Neurosurg 84(4): 170–5
153. Yokoyama T, Sugiyama K, Nishizawa S et al. (2001) The optimal stimulation site for chronic stimulation of the subthalamic nucleus in Parkinson's disease. Stereotact Funct Neurosurg 77(1–4): 61–7
154. Yoon TH, Hwang EJ, Shin DY et al. (2000) A micromachined silicon depth probe for multichannel neural recording. IEEE Trans Biomed Eng 47(8): 1082–1087

Implantable Cardiac Electrostimulation Devices

Rick McVenes and Ken Stokes

Abstract The history of bradycardia (too slow heart beat) goes back 300 years, but implantable pacemakers made their appearance in 1959. Since then, as pacemakers became more sophisticated, the indications for their use have expanded greatly. Today they are used to treat numerous rhythm disturbances including some forms of tachycardia (too fast a heart beat), heart failure, and even stroke (thromboembolism due to atrial fibrillation). Implantable cardioverter defibrillators (ICD) made their appearance in 1980. Today they are used to correct tachycardia, ventricular fibrillation, and even asystole (no heart beat) as well as heart failure patients. These are highly sophisticated devices made from very high reliability components.

1 Introduction

The history of bradycardia (too slow a heart beat, also known as Stokes-Adams disease) is 300 years old. The syncopal attacks which can occur as a result of heart block were initially attributed to epilepsy [1]. In 1827, Adams determined that the source of bradycardia was the heart, not the brain [2]. He was severely attacked by the scientific community at the time, but Stokes came to his defense in 1846 [3]. External pacemakers to treat Stokes-Adams disease first appeared in the 1930s. The age of implantable pacemakers was born in 1959. Early implantable defibrillators designed to treat tachycardia, ventricular fibrillation, or asystole made their appearance in 1980. Thus, artificial implantable cardioverter defibrillators (ICD) and pacemakers to control cardiac rhythm disturbances have a long and successful history, benefiting millions of patients. Modern ICDs and pacemakers are highly sophisticated devices with incredible capabilities.

R. McVenes (✉)
Leads Research, Cardiac Rhythm Disease Management Division, Medtronic, Inc.,
MVC 52, 8200 Coral Sea St. NE, Mounds View, MN 55112, USA
e-mail: rick.mcvenes@medtronic.com

D.D. Zhou, E. Greenbaum (eds.), *Implantable Neural Prostheses 1*,
Biological and Medical Physics, Biomedical Engineering,
DOI 10.1007/978-0-387-77261-5_7,

In this chapter we will first briefly review the origins and history of pacemakers and ICDs up to the present. Then we will summarize their components and design parameters. We will explore the reasons (indications) they are needed. Finally, we will briefly comment on their associated clinical complications and how these are managed or improved by design.

2 Pacemaker, ICD, and Lead Codes

Modern pacemakers and ICDs are complicated devices [4]. To make things simpler, pacing terminology involves the use of three or four letter codes to classify their function. The first letter signifies the chamber (ventricle or atrium) paced. The second letter tells us which chamber the device senses in. The third letter tells us how the pacemaker functions (is it triggered by a signal or inhibited). Thus, a VVI pacemaker paces the right ventricle, senses the right ventricle's R wave (the electrical activity resulting in contraction), and is inhibited when the ventricle contracts on its own. A VAT pacemaker paces in the ventricle, senses in the atrium, and triggers the stimulation pulse when it senses an atrial contraction (P wave). The letter "D" stands for "double". Thus, a DDD pacemaker paces both chambers, senses in both chambers and is both triggered and inhibited. When the letter "R" is used, as in VVIR, this signifies that the pacemaker is "rate responsive". That is, it automatically adjusts its rate according to the patient's needs.

3 Pacemakers and ICDs

3.1 External Pacemakers

In the late 1800s, reports characterizing the electrostimulation of the heart using external equipment began to appear [5, 6, 7, 8]. The first external electromechanical pacemaker is commonly attributed to Hyman (1932), although Booth and Lidwell reported successful human pacing 4 years earlier [9, 10]. Booth and Lidwell's device used a unipolar myocardial needle with a saline soaked indifferent plate electrode on the skin. Hyman used a hand-cranked pulse generator and bipolar transthoracic needles to effect cardiac-electrode contact (Fig. 1). An external AC current powered asynchronous pacemaker was introduced by Zoll in 1952 [11]. This was a large device by today's standards, transported on a cart (Fig. 2). In 1956, the first external "demand" (VVI) pacemaker was introduced by Leatham and Cook. The first fully portable, wearable battery powered external pulse generator, developed by Bakken, was applied clinically by Lillehei in 1957 (Fig. 3).[12]. This device used Teflon-insulated, multistranded stainless steel suture wire leads, applied transthoracically. Today, external pacemakers are typically used only in hospitals for temporary stimulation. A related external device, the pacing system analyzer (PSA), is used at implant or pulse generator replacement to test the leads.

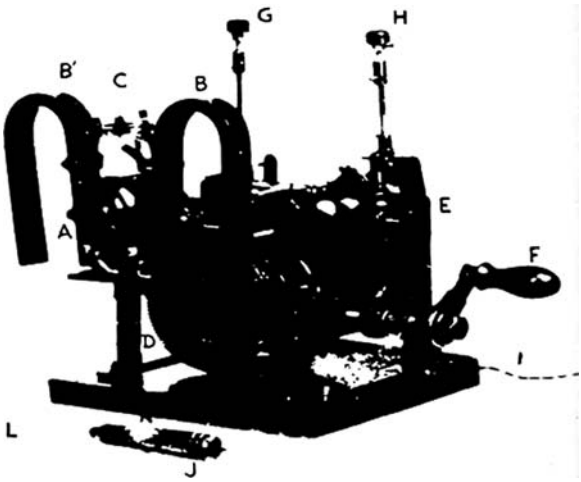

Fig. 1 The Hyman external pacemaker, operated by turning a crank (f). The lead was a bipolar needle inserted through the chest (j). The device was carried in a shoulder case. Courtesy of the Collections of the Bakken Library and Museum

Fig. 2 Zoll AC powered pacemaker (PM-65) introduced in 1952. The distance the patient can travel is limited to the length of the power cord, which must be plugged into a wall outlet. Courtesy of The Heart Rhythm Foundation

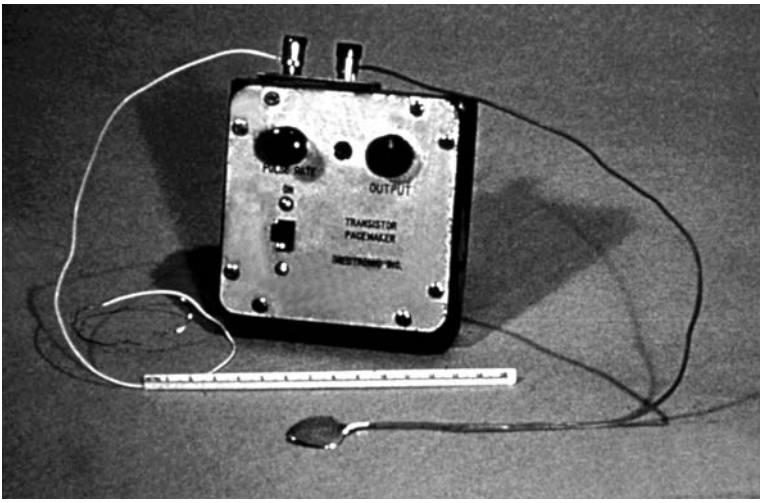

Fig. 3 The Bakken wearable external battery powered pacemaker, introduced in 1957. The leads are straight Teflon insulated wires, one implanted on the heart, the other a subcutaneous "indifferent" plate. Courtesy of the Collections of the Bakken Library and Museum

3.2 Artificial Implantable Ventricular Pacemakers

The first totally implantable pacemaker (asynchronous or VOO) was reported by Senning and Elmqvist in 1959 [13]. The first device worked only a short time, with stimulation thresholds rising to 20+ volts (which was above the pulse generator's capacity). These pacemakers required periodic recharging by induction from an external power source. Also in 1959, Chardack and Gage implanted a completely self-contained battery powered device developed by Greatbatch [14]. This was a hockey puck sized epoxy block containing cylindrical batteries, hand assembled circuitry, a hardwired multistranded lead, and a silicone rubber covering similar to a slightly later model shown in Fig. 4. The bare tips of the wires were inserted in and sutured to the heart muscle (myocardium). The Greatbatch device functioned successfully for over 1 year. Some early pacemakers similar to that shown in Fig. 4 were "programmable" (that is, rate could be adjusted at implant). The pulse generator had a "pigtail" adjacent to the lead. The tip could be cut off exposing three wires. The rate could then be determined by which two of the three wires were twisted together before sealing with medical adhesive. The next advance in "programmability" was the inclusion of one or two 10-turn potentiometers on the circumference of the pulse generator. One could palpate these, and insert a Keith needle percutaneously. Rotating the Keith needle in one potentiometer would cause rate changes. Rotating the Keith needle in the other potentiometer would change an output parameter. External (noninvasive) programmability was developed in the early 1970s. For example, an early Medtronic programmer used a hand-cranked

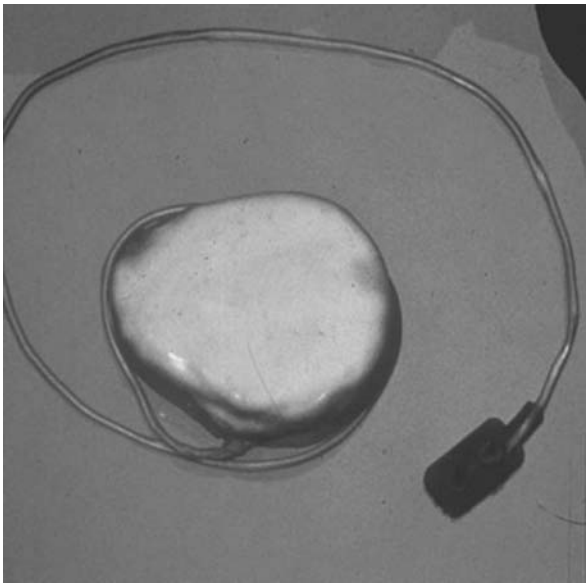

Fig. 4 Early 1960s Medtronic epoxy encapsulated, silicone rubber covered ventricular pacemaker powered by a battery of Hg–Zn cells. The lead is hardwired with a Hunter-Roth electrode that must be implanted using stab wounds in the heart made with a scalpel blade

external device that rotated a magnet over the implanted pacemaker to adjust rate and output parameters. Today, modern pulse generators are programmed noninvasively by sophisticated computerized machines using RF, obtaining information about the patient's and device's status by telemetry.

In the later 1960s, pulse generators were developed with connectors so that separate leads with terminals could be joined at the time of surgery. By this time, a number of manufacturers had entered the market, each with their own terminal designs as shown in Fig. 5. By the mid 1970s, the prevalent systems used a setscrew connection on a terminal pin with sealing rings (Fig. 6). Today the universal IS1 terminal allows implanters to "mix and match" leads and generators from different manufacturers. Sealing rings prevent fluid leakage when inserted into the connector. The terminal also provides strain relief for the lead when the connected assembly is tucked into its subcutaneous or intramuscular pocket.

The first automatic rate responsive VVIR pacemaker was introduced by Cammilli in 1976 [15]. This used an IrO_2 pH sensor with an Ag/AgCl reference electrode on the lead. The pacemaker's rate responded to exercise as well as emotional state. The problem with it was slow response time. It was reported that when a patient got into a short argument with his neighbor, the pacemaker sped up after he had sat down to calm his temper. Additionally, The FDA determined that Ag/AgCl was not biocompatible, so the device was not commercially successful. About the same time, Rickards and Norman introduced a VVIR pacemaker based on QT time interval [16]. This design was clinically successful. Today many different types of sensors are used to provide automatic rate response, including patient activity, accelerometers, stroke volume, respiration rate, oxygen saturation, core temperature, and more [17].

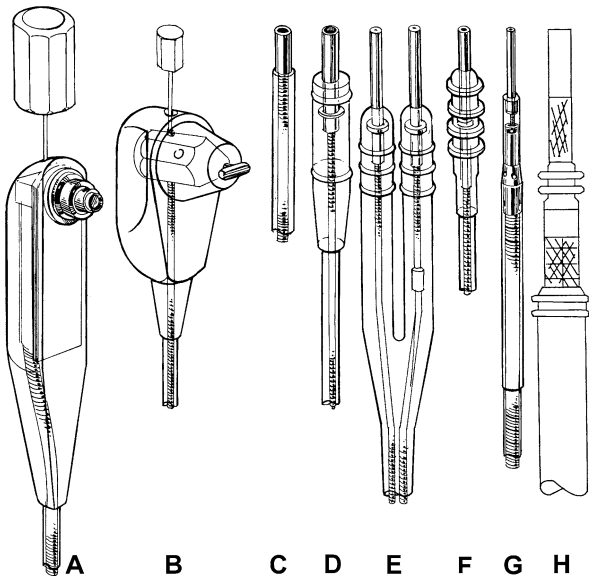

Fig. 5 Early terminal assemblies: (**A**) General Electric, (**B**) Pacesetter, (**C**) Vitatron, (**D**) Cordis 6 mm unipolar, (**E**) Medtronic 5 mm bipolar, (**F**) Intermedics, (**G**) Medtronic "in-line" bipolar, and (**H**) the IS1 universal terminal. A–E were used in the 1970s. By 1980, **A–C** were obsolete with most companies using a version of **D** or **E** (but not all the same size). All the designs except F were made with silicone rubber. The Intermedics design used injection molded polyurethane. The in-line terminal was developed in the 1980s while the IS1 made its appearance in the 1990s. Today, all terminals are IS1

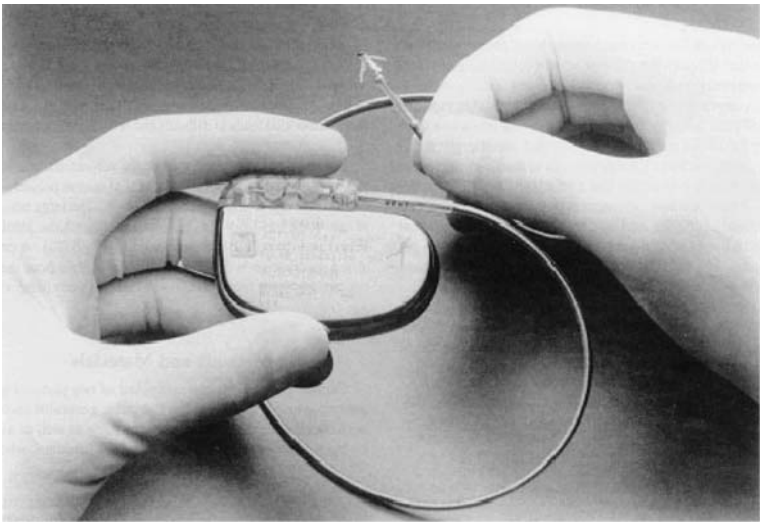

Fig. 6 An implantable bipolar pulse generator with an IS1 lead inserted in the connector

Early pacemakers were implanted using a thoracotomy to place the electrode(s) on the epicardial surface of the heart. However, a thoracotomy is a very traumatic procedure so that many elderly patients suffered complications as a result. In the early 1970s an epicardial lead was developed with a corkscrew electrode as shown in Fig. 7 [18]. This lead was accompanied by a new, less traumatic implant procedure. A small incision exposed the subxiphoid process at the bottom of the sternum. This was removed, giving direct access to the right ventricle. The lead, mounted on an introducer tool, was then screwed into the myocardium. While highly successful, this procedure still required general anesthesia.

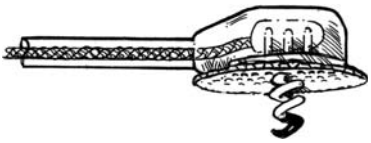

Fig. 7 Medtronic Model 6917 epi/myocardial lead. The electrode is a 6-mm long, 3-turn corkscrew. The proximal two turns are insulated with silicone rubber, exposing the distal 12 mm^2 Pt/Ir electrode. The design was later modified to have a 2-turn corkscrew with a 6-mm^2 electrode (Model 6917A) for a better right ventricular fit

An endocavitary transvenous lead was implanted by Furman and Robinson in 1958 with an external pulse generator [19]. Siddons and Davies reported a totally implantable transvenous system in 1963 [20]. As transvenous leads evolved, it became obvious that they were easier and less traumatic to implant than those requiring transthoracic approaches. The fact that transvenous implants usually do not require general anesthesia was a very important feature, making the procedure significantly safer. However, while the transvenous approach rapidly became more popular than the transthoracic, this method of implantation did not provide reliable results. Complications, including primarily dislodgment, required corrective reoperation in up to 40% of implants in 1977 [21]. The dislodgment problem has largely been solved by the introduction of two fixation mechanisms [22, 23].

Pacemaker and ICD electrode fixation mechanisms to prevent transvenous lead dislodgment typically fall into two categories, passive and active. Passively fixed electrodes have several small silicone rubber or polyurethane projections (called tines) just proximal from the tip, which engage the heart's endocardial structure to hold the electrode firmly in place (Fig. 8). The electrode does not penetrate the myocardium. Active fixation requires penetration of the myocardium to achieve stable electrode/cardiac positioning. Most commonly, these are corkscrew electrodes that are turned into the cardiac tissue (Fig. 9). Their advantage is that they do not require cardiac structure to engage in. These work well in an enlarge heart with relatively smooth endocardial surfaces. Also, the most advantageous place to position an electrode may not be in a part of the heart where there is endocardial structure. Most active fixation electrodes are

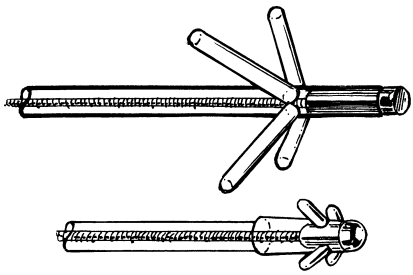

Fig. 8 An early unipolar lead tip with four, 10-mm long silicone rubber tines for fixation (*top*). A modern lead with shorter tines set closer to the distal electrode (*bottom*)

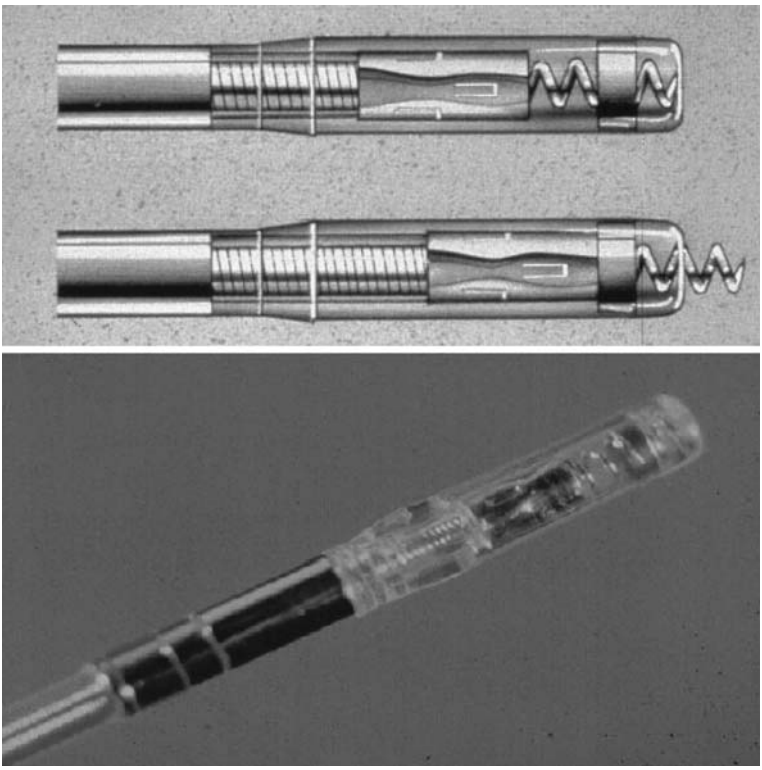

Fig. 9 An early Medtronic "Bisping" extendible/retractable screw-in distal tip, unipolar Model 6957 (*top*), and bipolar Model 4016 (*below*)

extendable and retractable so that they can be inserted without concern for damage to the cardiovasculature by the sharp tip. There are also leads with fixed and exposed helices that are inserted while counter rotating them to prevent damage. Then they are screwed into the myocardium by rotating the entire lead body in the other direction.

Ventricular leads are usually straight and flexible. A stylet is inserted into the lumen to stiffen it during the implant procedure. Typically the lead is inserted into the subclavian vein using an introducer kit as shown in Figs. 10 and 11 [24, 25]. A commonly used alternative is a cephalic cutdown and

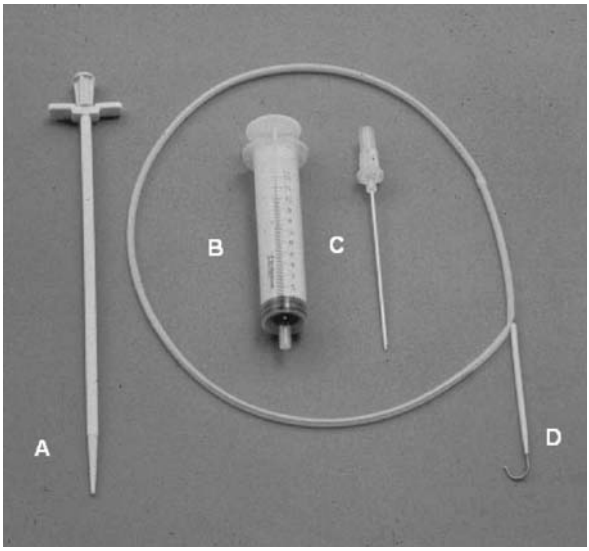

Fig. 10 A subclavian stick kit containing a splittable sheath containing a hollow dialtor (**A**), sterile syringe (**B**), and needle (**C**), and a guidewire in its protective package (**D**)

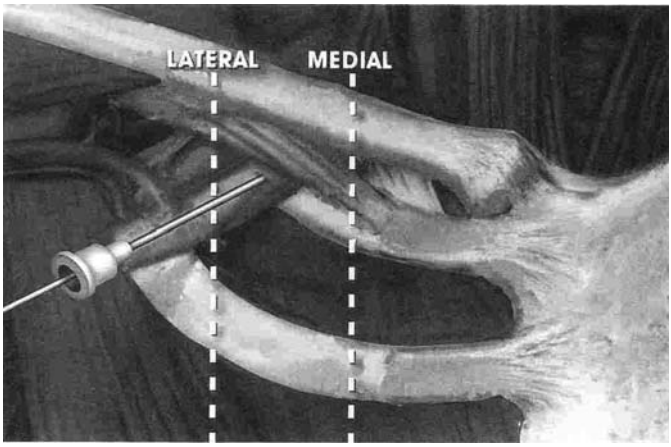

Fig. 11 The subclavian stick procedure is as follows: The subclavian vein is punctured with the needle. Then a guidewire is inserted into the heart, through the needle. The needle is removed and the introducer is inserted over the guidewire. The guidewire is removed (unless it is to be retained for a second introducer). The dialtor is removed and the lead inserted. Once the lead is in position, the sheath is split and removed

venotomy. The lead is advanced through the venous vasculature until the tip reaches the atrium. Typically, the distal portion of a passive fixation lead (with a curved end caused by bending the stylet prior to insertion into the lead) is then pressed against the atrial wall to form a "U", then it is backed through the bicuspid valve and allowed to flop into the ventricle. This helps prevent the tines from catching on the valve's chordae. The lead tip is advanced into position, typically the right ventricular apex. The stylet is removed and the lead body is adjusted to provide adequate slack. If electrical testing provides acceptable stimulation thresholds, cardiac signals, and pacing impedance, a ligature is used on an anchoring sleeve to fix the proximal end of the lead to muscle or fascia. The implant of a screw-in lead is similar although they typically do not need to be backed into the ventricle. These have the advantage of being implantable anywhere in the heart, requiring no endocardial structure to hold them in place.

Once the lead has been satisfactorily tested, the terminal pin is pushed into the pulse generator's connector until it is visibly positioned within the setscrew block. This also assures that the sealing rings are in place. A torque wrench is inserted through the silicone grommet, into the setscrew, which is then tightened on the pin. Then, the pulse generator is turned to wrap the excess lead around it and is placed in a subcutaneous or intramuscular pocket. Finally, the pocket is irrigated and closed.

3.3 Artificial Implantable Atrial Pacemakers

In the early 1960s, the indications for implantable pacemakers included primarily atrioventricular (AV) block (atrial impulses that normally control the ventricles rate are blocked resulting in bradycardia) [26, 27]. At the time, the physiologic importance of maintaining the normal temporal AV sequence was not generally appreciated [28]. In fact, transvenous atrial leads did not appear in the literature until 1969 [29]. In 1968 DeFrances described a patient with recurrent and refractory ventricular tachycardia controlled by permanent epicardial atrial pacing [30]. Atrial pacing was sometimes used in bradycardia patients with intact atrial-ventricular (AV) conduction.

Atrial leads are either straight (active fixation) or "J" shaped (Fig. 12). The "J" is straightened by a stylet prior to venous insertion. Once the lead is in the right atrium, the stylet is retracted and the distal "J" forms. Next the electrode tip is pulled into the right atrial appendage where the tines can engage pectinate muscles to hold it in place. Typically, passively fixed "J" leads are not placed elsewhere because most of the chamber has smooth, thin walls, which cannot interact with tines. Screw-in leads are a different matter. While "J" shaped extendable/retractable screw-ins have been used in the right atrial appendage, straight active fixation leads are more versatile. Usually the atrium is mapped to find the optimum p wave amplitudes and/or stimulation thresholds before the lead is fixed in place, connected to the pulse generator and implanted.

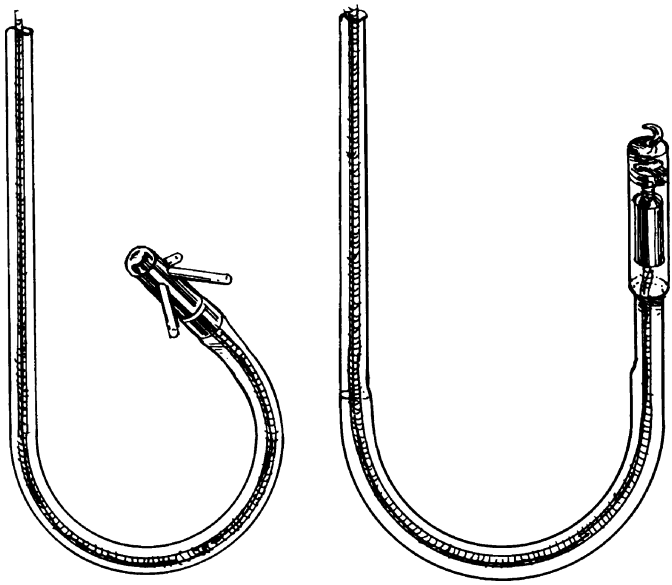

Fig. 12 *Left*, an atrial "J" shaped lead with passive (tined) fixation. A "J" shaped screw-in is shown to the *right*. Both lead types must be implanted in the atrial appendage. Straight screw-in leads (Fig. 9) are used in other locations within the atrium

Some specific atrial electrode sites are used for special purposes. For example, a lead screwed into Bachmann's bundle (a small spot on the interatrial septum) may be used to help prevent atrial fibrillation [31]. At this location, both right and left atria are stimulated. Even dual atrial pacing using one lead in the high right atrium and one under the left atrial appendage via the coronary sinus has been done to prevent atrial tachycardia [32].

Atrial-based pacing predominates today, primarily in the form of dual-chamber devices.

3.4 Dual-Chamber Pacemakers

In 1963 Nathan et al. implanted the first dual-chamber pacemaker (VAT) [33]. Funke patented the first fully automatic (DDD) pacemaker in 1978 [34]. These modalities offered the patient more physiological cardiac rhythm, but they were largely unused until the early 1980s. The reason was that two leads were required, one for the right atrium and one for the right ventricle. For many elderly patients the risk of thoracic surgery to place myocardial leads exceeded the disadvantages associated with single chamber pacing. Because the silicone rubber transvenous leads available at that time were relatively large, it was difficult to implant two in one vein. Positioning one often dislodged the other, making the implant procedure a frustrating experience. Two relatively large leads could more easily be

inserted through two different veins, but this required more surgery, and could restrict venous drainage from the head. The advent of small, lubricous polyurethane leads made the insertion of two in one vein a practical procedure so that DDD pacing could become relatively commonplace. Generally speaking, the leads and implant techniques are the same as for single chamber pacemakers. The exception is the need to insert two leads, preferably in one vein. Again, subclavian stick is the most widely used procedure. A popular technique uses two introducers. The first lead is inserted through the introducer sheath while the guide wire is retained in it. After the first lead is in position the sheath is removed and a second introducer is inserted over the guidewire, alongside the first lead. After the second lead is in position the second introducer and guidewire are removed, the leads tested, and the implant procedure completed.

Dual-chamber pacing and sensing (DDD) has been shown to provide superior hemodynamics compared to ventricular pacing and sensing (VVI) alone [35]. In fact, studies have shown that when patients with DDD pacemakers are reprogrammed to VVI (without the patient knowing which mode they are in), 83% reported new or worse symptoms. Thus, dual-chamber pacing has largely replaced single chamber devices.

Not all dual-chamber systems require pacing in the atrium, however. "Single pass" leads that sense and pace in the right ventricle, but only sense in the atrium (VAT or VDD) have been successfully developed, but their efficacy does not quite meet DDD performance and are not indicated for all patients [36, 37].

3.5 Cardiac Resynchronization Therapy (CRT) Devices (Pacing Both the Right and the Left Heart)

One of the common forms of congestive heart failure is left-sided intraventricular delay coupled with mechanical dyssynchrony. The interest in pacing for biventricular stimulation in patients with severe LV dysfunction was inspired by small initial studies. The results suggested that improved functional capacity could be achieved in these patients [38, 39]. The early results have now been validated in large clinical trials [40, 41, 42]. The early systems for CRT employed Y-adapters for biventricular stimulation. The first Y-adapters made one ventricular lead the cathode and the other the anode in a "split bipole" configuration. Failure to maintain capture at both sites occurred commonly, primarily on the lead connected to the anodal terminal. Reoperation to change or adjust the adaptors was often required [43, 44]. Subsequent Y-adapters and 1st generation biventricular pulse generator connectors shorted the two leads together to yield a "dual cathode" configuration. In these systems, individual pacing thresholds cannot be measured independently or directly, which is a distinct disadvantage. More recent systems provide independent channels for both ventricular outputs, which allows lead performance to be assed on both chambers and the timing between the two ventricular stimulation pulses to be adjusted. In addition, the evolution of multisite pacing requires new connectors

to accommodate the additional leads without adapters. The triple port IS1 connector was developed for atrial–biventricular stimulation (Fig. 13). A five-port version is needed for CRT in combination with a defibrillator (Fig. 14).

Transvenous implant on the LV requires cannulation of the coronary sinus (CS) and passage of a lead into a peripheral cardiac vein (CV). While the CS is routinely cannulated during standard electrophysiologic studies, accessing

Fig. 13 A cardiac rhythm-timing (heart failure) pacemaker, InSync Model 7277, with a connector module accommodating 3 leads

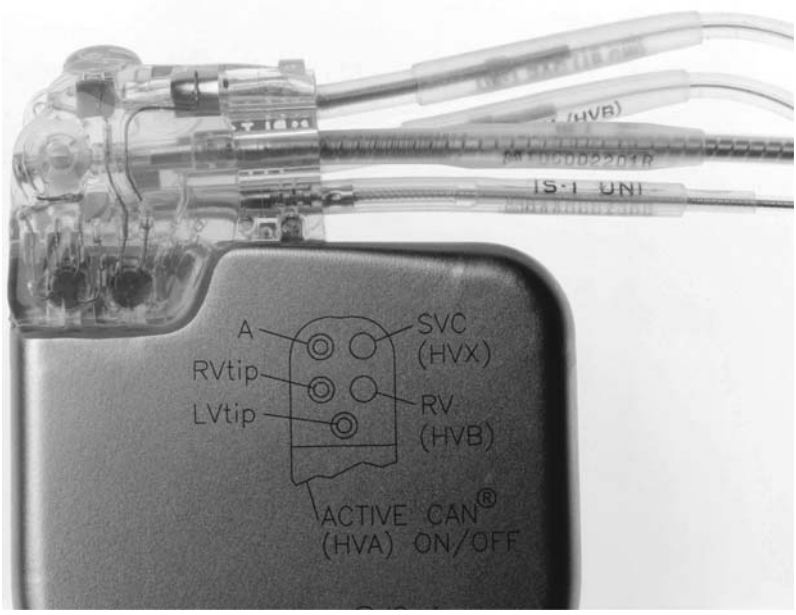

Fig. 14 A cardiac rhythm timing (heart failure) pacemaker/ICD with a connector module accommodating five leads

it from a superior approach in patients with LV and/or right atrial enlargement can be challenging. The CS exhibits marked anatomical variability. In some anatomical studies about 10% of the population presented no suitable vein for LV pacing via the CS [45]. Tortuosity or acute angulation of a tributary from the coronary sinus, cardiac vein, or valves at the tributary os can prevent access to a posterior or lateral branch [46, 47]. This technical challenge has fostered advances in the design of both lead and delivery systems. By redesigning the distal electrode assembly used on right heart leads, the most flexible tip assembly possible for better performance during implant was obtained. Some lead designs incorporated a preshaped distal end to facilitate introduction into CV tributaries (Fig. 15). Others used preformed shapes (like a "pig tail") or even tines to affect fixation. The addition of a guidewire or combined guidewire and stylet delivery has also improved implant success. Availability of more than one type of lead has enhanced the ability to achieve the posterolateral and lateral positions commonly associated with optimal effectiveness of biventricular stimulation [48].

Fig. 15 Transvenous left ventricular leads with continuous curves to aid introduction into the coronary sinus os. Medtronic Models 2187 (*upper*) and 4193 (*bottom*)

The design of delivery systems has also improved. The balloon catheter for CS venography has enhanced the identification of potential implant sites. More distal advancement of the delivery sheath into the CS and proximal venous system facilitates passage of the guidewire or lead tip to the level of the target cardiac venous tributary. One approach involves the addition of a soft distal section to the delivery sheath to allow advancement deeper into the CS or proximal cardiac veins while reducing the potential for CS dissection and perforation (Fig. 16). This sheath, when combined with the functionality of a steerable electrophysiologic catheter, provides both tip deflection and reach for engagement within a cardiac vein tributary. Recently, inner sheaths with varying tip angles have further improved the ability to "sub-select" or get into venous locations providing better hemodynamic outcomes.

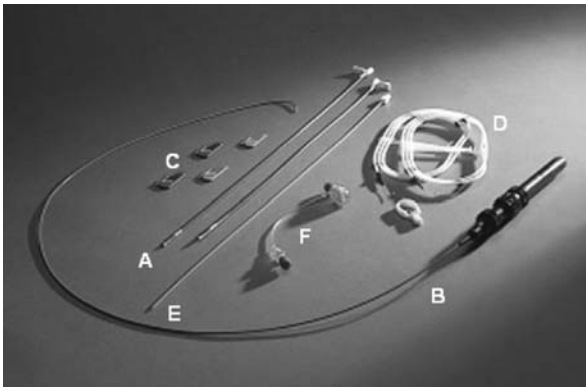

Fig. 16 Straight lead delivery sheaths with soft distal tips (**A**), steerable delivery system catheter (**B**), with slitters (**C**), guidewires (**D**), dilator (**E**), and hemostasis valve (**F**). Medtronic model 6218

Acceptable performance of a biventricular system in terms of stimulation thresholds and sensing is somewhat different from that of leads for traditional antibradycardia therapy. Greater priority has been given to LV lead design for successful implant rather than pulse generator longevity. This is because many early investigators considered that a 2- to 3-year pulse generator was of less consequence to this patient population, given their poor survival rate. Typically, while the LV lead's performance is generally acceptable, it has higher stimulation thresholds than RV electrodes, with larger standard deviations. Additionally, dislodgement and avoidance of phrenic nerve stimulation are higher priority needs driving lead design over electrical performance optimization.

The placement of permanent endocardial LV leads by transseptal puncture is feasible and requires long-term anticoagulation, but it is highly investigational because of the risk of catastrophic embolic complications [49, 50, 51, 52]. Mid-term follow-up of endocardial LV leads in a small number of patients has proved to be free of major complications. All the patients had failed transvenous LV implant attempts (presumably because they did not have a cardiac vein at the target location) and had a demonstrated need for biventricular stimulation. Autopsy revealed no adherent LV thrombus in one of four patients who have died from intractable heart failure or influenza in this series [53]. The left endocardial approach may have potential because it permits LV mapping to institute pacing at a site associated with the best hemodynamic performance or the optimal cardiac activation pattern or sequence [54].

The adoption of LV endocardial stimulation on a broad scale, however, would require a significant breakthrough in anticoagulation therapy, and a large clinical trial to establish safety.

Because heart failure patients are often prone to tachyarrhythmias, biventricular ICDs have largely replaced biventricular pacemakers.

3.6 Implantable Cardioverter Defibrillators

The implantable defibrillator [56] was conceived by Mirowski in 1960 [56]. The first defibrillator was implanted in a human in February 1980 [57]. A second-generation device which allowed the physician to program the therapy threshold rate noninvasively rather than predetermine it before ordering the device from the manufacturer was available by 1988 [58]. Because these devices required large, high-capacity batteries and components to deliver relatively large shocks, they were relatively large (Fig. 17). Early systems used large epicardial patch electrodes, which of course, necessitated the more traumatic transthoracic surgery. Early transvenous leads required up to three conductor coils and were relatively large in diameter. The third generation of ICDs became available in 1991 with programmable shock therapy [55].

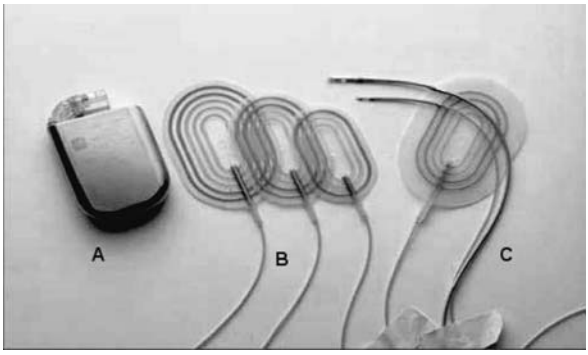

Fig. 17 An early implantable defibrillator (**A**) with four epicardial patch electrodes (**B**) and two bipolar transvenous active fixation leads (**C**)

Modern ICDs are capable of both pacing and defibrillation. Because of the need for more circuitry and a high-rate, high-capacity battery these devices are still substantially bigger than modern pacemakers. Modern ICDs for heart failure patients require five port connectors similar to that shown in Fig. 14. However, multi-port connectors take space, which significantly increases the size of the device. In fact, the connector module can be the major bulk of the device. The connector block is becoming more complex to fit leads with three or four electrodes. Thus, there exists debate among the manufacturers as to the design and standardization of new systems, to deal with the growing complexity of pacemaker and ICD connectivity.

4 Modern Pacemaker and ICD Components

4.1 Pacemaker Power Sources

Modern pacemakers typically use a single hermetically sealed lithium iodide (LiI) cell [59]. The earliest epoxy encapsulated pacemakers used mercury–zinc

cells. These are no longer used because they give off hydrogen gas, can swell if their vents are plugged, and do not provide the longevity of LiI cells. Nuclear batteries were also used between 1970 and 1982 [60]. One type used the β voltaic effect. A β emitter such as promethium 147 produces electrons which impinge on a semiconductor to produce an electric current. Another type used plutonium 238 initially, but then switched to plutonium oxide. The heat produced by nuclear decay was converted to electricity by a thermopile. At first glance it would seem that these power sources had significant benefits, such as 20 to 40-year longevity, obviating the need for reimplantation in most patients. However, pacemaker technology has advanced relatively quickly over the last 35 years. A patient with a fully functioning 20 + -year-old pacemaker will not benefit from technological advances. In addition, there were substantial federal nuclear regulatory issues. A patient wearing a nuclear pacemaker was considered fissionable material. Follow-up requirements were time consuming and rigorous. Once a patient died, or if the device had to be explanted for any reason, it was required by federal law to be retrieved and returned to the manufacturer, which was a substantial burden for physicians, undertakers, manufacturers, and patient's families. Imagine the shock of discovering that you had just cremated someone who had a plutonium 238-powered device in them!

4.2 ICD Power Sources

A pacemaker must deliver a shock of no more than 10 V (typically about 4–5 V) over 0.5–1 ms [57]. The energy of the pulse is typically 1–10 μJ. A defibrillator must deliver up to 40 J in a few milliseconds. Thus, LiI batteries are not sufficient for the task. Today, ICDs are powered by Li–silver vanadium oxide (SVO) batteries.

4.3 Pacemaker Circuitry Design Requirements

The first implantable pacemaker circuitry was made from "cordwood" (separate) components with soldered connections. In 1970, the most sophisticated "demand" (VVI) pacemaker had about 25 individual components. Today's pacemakers may have the equivalent of many thousands or even 10s of thousands of individual components in their integrated circuitry. Warren and Nelson describe the basic design elements as follows [55].

- Pace control includes sense amplifiers to detect the heart's intrinsic electrical signals which are used to track heart activity during an arrhythmia. It also includes pacing output and timing circuits.
- Rate adaptive circuitry includes amplifiers, filters and current sources for various types of sensors. These sensors determine the need for increased or reduced pacing rate.
- A microprocessor controls the overall system function. Typically an 8-byte design is sufficient but this can be as big as 32 KB.

- Random access memory is used for program space, storage of operating parameters, and storage of electrograms. This can require up to 512 KB.
- Telemetry control is dedicated to the specifics of communication protocol and telemetry schemes.
- System control contains the support circuitry for the microprocessor, including the telemetry interface.
- The voltage supply provides various currents and voltages to the system. Digital circuits operate at 2.2 V or less while analogue circuits typically require precision nanoampere inputs.

4.4 ICD Circuitry Design Elements

Warren and Nelson describe the basic design elements that differ from those in pacemakers as follows [55]:

- Read only memory provides sufficient nonvolatile memory for system start-up tasks and some program space. Program space requirements can be as high as 100 KB.
- RAM in an ICD must serve similar functions as in a pacemaker, but in addition must store several minutes of electrograms from several lead sources. RAM can be as high as 512 KB.
- The battery may include one or two Li-SVO cells.
- Low voltage supply must power 3 V or lower circuitry. Separate voltage supplies are needed for pacing (up to 5 V) and control of charging circuits (10–15 V).
- The high power supply, output switch, and defibrillation control provides and delivers the defibrillation shock.
- Pacing control sense amplifiers typically use automatic gain control. They must also be protected from the delivery of high-voltage defibrillation pulses.

4.5 Pacemaker and ICD Mechanical Components

Most pacemaker and ICD containers (cans) are made of titanium. Two halves containing the circuitry, battery, feedthroughs, and sometimes sensors are laser welded together in a helium atmosphere. Helium leak testing must show an acceptable level of hermeticy, typically a He leak rate $< 10^{-8}$ cc/s. The feedthroughs are typically high-quality ferrules encased in glass. At least one manufacturer uses niobium pins encased in sapphire. These are attached to stainless steel or titanium setscrew blocks designed to connect to the lead's terminal pin(s). Some newer designs may use other forms of connection, such as crown contacts, requiring fewer setscrews. The feedthroughs, setscrew blocks, or other electrical contact mechanisms are all embedded in an injection molded

polyurethane "header", providing ports for the lead terminals (Fig. 6). Setscrew access ports are sealed with silicone rubber "grommets". Setscrews are tightened or loosened with special torque wrenches.

4.6 Leads

Pacemaker leads are either unipolar or bipolar. Unipolar leads have only one electrode to be placed in the heart. The other electrode is on the pulse generator's metallic surface. These have the advantage of relative design simplicity and smaller diameters. On the other hand, these pacemakers pass their current through the heart back to the pacemaker can, through skeletal muscle. Thus, they can be subject to uncomfortable skeletal muscle stimulation at the pacemaker implant site. They are also subject to having their sense amplifiers fooled into thinking the heart is beating when it is not (oversensing) by detecting skeletal muscle noise. These complications are mitigated by implanting unipolar pulse generators with the electrically active side facing the skin to avoid contact with skeletal muscle, reducing the pulse generator's output, or adjusting its amplifier sensitivity. Bipolar leads have two electrodes, both of which are placed in the patient's heart. There is no electrical activity on the pacemaker can. Thus, these devices have the advantage of being immune to skeletal muscle oversensing and stimulation. Bipolar leads must have two conductors (compared to only one for unipolar). These have typically been metal (MP35N[1]) coils, but more recently microcables have come into use, especially in ICDs (Fig. 18).

Passively fixed electrodes are typically hemispherical in shape with about 4–8 mm^2 geometric surface area (size). They also have a surface coating or preparation, which produces a very high microscopic, electrolyte contacting surface area (Fig. 19). Some commonly used examples are platinum black, IrO_2, or TiN on a platinum base [61, 62, 63]. Vitreous carbon electrodes with a textured oxidized surface are also used on passively fixed leads [64]. The small electrode size provides efficient stimulation with high pacing impedance (to extend battery longevity) while the very high electrolyte contacting microscopic surface area provides high capacitance [65, 66]. Today, most electrodes also elute a trace of glucocorticosteroid, which helps suppress the foreign body response (inflammation and encapsulation) at the electrode tissue interface that can cause stimulation thresholds to markedly rise chronically [67].

ICD leads require very low electrical resistance to deliver their high-energy shocks without overheating. Today, most ICD high-voltage conductors are made by drawing an MP35N tube filled with a silver plug down into silver cored wire. The introduction of microcable conductors for the pacing function of the device has allowed newer designs to be much smaller in diameter. In addition to pacing electrodes, these leads must have a very large shocking electrode. This is typically made of platinum wire to allow mechanical flexibility.

---

[1] Dupont, an alloy of Ni, Co, Cr and Mo

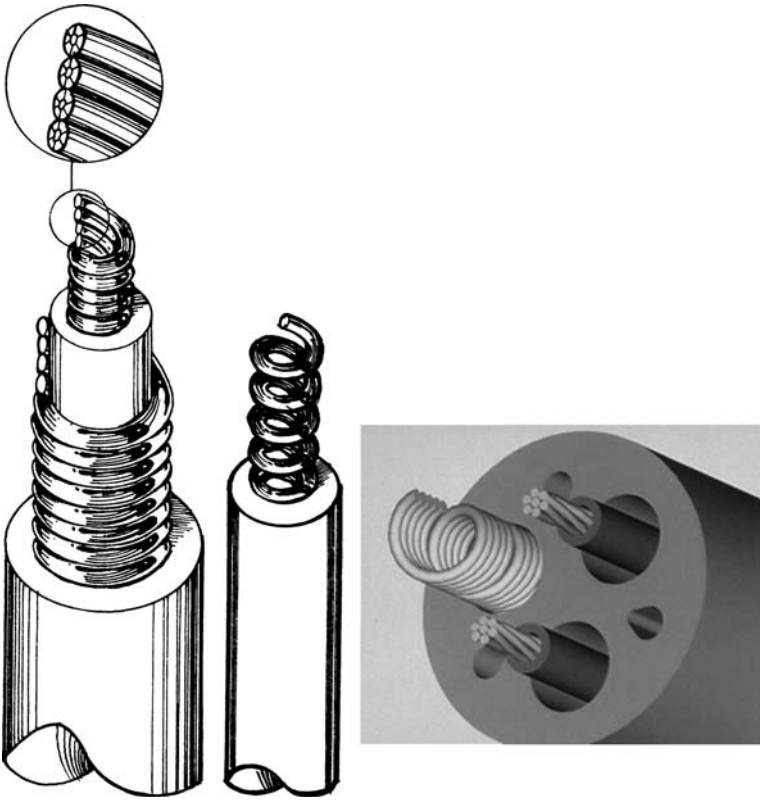

Fig. 18 A coaxial bipolar lead assembly (*left*), a unipolar lead's conductor assembly (*center*), and an ICD lead with a conductor coil and two microcables

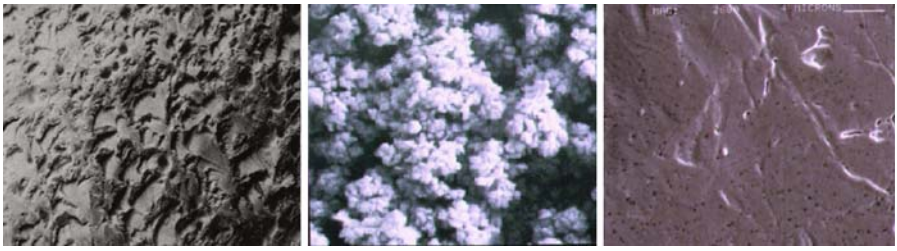

Fig. 19 Electron micrographs of electrode surfaces. *Left* – a St Jude Medical Model 412S/60 lead's activated carbon electrode surface (8000X), *center* – a Medtronic Model 4012 platinized electrode surface (4800X), and *right* – a Medtronic polished platinum electrode surface (7000X)

Electrical insulation is typically provided by either silicone rubber, a polyether polyurethane, or both. Silicone rubber has a long history of use. It is relatively flexible but weak with low tear resistance [68]. Thus, it is subject to mechanical damage both during implant and while in service. Polyurethane is

stiffer (higher modulus of elasticity) and much tougher with high tear resistance. In addition it is slippery in blood while silicone rubber tends to be sticky. Thus, polyurethane insulated leads can be smaller (thinner insulation), yet with similar or better implant characteristics (stiffness, torque control, lubricity in blood) [68]. These leads are much more resistant to mechanical damage. However, some softer polyether polyurethanes are subject to oxidative forms of damage, environmental stress cracking (ESC), and metal ion oxidation (MIO) [69, 70]. Modern polyurethane insulated leads use harder, more biostable materials with improved manufacturing processes. These continue to demonstrate excellent long-term performance in postmarket clinical studies [71]. Some leads also have a redundant insulation, typically eTFE, on each wire of the conductor coil, which serves to additionally improve hardware reliability [72].

4.7 Programmability and Automaticity

Until the 1990s most pulse generators had to be electrically tested and programmed. In most cases the pulse generator was left at factory preset values at implant. After about 6 weeks, the patient was retested, and the pacemaker's output adjusted to as low a voltage as could safely be used (typically about three times the stimulation threshold value) to minimize current drain from the battery. This procedure was necessary because older, pre-steroid eluting lead's thresholds typically increased significantly to a peak value (because of inflammation), then came down to an intermediate value (because of encapsulation). A high output was needed to assure "capture" during the peak phase. The advent of steroid elution coupled with high efficiency designs dramatically reduced or eliminated the peaking phenomenon, keeping chronic thresholds relatively low. Nonetheless, the practice of reprogramming 6 weeks post-implant continued. Toward the end of the 20th century, pacemakers that could determine if a pacing stimulus actually "captured" the ventricle were introduced [73, 74]. These used very low polarizing electrodes to detect the ventricular QRS complex or atrial P wave evoked by the pacing stimulus. If the stimulus was too low and the heart did not react, the stimulus would be increased and delivered again. Using this feature, the pulse generator could automatically set its output with a much lower safety factor, maximizing battery longevity without compromising patient safety. Then, pacemakers became truly automatic with artificial intelligence algorithms to learn the patient's specific situation and adjust themselves accordingly. Today, most pacemakers are simply implanted and the device adjusts itself according to the patient's needs.

5 Summary of Indications for Pacemaker Implant

There are many indications for the implant of pacemakers to treat bradycardia or manage rhythm complications as briefly summarized below. Of course, each individual patient must be evaluated to determine if pacing is in fact

appropriate. For example, an athlete in good physical condition may have a resting heart beat as low as 40, and be completely healthy with no need for a pacemaker. Another patient who is not very fit may indeed require a pacemaker to get his or her heart rate up from 40 to 72 beats per minute. A thorough review of indications is to be found on the ACC/AHA/NASPE web site [75]. But first let us look at how the heart's electrical conduction system works.

5.1 The Cardiac Conduction System

Figure 20 shows a cartoon of the heart's conduction system. In natural stimulation, electrical depolarization is initiated at the sinoatrial node at a typical intrinsic rate of 70–75 bpm. The atrium then depolarizes in a wave emanating from the sinoatrial node (or along tracks of oriented myocardial fibers), initiating a contraction. As the stimulus enters the atrioventricular node, its conduction

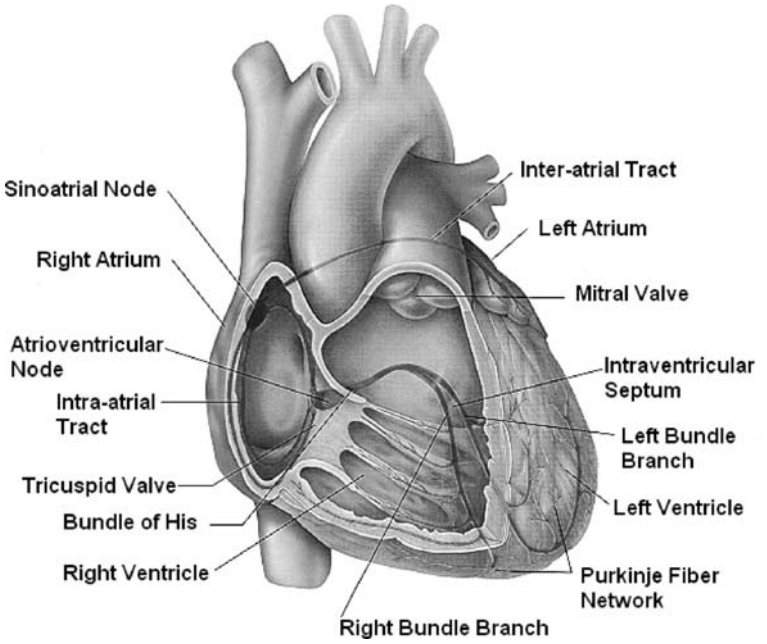

Fig. 20 A cartoon of the anatomically normal conduction system of the heart. In natural stimulation, depolarization is initiated at the sinoatrial (SA) node at a typical intrinsic rate of 70–75 bpm. The atrium then depolarizes in a wave emanating from the sinoatrial node (or along tracks of oriented myocardial fibers), initiating a contraction. As the stimulus enters the atrioventricular (AV) node, its conduction slows. This allows complete contraction of the atria before the impulse reaches the ventricles. As the impulse enters the His bundle, conduction velocity increases. The impulse is then transmitted through the left and right bundle branches (fascicles) and the Purkinje fibers throughout the right and left ventricular endocardial shells to initiate a ventricular contraction

slows. This allows complete contraction of the atria before the impulse reaches the ventricles. As the impulse enters the His bundle, conduction velocity increases. The impulse is then transmitted through the left and right bundle branches (fascicles) and the Purkinje fibers throughout the right and left ventricular endocardial shells. The subsequent depolarization of the ventricular muscle then generates a QRS complex on surface electrocardiography. When an interruption or abnormality in the conduction system occurs, other cells assume the role of pacemaker, at slower rates. For example, if the atrioventricular node or cells in the ventricle were forced to take over as the pacemaker, ventricular rate may fall to 40–60 bpm or less, which may require an artificial pacemaker.

5.2 Acquired AV Block

This is a condition where the electrical impulses from the atrium are blocked at the AV node (AV block) or within the ventricle's conduction system (fascicular block). It can occur because of fibrosis due to the normal aging process, myocardial infarction, cardiomyopathy, and other diseases. It can also be caused by accidentally cutting the heart's conduction system during cardiac surgery.

5.3 Sinus Node Dysfunction (Sick Sinus Syndrome or SSS)

Sick sinus syndrome is caused by electrophysiologic abnormalities of the sinus node and is the most common indication for pacing today [76]. It is caused by disorders that involve scarring, degeneration, or damage to the conduction system – including sarcoidosis, amyloidosis, Chagas disease, and cardiomyopathies. It is most common in elderly patients where the cause is often nonspecific, scar-like degeneration of the conduction system. Cardiac surgery is a common cause in children. It is also caused or worsened by medications such as digitalis, calcium channel blockers, beta-blockers, sympatholytic medications, and antiarrhythmics. SSS includes a number of arrhythmias including sinus bradycardia, sinus arrest, sinoatrial block, and paroxymal supraventricular tachyarrhythmias alternating with periods of bradycardia or asystole.

5.4 Prevention and Termination of Tachyarrhythmias

Reentrant rhythms including atrial flutter, paroxymal reentrant supraventricular tachycardia, and ventricular tachycardia can sometimes be prevented or terminated by a variety of pacing patterns including programmed stimulation and short bursts of rapid pacing [77].

5.5 Hypersensitive Carotid Sinus and Neurocardiogenic Syncope

Syncope (fainting due to poor blood supply to the head) or presyncope results from an extreme reflex response to carotid sinus stimulation. It also occurs in children, adolescents, and young adults with congenital heart disease [78]. Often patients present with symptomatic sinus bradycardia, bradycardia–tachycardia syndrome, congenital 3rd degree AV block, or advanced 2nd or 3rd degree AV block.

5.6 Cardiac Transplantation

Bradyarrhythmias after cardiac transplantation occur in 8–23% of patients, mostly associated with sinus node dysfunction. About 50% of these resolve in 6–12 months requiring no permanent pacing [79]. The remaining 50% may require permanent pacing.

5.7 Atrial Fibrillation (AF) and Flutter

Once AF is cardioverted there is a 50–60% recurrence in spite of antiarrhythmic drug therapy [77]. Ablation of the AV node with permanent pacing is effective in controlling the ventricular rate. AAI pacing results in increased patient survival, reduced heart failure, less AF, and fewer thromboembolic complications. Currently used algorithms are atrial overdrive, pacing in response to sudden change, and post-AF aggressive overdrive pacing.

5.8 Heart Failure

Heart failure is a progressive disorder in which damage to the heart causes weakening of the heart muscle [80]. The most common forms are congestive heart failure (CHF) and obstructive heart failure. Congestive heart failure is a condition where the heart cannot pump enough blood to keep the body's organs functioning properly. It can result from coronary artery disease, myocardial infarction where scar tissue interferes with the heart's function, high blood pressure, heart valve disease, cardiomyopathy, congenital defects, and infection (endocarditis and/or myocarditis). Limited improvement has been reported in patients with symptomatic dilated cardiomyopathy refractory to medical therapy, using dual-chamber pacing and a short AV delay. Thirty to forty percent of patients with congestive heart failure have intraventricular conduction abnormalities which progress over time. This leads to significant dyssynchrony in both LV contraction and relaxation. Biventricular pacing has been shown to produce improvements in NYHA class III or IV patients

Hypertrophic obstructive cardiomyopathy is a high LV outflow gradient due to enlargement of the intraventricular septum, obstructing blood flow from the left ventricle. Sometimes the enlarged septum distorts a mitral valve leaflet causing it to leak. It can be treated with dual-chamber pacing and a short AV delay.

6 Summary of Indications for ICD Implant

ICDs are usually thought of as being indicated to treat too fast heart rates (tachycardia, ventricular fibrillation) or cardiac arrest. However, it appears that many heart failure patients are also prone to tachyarrhythmias. Thus many now receive an ICD lead on the left ventricle via the coronary sinus so they can be paced for biventricular resynchronization, but can be defibrillated if need be. The indications for ICD implant are broken down into three classifications based on causative and risk factors, and comorbidities. The following examples are summarized. For a more thorough explanation see indication guidelines for the implant of ICDs which are provided by an ACC/AHA/NASPE web page [75]:

- Class I includes cardiac arrest due to ventricular fibrillation (VF) or tachycardia (VT), spontaneous sustained VT associated with structural heart disease, syncope of undetermined origin and nonsustained VT in patients with coronary artery disease, or prior myocardial infarction.
- Class II includes some less specific indications such as ejection fraction $< 30\%$ at least 1 month post-MI and 3 months post-artery revascularization or cardiac arrest presumed to be due to VF when electrophysiological testing is precluded. Severe symptoms in patients awaiting cardiac transplantation may require an ICD. Other indications include some inherited conditions, nonsustained VT with coronary artery disease, recurrent syncope of undetermined etiology with ventricular dysfunction and inducible VT, recurrent syncope of undetermined etiology or family history of unexplained sudden death, and syncope in patients with advanced structural heart disease.
- Class III includes syncope of undetermined cause when VT cannot be induced in electrophysiological examinations, incessant VT or VF, VT or VF resulting from arrhythmias amenable to surgical or catheter ablation or due to a transient reversible disorder. Significant psychiatric illnesses that may preclude follow-up may be a cause to implant an ICD. Terminal illness with projected life expectancy of ≤ 6 months or certain forms of coronary artery disease may also indicate the need for an implantable ICD. As noted above, ICDs are indicated for patients with NYHA class IV drug-refractory congestive heart failure who are not candidates for heart transplantation. In fact, biventricular resynchronization has even made it possible to take some patients off the transplant list.

7 Clinical Management of Complications, and Related Improvements Over Time

7.1 Medical Complications

Single chamber pacemakers did a good job of preserving quality of life, and in relatively few cases, saved lives. They did, however, occasionally develop complications. For example, when pacing a patient with intact atrial ventricular conduction, retrograde conduction may activate the atria after ventricular activation. This "pacemaker syndrome" results in a retrograde flow of blood from the ventricles to the atria with flooding of the jugular and pulmonary veins. Weakness or syncope can then occur as a result of lower cardiac output or congestive heart failure [81]. Another potential complication of ventricular pacing alone is cannon waves. Pacing the ventricle causes the tricuspid valve to close. If the atrium contracts against a closed valve, then blood is forced back through the venous system producing a throbbing in the neck [82]. Dual-chamber pacemakers resolve these complications by better maintaining AV synchrony.

As noted above, unipolar devices are also prone to oversensing and muscle stimulation. Infected pacemaker pockets appear to occur in about 1–2% of patients. Explant of the device, debriding and irrigating the pocket, and implanting a new system on the other side typically solves the problem. Twiddler's syndrome occurs when a patient plays with their generator, twisting the lead up and possibly even pulling it from the heart. This can also happen without the patient's intervention in physically active or obese people. Most pulse generators and ICDs have a suture hole so it can be fixed to fascia. Sometimes implanters will put the device in a polyester mesh bag. This induces fibrotic ingrowth to fix the generator in place. Some thin people, especially the elderly, have delicate skin. If implanted subcutaneously, the skin can be tight enough to develop pressure necrosis and the device can break through the skin. This is usually dealt with by implanting the device within the muscle planes, or in some extreme cases, using alternate sites with more "padding".

Some of the major complications that can occur with leads is dislodgment (the electrode pulls away from its implant site), perforation (the lead penetrates through the epicardium), exit block (thresholds higher than the device's output), failure to sense, and infection. In 1975, 40% of patients had to be reoperated on to reposition their dislodged leads [21]. By the mid-1980s, this had been reduced to 1–3% using tines and active fixation. Perforation can be life threatening because blood can fill the pericardial sack resulting in tamponade. In most cases today, perforation is mitigated by assuring that atraumatic electrode designs are matched to the stiffness of their lead bodies. Electrode fixation also helps. In most cases, when perforation occurs it is during implant. If the heart muscle is in adequate condition, the lead can be simply pulled back without complication. If there is bleeding into the pericardial sack, then the

blood must be removed by a pericardial needle stick. Exit block caused by excessive inflammation around the electrode was at one time a major complication. By the mid-1980s, this was mostly eliminated by steroid eluting electrodes [83]. Sensing has been greatly improved over the years because of design changes to both the amplifiers and the electrodes. Modern sense amplifiers have very high input impedances so that there is no attenuation of low-frequency cardiac signals. High capacitance electrodes also produce less distorted, higher fidelity signals. Of course, an infected lead must be explanted. Because chronic leads develop collagenous encapsulation over time, explant used to require open-heart surgery. Today the development of tools to safely remove embedded leads transvenously has made extraction a safer, more viable procedure [84].

7.2 Hardware Complications

Some examples of more recent issues that resulted in pacemaker or ICD advisories include the *possible* separation of interconnect wires from the hybrid circuit, premature battery depletion due to a battery short, fractured power supply wires, potential circuit overload, and potential delayed return to permanent settings once the programmer head is removed [71]. Some ICDs have also delivered shocks when not needed (a very painful event) while some others have failed to deliver the stimulus when needed. These situations are dealt with by advising physicians on how to test for the complication and manage the patient. If need be, the pulse generator or ICD can be relatively easily explanted and returned to the manufacturer. Meanwhile, manufacturers continually design and redesign devices for the highest possible reliability.

Some lead-related complications include insulation failure and conductor fracture. Conductor fracture may be visible on X-ray whereas insulation rupture is usually not. Analysis of lead performance is part of the patient's routine follow-up. Stimulation thresholds, sensing and impedance measurements can be used to determine if the lead is intact and functioning properly. One company, Medtronic, has conducted postmarket clinical studies on their leads for 25 years. If the actuarial survival of any lead falls below 95% in 5 years, an advisory is issued, again with information on how to test for the complication and how to manage the patients [71].

8 Conclusions

Electrical stimulation of the heart has a long history, going back 260 years. Implantable pacemakers and ICDs are only about 40 years old, but during that time they have undergone amazing improvements incorporating many new innovations and scientific discoveries. Single chamber pacemakers prevailed for the first 25 years before dual-chamber systems became practical. Because these provide better hemodynamics, and resolve some complications of single

chamber devices, they now predominate. Pacing used to be just for bradycardia patients. Today it is used to prevent tachyarrhythmias, atrial fibrillation (thus reducing the chances of stroke), and to improve the condition of heart failure patients. ICDs now treat most of the heart failure patients as well as prevent deadly ventricular fibrillation. Where once we just stimulated in one chamber we now routinely place leads in two or three chambers. Four-chamber pacing has even been reported. The devices keep getting smaller, more sophisticated, and more reliable.

References

1. Furman S (2000) Introduction: History of cardiac pacing. In: Ellenbogen KA, Kay GN and Wilkoff BL (eds) Clinical cardiac pacing and defibrillation, 2nd edn. WB Saunders, Philadelphia, pp. 1–13
2. Adams R (1827) Cases of diseases of the heart accompanied with pathological observations. Dublin Hosp Rep. 4: 396
3. Stokes R (1846) Observations on some cases of permanently low pulse. Dublin Q J Med Sci 2: 73
4. Bernstein AD and Parsonnet V (2000) Pacemaker, defibrillator, and lead codes. In: Ellenbogen KA, Kay GN and Wilkoff BL (eds) Clinical cardiac pacing and defibrillation, 2nd edn. WB Saunders, Philadelphia, pp. 327–332
5. Hoorweg JL (1892) Condensatorentladung und auseinandersetzung mit du Bois-Reymond. Pflugers Arch 52: 87–108
6. Weiss G (1902) Sur la possibilite' de render comparable entrre les appareils cervant a' l'excitation electrique. Arch Ital Biol 35: 413
7. Lapique L (1909) Definition experimentale de l'excitabilite. C R Soc Biol 67: 280
8. Nernst W (1908) Zur theorie des electrischen reizes. Pflugers Arch 122: 275–314
9. Schecter DC, Lillehei CW and Soffer A (1972) Background of clinical cardiac electrostimulation. NY St J Med 72: 605–609
10. Mond H, Sloman G and Edwards R (1981) The first artificial pacemaker. PACE 4: 60
11. Zoll P, et al. (1961) Long term electrical stimulation of the heart for Stokes-Adams disease. Ann Surg 154: 330
12. Lillehei CW, Gott VL, Hodges PC, et al. (1960) Transistor pacemaker for treatment of complete atrioventricular dissociation. JAMA 172: 2006–2010
13. Elmvquist R and Senning A (1959 and 1960) Implantable pacemaker for the heart. In: Smyth CN (ed.) Medical electronics, Iliffe & Sons Ltd, Paris and London
14. Greatbatch W and Chardack WM (1959) A transistorized implantable pacemaker for the long term correction of complete atrioventricular block. M Electron NEREM 48: 643
15. Cammilli L, Ricci D, Risani R, et al. (1979) PH triggered pacemaker and clinical results. In: Meere CD (ed.) Proceedings of the VIth world symposium on cardiac pacing. PACESYMP, Montreal, Chapter 19–8
16. Rickards AF and Norman J (1981) Relation between Q-T interval and heart rate: New design of physiologically adaptive cardiac pacer. Br Heart J 45: 56–61
17. Leung S-K, Lau C-P and Camm JA (2000) An overview of sensors: Ideal characteristics. Sensor combinations and automaticity. In: Ellenbogen KA, Kay GN and Wilkoff BL (eds.) Clinical cardiac pacing and defibrillation, 2nd edn. WB Saunders, Philadelphia, pp. 219–248
18. Hunter S, Boldiuc L, Long V, et al. (1973) A new myocardial pacemaker lead (sutureless). Chest 63: 430
19. Furman S and Robinson G (1958) The use of an intracardiac pacemaker in the correction of total heart block. Surg Forum 9: 245
20. Siddons H and Davies J (1968) A new technique for internal cardiac pacing. Lancet 2: 1204

21. Hori M (1977) Round table world survey. In: Watanabe Y (ed) Cardiac pacing. Excerpta Medica, Amsterdam p. 556
22. Painter MW, Harrington OB, Crosby VG, et al. (1979) Implantation of an endocardial tined lead to prevent early dislodgment. J Thorasc Cardiovas Surg 77: 249
23. Bisping HJ and Rupp H (1977) A new permanent transvenous electrode for fixation in the atrium. In: Watanabe Y (ed.) Proceedings of the Vth International symposium on cardiac pacing. Excerpta Medica, Amsterdam pp. 543–547
24. Littleford PO, Parsonnet V and Spector SD (1979) Method for rapid and atraumatic insertion of permanent endocardial electrodes through the subclavian vein. Am J Cardiol 43: 980
25. Belott PH and Reynolds DW (2000) Permanent pacemaker and implantable cardioverter-defibrillator implantation. In: Ellenbogen KA, Kay GN and Wilkoff BL (eds.) Clinical cardiac pacing and defibrillation, 2nd edn. WB Saunders, Philadelphia, pp. 573–644
26. Nissen RG, Holmes DR, Maloney JD, et al. (1979) Experience with permanent cardiac pacemakers in congenital heart disease. In: Meere C (ed.) PACESYMP, Montreal, Proceedings of the VIth world symposium on cardiac pacing, Chapter 23–2
27. Tabrisky J, Jobe WE, Newman MB, et al. (1967) Internal cardiac pacemakers. Amer J Roentgenology 100: 446–456
28. Benchimol A and Liggett MS (1966) Cardiac hemodynamics during stimulation of the right atrium, right ventricle, and left ventricle in normal and abnormal hearts. Circulation, XXXIII: 933–944
29. Smyth NPD, Vasarhely L, McNamara W, et al. (1969) A permanent transvenous atrial electrode catheter. J Thorac Cardiovasc Surg 58: 773
30. DeFrancis NA and Giordano RP (1968) Permanent epicardial atrial pacing in the treatment of refractory ventricular tachycardia. Am J Cardiol 22: 742–745
31. Padeletti L, Porciani MC, Michelucci A, et al. (1998) Interatrial septum pacing: A new approach to prevent paroxysmal atrial fibrillation. PACE 21(Pt. II): 797
32. Daubert C, Gras D, Leclercq C, et al. (1995) Biatrial synchronous pacing: A new therapeutic approach to prevent refractory atrial tachyarrhythmias. PACE 18(Pt. II): 1781
33. Nathan DA, Center S, Wu C-Y, et al. (1963) An implantable synchronous pacemaker for the long term correction of complete heart block. Circulation 27: 682–685
34. Funke HD (1979) Eighteen (18) months of clinical experience with the implantable optimized sequential stimulator. PACE 2: A-44 (251)
35. Faerestrand S and Ohm O-J (1985) A time-related study of the hemodynamic benefit of atrioventricular synchronous pacing Evaluated by Doppler echocardiography. PACE 8: 838–848
36. Santini M, MacCarter D, Knudson M, et al. (1981) Automatic atrial rate responsive VVI pacing: A simple physiological approach. PACE 4: A–72
37. Tse H-F, Lau C-P, Leung S-K, et al. (1996) Single lead DDD system; Comparative evaluation of unipolar, bipolar and overlapping biphasic stimulation and the effects of right atrial floating electrode location on atrial pacing and sensing. PACE 19(11 part II): 1758–1763
38. Bakker P, Sen KCA, de Jonge N, et al. (1995) Biventricular pacing improves functional capacity in patients with end-stage congestive heart failure. PACE 18(4 Pt. II): 825
39. Cazeau S, Ritter P, Lazarus A, et al. (1996) Multisite pacing for end-stage heart failure: Early experience PACE 19(Pt II): 1748–1757
40. Cazeau S, Leclercq C, Lavergne T, et al. (2001) Effects of multisite biventricular pacing in patients with heart failure and intraventricular conduction delay. N Engl J Med 344: 873–80
41. Abraham WT, Fisher WG, Smith AL, et al. (2002) Cardiac resynchronization in chronic heart failure, N Engl J Med 346:1845–1853
42. Bristow MR, Feldman AM, Saxon LA (2000) Heart failure management using implantable devices for ventricular resynchronization: Comparison of medial therapy, pacing, and defibrillation in chronic heart failure (COMPANION) trial. J Card Fail 6: 276–285
43. Ritter P, Gras D, Bakdach H, et al. (1998) Material-related complications of multisite pacing in end-stage heart failure. Archives Des Maladies Du Coeur Et Des Vaisseauz 91: 143

44. McVenes R, Stokes K, Christie M, et al. (1998) Technical aspects of simultaneous biventricular stimulation thresholds. Archives des Maladies du Coeur et des Vaisseauz 91(3): 152
45. VonLudinghausen M (1987) Clinical anatomy of cardiac veins, Vv. Cardiacae Surg Radiol Anat 9: 159–168
46. Hill MRS, Connors SP and Hassan A (2000) Coronary venous vasculature in congestive heart failure patients: Opportunities for left ventricular pacing. Europace. I: D238
47. Asirvatham SJ, Talreja DR, Gami AS, et al. (2001) Coronary venous drainage of the lateral left ventricle: Implications for biventricular pacing. Circulation 104(17): II–619
48. October 18, (2000) Medtronic Attain™ side-wire lead model 4191 study closure report 1.1
49. Garrigue S, Jaïs P, Espil G, et al. (2001) Comparison of chronic biventricular pacing between epicardial and endocardial left ventricular stimulation using Doppler tissue imaging in patients with heart failure. Am J Cardi 88: 858–862
50. Leclercq F, Hager FX, Marcia JC, et al. (1999) Left ventricular lead insertion using a modified transseptal catheterization technique: A totally endocardial approach for permanent biventricular pacing in end-stage heart failure. PACE 22: 1570–1575
51. Gold MR and Rashba EJ (1999) Left ventricular endocardial pacing: Don't try this at home. PACE 22: 1567–1569
52. Leclercq F, Kassnasrallah S, Macia JC et al. (2000) Transcranial doppler detection of microemboli during endocardial biventricular pacing in end-stage heart failure. J Am Coll Cardiol 35(Suppl A): 141–A34
53. Jais P, Takahashi A, Garrigue S, et al. (2000) Mid-term follow-up of endocardial biventricular pacing. PACE 23:1744–1747
54. McVenes R and Christie M (2002) LV endocardial and triple site stimulation–Insights to the mechanism of cardiac resynchronization. Europace 3(Suppl A): 176
55. Warren JA and Nelson JP (2000) Pacemaker and ICD pulse generator circuitry. In: Ellenbogen KA, Kay GN and Wilkoff BL (eds.) Clinical cardiac pacing and defibrillation, 2nd edn. WB Saunders, Philadelphia, pp. 194–216
56. Miroski M (1970) Standby automatic defibrillator. Arch Intern Med 126: 158
57. Thomas AC, Moser SA, Smutka ML, et al. (1988) Implantable defibrillation: Eight years of clinical experience. PACE11: 2053–2056
58. Winkle RA, Mead H, Ruder MA, et al. (1989) Long-term outcome with the automatic implantable cardioverted-defibrillator. J Am Coll Cardiol 13: 1353
59. Untereker DF, Shepard RB, Schmidt CL, et al. (2000) Power systems for implantable pacemakers, cardioverters and defibrillators. In: Ellenbogen KA, Kay GN and Wilkoff BL (eds) Clinical cardiac pacing and defibrillation, 2nd edn. WB Saunders, Philadelphia, pp. 167–193
60. Owens BB (ed) (1986) Batteries for implantable biomedical devices. Plenum, New York
61. Bornzin GA, Stokes KB and Wiebusch WA (1983) A low-threshold, low-polarization platinized endocardial electrode. PACE 6: A–70
62. DelBuffalo AGA, Schlaepfer J, Fromer M, et al. (1993) Acute and long-term ventricular stimulation thresholds with a new, iridium oxide-coated electrode. PACE 16: 1240
63. Schaldach M, Hubman M, Weikl A, et al. (1990) Sputter-deposited TiN electrode coatings for superior sensing and pacing performance. PACE 13: 1891
64. Elmqvist H, Schuller H and Richter G (1983) The carbon tip electrode. PACE 6: 436
65. Stokes KB, Taepke R and Gates J (August 1994) All impedances are not created equal: Expediency vs efficiency. Medtronic Sci Technol 3(1): 2–12
66. Stokes K (March 1995) Estimating pulse generator longevity. Medtronic Sci Technol J 3(2): 26–28
67. Stokes KB, Bornzin GA and Wiebusch WA (1983) A steroid-eluting, low-threshold, low-polarizing electrode. In: Steinbach K (ed.) Cardiac Pacing, Steinkopff verlag, Darmstadt, pp. 369–376
68. Stokes K and Cobian K (1982) Polyether polyurethanes for implantable pacemaker leads. Biomaterials 3: 225–231

69. Stokes KB, Frazer WA and Christopherson RA (1984) Environmental stress cracking in implanted polyurethanes. Second world congress on biomaterials, 10th Annual Meeting of the Society for Biomaterials p. 254
70. Stokes KB, Urbanski P and Upton J (1990) The in vivo autooxidation of polyether polyurethane by metal ions. J Biomater Sci, Poly Ed 1(3): 207–230
71. Medtronic Inc (2007) Cardiac rhythm disease management, Product Performance report, 2nd edn., Issue no 57. http://www.mwdtronic.com
72. Tyers F, Yeung J, Mills P, et al. (May 1997) 3 Year experience: New atrial and ventricular coradial bipolar leads. PACE 20(Pt II): 1475
73. Schüller H, Fahraeus T, Thuesen L, et al. (1995) First clinical experience with an automatic output adaption pacemaker based on evoked response. PACE 18(4, Pt II): 824
74. Livingston AR, Callaghan FJ, Byrd CL, et al. (1988) Atrial capture detection with endocardial electrodes. PACE 11(11 Pt2): 1770–1776
75. ACC/AHA/NASPE Guidelines: Indications for pacing and ICD therapy. http://www.patientcareonline
76. Gillis AM (2000) Sinus node disease. In: Ellenbogen KA, Kay GN and Wilkoff BL (eds) Clinical cardiac pacing and defibrillation, 2nd edn. WB Saunders, Philadelphia, pp. 405–425
77. Saksena S, Mehra R and Ellenbogen KA (2000) Pacing for prevention of tachyarrhythmias. In: Ellenbogen KA, Kay GN and Wilkoff BL (eds.) Clinical cardiac pacing and defibrillation, 2nd edn. WB Saunders, Philadelphia, pp. 479–496
78. Sheldon RS and Jaeger FJ (2000) Carotid sinus hypersensitivity and neurally mediated syncope. In: Ellenbogen KA, Kay GN and Wilkoff BL (eds.) Clinical cardiac pacing and defibrillation, 2nd edn. WB Saunders, Philadelphia, pp. 455–478
79. Wilkoff BL and Firstenberg MS (2000) Cardiac chronotropic responsiveness. In: Ellenbogen KA, Kay GN and Wilkoff BL (eds.) Clinical cardiac pacing and defibrillation, 2nd edn. WB Saunders, Philadelphia, pp. 508–532
80. Gold MR and Peters RW (2000) Pacing in patients with heart failure. In: Ellenbogen KA, Kay GN and Wilkoff BL (eds.) Clinical cardiac pacing and defibrillation, 2nd edn. WB Saunders, Philadelphia, pp. 497–507
81. Janosik DL and Ellenbogen KA (2000) Basic physiology of cardiac pacing and pacemaker syndrome. In: Ellenbogen KA, Kay GN and Wilkoff BL (eds.) Clinical cardiac pacing and defibrillation, 2nd edn. WB Saunders, Philadelphia, pp. 333–382
82. Morgan DE, Norman R, West RO, et al. (1986) Echocardiographic assessment of tricuspid regurgitation during ventricular demand pacing. Am J Cardiol 58(10): 1025–1029
83. King DH, Gillette PC, Shannon C, et al. (1983) A steroid eluting endocardial pacing for treatment of exit block. Am Heart 106: 1438
84. Byrd CL and Wilkoff BL (2000) Techniques and devices for extraction of pacemaker and implantable cardioverter-defibrillator leads. In: Ellenbogen KA, Kay GN and Wilkoff BL (eds.) Clinical cardiac pacing and defibrillation, 2nd edn. WB Saunders, Philadelphia, pp. 695–709

The Bion® Microstimulator and its Clinical Applications

Todd K. Whitehurst, Joseph H. Schulman, Kristen N. Jaax, and Rafael Carbunaru

Abstract The Bion® microstimulator is a miniature leadless implantable neurostimulator designed to be implanted through a minimally invasive procedure. The small profile of the microstimulator allows it to be implanted through a small incision or by injection. Additionally, the stimulating electrodes are mounted directly on the microstimulator, which eliminates possible complications associated with the use of a lead (e.g., migration). An RF-powered version of the Bion® microstimulator was developed over a decade ago and that device has been used in feasibility clinical studies for several functional electrical stimulation (FES) applications, including shoulder subluxation and post-stroke hand rehabilitation. It has also been explored in clinical applications for knee osteoarthritis rehabilitation, obstructive sleep apnea, and pressure ulcer prevention. A version of the Bion® microstimulator with a rechargeable battery has also been developed, and the first-generation battery-powered microstimulator was used in a feasibility clinical trial for headaches. It is also being used in a clinical trial for overactive bladder. Preclinical experiments on the use of the microstimulator for gastroesophageal reflux disease have also been promising. Battery-Powered Microstimulator-sensors with bidirectional propagated wave telemetry, capable of coordinating hundreds of injectable devices for stroke and quadriplegic patients, are presently in the last stages of development.

1 Introduction

The Bion® microstimulator was originally designed for Functional Electrical Stimulation (FES). It was developed as a means to provide small stimulators distributed across a patient's body without the need for interconnecting wires. Other systems implanted for FES, such as the Praxis system (Cochlear Ltd, Lane Cove, NSW, Australia) and the Freehand system (NeuroControl,

T.K. Whitehurst (✉)
Boston Scientific Neuromodulation, Valencia, CA 91355, USA
e-mail: todd.whitehurst@bsci.com

D.D. Zhou, E. Greenbaum (eds.), *Implantable Neural Prostheses 1*,
Biological and Medical Physics, Biomedical Engineering,
DOI 10.1007/978-0-387-77261-5_8,

Cleveland, OH, USA), utilize a central controller typically implanted in the trunk with a number of electrode leads directly connected from the central controller to the muscle targets in the limb(s) [1, 2]. The central controller activates the electrodes directly. While this architecture has proven effective for FES, the necessity of running an electrode lead through a limb joint (e.g., shoulder joint) increase the amount of stress on the lead and may result in lead fracture. Additionally, an infection in any one part of the body would tend to spread to the rest of the system, which has led to an explant of the entire system.

2 Development of Bion® Microstimulator

In the early 1990s other implanted magnetically powered systems consisting of a pacemaker sized device with between 8 and 24 leads were implanted for FES. Among these were the low-power 24-lead Praxis system (Cochlear Ltd, Lane Cove, NSW, Australia) designed to stimulate nerves, and the high-power 8 lead Freehand system (NeuroControl, Cleveland, OH, USA) designed to power both nerves and muscle sections [1, 2]. These devices utilized a central controller typically implanted in the trunk with a number of electrode leads directly connected to the targets in the limb(s). The central controller also activated the electrodes directly. Due to the arrangement of the leads, this design is sometimes referred to as the octopus type of stimulator and worked well but had several serious problems. For example, every wire had to be planned for in advance of the surgery, and excessive surgery was required to install or extract the systems. They were also prone to infection because of the large area of all the attached leads. By the time infection was detected the entire system was affected and had to be surgically removed.

The company making the Freehand system took it off the market after a few years due to the extensive surgery required. The company making the 24-lead Praxis System never went to commercial production after an infection in the first patient required the entire system to be surgically removed.

Commercial feasibility is essential to get a product to the public. On that note, the only multichannel stimulators that are commercially successful today are the nonmultiwire spinal cord stimulator and nonmultiwire cochlear implant. These systems are implanted in only one or two anatomical locations in the body, and thus the surgeries are relatively quick.

The Bion® microstimulator was developed to overcome the need to tunnel leads from a central controller. Each Bion® microstimulator is a self-contained implantable electrical stimulator that requires no lead. Each device contains at least one pair of electrodes (cathode and anode) for stimulation. Each device also contains all of the electronics necessary to deliver electrical stimulation, including programmable memory so that stimulation parameters may be programmed and stored. Additionally the devices contain a means of communication with an external programmer or controller, which is typically some type of

radiofrequency (RF) telemetry. The Bion® microstimulator contains a means of receiving RF energy from an applied RF field. The energy received is used to power the microstimulator. Some Bion® microstimulators also contain a rechargeable battery, and excess received energy may be used to charge the battery.

The Bion® microstimulator was designed to have a form factor that allows it to be implanted in a minimally invasive fashion. Bion® microstimulator devices thus far have been designed with a cylindrical form factor, in which the diameter is 2.0–3.3 mm and the length is 16–27 mm. This allows a Bion® microstimulator to be implanted in tissue in a manner similar to injection.

2.1 First-Generation RF-Powered Bion® Microstimulator

The first-generation Bion® microstimulator (RFB1) was originally proposed by G.E. Loeb et al. [3] as an RF-powered device. The first devices were designed and developed by researchers at Queens University (Kingston, ON, Canada), the Illinois Institute of Technology (Chicago, IL, USA), and the Alfred E. Mann Foundation (Valencia, CA, USA) with funding from the NIH Neural Prosthesis Program (Fig. 1). G. Loeb, P. Troyk, J. Schulman, and J. Gord produced the electrical design and specifications of the Bion®. G. Loeb conceived of the idea of using a tantalum oxide capacitor electrode that also served as the energy storage capacitor. J. Gord led the team at AMF that designed the first integrated circuit for the Bion®. P. Troyk designed and constructed the highly efficient Class E magnetic field transmitter to power the Bion®. An infrared laser welding station was constructed at the AMF by Primoz Strojnik to seal the glass case. The pulse width digital circuitry in the chip was designed by J. Wolfe. The RFB1 contained a ferrite wound coil next to the Integrated Circuit inside the glass case with the Tantalum oxide capacitor electrode outside the case. Subsequently, the RFB1 was produced by the Alfred Mann Institute for Biomedical Engineering at the University of Southern California (Los Angeles, CA).

Fig. 1 Photo of the first version of the glass-encased RF-powered microstimulator Bion®. From *left* to *right*: cylindrical shaped tantalum oxide coated open cell capacitor electrode attached via a tantalum stem which is hermetically sealed through a glass bead into the inside of the glass container. To the *right* of the stem is the 3 μm integrated circuit, followed by the coil-wrapped ferrite rod. On the *right* side is the iridium spherical-shaped electrode which is hermetically sealed to the glass case. (Reproduced from Ref. [4] with permission from IEEE)

The RFB1 was designed to be injected or implanted directly into a muscle for direct stimulation of muscle tissue or of the local motor nerves supplying the muscle (e.g., for stimulation at a motor point). The device encased the electronics in a hermetically sealed glass capsule. It had a single tantalum capacitor electrode (cathode) on the front tip of the microstimulator to provide charge-balanced stimulation. The single anode was an iridium electrode mounted at the other end of the cylinder. The device had a diameter of 2 mm and a length of 16 mm.

A block diagram of the control circuit is shown in Fig. 2. The RFB1 produced a wide range of possible programmable stimulation parameters, with a maximum pulse current of 30 mA, a maximum pulse width of 512 ms, and a maximum frequency of more than 500 Hz [5]. The device was designed to be powered and controlled by an external controller worn by the patient during use of the device. Each microstimulator had a unique 8-bit address, which allowed up to 255 devices to be controlled independently

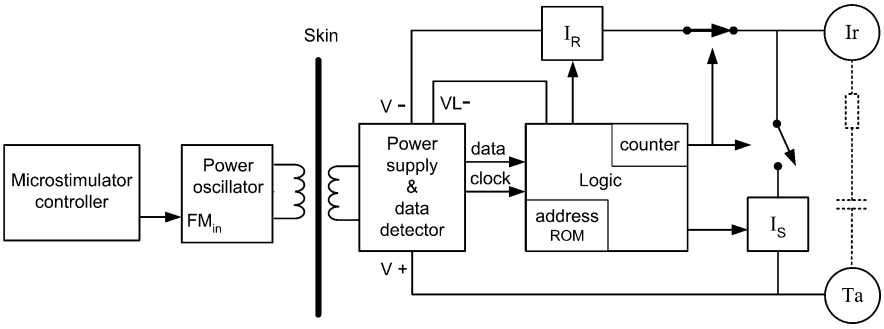

Fig. 2 Block diagram of control circuit and glass-encased RF-powered microstimulator. Reproduced from Ref. [4] with permission from IEEE

2.2 Second-Generation RF-Powered Bion® Microstimulator

The first-generation RF-powered Bion® microstimulator encased the electronics in a hermetically sealed glass package and effected stimulation with an external tantalum capacitor electrode. A second-generation RF-powered Bion® microstimulator (RFB2), shown in Fig. 3, has been developed by the Alfred E. Mann Foundation (Valencia, CA, USA). This device encases the electronics in a hermetic ceramic case, including a decoupling capacitor, and employs a platinum–iridium stimulation electrode. The microstimulator includes an eyelet through which a suture may be threaded, which facilitates straightforward explantation of the Bion® within the first week of implant, if necessary. The diameter of the RFB2 is 2.4 mm, and the length including the eyelet is 17.5 mm. The electronics core of the RFB2 is very similar to that of RFB1, so that RFB2 has the same stimulation parameters as RFB1 and also has 255 possible device addresses [6].

Fig. 3 Second-generation RF-powered Bion® microstimulator (RFB2)

Several changes were made to improve the RFB2 design (see Fig. 4). To address the high-energy requirement, the compliance voltage of the RF-powered microstimulator was increased from 9 to 18 V so very high currents could be delivered. The demodulation circuit was improved so the Class E power supplies could drive the microstimulators. The RF-powered microstimulators could now generate greater than 30 mA pulses.

Fig. 4 Ceramic case microstimulator component arrangement. Reproduced from Ref. [4] with permission from IEEE

Instead of having the coil side by side with the IC, it was decided to sandwich the ceramic hybrid and IC in between two half-cylinders of ferrite. The coil was wrapped around the entire assembly. This made the coil longer and more efficient in receiving energy from the AC magnetic field. These hybrids and ICs manufactured at the AMF pilot line were provided to Alfred E. Mann Institute for Biomedical Engineering at the University of Southern California

(AMI-USC) to assist their research and development efforts. AMI-USC installed them in glass cases with external tantalum oxide capacitors for animal and human use. Advanced Bionics Corporation (Valencia, CA) also used these circuits in battery-powered versions that were RF powered to test their insertion system for the urinary incontinence application.

A ceramic tube was designed to replace the glass case in some versions. Each end of the tube had metal parts brazed on. One end was sealed hermetically with a metal cap and the other end had a short metal cylinder brazed on. After all the components were loaded into the open cylinder end and attached electrically, the unit was vacuum baked for several days to drive all the moisture out, and then a metal cap was laser welded on. The wall of the ceramic tube was 0.010-in. thick, making the outside diameter 2.25-mm wide instead of the 2.00 mm of the glass walled versions. The three-point break strength was measured to be greater than 30 lb rather than the 5 lb measured in the same way on the glass case, although whether or not this additional strength is required remains uncertain.

There was a concern that the external tantalum oxide capacitor slug was accessible to handling. There was the possibility that a surgeon's scalpel might lose a particle of steel on the tantalum slug and short through the thin oxide coating. This would prevent the capacitor from holding charge and allow the dangerous condition of permitting continuous direct current to flow directly into the tissue. The best solution is to place a highly reliable capacitor inside the ceramic case (see Fig. 4). A counterargument to this is that a piece of steel breaking from a surgical scalpel is highly unlikely, and for it to then adhere to the tantalum is an even further unlikely scenario; and finally that a scratch in the tantalum oxide should immediately heal itself in any event.

Failures that occurred in the pilot production raised concerns about damage from static electricity due to handling the microstimulators in the operating room. Therefore, as an added protection, a series pair of opposing zener diodes were mounted on the ceramic substrate opposite to the side where the rectifier diode was mounted. The rectifier diode can be seen in the right side of Fig. 4. These zener diodes are the same as those used for defibrillation protection in cardiac pacemakers. One could argue that there is a possibility for the microstimulator to be implanted near the chest, and thus, defibrillator protection is not unreasonable. The production yield increased immediately after the zener diodes were introduced.

During surgery, the clinician must decide whether the implant is positioned properly and the threshold is at the desired value. At that point the microstimulator is released and left in the body. Sometimes, a slight last movement that occurs at the time of release displaces the implant and causes the threshold to be higher than desired, or there may be an undesired effect and the clinician may want to repeat the insertion. It is also possible, especially in initial applications that the desired physiological effect is not what it was supposed to be, and it is desirable to remove the device within a few days or a week after it has been installed. An eyelet allows for a simple removal within about a week or more if

dissolvable suture material was attached to it and left dangling near the entrance wound. An eyelet of platinum or iridium was welded on the anodic pulse end of some versions of the device. Also, if the implant needs to be removed, the eyelet is the safest place to strongly grab the Bion® without causing damage.

It became clear in the animal studies that a simple method was required for the clinician to accurately inject the microstimulators. A set of injection tools was designed to facilitate the device insertion (see Fig. 5). The insertion probe (A in Fig. 5) is insulated from a few millimeters below the top all the way down to about 1 mm from the edge of the tip. There are two types of probes available: one with a sharp point and one with a dull rounded point. The clinician selects the tip he requires depending on the type of tissue he is going through. The top of the probe is hooked up to an external portable pulse generator [7].

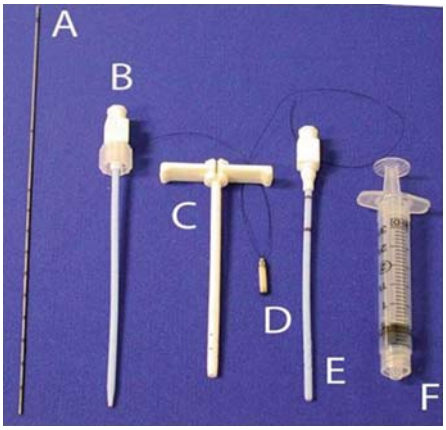

Fig. 5 Insertion tools: (**A**) insertion probe used for locating nerves, (**B**) dilation tool used to spread tissue, (**C**) microstimulator insertion tool or sheath, (**D**) microstimulator with dissolvable suture attached, (**E**) microstimulator ejector tool with two marks, (**F**) 3 ml syringe. (Reproduced from Ref. [7] with permission from IEEE)

Another system has been developed for Bion® implantation by H.M. Kaplan and G.E. Loeb at The Alfred Mann Institute at the University of Southern California (AMI-USC), who have designed, produced, and tested a single simple tool for implanting BIONs as an outpatient office procedure [8]. The implant is preloaded into the tip of the cannula of a two-piece insertion tool made from non-conductive polymers (Fig. 6). Trial stimulation pulses are generated by the implant as the tool is manipulated into the desired position. The implant is released by simply withdrawing the cannula over the implant, while an internal probe preserves both the relative location of the implant's electrodes with respect to the target and its axial orientation (which is important for implants containing motion sensors). The Bion® insertion tool (BIT) has been used by that group for over 50 Bion® implants in human subjects to date.

Fig. 6 Bion® insertion tool (BIT) developed by AMI-USC. The Bion® is preloaded and delivered in the tip of the polymeric cannula. (Originally published in Ref. [8] with permission)

2.3 First-Generation Battery-Powered Bion® Microstimulator

The first-generation battery-powered Bion® microstimulator (BPB1), shown in Fig. 7, was based on the RF-powered Bion®. It was designed and developed by Advanced Bionics. The BPB1 was designed to be injected or implanted adjacent to a peripheral nerve for chronic stimulation. The electronics of the device are encased in a hermetically sealed ceramic and titanium case. It has a single iridium-stimulating electrode (cathode) on the tip of the microstimulator. The single anode is an iridium electrode encompassing the surface of the distal of the cylinder. The device has a diameter of 3.3 mm and a length of 27 mm.

The BPB1 is capable of producing a wide range of possible programmable stimulation parameters, with a maximum pulse current of 12 mA, a maximum pulse width of 1000 ms, and a maximum frequency of more than 1000 Hz. The device is designed to be programmed by an external

Fig. 7 First-generation battery-powered Bion® microstimulator (BPB1)

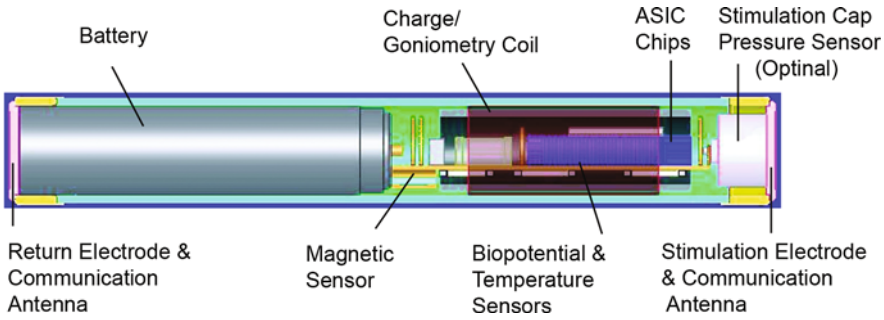

Fig. 8 BPB internal layout showing battery and electronics assembly (reproduced from Ref. [7] with permission from IEEE)

programmer during a fitting procedure with a clinician, and it includes a memory capable of storing a stimulation program. The system includes a remote control that allows a patient to adjust the stimulation within a range programmed by a clinician.

The internal layout of BPB1 with battery and electronics assembly is shown in Fig. 8. A 10 mW-h rechargeable Li-ion battery developed by Quallion (Sylmar, CA) is the main power source for the implant. This rechargeable battery allows the implanted device to operate as a standalone stimulator/sensor. The patient is given a charging system that allows charging at home. Charging of the device typically requires 1–2 h when the battery is maximally depleted. The time between charging depends on the programmed stimulation parameters and may vary from as long as 2 weeks to less than a day. The total life of the battery is expected to be up to 20 years [9].

2.4 Second-Generation Battery-Powered Bion® Microstimulator

A second-generation battery-powered Bion® microstimulator (BPB2) is under development by Advanced Bionics Corporation. That device will incorporate multiple stimulating electrodes and increased battery capacity in a form factor that is only modestly larger than the BPB1. Also under development is a portable battery-powered charger for the second-generation battery-powered Bion® microstimulator.

3 Clinical Applications of Bion® Microstimulator

3.1 RFB1 Applications

The RFB1 has been used in several feasibility clinical studies designed to explore the efficacy and safety of the device in rehabilitation of hypotrophic muscles. The clinical applications have included treatment of knee osteoarthritis and

rehabilitation of post-stroke shoulder subluxation and post-stroke hand contracture [5] and are described in more detail below.

3.1.1 RFB1 for Shoulder Subluxation in Post-Stroke Patients

Hemiplegic shoulder pain is common after a stroke. It can impede rehabilitation and thus may lead to long-term disability. The factors contributing to shoulder pain include subluxation and contractures. Transcutaneous electrical stimulation of the shoulder muscles has been demonstrated to reduce existing post-stroke shoulder subluxation and associated pain, although the effect is not maintained after discontinuation of the treatment. Intramuscular electrical stimulation of the supraspinatus, posterior deltoid, middle deltoid, and upper trapezius with a percutaneous stimulation system has also been shown to be efficacious in reducing hemiplegic shoulder pain at up to 12 months post-treatment. The typical treatment regimen for transcutaneous or percutaneous stimulation is one or more hours per day of stimulation for several weeks [10–13].

The RFB1 devices have been implanted in the middle deltoid and supraspinatus muscles (typically one device in each muscle) of post-stroke patients suffering from shoulder subluxation in two separate clinical studies, one at Queens University and another at California Rancho Los Amigos National Rehabilitation Center (Downey, CA, USA). The implanted devices were powered and controlled by an external controller, which included a coil that was placed over the affected shoulder. The external controller was programmed to activate the devices in order to effect stimulation of the muscles in which the devices were implanted. Each patient activated the external controller daily for at least an hour a day. Patients used the device for several weeks during the study, and they were allowed to continue with stimulation after the end of the study. The outcome measures included the visual analog scale (VAS) pain score; radiographic assessment of subluxation; and clinician assessment of range of motion, strength, and function [5, 14, 15].

The initial study at Queens University enrolled patients at 3–12 weeks following the stroke that caused a hemiplegic shoulder. Patients were randomized to an active group that received the implant immediately and a control group that received no implant (but who were then eligible for implant after the end of the control period). The outcome measures were assessed in each group at baseline and after 6 weeks. Fourteen patients were enrolled and nine were ultimately implanted. When assessed radiographically, subluxation demonstrated a statistically significant decrease in the active (stimulated) patients but not in the control patients [5, 14–16].

The study at California Rancho Los Amigos National Rehabilitation Center enrolled 14 patients, each at 6 months or greater following a stroke that caused a hemiplegic shoulder. Patients were randomized to an active group that received the implant immediately and a control group that received transcutaneous electrical muscle stimulation (but who were then eligible for implant after the end of the control period). The outcome measures were assessed in each group at

baseline and after 6 weeks. Ten total patients were implanted, and seven received transcutaneous electrical muscle stimulation. Three of these patients had the microstimulator implanted and activated following the control treatment of 6 weeks of transcutaneous stimulation. The patients using the microstimulator showed a significant decrease radiographically in subluxation, while the surface stimulation patients did not. Additionally, the microstimulator patients reported greater pain relief during active shoulder movements [5, 17].

3.1.2 RFB1 for Knee Osteoarthritis

In a feasibility clinical study at Istituto Ortopedico Gaetano Pini (Milan, Italy), the RFB1 was implanted for therapeutic muscle rehabilitation in patients with severe knee osteoarthritis who were considering total knee arthroplasty. Patients each received up to two microstimulators, one alongside the proximal femoral nerve to effect contraction of the quadriceps muscles and the other in the vastus medialis muscle. Patients were evaluated at baseline prior to implantation and after 12 weeks of stimulation. The outcome measures of the study included assessment of knee function by the Western Ontario McMaster (WOMAC) knee test score, the Knee Society Function score, VAS pain score, and the Knee Society Pain-Free index. Five patients were implanted and were trained to perform the therapy at home. A statistically significant improvement was observed in all outcome measures. Additionally, at least one patient was able to delay total knee arthroplasty surgery for over 3 years [5, 14–16].

3.1.3 RFB1 for Post-Stroke Hand Contractures

Hemiparetic post-stroke patients may demonstrate a flexion contracture of the hand, which may develop shortly after the stroke due to spastic flexor muscle activity in the hand. While some patients may recover limited ability for voluntary extension of the hand, they may remain disabled due to an inability to overcome the flexors with extensors that became hypotrophic following the stroke.

A feasibility clinical study by Baker et al. [18] of the RFB1 for post-stroke hand rehabilitation is in progress at California Rancho Los Amigos National Rehabilitation Center [5]. The microstimulator is being implanted for therapeutic muscle rehabilitation in patients with severe post-stroke hand contracture. Patients may receive up to four microstimulators, each implanted in muscles or at motor points to effect finger and wrist extension. Patients are randomized to an active group that received the implant immediately and a control group that receives transcutaneous electrical muscle stimulation but who are then eligible for implant after the end of the control period. Patients in the study are evaluated at baseline prior to implantation and after 12 weeks of stimulation. Eleven patients have been implanted with microstimulators, and six patients have completed the control period with surface stimulation. Five of these patients had the microstimulator implanted and activated following the

control treatment of 6 weeks of transcutaneous stimulation [17]. Results from this ongoing trial are not yet available.

In addition to strengthening muscles via open-loop stimulation, the external controller may be modified to sense the EMG of weak voluntary flexion, and this sensed signal may be used to trigger the devices to stimulate, thus initiating stronger flexion. The study may be extended to include evaluation of the efficacy of such triggered stimulation for hand rehabilitation.

3.1.4 RFB1 for Foot Drop

Foot drop is a significant weakness of ankle and toe dorsiflexion that may impair gait. When it is a sequela of stroke or spinal cord injury, it may be treated with electrical stimulation of the peroneal nerve. Transcutaneous electrical stimulation of the common peroneal nerve may be difficult to perform reliably in a system applied by a patient, and patients may find transcutaneous stimulation uncomfortable [19]. In a feasibility clinical study at the University of Alberta (Edmonton, Canada) by Weber et al.15, one patient with an incomplete spinal cord injury at C6/7 was implanted with three functional RFB1 devices, one at the motor point of the tibialis anterior muscle, which dorsiflexes and inverts the ankle; the second at the deep peroneal nerve, which activates tibialis anterior, extensor digitorum longus, and other muscles; and the third at the motor point of the peroneus longus muscle, which everts the foot and can compensate for the inversion action of the tibialis anterior.

The external controller was combined with a modified Walkaide 2 system (Innovative Neurotronics, a division of Hanger Orthopedic Group, Bethesda, MD, USA), which was able to sense the tilt of the lower leg (i.e., the angle of the lower leg relative to vertical). The controller thus initiated stimulation of the deep peroneal nerve when it detected the onset of the swing phase (i.e., maximum positive tilt was detected), and stimulation was turned off when the leg swung forward (i.e., a negative tilt angle was detected). When activated, the thee microstimulators were programmed to effect ankle and toe dorsiflexion. Three-dimensional video motion analysis of the ankle and foot trajectories during walking with stimulation demonstrated that the toe cleared the ground by approximately 3 cm, which was comparable to the toe clearance in the less affected contralateral leg of the patient. Additionally, unlike surface stimulation of the common peroneal nerve by the Walkaide 2 system, stimulation with the implanted microstimulators produced dorsiflexion without eversion [5, 20].

3.1.5 RFB1 for Pressure Ulcer Prevention

Pressure ulcers (PUs) are debilitating wounds caused by pressure and shear from unrelieved sitting. About 30% of immobilized patients suffer from PUs, and despite a multitude of therapies recurrence rates are as high as 60% annually, even after aggressive surgical repair. Using modern glass-encapsulated versions of the Bion®, Kaplan and Loeb at AMI-USC have

investigated the use of BIONs to prevent PUs [21]. BIONs have previously been demonstrated to activate strong muscle contractions with associated skeletal motion and increases in muscle bulk, strength, metabolic capacity, and vascularity. These effects counteract three major etiological factors of PUs: immobility, soft-tissue atrophy, and ischemia. To date three spinal cord injured patients have each had two BIONs implanted, during reconstructive flap surgery that they already required for PUs. In all cases it has been possible to subsequently stimulate the hamstring and gluteus maximus hip extensors selectively as desired, with promising early results. Once the efficacy of this novel therapy has been proven, its broader application is envisioned as a bilateral, prophylactic treatment, for all immobile patients at risk of PUs. BIONs would eventually be injected percutaneously, controlled, and powered via in-chair antennae.

3.2 RFB2 Applications

3.2.1 RFB2 for Post-Stroke Shoulder Subluxation

The RFB2 has been implanted in a feasibility clinical study at Akita University Hospital (Akita, Japan) in a 66-year-old male with a 5-year history of post-stroke shoulder subluxation. The patient's subluxation resulted in a VAS pain score of 7 at baseline. Two microstimulators were implanted, one next to the axillary nerve and the other at the motor point of the middle deltoid muscle. An external controller was programmed to activate the microstimulators to affect shoulder flexion. After daily stimulation for 6 months, the patient's pain decreased to 0 on the VAS. Stimulation was discontinued for months 6–12, and the patient reported persistent pain relief at 12 months, suggesting a significant carry-over effect [22].

3.2.2 RFB2 for Post-Stroke Hand and Arm Rehabilitation

A clinical feasibility study of post-stroke forearm rehabilitation using the RFB2 is in progress at the University of Southampton (Southampton, UK). Five to seven microstimulators are implanted in each patient at the motor points of the extensor muscles of the hand, wrist, and elbow. In the lower arm these muscles include the extensor carpi ulnaris and radialis, the extensor digitorum superficialis, the extensor pollicis longus, the abductor pollicis; and in the upper arm they include the medial and lateral heads of the triceps.

Seven patients with post-stroke arm and hand contracture (due to spastic flexion) have been enrolled to date. The external controller has several open-loop programs that may be triggered by the patient to activate the upper limb muscles in a coordinated manner, including one that opens the hand through stimulation of the wrist and finger extensors; another that facilitates voluntary grasping by switching off the finger extensors but maintaining wrist extension; and yet another that facilitates reaching through elbow extension. Patients in

the study use the system to facilitate rehabilitation of intrinsic muscle strength for a minimum of 2 hours per day for at least 12 weeks [23, 24]. Results from this ongoing trial are not yet available.

3.3 BPB1 Applications

The BPB1 has been used in two clinical studies designed to explore the efficacy and safety of the device for peripheral nerve stimulation. The clinical applications have included treatment of medically refractory overactive bladder and refractory headaches.

3.3.1 BPB1 for Overactive Bladder

Clinical feasibility studies have suggested that chronic pudendal nerve stimulation may significantly relieve symptoms of urinary urge incontinence (UUI) in up to 80% of severely affected patients [25, 26]. The BPB1 was designed to provide stimulation of the pudendal nerve while avoiding the complications attendant with a leaded system, such as lead migration. The BPB1 may be placed adjacent to the pudendal nerve at Alcock's canal via the perineum in an approach similar to a pudendal nerve block, as illustrated in Fig. 9. Figure 10(A) and 10(B) show the location of the Bion® microstimulator once it has been implanted adjacent to the pudendal nerve. The perineal incision wound is usually less than 4 mm wide and typically requires no stitches for surgical closing of the wound [27].

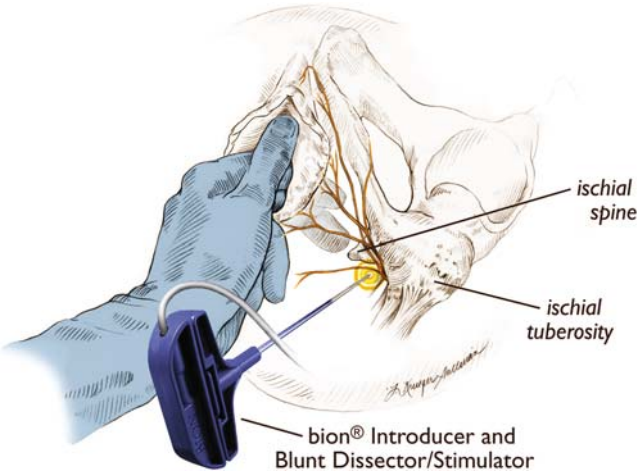

Fig. 9 Implantation of the Bion® microstimulator adjacent to the pudendal nerve using a custom blunt dissector and cannula

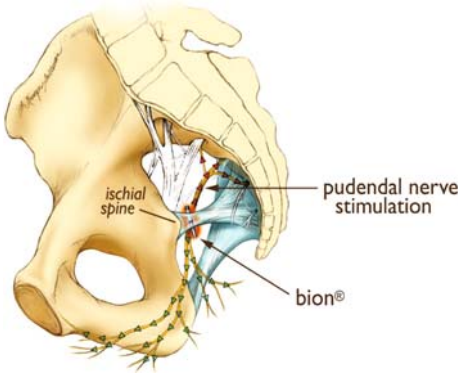

Fig. 10(A) Illustration of the Bion® microstimulator implanted adjacent to the pudendal nerve

Fig. 10(B) Radiograph of the Bion® microstimulator implanted adjacent to the pudendal nerve

All implanted patients are given a remote control and a charging system for their device. The remote control is a small device approximately the size of a mobile phone, which allows patients to adjust stimulation amplitude, activate and deactivate stimulation, and monitor the charge level of the rechargeable battery of the implanted device. The charging system consists of two components. During charging the patient sits on a padded RF coil. The coil is attached via a cable to an RF generator, which is plugged into an AC outlet. The charging system is designed for the patient to sit comfortably while charging for a period of 1–2 h. However, the microstimulator battery lasts for several days for most UUI patients, which means that most patients charge only a few minutes per day. The charging system is capable of charging Bion® microstimulators implanted up to 12 cm from the skin.

Initial clinical studies of the BPB1 for UUI were conducted in Europe at the Erasmus Medical Center (Rotterdam, The Netherlands) and University

Medical Center Schleswig-Holstein (Kiel, Germany). The primary outcome measure was a decrease in the number of leaks (as recorded in a 5-day patient voiding diary) at 45 days as compared to baseline. Eight patients were implanted with the microstimulator and six demonstrated a clinically significant response at 45 days [28–30].

A multi-center randomized controlled trial of the BPB1 for pudendal nerve stimulation for the treatment of UUI is currently in progress in the United States. Patients complete a baseline 5-day voiding diary that tracks the number of leaks per day and other associated information (e.g., number of incontinence pads used per day). The patients are randomized in a blinded fashion to a treatment group (50%) and a control group (50%), and then all patients are implanted. The patients in the treatment group are activated within a few days following implantation. The patients in the control group undergo a sham activation in which their device is blocked from providing stimulation pulses; however, they are told that their device has been activated, and their remote controls and charging systems function in a manner very similar to those of the treatment patients. At 45 days after the activation (or sham activation) of stimulation, patients complete a 5-day voiding diary, and then the control patients are activated. Patients also complete a 5-day voiding diary at 3 months, 6 months, and 1 year. The primary outcome measures are (1) the reduction in the number of leaks at 45 days as compared to baseline between the treatment and the control groups and (2) the reduction in the number of leaks at 1-year post-activation as compared to baseline for all patients. Approximately 80 patients have been implanted, and the trial is ongoing in the United States.

A similar trial for the treatment of urgency frequency syndrome (UF) is also in progress. The primary difference is that the primary outcome measure is the number of voids per day instead of leaks per day. Approximately 80 patients have been implanted in the UF trial as well, and the trial is ongoing in the United States.

3.3.2 BPB1 for Refractory Headaches

Several feasibility clinical trials have suggested that that chronic stimulation of the greater occipital nerve may improve symptoms in patients with frequent medically refractory migraines as well as in other severe headache syndromes [31–37]. The BPB1 has been implanted for chronic stimulation of the greater occipital nerve in several feasibility clinical trials for the treatment of refractory headaches. Using custom designed implant tools, a microstimulator may be implanted adjacent to the greater occipital nerve through a 4 mm incision at top of the neck [38]. Figure 11(A) and 11(B) show the location of the Bion® microstimulator once it has been implanted adjacent to the greater occipital nerve [39]. The patient is able to recharge by lying down on the same RF-charging coil as is described above for UUI, only the coil is padded as a pillow instead of a chair pad.

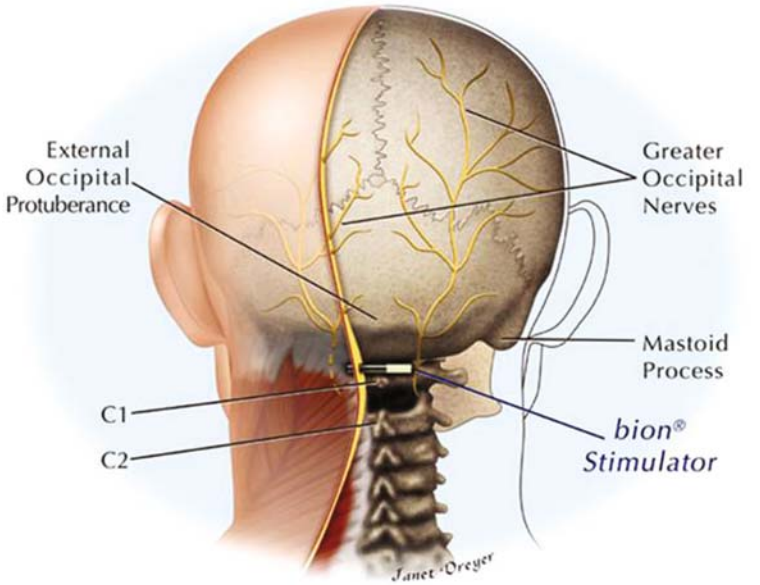

Fig. 11(A) Illustration of the Bion® microstimulator implanted adjacent to the greater occipital nerve

Fig. 11(B) Radiograph of the Bion® microstimulator implanted adjacent to the greater occipital nerve

Feasibility clinical studies of the BPB1 for refractory headache were conducted at the Michigan Head Pain and Neurological Institute (Ann Arbor, MI, USA), the Mayo Clinic (Scottsdale, AZ, USA), and the Institute of Neurology and National Hospital for Neurology and Neurosurgery, Queen Square (London, UK). The US centers included patients with frequent medically refractory migraine and chronic cluster headache. The UK center included patients with the aforementioned diagnoses as well as patients with hemicrania continua and SUNCT (short-lasting, unilateral, neuralgiform headache attacks with conjunctival injection and tearing). All patients were activated within a few days of implantation.

All of the patients in the feasibility studies completed a 28-day headache diary and a Migraine Disability Assessment (MIDAS) at baseline prior to implantation, and another 28-day diary was completed during the third month post-stimulation. The outcome measures included the change in a number of headache attributes at 12 weeks as compared to baseline including severity, frequency, and duration as well as the MIDAS as a measure of migraine-related disability.

A case report on one of the microstimulator patients describes a 56-year-old male with a 10-year history of refractory migraine prior to implant. At 3 months post-activation, he demonstrated a decrease in MIDAS score from class IV (severe disability) to class I (minimal or infrequent disability) and a decrease in average VAS score from 7/10 to 0/10 [39].

3.3.3 BPB1 for GERD (Preclinical)

Programmable stimulation under patient control to increase lower esophageal sphincter (LES) pressure may be useful in the control of gastroesophageal reflux disease (GERD). Acute experiments with endoscopic implantation of the BPB1 in the LES and selective stimulation of the LES were performed in three dogs. Baseline LES pressure prior to implantation was established via manometry. Once the microstimulator was implanted in the LES, manometry was repeated with activation and deactivation of microstimulator stimulation to observe the changes in LES pressure. The mean LES pressures at baseline in the three dogs were 13.0, 5.0, and 14.9 mmHg, and no significant change was observed immediately following implantation with the microstimulator deactivated. Following activation of stimulation, the resultant LES pressures were 62.1, 35.1, and 26.8 mmHg, respectively, a statistically and clinically significant increase. Endoscopic implantation of a microstimulator represents a novel approach to the treatment of GERD and possibly to other gastrointestinal motility disorders [40].

4 Summary

The Bion® microstimulator has demonstrated promising results in several clinical applications, including rehabilitation of hypotrophic muscles and stimulation of peripheral nerves for treatment of overactive bladder and migraine.

The novel form factor of the microstimulator allows it to be implanted via a minimally invasive procedure in a variety of locations in the body, and its small size allows it to be directly implanted in the limbs, neck, and head. Additionally, the battery-powered Bion® microstimulator contains a rechargeable battery that may last up to 20 years, offering a convenient alternative to larger implantable neurostimulation systems.

References

1. Johnston TE, Betz RR, Smith BT, et al. (2005) Implantable FES system for upright mobility and bladder and bowel function for individuals with spinal cord injury. Spinal Cord 43:713–723.
2. Taylor P, Esnouf J, Hobby J (2002) The functional impact of the Freehand System on tetraplegic hand function Clinical results. Spinal Cord 40:560–566.
3. Loeb GE, Zamin CJ, Schulman JH, et al. (1991) Injectable microstimulator for functional electrical stimulation. Med Biol Eng Comput 29:NS13–NS19.
4. Schulman JH, Mobley JF, Wolfe J, et al. (2006) A 1000+ Channel Bionic Communication System. Proceedings of the 28th IEEE EMBS Annual International Conference, New York City, USA, pp. 4333–4335.
5. Loeb GE, Richmond FJ, Baker LL (2006) The BION devices: injectable interfaces with peripheral nerves and muscles. Neurosurg Focus 15:20:E2.
6. Arcos I, Davis R, Fey K, et al. (2002) Second-generation microstimulator. Artif Organs 26:228–231.
7. Schulman JH (2008) The feasible FES system battery powered bion® stimulator. Proceedings of the IEEE 96(7):1226–1239
8. Kaplan HM, Loeb GE (2009) Design and fabrication of an injection tool for neuromuscular microstimulators. Ann Biomed Eng. Accepted for publication.
9. Carbunaru R, Whitehurst T, Jaax K (2004) Rechargeable battery-powered Bion microstimulators for neuromodulation. Conf Proc IEEE Eng Med Biol Soc 6:4193–4196.
10. Poduri KR (1993) Shoulder pain in stroke patients and its effect on rehabilitation. J Stroke Cerebrovascular Dis 3:261–266.
11. Teasell RW (1998) The Painful Hemiplegic Shoulder. Physical Medicine and Rehabilitation: State of the Art Reviews 12(3):489–500.
12. Linn SL, Granat MH, Lees KR (1999) Prevention of shoulder subluxation after stroke with electrical stimulation. Stroke 30:963–968.
13. Chae J, Yu DT, Walker ME, et al. (2005) Intramuscular electrical stimulation for hemiplegic shoulder pain: a 12-month follow-up of a multiple-center, randomized clinical trial. Am J Phys Med Rehabil 84(11):832–842.
14. Dupont AC, Bagg SD, Creasy JL, et al. (2001) Clinical trials of Bion injectable neuromuscular stimulators. Presented at the 6th Annual Conference of the International Functional Electrical Stimulation Society; June 16–21, 2001; Cleveland, OH, USA.
15. Dupont AC, Bagg SD, Baker L, et al. (2002) Therapeutic electrical stimulation with Bions: clinical trial report. Presented at the 2nd Joint Conference of the IEEE Engineering in Medicine and Biology Society and the Biomedical Engineering Society; October 23–26, 2002; Houston, TX, USA.
16. Dupont AC, Bagg SD, Creasy JL, et al. (2004) First clinical experience with Bion implants for therapeutic electrical stimulation. Neuromodulation 7:289–292.
17. Baker LL, Eberly V, Rakoski D, et al. (2006) Preliminary experience with implanted microstimulators for management of post-stroke impairments. J Neurol Phys Ther 30:209–222.

18. Baker LL, Palmer E, Waters RL, et al. (2004) Rehabilitation of the arm and hand following stroke - a clinical trial with Bions. Proceedings of the 26th Annual International Conference of the IEEE Engineering in Medicine and Biology Society; September 1–5, 2004, 2:4186–4188.
19. Lyons GM, Sinkjaer T, Burridge JH, et al. (2002) A review of portable FES-based neural orthoses for the correction of drop foot. IEEE Trans Neural Syst Rehabil Eng 10:260–279.
20. Weber DJ, Stein RB, Chan KM, et al. (2005) BIONic WalkAide for correcting foot drop. IEEE Trans Neural Syst Rehabil Eng 13:242–246.
21. Kaplan HM (2008) Neuromuscular Electrical Stimulation for Pressure Ulcer Prevention. PhD Dissertation, University of Southern California, Los Angeles, May 2008.
22. Shimada Y, Davis R, Matsunaga T, et al. (2006) Electrical stimulation using implantable radiofrequency microstimulators to relieve pain associated with shoulder subluxation in chronic hemiplegic stroke. Neuromodulation 9:234–238.
23. Burridge JH, Etherington R (2004) A preliminary clinical study using RF BION1 microstimulators to facilitate upper limb function in hemiplegia. Adv Clin Neurosci Rehabil 4:26–27.
24. Burridge JH, Etherington R, Cosendai G, et al. (2004) A preliminary clinical study using RF BION microstimulators to facilitate upper limb function in hemiplegia. Proceedings of the 9th Annual Conference of the International Functional Electrical Stimulation Society; September 6–9, 2004; Bournemouth, UK.
25. Peters KM, Feber KM, Bennett RC (2005) Sacral versus pudendal nerve stimulation for voiding dysfunction: a prospective, single-blinded, randomized, crossover trial. Neurourol Urodyn 24:643–647.
26. Spinelli M, Malaguti S, Giardiello G, et al. (2005) A new minimally invasive procedure for pudendal nerve stimulation to treat neurogenic bladder: description of the method and preliminary data. Neurourol Urodyn 24:305–309.
27. Buller JL, Peters KM (2007) The Bion microstimulator. In: Kreder K, Dmochowski D (eds). The Overactive Bladder: Evaluation and Management. Informa Healthcare, London, pp. 319–328.
28. Bosch JL (2005) The bion device: a minimally invasive implantable ministimulator for pudendal nerve neuromodulation in patients with detrusor overactivity incontinence. Urol Clin North Am 32:109–112.
29. Groen J, Amiel C, Bosch JL (2005) Chronic pudendal nerve neuromodulation in women with idiopathic refractory detrusor overactivity incontinence: results of a pilot study with a novel minimally invasive implantable mini-stimulator. Neurourol Urodyn 24:226–230.
30. Seif C, van der Horst C, Naumann CM, et al. (2005) Pudendal nerve stimulation therapy of the overactive bladder – an alternative to sacral neuromodulation? [Article in German] Aktuelle Urol 36:234–238.
31. Burns B, Watkins L, Goadsby PJ (2007) Treatment of medically intractable cluster headache by occipital nerve stimulation: long-term follow-up of eight patients. Lancet 369:1099–1106.
32. Magis D, Allena M, Bolla M, et al. (2007) Occipital nerve stimulation for drug-resistant chronic cluster headache: a prospective pilot study. Lancet Neurol 6:314–321.
33. Rogers LL, Swidan S (2007) Stimulation of the occipital nerve for the treatment of migraine: current state and future prospects. Acta Neurochir Suppl 97(Pt 1):121–128.
34. Schwedt TJ, Dodick DW, Hentz J, et al. (2007) Occipital nerve stimulation for chronic headache–long-term safety and efficacy. Cephalalgia 27:153–157.
35. Weiner RL (2007) Occipital neurostimulation for treatment of intractable headache syndromes. Acta Neurochir Suppl 97(Pt 1):129–133.
36. Matharu MS, Bartsch T, Ward N, et al. (2004) Central neuromodulation in chronic migraine patients with suboccipital stimulators: a PET study. Brain 127(Pt 1):220–230.
37. Popeney CA, Alo KM (2003) Peripheral neurostimulation for the treatment of chronic, disabling transformed migraine. Headache 43:369–375.

38. Trentman TL, Rosenfeld DM, Dodick DW, et al. (2006) Schwedt TJ. GON stimulation via the Bion microstimulator: implantation technique and stimulation parameters. Annual meeting of the American Society of Anesthesiologists; 2006; Chicago, IL, USA. Abstract:A333.
39. Rogers LL (2005) Unilateral occipital nerve stimulation for chronic migraine using a Bion microstimulator implant. 7th Congress of the International Neuromodulation Society (INS) Conference; June 10–13, 2005; Rome, Italy.
40. Clarke JO, Jagannath SB, Kalloo AN, et al. (2007) An endoscopically implantable device stimulates the lower esophageal sphincter on demand by remote control: a study using a canine model. Endoscopy 39:72–76.

Brain Control and Sensing of Artificial Limbs

Joseph H. Schulman

Abstract This chapter discusses the possibility of making an artificial limb that an amputee can control and feel as if it were his own. The technology is now available to make electrical connections to hundreds or thousands of neurons in the stump of an amputated limb. The extreme miniaturization that is now possible in combination with modern digital signal processing in radio communication and the advances in implantable technology over the last half century provide sufficient impetus for the development of such an advanced prosthesis. An approach using the concept of the Utah slanted bed of nails in conjunction with the subminiturization, high-speed low-power communications, and advanced biocompatible packaging technology developed at the Alfred Mann Foundation is described.

1 Introduction

The ability to make artificial limbs that have touch and proprioceptive feeling and joint movement similar or identical to the natural limb is now possible and will soon be a common reality. When a limb is amputated, in most cases, all the neurons that still have attached cell bodies remain viable. With the development of integrated circuits and digital signal processing, it is now possible to implant tiny multi-electrode wireless assemblies on peripheral nerves which can detect or cause neuronal spikes on hundreds or thousands of specific neurons. The electrical pulse signals on motor neurons can be used to control flexion and extension of artificial joints. Joint angle position and touch sensors on the artificial limb can be used to stimulate electrical pulses on the appropriate proprioceptive and touch sensory neurons.

This chapter describes some of the research and technology development going on in this field and a proposal to make a commercial version of a peripheral nerve interface. At the present time there is a large program funded

J.H. Schulman (✉)
Mann Medical Research Organization, Valencia, CA, USA
e-mail: joes@mannfbe.org

D.D. Zhou, E. Greenbaum (eds.), *Implantable Neural Prostheses 1*,
Biological and Medical Physics, Biomedical Engineering,
DOI 10.1007/978-0-387-77261-5_9,

by Defense Advanced Research Program Agency (DARPA) to develop high-quality artificial limbs. A major effort to make a peripheral nerve interface is in progress at many universities and laboratories. At the University of Michigan where major research to develop neuronal electrodes using integrated silicon chip technology has been ongoing for 20 years, there is research attempting to use this technology for the peripheral nerve interface [1].

Another approach is to redirect the nerves from the stump to another area such as the chest, so a non-invasive system such as surface electrodes can be used to detect or stimulate the appropriate neural signals [2]. A major program is also ongoing at University of Utah to develop a silicone slanted bed of nails electrode array with electronics built in to wirelessly power and communicate with prosthetic limbs [3]. This program seems to be the most promising in that theoretically it can provide the most data channels in and out of the nervous system with a small number of implantable devices [4].

At the Alfred Mann Foundation (AMF), Valencia CA, a major effort in miniaturization of neural sensing and stimulating electronics for the battery-powered injectable micro-devices has been ongoing for the last 10 years [5]. This includes high speed very low-power multiple channel radio communications [6], hermetic sealing, and biocompatible long lasting implantable packaging techniques [7]. In this chapter the design of a long-term reliable commercial product based on the Utah approach, using the AMF technology has been proposed.

2 Limb Loss and Electrical Neural Stimulation

2.1 Limb Loss in the United States

According to the Amputee-Coalition [8] in the year 2007 there were approximately two million people with missing limbs. They also report a yearly incidence of 185,000 new amputations per year. According to the Amputee-Coalition, Limb loss can occur due to trauma, infection, diabetes, vascular disease, and cancer. The majority of these are leg amputations in male patients as can be seen in the Tables 1 and 2. These numbers do not include people with missing fingers and toes.

Table 1 Limb loss in different amputee groupings [8]

Elbow to shoulder	3%
Wrist to elbow	4.6%
Above knee to lower thigh	32.6%
Ankle to above knee	53.6%

Table 2 Amputees grouped in years by age and gender in 1996 [8]

Age	18–44	45–64	65–74	75+
Population	293,000	305,000	395,000	223,000
Population				
Male	893,000			
Female	392,000			

2.2 Stimulation on Peripheral Nerves, Neurons, and Neuroma

There are four or more nerves controlling each limb depending on the closeness to the spinal cord (see Fig. 1). Each nerve has hundreds to thousands of neurons. The peripheral neurons that cause muscles to contract are called motor neurons and the peripheral neurons that carry information from the periphery to the central nervous system are called sensory neurons. All neurons are living biological cells and have a component called the cell body. The cell body contains organelles within it and normally supplies nutrients to the rest of the neuron.

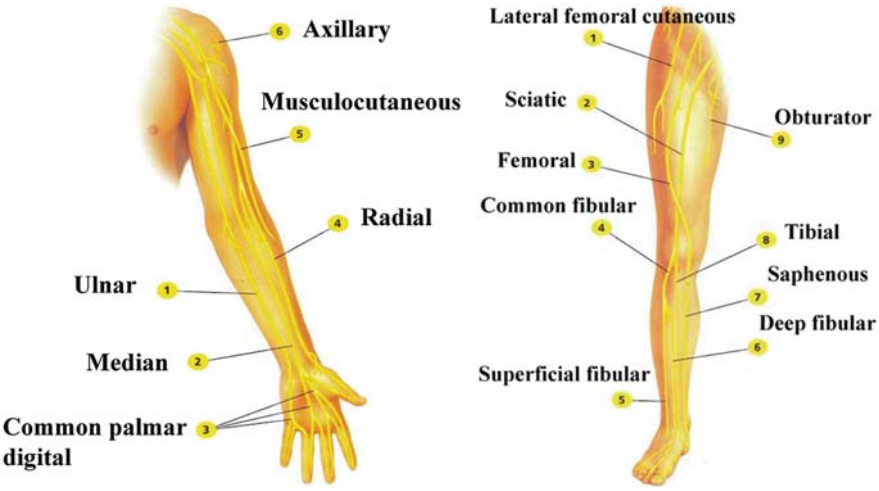

Fig. 1 The major nerves in the arm and leg. From each major nerve branches spread out to innervate every group of muscle fibers. Other branches spread out to monitor proprioceptors for joints and touch sensors

When a nerve is cut, the section of each neuron that is separated from its cell body stops functioning and dies. However the section that remains connected to the cell body remains viable. At the cut end of the viable part of the nerve, an irregular shaped end cap called a neuroma is formed to seal the opening. An oscilloscope attached to an electrode which is near a neuron will detect the electrical spikes traveling down the neuron. An electrical pulse generator when attached to the electrode can induce electrical spikes on a nearby neuron. These facts provide the means to interface peripheral neurons to an artificial limb.

3 Experiments on Humans and Animals

3.1 Development of the Utah Bed of Nails Electrode Array

In the 1990s Dr. Richard Norman and his group at the University of Utah developed the bed of nails (BON) electrode array for detecting and studying signals in the human brain [9], and individual neurons [10].

In other work, the sensed neural signals were above the +/− 20 μV noise level and were detectable with amplitude window and time window sorting [11].

In September, 2000 the *Journal of Neurophysiology* received an article from Branner, Stein, and Normann [12] describing the successful use of a novel slanted bed of nails (SBON) electrode to stimulate individual neurons in the cat sciatic nerve. The slanted bed of nails electrode was made using the same MEMs methods as the bed of nails (BON) electrode array [10] but with varying electrode length (see Fig. 2).

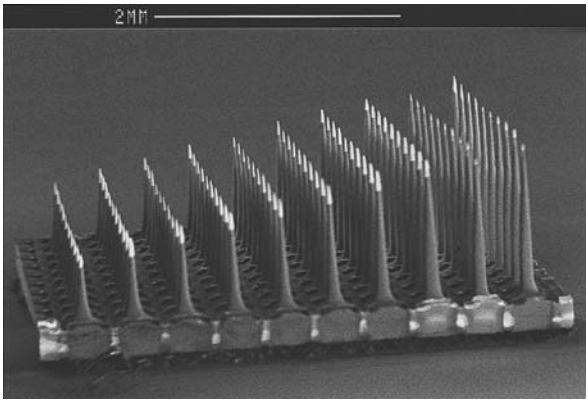

Fig. 2 Utah slanted bed of nails (BON): 100 electrodes in a 4.2 × 4.2 mm array. (Reproduced from Ref. [12] with permission from The American Physiological Society)

The slanted bed of nails (SBON) was designed to make electrical contact with different layers of neurons in a nerve. Maximum stimulation levels were reported to be less than 200 μA at 200 μs. A comparison between the BON and the SBON in Fig. 3 shows the position of the electrode tips in nerves.

3.2 First Human Implant to Control Robotic Devices

In 2002 a study was carried out by Professor Kevin Warwick and co-workers. [13] in England and in the United states in which a Utah BON 100 needle array was implanted in the medial nerve of Warwick's wrist. Twenty needles of the BON plus two indifferent electrodes were connected through a 22 wire cable which was

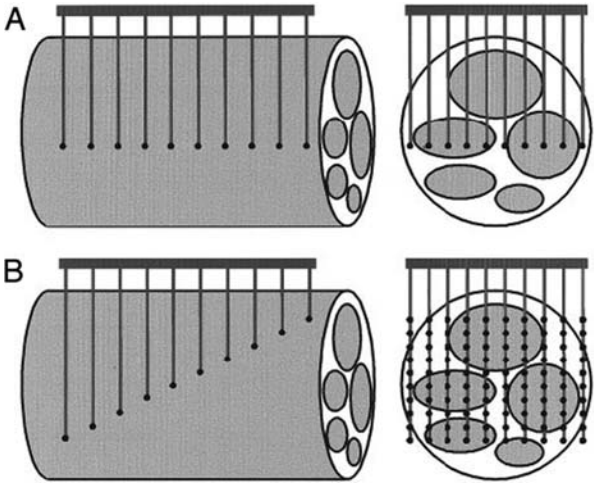

Fig. 3 Comparison of the Utah Electrode Array (UEA) and the Utah slanted electrode Array (USEA). The position of the electrodes and their tips in the nerve are shown in both pictures (from the side and the front). (**A**) All 100 electrodes of the UEA are 1 mm long. (**B**) The USEA has 10 electrode rows of varying length (0.5–1.5 mm). (Reproduced from Ref. [12] with permission from The American Physiological Society)

tunneled under the skin of the arm to a location below the elbow. At that location the cable was terminated at a connector mounted in the arm (see Fig. 4).

Fig. 4 This photo taken during the implant surgery shows the electrode passer used to position the array in the arm. (Reproduced from Ref. [13] with permission from Dr. K. Warwick)

Many experiments were performed, using nerve signals: Among these experiments one was to use his motor neuronal spike signals to control a robotic hand (see Fig. 5), and another was to use the neuronal spikes to steer and drive a wheel chair (see Fig. 6).

This prosthesis named "SNAVE" after its designer contains force and slip sensors in the fingers and palm and uses a microcontroller to co-ordinate the

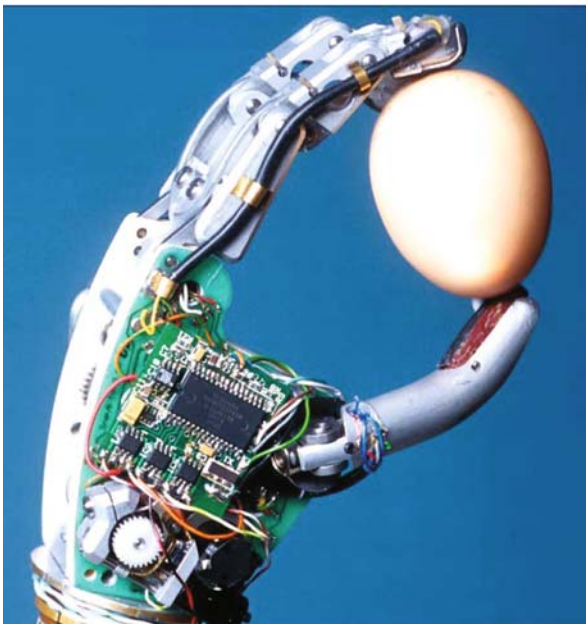

Fig. 5 Dr. Warwick at Columbia University in NY using only nerve signals operated an artificial hand prosthesis in Reading England via the Internet. (Reproduced from Ref. [14] with permission from Wiley-Blackwell)

operation. Joint flexion sensors allow for adaptation of the grip shape and for the force applied to the object to be modified by the microcontroller such that the lightest possible touch is applied.

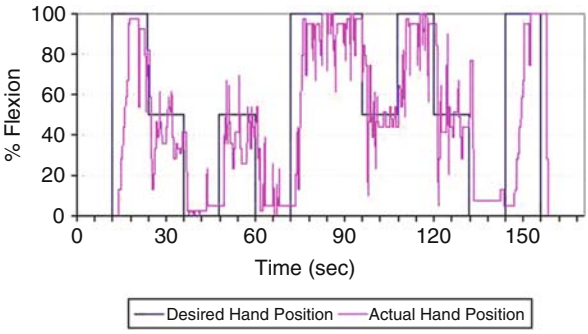

Fig. 6 The subject attempts to adjust the prosthetic hand flexion to reach the desired hand position. (Reproduced from Ref. [14] with permission from Wiley-Blackwell)

In this study, the integration value from the neural implant was broadcast to the prosthetic hand in order to set the hand flexion. Two thresholds were set such that the hand could achieve three set positions, full closed, 50% open, fully open. The on-board "intelligence" of the SNAVE hand was used to control the hand grasp function, such that the hand automatically grasped shut, if the activity was below the lowest threshold. The subject's ability to control the hand is shown in Fig. 7.

Fig. 7 Dr. Warwick, using only nerve signals, demonstrated the operation of a wheel chair. On the right is the sequencing indicator and controller box. (Reproduced from Ref. [13] with permission from Dr. K. Warwick)

The light sequencing box allowed him to rapidly select which motion he desired (forward, backward, left, or right). Closing his hand was the command signal to halt the sequence and initiate the movement. He was able to drive and navigate the wheelchair with this equipment.

The system operated for 3 months as the wires gradually broke, until only three of the wires were left operating (two indifferent and one electrode). The system was explanted on June 18, 2002, after an implantation period of 96 days. Following the explants it was determined that the Utah BON was undamaged. The breaking of the wires occurred where the cable left the arm. His median nerve apparently was not damaged. No perceivable loss of hand sensation or motion control was experienced by Dr. Warwick and was not detected by comparing tests taken before, during, and after explanation.

3.3 Testing of the Concept in Amputees

In August 2003 the American Society for Surgery of the Hand Journal received an article by Dhillon, Lawrence, Hutchinson and Horch [15] describing the residual function in Peripheral Nerve Stumps of Amputees, and its implications for neural control of Artificial Limbs. In eight amputee patients several

longitudinal intrafascicular electrodes were each implanted in micro-clusters of neurons in a fascicle. The experiments demonstrated that long-term patients could reliably generate motor control signals when they attempted to move their missing limb components. The patients also were able to repeatedly detect tactile and proprioceptive signals when specific neurons were stimulated. This and other work has demonstrated that many peripheral nerves in the stumps remain viable in the long-term amputee. The experimental setup is shown in Fig. 8. Other similar studies have confirmed these findings [16].

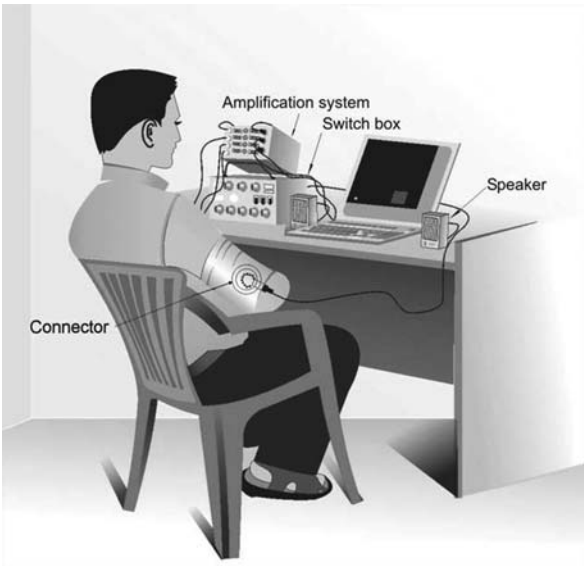

Fig. 8 Experimental setup for an amputee patient with several longitudinal intrafascicular electrodes implanted in micro-clusters of neurons in a fascicle. The cable from the saddle connector leads to a stimulating and recording setup controlled by a laptop computer. Motor signals were recorded in differential mode between a reference and an intraneural electrode. The signals were sent to a loudspeaker with a noise clipper and fed through an analog-to-digital converter to a battery-powered laptop computer (Reproduced from Ref. [15] with permission from Elsevier)

4 Implants: Designing the Ultimate Peripheral Nerve Interface

4.1 The Implant Design

In the human limb there are several peripheral nerves and their branches located at one or more muscle thicknesses away from the surface of the skin. Any wires coming from an attachment to the nerves to any location between the muscles and the skin will be pulled and pushed as the limb is moved and as the muscles

are contracted and relaxed. This pushing and pulling can damage any nerve the wires are attached to. The best solution is not to have any wires at all.

This can be accomplished by having a group of electrodes in which each electrode is in contact with a different neuron, and each electrode is connected to a small package at the surface of the nerve. This package must contain all the amplifiers, stimulators, power supplies, and other components. If the package is small enough and attached securely, limb and muscle movement should not displace or damage the electrode–neuron interface. This means

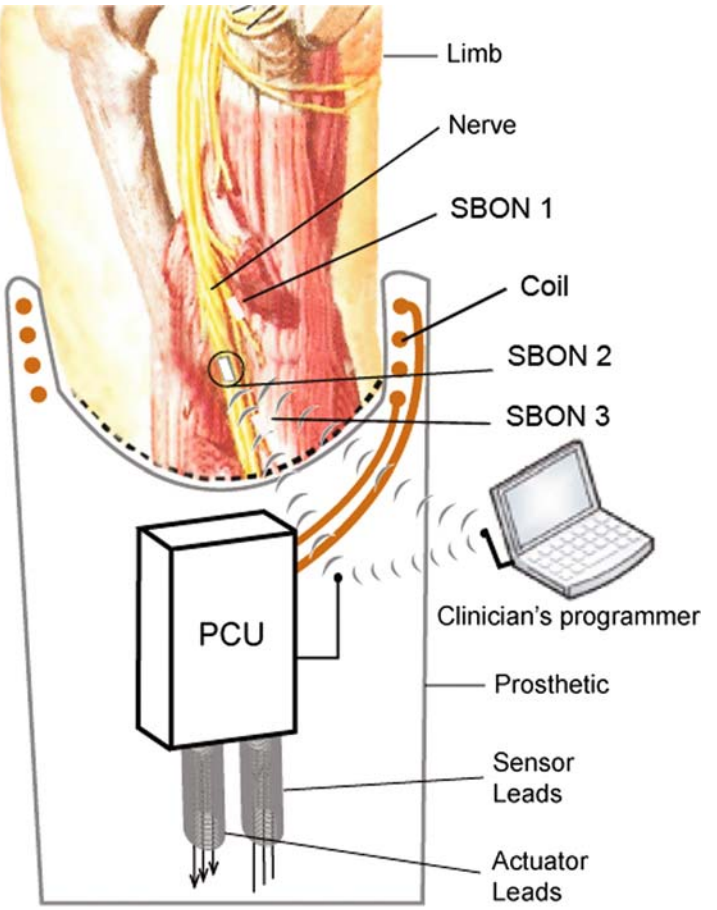

Fig. 9 A conceptual design showing three SBONs on different nerve locations, and the prosthetic with the primary coil in the socket wall of the prosthesis. The prosthetic control unit (PCU) contains the battery, and the data transceiver that (1) receives spike data from all of the SBONS on motor neurons and uses this data to control actuators on the prosthesis to cause flexion and extension and (2) to transmit to the SBONS sensed information from the prosthesis for touch and proprioception. The clinician's programmer is used to electrically fit the prosthesis to the peripheral nervous systems

that power has to be brought into the package through a wireless method, and the two-way communication between the limb and prosthetic must also be wireless.

The plan here is to use the concept of the Utah slanted bed of nails (SBON) in a totally wireless system. The "bed" of the SBON becomes the small package containing all the electronics. The prosthesis could contain the battery for powering the implant. The power should come from a closely coupled magnetic coil which acts as the primary winding of a transformer with the coil in the "bed" being the secondary winding. If the prosthesis has a socket into which fits the stump of the amputated limb, the primary coil can be wound in the socket wall coaxially with the secondary coil in the "bed" for optimum coupling (see Fig. 9).

4.2 Challenges and Problems in the Development of Implantable Miniature Peripheral Nerve Interface

There are several mechanical and electronic problems to overcome to develop a system that will stimulate and sense individual neurons in the peripheral nerves of an amputated limb. Certain requirements are necessary for miniaturization and to function without wires or cables.

4.2.1 Packaging Hermeticity

One way to look at the human body is to think of it as a bag of salt water with tissue suspended in it. Since high impedance integrated electronics would fail in salt water, all electronics must remain dry inside a container. Also the container must not be corroded by the salt water fluids of the body, and the container itself must not damage the body. The most efficient way to do this is to make the bed of the bed of nails one wall of the hermetic package. That means that each nail must conduct electrically via a hermetic feed-throughs to the inside of the package.

At the Mann Foundation over the last few decades we have developed titanium to ceramic feed-throughs technology in a variety of implantable devices. The brazed parts do not exhibit passive or active corrosion in saline, or any non-biocompatability effects. A bed of nails can be constructed out of an array of titanium feed-throughs brazed to a thin ceramic wall (see Fig. 10). This has the advantage that the ceramic wall with the brazed electrodes can be part of the hermetic package that contains the electronics. The titanium feed-throughs can be needle electrodes that are each brazed to a ceramic plate. Each electrode has a post that protrudes hermetically through the ceramic plate. The other end forms the needle electrode. Each electrode is coated with an insulator having an exposed platinum or iridium coated surface.

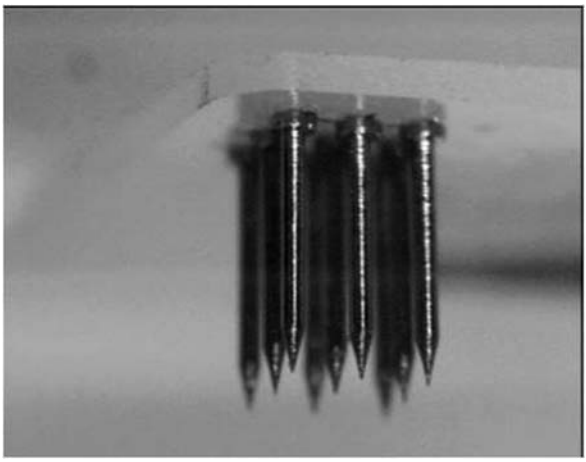

Fig. 10 Photo showing 3×3 titanium to ceramic brazed pin array in a ceramic plate

Another design uses a titanium feed-throughs post which has an iridium or platinum–iridium metal pin welded to it with a coated insulator except for the exposed electrode surface (see Fig. 11).

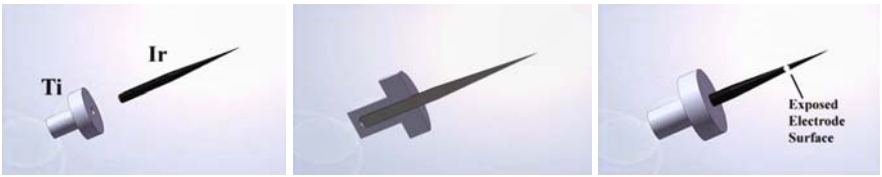

Fig. 11 This sequence shows an iridium pin welded to a titanium feed-through

The small space in the SBON package (i.e., "bed") containing all of the electronics must be hermetic. The "bed" is made out of a ceramic floor and contains the feed-throughs for the needle electrodes, and a ceramic roof. The roof may contain feed-throughs for indifferent electrodes. Also the titanium walls could be used as an indifferent electrode. The roof and floor are each brazed to a surrounding titanium wall that is about half of the "bed" thickness. The edges of the walls are designed to fit together. After the electronics are mounted in the floor and ceiling, the two halves are fitted to each other and the two titanium walls are welded together. This "bed" can be tested by sealing the package in a dry argon atmosphere with about 30% helium gas. After it is sealed it can be tested with a helium leak detector to confirm hermeticity. To provide a long hermetic life, it may be desirable to also insert a water absorbent getter inside the package.

4.2.2 Implant Size

Nerves vary in thickness depending on location and function. Nerves start out from the spinal cord relatively thick, between 5 and 10 mm in diameter, and get thinner as branches divide out to connect to muscles and other organs on their route to the distal ends of the limb. The thick nerves contain many hundreds or thousands of neurons. The branching nerves contain fewer and fewer fibers until very thin branches containing less than a hundred fibers connect to muscles. Since there is a possibility that the needles can sever one or more neurons when the BON is inserted into the nerve, it was decided that the BON should be inserted close to the amputated end of the nerve. The original BON designed by Dick Norman and his team was designed specifically for a flat area on the cortex of the human brain. We decided that since our bed of nails is designed for peripheral nerves close to the stump, we could make it more rectangular since it will lie parallel to the axis of the nerve. It was decided to take advantage of the nerve geometry and make an 8 by16 electrode array fitting on a foot print of about 5 $\times$ 10 mm. A diagonal view of the planned SBON design, with a 3 mm thick package forming the bed of the bed of nails is shown in Fig. 12. Figure 13 shows an internal view of the "bed".

4.2.3 Internal Construction of the Implant

The electronics needs to have the ability to either monitor or stimulate each of the 128 electrodes on the SBON simultaneously. The stimulation requires that

Fig. 12 Planned slanted bed of nails (SBON) showing a three millimeter thick electronics package in the form of the "bed". The needles are brazed through a floor composed of a ceramic plate. The sides are titanium walls brazed to the side of the ceramic floor and ceramic ceiling. The titanium walls of the floor and ceiling are welded together

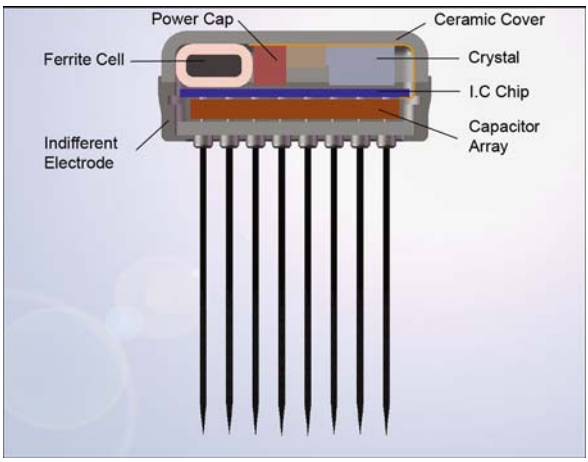

Fig. 13 Cross section of the SBON showing where the various components will be located

each electrode have a capacitor electrically in series with it to protect the tissue from direct current during stimulation. These capacitors are too large to be part of the integrated circuit. Each electrode needs its own isolated capacitor. A major design requirement for miniaturization is to reduce the amount of wires and connections as much as possible.

The integrated circuit will contain at least 64 amplifiers and 64 stimulator circuits that can be hooked up to any electrodes in unipolar or bipolar mode. To reduce the number of wires and wire bonds, it was decided to have the 128 capacitors required for stimulation electrodes mounted in an 8×16 array matching the needle post array to which they would be bumped. Bumping is an industrial process in which a precise machine aligns the electrical pads on one surface of a component with a matching set of pads on the surface of another component, and then simultaneously connects each pair of matching pads by using conductive epoxy, welding or some other means.

The capacitor array will be bumped to the electrode posts, and the integrated circuit will be bumped to the capacitor array. This eliminates the 128 connections between the IC and the cap array, and the 128 connections between the cap array and the bed nails. In Fig. 13 one can see the IC chip sitting on the capacitor array, and the capacitor array sitting on the ceramic plate which contains the posts of the electrode needles. Each needle post is bumped to one side of a specific capacitor in the array, and the other side of that capacitor is bumped to a pad on the IC chip.

4.2.4 Components on the Hybrid Circuit

On top of the chip will be a thin ceramic hybrid circuit with additional components which require wire connections to the large IC chip. These components are described in following sections.

4.2.5 Coil and Antenna

A ferrite wound coil is used to pick up the 125 kHz magnetic field energy for powering the device. A pole or loop antenna is designed to radiate and receive the propagated 400 mHz radio signals communicating with the prosthetic control unit (PCU).

4.2.6 Chip and Crystal Oscillator

An integrated circuit chip is used for converting the 125 kHz to a regulated dc voltage and a capacitor acts as a battery to store this energy for powering. A crystal provides an accurate frequency clock for timing and radio frequencies.

4.2.7 Indifferent Electrodes

At each end of the cap array there will be eight extra pads connected to eight extra bumped pads from the large IC chip. These 16 pads are used for wire-bonding between the large IC chip and the hybrid. This is the path for the IC to connect to the hybrid circuit. At this time only 10 wires are needed connecting the hybrid to the large IC chip.

When in unipolar mode there will be a requirement for several selectable indifferent electrodes in case there is a muscle generating a large EMG potential adjacent to one of the indifferent electrodes. Besides the metal band going around the sides of the bed, there will be four other indifferent circular electrodes mounted on the ceramic roof (cover).

4.2.8 Wireless Power

The power will be wirelessly transferred to the SBON via a 125 kHz magnetic field. The efficiency of the ferrite pickup coil is on the order of 1% or less. The circuit in the SBON is designed to protect the SBON from overheating if the field gets very large. The circuit reduces the excessive undesired power by causing the coil to be detuned. The low efficiency and the method of self-regulation permit the use of over 20 SBONs to be safely powered simultaneously from a single primary coil. The axis of the ferrite coil is aligned with the nerves which are aligned with the limb axis. The prosthetic wall of the socket contains a coil which has its axis aligned with the axis of the limb.

4.2.9 Wireless Communication

Each SBON must be able to communicate all spike data detected by its amplifiers connected to the motor neurons to the actuator circuits controlling the appropriate joint, and simultaneously transmit all the sensory signals detected by the sensors in the prosthesis to the stimulators connected to the appropriate sensory neurons (see Fig. 14).

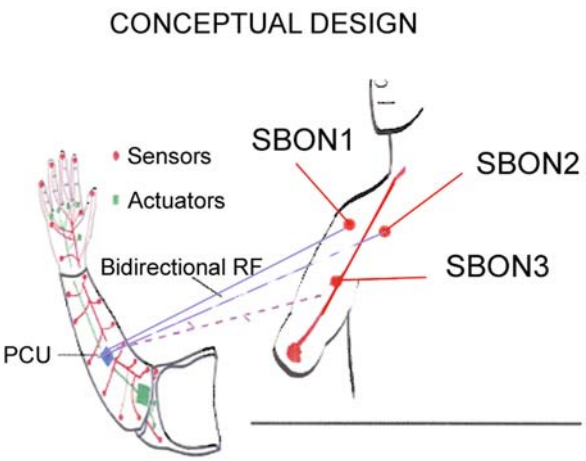

Fig. 14 Communication path between the three SBONs mounted on the nerve and the prosthetic control unit (PCU)

The communication channel used is a UHF channel in the Medical Micropower Band presently being presented to the FCC and NTIA for approval by the Alfred Mann Foundation (AMF). It consists of four 5 MHz wide bands in the 410–460 MHz region. Each band can simultaneously communicate in both directions to 850 electrode channels each at a rate of about 100 communications per second for each electrode. Each SBON will only use the number of channels that it needs. The communication method uses Time Domain Multiplexed Access (TDMA). There are 850 receive time slots and 850 transmit time slots in each 10 ms frame. Fifteen bits of data are sent and 10 bits of data are received in the form of Quad-Phase modulation 100 times per second. Each electrode channel is assigned a specific 5 μs time slot. Each electrode channel receives the 15 data bits plus 15 forward error detection bits during its receive 5 μs time slot and sends back 10 data bits plus 10 forward error detection bits in a 5 μs transmitting time slot. These propagated UHF radio signals will travel through about four inches of tissue and be reliably detected. Each 5 μs RF energy burst is about 1 mW of effective radiated power.

4.2.10 Prosthetic Master Control Unit (PMCU)

The PCU is a computerized battery-powered device that is used to co-ordinate the artificial limb for the patient by properly routing the sensor and actuator signals between the motor and the sensory neurons.

The prosthesis contains a PCU that has five operational functions:

1. Generate a 125 kHz magnetic field to power the SBON.
2. Transmit a UHF radio signal to the SBON using the Medical Micropower Band protocol.
3. Receive a UHF radio signal from the SBON using the Medical Micropower Band protocol.

4. Send command signals from the patient's motor neurons to the actuators in the artificial limb.
5. Send sensor signals from the artificial limb to stimulate the appropriate patients sensory neurons.

4.2.11 Clinicians Fitting Unit

The clinicians fitting unit is a notebook computer designed to permit the clinician to fit each sensor on the artificial limb to the proper sensory neuron, and to fit each motor neuron to the proper actuator. It will permit oscilloscopic recording of individual sensory units with a resolution of 30,000 samples/second, and adjust the data reduction circuit in the SBON to permit the patient to control his limb.

Each voltage amplifier has a programmable data reduction circuit. The circuit has a spike peak height window detection circuit for positive and negative spikes and a time window circuit for the spike width. The thresholds to the positive and negative spike window circuits and the time window can be adjusted by the clinician to select out a specific spike. If the electrodes pick up a great many spikes within the 10 ms windows, the clinician can use a rectify and integrate mode to get a high and low figure of merit acceptance value. From a review of the signals picked up with the BON devices, it appears that these two selection routines will always be sufficient to select the proper spikes or group of spikes required to control the actuators.

5 Conclusion

This study indicates that it is possible to construct a robust SBON peripheral nerve interface with a bed that is between 2 and 3 mm thick that contains all the electronics for a completely wireless implantable system. Based on Bion^{TM} test data [4–7], it appears that a lifetime in excess of 80 years will be possible for such a device. The titanium or iridium metal electrode nails in such a device is very sturdy and will bend without breaking if accidental lateral forces are applied. This method of packaging is now used successfully in many implantable devices.

Acknowledgment The author wishes to thank the Alfred Mann Foundation for funding this study and providing information on their brazing, communication and implantable technologies.

References

1. Kipke DR, Shain W, Buzsaki G, et al. (2008) Advanced Neurotechnologies for Chronic Neural Interfaces: New Horizons and Clinical Opportunities. J Neurosci 46:11830–11838

2. Kuiken T, Marasco PD, Blair LA, et al. (2007) Redirection of cutaneous sensation from the hand to the chest skin of human amputees with targeted reinnervation. The National Academy of Sciences of the USA, PNAS 104(50):20061–20066
3. www.physorg.com/news65100472.html. University of Utah to help building bionic arm. April 24, 2006
4. Schulman JH, Mobley P, Wolfe J, et al. (2006) A 1000 + Channel Bionic Communication System, *Proceedings of the 28th IEEE EMBS Annual International Conference*, New York City, NY, Sept., 2006, pp. 4333–4335
5. www.aemf.org. Alfred Mann Foundation for Scientific Research, Valencia, CA, USA
6. Schulman J, Mobley P, Wolfe J, et al. (2006) An Implantable Bionic Network of Injectable Neural Prosthetic Devices: The Future Platform for Functional Stimulation and Sensing to Restore Movement and Sensation. In: Bronzino JD (ed) Biomedical Engineering Fundamentals, The Biomedical Engineering Handbook Series, Chapter 34, Third Edition Trinity College, Hartford, Connecticut, CRC Press, USA
7. Jiang G, Mishler D, Davis R, et al. (2005) Zirconia to Ti-6Al-4 V braze joint for implantable biomedical device, J Biomed Mater Res: Part B – Applied Biomatls 72B:316–321
8. www.amputee.coalition.org and the National Limb Loss Information Center (NLLIC)
9. Nordhausen CT, Rousche PJ,Normann RA (1994) Optimizing Recording Capabilities of the Utah Intracortical Electrode Array. Brain Res 637(1–2):27–36
10. Rousche PS, Normann RA (1998) Chronic Recording Capability of the Utah Intracortical Electrode Array in Cat Sensory Cortex. J Neurosi Meth 82:1–15
11. Private communications with Dr. Richard Stein.
12. Branner A, Stein RB, Normann RA (2001) Selective Stimulation of Cat Sciatic Nerve Using an Array of Varying Length Microelectrodes. J Neurophysiol 85:1585–1594
13. Warwick K, Gasson M, Hutt B, et al. (2003) The Application of Implant Technology for Cybernetic Systems. Arch Neurol 60:1369–1373
14. Gasson M, Hutt B, Goodhew I, et al. (2005) Invasive Neural Prosthesis for Neural Signal Detection and Nerve Stimulation. Int J Adapt Control Signal Process 19:365–375
15. Dhillion GS, Lawrence SM, Hutchinson DT, et al. (2004) Residual Function in Peripheral Nerve Stumps of Amputees: Implications for Neural Control of Artificial Limbs. J Hand Surg 29(4):605–615
16. Jia X, Koenig MA, Zhang X, et al. (2007) Residual Motor signal in Long-term Human Severed Peripheral Nerves and Feasibility of Neural signal-controlled Artificial Limb. J Hand Surg 32A:657–666

Magnetic Stimulation of Neural Tissue: Techniques and System Design

Eric Basham, Zhi Yang, Natalia Tchemodanov, and Wentai Liu

Abstract Magnetic stimulation of neural tissue is an attractive technology because neural excitation may be affected without the implantation of electrodes. This chapter provides a brief overview of the technology and relevant literature. While extensive magnetic stimulation modeling and clinical experimentation work has been presented, considerably less quantitative in vitro work has been performed. In vitro experiments are critical for characterizing the site of action, the structures stimulated, and the long-term tissue histological effects. In vitro systems may also facilitate the development of novel magnetic stimulation approaches. To demystify magnetic stimulation systems, this chapter presents an in vitro experimental system using a systematic design methodology. The modeling methods are designed to aid experimentation. Circuit schematics, test rigs, and supplier information are given to support practical implementation of this design methodology. Example neural preparations and their modeling and use are also covered. Finally, as an alternative to pulsed discharge circuits for magnetic stimulation, this chapter shows how to use a circuit to deliver asymmetric current pulses to generate the magnetic field.

1 Introduction

Magnetic stimulation of neural tissue is an intriguing technology because stimulation may be affected without direct contact to the tissue under study. Magnetic stimulation has advantages over electrical stimulation in biocompatibility, bioresistance, and operational biotoxicity. Rather than creating an electric field via the injection of current, as in electrical stimulation, magnetic stimulation arises as a result of the induced fields created within the tissue. A conceptualized system is shown in Fig. 1. In short, a time-varying current flowing through a coil generates a time-varying magnetic field. The time-varying magnetic field induces an electrical field within

E. Basham (✉)
Department of Electrical Engineering, University of California, Santa Cruz, CA, USA
e-mail: basham.eric@gmail.com

D.D. Zhou, E. Greenbaum (eds.), *Implantable Neural Prostheses 1*,
Biological and Medical Physics, Biomedical Engineering,
DOI 10.1007/978-0-387-77261-5_10,

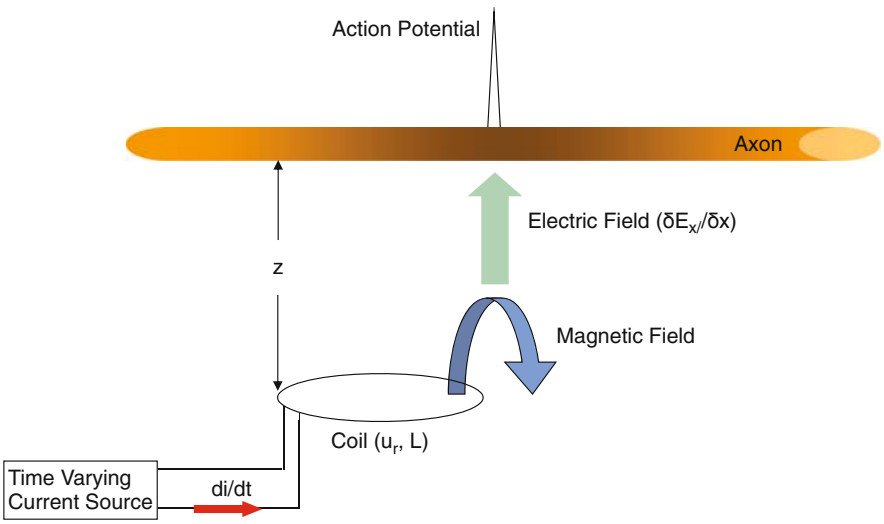

Fig. 1 Magnetic stimulation conceptual system overview. Critical system design parameters are the current ramp rate of change di/dt, the coil relative permeability u_r, inductance L, and the coil distance from the nerve z. The spatially varying electric field $\partial E_x/\partial x$ produced depolarizes the axon, shown as the shaded area along the axon, and leads to the initiation of an action potential

the tissue. During magnetic stimulation, the stimulating coil may be sealed and remain completely isolated from the target tissue. Since there is no metal–electrolyte interface, as is the case with electrodes used for electrical stimulation, issues of charge transfer, electrode surface modification, and corrosion are mitigated. In addition, magnetic fields penetrate unattenuated through non-conductive tissue because the permeability of tissue at low frequencies (<50 kHz) is near unity.

Since no direct electrical connection between the target tissue and the device is required, magnetic stimulation applied externally may be used to stimulate neural tissue without surgical implantation of electrodes. One of the most important applications of external excitation of neural tissue is transcranial magnetic stimulation (TMS). TMS is used for mapping functional areas of the brain, sleep studies, and the treatment of depression. External magnetic stimulation has also been used as an alternative to functional electrical stimulation (FES) to mitigate incontinence, treat pain [1], evaluate spinal function, and as a diagnostic tool for evaluation of nerve damage [2]. Reviews of magnetic stimulation and TMS in particular are available in [3–8].

Magnetic stimulation with traditional methods confounds in vitro experimentation as the area of effect is quite large and interferes with standard electrophysiology recording equipment. The resulting electromagnetic interference and mechanical constraints are especially evident in adherent cell electrophysiological studies of magnetic stimulation. Typically, only large and long neural preparations (centimeters in length) can be used for experimentation. A properly scaled system also facilitates the study of the histological effects of magnetic stimulation

and aids in the investigation of pulsed electromagnetic fields on nerve regrowth. These are both active areas of investigation [9–11]. Currently, commercially available systems or system descriptions are lacking for important neuroscience animal models such as rat or mouse. Scaled magnetic stimulation systems may also facilitate animal model experimentation and lead to insight not available through clinical experimentation.

While extensive magnetic stimulation modeling work has been presented [12–17], considerably less quantitative in vitro work has been performed [18–20]. In vitro experiments are critical for characterizing the site of action, structures stimulated, and the long-term tissue histological effects of magnetic stimulation. The disparity in experimental versus modeling research is predominantly due to the difficulty in understanding the electromagnetic interaction with neural tissue during experimentation. For example, inserting electric probes into the tissue during stimulation alters the fields produced and thus the experimental results.

There is still some debate about the exact nature of the interaction of magnetic fields with nervous tissue [21–23], exemplifying the need for flexible, quantitative experimental systems. In a recent clinical evaluation of repetitive TMS (rTMS), the key difference in efficacy was found to link closely with the manufacturer model (and thus the specific waveform) generating the biphasic pulse [24].

Modifying full-scale magnetic stimulation systems in a clinical environment presents significant challenges to proof of concept experimentation. As an example, there is little data that covers co-stimulation (pairing electrical stimulus with magnetic stimulus) and paired pulse protocols. Rapidly reconfigurable in vitro systems can be invaluable for developing better predictive models, correlating effects of clinical experiments [25], and developing proof of concept systems.

In the following chapter, we outline a method that relies on the use of first-order estimates to facilitate experimentation. We hope to demystify magnetic stimulation experiments by simplifying the modeling methods and describing the experimental apparatus. Since magnetic stimulation systems are more complex than electrical stimulation systems, both from the perspective of modeling and apparatus, we touch on design techniques for the modeling, computer control, data acquisition, coil design, circuit design, and recording methods. We then use a scaled magnetic stimulation system to investigate a new approach to magnetic stimulation circuit design. Two example neurological preparations and the reasoning for their use are also covered. While at some points the discussion may appear oversimplified or pedantic, the focus of this chapter is to facilitate lab experimentation and offer a conceptual starting point for further experimentation.

2 Field-Based Comparison of Electrical and Magnetic Stimulation

Compared to magnetic stimulation of neural tissue, electrical stimulation is well understood and well characterized. In 1947, Hodgkin and Rushton reported the first experimental application of passive cable theory to axons [26]. A significant review of experimental results of extracellular electrical stimulation later

occurred in [27], and the author presented an instructional chapter oriented toward laboratory practice and qualitative analysis in [28]. In [29], Rattay introduced an efficient quantitative approach for modeling the response of an axon to extracellular stimulation. The method introduced the concept of the "activation function" for prediction of extracellular stimulation response. For extracellular electrical stimulation, the second derivative of the external potential in the direction of the axon is responsible for activation of the axon. Rattay's work focused on the derivation of a modified form of the cable equation that included a source term shown on the left-hand side of Equation (1)

$$\lambda_m^2 \frac{\partial^2 V_e(x,t)}{\partial x^2} = -\lambda_m^2 \frac{\partial^2 V_m(x,t)}{\partial x^2} + \tau \frac{\partial V_m(x,t)}{\partial t} + V_m(x,t), \tag{1}$$

where the length and time constants of the neural membrane (λ_m and τ_m, respectively) are defined as

$$\lambda_m = \sqrt{\frac{r_m}{r_i}} \text{ and } \tau_m = c_m r_m \tag{2}$$

V_m is the transmembrane voltage defined as the voltage difference between the intracellular and the extracellular fluid ($V_m = V_{intracellular} - V_{extracellular}$), r_m is membrane resistance times unit length ($k\Omega \cdot cm$ axon length), r_i is intracellular resistance ($\Omega \cdot cm^{-1}$), c_m is membrane capacitance per unit length ($F \cdot cm^{-1}$). V_e is the stimulating electrode voltage and the axon lies along the x axis as depicted in Fig. 2. Both V_e and V_m are functions of location and time. Setting V_m to zero leads to the definition of the "activating function", $\lambda^2 \cdot \partial E_e / \partial x$, which is useful for determining the initial change in V_m.

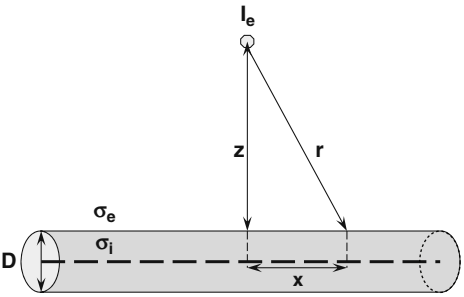

Fig. 2 Geometric description of stimulation of a long uniform fiber by a point source. An extracellular point current source I_e is located a distance z from the cylindrical fiber of diameter D and intracellular conductivity σ_i. Fiber and source are immersed into an unbound extracellular medium of uniform conductivity σ_e. The geometrical representation is used to derive the electrical field distribution along the fiber

The activating function allows estimation of stimulation based on the membrane length constant and the spatially varying electric field [30]. The activation function provides a method to quantitatively predict the behavior of the axon to external electrical fields. Regions of the cable where $\partial^2 V_e / \partial x^2$

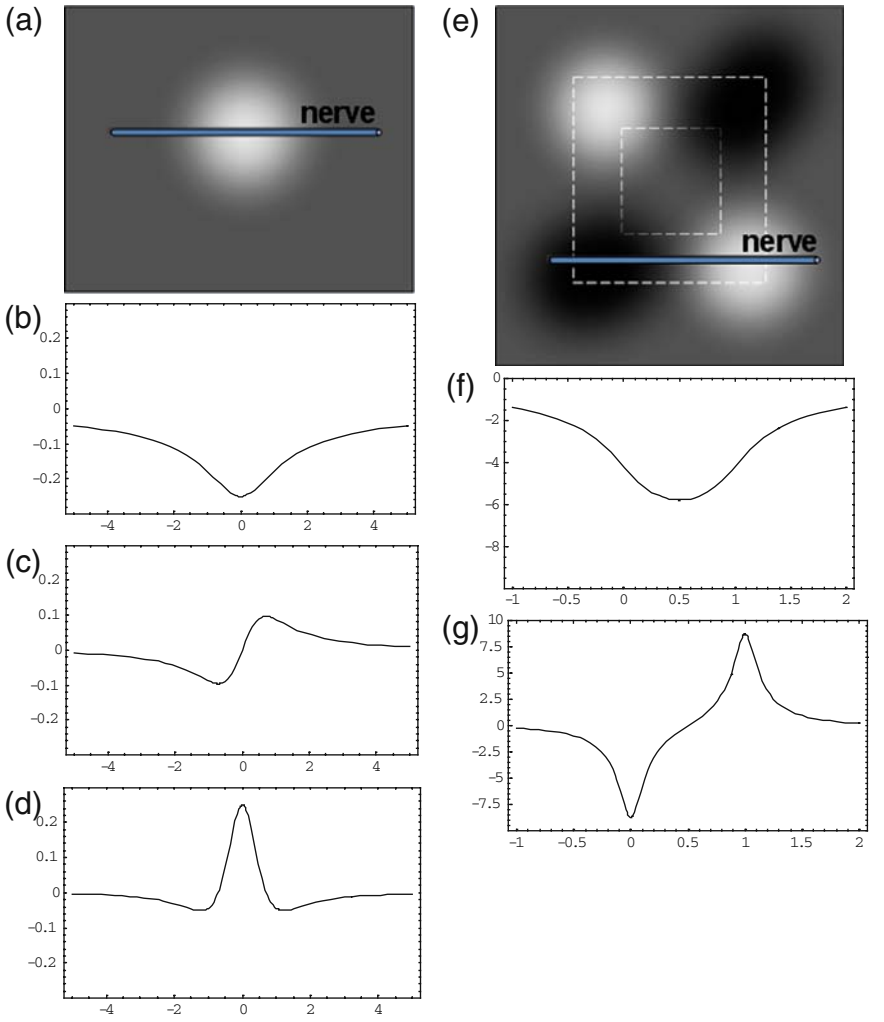

Fig. 3 Diagrammatic comparison of fields induced by a cathodal point source (**a**–**d**) and a square magnetic stimulation coil (**e**–**g**). (**a**) nerve lies above the point source and the shaded area represents the magnitude of the spatially varying electric field. With the nerve fiber placed as shown in (**a**), (**b**) shows the magnitude of the extracellular potential V_e along the fiber, (**c**) shows the magnitude of the electric field along the fiber, and (**d**) shows the derivative of electric field along the fiber for cathodal electrical stimulation. (**e**) nerve lies above the coil and the shaded area represents the positive magnitude (*light shading*) and negative magnitude (*dark shading*) of the spatially varying electric field. With the nerve fiber placed as shown in (**e**), (**f**) shows the magnitude of the electric field along the fiber, and (**g**) shows the derivative of electric field along the fiber for magnetic stimulation. Comparing the two methods, cathodal electrical stimulation generates a single depolarizing peak and two much smaller hyperpolarizing peaks, while magnetic stimulation generates a hyperpolarizing and a depolarizing peak of approximately equal magnitude. As a note: the situation for anodic electrical stimulation varies slightly as a strong hyperpolarizing peak and two small depolarizing peaks are generated. Excitation occurs when the small depolarizing peaks reach the necessary magnitude to fully depolarize the fiber. Typically 5–7 times as much current are required to stimulate anodically as cathodically

were greater than zero were shown to be depolarized. Regions where $\partial^2 V_e/\partial x^2$ are less than zero are predicted to be hyperpolarized, as depicted in Fig. 3.

$$V_e = \frac{I_e}{4\pi\sigma(x^2 + z^2)} \tag{3}$$

The electric field is equal to the gradient of the scalar potential, V_e, from the point source electrode

$$\vec{E}_e = \frac{\partial V_e}{\partial x} = \frac{I_e x}{4\pi\sigma(x^2 + z^2)^{\frac{3}{2}}} \tag{4}$$

where I_e is the current injected by the point electrode, σ is the extracellular medium conductivity, and z is the distance between the point source and the axon. The spatially varying electric field from a point source electrode at a height, z, above the axon is

$$\frac{\partial \vec{E}_e}{\partial x} = \frac{I_e(2x^2 - z^2)}{4\pi\sigma(x^2 + z^2)^{\frac{5}{2}}}. \tag{5}$$

Thus, we can directly calculate $\delta E_e/\delta x$ from Equation (5) given the electrode input current, extracellular conductivity, position of the electrode, and the cable equation. With the source term modified to reflect the spatially varying electric field the cable equation is

$$\lambda^2 \frac{I_e(2x^2 - z^2)}{4\pi\sigma(x^2 + z^2)^{\frac{5}{2}}} = \lambda^2 \frac{\partial \vec{E}_e}{\partial x} = -\lambda_m^2 \frac{\partial^2 V_m(x,t)}{\partial x^2} + \tau \frac{\partial V_m(x,t)}{\partial t} + V_m(x,t). \tag{6}$$

There is some debate in the literature as to whether the activation function is more conveniently defined as $\partial E_e/\partial x$ or as $\lambda^2 \cdot \partial E_e/\partial x$ [31], but here we use activating function to refer to $\lambda^2 \cdot \partial E_e/\partial x$, and define the spatially varying electric field as $\delta E_e/\delta x$, that is, the rate of change of the electric field with respect to the *x* axis.

The cable model provides insight into the interaction between the electric fields and the neural tissue, but it does not completely describe the dynamics of the system. The peak spatially varying electric field and the length of time the electric field is maintained are both essential components to understanding the generation of an action potential in neural tissue. For example, the activating function fails to correctly predict the depolarized or hyperpolarized regions for longer time periods or wider areas of stimulation (p. 214, [32]). Vexing questions about the validity of the activation function remain [33, 34]. These inconsistencies have led to efforts to improve the passive cable model's predictive capability via simulation [23, 35–40].

Several time points should be collected to facilitate the correlation of modeling and experimental data. The plot of time point versus stimulus strength is called a strength-duration curve. The strength-duration curve is an invaluable experimental metric. Analysis of experimental data can be used to obtain an estimate of τ_m through fitting of Equation (7). The curves can also be qualitatively compared and the comparison can provide some insight into physiological conditions.

$$I_{th} = \frac{I_{rheobase}}{\left(1 - e^{-\left(\frac{t_{duration}}{\tau}\right)}\right)}. \tag{7}$$

In this equation, I_{th} is the current stimulus threshold sufficient to generate a neural response (action potential) in 50% of the trials. $t_{duration}$ is the length of the experimental stimulus pulse, and τ_m is the membrane time constant as defined in Equation (2). $I_{rheobase}$ is the minimum current stimulus that produces any response as $t \to \infty$. Chronaxy is defined as the duration at which stimulus occurs at twice the rheobase. During actual experimentation, the rheobase is estimated at approximately 10× the chronaxy of the nerve. More information on the derivation and application of the strength–duration curve may be found in [41].

Using I_{th} as the dependant variable of the strength–duration curve for characterization of nerves and axons discards important information about the actual mechanism of excitation. An improved method is the use of $\delta E_e/\delta x$, as derived in Equation (5). Further verification is possible by measuring strength–duration curves at several distances above the nerve. However, the range at which stimulus will occur at any input current will vary as a function of the membrane constants, pulse polarity, and diameter of the axon as shown in Fig. 4.

Using $\delta E_e/\delta x$ as the ordinate of a strength–duration curve allows the comparison of electric fields generated by sources other than a point source electrode. For example, an equivalent cable expression to the cable equation with an electrical source term (Equation 8) for magnetic stimulation was presented in [15]. The spatially varying electric field was derived from fundamental electromagnetic principles.

$$\lambda_m^2 \frac{\partial \vec{E}_x(x,t)}{\partial x} = -\lambda_m^2 \frac{\partial^2 V_m(x,t)}{\partial x^2} + \tau \frac{\partial V_m(x,t)}{\partial t} + V_m(x,t) \tag{8}$$

where E_x is the x component of the magnetically induced electric field. The derivation of (Equation 8) assumes the fiber lies along the x axis parallel to the plane of the coil. Early reports of magnetic stimulation used a magnetic field strength term to report strength–duration curves (e.g., [42]). However, comparing the values of electrically and magnetically induced spatially varying electric fields ($\delta E_e/\delta x$ and $\delta E_x/\delta x$) allows a first-order comparison between magnetic and electrical stimulation.

There is still some debate as to whether the magnetically induced $\delta E_x/\delta x$ is applicable to neural stimulation [43]. A controlled, quantitative, experimental approach allows the investigation of conflicting clinical and experimental evidence and should provide insight into the discrepancy between simulation and experimental data. Cable equation modeling seems to lend itself to

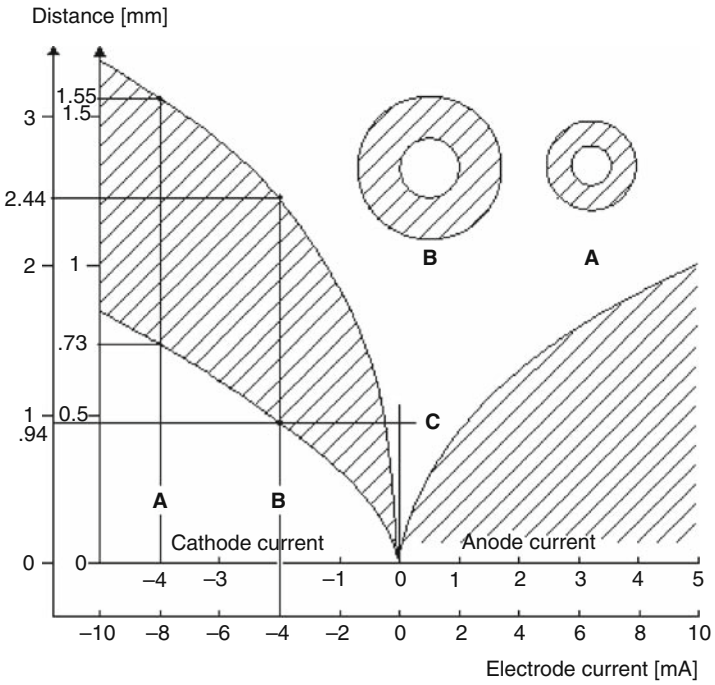

Fig. 4 Current-distance relationship for unmyelinated fibers. Excitation occurs for points lying in the shaded region. For cathodal stimulation, a minimum distance arises at the point where anodal block prevents the escape of the action impulse. For anodal stimulation, block does not occur; thus there is no lower limit on the source-fiber distance. The inner scales are for a fiber diameter of 9.6 μm, and the outer for a diameter of 38.4 μm. Scaling the excitation with respect to both current strength, source-fiber distance, and fiber diameter leaves the solution unchanged (from [29])

certain neurological preparations, notably long, relatively uniform nerve fibers. Scaling a magnetic stimulation system to allow the use of smaller and more varied preparations with varying axonal diameter and membrane constants can further facilitate modeling. Several candidate neural preparations are well characterized and include information on the membrane constants and the diameter of individual axons. For dynamic modeling, the active properties of the membrane must be solved or simulated [15, 44]. Using well-characterized preparations allows simulation of the cable equation and several freely available packages are designed to assist with cable modeling, including NEURON (http://www.neuron.yale.edu/neuron/) [45] and GENESIS (http://www.genesis-sim.org/GENESIS/) [46]. Neurocal is a simplified package written in MATLAB that is very easy to use and modify [47]. Combining easily modeled, well-documented neurological preparations with simple lab experiments and accurate, easy to use active cable equation simulators is a powerful application of the engineering methodology of simulate, design, fabricate, and test.

3 Magnetic Modeling

There are several different approaches to determining the source term in the cable equation for magnetic stimulation. In any case, the goal is the same: determine the unknown experiential variables from the known experimental parameters. For magnetic stimulation, the unknown terms are the induced electrical field and the spatial variation of the induced electric field, while the design parameters are the time-varying input current, coil shape, turn number, and expected depth of stimulation. The required excitation threshold may be determined using methods outlined in the prior section, but to some degree may also be considered an experimental variable. In the final section, we will cover selection of neural preparations with widely varying membrane properties which are useful for testing the same experimental set-up with neural preparations having differing excitability thresholds.

Finite Element Methods (FEM) can provide answers directly by solving the fundamental electromagnetics problems at each point of a finely discretized physical model. Ansoft, COMSOL, Quickfield, and MATLAB are finite element analysis software packages that have been applied to magnetic stimulation modeling. All of these packages also have a free or low-cost student version. Texts that introduce the software concurrently with electromagnetic principles include for Ansoft [48], for Quickfield and MATLAB [49], and for MATLAB specifically [50]. Magnetic stimulation modeling becomes complex quickly as realistic models are developed. These packages also have a significant learning curve to master and apply appropriately. In addition, finite element models can be computationally time consuming to evaluate. These reasons make finite element methods applied to magnetic stimulation more appropriate for design verification than design.

Analytical solutions address these concerns. Derivation of the fields involved in magnetic stimulation can be daunting for those less experienced with electromagnetics. In many reviews of magnetic stimulation the authors skim the general approach and leave the reader without the tools necessary to aid experimentation. We outline the general approach to the derivation of the fields involved in magnetic stimulation and subsequently provide the reader with analytical formulas that can provide first-order estimates of the source term in the passive cable model equation. For readers with advanced electromagnetic understanding, there are alternate approaches to determining the relevant electrical fields. We have provided one example in the appendix covering scaling and the use of ferrite solenoid cores.

While the goal is to model the induced electric field $\vec{E}$ directly from the input current and physical coil parameters, the magnetic vector potential $\vec{A}$ is a more convenient way of deriving the induced electric fields. While the electric field, $\vec{E}$, can be described as the gradient of the scalar potential V (as outlined in the section above on cable modeling), there is no generalized scalar potential for magnetic field. However, the magnetic field, $\vec{B}$, can be obtained by taking the curl of the magnetic vector potential, $\vec{A}$.

$$\vec{B} = \nabla \times \vec{A} \tag{9}$$

The electric field, **E**, is related to the time-varying magnetic field by

$$\nabla \times \vec{E} = -\frac{\partial \vec{B}}{\partial t} \tag{10}$$

Substituting and solving, we obtain

$$\vec{E} = -\frac{\partial \vec{A}}{\partial t} - \nabla V \tag{11}$$

Since there is assumed to be no charge on the coil and the current distribution in the coil is determined to be uniform (i.e. quasistatic conditions), Equation (11) reduces to

$$\vec{E} = -\frac{\partial \vec{A}}{\partial t} \tag{12}$$

The magnetic vector potential is related to the physical dimensions of the coil according to Fig. 5.

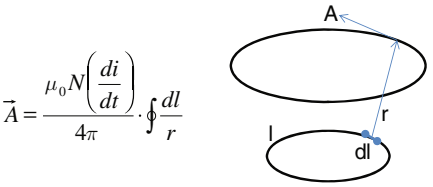

Fig. 5 Geometrical derivation of the magnetic vector potential A. The lower loop is the coil and the upper loop the region around which the magnetic vector potential is calculated

Much of the challenge in determining the electrical field induced by time-varying magnetic fields arises in accounting for the charge accumulation at the boundary interface between air and tissue. Several articles are available that address boundary condition modeling [51–56]. The interested reader is referred to them for more information. In the method presented in [57], for experimental conditions where the tissue interface is parallel to the plane of the coil, the electric field $\vec{E}_x$ can be calculated by numerically integrating along the line:

$$\partial \vec{E}_x = -\frac{\mu_0 N\left(\frac{di}{dt}\right)}{4\pi}\left\{\left[\frac{dl_x}{R} + \frac{(x-x_0)dl_z}{\rho^2}\cdot\left(1-\frac{z_0-z}{R}\right)\right]\hat{x} + \left[\frac{dl_y}{R} + \frac{(y-y_0)dl_z}{\rho^2}\left(1-\frac{z_o-z}{R}\right)\right]\hat{y}\right\} \tag{13}$$

where the coil element lies at (x_0, y_0, z_0), the electric field is calculated at (x,y,z), N is the number of coil turns, di/dt is the rate of change of the coil input current, μ_0 is the permittivity of free space and

$$\rho = \sqrt{(x-x_0)^2 + (y-y_0)^2} \tag{14}$$

$$R = \sqrt{(x - x_0)^2 + (y - y_0)^2 + (z - z_0)^2}. \tag{15}$$

The problem can be significantly simplified if the coil is planar and square. If the coil is in the x–y plane with $z_o = 0$, and if no coil element lies in the z axis, that is, all coil elements are parallel to the air–tissue interface, then Equation (13) simplifies to Equation (16). We omit the derivations of $\vec{E}_y$ and $\delta E_y/\delta y$ because they are similar in form. While all elements in a square coil are parallel and assumed to be tightly packed, the width of the coil has finite dimensions with respect to the coil diameter, even more so for coils with small diameter. These assumptions introduce error, in some cases significant, but suffice for derivation of first-order design equations.

$$\partial \vec{E}_x = -\frac{\mu_0 N \left(\frac{di}{dt}\right)}{4\pi} \cdot \frac{1}{R} dl_x \tag{16}$$

Integrating the expression with respect the x component of the line yields the general form

$$\vec{E}_x = -\frac{\mu_0 N \left(\frac{di}{dt}\right)}{4\pi} \cdot \ln\left[x - x_0 + \sqrt{(x - x_0)^2 + (y - y_0)^2 + (z - z_0)^2}\right]\Bigg|_{x_{01}}^{x_{02}} \tag{17}$$

A square coil has a side length of (a) and is oriented such that one corner of the coil is at (0,0) and the opposite corner is at (a,a). Two elements of the coil lie along the x axis. The first element starts at (0,0) and ends at (a,0). The expression is evaluated from 0 to a as

$$\vec{E}_x = -\frac{\mu_0 N \left(\frac{di}{dt}\right)}{4\pi} \cdot \ln\left[x - x_0 + \sqrt{(x - x_0)^2 + y^2 + z^2}\right]\Bigg|_0^a \tag{18}$$

and simplifies to

$$\vec{E}_x = -\frac{\mu_0 N \left(\frac{di}{dt}\right)}{4\pi} \cdot \ln\left[\frac{x - a + \sqrt{(x - a)^2 + y^2 + z^2}}{x + \sqrt{x^2 + y^2 + z^2}}\right]_x \tag{19}$$

For the side of the coil at $y = a$, the second element that lies along the x axis, with current moving from a to 0

$$\vec{E}_x = -\frac{\mu_0 N\left(\frac{di}{dt}\right)}{4\pi} \cdot \ln\left[x - x_0 + \sqrt{(x-x_0)^2 + y - a^2 + z^2}\right]\Bigg|_a^0 \tag{20}$$

and similarly simplifies to

$$\vec{E}_x = -\frac{\mu_0 N\left(\frac{di}{dt}\right)}{4\pi} \cdot \ln\left[\frac{x + \sqrt{x^2 + (a-y)^2 + z^2}}{x - a + \sqrt{(x-a)^2 + (a-y)^2 + z^2}}\right] \tag{21}$$

For the full expression for the electric field around the coil, the expressions are summed to produce

$$\vec{E}_x = -\frac{\mu_0 N\left(\frac{di}{dt}\right)}{4\pi} \cdot \ln\left[\frac{\left(x - a + \sqrt{(x-a)^2 + y^2 + z^2}\right) \cdot \left(x + \sqrt{x^2 + (a-y)^2 + z^2}\right)}{\left(x + \sqrt{x^2 + y^2 + z^2}\right) \cdot \left(x - a + \sqrt{(x-a)^2 + (a-y)^2 + z^2}\right)}\right] \tag{22}$$

Evaluation of the above expression on an x and y plane for a fixed z (height above the coil) will graph the electric field that an axon lying along the x axis will be exposed to during a current pulse.

As seen in Fig. 6b, a maximum rate of change of the electric field occurs at each corner of the coil and a minimum rate of change occurs in the center of each winding. It becomes useful to have an expression for the spatially varying electric field. This is the source term, or excitation function, for long straight axons. As before, the spatially varying electric field may be evaluated by numerically integrating along the length of the coil

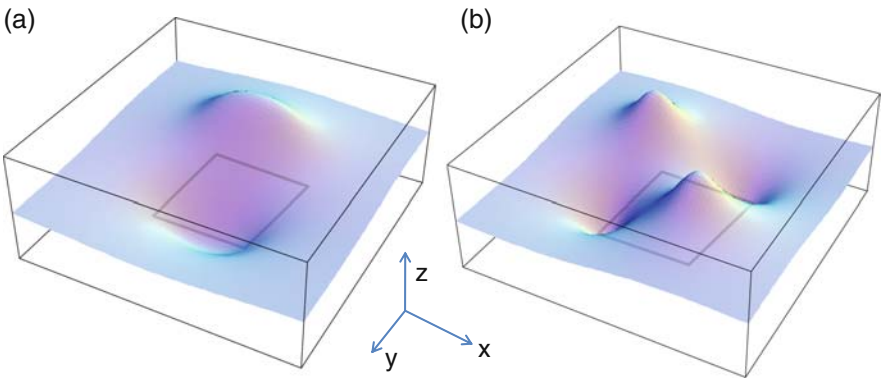

Fig. 6 Fields generated above a unit sized square coil. Square coils are shown in grey. (**a**) the z axis shows the relative magnitude of the e field generated above the coil (**b**) the magnitude of spatial distribution of $\partial E_x/\partial x$ maxima and minima generated by square coil. Compare with alternative views in Fig. 3. and Fig. 7

$$d\left[\frac{\partial \vec{E}_x}{\partial x}\right] = \frac{\mu_0 N\left(\frac{di}{dt}\right)}{4\pi} \cdot \left\{\left[\frac{x-x_0}{R^3}\right]dl_x - \left[\frac{(y-y_0)^2-(x-x_0)^2}{\rho^4}\right] \cdot \left[1+\frac{z-z_0}{R}\right]dl_z + \left[\frac{(x-x_0)^2(z-z_0)}{\rho^2 R^3}\right]dl_z\right\} \tag{23}$$

As before, Equation (23) is simplified for the case where the elements of the coil lie in the $z_o = 0$ plane and for square coils with elements lying only along the x axis to

$$d\left[\frac{\partial \vec{E}_x}{\partial x}\right] = -\frac{\mu_0 N\left(\frac{di}{dt}\right)}{4\pi} \cdot \frac{x-x_o}{R^3} dl_x \tag{24}$$

Alternatively, we can directly evaluate the derivative of the closed form analytical solution for the electric field from Equation (22). The resultant expression after simplification is

$$\frac{\partial \vec{E}_x}{\partial x} = -\frac{\mu_0 N\left(\frac{di}{dt}\right)}{4\pi} \cdot \left[\frac{1}{\sqrt{(a-x)^2+y^2+z^2}} + \frac{1}{\sqrt{x^2+(a-y)^2+z^2}} - \frac{1}{\sqrt{(a-x)^2+(a-y)^2+z^2}} - \frac{1}{\sqrt{x^2+y^2+z^2}}\right] \tag{25}$$

The plot of the spatially varying electric field is shown in Fig. 6b for the unit coil case ($a = 1$) at a height (¼*a) above the coil. The figure shows four loci of excitation. The peak electric field and locus of excitation for long straight nerves will occur at the corners of square coil windings as shown in Fig. 3. By setting $y = 0$ in Equation (25), the $\delta E_x/\delta x$ can be plotted for nerves lying along the x axis. An example at a height of 1/4a is shown in Fig. 7. The production of a symmetrical anodic and cathodic pulse is consistent with clinical results from the stimulation of myelinated nerves. This demonstrates the possibility of nerve impulse blocking as a function of coil orientation [58].

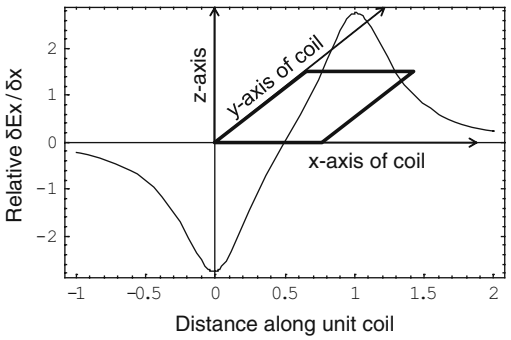

Fig. 7 Planar slice view of the spatially varying electric field magnitude along the fiber. Fiber is assumed to lie along the *x-axis*

Square coils are employed for three reasons. First, the experimenter can align the nerve tissue with the predicted maximum field. Round coils typically have peaks at the top third and bottom third of the coil, which can be challenging to repeatably locate during experimentation. In square core coils, the peaks align with the corners. Second, a square core coil with no winding elements along the z-axis and winding elements parallel to the x and y axis allows an analytical solution to Equations (13) and (23). Third, square coils have been shown in simulation to have approximately 20% larger effect per unit current than properly aligned round coils [57].

The closed form analytical Equation (25) ($\delta E_x/\delta x$) provides a design tool for magnetic stimulation. Given the depth of stimulation (z) and threshold of stimulation ($\delta E_x/\delta x$), requirements for current rise time (di/dt), coil size (a), and number of turns (N) can be directly evaluated. Rapid evaluation of coil and circuit designs and guidance for determining current requirements are possible using this equation.

The stimulus efficiency of different combinations of stimulation depth to coil diameter can be evaluated with the closed form solutions. Setting the x to 0 (the peak $\delta E_x/\delta x$ field), $y = 0$, and making the substitution with the unitless term ζ, which defines the ratio between coil side length and depth of stimulation [59] as

$$a = \frac{z}{\varsigma} \tag{26}$$

Equation (25) reduces to

$$\frac{\partial \vec{E}_x}{\partial x} = -\frac{\mu_0 N\left(\frac{di}{dt}\right)}{4\pi} \cdot \left[1 - \frac{2}{\sqrt{\frac{1}{\varsigma^2}+1}} + \frac{1}{\sqrt{\frac{2}{\varsigma^2}+1}}\right] \tag{27}$$

Similar equations may be derived for double square coils and quad square (or butterfly) coils and show that additional windings at the locus of excitation multiply the effect by either 2 (double square coils) or 4 (quad square coils). In Fig. 8, the results have been plotted. The energy required for magnetic

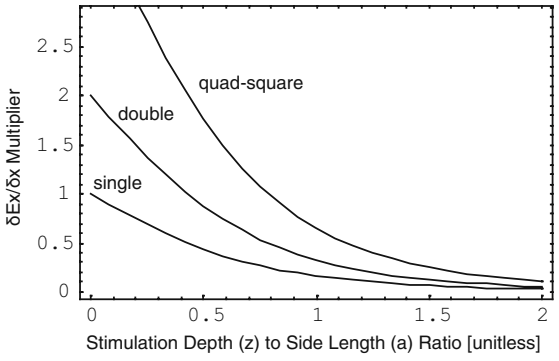

Fig. 8 Efficiency of magnetic stimulation as a function of distance to site of stimulation and coil geometry. The efficiency of magnetic stimulation falls rapidly as the penetration target depth becomes equal to the coil side length

stimulation of nerves increases dramatically as the coil is moved further away from the tissue. The area of effect also increases, leading to less focused area of stimulation. A similar approach is used to analyze quad coil cores with variable intercoil spacing [60].

The value of the load inductance is important for current source design, and in the case of a pulse discharge stimulator system directly affects the stimulus pulse width. An approximation for the inductance of a flat circular coil is [61]

$$L = \mu_0 N^2 r\left[0.48 \ln\left(1 + \pi\frac{r}{h}\right) + 0.52 \cdot r \sinh\left(\frac{r}{h}\right)\right] \tag{28}$$

where h (the height of the coil) is approximated as the thickness of one turn, r is the coil radius, N is the number of turns, and μ_o is permittivity of free space.

Similarly for a flat square coil, inductance is calculated as [61]

$$L = \mu_0 N^2 a\left(\frac{2}{\pi}\right)\left(\ln\left(1 + \pi\frac{a}{2h}\right) + \frac{1}{3.64 + 4\frac{h}{a} + 4.51\left(\frac{h}{a}\right)^2}\right) \tag{29}$$

where h (the height of the coil) is approximated as the thickness of one turn, a is the coil side length, N is the number of turns, and μ_o is permittivity of free space. An alternate calculation method for planar square and round coils is found in [62] and an online calculator is available at http://smirc.stanford.edu/spiralCalc.html.

The peak *B* field is often reported as a figure of merit, and so formulas are included for comparative and design estimation. *B* field formulas allow comparison to clinical experimental systems when B is the reported value. However, a more relevant comparison is the induced electric field or the spatially varying induced electric field.

To calculate the B field of a ring coil at height of z = 0, i.e., the x–y plane of the coil

$$B = \sum_i \frac{\sqrt{2}\mu_o I}{\pi R} \approx \frac{\sqrt{2}\mu_o NI}{\pi R} \tag{30}$$

where R is radius of the ring coil in cm, N is number of windings, and I is current in mA. The magnetic induction B = μH will be calculated in nT. To calculate the B field at a height above the center of the round coil along the z axis

$$B_z(z) = \frac{62.83NI}{R}\left[\frac{1}{\left(1 + \left(\frac{z}{R}\right)^2\right)^{3/2}}\right] \tag{31}$$

where z is the distance from the coil center along the coil axis.

To calculate the B field of a planar square coil at z = 0, i.e., the x–y plane of the coil

$$B = \sum_i \frac{\mu_o I}{a} \approx \frac{\mu_o N I}{a} \tag{32}$$

where a is the coil side length in cm, N is number of windings, and I is current in mA. The magnetic induction B = μH will be calculated in nT. To calculate the B field at a height above the center of the square coil along the z axis

$$B_z(z) = 40NI \frac{\sqrt{a^2 + z^2}}{2 + \left(2\frac{z}{a}\right)^2} \tag{33}$$

Other coil and nerve arrangements have been presented and have been shown to have advantages over parallel nerve–coil arrangements. Bent nerves are exposed to different extracelluar electric field distributions than straight nerves in the same electric field. If the bend is at the peak electric field, a maximum electric field gradient is induced and the source term is more accurately described as a function of E_x than of $\delta E_x/\delta x$ [18]. The peak electric field and locus of excitation for bent nerves occur midway along the coil windings oriented along the x axis. A perpendicular coil–nerve arrangement has a very low threshold for stimulation in vitro for relatively long periods of sinusoidal excitation and is also modeled in a simplified manner in [51]. In a perpendicular orientation, however, a comparative application of an electrically induced $\delta E_e/\delta x$ can be challenging. Other coil shapes such as the cone [63], crown [64], HESED [65], and Slinky [66] coils used primarily to improve the depth of effect in transcranial magnetic stimulation systems present similar challenges to simple first order modeling. With FEA modeling design verification and careful manufacture, there is no reason alternate coil topologies could not be applied to an in vitro magnetic stimulation system.

4 Core

One approach to decreasing the current requirements is to increase the flux in the inductor loop. A core is a very effective way of increasing the magnetic flux. There are several examples in the literature of ferrite and iron cores used for clinical magnetic stimulation [51, 67–71] and in vitro experimentation [51, 70, 72–75]. An alternate method of including a core is in [69] where FEA simulation showed a 50% increase by incorporating a cylindrical plate twice the thickness and 30% larger than the coil diameter. Cores function essentially as flux concentrators, and electric field is related to flux density as described by Faradays law

$$\nabla \times \vec{E} = -\frac{\partial \vec{B}}{\partial t}. \tag{34}$$

The inclusion of a core is analogous to increasing the number of windings and thus the magnetic field capable of generating an electric field for magnetic stimulation

$$B \propto \mu_r \mu_0 nI \tag{35}$$

where μ_r is the relative permeability of the core, n is the turn density, and I is current. A straightforward algebraic method to estimate the equivalent permeability, μ_{eq}, is to employ the reluctance path method (also called the reluctance method, magnetic circuit method, or permeance method). Two excellent resources for further information on this approach are [48, 76]. The reluctance path method employs an analogy for electric circuits where current (A) is analogous to flux (Wb), electromotive force (V) is analogous to magnetomotive force (A-turns), and resistance (Ω) is analogous to reluctance (ℜ). Figure 9a shows the equivalent magnetic circuit.

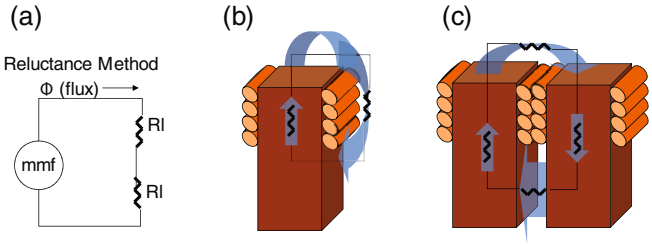

Fig. 9 Reluctance path method for estimating relative permeability. (**a**) is the reluctance path model abstraction (**b**) and (**c**) are examples of square solenoid coils

$$\Re_{ttl} = \frac{l_g}{\mu_0 A_c} + \frac{MPL}{\mu_0 \mu_r A_c} \tag{36}$$

For purposes of estimation, the core becomes a gapped inductor with an equivalent distributed permeability, μ_{eq}, defined by

$$\mu_{eq} = \frac{\mu_r}{1 + \mu_r \dfrac{l_g}{MPL}} \tag{37}$$

where l_g is distance the magnetic flux travels through (gap length), and MPL is the total length of the flux path. Using the estimated equivalent permeability, the closed form analytical coil equations allow quick estimation of the spatially

varying electric field component at any point using a variety of core dimensions and core types. For topologies with large air gaps, an improved estimate of inductance is obtained by approximating the fringing flux [77], according to

$$F = 1 + \frac{l_g}{\sqrt{A_c}} \ln \frac{2 \cdot G}{l_g} \tag{38}$$

where L is the inductance, F is the fringing flux, l_g is the summation of the gap lengths, A_c is the core area, and G is the height of the winding. The load inductance is then estimated as

$$L' = LF \tag{39}$$

A further improved method of estimating the fringing flux for more complex geometries is found in [78].

Using cores in stimulation coils allows the reduction of the coil size while maintaining the necessary flux to induce excitation. Two important details come to light using this approach. First, from Equation (25), field focality improves as z is reduced and the dimensions of the coil are reduced. The resultant scaling allows the interaction of the system with precise structures in the neural tissue under study. Second, the current requirements to generate a $\delta E_x/\delta x$ of the correct magnitude fall significantly with the inclusion of a core. Comparable in vitro magnetic stimulation experiments employ di/dt ramps greater than 10 A/μs. By reducing the size of the coil and moving the site of stimulation closer to the coil, the current ramp requirement can be reduced to on the order of 0.16 A/μs (see appendix). Thus, for in vitro experimentation, an improvement in both field focality and significant reduction in energy required is obtained by moving the tissue under study closer to the stimulating coils.

One caveat to using a core as a flux concentrator is that the core must have an operational frequency above the highest frequency component of the driving waveform to reduce power losses due to the core. For single pulse magnetic stimulation systems, iron, steel, and permalloy cores can be used provided they do not saturate. The frequency range for multiple pulse magnetic stimulation requires operation in the 200 kHz–1 Mhz frequency. Multiple pulse stimulation uses consecutive pulses, as opposed to rTMS, which is a single pulse system at a repetition rate of about 1 Hz. The rapid rise times mandate the use of ferrite cores as the high-frequency operation exceeds most steel core and permalloy core performance specifications. The cores tested in the multiple pulse experiments presented later employ cores from Fair-Rite Products Corporation (www.fair-rite.com) of material 77. Performance up to 3 MHz is possible with alternate materials, such as material 61. Custom machining for many shapes is available from several manufacturers such as Elna Magnetics (www.elnamagnetics.com). I cores, E cores, and square U cores can be used providing they have a square cross section. If the cross section is rectangular, slight modification of the design equations is required. Ferrite cores are essentially a ceramic, and often shatter

or split when cut. Use diamond bit rotary tool bits and saw blades when cutting E or U cores and avoid cutting the wound part of the core.

Further improvements in the resistance loss due to high-frequency effects are possible by using litz wire as opposed to solid core wire or standard stranded wire. Litz wire is a bundle of individually insulated wire woven together to reduce the skin effect and proximity effect losses in conductors. For a closed form design approach to wound components using solid and litz wire, please see [79]. As the current pulse delivered from the magnetic stimulator changes from an undamped and nearly sinusoidal waveform to a damped and less harmonic waveform, core losses become more challenging to estimate. In reality, the processes of energy dissipation in a core under transient non-sinusoidal excitation are considerably more complex. Applying transient currents to ferrite core inductors results in losses from magnetic diffusion time and generation of eddy currents [80-83]. These effects may be severe and challenging to estimate. Since these small core coils are relatively easy to fabricate and few are needed, it is reasonable to estimate their performance, build, test, and tune the inductors.

An impedance analyzer can be an invaluable tool to characterize the fabricated inductors. Since the tissue properties naturally vary so widely from preparation to preparation, the components of a magnetic stimulation systems must perform over a wide range. As long as the stimulation core is properly characterized, analytical evaluation of the data collected is possible. We used a Hewlett Packard 4192A impedance analyzer with a custom interface written in Lab View (code available upon request from the authors) to verify the self-resonant frequency of the coil was above the operating frequency of the circuit, see Fig. 10. The Agilent 4194A and the new 4294A include a built-in equivalent circuit calculator. The impedance analyzers are also helpful for characterizing the pulse discharge capacitors equivalent series inductances and resistances.

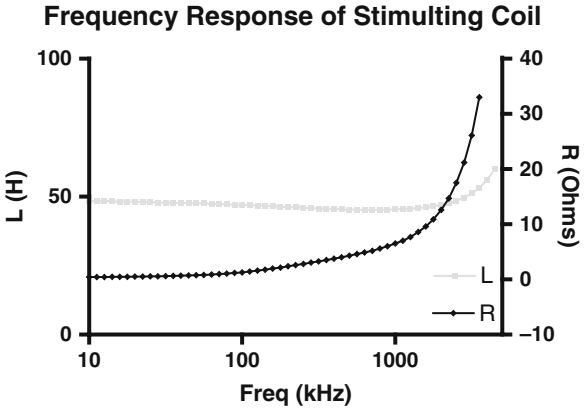

Fig. 10 Measurement results of small signal coil impedance. Coil resistance is negligible below 200 Hz, but becomes significant at 2 Mhz

In circuit operation was confirmed by analyzing the Vin/Iout waveform phase shift and shown to have a roll-off frequency above 1 MHz. In this manner, the low current and pulsed high-current performance of the cores may be verified. These two techniques were used because the 4192A cannot source high currents and because instrumentation for low frequency, high-current inductance measurement is not typically available and would likely overheat the coil as these coils are designed for a pulsed circuit topology, not continuous operation.

5 Systems for Magnetic Stimulation

One option for performing magnetic stimulation experiments in the laboratory is to purchase a commercially available system. Commercially available systems can deliver currents and voltages capable of stimulating neuronal tissue centimeters away from the coil, but are expensive because of the necessary interlocks and the inclusion of high-power components. Commercially available systems also are challenging to modify when working with smaller scale systems. Due to their intended use, they may be less configurable for a wide range of pulse shapes and pulse protocols.

Constructing a smaller scale system allows the inexpensive evaluation of new coil excitation circuit topologies. The critical component of a magnetic stimulation system is the power switch used to control current through the load coil. New power devices and pulse capacitors are continually under development [84–86] and supply the need for such devices in industrial applications. Switching strategies and circuit topologies can be tested in a smaller scale system before full power devices become commercially available. For readers interested in the details of full-scale magnetic stimulation system construction, descriptions are available in [64, 87]. Both of these sources present relatively detailed circuit schematics and application notes. Overviews of magnetic stimulation system design are presented in [68, 88].

In the following sections two complete, documented, magnetic stimulation systems suitable for laboratory scale experiments and in vitro magnetic stimulation experiments are presented. The described systems are very dangerous, even though they are reduced in scale. Discharges may reach 100 J. Proper expertise with power electronics and safety protocols are compulsory. The most significant technical standard is IEC-601 *Medical Electrical Equipment* and there is an excellent approach to safety in laboratory practice in [87, 89]. Minimally, systems must have appropriate lockouts and the power components must be enclosed. Catastrophic failure of pulse discharge capacitors and the load coil is of particular concern.

6 Pulsed System

Maintaining a current ramp for the length of time required to stimulate neural tissue can confound the design of a current amplifier output stage. Depending on the τ_m and λ_m of the tissue under study, stimulation times range from hundreds of microseconds to a few milliseconds. The common strategy is to use thyristor triggered pulse discharge circuit, as in Fig. 11. The tuned LCR pulse discharge circuit is used to produce a waveform with a damped sinusoidal pulse. The pulse shape is a function of the stimulating coil, the capacitor bank, and the parasitic resistance of the system according to Equation (40).

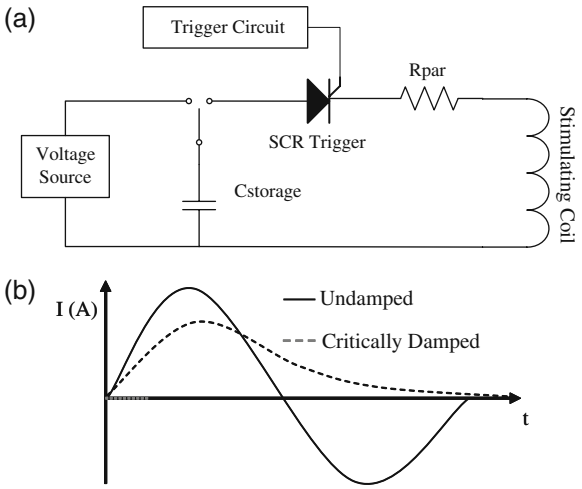

Fig. 11 Typical circuit implementation of a magnetic stimulation circuit. Circuit. (**a**) A SCR triggered pulse discharge circuit implementation of a time varying current source as in Fig. 1. (**b**) Resulting current waveform output (**b**). The system produces different current waveforms and thus different electric fields with varying shape, pulse width and magnitude as a function of the parasitic resistance Rpar in the system, the storage capacitance Cstorage and the inductance of the stimulating coil

$$I(t) = \frac{V}{\beta L} e^{-\alpha t} \sin \beta t \tag{40}$$

where

$$\beta = \sqrt{\frac{1}{LC} - \frac{R^2}{4L^2}} \text{ and } \alpha = \frac{R}{2L} \tag{41}$$

Shorter pulses have been shown to be more energy efficient in pulse discharge circuits [59], while the most energy efficient time point to electrically stimulate

neural tissue is at the chronaxy of the nerve [90]. Due to losses in the stimulation coil and restrictions on the circuit design window, pulse discharge circuits often operate on much shorter timescales than the chronaxy of the nerve under study.

Undamped systems are called rapid rate stimulators, and up to 40% of the stimulation energy may be returned to the capacitor bank. While damped systems induce a pair of rectangular electric field pulses, an undamped system produces a set of triphasic pulses [91]. Although the exact mechanism is not known, there is some evidence that stimulus thresholds are lower than the equivalent damped system [88]. This is a conundrum because biphasic electrical stimulation is generally less efficacious than monophasic stimulation.

Recently, a well-documented pulsed discharge system using a novel application of a power device was presented in [64]. The pulsed system we employ in our lab is a modification of this full-scale experimental TMS system. Hopefully, a detailed example will provide insight for users constructing their own systems. A complete system diagram is shown in Fig.12.

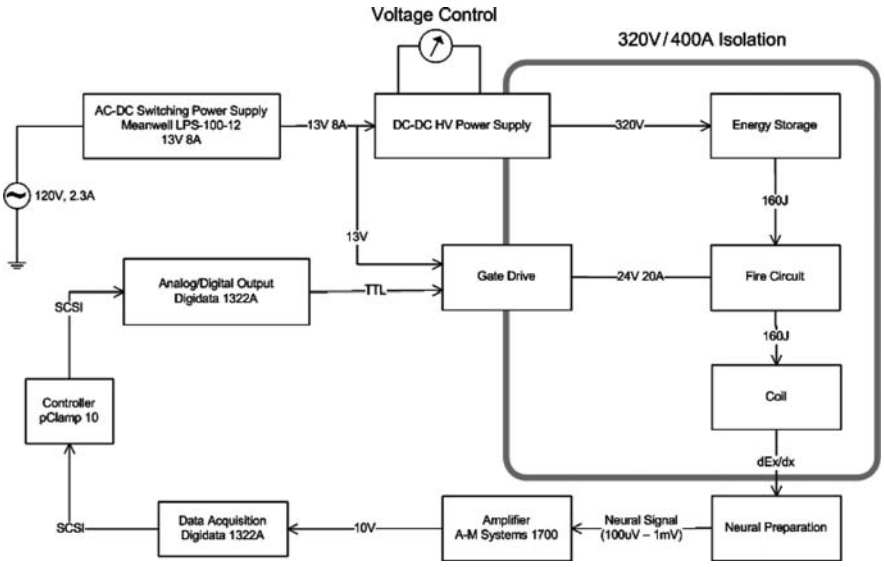

Fig. 12 Block diagram of a pulsed discharge magnetic stimulation and recording system. The grey border shows the electrical isolation area, however, extreme caution must be exercised when using these systems as lethal high voltages are present

A standard switching AC to DC converter (Mean Well LPS-100-12) with isolated outputs provides power to a custom built high-voltage DC power supply. There are several options to provide an adjustable high voltage for capacitor charging, such as a rectified output variac, but flyback transformers [92] have significant advantages for small-scale systems. In contrast to line transformers, flyback transformers utilize relatively small, high-frequency cores so 60 Hz noise

near the recording apparatus is mitigated. The LT3750 (Linear Technology, Milpitas, CA) capacitor charger controller is a discontinuous mode flyback transformer intended to charge flash capacitors for consumer applications.

The photoflash capacitors we used leaked significantly until they were held at voltage for several hours. Reforming capacitors is less of a problem than in the past but pulse discharge capacitors can be exposed harsh operating conditions. An auto refresh circuit or regulated charger can also be useful for conditioning capacitors. Linear Technology offers several flyback-based regulated capacitor chargers that employ secondary side sensing, but these do not isolate the primary and secondary parts of the circuit. By adding refresh circuitry, the primary and secondary side can be completely isolated. Auto refresh provides primary–secondary isolation but differs significantly from secondary side sensing in that a runaway condition may occur where charging occurs after the target voltage is reached. To avoid a runaway condition, the capacitor bank leakage should be characterized and the component values for R_t and C_t should be set such that

$$R_t C_t > \frac{2 I_{PK} L_{\mathrm{Pr}\,imary}}{I_{Lk} V_{input}} \tag{42}$$

where I_{PK} is the leakage current, $L_{Primary}$ is the transformer primary inductance, I_{LK} is the capacitor bank leakage current, V_{input} is the primary side voltage supply, R_t is the resistance, and C_t is the capacitance shown in Fig. 13. The adjustable flyback-based high-voltage DC power supply can deliver a peak current of 7 A. Voltage is controllable from 20 to 320 V. Several LT3750 devices can be paralleled to provide faster charge rates for higher current charge rates and/or larger capacitances.

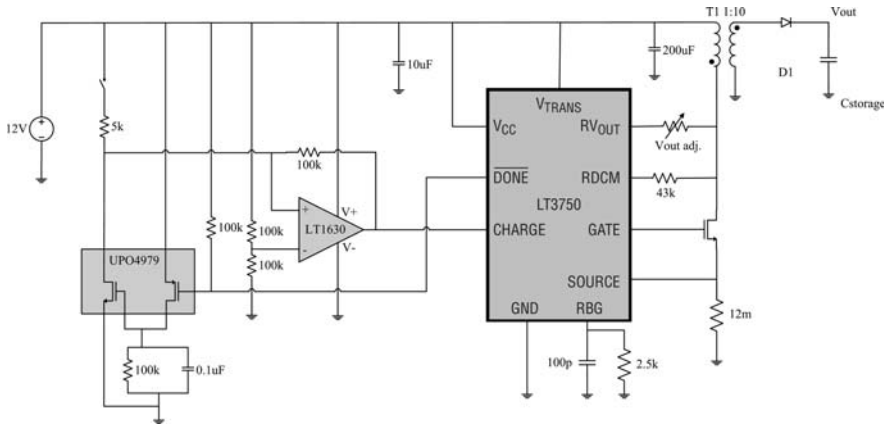

Fig. 13 High voltage power DC power supply. Output voltage is controlled by a refresh circuit. A refresh circuit has an isolation advantage, but runaway conditions can occur. Alternatively a circuit based on the LT3751 can be used to charge the capacitor bank. Flyback power supplies are well suited to laboratory scale magnetic stimulation systems because they provide isolation and be employed in parallel to provide increased current

Commonly available photoflash capacitors are adequate for energy storage in small-scale magnetic stimulation systems. These typically have an upper voltage limit of 320 V and are designed for high-current discharge, usually by the designation "photo" on the component markings and specified by the manufacturer for pulse discharge or photoflash applications. It is incredibly important not to exceed the voltage or polarity of photoflash capacitors. Doing either may result in catastrophic failure. Capacitor manufacturers recommended by Linear Technology for the LT3750 include Rubycon, Cornell-Dublier, and NWL. For higher voltage requirements, capacitors can be placed in series or specialized pulse discharge capacitors may be obtained from General Atomics Energy Products, San Diego, CA (www.gaep.com).

Mechanical switches are used to toggle banks of capacitors with values of 100, 200, 400, 800, and 1600 uF. This arrangement allows for variable capacitor storage from 100 to 3100 uF. Each capacitor bank includes a discharge circuit to be used before mechanical switching or to safely discharge the storage bank. Mechanical switches are less appropriate for full-scale systems. Full-scale systems that employ banks of capacitors switched by power devices have been presented [93, 94], but these systems can be bulky, complex, and expensive.

A silicon-controlled rectifier cannot stop current flowing once it has been triggered. Only one stimulation pulse width is available for a particular capacitance and load inductance. The controllable pulse-width (cTMS) system employs an insulated gate bipolar transistor (IGBT) to truncate the pulse. Truncating the pulse allows the testing of several time points along a fictive strength–duration curve without a large hardware overhead, which can interrupt experiments. Since the di/dt slope, and ultimately the E_x and $\delta E_x/\delta x$, is set by the voltage stored on the capacitor bank and the load inductance, longer pulse widths can be obtained with a larger capacitance. It is critical to completely discharge the capacitor bank before switching or destructive welding may occur. For both SCRs and IGBTs, it is important not to exceed the maximum pulse voltage, maximum pulse current, or the di/dt and dv/dt ratings. While IGBTs can tolerate some current pulses exceeding their operational specs, the maximum collector emitter voltage must never be exceeded. For a comfortable margin of error for flyback conditions, use devices with a greater than required V_{ce} rating.

In any high-voltage circuit driving a nearly pure inductive load transient suppression is important. The discrete devices used to shunt inductive spikes, i.e., snubber components, can be mounted directly to the terminals of the IGBT to reduce stray impedance. A diode snubber is available as an integrated component from Cornell–Dublier in the SCM line. WIMA and EPCOS both supply snubber capacitors that mount directly to IGBT modules as well. Use of these devices further reduce terminal impedances. For pulse discharge systems, snubbers and flyback protection are critical. For information on the practical applications of subber circuits, see [95–97].

IGBTs are best operated using gate driver circuits [98]. Gate driver circuits provide sharp transition pulses of the required current to drive the large capacitive gate in an IGBT. IGBT driver circuits can be constructed according to the application notes available on the PowerEx website www.pwrx.com. For lower

voltages (<1400 V) and lower current (<1200 A), PowerEx has made several development kits available, such as the BG2A. A driver board for the CM600 series is also available from Eastern Voltage Research Corporation (http://www.easternvoltageresearch.com). Voltages exceed 2500 V in the full-scale cTMS system and a high-voltage optically isolated IGBT driver (AP-1318) is available from Applied Power Systems (Hicksville, NY). All of these IGBT driver systems optically isolate the gate from the input signal. Isolation is important for safety reasons and to protect the computer-controlled TTL outputs. In the scaled system, the high-power components are optically or mechanically isolated from the data acquisition and control unit. Trigger timing is controlled and recorded simultaneously with the output response by a software/hardware data acquisition system. Further information on data acquisition and control for is covered later in the chapter.

As interest in magnetic stimulation rises and new power devices become available, look to sources which cover high-energy pulsed magnetic discharge and circuit design, such as [99, 100]. An alternate approach is presented in [101]. Essentially, the ramp decay rate is controlled by an H-bridge. The transistors in the high-power H-bridge are switched on and off to create a stepped ramp decay.

6.1 Scaling

Scaling issues are of particular concern in a pulsed discharge magnetic stimulation system. For a critically damped RLC circuit, $(V_o/L)_{max} = (di/dt)_{max}$ and as a result

$$\frac{\partial E_x}{\partial x}_{\max} \propto \frac{V_o}{L} \tag{43}$$

So the scaling limits for magnetic stimulation depend on inductance and $\delta E_x/\delta x$. Inductance scales by u_r, N^2, $A_c{}^2$, while $\delta E_x/\delta x$ scales by di/dt, u_r, N, z. As shown in Fig. 8, A_c directly impacts the optimal z, i.e., the ratio of coil diameter to stimulation depth. Setting V_o to a maximum fixed value, as radius increases for a fixed number of turns, L increases and di/dt and thus $\delta E_x/\delta x$ falls. Scaling is covered in depth in the appendix and [102]. $\delta E_x/\delta x$ and pulse width are both functions of C, V_o, and L and $R_{parasitic}$. A simple spreadsheet can be a valuable way to explore the design space. Analysis should include effects of coil heating. The upper limit to the peak current discharge is often the cross sectional area of the fine wire used in construction of the load coil. Temperature change in a wire is measured by

$$\Delta T = \rho \left(\frac{I}{A}\right)^2 \frac{PW}{1x10^6} \cdot \frac{c}{\rho_{den}} \tag{44}$$

where ΔT is the temperature change in Kelvin, c is the specific heat (0.385 J/gm K), ρ_{den} is the wire density (copper is 8.96 g/^{3}), I is the current in Amps, PW is the pulse time duration, and A is area in meters. Coil heating and destructive failures are a function of the time the current flows in a wire according to (pp. 4–74 to 4–79 [103]).

$$I_{\max} = \frac{A\sqrt{\log\left(\frac{1 + T_m - T_a}{234 - \rho_{den}}\right)}}{33\left(\frac{PW}{100000}\right)} \tag{45}$$

where I_{max} is current in Amperes, T_m is the melting point in Celsius (1083°C for copper), and T_a is the ambient temperature in Celsius.

7 Current Source System

7.1 Overview

Stimulating at the chronaxy of the nerve is the most energy efficient method of stimulation [64, 104]. However, by stimulating near the rheobase of the axon, significant simplification of the electronics is possible. According to Equation (25), the di/dt scales linearly with the $\delta E_x/\delta x$ for a fixed coil topology. Reducing the di/dt by half has the effect of reducing the current peak by half. Since $V = L \cdot di/dt$ is the peak voltage required to obtain that current ramp (ignoring the resistive losses in the circuit for simplification), then this in turn reduces the system voltage requirements by half as well. Power device switching speed varies greatly with the required peak voltage and current rating, which makes a wider array of higher speed semiconductor devices available for different pulsing strategies.

One approach to create longer pulses is to use a sawtooth to generate several concurrent current ramps as in Fig. 14. The asymmetric sawtooth (long rise time, short fall time) also allows a significant reduction in the power dissipated in the inductor as $P = I^2R$, provided the waveform has no DC component. Reducing current and extending the stimulation time should result in significant energy savings, since power is consumed to the square of the current. The

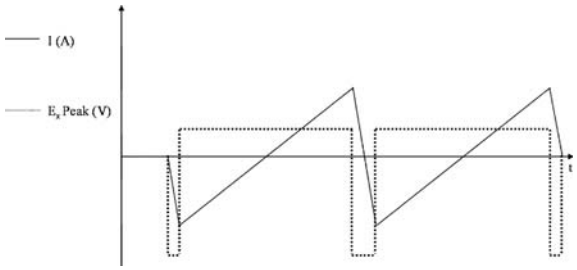

Fig. 14 Sawtooth current waveform and the resultant asymmetric biphasic electric fields produced by coil excitation. The dotted line is the induced E field, the solid line is the current waveform through the inductor

current supplied to the load is a function of the inductance of the coil when using pulse discharge circuits. In contrast, the current supplied to the load with an asymmetric current source is independent of the load. Decoupling the load from the system performance provides the opportunity to test different inductances without having to redesign the stimulus system or make it overly complex to support a wide experimental range.

Using the sawtooth current driver approach also decouples the induced waveform from the coil electrical properties [38] allowing easier investigation of wave shape variation effects on neural responses. Significant effects of waveform shape have been shown in electrical stimulation modeling [104], confirmed in our lab experimentally and shown clinically for magnetic stimulation in peripheral nerves [105]. Control over waveform shape also enables the evaluation of pulse shape-mediated nerve recruitment [106, 107]. Current driver topologies can deliver much more linear di/dt ramps than a pulse discharge system. The more linear the current ramp is, the more uniform the electric field throughout the course of the pulse, since the induced electric field is a function of di/dt. In clinical functional magnetic stimulation experiments, a constant current ramp has been shown to have lower stimulation thresholds than the commonly used damped sinusoidal waveform [108].

The effects of the polarity of the $\delta E_x/\delta x$ waveform may be observed by changing the polarity of the input waveform. A series of pulses also creates an opportunity to test magnetic stimulation effects at longer durations than in the typical pulse discharge circuit. The ability to test the effects of waveform shape on stimulation threshold is a necessary component of a quantitative magnetic stimulation system.

7.2 Circuit Design

An analysis of scaling (see Appendix) shows that the current required for small-scale magnetic stimulation (about $\sim$0.16 A/μs) is well within the range of a power amplifier topology. It is critical that the transition edge of a sawtooth waveform be as short as possible to prevent hyperpolarizing effects on the neural membrane, or worse, inactivating the Na^+ ion channels, thereby increasing the energy requirements for stimulation. A grounded load V–I converter, such as an improved Howland VCCS (Fig. 15) [109], is typically used in this application. For a typical Howland current source, the output impedance falls as the signal frequency increases. According to Equation (46), the output impedance appears capacitive as the effects of finite open loop gain come into play [110]

$$C_{eq} = \frac{R_1 + R_2}{2\pi f_o R_3 R_4} \tag{46}$$

where f_o is the gain bandwidth product of the amplifier, and R1, R2, R3, and R4 are resistances as in Fig. 15. When driven with a sharp transition pulse past

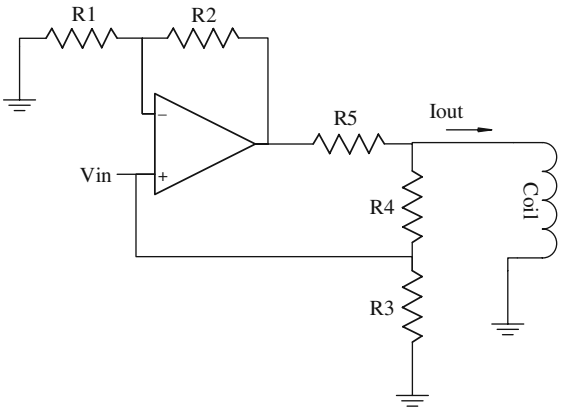

Fig. 15 Improved howland current source (inverting). R3 functions as the sense resistor. The coil is not part of the feedback loop

the unity gain bandwidth frequency, the lowered output impedance of the amplifier and the nearly pure inductance of a magnetic stimulator coil form an LC tank. The driver circuit becomes unstable as evidenced by high-frequency oscillations at the output (see Fig. 16). The drop in amplifier output impedance is often further degraded by the desire of the designer to employ low-value resistances in the feedback path to improve frequency response. Small feedback resistance values reduce the output impedance and degrade accuracy due to component tolerance variation.

The more appropriate approach is to include the reactive load inside the feedback loop. The floating load current source topology, Fig. 17, is particularly

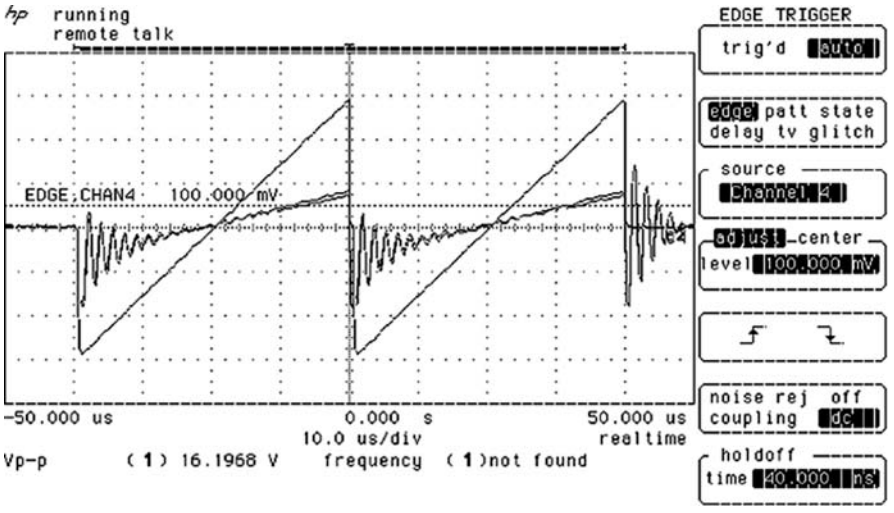

Fig. 16 Ringing at output of inductively loaded current source. Typical results obtained by loading a current source with a nearly pure inductive load and a sawtooth input waveform. The effective output capacitance can be estimated by measuring the frequency of the ringing waveform when the inductor is excited with a step input

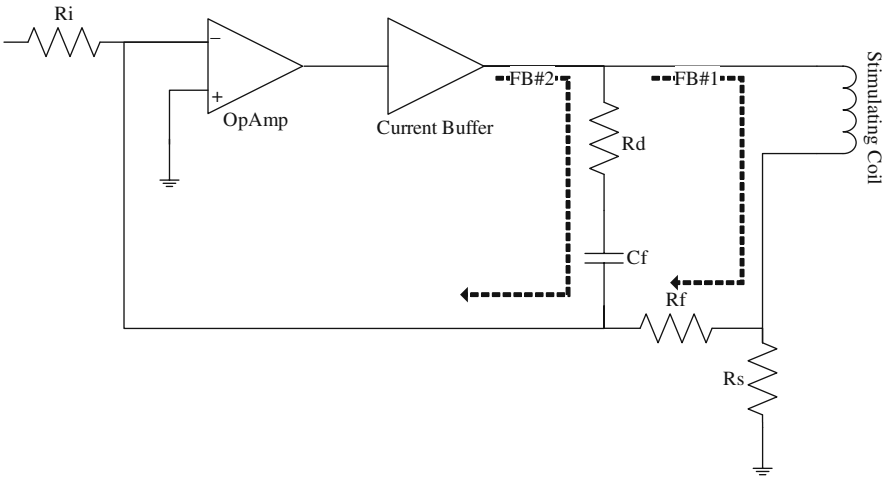

Fig. 17 Floating load current source topology. The operational amplifier and the current buffer function as a composite amplifier. By including the load coil in a feedback loop current waveforms can be supplied to the load while maintaining stability. A second feedback path provides additional high frequency stability and improved step transition response

appropriate for magnetic stimulation as the coil is always isolated from the preparation (and the patient in clinical applications). Both terminals of the inductor are available and it may be placed into the feedback loop and compensated. The floating load current source is insensitive to component tolerance mismatch that plagues the improved Howland current source. In Fig. 17, Rs functions as a sense resistor, thus the current across the load is defined as

$$I_{load} = -\frac{V_{in}}{R_s}\frac{R_f}{R_{in}} \tag{47}$$

7.3 Rate of Closure Stability Analysis

The method used to analyze this circuit uses rate of closure feedback loop analysis [111]. The open loop gain of the amplifier is plotted. The feedback factor, $ß = V_{fb}/V_{out}$, of each independent feedback path is calculated and then the inverse ($1/ß$) is plotted. The closed loop gain follows the lowest feedback path, as in Fig. 18. The difference between the closed loop gain and the open loop gain is the circuit's loop gain and graphically equivalent to the area between the feedback plot and the open loop gain. For the case of the floating load current source, the DC loop response is calculated when the inductor is shorted as

$$V_{fb} = V_{out}\frac{Ri}{Rf + Ri}\cdot\frac{Rs(Rf + Ri)}{RlRs + Rf(Rl + Rs) + Ri(Rl + Rs)} \tag{48}$$

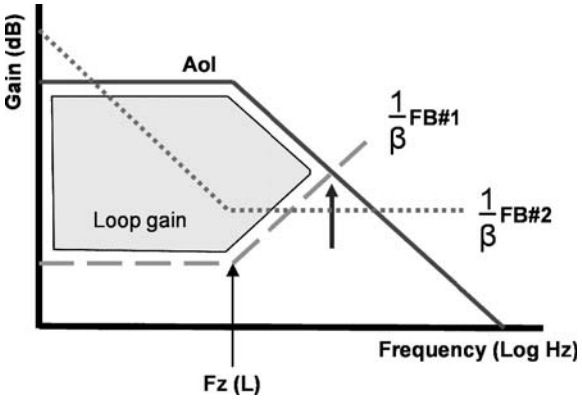

Fig. 18 Beta feedback Analysis for multiple feedback paths. The dashed line is the feedback path formed by the inductor, Rf and Rs. Fz (L) denotes the zero created by including the active load in the feedback loop. The dotted line is the feedback path through the Rd and Cf high frequency shunt. The solid line represents the open loop gain of the amplifier and the buffer stage. The arrow denotes a loop closure rate of 40 dB when the second feedback path is not present indicating an instability condition. By including a second feedback path with a zero the closed loop response (i.e. following the lowest line across the bode plot) splits the 40 dB loop closure rate into 2, 20 dB loop closures

The first feedback loop (FB#1 in Fig. 18) is through the inductor and the zero in the feedback path is defined by the inductance and parasitic resistance of the load as

$$f_z(L) = \frac{Rs - Rl}{2\pi f L_{load}} \tag{49}$$

If a second feedback path is not in place, the feedback loop and the amplifier's open loop gain plot intersect with a closure rate of 40 dB. A rate of closure of 40 dB corresponds to a phase shift of 180° and oscillatory behavior. To compensate, a second feedback path with a feedback path zero (capacitor) is added to the circuit (FB#2 in Fig. 18). The value of the capacitor is set below the feedback path of the load feedback path and the resistance is set to provide a rate of loop closure of 20 dB and also at least 20 dB greater than the DC gain [110, 112]. The second feedback loop zero is defined by the feedback capacitor and the feedback resistance as

$$f_z(C) = \frac{1}{2\pi R_d C_f} \tag{50}$$

Rate of closure is a powerful technique, but for a complete analysis it is important to check the open loop phase shift throughout the gain bandwidth. This may be estimated using hand plots or spreadsheets [113], but the use of Tian's method [114] for feedback loop analysis is more accurate and handily implemented in SPICE.

SwitcherCAD from Linear Technology bears mention [115]. SwitcherCAD is a free SPICE program available from Linear Technology. It is well supported by an active internet community (LT SPICE at yahoo groups), which includes a wide variety of uploaded test jigs and component SPICE models. For example, Tian's and Middlebrook's methods for feedback loop analysis are implemented directly in examples. It uses a compact description for component parasitic modeling that greatly improves both accuracy and speed, and improves convergence for simulation of pulsed systems.

7.4 Output Stage Design Details

There are a few implementation caveats to the floating load current source topology approach. Inductance of the sense resistor must be minimized to prevent peaking and oscillation. The value of R_s impacts the loop gain and larger values improve both the power bandwidth and the settling time according to Equation (49). In this topology, the entire current flows through the current sense resistor and larger values will increase the voltage drive requirement. Unfortunately, monolithic operational amplifiers that have the necessary gain bandwidth and drive current in the ampere range are not available. To meet this need, we built a composite amplifier using a commercially available current feedback amplifier (LT1468) and implemented a discrete power output stage. Current feedback amplifiers are ideal for this application as they provide moderate gains and a high unity gain bandwidth frequency with excellent drive capabilities.

The power output stage bipolar junction transistor (BJT) power devices were selected because of their low output resistance, reduced drive requirements, and immunity to inductive kickback spikes, which can destroy field effect metal oxide semiconductor transistors. However, it is generally difficult to find radio frequency (RF) power PNP devices. The lack of high-speed PNP devices can be resolved by using composite devices [116]. Careful design is important because composite devices may develop local oscillations and have bandwidth limitations.

Composite devices (Darlington or composite PNP) are required because the gain of power RF BJT devices is generally low. RF devices are used because the current booster stage must be significantly faster than the driving operational amplifier. Figure 18 shows the speed requirement of the current booster stage. If the current booster stage has a 3 db roll off below the unity gain bandwidth of the amplifier, it will introduce an additional pole and invite oscillation. If the current feedback stage cannot respond to the output control signal from the amplifier, then the output will oscillate while the current booster continually tries to catch up to the feedback signal measured at the sense resistor. To prevent the addition of poles in the feedback loop, the midband gain of the power stage must extend past the unity gain frequency of the amplifier [117, 118].

Placing a reactive load inside the feedback loop requires particular attention when switching currents. Switched currents result in sharp flyback

pulses from the inductive load. Flyback voltage pulses can damage components and create intermittent failures. The most effective way to dissipate flyback voltage pulses is to include discrete ultrafast recovery flyback diodes (Fig. 19, clamping diodes shown on the right). With proper selection of components the parasitic capacitance added to the output is negligible. Additional protection from flyback pulses is achieved by using unidirectional zener diodes on the power supply rails [119].

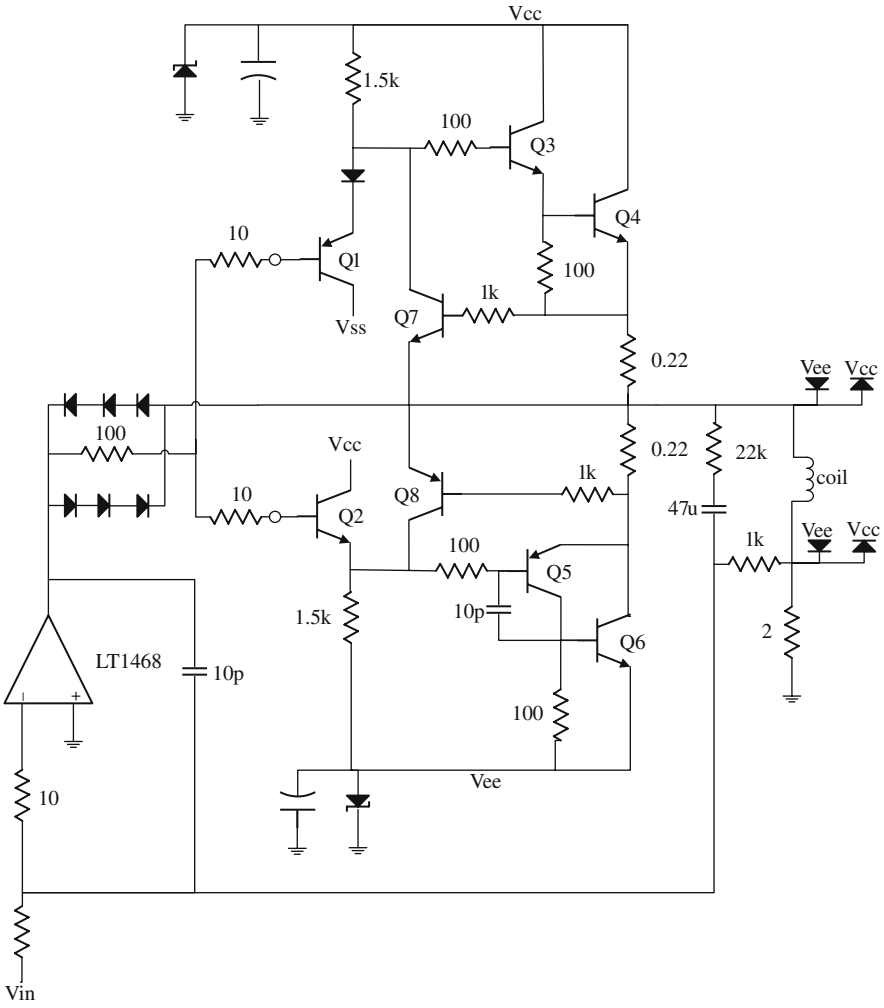

Fig. 19 Reactive load driver circuit. Example of a complete linear current source circuit with the reactive load inside the feedback loop. Circuit is capable of delivering 4App. Transistors are Advanced Semiconductor Q1,Q8 = 2N2907 Q2,Q7 = 2N2222 Q3 = 2N3866 Q5 = 2N5160 Q4, Q6 = 2N3632, input diodes are 1N4148, clamping diodes are BAV99, zener deiodes are 1.5KE16A, electrolytic caps are low ESR, 2200uF. Vcc and Vee are +16V and −16 V respectively

7.4.1 Scaling

The advantage to using a controlled current source rather than a pulse discharge circuit is that the waveform delivered is nearly independent of the load coil. Different coil topologies may be directly compared, and waveforms reversed in polarity and changed in shape and duration during experimentation.

7.5 Circuit Testing

In the following, we present several methods of testing and evaluation of the sawtooth current generator. Hopefully, examples of testing will help users characterize and debug their systems quickly.

7.5.1 Verification of the Current Waveforms

The entire system was tested with a range of inductances from 5 to 100 μH, with and without cores, to verify whether system was stable. The test inductors ranged from low parasitic resistances of 10s of milliohms to 1 Ohm. Figures 20, 21, and 22 show typical simulation and measurement results from a 20 μH coil. It is important to use precise probing techniques as the inductance of the probe placed on the output terminal to the coil can influence the measured waveform for this circuit topology.

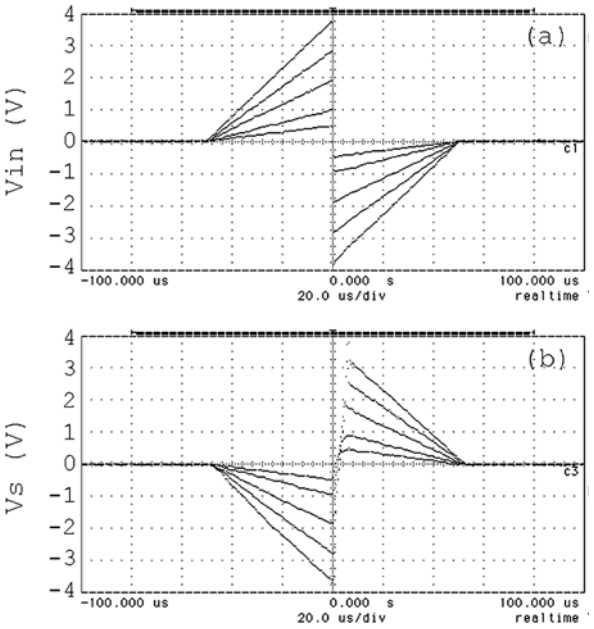

Fig. 20 Increasing current waveform response of reactive load driver circuit. Measured responses of ramp pulse swept in increasing input voltage for the reactive load driver circuit. (**a**) input voltage waveforms (**b**) measured voltage across the 2 ohm sense resistor, similar to line C2 in Fig. 21

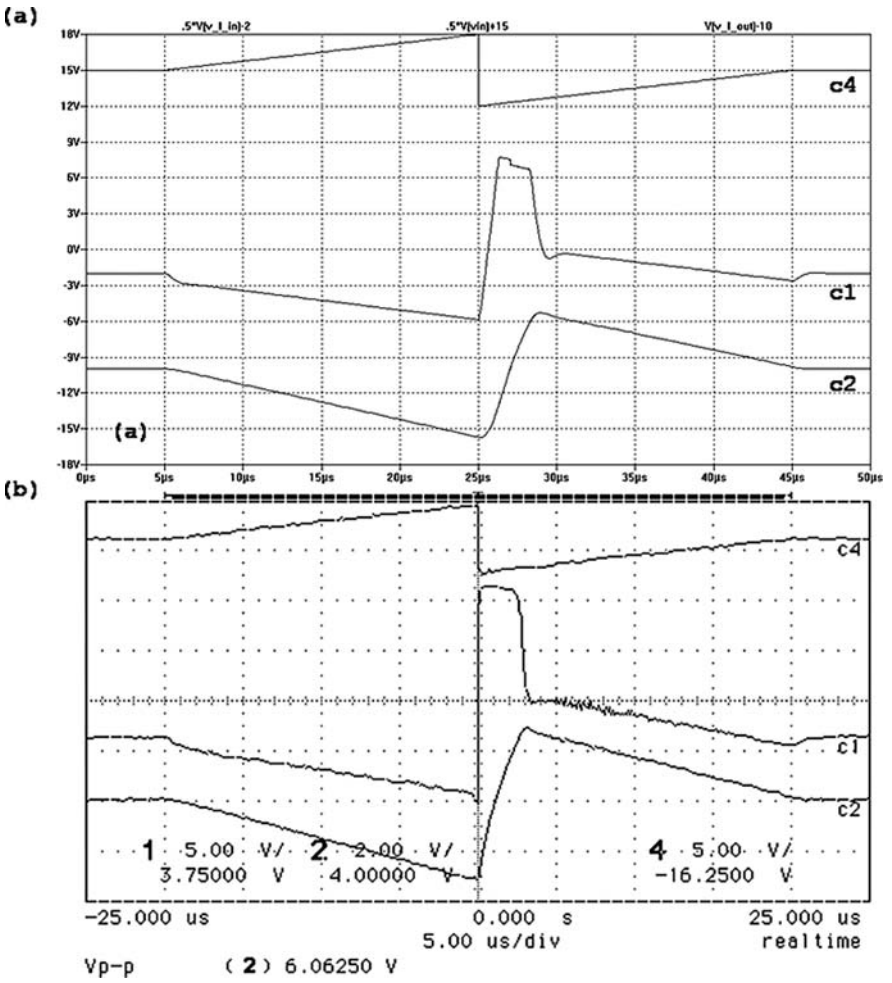

Fig. 21 Simulated and measured responses of a single ramp pulse for the reactive load driver circuit. (**a**) Waveforms from LT Spice simulation (**b**) measured response. C4 is the input waveform, C1 is the voltage at the load, C2 is the voltage across the sense resistor

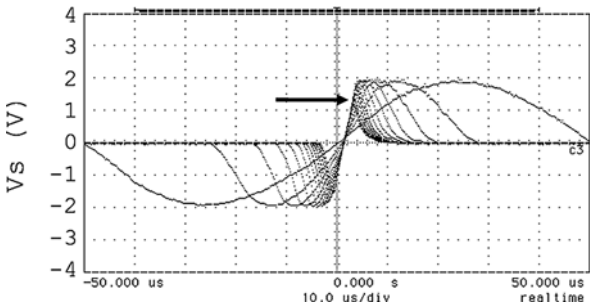

Fig. 22 Frequency performance of reactive load driver circuit. Sine wave sweep of increasing frequency at half power measured at the sense resistor. The 3 db roll off was measured at 129 kHz, indicated by bold arrow

7.5.2 Verification of the Electric Field

To verify that the electric field was generated by the time-varying current pulse as predicted, a pickup coil was placed over the coil as the circuit generated single current sawtooth waveforms. The signal from the pickup coil was amplified using an INA111 instrumentation opamp (Texas Instruments, TX) with a gain of 10X. The TI INA111 has a very high-frequency response and an adjustable gain. Users should carefully consider the peak amplitude of the induced potential and include an input protection network for testing their coils if necessary. The electric field produced from a triangular current ramp should be a square wave as shown in Fig. 23. While [120-122] discuss probe construction for measuring electric fields above and inside solenoid inductors, probe construction, accurate measurements, and proper alignment on the submillimeter scale proved unreasonable.

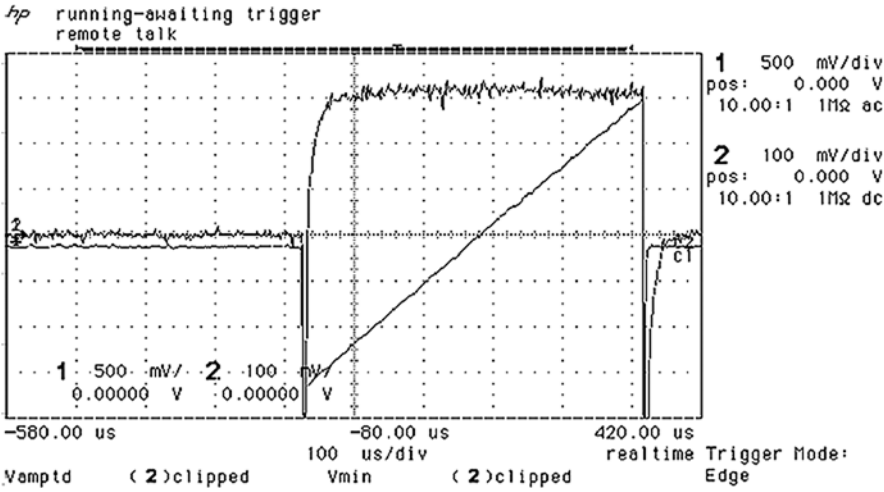

Fig. 23 Measurement of electric filed generated in situ. Ramp output waveform and measured response from pickup coil area shown

8 Neural Preparations

Required excitation threshold is determined from the physiological parameters of the neural model under study. As previously discussed, the spatial rate of change of the electric field along the length of the axon ($\partial E_x/\partial x$) has been shown to predict extracellular neural electrical stimulation (see review in [30]). Clearly, the spatial rate of change of the electric field along the length of the axon is one experimental variable. However, the space and length constants of the tissue under study are also

experimental variables. Little study has been completed to investigate the effect of waveform shape and pulse-width variation on preparations with varying time and length constants. Both the length and the time constants are functions of passive membrane properties r_m, r_i, c_m (Equation 51), which depend on membrane surface area as well as its intrinsic resistive and capacitive characteristics such as density of ion channels and membrane thickness and determine both the variation of excitability of the cell and the propagation speed of the action potential.

$$\lambda_m = \sqrt{\frac{r_m}{r_i}} \text{ and } \tau_m = c_m r_m \tag{51}$$

In Equation (52) C_m, R_m, R_i are the size-independent-specific membrane properties in $(F \cdot cm^{-2})$, $(k\Omega \cdot cm^2)$, and $(\Omega \cdot cm^{-2})$, respectively; a (cm) is the fiber radius:

$$c_m = C_m 2\pi a \quad [F/cm] \qquad r_m = \frac{R_m}{2\pi a} \quad [k\Omega \cdot cm] \qquad r_i = R_i/\pi a^2 \quad [\Omega/cm] \tag{52}$$

In the absence of myelination, diameter variations control the efficacy of neural signaling by determining the length constant, which is proportional to the square root of the radius of the process [123]. Larger processes have both lower thresholds for extracellular stimulation and faster propagation velocities, resulting in longer length constants. In the ideal case where the cell can be modeled by a lumped $r_m c_m$ model, the time constant τ_m is independent of axon diameter, since c_m and r_m are reciprocally dependent on the size of the cell. In this idealized case, τ_m is a measure of the excitability of the cell that depends on its intrinsic properties rather than size. Thus, both different cell types (motor neuron versus sensory neuron) and different areas of the cell (axon hillock versus soma) may have different time constants, and thus different excitabilities, with shorter time constants corresponding to faster signaling.

Experimentally, λ_m and τ_m can be elucidated from published or directly measured passive membrane properties as well as the strength–duration curve. Membrane capacitance depends on the intrinsic properties of the phospholipid bilayer, with the specific capacitance per unit area of all biological membranes, C_m, equaling approximately 1 $\mu F/cm^2$. A useful tool for measuring membrane properties in the lab is Neurofit [124], a MATLAB-based software package that allows the extraction of active as well as passive properties of the membrane from voltage-clamp experiments.

Experimental derivation of a strength–duration curve using a point source electrode is the first step to magnetic stimulation experiments, because it allows the extraction of a series of stimulus magnitudes and durations that are sufficient to stimulate tissue at a specific distance between fiber and current source. Additionally, qualitative analysis of the curve shape can tell important things about passive properties of the neural preparation. At rheobase, the membrane

is essentially voltage-clamped at just below threshold voltage, and the stimulus current is equal to ionic current. According to Equation (53), I_{rh} is dependent on and will increase with the size of the cell:

$$V_{th} = \lim_{t \to \infty} \left[I_{th} r_m (1 - e^{-t/\tau_m}) \right] = I_{rh} r_m \tag{53}$$

Thus, rheobases of cells with a larger diameter will be shifted up on the strength–duration curve.

The chronaxy, or the minimum pulse duration needed to reach V_{th} when pulse strength is twice the rheobase, estimates a pulse length with a reasonably low stimulus. With some limitation chronaxy provides a relationship between an experimentally derived strength–duration curve and the time constant:

$$t_{chronaxy} = \tau_m \ln 2 \tag{53a}$$

Thus, while rheobase is dependent on the surface area of the cell, the chronaxy depends on the specific membrane resistance, and thus on density of ion channels, rather than size of the cell. However, Equation (53a) is derived from the isopotential lumped r_m c_m model, where the stimulus is expressed in terms of transmembrane current. In axons, and cells with non-spherical morphologies, as well as experiments where the stimulus is a change in extracellular potential gradient, this relationship is not as clear, and chronaxy does exhibit some dependence on fiber shape, size, as well as distance of point current source from fiber [125]. However, this variation is much less significant than the variations we see in rheobase and the space constant [125]. Generally, the chronaxy estimates a pulse length with a reasonably low stimulus that is sufficient to depolarize the cell. In general, faster-signaling fibers exhibit shorter chronaxy values.

In the case of extracellular stimulation of an axon trunk, this variation in passive properties leads to the recruitment order where larger diameter axons are recruited at lower stimulus magnitudes than smaller diameter ones.

While this recruitment order may be convenient in terms of experimentation, since it allows the excitation of a small subgroup of large axons while stimulating an entire nerve trunk, it also makes it difficult to selectively stimulate smaller axons without stimulating larger ones. It is possible to suppress the extracellular voltage gradient for fibers within a specific diameter range, by using arrays of multiple electrodes [126], however, for magnetic stimulation this would require a number of closely spaced coils.

Having neural preparations with a variety of fiber diameters, as well as a spatially defined distribution of axon diameters, facilitates recruitment studies by enabling the selection of axon fiber by distance from stimulus source as

Table 1 Cable parameters for various neural structures of Helix aspersa and Procambrius clarkii

	τ (ms)	λ (mm)	Diameter (μm)	R_m (Ω-cm^2)	R_i (Ω-cm)	C_m (μF/cm^2)	ref.
P. clarkii							
Medial giant axon*	2.9±0.9	4.0±1.0	201±32	1664±592	56±26	1.7±0.6	[127]
Lateral giant axon	1.4	2.6	100	2530	90	0.6	[128]
Sensory axon	9.2	0.9	18	2617	160	3.5	[129]
H. aspersa							
Soma	20–250						[130]
Olfactory interneurons		0.274[ii] (0.091–0.612)[iii]	0.5	4000[i]	80[i]		[131]
Optic nerve			0.1				[132]
Intestinal nerve, ovotestis branch			0.05–2.1				[133]

*Standard deviation sample data available

[i]Value averaged from other relevant snail species

[ii]Estimate obtained from R_m and R_i values averaged from other snail species

[iii]Estimate obtained from R_m and R_i extremes

well as by fiber diameter. The medial and lateral giant axons in the crayfish abdominal nerve cord are an excellent example. Table 1 displays some useful cable parameters for two neural preparations discussed in the following section.

9 Selection

In selecting a neural preparation, several factors should be considered. Specific structures must be repeatably and reliably located to allow testing of similar structures from experiment to experiment. The preparation should be asymmetric – offering both large and small axons for study of recruitment and different stimulus thresholds. Spatially defined nerve morphologies allow the experimenter to explicitly determine the distance from source to fiber. Stability under a wide temperature range allows alteration of the temperature-dependant length constant. Preparations that are pH insensitive permit short-duration charge-imbalanced stimulation, which greatly simplifies modeling of electric fields used for control experiments. Invertebrate preparations meet these criteria and have proved to be an invaluable neurobiological model [134]. In addition, axons of these organisms are unmyelinated, which further simplifies correlation between modeling and experimental data. Unmyelinated nerves may also serve as a model of human pain afferents in pulsed electromagnetic field pain therapy [1] and for studies on unmyelinated axons in the human brain and organs [135].

The use of a stimulating coil with cores allows the use of physically smaller neurobiological preparations. Here we use two neural preparations to evaluate the effects of magnetic stimulation on unmyelinated nerves and demonstrate magnetic stimulation with a ferrite core stimulation coil.

The abdominal nerve cord from *P. clarkii* makes an excellent neurobiological preparation because it is extensively studied. The nerve cord has several structures that are easy to locate and allow the orientation of known morphological structures. The lateral and medial giant axons are easily located (Fig. 24). In addition, crayfish have several sensory non-spiking afferents that may permit the study of magnetic stimulation effects on non-spiking neurons.

The circumesophageal ring from *H. aspersa* (Fig. 25) is another useful model. *H. aspersa* makes an excellent model because the circumesophageal ring contains individual cells and nerves that can be located repeatably [136]. Specifically, the pedal and optic nerves serve as excellent material for relatively long, uniform nerves. Moreover, the snail eye stalk containing both the olfactory and the optic nerve is susceptible to tactile stimulation [137]. The length and time constants of *H. aspersa* and *P. clarkii* are also greatly different, permitting a range of experimental conditions to test the validity of Equations (6) and (8).

Both of these neurobiological preparations are thoroughly documented as part of a laboratory curriculum [138, 139], and specimens are inexpensively obtained from biological supply houses. The space constant may be varied by

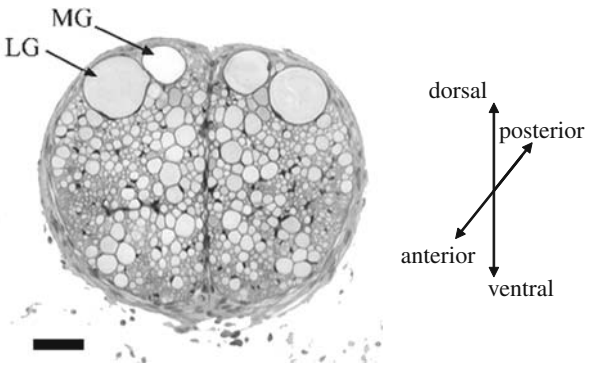

Fig. 24 Transverse section of the crayfish abdominal nerve cord. Lateral Giant neuron (LG) and Medial Giant neuron (MG) are clearly seen near the top (dorsal side) of the figure. Black bar is approximately 100 μM. Reprinted with permission from [158]

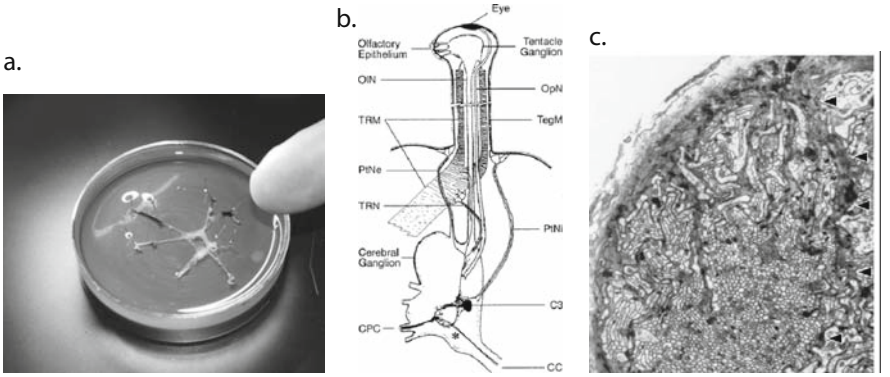

Fig. 25 *Helix Aspersa* morphological details. (**a**) dorsal view of circumoesophageal ring showing eye stalks. The black spots at the 10 o'clock and 2 o'clock positions are the eyes. Preparation is shown in a 30 mm Petri dish with the neural preparation pinned to a sylgard-184 substrate. (**b**) diagrammatic cross section of the eye stalk, reprinted with permission from [159] (**c**) Cross section of the intestinal nerve, ovotestis branch [133]. The densely packed small (0.2 μm – 0.5 μm) axons typical of *H. Aspersa* nerves are clearly seen

changes in external salt concentration or temperature because the preparations are robust. In both *H. aspersa and P. clarkii* oscillatory structures have been located that produce rhythmic repeatable patterns [140, 141]. These structures offer the opportunity to study subtle effects of magnetic fields on structures with a strong intrinsic behavior.

10 Methods

10.1 Data Acquisition and Control

While it is beyond the scope of this chapter to discuss an entire electrophysiology recording and stimulation system, we will include a few resources. It is probably best to learn techniques and about the equipment from users in an active lab. If this

is not possible, several excellent resources exist. Details of construction of an electrophysiology station are reviewed in [142] and exhaustive details on methods of recording and stimulation are covered in [143, 144]. A computer-controlled data acquisition system is a must for magnetic stimulation systems. Computer control provides some measure of safety for the operator during discharge and enables for precise measurement. Exact timing information is required to determine when the magnetic stimulation pulse was generated and when and where the neural signal is generated. This requires tens of microseconds timing accuracy to correctly infer propagation velocity and thus the locus of excitation for small neural preparations. An excellent resource for data acquisition systems is [145].

Given time, equipment can be constructed in the lab or purchased second hand. An inexpensive recording amplifier described in [146] and stimulators are described in [147-149]. The current and voltage compliance of the stimulator increase significantly as the distance increases from the point source to the neural cable. Telescoping amplifier methods [150] are easily employed to extend the operating range of stimulators.

MATLAB has gained wide acceptance as a development platform for the acquisition and analysis of electrophysiological data. Notably among these tools are several free packages. Gprime is a free package for data acquisition and control that works with a wide range of National Instruments data acquisition cards, can perform rudimentary spike sorting, and supply a synchronized signal to a stimulator [151]. SigTool is a suite of processing tools for the analysis of neural data with a wide range of import capabilities for commercial data acquisition systems [152]. SigTool calls wave_clus to perform spike sorting and clustering and wave_clus is also a standalone analysis package [153]. Wave_clus has both tutorials and sample data available at http://www.vis.caltech.edu/~rodri/Wave_clus/Wave_clus_home.htm.

10.1.1 Electrophysiological Recording and Stimulation

To record electrophysiological signals, we employ both suction electrodes and custom designed recording chambers based on a cuff electrode recording apparatus. Suction electrode recordings from nerve trunks yield compound action potentials from a group of neurons, however, due to diameter-based recruitment the recorded CAP constitutes of spikes from only a small subgroup of the larger axons, while offering a relative ease of handling and robust experimental protocol. Suction electrodes can be easily constructed [149]. Significant improvements in recording stability and signal fidelity are possible with the use of glass suction electrodes made from smooth wall micropipette glass, flamed to form a smooth hourglass shape opening (as shown in Fig. 26). A successful recording will produce very stable, reproducible signals over several hours. We have been able to successfully apply spike sorting to extracellularly recorded action potentials using these suction electrodes.

The cuff electrode recording chamber is based on the apparatus presented in [154]. The chamber is constructed by tying fine gauge electrode wire around a

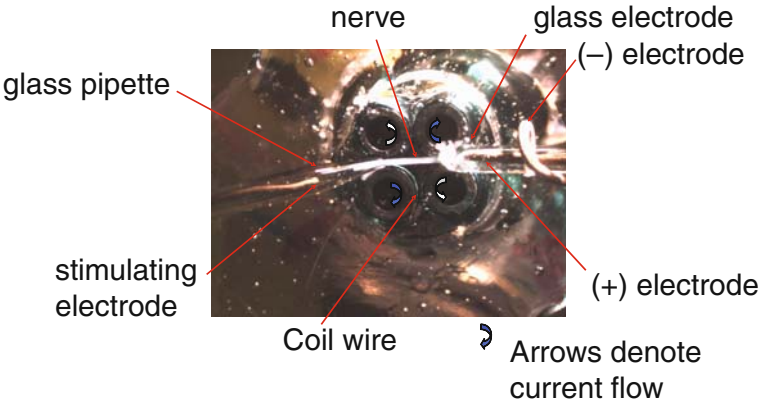

Fig. 26 Top view of magnetic stimulation and suction electrode rig

Teflon tube of the approximate diameter of the nerve under study. Teflon sleeving assortments are available from Sparky Electronics, Fresno, CA and Fry's Electronics, San Jose, CA 95112. Gold and silver are appropriate wires for the recording and a significant decrease in noise is observed when the silver wire is chlorided. Platinum wire can be stiff even at very fine gauge sizes. Fine gauge precious metal wire is available from A-M Systems, MWS Wire Industries, Westlake Village, CA 91362 and California Fine Wire, Grover Beach, CA 93483-0446. The assembly is taped or pinned down over a sheet of polyimide roughened to facilitate adhesion. Insulted wires to interface with the recording amplifier are silver epoxied to the free end of the recording wire. The entire assembly is then covered with SYLGARD® 184 (Dow Corning) silicone elastomer and cured. After curing, the apparatus is trimmed to size and the Teflon tube is removed. The resulting device is shown in Fig. 27. A hole is drilled in the bottom of a Petri dish and the whole apparatus glued to the bottom of the Petri dish. Since the KAPTON is a known thickness, and an excellent insulator, small nerves can placed with reasonable repeatability close to the coil.

In our set-up electrophysiological signals were recorded using glass suction electrodes filled with bath saline. Signals were amplified by an A-M Systems model 1700 amplifier (www.a-msystems.com) set at a gain of 1000× and hardware filtered at 10 Hz and 5 kHz. Axon Instruments pClamp (http://www.moleculardevices.com) was used for data collection and triggering of both magnetic and electrical pulse generators. Data were digitally filtered at 100 Hz and 5 kHz.

Electrical stimulation was performed using a S8800 Grass Technologies stimulator (http://www.grasstechnologies.com). A custom designed modified Howland current source triggered directly form the output of the Grass S8800 provided the current pulse to the preparation. Magnetic stimulation was accomplished using an Agilent 33120A arbitrary waveform generator driving a high-power V–I converter or a thyristor triggered pulse discharge circuit. Further details on the circuits may

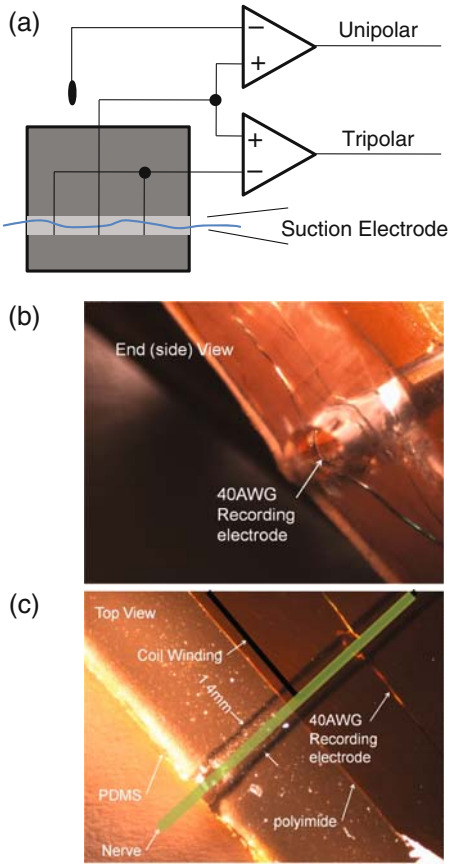

Fig. 27 Modified nerve cuff recording apparatus. (**a**) system diagram and recording hook up to amplifier. (**b**) end view (**c**) top view

be obtained from [155]. Axon Instruments Clampfit was used for threshold windowing and peak alignment.

10.1.2 Tissue Culture

Snails can be obtained from biological supply houses. Adults with shells 2–3 cm in diameter are used for recording. Snails are fed a diet of cornmeal or bird seed and provided oyster shells as a calcium source. Light, maintained at 12 h cycles, can be inversed such that the snails are active during the day. Individual specimens were anesthetized with 2 ml cold (10°C) 50 mM $MgCl_2$ and prepared as in [138]. The nerves in the eyestalk as well as the pedal nerves located on the ventral surface of the subesophageal ganglia are good targets for magnetic stimulation because of their length as well as readily recordable CAPs.

Crawfish adults are 7–11 cm in length. Specimens should be kept in individual tanks and maintained on a mixed diet of vegetable and protein matter. Dissection can be performed by anesthetizing the animal in an ice bath and cutting off the tail (abdomen). The abdomen is pinned ventral side up and bathed in crawdad

saline prepared as in [138]. Swimmerets need to be removed and the cuticle cut along the sides of the carapace of the abdominal section. The cuticle can then be carefully removed, the abdominal nerve cord freed from the surrounding muscle tissue, and lifted into clean crawdad saline solution.

11 Results

A large shift in the chronaxy of the strength–duration curve would be expected from the difference in physiology and morphology between *H. aspera* and *P. clarkii*. As shown in Fig. 28, the chronaxy of *H. aspersa* and *P. clarkii* vary by approximately 20 times. The rheobase varied much less, by approximately two.

Initial testing results of magnetic stimulation appear promising. Figure 29(a and b) show magnetic stimulation of single action potentials using ferrite cores. For Fig. 29a, the core used was a 22 μH coil stimulated with a linear saw tooth current ramp of 0.1 A/μs for 250 μS. For Fig. 29b, the magnetic pulse was

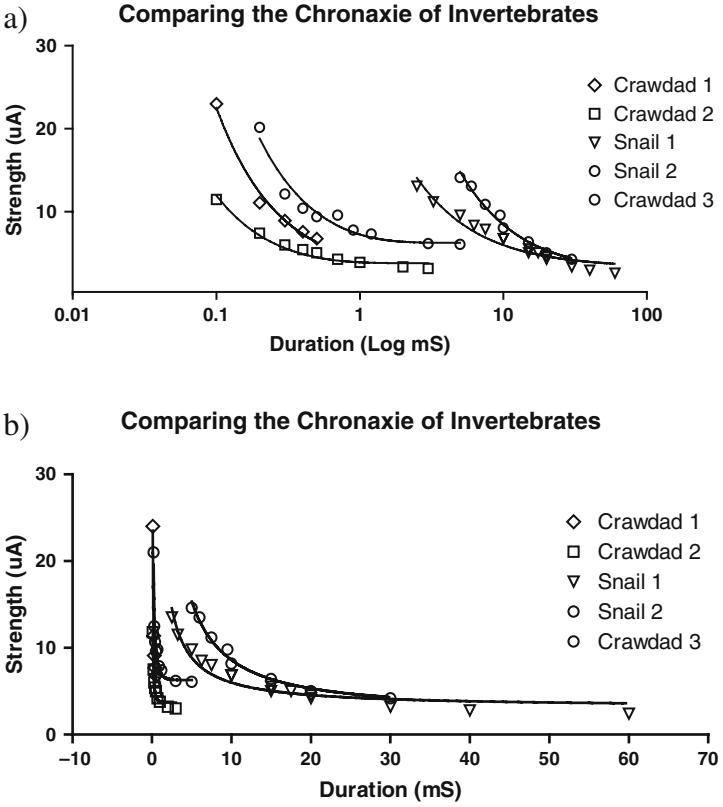

Fig. 28 Comparison of strength-duration curves of invertebrates. Experimentally derived strength-duration curves using electrical stimulation and suction electrodes. (**a**) shows a log-linear plot and (**b**) shows a linear-linear plot. Similar rheobase, but the chronaxy varies by as much as an order of magnitude. Curve fitting was performed using a non-linear fit to the exponential strength-duration equation

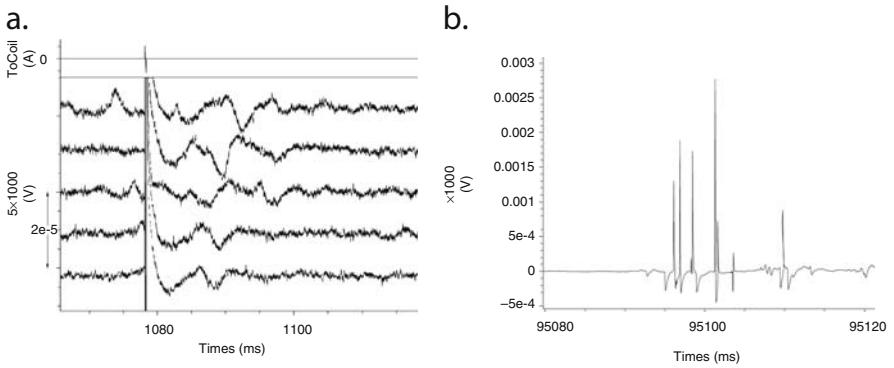

Fig. 29 Magnetically generated action potentials. (**a**) Single Action potential generated by magnetic stimulation with ferrite core using *H. Aspersa* neurobiological preparation. Upper trace is the current delivered to the coil. Lower 5 traces are recorded responses from repetitive sweeps. The stimulus artifact aligns with the spike in the upper trace. (**b**) set of individual action potentials generated by magnetic stimulation with ferrite core using *P. Clarkii* neurobiological preparation. Note the stimulus artifact to the left of the first action potential

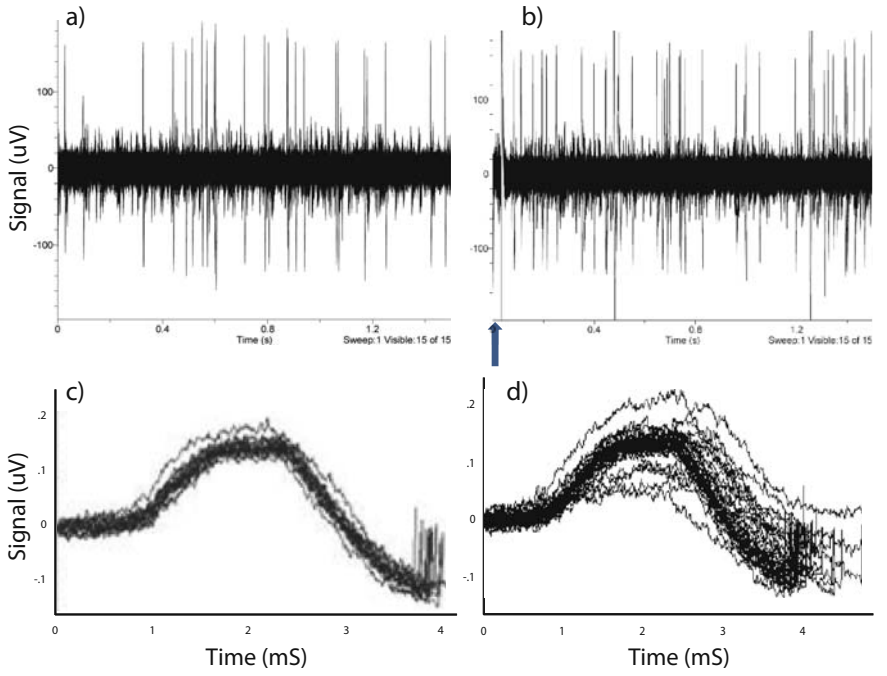

Fig. 30 Variation in spiking frequency and action potential shape induced by magnetic stimulation. (**a**) 19 neural spikes recorded without stimulus (**b**) 36 neural spikes recorded with stimulus (**c**) Aligned action potentials from (**a**) (**d**) Aligned action potentials from (**b**). Data is 15 sweeps 30s apart. Arrow in (**b**) denotes magnetic stimulation stimulus artifact

generated with a thyristor triggered circuit using a bank of 1000 μF flash capacitors charged to 200 V. The coil was a rectangular coil 2.2 mm by 4.4 mm of material 73 wound to an impedance value of 24 μH.

Subthreshold stimuli will not elicit an action potential but should alter the intrinsic behavior of oscillatory firing patterns. The effect of subthreshold magnetic stimulation alters both the firing frequency and the shape of the recorded action potentials in Fig. 30b and 30d. The change in spiking frequency and the variation of action potential shape are clear evidence of subthreshold interaction of magnetic fields with neural tissue.

12 Conclusion

Magnetic stimulation of neural tissue has a wide range of clinical applications. However, the future development of the field depends upon development of improved technologies and quantitative models are a part of this development. To further this goal we outlined a complete approach to developing small-scale magnetic stimulation experiments and showed how it could be applied to novel circuit topologies. The use of ferrite cores has allowed magnetic stimulation to be scaled to the point that a wide variety of neurobiological preparations are available for study. With new preparations comes new opportunities for investigation and understanding. Using a wide array of neurobiological preparations offers the opportunity to investigate the finer details of magnetic stimulation including magnetic stimulation nerve recruitment, blocking studies, and long-term histological effects.

Acknowledgment The authors would like to acknowledge Dr. David Tauck of Santa Clara University for his guidance during the dissections and electrophysiological experiments, Bennett Lee for his assistance with the neural preparations, Dr. David Parent for valuable technical discussion on coil and circuit design and numerical analysis, and Melissa Wibom for draft editing assistance. We would like to acknowledge the NSF for their funding support.

Appendix: Modeling Magnetic Stimulation with Solenoid Coil

The circular E field generated by a solenoid coil with core (shown in Fig. 31) can be approximated as

$$E \approx \begin{cases} \alpha \dfrac{r}{2} u_r u_0 n \dfrac{dI}{dt}, r < \rho, z << \rho \\ \alpha \dfrac{\rho^2}{2r} u_r u_0 n \dfrac{dI}{dt}, r > \rho, z << \rho, \end{cases} \tag{54}$$

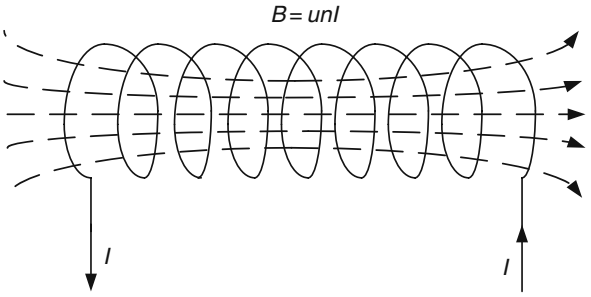

Fig. 31 Illustration of magnetic field flux generated by long sinusoid coil

where α ($0 < \alpha < 1$) is a parameter to compensate the distance between the coil and the neural tissue, ρ denotes the radius of the inductor, and r represents the distance from the point of interest to the center of the current loop.

Within the circular loop, the E field derivative can be evaluated in x–y coordinates as

$$E = E_x\hat{x} + E_y\hat{y} = -\frac{y}{2}\alpha u_r u_0 n\frac{dI}{dt}\hat{x} + \frac{x}{2}\alpha u_r u_0 n\frac{dI}{dt}\hat{y}. \tag{55}$$

From Equation (55), the spatial derivative of the E field is almost zero, given $r \leq \rho$

$$\begin{cases} \dfrac{\partial E_x}{\partial x} = -\dfrac{\partial\alpha\dfrac{y}{2}u_r u_0 n\dfrac{dI}{dt}}{\partial x} = 0, r < \rho, z << \rho \\ \dfrac{\partial E_y}{\partial y} = \dfrac{\partial\alpha\dfrac{x}{2}u_r u_0 n\dfrac{dI}{dt}}{\partial y} = 0, r < \rho, z << \rho. \end{cases} \tag{56}$$

Equation (56) shows that a neuron directly above a solenoid coil is difficult to stimulate. This property is irrelevant to the geometry variation of neurons and it indicates potentially improved spatial selectivity compared with functional electric stimulation, where neurons close to the electrode are all stimulated.

If a part of the neuron or the whole neuron is located outside the current loop (shown in Fig. 32, the right upper neuron), the E field derivative can be derived from (54) as

$$E = E_x\hat{x} + E_y\hat{y} = -\alpha\frac{y}{2}\frac{\rho^2}{r^2}u_r u_0 n\frac{dI}{dt}\hat{x} + \alpha\frac{x}{2}\frac{\rho^2}{r^2}u_r u_0 n\frac{dI}{dt}\hat{y}. \tag{57}$$

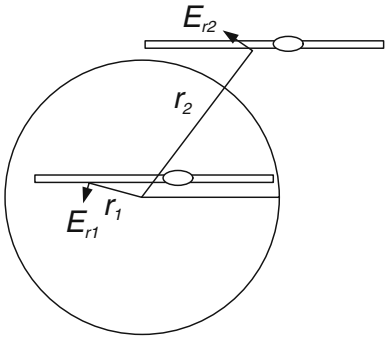

Fig. 32 Illustration of nerve location and orientation referred to the stimulating coil that is indicated by the circle

In this case, the spatial derivative of the E field is non-zero, as r is a function of both x and y, thus

$$\begin{cases} \dfrac{\partial E_x}{\partial x} = -\dfrac{\partial \alpha \dfrac{y}{2}\dfrac{\rho^2}{r^2} u_r u_0 n \dfrac{dI}{dt}}{\partial x} = -\dfrac{y}{2}\alpha\rho^2 u_r u_0 n \dfrac{dI}{dt}\dfrac{\partial r^{-2}}{\partial x} = \alpha\rho^2 u_r u_0 n \dfrac{dI}{dt}\dfrac{xy}{r^4}, r > \rho, z << \rho \\ \dfrac{\partial E_y}{\partial y} = \dfrac{\partial \alpha \dfrac{x}{2}\dfrac{\rho}{r^2} u_r u_0 n \dfrac{dI}{dt}}{\partial y} = \dfrac{x}{2}\alpha\rho^2 u_r u_0 n \dfrac{dI}{dt}\dfrac{\partial r^{-2}}{\partial y} = -\alpha\rho^2 u_r u_0 n \dfrac{dI}{dt}\dfrac{xy}{r^4}, r > \rho, z << \rho \end{cases} \tag{58}$$

According to Equation (58), the maximum spatial derivative is obtained when

$$|x| = |y| = \frac{\sqrt{2}}{2}\rho$$

The maximum spatial derivative of the E field over both x and y axes are

$$\left|\frac{\partial E_x}{\partial x}\right| = \left|\frac{\partial E_y}{\partial y}\right| = \frac{1}{2}\alpha u_r u_0 n \frac{dI}{dt}. \tag{59}$$

Equations (58) and (59) suggest an optimal coil–axon configuration, this shown in Fig. 33. To achieve, two conditions should be satisfied: (1) the membrane segment should be close to the current loop and (2) the axon's direction is approximately 45° deviated from the radius.

Other configurations, e.g., neuron inside the coil radius (Fig. 32), or the axon crossing the coil center (Fig. 34a), or neuron completely outside the coil radius (Fig. 34b), introduce a smaller E field derivative compared with the optimal configuration. In all cases, the spatial derivative of E field can be evaluated using Equation (58).

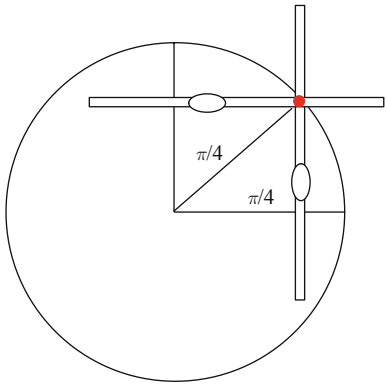

Fig. 33 Optimal nerve location and orientation that maximizes the induced E field derivative

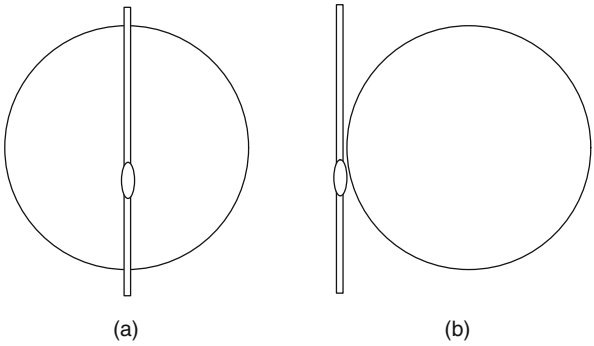

Fig. 34 (**a**) Not excitable coil nerve geoemtry Configuration. (**b**) excitable, but less preferreable configuration compared with Fig. 33.

Current Slew Rate and Power Consumption

14.1 Slew Rate

A magnetically induced spatially varying E field of about 10 kV/m^2 is required for a duration near the chronaxy of the nerve to stimulate neurons [59, 156, 157]. Given a conventional air–core coil with diameter on the order of a few cm, a current slew rate greater than 10 A/us is required for excitation of neural tissue placed with a few mm. According to Equation (59), the maximum spatial derivative of E field generated by a solenoid coil is

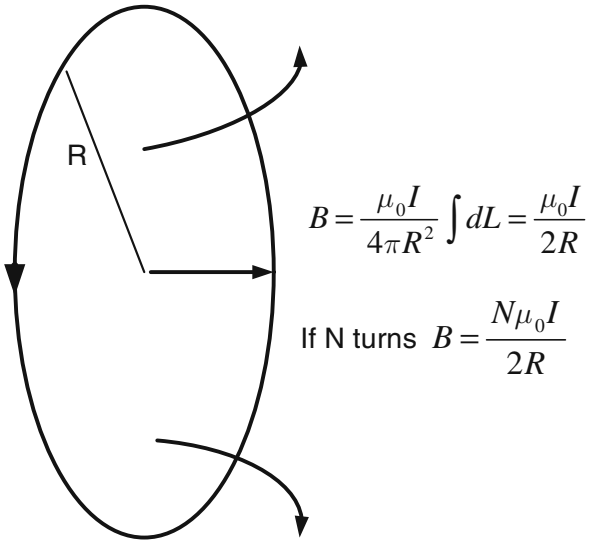

Fig. 35 Illustration of magnetic field flux generated by a current loop or N superimposed current loops

$$\frac{1}{2}\alpha u_r u_0 n \frac{dI}{dt}.$$

Given $u_0 = 4\pi \times 10^{-7}$ and the required current slew rate is

$$\frac{dI}{dt}_{Threshold} = 1.6 \times 10^{10} \frac{L}{\alpha \mu_r N} \tag{60}$$

where N is the number of turns, L is the coil height and

$$\frac{dE}{dx}_{Threshold} = 10^{10} V/m^2.$$

Using values reasonable to implement experimentally; N = 100, $\mu_r = 20$, $\alpha = 0.5$, and L = 1 cm, we have

$$\frac{dI}{dt}_{Threshold} = 1.6 \times 10^5 A/S = 0.16 A/\mu S. \tag{61}$$

According to Equation (59) and numeric examples shown in Equations (60) and (61), the loop diameter of a solenoid coil does not influence the required current slew rate to activate neurons.

14.2 Power Consumption

The required energy per pulse to active a neuron is

$$\int 0.5I^2 R_{res} dt = \int 0.5\left(\frac{dI}{dt_{Threshold}} t\right)^2 R_{res} dt = 0.17 \frac{dI^2}{dt_{Threshold}} R_{res} T^3, \quad (62)$$

where T is the current pulse width and R_{res} is the coil resistance. For a 100 μS pulse with a 1 Ω coil resistance, the dissipated energy is only 4 mJ. The technique of using biphasic sawtooth waveform can further reduce power dissipation by half.

15 Scaling with Planar Coil

Similar to Equation (54), the E field generated by a circular planar coil is approximated as

$$E \approx \begin{cases} \alpha \frac{r}{2\rho} u_r u_0 N \frac{dI}{dt}, r < \rho, z << \rho \\ \alpha \frac{\rho}{2r} u_r u_0 N \frac{dI}{dt}, r > \rho, z << \rho \end{cases} \quad (63)$$

For Case I, where $r < \rho$, following Equation (63), neurons inside the coil radius are less excitable. It is important to note that Equation (63) is approximate and a small E field spatial derivative still exists.

For Case II, where$r > \rho$, the field is approximated as

$$E = E_x \hat{x} + E_y \hat{y} = -\alpha \frac{y}{2} \frac{\rho}{r^2} u_r u_0 N \frac{dI}{dt} \hat{x} + \alpha \frac{x}{2} \frac{\rho}{r^2} u_r u_0 N \frac{dI}{dt} \hat{y}, \quad (64)$$

where the spatial derivative of E field can be obtained from Equation (64) as

$$\begin{cases} \frac{\partial E_x}{\partial x} = -\frac{\partial \alpha \frac{y}{2} \frac{\rho}{r^2} u_r u_0 N \frac{dI}{dt}}{\partial x} = -\alpha \frac{y}{2} \rho u_r u_0 N \frac{dI}{dt} \frac{\partial r^{-2}}{\partial x} = \alpha \rho u_r u_0 N \frac{dI}{dt} \frac{xy}{r^4}, r > \rho, z << \rho \\ \frac{\partial E_y}{\partial y} = \frac{\partial \alpha \frac{x}{2} \frac{\rho}{r^2} u_r u_0 N \frac{dI}{dt}}{\partial y} = \alpha \frac{x}{2} \rho u_r u_0 N \frac{dI}{dt} \frac{\partial r^{-2}}{\partial y} = -\alpha \rho u_r u_0 N \frac{dI}{dt} \frac{xy}{r^4}, r > \rho, z << \rho \end{cases} \quad (65)$$

The maximum E field spatial derivative is achieved when $|x| = |y| = \frac{\sqrt{2}}{2}\rho$

$$\left|\frac{\partial E_x}{\partial x}\right| = \left|\frac{\partial E_y}{\partial y}\right| = \frac{1}{2} u_r u_0 \frac{N}{\alpha\rho}\frac{dI}{dt} \tag{66}$$

Comparing Equation (66) to (59), the spatial derivative is related to the loop radius ρ. With planar coils, reducing the loop radius can increase the E field spatial derivative. A few numeric examples are included below to describe the scaling effect.

Case A: 20 turns, $\rho = 4$ cm and $u_r = 1$, the required minimal current slew rate is

$$\frac{dI}{dt} = 3 \times 10^7 A/S = 30 A/\mu S$$

Case B: 20 turns, $\rho = 4$ mm and $u_r = 1$, the required minimal current slew rate is

$$\frac{dI}{dt} = 3 \times 10^6 A/S = 3 A/\mu S$$

References

1. Weintraub, M.I. and S.P. Cole, *Pulsed magnetic field therapy in refractory neuropathic pain secondary to peripheral neuropathy: electrodiagnostic parameters – pilot study*. Neurorehabilitation and Neural Repair, 2004, **18**(1): 42.
2. Pujol, J., et al., *The effect of repetitive magnetic stimulation on localized musculoskeletal pain*. Neuroreport, 1998, **9**(8): 1745–1748.
3. Basser, P.J. and B.J. Roth, *New currents in electrical stimulation of excitable tissues*. Annual Review of Biomedical Engineering, 2000, **2**(1): 377–397.
4. Barker, A.T., *The history and basic principles of magnetic nerve stimulation*. Electroencephalogr Clin Neurophysiol Suppl, 1999, **51**: 3–21.
5. Geddes, L.A., *History of magnetic stimulation of the nervous system*. J Clin Neurophysiol, 1991, **8**(1): 3–9.
6. Hallett, M., *Transcranial magnetic stimulation and the human brain*. Nature, 2000, **406**(6792): 147–150.
7. George, M.S., et al., *Transcranial magnetic stimulation*. Neurosurgery Clinics of North America, 2003, **14**(2): 283–301.
8. Hallett, M., *Transcranial magnetic stimulation: a primer*. Neuron, 2007, **55**(2): 187–199.
9. Kato, M., *Electromagnetics in biology*. 2006, Tokyo: Springer. xv, 324p.
10. Ji, R.-R., et al., *Repetitive transcranial magnetic stimulation activates specific regions in rat brain*. Proceedings of the National Academy of Sciences of the United States of America, 1998, **95**(26): 15635–15640.
11. Li, G.N. and D. Hoffman-Kim, *Tissue-engineered platforms of axon guidance*. Tissue Engineering Part B: Reviews, 2008, **14**(1): 33–51.
12. Eaton, H.A.C. *The electric field induced in a spherical volume conductor by a Magnetic Coil*. in *Engineering in Medicine and Biology Society, 1990, Proceedings of the Twelfth Annual International Conference of the IEEE*. 1990.
13. Bencsik, M., R. Bowtell, and R.M. Bowley, *Electric fields induced in a spherical volume conductor by temporally varying magnetic field gradients*. Physics in Medicine and Biology, 2002(4): 557–576.

14. Ravazzani, P., et al., *Magnetic stimulation of the nervous system: Induced electric field in unbounded, semi-infinite, spherical, and cylindrical media*. Annals of Biomedical Engineering, 1996, **24**(5): 606–616.
15. Roth, B.J. and P.J. Basser, *A model of the stimulation of a nerve fiber by electromagnetic induction*. Biomedical Engineering, IEEE Transactions on, 1990, **37**(6): 588–597.
16. Miranda, P.C., et al., *Tissue heterogeneity as a mechanism for localized neural stimulation by applied electric fields*. Physics in Medicine and Biology, 2007, **52**(18): 5603–5617.
17. Ye, H., M. Cotic, and P.L. Carlen, *Transmembrane potential induced in a spherical cell model under low-frequency magnetic stimulation*. Journal of Neural Engineering, 2007, **4**(3): 283–293.
18. Rotem, A. and E. Moses, *Magnetic stimulation of curved nerves*. Biomedical Engineering, IEEE Transactions on, 2006, **53**(3): 414–420.
19. Rotem, A. and E. Moses, *Magnetic stimulation of one-dimensional neuronal cultures*. Biophysical Journal, 2008.
20. References, S., et al., *Magnetic coil stimulation of straight and bent amphibian and mammalian peripheral nerve in vitro: locus of excitation*. Journal of Physiology, 1993, **460**: 201–219.
21. Hsu, K.H., S.S. Nagarajan, and D.M. Durand, *Analysis of efficiency of magnetic stimulation*. Biomedical Engineering, IEEE Transactions on, 2003, **50**(11): 1276–1285.
22. Engstrom, S. and R. Fitzsimmons, *Five hypotheses to examine the nature of magnetic field transduction in biological systems*. Bioelectromagnetics, 1999, **20**(7): 423–430.
23. Struijk, J.J. and V. Schnabel, *Difference between electrical and magnetic nerve stimulation: a case for the transverse field?* Engineering in Medicine and Biology Society, 2001. Proceedings of the 23rd Annual International Conference of the IEEE, 2001, **1**.
24. Wasserman, E., C.M. Epstein, and U. Ziemann, *The Oxford handbook of transcranial stimulation*. 2008, Oxford; New York: Oxford University Press. xiv, 747p.
25. Ridding, M.C. and J.C. Rothwell, *Is there a future for therapeutic use of transcranial magnetic stimulation?* Nature Reviews and Neuroscience, 2007, **8**(7): 559–567.
26. Hodgkin, A.L. and W.A.H. Rushton, *The electrical constants of a crustacean nerve fibre*. Proceedings of the Royal Society of London. Series B, Biological Sciences (1934–1990), 1946, **133**(873): 444–479.
27. Ranck, J.B., *Which elements are excited in electrical stimulation of mammalian central nervous system: a review*. Brain Research, 1975, **98**(3): 417–440.
28. Patterson, M.M. and R.P. Kesner, *Electrical stimulation research techniques*. Methods in physiological psychology, 1981. New York: Academic Press. xv, 370p.
29. Rattay, F., *Ways to approximate current-distance relations for electrically stimulated fibers*. Journal of Theoretical Biology, 1987, **125**(3): 339–349.
30. Rattay, F., *Analysis of models for extracellular fiber stimulation*. Biomedical Engineering, IEEE Transactions on, 1989, **36**(7): 676–682.
31. Roth, B.J., *Mechanisms for electrical stimulation of excitable tissue*. Crit Rev Biomed Eng, 1994, **22**(3–4): 253–305.
32. Plonsey, R. and R.C. Barr, *Bioelectricity: a quantitative approach*. 3rd ed. 2007, New York: Springer. xiv, 528p.
33. Schnabel, V. and J.J. Struijk, *Evaluation of the cable model for electrical stimulation of unmyelinated nerve fibers*. Biomedical Engineering, IEEE Transactions on 2001, **48**(9): 1027–1033.
34. Zierhofer, C.M. and C.M. Zierhofer, *Analysis of a linear model for electrical stimulation of axons-critical remarks on the "activating function concept"*. Biomedical Engineering, IEEE Transactions on, 2001, **48**(2): 173–184.
35. Hui, Y., et al. *A New Model and improved cable function for representing the activating peripheral nerves by a transverse electric field during magnetic stimulation*. In Neural Engineering, 2005. Conference Proceedings. 2nd International IEEE EMBS Conference on. 2005.
36. Nagarajan, S.S., S.S. Nagarajan, and D.M. Durand, *A generalized cable equation for magnetic stimulation of axons*. Biomedical Engineering, IEEE Transactions on, 1996, **43**(3): 304–312.

37. Struijk, J.J. and D.M. Durand. *Magnetic peripheral nerve stimulation: axial versus transverse fields*. in *[Engineering in Medicine and Biology, 1999. 21st Annual Conf. and the 1999 Annual Fall Meeting of the Biomedical Engineering Soc.]* BMES/EMBS Conference, 1999. Proceedings of the First Joint. 1999.
38. Hsu, K.H. and D.M. Durand, *Prediction of neural excitation during magnetic stimulation usingpassive cable models*. Biomedical Engineering, IEEE Transactions on, 2000, **47**(4): 463–471.
39. Kai-Hsiung, H. and D.M. Durand. *Determination of excitation thresholds of nerve fibers during magnetic stimulation*. in *Engineering in Medicine and Biology Society, 1996*. Bridging Disciplines for Biomedicine. Proceedings of the 18th Annual International Conference of the IEEE. 1996.
40. Suarez-Antola, R.E. *The time constants for the electric stimulation of nerve an muscle fibers by point electrodes*. in *Neural Engineering, 2005. Conference Proceedings*. 2nd International IEEE EMBS Conference on. 2005.
41. Malmivuo, J. and R. Plonsey, *Bioelectromagnetism: principles and applications of bioelectric and biomagnetic fields*. 1995, New York: Oxford University Press. xxii, 482.
42. Irnich, W., *Electrostimulation by time-varying magnetic fields*. Magnetic Resonance Materials in Physics, Biology and Medicine, 1994, **2**(1): 43–49.
43. Ruohonen, J., et al., *Transverse-field activation mechanism in magnetic stimulation of peripheral nerves*. Electroencephalography and Clinical Neurophysiology/Electromyography and Motor Control, 1996, **101**(2): 167–174.
44. Roth, B.J., B.J. Roth, and P.J. Basser, *A model of the stimulation of a nerve fiber by electromagnetic induction*. Biomedical Engineering, IEEE Transactions on, 1990, **37**(6): 588–597.
45. Carnevale, N.T. and M.L. Hines, *The Neuron book*. 2006, Cambridge, UK; New York: Cambridge University Press. xix, 457p.
46. Bower, J.M. and D. Beeman, *The book of Genesis: exploring realistic neural models with the GEneral NEural SImulation System*. 1998. Springer-Verlag New York, Inc. New York.
47. Zeng, L. and M.D. Dominique, *Extracellular voltage profile for reversing the recruitment order of peripheral nerve stimulation: a simulation study*. Journal of Neural Engineering, 2004, 4: 202.
48. Brauer, J.R., *Magnetic actuators and sensors*. 2006, Hoboken, NJ: Wiley. xii, 308p.
49. Claycomb, J.R., *Applied electromagnetics using QuickField & MATLAB*. 2008, Hingham, Mass: Infinity Science Press.
50. Lonngren, K.E., S.V. Savov, and R.J. Jost, *Fundamentals of electromagnetics with MATLAB*. 2007, Raleigh, NC: SciTech Pub. xx, 528p.
51. Davey, K., L. Luo, and D.A. Ross, *Toward functional magnetic stimulation (FMS) theory and experiment*. Biomedical Engineering, IEEE Transactions on, 1994, **41**(11): 1024–1030.
52. Nagarajan, S.S., D.M. Durand, and E.N. Warman, *Effects of induced electric fields on finite neuronal structures: a simulation study*. Biomedical Engineering, IEEE Transactions on, 1993, **40**(11): 1175–1188.
53. Durand, D., A.S. Ferguson, and T. Dalbasti, *Effect of surface boundary on neuronal magnetic stimulation*. Biomedical Engineering, IEEE Transactions on, 1992, **39**(1): 58–64.
54. Davey, K. and M. Riehl, *Designing transcranial magnetic stimulation systems*. Magnetics, IEEE Transactions on, 2005, **41**(3): 1142–1148.
55. Ren, L. and S. Ueno, *Calculating the activating function of nerve excitation in inhomogeneous volume conductor during magnetic stimulation using the finite element method*. Magnetics, IEEE Transactions on, 2000, **36**(4): 1796–1799.
56. Mathis, J., et al., *The boundary effect in magnetic stimulation. Analysis at the peripheral nerve*. Electroencephalography and Clinical Neurophysiology/Electromyography and Motor Control, 1995, **97**(5): 238–245.
57. Esselle, K.P. and M.A. Stuchly, *Neural stimulation with magnetic fields: analysis of induced electric fields*. Biomedical Engineering, IEEE Transactions on, 1992, **39**(7): 693–700.

58. Olree, K.S. and K.W. Horch, *Differential activation and block of peripheral nerve fibers by magnetic fields*. Muscle and Nerve, 2006, **34**(2): 189–196.
59. Alkhateeb, A. and R.P. Gaumond. *Excitation of frog sciatic nerve using pulsed magnetic fields effect of waveform variations*. in *Engineering in Medicine and Biology Society, 1995, IEEE 17th Annual Conference*. 1995.
60. Sommers, J.D. and R.P. Gaumond. *Spacing analysis of a focal magnetic stimulating coil*. 1997.
61. Wheeler, H.A., *Inductance formulas for circular and square coils*. Proceedings of the Ieee, 1982, **70**(12): 1449–1450.
62. Mohan, S.S., et al., *Simple accurate expressions for planar spiral inductances*. Ieee Journal of Solid-State Circuits, 1999, **34**(10): 1419–1424.
63. Lontis, E.R., M. Voigt, and J.J. Struijk, *Focality assessment in transcranial magnetic stimulation with double and cone coils*. Journal of Clinical Neurophysiology, 2006, **23**(5): 463.
64. Peterchev, A.V., R. Jalinous, and S.H. Lisanby, *A transcranial magnetic stimulator inducing near-rectangular pulses with controllable pulse width (cTMS)*. Biomedical Engineering, IEEE Transactions on, 2008, **55**(1): 257–266.
65. Bronzino, J.D., A. Zangen, Y. Roth, B. Voller, and M. Hallett, *"Transcranial magnetic stimulation of deep brain regions: evidence for efficacy of the H-coil" in The biomedical engineering handbook*. 3rd ed. The electrical engineering handbook series. 2006, Boca Raton: CRC/Taylor and Francis.
66. Ren, C., P.P. Tarjan, and D.B. Popovic, *A novel electric design for electromagnetic stimulation-the Slinkycoil*. Biomedical Engineering, IEEE Transactions on, 1995, **42**(9): 918–925.
67. Han, B., et al., *Some technical aspects of magnetic stimulation coil design with the ferromagnetic effect*. Medical and Biological Engineering and Computing, 2003, **41**(5): 516–518.
68. Davey, K. and C.M. Epstein, *Magnetic stimulation coil and circuit design*. Biomedical Engineering, IEEE Transactions on, 2000, **47**(11): 1493–1499.
69. Han, B.H., et al., *Some technical aspects of magnetic stimulation coil design with the ferromagnetic effect*. Medical and Biological Engineering and Computing, 2003, **41**(5): 516–518.
70. Epstein, C.M. and K.R. Davey, *Iron-core coils for transcranial magnetic stimulation*. Journal of Clinical Neurophysiology, 2002, **19**(4): 376.
71. Salvador, R., et al., *High-permeability core coils for transcranial magnetic stimulation of deep brain regions*. In *Engineering in Medicine and Biology Society, 2007*. EMBS 2007. 29th Annual International Conference of the IEEE. 2007.
72. Åke Öberg, P., *Magnetic stimulation of nerve tissue*. Medical and Biological Engineering and Computing, 1973, **11**(1): 55–64.
73. Maass, J. and M. Asa, *Contactless nerve stimulation and signal detection by inductive transducer*. Magnetics, IEEE Transactions on, 1970, **6**(2): 322–326.
74. Ueno, S., P. Lövsund, and P. Öberg, *Effect of time-varying magnetic fields on the action potential in lobster giant axon*. Medical and Biological Engineering and Computing, 1986, **24**(5): 521–526.
75. Ueno, S., et al., *Capacitive stimulatory effect in magnetic stimulation of nerve tissue*. Magnetics, IEEE Transactions on, 1978, **14**(5): 958–960.
76. van den Bossche, A., *Inductors and transformers for power electronics*. 2005. Boca Raton, FL: CRC Press.
77. McLyman, C.W.T., W.T. McLyman, and M. McLyman, *Transformer and inductor design handbook*. 2004. Boca Raton, FL: CRC Press.
78. Van den Bossche, A., V. Valchev, and T. Filchev. *Improved approximation for fringing permeances in gapped inductors*. in *Industry Applications Conference, 2002, 37th IAS Annual Meeting. Conference Record of the*. 2002.
79. Zhi, Y., L. Wentai, and E. Basham, *Inductor modeling in wireless links for implantable electronics*. Magnetics, IEEE Transactions on, 2007, **43**(10): 3851–3860.

80. Brauer, J.R. and I.D. Mayergoyz, *Finite-element computation of nonlinear magnetic diffusion and its effects when coupled to electrical, mechanical, and hydraulic systems*. Magnetics, IEEE Transactions on, 2004, **40**(2): 537–540.
81. Venkatachalam, K., et al., *Accurate prediction of ferrite core loss with nonsinusoidal waveforms using only Steinmetz parameters*. Computers in Power Electronics, 2002, Proceedings. 2002 IEEE Workshop on, 2002: 36–41.
82. Jieli, L., et al. *Improved calculation of core loss with nonsinusoidal waveforms*. In *Industry Applications Conference, 2001*, *Thirty-Sixth IAS Annual Meeting*. Conference Record of the 2001 IEEE. 2001.
83. Hurley, W.G., E. Gath, and J.G. Breslin, *Optimizing the AC resistance of multilayer transformer windings with arbitrary current waveforms*. Power Electronics, IEEE Transactions on, 2000, **15**(2): 369–376.
84. Travis, B., *IGBTs and MOSFETs vie for applications*. EDN, 1999, **44**(9): 77–88.
85. Burke, A., *Ultracapacitors: why, how, and where is the technology*. Journal of Power Sources, 2000, **91**(1): 37–50.
86. Slenes, K.M., et al., *Pulse power capability of high energy density capacitors based on anew dielectric material*. Magnetics, IEEE Transactions on, 2001, **37**(1 Part 1): 324–327.
87. Prutchi, D. and M. Norris, *Design and development of medical electronic instrumentation: a practical perspective of the design, construction, and test of medical devices*. 2005, Hoboken, NJ: Wiley-Interscience, xv, 461p.
88. Pascual-Leone, A., *Handbook of transcranial magnetic stimulation*. 2002, New York: Arnold; Oxford University Press [distributor], x, 406p.
89. Webster, J.G. and J.W. Clark, *Medical instrumentation : application and design*. 3rd ed. 1998, New York: Wiley, xix, 691 p.
90. Geddes, L.A., *Accuracy limitations of chronaxie values*. Biomedical Engineering, IEEE Transactions on, 2004, **51**(1): 176–181.
91. Beecroft, S.I., A. Alkhateeb, and R. Gaumond. *Nerve fiber stimulation threshold for multiphase stimuli*. In *Bioengineering Conference, 1994*. Proceedings of the 1994 20th Annual Northeast. 1994.
92. Pressman, A.I., *Switching power supply design*. 2nd ed. 1998, New York: McGraw-Hill, xviii, 682p.
93. Han, B.H., et al. *Development of four-channel magnetic nerve stimulator*. in *Engineering in Medicine and Biology Society, 2001*. Proceedings of the 23rd Annual International Conference of the IEEE. 2001.
94. Polson, M.J., A.T. Barker, and I.L. Freeston, *Stimulation of nerve trunks with time-varying magnetic fields*. Med Biol Eng Comput, 1982, **20**(2): 243–244.
95. Guide, C.D.A., *Application guide, snubber capacitors*. http://www.cde.com/catalogs/igbtAPPguide.pdf.
96. Severns, R., *Design of snubbers for power circuits*. Cornell Dublier Technical Papers, online at http://www.cde.com/tech/design.pdf.
97. Whites, K., *RL Circuits, inductive kick, diode snubbers, lecture 4 EE322*. http://whites.sdsmt.edu/classes/ee322/class_notes/322Lecture4.pdf, 2006.
98. Motto, E., *Hybrid circuits simplify IGBT modul gate drive*, in *PCIM*. 1999. Europe.
99. Kratz, R. and P. Wyder, *Principles of pulsed magnet design*. Engineering materials. 2002, Berlin; New York: Springer, ix, 181p.
100. Smith, P.W., *Transient electronics: pulsed circuit technology*. 2002, New York: John Wiley, xi, 272 p.
101. Perreault, D. and S. Mogren, *Magnetic Stimulator Power and Control Circuit*, R.B. CArr (ed.) USPTO, 2003, Engineering, Onc: USA.
102. Basser, P.J., P.J. Basser, and B.J. Roth. *Scaling laws for electromagnetic stimulation of an axon*. In *Engineering in Medicine and Biology Society, 1990*. Proceedings of the Twelfth Annual International Conference of the IEEE. 1990.

103. Fink, D.G. and H.W. Beaty, *Standard handbook for electrical engineers*. 1999, New York: McGraw-Hill., p. v.
104. Mesut, S. and T. Yanmei, *Non-rectangular waveforms for neural stimulation with practical electrodes*. Journal of Neural Engineering, 2007, **3**: 227.
105. Wada, S., et al., *Effects of stimulus waveform on magnetic nerve stimulation*. Japanese Journal of Applied Physics Part 1-Regular Papers Short Notes and Review Papers, 1996, **35**(3): 1983–1988.
106. Grill, W.M., W.M. Grill, and J.T. Mortimer, *Stimulus waveforms for selective neural stimulation*. Engineering in Medicine and Biology Magazine, IEEE, 1995, **14**(4): 375–385.
107. Accornero, N., et al., *Selective activation of peripheral-nerve fiber groups of different diameter by triangular shaped stimulus pulses*. Journal of Physiology-London, 1977, **273**(3): 539–560.
108. Havel, W.J., et al., *Comparison of rectangular and damped sinusoidal dB/dt waveforms in magnetic stimulation*. Magnetics, IEEE Transactions on, 1997, **33**(5): 4269–4271.
109. Franco, S., *Design with operational amplifiers and analog integrated circuits*. 3rd ed. McGraw-Hill series in electrical and computer engineering. 2002, New York: McGraw-Hill, xiv, 658p.
110. Steele, J. and T. Green, *Tame those versatile current source circuits*. Elec. Des, 1992: 61–72.
111. Smith, S., A.S. Sedra, and K.C. Smith, *Microelectronic circuits,* 4th ed. 1998, New York: Oxford University Press.
112. Microtechnology, A., *Application note 19*, 2004 online at: http://apex.cirrus.com/en/products/apex/documents.html.
113. Microtechnology, A., *Loop stability with reactive loads*, in *Application Note 38*, 2007 online at: http://apex.cirrus.com/en/products/apex/documents.html.
114. Tian, M., et al., *Striving for small-signal stability*. Circuits and Devices Magazine, IEEE, 2001, **17**(1): 31–41.
115. Engelhardt, M., *Simulationsprogramm LT_SPICE (SwitcherCAD III)*.
116. Gray, P.R., *Analysis and design of analog integrated circuits*. 4th ed. 2001, New York: Wiley, xviii, 875p.
117. Williams, J., *High speed amplifier techniques, Linear Technology Corporation*. Application Note 47, 1991.
118. Williams, J., *Power gain stages for monolithic amplifiers, Linear Technology Corporation*. Application Note 18, March 1986.
119. Steele, J., *Protect those expensive power Op amps*. Electronic Design, 1991.
120. Stenzel, R.L., *A new probe for measuring small electric fields in plasmas*. Review of Scientific Instruments, 1991, **62**: 130.
121. Glover, P.M. and R. Bowtell, *Measurement of electric fields due to time-varying magnetic field gradients using dipole probes*. Physics in Medicine and Biology, 2007, **52**(17): 5119–5130.
122. Soonchil, L.E.E., L.E.E. Yongkwan, and Y.U. Insuk, *Electric field in solenoids*. Japanese Journal of Applied Physics, 2005, **44**(7A): 5244–5248.
123. Kandel, E.R., J.H. Schwartz, and T.M. Jessell, *Principles of neural science*. 4th ed. 2000, New York: McGraw-Hill, Health Professions Division, xli, 1414p.
124. Willms, A.R., *Neurofit: software for fitting Hodgkin-Huxley models to voltage-clamp data*. Journal of Neuroscience Methods, 2002. **121**: 139–150.
125. Horch, K.W. and G.S. Dhillon, *Neuroprosthetics theory and practice*. Series on bioengineering and biomedical engineering. 2004, River Edge, NJ: World Scientific, xxv, 1261p.
126. Lertmanorat, Z. and D.M. Durand, *A novel electrode array for diameter-dependent control of axonal excitability: a Simulation study*. Biomedical Engineering, IEEE Transactions on 2004, **51**(7): 1242–50.
127. Glantz, R.M. and T. Viancour, *Integrative properties of crayfish medial giant neuron: steady-state model*. J Neurophysiol, 1983, **50**(5): 1122–1142.

128. Watanabe, A. and H. Grundfest, *Impulse propagation at the septal and commissural junctions of crayfish lateral giant axons*. The Journal of General Physiology, 1961, **45**(2): 267–308.
129. Mellon, D. and C. Kaars, *Role of regional cellular geometry in conduction of excitation along a sensory neuron*. Journal of Neurophysiology, 1974, **37**(6): 1228–1238.
130. Haynes, L.W. and G.A. Kerkut, *Response time constants in snail neurones*. Cellular and Molecular Life Sciences (CMLS), 1977, **33**(11): 1482–1483.
131. Ratte, S. and R. Chase, *Synapse distribution of olfactory interneurons in the procerebrum of the snail Helix aspersa*. The Journal of Comparative Neurology, 2000, **417**(3): 366–384.
132. Gillary, H.L., *Electrical responses from the eye ofHelix to photic stimulation and simultaneous electrical stimulation of the optic nerve*. Vision Research, 1970, **10**(10): 977–991.
133. Antkowiak, T. and R. Chase, *Sensory innervation of the ovotestis in the snail Helix aspersa*. Journal of Experimental Biology, 2003, **206**(22): 3913–3921.
134. Clarac, F. and E. Pearlstein, *Invertebrate preparations and their contribution to neurobiology in the second half of the 20th century*. Brain Research Reviews, 2007, **54**(1): 113–161.
135. William, R.K., *Opportunities afforded by the study of unmyelinated nerves in skin and other organs*. Muscle and Nerve, 2004, **29**(6): 756–767.
136. Kerkut, G.A., et al., *Mapping of nerve cells in the suboesophageal ganglia of Helix aspersa*. Comparative Biochemistry and Physiology A, 1975, **50**(1A): 1–25.
137. Prescott, S. and R. Chase, *Two types of plasticity in the tentacle withdrawal reflex of Helix aspersa are dissociated by tissue location and response measure*. Journal of Comparative Physiology A: Sensory, Neural, and Behavioral Physiology, 1996, **179**(3): 407–414.
138. Wyttenbach, R.A., et al., *Crawdad a CD-ROM lab manual for neurophysiology*. 1999, Sinauer Associates.
139. Olivo, R.F., *An online lab manual for neurophysiology*. Journal of Undergraduate Neuroscience Education, 2003, **2**: A16–A22.
140. Cattaert, D. and D. Le Ray, *Adaptive motor control in crayfish*. Progress in Neurobiology, 2001, **63**(2): 199–240.
141. Jacklet, J.W., *Neuronal and cellular oscillators*. Cellular clocks. 1989, New York: Marcel Dekker, xiii, 553p.
142. Kettenmann, H. and R. Grantyn, *Practical electrophysiological methods: a guide for in vitro studies in vertebrate neurobiology*. 1992. New York: Wiley-Liss, xviii, 449p.
143. Stamford, J.A., *Monitoring neuronal activity: a practical approach*. Practical approach series. 1992. Oxford; New York: IRL Press at Oxford University Press, xxii, 294p.
144. Purves, R.D., *Microelectrode methods for intracellular recording and ionophoresis*. Biological techniques series. 1981. London; New York: Academic Press, x, 146p.
145. Dempster, J. and J. Dempster, *The laboratory computer : a practical guide for physiologists and neuroscientists*. Biological techniques series. 2001. San Diego: Academic Press, xii, 354.
146. Land, B.R., R.A. Wyttenbach, and B.R. Johnson, *Tools for physiology labs: an inexpensive high-performance amplifier and electrode for extracellular recording*. Journal of Neuroscience Methods, 2001, **106**(1): 47–55.
147. Guclu, B., *Low-cost computer-controlled current stimulator for the student laboratory*. Advances in Physiology Education, 2007, **31**(2): 223–231.
148. Wagenaar, D.A. and S.M. Potter, *A versatile all-channel stimulator for electrode arrays, with real-time control*. Journal of Neural Engineering, 2004, **1**(1): 39–45.
149. Land, B.R., et al., *Tools for physiology labs: inexpensive equipment for physiological stimulation*. Journal of Undergraduate Neuroscience Education, 2004, **3**: A30–A35.
150. Eagar, D., *Application Note 87*. Linear Technology.

151. Lott, G., *Hybridizing cellular and behavioral neurobiology with modern engineering tools: microelectronics, microfabricated devices, and software solutions for physiology*. 2007, New York: Cornell University.
152. Lidierth, M., *SigTool: a matlab-based environment for sharing laboratory-developed software to analyze biological signals*. Journal of Neuroscience Methods, 2009, **178**: 188–196.
153. Quiroga, R.Q., Z. Nadasdy, and Y. Ben-Shaul, *Unsupervised spike detection and sorting with wavelets and superparamagnetic clustering*. 2004. Cambridge, MA: MIT Press, pp. 1661–1687.
154. Fitzgerald, J., *Recording with microchannel electrodes in a noisy environment*. 2008.
155. Basham, E., W. Liu, and Y. Zhi, *A System for quantitative analysis of magnetic neural stimulation*. 2008, in review.
156. Hsu, K.H. and D.M. Durand, *A 3-D differential coil design for localized magnetic stimulation*. Biomedical Engineering, IEEE Transactions on, 2001, **48**(10).
157. Maccabee, P.J., et al., *Magnetic coil stimulation of straight and bent amphibian and mammalian peripheral nerve in vitro: locus of excitation*. Journal of Physiology (London), 1993, **460**: 201–219.
158. Mulloney, B., N. Tschuluun, and W. M. Hall, *Architectonics of crayfish ganglia*. Microscopy Research and Technique, 2003, **60**: 253–265.
159. Prescott, S. A., N. Gill, and R. Chase, *Neural Circuit Mediating Tentacle Withdrawal in Helix aspersa, With Specific Reference to the Competence of the Motor Neuron C3*. Journal of Neurophysiol, 1997, **78**: 2951–2965, December 1, 1997.

Regulatory Approval of Implantable Medical Devices in the United States and Europe

Mike Colvin

Abstract There has been explosive growth in the medical device arena in the last decade with over 9,000 major medical device submissions received by the FDA in 2007 alone. This has affected the timing, approval speed, costs, and strategies used for regulatory approval. Important differences have evolved in the clinical and regulatory environment between the United States and Europe regarding the costs, timeliness, clinical trials, and commercial availability of medical devices. This chapter gives a brief overview of the similarities and differences in the process of obtaining regulatory approval in the United States and Europe.

1 Introduction

Important differences have evolved in the clinical-regulatory environment between the United States and Europe. These differences have impacted the locations of clinical testing and consequently the timing of commercialization of medical devices in these countries. US regulatory requirements are usually more extensive and require additional time and resources compared with those of other countries [1]. This chapter summarizes the major similarities and differences between the regulatory, clinical processes, and regulatory approval that occur in the United States and Europe.

2 Regulatory Affairs Approval Process in the United States

Medical devices are regulated in the United States by the Center for Devices and Radiological Health (CDRH) of the FDA. The charter of the FDA/CDRH is to facilitate and protect the public health by making safe and effective medical

M. Colvin (✉)
Boston Scientific Neuromodulation Corporation, Valencia, CA 91355, USA
e-mail: michael.colvin@bsci.com

D.D. Zhou, E. Greenbaum (eds.), *Implantable Neural Prostheses 1*,
Biological and Medical Physics, Biomedical Engineering,
DOI 10.1007/978-0-387-77261-5_11,

devices available in a timely fashion. The metric for measuring safety and efficacy is determined in part by the risk associated with the device in question. Devices are classified according to their perceived risk using a three-tiered system (i.e., class I, II, or III).

2.1 Classification Panels

Most medical devices can be classified by finding the matching description of the device in Title 21 of the Code of Federal Regulations (CFR), parts 862–892. FDA has classified and described over 1,700 distinct types of devices and organized them in the CFR into 16 medical specialty "panels". These panels are found in Parts 862 through 892 in the CFR. For each of the devices classified by the FDA the CFR gives a general description including the intended use, the class to which the device belongs (i.e., class I, II, or III), and information about marketing requirements. Devices should meet the definition in a classification regulation contained in 21 CFR 862–892. The classifications are as follows:

868 Anesthesiology
870 Cardiovascular
862 Clinical Chemistry and Clinical Toxicology
872 Dental
874 Ear, Nose, and Throat
876 Gastroenterology and Urology
878 General and Plastic Surgery
880 General Hospital and Personal Use
864 Hematology and Pathology
866 Immunology and Microbiology
882 Neurology
884 Obstetrical and Gynecological
886 Ophthalmic
888 Orthopedic
890 Physical Medicine
892 Radiology

2.1.1 Class I Devices

These devices (lowest risk) are subject to general controls, which are published standards pertaining to labeling, manufacturing, post-market surveillance, and reporting. Devices are placed into class I when there is reasonable assurance that general controls alone are adequate to assure safety and effectiveness. Devices in this category include tongue depressors, bedpans, elastic bandages, examination gloves, hand-held surgical instruments, and other similar types of common equipment.

The general controls that typically apply to class I devices include prohibitions against adulteration and misbranding, requirements for establishing registration and device listing, adverse event reporting, and good manufacturing practices. Furthermore, FDA has jurisdiction including product seizure, injunction, criminal prosecution, civil penalties, and recall authority. Formal FDA review is not required for most class I devices before their market introduction [2].

2.1.2 Class II Devices

These are higher risk devices for which general controls alone have not been found to suffice in order to provide reasonable assurance of safety and efficacy, but for which there is adequate information available to establish special controls. Special controls may include performance standards, design controls, and post-market surveillance programs. Devices in this class are typically non-invasive and include X-ray machines, powered wheelchairs, infusion pumps, surgical drapes, surgical needles and suture material, and acupuncture needles. In addition to special controls, most class II devices require FDA clearance of a premarket notification application [(510(k)] before the device may be marketed. In the 510(k) application, the medical device manufacturer must provide data to demonstrate that the new device is "substantially equivalent" to an existing approved marketed device.

A device is substantially equivalent if, in comparison to a predicate (1) it has the same intended use as the predicate, (2) it has the same technological characteristics as the predicate, or (3) it has the same intended use as the predicate. If the device has different technological characteristics it is also considered substantially equivalent if the information submitted to FDA: (1) does not raise new questions of safety and effectiveness and (2) demonstrates that the device is at least as safe and effective as the legally marketed device.

A claim of substantial equivalence does not mean the new and predicate devices must be identical. Substantial equivalence is established with respect to intended use, design, energy used or delivered, materials, chemical composition, manufacturing process, performance, safety, effectiveness, labeling, biocompatibility, standards, and other characteristics, as applicable. A device may not be marketed in the United States until the submitter receives a letter declaring the device substantially equivalent.

Although substantial equivalence can usually be demonstrated on the basis of bench and animal testing alone, approximately 10% of 510(k) applications have included clinical data [3]. If clinical data are to be obtained, approval may only require an Institutional Review Board (IRB). No investigational device exemption (IDE) may be required. An investigational device exemption (IDE) allows the investigational device to be used in a clinical study in order to collect safety and effectiveness data required to support a premarket approval (PMA) application or a premarket notification [510(k)] submission to FDA. Clinical studies are most often conducted to support a PMA. Only a small percentage of

510(k)s require clinical data to support the application. Investigational use also includes clinical evaluation of certain modifications or new intended uses of legally marketed devices. All clinical evaluations of investigational devices, unless exempt, must have an approved IDE before the study is initiated.

Clinical evaluation of devices that have not been cleared for marketing requires the following:

- an IDE approved by an Institutional Review Board (IRB). Refer to clinical trials section below. If the study involves a significant risk device, the IDE must also be approved by FDA;
- informed consent from all patients;
- labeling for investigational use only;
- monitoring of the study and;
- required records and reports.

A device that has not been cleared or approved for marketing cannot be legally provided to a user for its intended human use unless several ordinarily applicable rules are waived. An approved IDE provides for exemption from these rules in order for a sponsor to distribute the device and conduct human clinical studies.

2.1.3 Class III Devices

These include devices (highest risk) such as heart valves, coronary stents, silicone gel-filled breast implants, implanted cerebral stimulators, implantable pacemaker pulse generators, and endosseous (intra-bone) implants. These devices are either life-sustaining/supporting, of substantial importance in preventing impairment of human health, or present a high risk of illness or injury. Consequently, general and special controls alone are not adequate to provide reasonable assurance of safety and efficacy. Most class III devices require FDA approval of a premarket approval application (PMA) before they can be legally marketed. Approval of the PMA generally requires clinical data demonstrating a reasonable assurance that the device is safe and efficacious, i.e., the benefits outweigh the risks for the intended target patient population [4].

The first and debatably most important step in this process is the pre-IDE meeting, in which the organization meets with FDA/CDRH to present data about the device, its clinical development program, and its intended patient population/use after approval. The number of patients/samples to be enrolled should be determined ahead of time on sound statistical analysis. The pre-IDE meeting is free to the sponsor; it provides greater assurance of a well-prepared submission, shortened review times, and has the potential to save research dollars. The FDA/CDRH staff will review the existing bench and animal studies that have been conducted. They will also review any relevant clinical data on similar use devices or clinical data obtained abroad. They then will give informal non-binding suggestions regarding any further animal or bench data that should be performed. They will also comment and make suggestions on the

proposed future clinical study design. With this input, the sponsor will prepare and then submit an IDE application to FDA/CDRH for formal review.

The pre-IDE meeting is quite controversial in many companies. On one side of the argument the sponsor may not want to disclose confidential information so early on with the FDA. There may also be concern that the FDA will suggest additional bench and/or animal studies that they had not been planned. Although these suggestions are informal and non-binding, they would nonetheless be on the table. If they are not performed this could lead to future issues between the company and the CDRH, unexpected delays, and increased costs. Also the FDA might feel that the company has something to conceal if they keep their data too "close to their vest."

The other side of the argument is that it is best to be upfront with the FDA as early as possible. The idea is to have open discussions with the FDA and negotiate any future testing to be performed. With this approach, both parties have had plenty of time to discuss and come to agreement on outstanding issues prior to IDE submittal. Thus, the potential for surprises that could impact the development schedule has been greatly minimized. The author strongly supports the latter approach; it has saved much time to market, kept testing costs to a minimum, minimized delays, and increased trust between the two parties.

2.2 Clinical Phase

Clinical development of a new class III device is typically divided into two phases: a pilot and a pivotal trial.

2.2.1 Pilot Trial

The first clinical assessment of a device after bench, in vivo biocompatibility testing, and animal testing is a pilot trial. The purpose of the pilot trial is to establish the basic safety of the device in human subjects and to demonstrate initial indications of effectiveness. It also serves to assist in the design of the subsequent pivotal trial phase. The pilot phase testing is normally limited to a smaller subject population (typically less than 100 subjects at several different centers). The pilot trial will typically last from 3 months to a year depending on the complexity of the device.

2.2.2 Pivotal Trial

The purpose of the pivotal trial is to generate data to establish that the device is safe and efficacious in the patient population for which the device is indicated. During the pivotal trial, the dialogue increases between the FDA/CDRH and the company. The specifics of the pivotal trial are well defined; this includes choosing the patient population, the type of control group to be used, and how

the control group will be measured against the device group under evaluation. For first-use devices, e.g., cerebral drug delivery, where there is minimal data regarding short- or long-term safety and efficacy, the FDA/CDRH usually will require prospective randomized controlled studies.

Most devices under evaluation with the FDA/CDRH are similar to pre-existing approved devices, e.g., an angioplasty balloon/stent system or a spinal cord stimulator. If the FDA/CDRH has substantial data on the device class, comparisons may be made with historical data or objective performance criteria. When little data on the existing device class are available, the FDA typically requires a randomized rather than a single-arm study. The new device will be compared against simultaneous controls treated with the best known current medical practice. That comparison may be designed to show that the new treatment/device is superior to the best known current medical practice. For new indications, the new device must have equivalent or better outcomes when compared with a previously approved device utilized for an older application.

The specifics of the study design may have a profound impact on the time and cost of getting a new device to market. The primary endpoint of a pivotal trial for a new-class, class III device is usually a clinical endpoint. Depending on the endpoints negotiated, the pivotal trial typically requires enrollment of large patient populations at multiple centers with appropriate follow-up over a period of 1–2 years. The trial must be conducted according to good clinical practices standards with approval of the IRB at each participating center.

2.3 Clinical Trials

Once the FDA/CDRH has approved the IDE, the sponsor must formally begin the subject recruitment process to ensure study enrollment in a timely manner. Each site has its own regulations regarding participation in clinical studies, which typically can be divided into three sections:

(1) Human research
(2) Contract
(3) Conflict of interest.

Every medical device trial clinical site is federally mandated to have an Institutional Review Board (IRB) responsible to ensure the protection of the rights, safety, and welfare of research subjects. The FDA has regulatory oversight approval of the IRB protocols involving medical devices. The Office of Protection from Research Risks (OPRR) is responsible for the regulatory oversight approval regarding all human research and is in direct communication with the FDA/CDRH. Products not regulated by the FDA that involve human subjects fall under the regulations and oversight of the OPRR. Both the FDA and the OPRR are in the Department of Health and Human Services. Each IRB

must meet the standards for the requirements, leadership, and processes set forth by the Department of Health and Human Services. IRBs are subject to periodic audits by the FDA to ensure that records, processes, and procedures are in compliance with regulations [5, 6].

Working with the sponsor, the principal investigator prepares an application to the IRB at his/her institution that includes the consent form describing in lay language the device, the inclusion and exclusion criteria for the trial, the proposed clinical study, and a draft consent form describing the risks and benefits of participation in the study. The IRB then formally reviews the application. The IRB typically requests changes, usually to the informed consent documents. The IRB process from start to finish usually takes around 3 months, although this can take considerably longer.

The company must also negotiate agreements with each clinical site addressing the many issues associated with the clinical trial. This includes the study costs/reimbursement, e.g., cost per patient enrolled and overhead. These agreements typically include an indemnification clause and the assignment of intellectual property ownership rights of new discoveries made over the course of the study.

The resources and efforts required at each clinical site to comply with the high-quality research necessary during the IDE study are formidable. The clinical site must dedicate additional resources, including physicians and nursing staff to ensure high-quality clinical research. The role of the research director is critical to the success of all phases of the trial, including general study management, IRB process, patient recruitment, and accurate completion of the case report forms. The sponsor is responsible for ensuring that each clinical site has the necessary resources in place to fulfill the requirements of the study protocol. The clinical research staff is not part of the hospital's salaried nursing staff. The per-patient costs include any charges the patient incurs to complete the study, including any diagnostic procedures and studies, clinic visits and travel, and research nurses' salaries. It frequently takes approximately 3–6 months to complete the patient recruitment for each clinical site.

Pivotal studies required for a PMA application are typically large multicenter randomized trials and often represent the largest commercial risk and expense in the development process of a new device.

2.4 Types of Domestic Applications

2.4.1 Premarket Notifications or 510(k)s

These are applications used when the intent is to market a type of device that may be substantially equivalent to a legally marketed device that was not subject to premarket approval.

2.4.2 Expedited PMAs

These are used when FDA has granted priority status to an application to market a medical device because it is intended to treat or diagnose a life-threatening or irreversibly debilitating disease or condition and to address an unmet medical need.

2.4.3 Premarket Reports

They are applications required for high-risk devices originally approved for a single use (i.e., use on a single patient during a single procedure) that a manufacturer has reprocessed for additional use.

2.4.4 Panel-Track Supplements

They are applications used to supplement approved PMAs or premarket reports. These supplements typically request approval of a significant change in the design or performance of a device, or for a new purpose for using a device.

2.4.5 180-Day PMA Supplements

These are also used to supplement approved PMAs or premarket reports. These supplements typically request approval of a significant change in aspects of a device, such as its design, specifications, or labeling, when demonstration of reasonable assurance of safety and effectiveness either does not require new clinical data or requires only limited clinical data.

2.4.6 Real-Time PMA Supplements

They are a supplement to an approved premarket application or premarket report that requests a minor change to the device, such as a minor change to the design of the device, software, sterilization, or labeling, and for which the applicant [PMA holder] has requested and the agency has granted a meeting or similar forum to jointly review and determine the status of the supplement.

2.4.7 Original Premarket Approval (PMA)

These applications are generally required when the device is new or when the risks associated with the device are considerable (as would be the case if the device is to be implanted in the body for life-supporting purposes).

2.5 The 510(k) Review Process

Under the 510(k) review process, FDA reviews applications to market a device that may be substantially equivalent to a legally marketed device that was not subject to premarket approval.

The information required in a 510(k) submission is defined 21 CFR 807.87. A 510(k) submission includes (1) device trade or proprietary name, common or usual name or classification, class of the device (class I, II, or III); (2) submitter's name and address, contact person, telephone number and fax number, representative/consultant if applicable; (3) name and address of manufacturing/packaging/sterilization facilities, registration number of each manufacturing facility; (4) action taken to comply with the requirements of the special controls; (5) proposed labels, labeling, and advertisements to describe the device, its intended use, and the directions for its use; and (6) a 510(k) summary or a 510(k) statement.

For Class III medical device, the following are included: (1) a Class III certification and a class III summary; (2) photographs of the device, engineering drawings of the device; (3) identification of the marketed device(s) to which equivalence is claimed including labeling and description of the medical device; (4) statement of similarities and/or differences with marketed device(s); (5) data to show consequences and effects of a modified device, performance data (bench, animal, clinical).

The following are also included: (1) sterilization information (as applicable); (2) software development, verification, and validation information; (3) hardware design and development information; (4) information requested in specific guidance documents (as applicable); (5) kit certification statement (for a 510(k) submission with kit components only); and (6) truthful and accurate statement.

Depending on the complexity of the new or modified medical device, the FDA Review of a 510(k) submission takes between 20 and 90+ days. The more complex the changes or comparison required to support the safety and effectiveness of the new or modified medical device, the longer the FDA review process.

First the FDA staff conducts a scientific review of the application (refer to Fig. 1). When a 510(k) application lacks information necessary for FDA to reach a decision, the agency may issue an "additional information" letter that indicates that the information is insufficient. The manufacturer may then submit additional information. Once FDA has obtained sufficient information from the manufacturer, FDA may make one of three decisions: FDA may decide that (1) the device is substantially equivalent and therefore may be marketed, (2) the device is not substantially equivalent and may not be marketed, or (3) a 510(k) application was not required because the product is not regulated as a device or the device is exempt from the requirements for premarket notification.

2.6 The PMA Process

Under the PMA review process, FDA reviews applications for new devices or those for which risks associated with the device are considerable. Applications reviewed under this process include original PMAs, expedited PMAs, premarket reports, panel-track supplements, and 180-day PMA supplements.

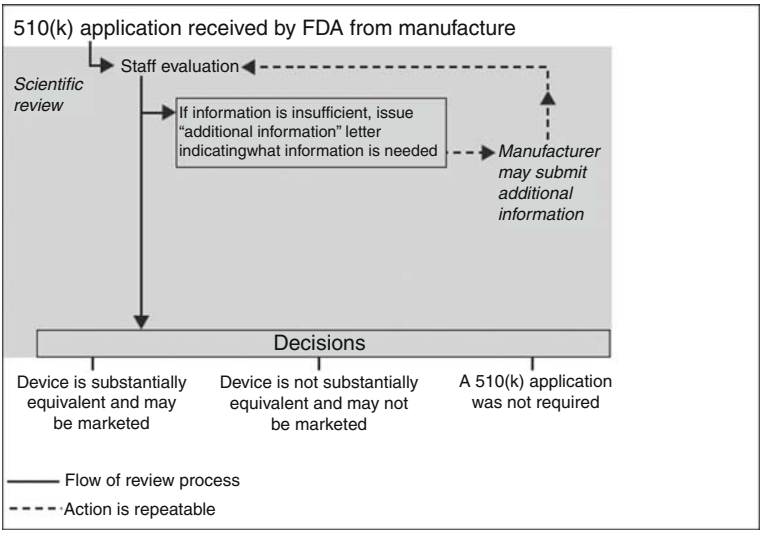

Fig. 1 510(k) Review process (United States accountability Office-GAO-05-1042
Note: This flow chart presents the typical review process to determine whether a 510(k) application is required and, if so, whether a device is substantially equivalent to a legally marketed device that was not subject to premarket approval
Source: GAO.

The PMA application content includes (1) full reports of all information, published or known to or which should reasonably be known to the applicant, concerning investigations which have been made to show whether or not such device is safe and effective; (2) a full statement of the components, ingredients, and properties and of the principle or principles of operation of such device; (3) a full description of the methods used in, and the facilities and controls used for, the manufacture, processing, and, when relevant, packing and installation of such device; and (4) an identifying reference to any performance standard under Section 514 which would be applicable to any aspect of such device if it were a class II device, and either adequate information to show that such aspect of such device fully meets such performance standard or adequate information to justify any deviation from such standards.

The PMA application content also includes (1) such samples of such device and of components thereof as the Secretary may reasonably require, except that where the submission of such samples is impracticable or unduly burdensome, the requirement of this subparagraph may be met by the submission of complete information concerning the location of one or more such devices readily available for examination and testing; (2) specimens of the labeling proposed to be used for such device; and (3) such other information relevant to the subject matter of the application as the secretary, with the concurrence of the appropriate panel under Section 513, may require.

After an initial screening of an application and determination that the review should proceed (this initial screening is called a filing review), FDA multidisciplinary staff conduct a scientific review of the application. The scientific review can include reviews of results from clinical investigations of the device that involve human subjects. FDA also reviews nonclinical studies of the device, and studies that may include microbiological, toxicological, and engineering tests (see Fig. 2). If FDA determines that it needs significant additional information to complete its scientific review, FDA issues a "major deficiency letter" to the manufacturer identifying the information that is required. The manufacturer can respond to FDA's request by submitting an amendment to the

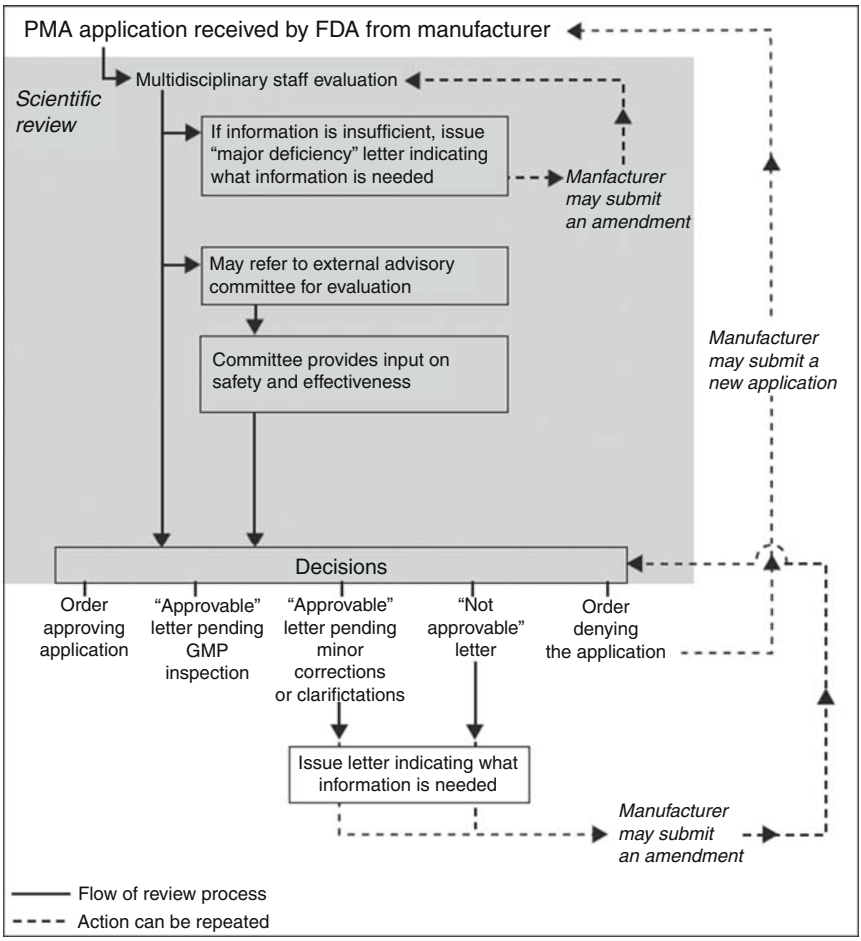

Fig. 2 The PMA review process (United States accountability office-GAO-05-1042
Note: This flow chart presents the typical review process for application for which FDA has conducted an initial screening and determined that the review should proceed
Source: GAO.

original application. FDA then proceeds with its review of the amended application. FDA can issue additional major deficiency letters and review additional amendments until FDA determines that it has sufficient information to make a decision.

As part of its review, FDA may refer applications to an external advisory committee for evaluation. FDA takes this step when a device is the first of its kind or when the agency believes it would be useful to have independent expertise and technical assistance to properly evaluate the safety and effectiveness of the device. For example, approximately 22% of PMAs and expedited PMAs were referred to external advisory committees in fiscal years 2002 and 2003. The percentage in fiscal year 2004 was closer to 40%. FDA does not refer 180-Day PMA Supplements to external advisory committees. For applications referred to an advisory committee, the committee provides input to FDA on the safety and effectiveness of the devices.

The FDA has a statutory 180-day review cycle for PMA applications. Often PMA applications require medical advisory board review prior to the FDA granting approval to market the medical device. A facility inspection verifying the manufacturing systems present to manufacture the medical device is usually performed prior to FDA PMA approval. FDA approval of a PMA often requires significantly more than 180 days.

2.7 Humanitarian Device Exemptions (HDEs)

An HDE application is essentially the same as a PMA in both form and content but is exempt from the effectiveness requirement of a PMA. Even though the HDE is not required to contain the results of scientifically valid clinical investigations demonstrating that the device is effective for its intended purpose, the application must contain sufficient information for FDA to determine, as required by statute, that the device does not pose an unreasonable or significant risk of illness or injury to patients and that the probable benefit to health outweighs the risk of injury or illness from its use. An HDE application must also contain information that will allow FDA to make the other determinations required by the act. In order to submit an HDE application for a medical device, the medical device must first meet the definition of a humanitarian use device (HUD) under 21 CFR 814.3(n). A HUD is a "medical device intended to benefit patients in the treatment or diagnosis of a disease or condition that affects or is manifested in fewer than 4,000 individuals in the United States per year." An approved HDE authorizes marketing of the humanitarian use device (HUD).

FDA Performance/Timeliness (Tables from Office of Device Evaluation Annual Report)

The number of major FDA submissions received from 1997 to 2007 is shown in Table 1. As shown in Table 1, during FY 06, ODE received 9,415 major submissions, up from 8,690 in FY 05. Of the 25 original PMAs and 21 panel-track supplements received in FY 06, 2 were granted expedited status.

Table 1 Major FDA submissions received: 1997 to 2007 (United States accountability office-GAO-05-1042)

TYPE OF SUBMISSION	1997 ODE& OIVD	1998 ODE& OIVD	1999 ODE& OIVD	2000 ODE& OIVD	2001 ODE& OIVD	2002 ODE& OIVD	2003 ODE& OIVD	2004 ODE Only	2005 ODE Only	2006 ODE Only	2007 ODE Only
Original PMAs PMA	66	48	64	67	71	49	54	37	43	25	31
Supplements	409	517	557	546	641	645	666	565	712	1,113	1,087
Original IDEs	297	322	304	311	283	312	242	222	226	251	211
IDE Supplements	3,776	4,277	4,127	4,388	4,810	4,722	4,415	4,297	4.264	4,485	4,345
510(k)s	5,049	4,623	4,458	4,202	4,248	4,320	4,247	3,107	3,130	3,240	3,192
Original HDE HDE	4	8	12	11	5	5	10	9	4	4	6
Supplements	0	0	4	10	16	16	29	28	24	53	23
513(g)s	29	34	43	59	82	104	156	239	287	244	381
Total	9,630	9,829	9,569	9,594	10,156	10,192	9,819	8,504	8,690	9,415	9,276

ODE: Office of Device Evaluation
OIVD: Office for In Vitro Diagnostics

Table 2 Major submissions completed FY 1997–FY 2007 (United States accountability office-GAO-05-1042)

TYPE OF SUBMISSION	1997 ODE &OIVD	1998 ODE &OIVD	1999 ODE &OIVD	2000 ODE &OIVD	2001 ODE &OIVD	2002 ODE &OIVD	2003 ODE &OVID	2004 ODE Only	2005 ODE Only	2006 ODE Only	2007 ODE Only
Original PMAs	48	40	36	42	53	41	31	29	28	27	27
PMA Supplements	401	421	440	474	442	533	494	424	354	594	578
Original IDEs	272	325	305	320	284	307	246	217	238	234	214
IDE Amendments	220	225	268	251	207	251	217	162	208	178	163
IDE Supplements	3,777	4,209	4,224	4,335	4,802	4,711	4,424	4,336	4,226	4,430	4,324
510(k)s	5,155	5,229	4,593	4,397	4,150	4,376	4,132	3,376	3,184	3,080	3,052
Original HDE	2	4	6	6	4	10	2	6	2	3	2
HDE Supplements	0	0	3	10	11	14	24	22	31	69	47
Total	9,875	10,453	9,876	9,835	9,953	10,243	9,570	8,573	8,272	8,615	8,407

Of the 31 original PMAs and 4 panel-track supplements received in FY 07, 2 were granted expedited status. Similarly, two original and PMA panel-track supplements received expedited status in FY 06. In FY 07, 18 of the 31 (58%) original PMAs were submitted as modular PMAs as compared to 11 (44%) modular PMAs submitted in FY 06.

The major submissions completed from 1997 to 2007 are shown in Table 2. The table summarizes the actions that ODE completed in fiscal years 1997–2007. Note that decisions may be made in one fiscal year for an application that was submitted in a previous fiscal year.

ODE & OIVD in Table 2 are included in 1997 through 2003; 2004 through 2007 include ODE only.

3 European Regulatory Approval Process

Although there are many similarities in the regulatory process in the United States and countries within the European Union, there are important differences that impact the time and cost associated with the introduction of a new medical device. Below, three illustrative examples are outlined: use of Notified Bodies, criteria for approval, and local site (Ethics review board/site negotiation).

3.1 European Union (EU) Regulatory Approval

The EU system relies heavily on Notified Bodies, which are independent commercial organizations to implement regulatory control over medical devices. Notified Bodies have the ability to issue the CE mark, the official regulatory approval marking required for medical devices. Notified Bodies are designated, monitored, and audited by the pertinent member states via the national competent authorities. Many functions performed by the FDA/CDRH within the United States are performed by Notified Bodies, including medical device certification, assessment and verification of quality systems, device type designation, and the review of the design history files for high-risk devices [7, 8].

3.1.1 Competent Authority

Each member state has a national regulatory oversight agency, which is known as the competent authority. The main responsibilities of the competent authority are as follows:

- The maintenance of a register of devices manufacturers and the medical devices that they place on the market.
- Ensure only CE marked devices are on the market.
- The establishment and administration of a vigilance system for incidents attributable to devices including the withdrawal of unsafe devices.

- The examination and approval (if acceptable) of applications for performance evaluation including clinical investigations.
- The designation and monitoring of Notified Bodies.
- Ensuring that the applicable directives and any modifications are ratified into national law.

3.1.2 Notified Bodies

Currently, there are more than 75 active Notified Bodies within Europe. A company is free to choose any Notified Body selected to cover the particular class of device under review. After approval, post-market surveillance functions are the responsibility of the member state via the competent authority. Notified Bodies typically function in a confidential manner, providing little visibility on their criteria required for approval. This flexibility allows for a high degree of variation as well as competition among Notified Bodies. They act independently of each other and it is not uncommon for the criteria required for product approval to vary. Therefore, a company should be encouraged to choose a notified body that is best suited for their particular device.

Notified Bodies are perceived by commerce to be less bureaucratic organizations that can respond more quickly and efficiently than the FDA. However, the flexibility granted to Notified Bodies can be offset by a system that is inherently more fragmented and highly variable. This has resulted in the approval and continued marketing of devices in Europe that failed efficacy trials in the United States.

Criteria for approval of high-risk devices are different in the European Union. To receive approval to market a class III high-risk (and some class II) device in the United States, the manufacturer must demonstrate the device to be reasonably safe and efficacious, which typically requires a prospective, randomized controlled clinical trial. To receive approval to market a device in the European Union, the manufacturer must demonstrate that the device is safe and that it performs in a manner consistent with the manufacturer's intended use. This difference has a profound impact on the size and scope of the clinical studies for regulatory approval.

3.2 European Device Classification

There are four main classes of devices in Europe: classes I, IIa, IIb, and III. Like in the United States class I devices are the lowest risk and class III devices are the highest.

3.2.1 Class I

Class I devices are low risk and manufacturers are often self certifying. Examples are stethoscopes, scalpels, hospital beds, and wheelchairs. The manufacturer has to produce a technical file, including product test results to relevant

standards. In addition, manufacturers of sterile products and devices with a measuring function must apply to a Notified Body for certification of the aspects of manufacture relating to sterility or metrology.

3.2.2 Class IIa

Class IIa are low-medium risk devices. Examples include hearing aids, electrocardiographs, and ultrasonic diagnostic equipment. Clinical safety prior to CE marking is often demonstrated by reference to other similar CE marked devices.

3.2.3 Class IIb

Class IIb are medium-high-risk devices. Examples include surgical lasers, infusion pumps (non-implantable), ventilators, and intensive care monitoring equipment. Clinical safety prior to CE marking may have to be demonstrated by clinical investigation.

3.2.4 Class III

Class III devices are considered to be of highest risk. Examples are balloon catheters and prosthetic heart valves. Such devices may employ new materials or components, have no established history of performance or target a new indication or where a significant change in the original intended use of the product is planned.

Class III devices require that a design dossier be prepared that must be reviewed by the Notified Body prior to CE marking. Clinical safety prior to CE marking is typically demonstrated by clinical investigation. CE marking clinical investigations must meet the minimum acceptable requirements.

4 Conclusion

As this chapter highlights, the demonstration of safety and efficacy for a new medical device is an extensive, arduous, and an expensive developmental path that spans early feasibility work to introduction of a device into the marketplace. By understanding this path and its complexities we can make most efficient use of this overall process, minimize cost, and have a streamlined and timely approval process. This brief review outlines the overall process and highlights some of the main differences in the clinical and regulatory pathways in the United States and Europe.

Considering these differences helps us understand why much early device clinical testing takes place outside of the United States. It also explains why the introduction of new devices into the market place is usually significantly faster in Europe when compared to the United States. This is a result of the intrinsic

differences in the criteria for approval and the process required to obtain approval. In particular, the CE Mark process requires the demonstration of safety only (and not efficacy). It relies a great deal on independent Notified Bodies to regulate the approval and post-approval process. By comparison, in the United States the approval of a high-risk device requires demonstration of both safety and efficacy and is more highly regulated (by a governmental agency CDRH/FDA). Integrated together, these factors account for the 1- to 3-year delays in the introduction of a new device into the clinical market place in the United States as compared with Europe.

Each system has its own strengths and weaknesses that must be evaluated within the framework of the different health systems. Through better understanding of these systems, we can make improvements toward improving speed and efficiency in obtaining both US and European device approval, without compromising the safety and efficacy of the device.

References

1. Chai JY. Medical device regulation in the United States and the European Union: a comparative study. Food and Drug Law Journal, 55: 57–80 (2000).
2. 21 USC §360.
3. 21 USC § 360(c).
4. Medical Device Amendments of 1976, Pub L No 94-295 (1976).
5. Food and Drug Administration Modernization Act of 1997, Pub L No 105–115 (1997).
6. 21 CFR 56 (2003).
7. US Food and Drug Administration web site. Available at: http://www.fda.gov.
8. Council Directive 98/97/European Economic Community. Annex I.A. 3–5; O.J. (L331) 15. 6. Page 8 GAO-05-1042 FDA's Review of Device Applications, (1998).

Index